Mirtat Bouroushian

**Editor** F. Scholz

# Electrochemistry of Metal Chalcogenides

Springer

# Electrochemistry of Metal Chalcogenides

# Monographs in Electrochemistry

Surprisingly, a large number of important topics in electrochemistry is not covered by up-to-date monographs and series on the market, some topics are even not covered at all. The series *Monographs in Electrochemistry* fills this gap by publishing indepth monographs written by experienced and distinguished electrochemists, covering both theory and applications. The focus is set on existing as well as emerging methods for researchers, engineers, and practitioners active in the many and often interdisciplinary fields, where electrochemistry plays a key role. These fields will range – among others – from analytical and environmental sciences to sensors, materials sciences and biochemical research.

Information about published and forthcoming volumes is available at
http://www.springer.com/series/7386

**Series Editor**: Fritz Scholz, University of Greifswald, Germany

Mirtat Bouroushian

# Electrochemistry of Metal Chalcogenides

## Springer

Dr. Mirtat Bouroushian
National Technical University of Athens
Dept. of Chemical Sciences
School of Chemical Engineering
Heroon Polytechniou Str. 9
Zographos Campus
157 73 Athens
Greece
mirtatb@central.ntua.gr

*Cover design*: Integra Software Services Pvt. Ltd., Pondicherry

Printed on acid-free paper

# Preface

This monograph is devoted to the electrochemistry of metal chalcogenides, a group of chemical compounds which possess very interesting properties for applications in various areas, e.g., electronics and optics, ion-sensitive electrodes, solar energy harvesting, fuel cells, catalysis, and passivation. The role which electrochemistry plays in studies of metal chalcogenides is twofold: on one side it is a synthesis tool and on the other side it can be utilized for the characterization and analysis of these compounds. It is thus a basic requirement that the fundamentals of electrochemical thermodynamics and kinetics of these systems are thoroughly studied and documented. The author Mirtat Bouroushian from the National Technical University of Athens must be given full credit for presenting the first book completely devoted to the electrochemistry of metal chalcogenides, a research topic to which he has made numerous own contributions. This monograph gives a well-balanced description of the properties of chalcogens and their major chemical compounds together with the state-of-the-art electrochemical synthesis of various metal chalcogenide phases and their characterization, as well as an account of the wide range of applications. Everybody who works with metal chalcogenides, and of course especially anybody dealing with the electrochemistry of these compounds, will find this monograph a very rich source of carefully and critically compiled information. I am sure that industrial electrochemists and researchers in institutes and universities as well as graduate students of material science, physics, electronics, and chemistry will highly appreciate to have this monograph at hands during their daily work.

January 2010
Fritz Scholz
Editor of the series *Monographs in Electrochemistry*

# Contents

# Introduction

Metal chalcogenide (MCh) materials range from common oxides and sulfides, selenides, and tellurides, to complex compound or solid solution systems containing different metal or chalcogen elements in various oxidation states and varying proportions. Owing to their wide spectrum of properties, these materials relate to a large variety of existing and potential applications in electronics, optics, magnetics, solar energy conversion, catalysis, passivation, ion sensing, batteries, and fuel cells.

The present monograph aims for a systematic presentation of metal chalcogenides and the electrochemical material science relevant to this family of compounds. More than an introduction and less than a handbook, it is an attempt to give a comprehensive coverage of achievements, complications, and prospects in this area.

This book regards in particular the systems relevant to the sulfur sub-group elements, i.e., sulfur, selenium, and tellurium. The reasons for this approach are fairly obvious. The metal compounds of the heavier congeners of oxygen, especially those of selenium and tellurium, are notably less known and not systematically studied compared to the corresponding oxides (and also to other inorganic compounds like halogenides). Thus, the need arises to fill this gap, which, aside from the normal pace, is stimulated further by the unprecedented advancements that have been encountered in the chemistry and technology of these materials in the last decades. Adoption of this approach appears to be reasonable also in view of the immense breadth of the surveyed field and its multidisciplinary character: the common binary MCh compounds alone, excluding the oxides as well as the compounds of actinides and lanthanides, are more than a hundred, and it is rather difficult to contemplate the number of multielement combinations.

The role of electrochemistry in synthesis, development, and characterization of the MCh materials and related devices is vital and of increasing importance, although it remains uncharted as to its content and borders. Electrochemistry as a preparation tool offers the advantages of soft chemistry to access bulk, thin film, and epitaxial growth of a wide range of alloys and compounds, while as a characterization tool provides exceptional assistance in specifying the physicochemical properties of materials. Moreover, quite important applications and modern devices base their operation on electrochemical principles. Thereupon, our scope in the first place was to organize existing facts on the electrochemistry of metal chalcogenides

regarding their synthesis, properties, and applications. In parallel, we hope to provide an outlook of the field that opens up for the electrochemist or material scientist to explore, considering that not only have a lot of technologically interesting MChs not yet been the object of electrochemical investigation, but also numerous systems are completely unknown from this point of view.

This book is designed as follows: The fundamentals of chalcogen chemistry and their compounds are presented in the first chapter where also a brief, though systematic, description is attempted of the metal chalcogenide solids on the basis of the Periodic Table, in terms of their structure and key properties. A general discussion on the electrochemistry of the chalcogens is the subject of the second chapter, where the basic equilibrium data are also provided for the aqueous chalcogen systems. Available facts and inferences regarding conventional films and novel structures of MChs prepared via the electrochemical route are illustrated in Chaps. 3 and 4, following an introduction to the principles underlying the electrochemical formation of inorganic compounds and alloys, along with an outline of relevant preparation procedures. Insights into the fundamentals of photoelectrochemistry and research results sorted either from a material-oriented point of view or by the aspect of important light-induced processes constitute the subject matter of Chap. 5. Finally, topics on catalysis, mainly related to fuel cells, intercalation electrodes, batteries, and ion-sensing applications are introduced and discussed in Chap. 6.

For realizing this monograph, I am deeply indebted to the Editor, Professor Fritz Scholz who first suggested the idea and vigorously sustained the project in every way with great enthusiasm. I also thank Dr. T. Kosanovic (NTUA) and greatly acknowledge her contribution to data collection and figure editing. Finally, special thanks are due to D. Vasilakopoulos (NTUA) for his continual support.

Mirtat Bouroushian

# Chapter 1
# Chalcogens and Metal Chalcogenides

## 1.1 The Chalcogens

It is common that the three heaviest elements of the sulfur sub-group, namely selenium, tellurium, and polonium, be collectively referred to as the "chalcogens," and the term chalcogen be addressed only for these elements – in practice, only for the chemically and technologically important selenium and tellurium; however, according to the official guides to inorganic nomenclature, the term applies equally to all the elements in Group 16 of the Periodic Table, thus being proper also for oxygen and sulfur. On the other hand, several textbooks imply that oxygen is excluded from the chalcogens, this probably being the consequence of having discussed the chemistry of oxygen in a separate chapter [1].

The term "chalcogen" was proposed around 1930 by Werner Fischer (Fig. 1.1), when he worked in the group of Wilhelm Biltz at the University of Hannover, to denote the elements of Group 16 [2]. It was quickly accepted among German chemists, and it was Heinrich Remy who recommended its official use in 1938 while being a member of the Committee of the International Union of Chemistry (later IUPAC) for the Reform of the Nomenclature of Inorganic Chemistry. Following this, it was internationally accepted that the elements oxygen, sulfur, selenium, and tellurium will be called chalcogens and their compounds chalcogenides. The term derives from the Greek terms $\chi\alpha\lambda\kappa\acute{o}\varsigma$ meaning copper and $\gamma\varepsilon\nu\nu\acute{\omega}$ meaning giving birth, and it was meant in the sense of "ore-forming element" (cf. "hydrogen" similarly originating from $\acute{\upsilon}\delta\omega\rho$ meaning water; also "oxygen", etc.).

As a matter of fact, this book is concerned with sulfur, selenium, and tellurium as components of compound or solid solution systems in which metallic or semimetallic elements, whatsoever, participate as well. In particular, it is focused on the electrochemistry of the inorganic compounds of sulfur, selenium, and tellurium with metals and semimetals, which collectively may be termed as metal chalcogenide (MCh) systems.

**Fig. 1.1** The German inorganic chemist Werner Fischer (August 21, 1902, Elberfeld–August 16, 2001, Freiburg im Breisgau) introduced the term "chalcogen" [Courtesy of *Gesellschaft Deutscher Chemiker*, and photo atelier *Binz* (Mannheim)]



## 1.1.1 History and Occurrence

*Sulfur* has been known from prehistoric years, and its name conveys a certain metaphysical value due to the natural presence of the element in regions of volcanic activity and its burning properties. Probably no other element, with the exception of gold, has received such mystical quality. Sulfur was assumed to represent *heat*, one of the three elementary principles in which matter could be resolved, the other two being *solidity* and *liquidity*, identified, respectively, with salt and mercury. The old name of the element was brimstone (*brennstein*, "the stone that burns"), and alchemists used the name sulfur to designate all combustible substances. "Brimstone" sulfur has been central to their efforts to transmute lead to gold by transferring the yellow color of sulfur into the base metal. Sulfur was also associated with the phlogiston theory of combustion introduced by Georg Stahl (1660–1734). This theory proposed that the more phlogiston an object contained, the more easily it burned. On being burned, the object lost its phlogiston and became

a new substance incapable of being burned further. Inasmuch as sulfur could be burned with almost no residue, it was thought to be essentially pure phlogiston. By the end of the eighteenth century, Davy described sulfur as a resinous material which contained hydrogen and oxygen as essential ingredients. Gay-Lussac firmly established its elementary nature in 1809.

*Selenium* was discovered in 1817 by J. J. Berzelius (1779–1848) and J. G. Gahn (1745–1818) in the sediment taken from the lead chamber of a sulfuric acid plant in Gripsholm, Sweden. Its name was derived from the Greek word $\sigma\varepsilon\lambda\acute{\eta}\nu\eta$ (*selene*), for moon, because of its chemical similarity to tellurium-earth.

*Tellurium* was the first of the three elements S, Se, and Te to be recognized as an element. F. J. Müller von Reichenstein (ca. 1740–1825) extracted it from a Transylvanian ore and identified it as a new "metal" in 1782, while M. H. Klaproth (1743–1817) isolated it in 1798 and named it from the Latin *tellus*, meaning earth.

Sulfur exists widely in the Earth both as the free element and in a variety of combined forms (mainly sulfides and sulfates). It ranks 16th in order of abundance among the elements, making up about 0.05% of the Earth's crust, while its total contribution, both free and combined, to crystal rock is 340 ppm; this is only about one-third the value listed for phosphorus (1,120 ppm), but it is nearly twice the value for carbon (180 ppm). Note in comparison that oxygen is the most abundant of all the elements (49.4% of the Earth's crust and 23% by weight of the atmosphere). Sulfur occurs in numerous sulfide ores of metals, including those of iron, zinc, lead, and copper, as well as in the form of various sulfates such as gypsum and anhydrite ($CaSO_4$) and alums (Table 1.1). The most economically important deposits of the element are associated with gypsum and limestone sedimentary rock formations, while limited amounts are found in volcanic regions. Sulfur is quite reactive and combines directly with most other elements at elevated temperatures. It does not combine directly with certain non-metals (iodine, tellurium, nitrogen, noble gases) or noble metals (iridium, platinum, gold). Organosulfur compounds are found in petroleum and coal. Sulfur is an essential element for life and is found in two amino acids, cysteine and methionine. It is important for the tertiary structure of proteins through S–S links. It is involved in vitamins, fat metabolism, and detoxification processes.

**Table 1.1** Some minerals of the chalcogens

| The most important minerals of sulfur | The most abundant minerals of selenium and tellurium |
|---|---|
| *Sulfides* of lead (galena PbS), molybdenum (molybdenite $MoS_2$), iron (pyrite $FeS_2$), zinc (sphalerite ZnS), and mercury (cinnabar HgS) | *Selenides* of lead (Pb), copper (Cu), silver (Ag), mercury (Hg), and nickel (Ni), e.g., clausthalite PbSe; crookesite $(Cu,Tl,Ag)_2Se$; eucairite $(Cu,Ag)_2Se$ |
| *Sulfates* of the Group II metals including epsomite ($MgSO_4 \cdot 7H_2O$), gypsum ($CaSO_4 \cdot 2H_2O$), celestite ($SrSO_4$), and barite ($BaSO_4$) | *Tellurides* of lead (Pb), copper (Cu), silver (Ag), gold (Au), and antimony (Sb), e.g., calaverite $AuTe_2$; nagyagite $Au_2Sb_2Pb_{10}Te_6S_{15}$; petzite $Ag_3AuTe_2$ |

Selenium and tellurium are comparatively rare elements, being 66th and 73rd, respectively, in order of crystal abundance; selenium comprises 0.05 ppm of the Earth's crust (comparable to Ag 0.08 and Hg 0.015 ppm) and Te comprises 0.002 ppm (about as rare as Ir 0.001 or Au 0.004). Native selenium and tellurium usually occur in conjunction with sulfur, in particular as selenide and telluride impurities in metal sulfide ores. Selenium occurs also in volcanic eruptions, soil, and waters in variable quantities. Many of the mineral deposits of selenium and tellurium (Table 1.1) occur together with the sulfides of chalcophilic metals, e.g., Cu, Ag, Au, Zn, Cd, Hg; Fe, Co, Ni; Pb, As, Bi. Sometimes the minerals are partly oxidized, e.g., $MSeO_3 \cdot 2H_2O$ (M $=$ Ni, Cu, Pb), $PbTeO_3$, $Fe_2(TeO_3)_3 \cdot 2H_2O$, $FeTeO_4$, $Hg_2TeO_4$, $Bi_2TeO_4(OH)_4$. Selenolite, $SeO_2$, and tellurite, $TeO_2$, are also found to occur in nature. Selenium, in trace amounts, is a biologically essential element for vertebrates, but can be toxic when introduced in larger quantities. Elemental tellurium has relatively low toxicity. It is converted in the body to dimethyl telluride.

Polonium, completing the elements of Group 16, is radioactive and one of the rarest naturally occurring elements (about $3 \times 10^{-14}\%$ of the Earth's crust). The main natural source of polonium is uranium ores, which contain about $10^{-4}$g of Po per ton. The isotope 210-Po, occurring in uranium (and also thorium) minerals as an intermediate in the radioactive decay series, was discovered by M. S. Curie in 1898.

Eighteen isotopes of sulfur, 17 of selenium, 21 of tellurium, and 27 of polonium have been registered; of these, 4 sulfur, 6 selenium, and 8 tellurium isotopes are stable, while there is no stable isotope of polonium. None of the naturally occurring isotopes of Se is radioactive; its radioisotopes are by-products of the nuclear reactor and neutron activation technology. The naturally occurring, stable isotopes of S, Se, and Te are included in Table 1.2.

**Table 1.2** Naturally occurring, stable isotopes of sulfur, selenium, and tellurium

| $^{32}S$ | 95.1% | $^{80}Se$ | 49.82% | $^{130}Te$ | 34.48% |
|---|---|---|---|---|---|
| $^{34}S$ | 4.2% | $^{78}Se$ | 23.52% | $^{128}Te$ | 31.79% |
| $^{33}S$ | 0.7% | $^{76}Se$ | 9.02% | $^{126}Te$ | 18.71% |
| $^{36}S$ | 0.02% | $^{82}Se$ | 9.19% | $^{125}Te$ | 6.99% |
| | | $^{77}Se$ | 7.58% | $^{124}Te$ | 4.61% |
| | | $^{74}Se$ | 0.87% | $^{123}Te$ | 0.87% |
| | | | | $^{122}Te$ | 2.46% |

## 1.1.2 Production and Uses

Sulfur for commercial purposes is derived mainly from native elemental sulfur mined by the *Frasch* process. Large quantities of sulfur are also recovered from the roasting of metal sulfides and the refining of crude oil, i.e., from the sulfur by-products of purified "sour" natural gas and petroleum (the designation *sour* is generally associated with high-sulfur petroleum products). Reserves of elemental sulfur in evaporite and volcanic deposits and of sulfur associated with natural gas,

petroleum, tar sands, and metal sulfides are quite large, amounting to about 5 billion tons. On the other hand, the sulfur in gypsum and anhydrite is almost limitless, and some 600 billion tons of the element is contained in coal, oil shale, and shale rich in organic matter, but low-cost methods to recover sulfur from these sources have not been developed.

The commercial uses of sulfur are primarily in the manufacture of phosphate and ammonium fertilizer end-products, but it is also widely used in the synthesis of other chemicals and products (e.g., in detergents, gunpowder, matches, insecticides, agrichemicals, dyestuffs, and fungicides), in petroleum refining, and in metallurgical applications. One of the direct uses of sulfur is in vulcanization of rubber. It reacts directly with methane to give carbon disulfide, which is used to manufacture cellophane and rayon. Approximately 85% (1989) of elemental sulfur is converted to sulfuric acid, whose principal use is in the extraction of phosphate ores for the production of fertilizer manufacturing. Other applications of sulfuric acid include oil refining, wastewater processing, and mineral extraction. Sodium and ammonium thiosulfate are used as fixing agents in silver-based photography. Sulfites derived from burning sulfur are extensively used to bleach paper and as preservatives in dried fruits.

Selenium and tellurium are rare elements widely distributed within the Earth's crust, so they do not occur in concentrations high enough to justify mining solely for their content. Also, their commercial values and chemical uses are insignificant compared to those of sulfur. Like other "minor" metals (such as Cd, In, Ga, and Ge), Se and Te are by-products of base metal smelting. They are recovered along with non-ferrous metal mining, mostly from the anode slimes associated with electrolytic refining of copper. The elements are recovered from the slimes by pyrometallurgical methods and are converted to alkali selenite and tellurite in the process. Selenium is almost completely separated from tellurium by neutralizing the alkaline solution with sulfuric acid. Tellurium precipitates as the hydrated dioxide, while the more acidic selenous acid remains in solution, from which 99.5% pure selenium is precipitated by sulfur dioxide. Tellurium can be obtained by electrolysis of a solution of tellurium dioxide in a mixture of sulfuric acid and hydrofluoric acid. If a lead cathode is used the deposit is coherent. Metallic Te can also be obtained by electrolysis of alkaline solutions of tellurium dioxide. Both elements are recovered also from flue dusts of combustion chambers for sulfur ores of silver and gold and from lead chambers in sulfuric acid manufacture. Electrochemical processes are used in order to extract selenium, in separating selenium from tellurium, in refining concentrated sulfuric acid from selenium, and in the electrorefining of selenium. For the electrorefining of tellurium it is desirable to prepare the electrolyte by anodic dissolution of the element, which is carried out usually in alkaline solutions.

Owing to its major production source, the reserve base for selenium is based on copper deposits. An assessment of US copper resources indicated that the identified and undiscovered resources total about 550 million metric tons, almost eight times the estimated US copper reserve base. An estimated 41,000 tons of wet copper anode slimes are generated annually. Slimes resulting from primary metal refining can have average selenium concentrations of about 10%, increasing to as high as

40% in a few cases. A 2006 survey of 56 worldwide electrolytic copper refiners showed that 52 and 45 plants, respectively, reported selenium and tellurium in their slimes. The selenium-containing slimes averaged 7% selenium by weight, with a few containing as much as 25% selenium. Tellurium concentrations were generally lower and averaged 2%. On the other hand, coal generally contains between 0.5 and 12 ppm of selenium, or about 80–90 times the average for copper deposits. However, the recovery of selenium from coal, although technically feasible, does not appear likely in the foreseeable future because of the high volatility of the element [3].

Useful information on the major industrial applications of selenium and tellurium can be traced in the old (1942), yet still expedient review of Waitkins et al. [4], based on most of the early (pre-war) references on the subject. Not much has changed since then, at least with regard to the industrial uses of these elements.

Selenium has several important commercial uses, the most important being in xerography, a process that takes advantage of the photoconductor properties of gray, "metallic" selenium. In fact, selenium is one of the most significant semiconductors and one of the first substances found to possess photoelectric conductivity.[1] Applications of semiconducting Se include rectifiers, solar cells, and photographic exposure meters. The element exhibits excellent glass-forming properties and it is used to color glass; its optical properties have also been extensively studied. Chemical and pigment uses of selenium include agricultural, industrial, and pharmaceutical applications. Despite the fact that selenium and its compounds are poisonous, trace amounts of the element are essential for the majority of higher animals, because of its anti-oxidative and pre-oxidative effects. Selenium colloids have been demonstrated for uses in nutritional supplements and medical diagnostics. Se-75 is one of the more useful radionuclides; it is widely used in biological tracer experiments and diagnostic procedures, as having a convenient gamma-ray for counting and half-life (120 days) more than adequate to allow complete chemical separation from other activities.

Metallurgical grade selenium has been used as an additive to cast iron, copper, lead, and steel alloys, in order to improve machinability and casting and forming properties. Its alloy with bismuth serves as a lead substitute in plumbing fixtures, in order to reduce lead in potable water supplies. The addition of a small amount, about 0.02% by weight, of selenium to low-antimony lead alloys used in the support grid of lead-acid batteries improves the casting and mechanical properties of the alloy. Cadmium sulfoselenide compounds have been used as pigments in ceramics, glazes, paints, and plastics, but because of the relatively high cost and toxicity of Cd-based pigments, their use is generally restricted to applications where they are uniquely suited. Additionally, selenium is used in catalysts to enhance selective oxidation; in plating solutions to improve appearance and durability; in blasting caps and gun bluing; in coating digital X-ray detectors; and in zinc selenide for infrared windows in carbon dioxide lasers. Selenium dioxide and certain organoselenium compounds

---

[1]It was discovered in 1873 that a small selenium bar in a telegraph circuit acts as a photoelectric resistor.

are gaining favor as versatile reagents in specialized organic syntheses, but these applications are at present minor.

The leading use of tellurium is as metallurgical additive, namely in steel production as a free-machining additive, in copper to improve machinability without reducing conductivity, in lead to improve resistance to vibration and fatigue, in cast iron to help control the depth of chill, and in malleable iron as a carbide stabilizer. Tellurium is also used in the chemical industry as a vulcanizing agent and accelerator in the processing of rubber and as a component of catalysts for synthetic fiber production. Other applications include its use in blasting caps and as a pigment to produce blue and brown colors in ceramics and glass. High-purity tellurium is increasingly used in electronic applications, such as thermal imaging, thermoelectrics, phase change memory, and photoelectric devices. The leading end-use among these applications is in the production of cadmium telluride-based solar cells. By 2010, it is projected that global CdTe cell production capacity will reach 608 MW. Mercury cadmium telluride is an important tellurium compound used in thermal imaging devices and infrared sensors. Semiconducting bismuth telluride is used in thermoelectric cooling devices employed in electronics and consumer products.

### 1.1.3 Allotropy – States of Matter

Basic physical properties of sulfur, selenium, and tellurium are indicated in Table 1.3. Downward the sulfur sub-group, the metallic character increases from sulfur to polonium, so that whereas there exist various non-metallic allotropic states of elementary sulfur, only one allotropic form of selenium is (semi)metallic, and the (semi)metallic form of tellurium is the most common for this element. Polonium is a typical metal. Physically, this trend is reflected in the electrical properties of the elements: oxygen and sulfur are insulators, selenium and tellurium behave as semiconductors, and polonium is a typical metallic conductor. The temperature coefficient of resistivity for S, Se, and Te is negative, which is usually considered

**Table 1.3** Some physical properties of sulfur, selenium, and tellurium

|  | S | Se | Te |
| --- | --- | --- | --- |
| Atomic mass | 32.07 | 78.96 | 127.60 |
| Atomic number | 16 | 34 | 52 |
| Electronic structure | $[Ne]3s^23p^4$ | $[Ar]3d^{10}4s^24p^4$ | $[Kr]4d^{10}5s^25p^4$ |
| Melting point (°C) | 119 ($S_\beta$) | 220.5 (gray) | 449.8 |
| Boiling point (°C) | 444.6 | 684.8 | 989.8 |
| Density (g cm$^{-3}$) | 2.06 ($S_\alpha$) | 4.82 (gray) | 6.25 |
| Atomic radius ($10^{-10}$ m) | 1.00 | 1.40 | 1.37 |
| $X^{(II)}$ covalent radius ($10^{-10}$ m) | 1.03 | 1.16 | 1.37 |
| Electronegativity (Allred–Rochow; Pauling) | 2.44; 2.58 | 2.48; 2.55 | 2.01; 2.10 |
| First ionization potential (eV) | 10.38 | 9.75 | 9.01 |

characteristic of non-metals. Polonium has resistivity typical of a true metal with a positive temperature coefficient.

Numerous allotropic modifications (perhaps 30 or more) are known for solid sulfur, more than for any other element, manifesting its exceptional ability to form rings or chains of various atomicities and forms. Ordinary sulfur (orthorhombic) is a pale-yellow solid at room temperature and consists of puckered rings of $S_8$ molecules. In its various allotropic forms, solid crystalline sulfur exists either as rings of mostly 6–12 atoms (cyclo-sulfur) or as chains of sulfur atoms (catena-sulfur). The most common ring form, cyclo-octasulfur, $S_8$, has three principal allotropes. Orthorhombic sulfur, $S_\alpha$, the thermodynamically stable form under ordinary conditions, when heated slowly changes to monoclinic sulfur at 95.5 °C. When heated rapidly, orthorhombic sulfur melts at 112.8 °C without assuming the monoclinic form. Monoclinic sulfur, $S_\beta$, crystallizes above 95.5 °C when melted sulfur is cooled slowly, and melts at 119 °C. $S_\beta$ is stable above 95.5 °C but converts to $S_\alpha$ when residing at room temperature. Another monoclinic allotrope, $S_\gamma$, crystallizes when a solution of sulfur in toluene or ethanolic ammonium sulfide is evaporated to dryness at a temperature above 95.5 °C. The $S_\gamma$ form melts at 106.8 °C and slowly changes to $S_\alpha$ and/or $S_\beta$.

Because of the conversion of orthorhombic sulfur to monoclinic form, the above values of melting points are difficult to observe, as the resulting allotropic mixture melts at only 115 °C. Amorphous or "plastic" sulfur can be produced through the rapid cooling of molten sulfur. X-ray crystallographic studies show that the amorphous form may have a helical structure with eight atoms per turn. This form is metastable at room temperature and gradually reverts back to crystalline within hours to days but this conversion can be rapidly catalyzed.

A notable property of sulfur in its molten state is that, unlike most other liquids, its viscosity increases massively above a certain temperature, due to the formation of polymers. Upon melting, sulfur forms a thin, straw-colored liquid, still containing $S_8$ molecules. If liquid sulfur is heated to temperatures near 160 °C, the $S_8$ rings rupture and the ends of the chains combine to form $S_{16}$, $S_{24}$, and $S_{32}$ species. The melt darkens to a rich orange-brown, and a tremendous increase in viscosity (10,000-fold) is observed as the long chains twist and tangle. Above 190 °C, however, the viscosity is progressively decreased due to depolymerization as the extended chains break into shorter fragments; when the boiling point (444 °C) is finally reached, liquid sulfur is once again very thin and runny. Sulfur vapor consists of acyclic $S_8$, $S_6$, $S_4$, and $S_2$ molecules, with the smaller molecules dominating at higher temperatures. At 1,000 °C, most of the molecules are probably $S_2$, which, like $O_2$ molecules, are paramagnetic. At 2,000 °C, it is estimated that nearly half the diatomic $S_2$ molecules dissociate into sulfur atoms.

The allotropy of selenium presents some analogies with that of sulfur. Most authors distinguish three general forms: amorphous, crystalline trigonal (t-Se, consisting of helical Se chains), and monoclinic (m-Se, consisting of puckered $Se_8$ rings). Crystalline t-Se is the most stable form at ambient conditions. In fact, three monoclinic modifications (α, β, γ) exist, distinct only by the different stacking of the $Se_8$ "molecules". These convert to the trigonal form at temperatures above 110 °C. The non-crystalline modifications are red (amorphous) selenium, which is a hard,

brittle glass (stable at temperatures below 31 °C), and black (vitreous) selenium, stable at 31–230 °C (m.p.). These convert spontaneously to the crystalline form at 70–120 °C.

Red selenium, originally known as α-selenium, is precipitated when aqueous selenous acid is treated with sulfur dioxide or other reducing agents and when aqueous selenocyanates are acidified; it is also formed by the condensation of selenium vapor on cold surfaces. This amorphous (glass) modification has a chain structure resembling that of trigonal selenium, somewhat deformed. Vitreous, or black, selenium – a brittle opaque, dark red-brown to bluish-black lustrous solid, obtained when molten selenium is cooled suddenly – is the ordinary commercial form of the element. It does not melt sharply, but softens at about 50 °C and rapidly transforms to hexagonal selenium at 180–190 °C. Vitreous selenium is much more complex than any other modification and its polymer rings may contain up to 1,000 atoms.

Trigonal selenium is variously called metallic gray or black selenium and occurs in lustrous hexagonal crystals, which melt at 220.5 °C. Its structure, which has no sulfur analogue, consists of infinite, unbranched helical chains. Its density, 4.82 g cm$^{-3}$, is the highest of any form of the element. Trigonal selenium is a semiconductor (intrinsic p-type with a rather indirect transition at about 1.85 eV [5]), and its electronic and photoelectric properties are the basis for many industrial uses of this element.

The structural diversity of the allotropic forms of the chalcogen elements diminishes when moving from sulfur to selenium and tellurium; polymeric tellurium is the only stable form of this element known to date, and only one crystalline form is known for certain, a silvery white, semimetallic solid which consists of helical polymeric chains. The structure is isomorphous with gray Se, but the chains are appreciable closer together than are the selenium chains. Crystalline tellurium has a metallic luster, but it is a poor conductor of heat and has the electrical properties of a semiconductor rather than those of a metal. It is quite brittle and insoluble in any liquid with which it does not react. Although a so-called amorphous form of tellurium is precipitated when aqueous tellurous acid is treated with reducing agents, such as sulfur dioxide, it is probable that this is merely finely divided crystalline tellurium. Trigonal Se and Te appear to form a continuous range of solid solutions, in which there is fairly random alternation of Se and Te atoms in the infinite chains.

The trend toward more metallic character of the elements in Group 16 is complete at polonium, which has two allotropes, both with typically metallic structures: α-cubic, which converts at 36 °C to β-rhombohedral (m.p. 254 °C).

Selenium is less complex than sulfur in the molten state, wherein cyclic $Se_6$, $Se_7$, and $Se_8$ species are present. The chain length of the selenium polymers in the melt is progressively reduced with increasing temperature. In fact, according to studies of electrical resistivity of molten selenium, it appears that as the chains in the liquid are thermally destroyed, selenium changes from a semiconductor to a metallic conductor. In the gas above gray or liquid selenium there is a temperature-dependent mixture of $Se_n$ species ($n = 2$–10). From vapor density determinations, it is concluded that $Se_8$ molecules are present below 550 °C. The vapor is yellow at the boiling point (685 °C), and dissociation to selenium species with lower atomicity occurs at higher temperatures.

Liquid tellurium boils at 990 °C to a golden yellow vapor, with density that corresponds to the molecular formula $Te_2$. Likewise, in polonium vapor only $Po_2$ species are present. Clearly, the decreasing complexity of the solid state of the three elements Se, Te, and Po, as compared to sulfur, is reflected in the vapor state.

## *1.1.4 Chemical Properties and Compounds*

Within the main group 16, there are great differences between the chemistry of oxygen and that of sulfur, with more gradual variations through the sequence sulfur to polonium. This is in accord with the general rule found for non-transition elements, dictating that the first of those in each main group (i.e., from Li to Ne) displays some anomalous properties relative to the later members of the group. One manifestation of this rule is that the maximum coordination number for the first element is four, while the maximum for the remainder of the group can be five, six, or even seven (as in $IF_7$). From a descriptive aspect, this is possibly due to the small size of the elements in the first long-row period, making them unable to accommodate more than four large ligand atoms. In fact, the heavier elements may utilize *d* orbitals in bonding, so that their maximum coordination number is not limited to four, nor is the valence limited to two as for oxygen. Thus, sulfur forms several hexacoordinate compounds (e.g., $SF_6$), while for tellurium, six is the characteristic coordination number. In addition, sulfur has a strong tendency to catenation, which manifests itself not only in the many forms of the element that all contain $S_n$ rings of various sizes, but also in polysulfide ions ($S_n^{2-}$) – unlike oxygen for which only the di- and trinuclear homopolyatomic anions $O_2^{2-}$, $O_2^{-}$, and $O_3^{2-}$ are known. Although Se and Te have a smaller tendency to catenation, they also form rings and long chains in their elemental forms. None of these chains is branched because the valence of the element is only two. Catenation is not restricted to the elemental forms; many compounds, particularly of sulfur, contain rings and chains, of which the latter might be regarded as oligomers stabilized by end-stopping groups, such as –H (polysulfanes), –Cl (polychlorosulfanes), or $-SO_3^{-}$(polythionates).

Another major difference among the first row elements and the others, in the main groups 14–16, is that C, N, and O form particularly strong π bonds with themselves and with each other. This gives rise to allotropes (e.g., graphite, $O_2$, $O_3$) and compounds (e.g., alkenes, alkynes, aromatics, $CO_2$, $NO_3^{-}$, $CN^{-}$) having no counterpart for the heavier elements. Specifically, the relatively poor capacity for π-bonding among second long-row elements is reflected by the lack of evidence for the existence of NS and $NS_2$, i.e., the sulfur analogues of the common oxides of nitrogen NO and $NO_2$.[2] In effect, the two π-bonded allotropes of oxygen, $O_2$ and $O_3$, are unique in type, since the other group 16 members either form rings and chains containing single bonds (S, Se, Te) or metallic lattices (Po).

_____

[2] However, on account of the particularly short C–S distances, multiple bonds (probably of the $d_\pi - p_\pi$ type) between hypervalent sulfur and carbon occur in a number of species.

On account of their $ns^2np^4$ outer electronic configurations, the chemistry of the chalcogens is predominantly non-metallic with a gradually increasing metallic character with atomic mass, the same as in each of the Groups 14–17. Thus, while there is some evidence of metallic character appearing for selenium in the formation of one or two basic salts in which the element might be regarded as having some cationic properties, this trend becomes more obvious with tellurium, although all its simple salts are still basic. Polonium forms both normal and basic salts, the latter being formally analogous to those formed by tellurium. The high ionization energies of chalcogens (X) rule out the possibility of a rare gas configuration produced by loss of all six outer electrons to give $X^{6+}$ ions. Even $X^{4+}$ ions probably do not exist in any compounds with the possible exception of one form of $PoO_2$. The more usual ways that the chalcogens complete the noble gas configuration are by forming.

(i)   "chalconide" ions, i.e., doubly charged chalcogen anions ($S^{2-}$, $Se^{2-}$, $Te^{2-}$). These ions exist only in the salts of the most electropositive elements, such as alkali metal sulfides, selenides, and tellurides;

(ii)  two electron-pair (covalent) bonds, e.g., in $H_2S$, $(CH_3)_2Se$, $SCl_2$;

(iii) $MX^-$ ions with one bond and one negative charge, e.g., $HS^-$, $RS^-$;

(iv)  "onium" cations with three bonds and one positive charge, such as those derived from the hydroxonium, $H_3O^+$, or sulfoxonium $H_3S^+$ ions, e.g., $R_3S^+$.

The stability of chalconide (ionic) compounds decreases from oxygen to tellurium; treatment with water produces XH– with X = O or S (hydroxyl and thiol radicals, respectively), but $XH_2$ with X = Se or Te. On warming, aqueous solutions of $HS^-$ evolve hydrogen sulfide, evidencing that the hydrosulfide ion is much less stable than hydroxide.

All the chalcogens form electron-pair compounds in which the element is bivalent, with two lone pairs of electrons, the best known examples being organic compounds. Also, many organo-substituted onium salts are known for the whole group and are generally prepared by addition of an alkyl iodide to a diorganochalcogen. In addition, many hypervalent $XQ_4$ and $XQ_6$ derivatives are known for all three S, Se, Te. Therefore, in total, apart from the ionic valence –2, formal oxidation states of 0, +2, +4, and +6 are typically encountered for the chalcogen elements.

All forms of elemental sulfur are very weakly soluble ($10^{-8}$ M at 298 K) in water. In most organic solvents, sulfur solubilizes with the ring $S_8$ molecules maintained, as in DMSO, DMF, $CS_2$, and methanol. Sulfur $S_8$ can be dissolved also through a disproportionation process, which is reversible only in liquid ammonia. Elemental selenium is very insoluble in aqueous systems and is generally resistant to either oxidation or reduction. It is therefore considered non-toxic to aqueous-based, biological systems. Tellurium is insoluble in all solvents that do not react with it. All three elements are not affected by non-oxidizing acids, but the more metallic Po will dissolve in concentrated HCl as well as in $H_2SO_4$ and $HNO_3$, giving solutions of $Po^{2+}$ and then $Po^{4+}$.

### 1.1.4.1 Hydrides

The hydrides of sulfur are called *sulfanes*. Hydrogen sulfide, $H_2S$, is the most important and most stable. It is a colorless, poisonous gas whose odor is recognized as that of rotten eggs. In aqueous solution, $H_2S$ is a very weak acid ($pK_{a1}$ 7.04, $pK_{a2}$ 14.9). Sulfur forms also $M_2H_2$ hydrides (similar to oxygen peroxide), which are non-planar molecules, as well as hydrides containing chains of more than two sulfur atoms. These higher sulfanes (polysulfanes) are thermodynamically unstable with respect to $H_2S$ and sulfur and owe their metastable existence at room temperature to rather high activation energy for the decomposition. The $H_2S_n$ sulfanes with $n = 3$–8 have been isolated in a pure state, and others up to $n = 17$ or 18 have been obtained in an impure form. Bulk (kilogram) quantities of the sulfanes may be made either via acid hydrolysis of sodium polysulfides ($Na_2S_x$) or from chlorosulfanes $S_yCl_2$.

The hydrides of selenium and tellurium, $H_2Se$ and $H_2Te$, are extremely toxic, highly malodorous gases, which condense to colorless liquids. Gaseous $H_2Se$ is 15 times more dangerous than $H_2S$, based on threshold limit values; however, in fact, $H_2Se$ turns out to be safer than $H_2S$ as it is easily oxidized biologically to non-toxic elemental red selenium. Although the heats of formation of $H_2Se$ and $H_2Te$ gases are positive (more endothermic for Te hydride), they decompose only slowly at room temperature. $H_2Se$ is more stable than $H_2Te$ due to a combination of the increasing radii from Se to Te, leading to an increased H–X bond length, and the decreasing electronegativity, resulting in the H–Te bond being almost completely non-polar. The gases are fairly soluble in water, dissociating to the $HX^-$ and $X^{2-}$ ions, and yield acidic solutions which precipitate selenides and tellurides of many metals from solutions of their salts; however, since both hydrides are easily oxidized, particularly in aqueous solution by air, elementary Se or Te is often precipitated as well. The stability trend of the gases is observed also in the acidity of their aqueous solutions, as shown by the increase in the acid dissociation constants; aqueous $H_2Se$ is a moderately strong acid ($pK_{a1}$ 3.88, $pK_{a2}$ 11 at 25 °C), while aqueous $H_2Te$ is almost as acidic as phosphoric acid and more acidic than hydrofluoric acid.

### 1.1.4.2 Oxides and Oxoacids

Within the sulfur sub-group, there are two main types of oxides, the dioxides $X^{IV}O_2$ (X = S, Se, Te, Po) and the trioxides $X^{VI}O_3$ (X = S, Se, Te). In addition, sulfur also forms disulfur monoxide, $S_2O$. Transient XO species are known in the gaseous phase for S, Se, and Te. Polonium forms a black monoxide PoO.

When heated, S, Se, Te (and Po) burn in air to give the dioxides $XO_2$, and react with halogens, most metals, and non-metals at moderate temperatures to form chalcogenides. Chalcogenides in general are thermodynamically unstable in the presence of oxygen. Thus, when fresh sulfide surfaces are exposed during mining, crushing, and grinding, or conditioned in flotation cells containing dissolved oxygen, some degree of oxidation of the surface is expected.

*Sulfur dioxide* is a colorless gas with a suffocating smell, which at 10 °C and normal pressure is condensed to a colorless liquid. It is made on a vast industrial

scale by burning sulfur or $H_2S$ or by roasting sulfide ores as part of the pyrometallurgy of zinc, molybdenum, and other metals. The burning of high-sulfur coals and fuel oil serves as the major source of $SO_2$ produced as an environmental pollutant. Sulfur dioxide gas is readily soluble in water (45 vol per 1 vol of water at 15 °C). Most of the commercially prepared $SO_2$ is oxidatively converted to the trioxide $SO_3$, which is subsequently used to manufacture sulfuric acid. The trioxide is a colorless, polymorphic crystalline solid (b.p. 44.52 °C). In the liquid and solid states, $SO_3$ trimerizes to form $S_3O_9$.

*Selenium dioxide* (naturally occurring selenolite) is a white solid, which can be formed by burning elemental selenium in air, by oxidizing it with nitric acid, or by dehydrating selenous acid. It is readily reduced to the elemental state by ammonia, hydrazine, aqueous sulfur dioxide, or a number of organic compounds. It is soluble in water (38.4 g per 100 ml at 14 °C) and forms selenous acid when dissolved in hot water. *Tellurium dioxide* (naturally occurring tellurite) is a white solid that can be prepared directly from the elements or by dehydrating tellurous acid or by the oxidation of tellurium with dilute nitric acid. $TeO_2$ is very sparingly soluble in water.

Sulfur dioxide exists as a V-shaped molecule, like water, in the gaseous state and sulfur trioxide as a planar triangular molecule. The dioxides of Se and Te do not exist as discrete, gas molecules. Solid sulfur dioxide contains discrete $SO_2$ molecules. Both $SeO_2$ and $TeO_2$ occur as polymeric solids; $SeO_2$ consists of infinite chains, whereas $TeO_2$ is essentially an ionic solid having a rutile structure. Unlike $SO_3$, the trioxides $SeO_3$ and $TeO_3$ are not obtained by oxidation of the dioxide. They are usually prepared by dehydration of their respective oxoacids: $H_2Se^{VI}O_4$ and $Te^{VI}(OH)_6$ (or $H_6TeO_6$).

$SO_2$ and $SO_3$ are (formally) the acid anhydrides of sulfurous acid and sulfuric acid, respectively. Sulfurous acid ($H_2S^{IV}O_3$) is a weak acid that does not exist in the free state; $SO_2$, although formally the anhydride of $H_2SO_3$, dissolves in water as $(SO_2)$aq with little or no formation of the free acid. However, many salts containing sulfite and bisulfite ions are known, for example $Na_2SO_3$ and $NaHSO_3$. In general, the sulfites are stable and are commercially important in food processing, paper industry, and photography. Sulfuric acid ($H_2S^{VI}O_4$) is the globally most important commercially prepared compound.

Selenium in the +IV oxidation state exists as the weak *selenous acid*, $H_2SeO_3$ ($pK_{a1}$ 2.6), and as a number of inorganic selenites, which in solution are highly toxic. In aqueous solution, dissolved selenite exists predominantly as the biselenite ion (pH range 3.5–9). *Tellurous acid*, $H_2TeO_3$, is similar to but weaker than selenous acid. Unlike $H_2SO_3$, both $H_2SeO_3$ and $H_2TeO_3$ can be isolated in stable form. Both are white solids that can be easily converted to the respective dioxide by dehydration in a jet of dry air.

The higher acids, *selenic* ($H_2SeO_4$) and *telluric* ($H_2TeO_4$), containing the chalcogen in the +VI oxidation state, are also known; these correspond to the sulfuric acid.

Selenic acid, $H_2SeO_4$, is a strong acid ($K_{a1}$ 2) and the solubility of its salts parallels that of the corresponding sulfates. It is formed by the oxidation of selenous acid or elemental selenium with strong oxidizing agents in the presence of water. Telluric acid, $H_2TeO_4$, or tellurates are obtained by oxidation of tellurides,

tellurium, or $TeO_2$ with hydrogen peroxide, or chromic acid in nitric solution, or chlorine. Tellurates can be reduced with difficulty to tellurides. Notably, unlike sulfur and selenium, Te(VI) forms a hexahydroxo-acid $Te(OH)_6$ (orthotelluric acid): on evaporation, telluric acid solutions give cubic or clinorhombic crystals of the trihydrate $TeO_3 \cdot 3H_2O$, or orthotelluric acid $H_6TeO_6$, which is very soluble in water.

The scarcity of data concerning complexation reactions especially of the heavier chalcogens has led researchers to calculate a number of dissociation constants from thermodynamic data. Séby et al. [6] provided recently a critical review and evaluation of the accuracy of selenium acid–base equilibrium constants reported in the literature, for the diprotic acids $H_2Se$, $H_2SeO_3$, and $H_2SeO_4$ at 25 °C and 1 bar pressure, along with the methods of their determination, the corresponding ionic media and ionic strengths. They determined also the solubility constants of the various solid phases, in the form of which inorganic selenium can exist for the –II, +IV, and +VI oxidation states (metal selenides, selenites, and selenates).

Let us add here that despite the general similarities of selenium and sulfur in their chemical properties, the chemistry of selenium differs from that of sulfur in two important aspects: their oxoanions are not similarly reduced, and their hydrides have different acid strengths. For example, Se(+IV) tends to undergo reduction to Se(–II), whereas S(+IV) tends to undergo oxidation. This difference is evidenced by the ability of selenous acid to oxidize sulfurous acid:

$$H_2SeO_3 + 2H_2SO_3 \rightarrow Se^0 + 2H_2SO_4 + H_2O$$
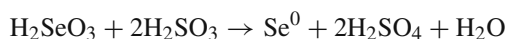
Although the oxoacids of selenium and sulfur have comparable acid strengths ($pK_{a1}$ 2.6 vs. $pK_a$ 1.9, respectively, for the quadrivalent species; $pK_a$ 3 for both the hexavalent species), the hydride $H_2Se$ is much more acidic than $H_2S$ ($pK_{a1}$ 3.9 vs. 7.0). Thus, while thiols such as cysteine are mainly protonated at physiological pH, selenols such as selenocysteine are predominantly dissociated under the same conditions.

### 1.1.4.3  Thio- and Seleno-sulfates

Elemental sulfur dissolves in boiling aqueous sodium sulfite solutions with the formation of sodium thiosulfate ($Na_2S_2O_3$). The reaction proceeds quantitatively if sulfur and excess sodium sulfite are boiled for some time in weakly alkaline solutions. In the cold, however, practically no reaction occurs. Alternatively, thiosulfate can be produced quantitatively in solution phase by using organic solvents to first dissolve sulfur and then accomplish the reaction with aqueous sulfite. In a parallel reaction, elemental selenium dissolves in alkaline sulfite solution to produce selenosulfate, $SeSO_3^{2-}$:

$$Se(s) + SO_3^{2-}(aq) \rightleftharpoons SeSO_3^{2-}(aq)$$
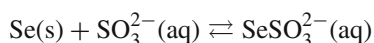
The formation constants for this equilibrium at temperatures from 0 to 35 °C have been reported by Ball and Milne [7].

Selenosulfate is an analogue of thiosulfate wherein one of the S atoms is replaced by a Se atom. Thiosulfate and selenosulfate anions are known to have tetrahedral structure as constituting the S and Se analogues, respectively, of the sulfate $SO_4^{2-}$ anion. The isomeric thioselenate anion $SSeO_3^{2-}$ is not produced by the reaction of sulfur with selenite nor is the selenoselenate ion $Se_2O_3^{2-}$ formed from selenium and selenite. Actually, $SSeO_3^{2-}$ may be produced as a metal salt by boiling an aqueous solution of selenite with sulfur, but in aqueous solution thioselenates are not stable and isomerize to selenosulfates.

Colloidal sulfur (selenium) can be produced readily from the disproportionation of aqueous thiosulfate (selenosulfate) with dilute acids:

$$S_2O_3^{2-} + 2H^+ \rightarrow S + SO_2 + H_2O$$

$$SeSO_3^{2-} + 2H^+ \rightarrow Se + SO_2 + H_2O$$
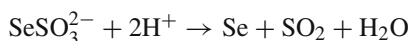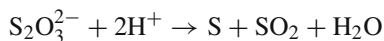
### 1.1.4.4 Polychalcogenide Ions

The characteristic strong tendency of sulfur and its heavier congeners to catenate is reflected in the wide range of polychalcogenide ions, i.e., reduced forms of the elements, that may be discrete in highly ionic salts or dissolved in polar solvents.

Alkali metal polysulfide solutions are known to contain unbranched, chain-like sulfur anions $S_n^{2-}$ in the range $n = 2$–6, while in addition, $S_7^{2-}$ and $S_8^{2-}$ can be crystallized by employing alkylammonium cations. Speciation analysis of aqueous alkali metal polyselenide solutions has shown formation of $Se_n^{2-}$ anions with $n = 2$–5, while those with $n = 3$–6 have been detected in DMF [8, 9]. While it is difficult to stabilize the long-chain free polyselenides in solution, they can be isolated as salts through the use of long-chain quaternary ammonium or phosphonium cations or alkali metal crown ethers. In total, uncoordinated polyselenides with $n = 2$–11 have been synthesized by a variety of methods and characterized in the solid state. Polytellurides $Te_n^{2-}$ with $n = 2$–4, completely analogous to those of the lower chalcogens, have been identified also in alkali metal solutions [10–12], while $Te_n^{2-}$ ions with $n = 2$–6, 8, 12, and 13 have been structurally characterized in the solid state. One feature of the polytelluride anions is that both the terminal and the internal bond distances are generally shorter than in elemental tellurium. Mixed polychalcogenide anions have also been synthesized [13, 14].

Simple cations are unknown within Group 16 (besides Po), but several highly colored polyatomic cations (*cationic clusters*), like $S_4^{2+}$, $S_8^{2+}$, $Se_4^{2+}$, $Se_8^{2+}$, $Te_4^{2+}$, and $Te_6^{4+}$, have been isolated in non-aqueous media [15]. Some mixed chalcogen cationic clusters have also been reported. These are all unstable in water.

Aqueous polysulfide solutions have been widely investigated as primary electrolytes in photoelectrochemical solar cells (PEC; Chap. 5). The complexity of these solutions arising from the overlap of multiple chemical equilibria is well

documented. Giggenbach [16] has provided evidence that the species in near-neutral aqueous sodium polysulfide solution may be related by the equilibria.

$$H_2S \rightleftharpoons H^+ + HS^-$$
$$HS^- \rightleftharpoons H^+ + S^{2-}$$
$$H_2O \rightleftharpoons H^+ + OH^-$$
$$HS^- + OH^- \rightleftharpoons S^{2-} + H_2O$$
$$S_3^{2-} + HS^- + OH^- \rightleftharpoons 2S_2^{2-} + H_2O$$
$$2S_4^{2-} + HS^- + OH^- \rightleftharpoons 3S_3^{2-} + H_2O$$
$$3S_5^{2-} + HS^- + OH^- \rightleftharpoons 4S_4^{2-} + H_2O$$
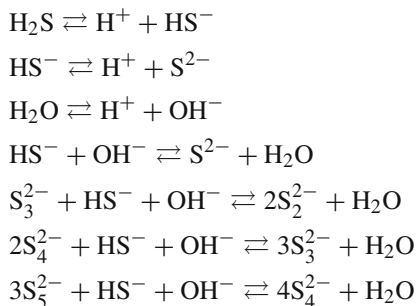
Dissociation of polysulfide ions into radicals $S_2^{\cdot-}$ or $S_3^{\cdot-}$, and disproportionation into sulfide and thiosulfate become significant at temperatures above 150 °C. In fact, in near-neutral solutions, polysulfide ions are stable with respect to this disproportionation up to 240 °C; however, at pH > 8 polysulfide ions become metastable, even at room temperature.

Licht et al. [17] developed a method of numerical analysis to describe the above-quoted equilibria of the 11 participating species (including alkali metal cations) in aqueous polysulfide solution, upon simple input to the algorithm of the temperature and initial concentration of sulfur, alkali metal hydroxide, and alkali metal hydrosulfide in solution. The equilibria constants were evaluated by compensation of the polysulfide absorption spectrum for the effects of HS$^-$ absorption and by computer analysis of the resultant spectra. Results from these calculations were used to demonstrate that the electrolyte is unstable, and that gradual degradation of polysulfide-based PECs (in the long term) can be attributed to this factor (Chap. 5).

Liquid ammonia solutions of lithium polysulfides have been characterized by Dubois et al. [18]. The least reduced polysulfide was shown to be $S_6^{2-}$ (not found previously *in aquo*) lying in a strongly temperature-dependent equilibrium with the radical $S_3^{\cdot-}$.

Complex equilibria among multiple species are typical also of polyselenide and polytelluride solutions. Aqueous polyselenide solutions have been employed as electrolytes in high-efficiency PEC with photoanodes made of gallium arsenide and cadmium chalcogenides (Chap. 5). Unlike polysulfides, the fundamental equilibria constraining the distribution of polyselenide species have not been meticulously characterized [19].

## 1.2 The Metal Chalcogenides

### 1.2.1 Solids, Complexes, and Clusters

The chalcogens have a rich metal chemistry both in molecular compounds and in the solid state, on account of their ability to catenate and to bind to multiple metal centers.

The chemistry of soluble metal chalcogenide complexes, either containing chalcogen–chalcogen bonds or only chalcogen–metal, has been studied extensively primarily for sulfur, and after the mid-1970s for selenium and tellurium as well. Metal–sulfur systems have a long chemical history in all aspects, but from the 1960s the interest in the related complexes was renewed, owing to their significance in bioinorganic chemistry and to hydrodesulfurization and other catalytic processes. The early progress in the identification of the many possible coordination modes available for sulfide ligands has been summarized neatly by Vahrenkamp [20]. A large number of synthetic molecular transition metal complexes with either terminal or bridging sulfide ligands have been reported and their catalytic activity has been reviewed [21, 22]. The coordination modes and structural types of soluble metal selenides and tellurides, synthesized in solution or in the solid state, have been sorted and described in the seminal review by Ansari and Ibers [23]. An excellent introduction to the synthetic and structural coordination chemistry of inorganic selenide and telluride ligands, covering all the facts up to 1993, can be found in Roof and Kolis [24], with the emphasis on compounds of mostly molecular nature.

The metal–polychalcogenide chemistry in the liquid and solid states has experienced unprecedented development in the past two decades [9]. Various types of polychalcogenide anionic clusters have been found, which serve as chelating ligands to transition metals retaining the typical terminal or bridging coordination mode of the simple chalcogenide ions and augmenting their bonding versatility by participating in 3- to 8-membered chelate rings. Polychalcogenide chains are characterized by conformational flexibility and variable nuclearity, being thus highly suitable bridging ligands for the construction of solid-state *polychalcogenido-metalate networks* in the presence of structure-directing counter cations. Notably, compounds of selenium and tellurium show structural types, some of which are unknown in sulfur chemistry. In particular, tellurium, with its larger size, diffuse orbitals, and increased metallic character, is found to possess a much more non-classical chemistry than its congeners, evidencing a presently well-documented potential for unusual structures and bonding. Kanatzidis [25] has summarized the experience and prospective in the field of inorganic chemistry of tellurium, stressing that both the compositions and structures of tellurides are unpredictable.

A large diversity of stoichiometries and structures, which is rather difficult to rationalize briefly, even considering only the binary combinations, is found in the solid chalcogenide compounds/alloys of the main group and transition metals and metalloids. In addition, non-stoichiometry in a single phase abounds for these solids, particularly for the transition metal compounds, where electronegativity differences are minimal and variable valency is favored. In general, "chalcogen-rich" and "metal-rich" phases occur for almost all systems of interest, and very often complex bonding is assumed in order to account for the observed structural features. For instance, according to the degree of sulfur–sulfur bonding, the transition metal sulfides would be classified as "sulfur-rich" phases featuring S–S bonding, usually in the form of persulfido units $S_2^{2-}$ (as exemplified principally by $FeS_2$) or compounds like $TiS_3$ and $TaS_3$ containing both per- and monosulfido units. There would be also a broad class of transition metal sulfides including members with isolated sulfide ($S^{2-}$) centers, e.g., $MoS_2$ and FeS. On the other hand, one would encounter

metal-rich phases (like $Ta_3S_2$) exhibiting metal–metal bonding, even to the point that they should be considered as being metallic alloys. Clearly, atom sizes, valence electron concentrations, and metal-to-non-metal proportions play key roles in the determination of structural features and types.

Metal chalcogenides have played a major role in the field of *low-dimensional solids*. It was the unraveling of the origin of the resistivity anomalies observed in layered transition MChs that stimulated the interest in low-dimensional inorganic materials. Metal clustering and low-dimensional structures are frequently found among transition MChs, as a consequence of the fact that, in contrast to the ionic 3D-type oxides, these compounds tend to form covalent structures, so that the reduced relative charge on the metal favors metal–metal bonding. In the metal-rich compounds,[3] preferred coordination polyhedra occur for the non-metal (chalcogen) atoms. The linkage of these polyhedra takes place in such a way that they often end up with an arrangement identical to that known from isolated metal clusters. However, clusters are rarely isolated in the chalcogenide structures. They condense by sharing common vertices, edges, or faces, or more unusually they may be connected via significant chemical bonding between the vertices. They also form columns, in which the central metal atoms interact to give chains running in the same direction. In layered chalcogenides, which have enough *d*-electrons for significant M–M bonding in two dimensions, the dimensionality of M–M interactions is increased to two. Further, in certain cases, the cluster network is best regarded as a 3D metal framework, i.e., as a metal packing arrangement. It may be emphasized in this connection that the occurrence of M–M bonds in MChs has substantiated the use of classification schemes based on structural elements rather than oxidation numbers, rationalizing thus the coincidental integer values of the oxidation state of transition metals and consequently the apparent stoichiometries [26].

The complexes in which metal clusters are coordinated by chalcogenide or polychalcogenide ligands occupy a special position among the so-called inorganic or *high-valence clusters*, the most characteristic being those of 4*d*- and 5*d*-metals of Groups 5–7. Currently, the chalcogenide cluster chemistry of the main group and *d*-transition metals is firmly established. The area has been the subject of several reviews [27, 28]. A recent survey of new and older results for the early transition MChs has been given by Fedorov et al. [29]. Considerably less developed is the cluster chemistry of the lanthanoids. Ionic lanthanides form comparatively unstable compounds with S, Se, and Te, so that as-composed clusters are rare [30].

The fabrication of inorganic *nanoclusters*[4] on a surface, or inside a homogeneous medium, lies at the cutting edge of nanoscience, design, and technology of applications. Mesoscopic inorganic clusters, bearing both molecular and solid-state

---

[3] Actually, those containing M–M bonds.

[4] The term "nanosized cluster" or "nanocluster" or simply "cluster" is used presently to denote a particle of any kind of matter, the size of which is greater than that of a typical molecule, but is too small to exhibit characteristic bulk properties. Such particles enter the size regime of mesoscopic materials.

characteristics, represent a unique prospect to developing novel materials with superior physical properties. Thereupon a wide scientific and technological interest has been directed to clusters derived from MChs that may serve as models for solid-state compounds and can be used as precursors in the production of unusual "bulk" phases. Synthetic studies with covalent metals (Zn, Cd, Hg, Cu, Ag) have produced extremely large metal chalcogenide cluster compounds with precisely defined cluster surfaces and internal, chalcogenido-encapsulated metal atoms, or metal clusters surrounded by protecting chalcogenide ligands ([31] and references therein). Most of the internal atoms in these species have coordination environments that resemble the environments found in bulk solid-state materials. Important uses in this connection are in the synthesis of new catalysts (Chap. 6), superconductors, and non-linear optical materials [32]. In parallel, developments in this field have provided considerable insight into the size-dependent physical properties of quantum-confined systems [33, 34].

## 1.2.2 Common Solid Structures

Binary metal chalcogenides of great variety occur, since with a given chalcogen many metals and metalloids form several compounds and sometimes long series of compounds. Although complex structures are not unusual, for a large part the binary compounds belong or relate to the very basic structural types and may be approached easily in a descriptive manner. "Three-dimensional" structures, commonly the cubic NaCl (rock salt; RS) and zinc blende (ZB), or the hexagonal NiAs and wurtzite (W) types, as well as "2D" layer-lattice varieties related to the $CdI_2$ type, are the major structure types observed (Fig. 1.2). The simple compounds formed by selenium and tellurium are generally isomorphous with their sulfide analogues, although there are differences, especially for tellurides. Polonium is distinctly metallic in many aspects; however it also shows non-metal characteristics by forming numerous polonides (MPo), which are often isostructural with tellurides and appear to be fairly ionic.

Chalcogenides can be formally derived from the hydrides; in particular, the more electropositive metals (e.g., Groups 1 and 2) may be considered to give chalconide "salts" of the corresponding hydrides. Passing by the 4:8-coordinated anti-fluorite forms of alkali metal chalcogenides, one finds that the alkaline earth compounds as well as many other monochalcogenides of rather less basic metals (e.g., the monosulfides of Pb, Mn, La, Ce, Pr, Nd, Sm, Eu, Tb, Ho, Th, U, Pu) adopt the 6:6 NaCl-type structure. With cations of increasing polarizing power and increasingly readily polarized chalcogenide anions, the ionic RS structure gives way to the ZB and W types, in both of which the ions are in tetrahedral coordination (but different packing arrangement). Thus, the increasing covalency of many metals in the later transition-element groups affords chalcogenide structures with lower coordination numbers; for example, the monosulfides of Be, Zn, Cd, and Hg adopt the ZB structure, while those of Zn, Cd, and Mn adopt the W one; also, the sesquichalcogenides ($M_2X_3$) of main group III (13) metals have defect tetrahedral,
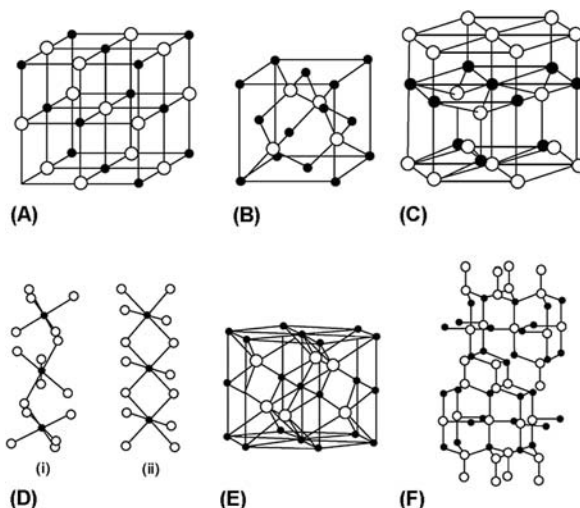
**Fig. 1.2** Crystal structures of the major sulfides (metal atoms are shown as *smaller* or *black* spheres): (**A**) galena (PbS) structure (rock salt); (**B**) sphalerite (ZnS) structure (zinc blende); (**C**) wurtzite (ZnS) structure; (**D**) pyrite structure and the linkage of metal–sulfur octahedra along the *c*-axis direction in (*i*) pyrite (FeS$_2$) and (*ii*) marcasite (FeS$_2$); (**E**) niccolite (NiAs) structure; (**F**) covellite (CuS) structure (layered). (Adapted from Vaughan DJ (2005) Sulphides. In Selley RC, Robin L, Cocks M, Plimer IR (eds.) Encyclopedia of Geology, MINERALS, Elsevier p 574 (doi:10.1016/B0-12-369396-9/00276-8))

mainly W, structures with various patterns of vacant lattice sites. When the bonding becomes more metallic, the 6:6 NiAs structure is observed, where the metal is now of octahedral coordination. This can be regarded as transitional between the RS structure and the more highly coordinated structures typical of pure metals. Most first row (3*d*) transition metal monochalcogenides MX (M = Ti, V, Cr, Fe, Co, Ni) come under this case. These compounds often contain vacancies at the metal site, so that the crystal becomes distorted owing to vacancy ordering which varies with temperature as well as composition. Their magnetic and electrical properties are generally complex and depend on the type of vacancy order.

Most transition elements react with chalcogen atoms to give dichalcogenides MX$_2$ with a precise 1:2 stoichiometry, crystallizing in either 2D or 3D structures, as originating from the competition between cationic *d* levels and anionic *sp* levels. The "2D" layered structures, which can be formulated as M$^{IV+}$(X$^{II-}$)$_2$, consist of sandwiched sheets of the X–M–X form, separated by a "van der Waals" gap between the X layers of adjacent sheets. Inside the sheets, the coordination of the metal ions is sixfold, either octahedral (as in the 1T polytype, which is more commonly denoted as the CdI$_2$ structure) or a body-centered trigonal prism (2H polytype) (Fig. 1.5). Note that the layered structures may be thought of as originating from vacancy ordering of the basic 3D types, in view of the fact that a defect NiAs structure in which every other plane of Ni atoms has been removed corresponds to the ideal 1T (CdI$_2$) arrangement.

| Li | Be |    |    | Octahedral |    |    | Trigonal Prismatic |    |    |    |    |    | B | C |
|----|----|----|----|----|----|----|----|----|----|----|----|----|----|----|
| Na | Mg |    |    |    |    |    |    |    |    |    |    |    | Al | Si |
| K  | Ca | Sc | Ti | V  | Cr | Mn | Fe | Co | Ni | Cu | Zn |    | Ga | Ge |
| Rb | Sr | Y  | Zr | Nb | Mo | Tc | Ru | Rh | Pd | Ag | Cd |    | In | Sn |
| Cs | Ba | La | Hf | Ta | W  | Re | Os | Ir | Pt | Au | Hg |    | Tl | Pb |

**Fig. 1.3** Elements forming layered sulfides or selenides with the metal in octahedral or trigonal prismatic coordination (niobium and tantalum are found in both). (Adapted from [35])

Two-thirds of the about 60 $MX_2$ compounds assume layered structures, found in particular for all the early transition metals of Groups 4–7 (with the exception of manganese) (Fig. 1.3). The non-layered $MX_2$ compounds assume a quite different structure motif and occur exclusively in Group VIII and beyond. Most of these materials are composed of infinite "3D" networks of metal atoms and discrete $X_2$ units with an X–X distance almost equal to that expected for an X–X single bond. Two structures of close similarity exist in this connection: pyrite (e.g., for the disulfides of Fe, Mn, Co, Ni, Cu, Ru, Os) and marcasite (known only for $FeS_2$ among the disulfides). Dichalcogenides of this type can be formulated, respectively, as $M^{II+}(X_2)^{II-}$ or $M^{I+}(X_2)^{I-}$. The marcasite structure (C18) is closely related to that of rutile (C4) adopted by many of the $MO_2$ oxides (e.g., $TiO_2$). In addition, a special 3D structure with half the anions present as $X_2$ pairs occurs, denoted as the $IrSe_2$ type. In the predominantly 3D region of the $d$-block compounds, one finds also the $PdS_2$ and $PdSe_2$ phases which exhibit a specific 2D arrangement owing to the special square coordination exerted by the palladium atom.

The layered transition metal dichalcogenides, although comprising a structurally and chemically well-defined family, display a number of remarkable characteristics, such as broad homogeneity ranges, order–disorder transitions, strong $d$–$p$ covalent mixing, and fast ionic diffusion. They cover actually a wide spectrum of electrical properties ranging from insulators like $HfS_2$, through semiconductors like $MoS_2$ and semi-metals like $WTe_2$ and $TcS_2$, to true metals like $NbS_2$ and $VSe_2$; they exhibit also intriguing magnetic and metal–insulator transitions, unusually high melting points, or superconductivity at high temperatures. In effect, this class of compounds has been most important in pioneering investigations on unusual electronic phenomena such as superconductivity, quantum size effects, and charge density waves (i.e., coupled fluctuations of electronic density and atomic positions along a conducting chain or layer). Moreover, their 2D nature is associated with a very rich intercalation chemistry with many potential applications. For an extensive description of the various arrangements and polytypes in the layered $MX_2$ phases, the reader should consult the reviews of Whittingham [35] and Rouxel [36].

Noteworthy also is the extensive compilation of early data on layered $MX_2$ given by Wilson and Yoffe [37], who worked out a group-by-group correlation of transmission spectra of the compounds to available electrical and structural data and produced band models in accord with a molecular orbital approach.

### 1.2.3 Ternary Compounds and Alloys

The ternary compounds of chalcogens with two different metal or metalloid constituents comprise several families and classes of materials. To quote but a single example, a major family of ternary chalcogenides with very interesting properties and applications is those having the $AB_2X_4$ stoichiometry (A, B = metal cations, X = S, Se, Te), of which several structural types have been identified, namely $Th_3P_4$, $CaFe_2O_4$, $K_2SO_4$, olivine, spinel, $Cr_3Se_4$, $Ag_2HgI_4$, $Yb_3S_4$, monoclinic types, $MnY_2S_4$, etc. [38]. In particular, chalcogenide spinels ($AB_2X_4$), such as the chalcochromites $MCr_2X_4$ (M = Ba, Cd, Co, Zn, Fe, Cu, Hg; also $CuCr_2S_3Se$, $CuCr_2S_{2.5}Se_{1.5}$); thiocobaltites $MCo_2S_4$ (M = Cu, Co); thiorhodites $M_xRh_{3-x}S_4$ (M = Cu, Co, Fe); thioaluminates $MAl_2S_4$ (M = Zn, Cr) [39], very often feature unusual combinations of magnetic, semiconducting, and optical properties.

Examples of known ternary (and quaternary) chalcogenide compounds, classified according to a formal valence combination scheme, are given in Table 1.4. These compounds were collected from a compilation of Madelung [40] regarding semiconductor materials. To be sure, numerous other systems exist. Some important ternary compounds or classes will be considered in the relevant sections of the present chapter.

Solid solutions are very common among structurally related compounds. Just as metallic elements of similar structure and atomic properties form alloys, certain chemical compounds can be combined to produce derivative solid solutions, which may permit realization of properties not found in either of the precursors. The combinations of binary compounds with common "anion" or common "cation" element, such as the "isovalent alloys" of IV–VI, III–V, II–VI, or I–VII members, are of considerable scientific and technological interest as their solid-state properties (e.g., electric and optical such as type of conductivity, current carrier density, band gap) modulate regularly over a wide range through variations in composition. A general descriptive scheme for such alloys is as follows [41].

Consider the ternary system $A_xB_{1-x}C$, having some range of mutual solid solubility for its binary constituents AC and BC at some composition and temperature range. Given that this system would be definitely observed to have a single phase with a structure denoted as α, it can be classified structurally into one of three possible types:

– If the binary constituents AC and BC both have the structure α as their stable form in the temperature range $\{T\}$, then the alloy is of "Type I" and one observes a single Bravais lattice of the type α at all alloy compositions for which solid

**Table 1.4**  Some ternary (and quaternary) semiconductor chalcogenides

| Formal valence combination | Examples |
|---|---|
| $I_x$–$III_y$–$VI_z$ | $ABX_2$ chalcopyrites (A = Cu, Ag; B = Al, Ga, In, Tl; X = S, Se, Te); $Cu_3In_5Se_9$, $Cu_3Ga_5Se_9$, $Ag_3In_5Se_9$, $Cu_2Ga_4Te_7$, $Cu_2In_4Te_7$, $CuIn_3Te_5$, $AgIn_3Te_5$, $AgIn_5Se_8$, $AgIn_9Te_{14}$, $AgIn_5Se_8$, $Cu_5TlSe_3$ |
| $I_x$–$IV_y$–$VI_z$ | $I_8$–IV–$VI_6$: $Ag_8GeS_6$, $Ag_8SnS_6$, $Ag_8SiSe_6$, $Ag_8GeSe_6$, $Ag_8SnSe_6$, $Ag_8GeTe_6$, $Cu_8GeS_6$; $I_4$–$IV_3$–$VI_5$: $Cu_4Ge_3S_5$, $Cu_4Ge_3Se_5$, $Cu_4Sn_3Se_5$; $Cu_4SnS_4$, $Ag_3Ge_8Se_9$ |
| $I_x$–$V_y$–$VI_z$ | $A_3BX_3$, $ABX_2$, and ABX (A = Cu, Ag; B = As, Sb, Bi; X = S or Se) |
| $II_x$–$III_y$–$VI_z$ | $II$–$III_2$–$VI_4$: $ZnIn_2X_4$, $CdGa_2X_4$, $CdIn_2X_4$, $CdTl_2X_4$, $HgGa_2X_4$ (ordered vacancy compounds); $II$–$III$–$VI_2$: $ZnTlX_2$, $CdInX_2$, $CdTlX_2$, $HgTlX_2$; $Zn_2In_2S_5$, $Zn_3In_2S_6$, $Hg_5Ga_2Te_8$, $Hg_3In_2Te_6$ (ordered vacancy compounds) |
| $II_x$–$V_y$–$VI_z$ | $Hg_3PS_3$, $Hg_3PS_4$ |
| $III_x$–$V_y$–$VI_z$ | $TlAsX_2$, $TlBiX_2$, $Ga_6Sb_5Te$, $In_6Sb_5Te$, $In_7SbTe_6$ |
| $IV_x$–$V_y$–$VI_z$ | $Sn_2P_2S_6$, $PbSb_2S_4$, $GeSb_2Te_4$, $GeBi_2Te_4$, $GeSb_4Te_7$, $GeBi_4Te_7$, $PbBi_4Te_7$ |
| $IV_x$–$V_y$–$VI_z$ | $PbNb_2S_5$, $PbNb_2Se_5$, $PbNbS_3$, $SnNb_2Se_5$, $SnVSe_3$ |
| $I_2$–II–IV–$VI_4$ | $Cu_2ZnSiS_4$, $Cu_2ZnSiSe_4$, $Cu_2ZnGeS_4$, $Cu_2ZnGeSe_4$ (44 compounds of the type) |
| I–III–IV–$VI_4$ | $CuAlGeSe_4$, $CuAlSnSe_4$, $CuGaGeSe_4$, $CuGaSnSe_4$, $CuInGeSe_4$, $CuInSnSe_4$; $AgAlGeSe_4$, $AgAlSnSe_4$, $AgGaGeSe_4$, $AgGaSnSe_4$, $AgInGeSe_4$, $AgInSnSe_4$ |

solubility exists. Actually, such is the case for the vast majority of the isovalent, "pseudobinary" IV–VI, III–V, II–VI, and I–VII alloys which, despite substitutional disorder or tendencies to order, retain in solution their diamond-like, zinc blende, wurtzite, and rock salt "substructures," respectively.

–  An alloy is said to be of "Type II" if neither the AC nor the BC component has the structure α as its stable crystal form at the temperature range $\{T\}$. Instead, another phase (β) is stable at $\{T\}$, whereas the α-phase does exist in the phase diagram of the constituents at some different temperature range. It then appears that the alloy environment stabilizes the high-temperature phase of the constituent binary systems. Type II alloys exhibit a α ⇌ β phase transition at some critical composition $x_c$, which generally depends on the preparation conditions and temperature. Correspondingly, the alloy properties (e.g., lattice constant, band gaps) often show a derivative discontinuity at $x_c$.

–  If neither the AC nor the BC component exhibits in any part of its (zero pressure) $(x, T)$ phase diagram the structure α, which though exists in their solid solution, then the latter is of "Type III". In this case, the alloy environment stabilizes a structure which is fundamentally new to at least one of its components. Such alloy-stabilized phases with no counterpart in the phase diagram of the constituent components can be formed in bulk equilibrium growth and may be distinguished from the unusual alloy phases that are known to form in extreme non-equilibrium growth methods and in epitaxial forms.

Pseudobinary II–VI systems or ternaries containing manganese will be discussed in the respective sections.

### 1.2.4 Intercalation Phases

The concept of tailoring the properties of materials by intercalating guest species in a host crystal is not only of major academic interest because of the intriguing structural and electric properties of the as-formed intercalation phases, but also of technological significance in various fields including battery and sensor development (Chap. 6). Chalcogenide hosts are usually adequately conductive, so that the extent of intercalation of ionic species is affected and can be controlled by oxidation/reduction of the host lattice, conveniently carried out by electrochemical charge transfer.

The 2D layered structures of Group 4–6 transition metal dichalcogenides $MX_2$ (M = Ti, Zr, Hf, Nb, Ta, Mo, W) as well as of the ternary alkali metal/$3d$-metal systems $AMX_2$ (A = alkali metal; M = Ti, V, Cr, Mn, Fe, Co, Ni) are capable of intercalating various guest species. The most well investigated is the intercalation of alkali metals (A) to dichalcogenide hosts, resulting in the formation of $A_xMX_2$ phases ($0 < x \leq 1$; M = Ti, Zr, Hf, V, Nb, Ta, Mo, W; X = mainly S, Se), which, in effect, have served for fundamental studies of the intercalation-induced structural changes and charge transfer. Transition metal derivatives of layered sulfides and selenides are also known, forming intercalates of the type $M'_xMX_2$ (M' = $3d$ transition metal, M = Nb, Ta; X = S, Se). Interestingly, ditellurides form metal-rich layer compounds rather than intercalation phases, such as $MM'Te_2$ (M' = Fe, Co, Ni; M = Nb, Ta), stabilized by strong bonding interactions between early and late transition metals (see Sect. 1.2.7.5 for Group VA). Intercalation processes regard also 3D lattices, i.e., the Chevrel phases $M_xMo_6X_8$ (intercalation into intersecting channels – Sect. 1.2.7.6 for Group VIA), $Nb_3X_4$ (X = S, Se), $A_xTi_3S_4$, $Tl_xV_3S_4$ (intercalation into tunnels), as well as 1D structures, i.e., $MX_3$ (M = Ti, Zr, Hf; X = S, Se), $AFeS_2$ (A = Na to Cs), $AMo_3X_3$ (A = alkali metal; X = S, Se) [28, 42–44].

Of special interest to intercalation studies are complex non-stoichiometric systems, such as the so-called "misfit" layer chalcogenides that were first synthesized in the 1960s [45]. Typically, the "misfit compounds" present an asymmetry along the $c$-axis, evidencing an inclination of the unit cell in this direction, due to lattice mismatch in, say, the $b$-axis; therefore these solids prefer to fold and/or adopt a hollow-fiber structure, crystallizing in either platelet form or as hollow whiskers. One of the first studied examples of such a misfit compound has been the kaolinite mineral.

### 1.2.5 Chalcogenide Glasses

The unique features of chalcogenide glasses (Chap. 6), such as quasi-stability, photoconductivity, infrared transparency, non-linear optical properties, and ionic

conduction, have led to a wealth of applications, several of which are commercially available or practically utilized [46].

By quasi-stability (or bi-stability) it is meant that these materials undergo an easily reversible thermally driven change from amorphous to crystalline phase, a phenomenon that can be exploited for electrical or optical switching purposes or for encoding binary information. Electrical switching in chalcogenide semiconductors came to prominence in the 1960s, when the amorphous $Te_{48}As_{30}Si_{12}Ge_{10}$ system was found to display sharp, reversible transitions in electrical resistance above a threshold voltage, upon bias [47]. Local switching by optical means is already of great commercial significance in erasable high-density optical memories (CD-RWs) utilizing semiconductor lasers and chalcogenides such as GeSbTe in the form of films with a thickness of $\sim$15 nm. In these systems, data writing is done by means of laser light heating and data reading by measuring the difference in reflectivity of the laser light from each of the two phases. The reversibility of the transition between the amorphous and crystalline states is remarkable and has been shown to be stable over $10^{12}$ repeated read–write cycles. Alternatively, bringing on the amorphous–crystalline transformation by electrical means forms the basis of phase-change random-access memory (PC-RAM), which operates much as the flash memory and magnetoresistive RAM (MRAM), as far as the electrodes are concerned, except that the memory bit cell consists of a bi-stable chalcogenide material. The phase change of CeSbTe glasses is accompanied by several orders of magnitude change in conductivity, thus providing a high reading signal-to-noise ratio [48].

On account of their photoconductive properties, chalcogenides glasses are used in applications such as photoreceptors in copying machines and X-ray imaging plates. Regarding purely optical applications, they are utilized for IR optical components such as lenses and windows and also IR-transmitting optical fibers. Chalcogenide fibers incorporating rare-earth ions, such as $Er^{3+}$, have been considered promising for optical amplifier applications.

As exhibiting significant ionic conductivities, chalcogenide glasses are utilized for the fabrication of high-sensitivity ionic sensors. In this connection, lithium-containing glasses have been investigated as solid-state electrolytes in all-solid-state batteries. Ionic transport in such materials can be useful also for data storage; a functional solid electrolyte consisting of crystalline metallic islands of $Ag_2Se$ dispersed in an amorphous semiconducting matrix of $Ge_2Se_3$ was described recently [49]. Technologies exploiting phase-change and electrolytic chalcogenide devices are evolving convergently. Both technologies present exciting opportunities that are not restricted to memory applications, but include cognitive computing and reconfigurable logic circuits [49].

### 1.2.6 Materials Synthesis

Various microstructures and configurations are possible for useful solid materials, including bulk single crystals and epitaxial layers, polycrystalline articles or thin films with controlled grain size (including micro- and nanocrystalline

phases), amorphous materials, composites, structured materials (e.g., multilayers, superlattices), hybrids, and combinations thereof. Synthetic methods available for solid-state chemistry include the conventional direct combination high-temperature techniques, synthesis from fluxes and melts, vacuum/high-temperature deposition from gas phase, hydrothermal synthesis, and synthesis from solutions. Emerging approaches include synthesis of alloys from suspensions of pre-formed metal nanoparticles, synthesis of extended frameworks by directed assembly of large molecular building blocks, low-temperature synthesis of nanostructured metal oxides and chalcogenides, salt-inclusion synthesis, and a range of preparation techniques for porous materials [50].

Traditional solid-state synthesis involves the direct reaction of stoichiometric quantities of pure elements and precursors in the solid state, at relatively high temperatures (ca. 1,000 °C). Briefly, reactants are measured out in a specific ratio, ground together, pressed into a pellet, and heated in order to facilitate interdiffusion and compound formation. The products are often in powdery and multiphase form, and prolonged annealing is necessary in order to manufacture larger crystals and pure end-products. In this manner, thermodynamically stable products under the reaction conditions are obtained, while rational design of desired products is limited, as little, if any, control is possible over the formation of metastable intermediates.[5]

Direct combination of chalcogen elements with most metals at temperatures 400–1,000 °C in the absence of air leads to the formation of MCh phases. For example, binary II–VI and IV–VI chalcogenides such as the selenides and tellurides of Cd, Hg, Pb, Sn, and Ge may be effectively prepared by mixing the elements in a quartz ampoule and heating to a temperature little above the melting point of the compound, in a rocking furnace. After reaction (for several hours) the ampoule is either quenched (giving amorphous phases) or slowly cooled to room temperature. Post-annealing of the product for 1–2 weeks under high vacuum without melting is usually required for the completion of the reactions. The nature of the products for a given reaction usually depends on the ratios of reactants, the temperature of the reaction, and other conditions.

Low-temperature solid-state synthesis is preferred in most cases, where appropriate, for obvious reasons such as energy and cost economy and process safety or for critical concerns regarding the accessibility of compounds that are stable only at low temperatures or non-equilibrium phases, i.e., compounds thermodynamically unstable with respect to the obtained phase (e.g., a ternary instead of binary phase). The use of low-temperature eutectics as solvents for the reactants, hydrothermal growth

---

[5] The mechanism of these reactions is generally not considered, unlike the reactions lying in the realm of molecular chemistry, i.e., organic reactions, where kinetic control over intermediate and product species allows for recognizing details of the mechanism, that is, of the structure of functional groups present in a molecule. Note also that with organic reactions the true thermodynamic minimum for a particular combination of elements is usually irrelevant. (Stein A, Keller SW, Mallouk TE (1993) Turning down the heat: Design and mechanism in solid-state synthesis. Science 259: 1558–1564.)

**Fig. 1.4** SEM images of caved cuboctahedral hexagonal copper sulfide (CuS covellite) crystals, synthesized by a solvothermal process in ethylene glycol, at 140 °C. (Reprinted in gray scale with permission from [52]. Copyright 2009, American Chemical Society)
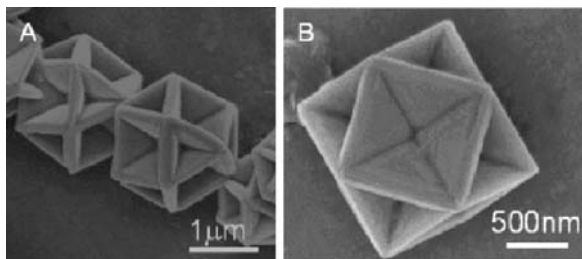


conditions, and solution growth are possible routes to accomplish a range of possibilities in materials synthesis. Much effort has been put during the last years toward solvothermal synthesis of MChs. In a typical process, a metal and/or a metallic salt is heated in a solvent (benzene, toluene, pyridine, ethylenediamine, water, etc.) at 100–200 °C in the presence of an excess of chalcogen (e.g., [51]). An astonishing example of obtaining well-defined cuboctahedral crystals of copper sulfide by a solution reaction in ethylene glycol [52] is shown in Fig. 1.4.

Many inorganic materials having vital roles in advanced technologies are prepared in the form of thin films. Methods of thin film preparation/processing can be divided into *dry processes* carried out in gas phase and *wet processes* carried out in liquid phase. The first group includes techniques such as vacuum evaporation, chemical vapor deposition (CVD), molecular beam epitaxy (MBE), and sputtering. These gas-phase techniques require high vacuum and/or temperature and have the advantages of high controllability in film growth and the feasibility to obtain a pure material, since one can simply exclude the unwanted chemical species from the system. A fine control of the growth process is possible due to many tunable variables, such as substrate conditions and gas pressure. Shortcomings are the high energy needed for the film processing, along with emission of gaseous waste materials [53].

Electrodeposition, anodization, electroconversion, electrophoresis, electroless deposition, spray pyrolysis, dip growth, and chemical bath deposition comprise some of the wet growth techniques, which are rather indispensable when it comes to the deposition/growth of large-area thin films, as dictated by considerations of simplicity, economics, and input energy. In particular, such processes implemented in water have the highest advantages in suppressing cost and environmental impact [54, 55]. Wet processes at low/ambient temperature and pressure are elegantly called *soft-solution processing* (SSP) techniques. They are found to be most appropriate when the alteration of the substrate must be avoided or limited to the surface, as in the formation of buffer layers on a photoactive material in solar cell applications.

Metal chalcogenides, apart from their technological significance in industrial applications, have played an important role in the development of new synthetic concepts and methods in the area of solid-state chemistry. A great example is alkali metal intercalation into $TiS_2$ (Chap. 6) first reported three decades ago, which highlighted the then-novel synthetic approach called "soft chemistry" (*chimie douce*). This low-temperature process allows for new compounds to be obtained while retaining the structural framework of the precursor. Related to this concept is the

reactive flux method that has proven to be widely applicable to the preparation of multinary MChs, especially low-dimensional polychalcogenides with unprecedented structures [56]. We should underscore finally the developing approaches for low-temperature synthesis of MChs in small length (nanometric) scales, which have proved quite fruitful [57].

### *1.2.7 An Account of the Periodic Table*

#### 1.2.7.1  Group IA (1). Lithium, Sodium, Potassium, Rubidium, Cesium

The alkali metals (A) react directly with sulfur at moderate temperatures in the absence of air to form compounds of formula $A_2S_n$ ($n = 1, 2, 3, 4, 5,$ or 6). The bonding in these sulfides is generally complex, and the polysulfide ions are present in the crystal lattice as zigzag chains. The higher sulfides are more conveniently prepared by reaction of the elements in anhydrous liquid ammonia. Similar alkali metal polyselenides, $A_2Se_n$, have been made by dissolving selenium in aqueous alkali metal selenide or by reacting the metal with an excess of selenium in anhydrous liquid ammonia. Analogous polytellurides exist, while alkali metal hydrogen sulfides and selenides, AHX, are also known. All of these compounds are, however, rather unstable and are readily oxidized in air.

The dialkali compounds $A_2X$ (A = Li to Rb; X = S, Se, Te) adopt, under normal conditions, the anti-fluorite structure (4:8 coordination), where the alkali metal ions occupy the F positions and the chalcogen ions the Ca positions of a fluorite cell. The $Cs_2X$ compounds crystallize in an anti-$PbCl_2$ type structure (the oxide, $Cs_2O$, assumes the anti-$CdCl_2$ type). $Rb_2Te$ is an exception within the dialkali monochalcogenides, as it can exist in two modifications at room temperature: a metastable one of the anti-$CaF_2$ type and a stable anti-cotunnite type, while there exist also further polymorphic high-temperature phases [58]. The anti-$CaF_2$ type $A_2X$ compounds have large lattice spacing due to their large ionic radius of cations and many of them are wide-band gap semiconductors with transparency.

All the dialkali monosulfides are soluble in water and give alkaline solutions. The tellurides are instantly decomposed by air. They are soluble in water, but the solutions are easily oxidized to red polytellurides. The alkali metal tellurides are strong reducing agents which reduce tellurites to metallic tellurium.

Tellurium-rich alkali metal tellurides are quite interesting novel chalcogenides with remarkable structural and transport properties. These materials have a tendency to contain defective square planar tellurium lattices as part of their structures and encompass a low-dimensional metallic nature. Notable are the recently synthesized cesium tellurides $Cs_3Te_{22}$, $Cs_4Te_{28}$, and $Cs_2Te_{13}$ [59]. The discovery of the cyclo-$Te_8$ octatellurium ring in the solid-state structure of $Cs_3T_{22}$ has been an important landmark in polychalcogenide chemistry. The $Te_8$ "molecule", the stability of which has been debated by chemists for a long time, completes the chalcogen series $S_8$, $Se_8$, and $Te_8$; this tellurium derivative has the expected puckered ring structure even though it is rather not a true allotrope since it coexists with other components in $Cs_3T_{22}$ and related materials.

Most commonly available alkali metal chalcogenides[6]:

Lithium sulfide, $Li_2S$; sodium selenide, $Na_2Se$; sodium sulfide, $Na_2S$; sodium hydrogen sulfide dihydrate, $NaHS \cdot 2H_2O$; sodium sulfide nonahydrate, $Na_2S \cdot 9H_2O$; sodium sulfide pentahydrate, $Na_2S \cdot 5H_2O$; potassium selenide, $K_2Se$; potassium sulfide, $K_2S$; potassium hydrogen sulfide, $KHS$; potassium hydrogen sulfide hemihydrate, $KHS \cdot 1/2H_2O$; potassium sulfide pentahydrate, $K_2S \cdot 5H_2O$; rubidium selenide, $Rb_2Se$; rubidium sulfide, $Rb_2S$.

### 1.2.7.2  Group IIA (2). Beryllium, Magnesium, Calcium, Strontium, Barium

The monosulfides of the alkaline earth metals crystallize in the rock salt (MgS, CaS, SrS, BaS) and zinc blende (BeS) structures. BaS is insoluble in water, while the other monosulfides are sparingly soluble but hydrolyzed on warming (except MgS that is completely hydrolyzed). The monoselenides are isomorphous to the sulfides. The monotellurides CaTe, SrTe, BaTe adopt the rock salt structure, while BeTe has the zinc blende and MgTe the wurtzite structure. Alkaline earth polysulfides may be prepared by boiling a solution or suspension of the metal hydroxide with sulfur, e.g.,

$$3Ca(OH)_2 + 12S \rightleftarrows 2CaS_5 + CaS_2O_3 + 3H_2O$$

Beryllium chalcogenides BeX (X = S, Se, Te) are covalent compounds that have similar structure and bonding with the Group III–IV semiconductors (in particular with the boron compounds BN, BP, BAs, and BSb). They present large band gaps (2.7–5.5 eV), and are potentially attractive materials for semiconductor–insulator applications such as blue-green laser diodes and laser-emitting diodes. The lattice constants of BeSe and BeTe are close to those of GaAs and ZnSe.

Most commonly available alkaline earth metal chalcogenides[7]:

Beryllium sulfide, BeS; beryllium selenide, BeSe; beryllium telluride, BeTe; beryllium polonide, BePo; magnesium sulfide, MgS; magnesium selenide, MgSe; magnesium telluride, MgTe; calcium sulfide, CaS (oldhamite); calcium selenide, CaSe; calcium telluride, CaTe; strontium sulfide, SrS; strontium selenide, SrSe; barium sulfide, BaS; barium selenide, BaSe; barium hydrosulfide, $Ba(HS)_2$; barium hydrosulfide tetrahydrate, $Ba(HS)_2 – 4H_2O$.

### 1.2.7.3  Group IIIA (3). Scandium, Yttrium, Lanthanoids, Actinoids

The rare earth elements (R) are those from atomic numbers 57–71, emanating as a particular series from the parent element lanthanum (atomic no. 57). The set of 14 elements from cerium (58) through lutetium (71) inclusive are commonly known as the lanthanoid (or lanthanide; Ln) series. The rare earths form a bridge at the

---

[6] As listed in MatWeb database: http://www.matweb.com/search/MaterialGroupSearch.aspx. Mineral names and corresponding exact or empirical formulas of the substances are given, as found.

[7] Ibid., p. 29.

sixth period between the very reactive metallic elements Cs and Ba and the transition element series beginning with hafnium (Hf). They represent the largest group of chemically similar elements, but their physical properties differ markedly due to subtle features of electronic structure. Because of the similarity between all of the R elements, their separation and recovery in pure form have been extremely difficult. The *d* transition metal elements yttrium and scandium are sometimes included in the group of R elements; in fact, there are adequate reasons to consider Y as a rare earth, but the inclusion of Sc is less common and more controversial [60].

The rare earth elements form chalcogenides of stoichiometry similar to those of the oxides (e.g., $RX_2$, $R_2X_3$, $R_3X_4$, and RX); however, these materials are very different from the oxides and cannot be treated by using the same concepts, due to *mixed valence* effects. In general, binary and ternary rare earth chalcogenides adopt a wide range of structure types and display a variety of physical properties, having potential applications as semiconducting, luminescent, magneto-optical materials, and infrared windows.

Most monochalcogenides of the Group 3 metals adopt the rock salt (NaCl) structure. Note that the crystal chemistry of divalent europium is very similar to that of the alkaline earths, particularly strontium, as the radius of $Eu^{2+}$ is almost the same as that of $Sr^{2+}$. For the Yb compounds, the cell dimensions are practically identical with those of the Ca compounds.

The sesquichalcogenides $R_2X_3$ (X = S, Se, Te) crystallize in many modifications (α, β, γ, δ, η, ε). The most common is the high-temperature γ modification which has a cubic $Th_3P_4$-type structure. The $Ln_2X_3$ compounds (Ln = La to Gd) crystallize principally in a defect-type $Th_3P_4$ structure involving a random arrangement of metal atoms in the 8-coordinate positions, of which $Ce_2S_3$ is a well-known example. $Ce_3S_4$ assumes a closely related structure, differing with respect to Ce vacancies, as all the metal positions are occupied. Interestingly, the cubic cell dimension of cerium sulfides decreases with increase in metal content, i.e., from $Ce_2S_3$ to $Ce_3S_4$, presumably due to additional metallic bonding or a change in type of bonding, from ionic in the red $Ce_2S_3$ to metallic in the gray-black $Ce_3S_4$. In general, increasing the metal content from the stoichiometric $R_2X_3$ changes the material from an insulator or semiconductor to a semimetal and finally to a metallic substance. Thus, stoichiometric compounds $Ln_2X_3$ are wide gap semiconductors with a wide transparency range and high refraction. Increasing the metal content leads to superconductivity in the $LaS_{1.5}$ to $LaS_{1.33}$ system and magnetic ordering in most of the remaining rare-earth systems which have an unfilled 4*f* subshell.

An unusual variety of metal-rich chalcogenides is found among the earliest transition metals. Scandium and yttrium as well as their heavier 4*f* analogues (lanthanides) have been recent sources of a number of new metal-rich chalcogenide structures, such as the telluride $Sc_2Te$, featuring chain or puckered sheet aggregates of metal atoms that are separated by a layer of individual chalcogenide atoms; or $Sc_8Te_3$, containing two types of complex-puckered metal sheets separated by chalcogenide anions. The known structures can be divided into two groups: (1) those unique (so far) to Sc, Y, etc., and (2) those for which an electron-richer isotype is also stable for a group IVA metal, Ti or Zr especially [61].

From the immense variety of the known ternary rare earth chalcogenides we may refer first to A:R:X systems containing heavy alkali metals (A = K, Rb, Cs; R = Sc, Y, La, Ce to Lu; X = S, Se, Te) with different molar ratios of the three components. The $ARX_2$ compounds with α-$NaFeO_2$ or β-$RbScO_2$ type trigonal or hexagonal layered structures feature octahedral coordination for the $R^{3+}$ cations and octahedral (α-$NaFeO_2$ type) or trigonal prismatic coordination (β-$RbScO_2$ type) for the $A^+$ cations. A large $R^{3+}$ variety for $A_3R_7X_{12}$-type compounds of the $Cs_3Y_7Se_{12}$-type structure can be found, having poorer alkali metal composition A:R:X = $1:2\frac{1}{3}:4$ with A = K, Rb, Cs and X = S, Se, Te; also, the even smaller ratio of A:R:X = 1:3:5 is reported, represented so far only by the selenide compound $CsEr_3Se_5$. The structures of these compounds consist of edge- and vertex-sharing $[RX_6]^{9-}$ octahedra frameworks, just like the layered $ARX_2$ phases that provide channels to take up the $A^+$ cations. For the $A_3R_7X_{12}$-type compounds, "triple" channels are present able to accommodate three $A^+$ cations at a time, while $CsEr_3Se_5$ displays "double" channels able to incorporate two of them. Analogous "single" channel A:R:X = 1:5:8 structures were found recently to be represented by the $RbSc_5Te_8$ telluride [62].

We note also ternary alkaline earth materials suitable for high-temperature thermoelectric applications, such as

– the lanthanide sulfides $La_{3-x}A_xS_4$ (A = Ca, Ba; $x$ = 0–0.8) crystallizing in a $Th_3P_4$-type structure [63];
– the recently characterized $BaR_2Te_4$ telluride series (R = Y, Sm to Tm), crystallizing in the calcium ferrite type $CaFe_2O_4$, i.e., a 3D network of edge- and corner-sharing $RTe_6$ octahedra;
– the newly discovered $SrSc_2Te_4$ and $BaSc_2Te_4$, which comprise electron-precise materials exhibiting band gaps 0.1 and 0.2 eV, respectively [64].

Finally, known are the lanthanide-ytterbium series $LnYbX_3$ (Ln = La, Ce, Pr, Nd, and Sm); the lanthanide chalcogenides with group IVB elements $Ln_2QX_5$ (Q = Ge, Sn); and the IA- or IIB-metal rare earth systems: $Cu_3RX_3$, $Cu_5RX_4$, $ZnR_2X_4$, $CdR_2X_4$ (R = Sc, Y, La, Pr, Sm, Gd, Tb to Lu).

Quaternary chalcogenides of the type A:Ln:M:X, containing three metal elements from different blocks of the Periodic Table (A is an alkali or alkaline earth metal, Ln is an *f*-block lanthanide or scandium, M is a *p*-block main group or a *d*-block transition metal, and X is S or Se) are also known [65].

The *actinoid elements* (or actinides; An) constitute a series of 14 elements which are formed by the progressive filling of the 5*f* electron shell and follow actinium in the periodic table (atomic numbers 90–103). All of the isotopes of the actinide elements are radioactive and only four of the primordial isotopes, $^{232}$Th, $^{235}$U, $^{238}$U, and $^{244}$Pu, have a sufficient long half-life for there to be any of these left in nature.

The structural chemistry of the actinides is often similar to that of lighter transition metals, such as Zr and Hf, and to that of the lanthanides; however, the diffuse nature of the 5*f* orbitals leads to some differences and specifically to interesting magnetic and electrical properties. The actinide sulfides are generally isostructural with the selenides, but not with the analogous tellurides. The binary chalcogenides of uranium and thorium have been discussed in detail [66], but the structural

chemistry of the transuranium element chalcogenides is far less developed. The monosulfides adopt defect NaCl structures (uranium monosulfide, US, is referred to as simple cubic rather than fcc), without being, however, simple ionic crystals. The sesquisulfides of Th, U, and Np have the $Sb_2S_3$ (chain) structure, while those of Ac, Pu, and Am have structures closely related to that of $Th_3P_4$.

Semimetallic behavior and non-stoichiometry are observed for the actinide chalcogenides; the ionic, NaCl-type, AnX as well as the tetragonal $UX_2$ and UXY compounds (with X and Y being elements of Group 15 or 16) are good conductors of heat and electricity, due to a partially filled conduction band. Further, $An_3X_4$ compounds (with bcc structures) are known to be metallic [67]. A few ternary actinide systems have been studied. The perovskite structure is the type adopted by ternary uranium sulfides and selenides of the formula $ABX_3$. Uranium compounds of this stoichiometry are known for Sc, V to Ni, Pd, Ru, Rh, and Ba. Thorium compounds are known for Cr, Fe, and Mn. No telluride analogues have been reported.

Most commonly available Group 3–16 binary chalcogenides[8]:

Scandium sulfide, $Sc_2S_3$; scandium selenide, $Sc_2Se_3$; scandium telluride, $Sc_2Te_3$; yttrium sulfide, $Y_2S_3$; lanthanum sulfide, $La_2S_3$; lanthanum sulfide, LaS; cerium(III) sulfide, $Ce_2S_3$; cerium(II) sulfide, CeS; praseodymium sulfide, $Pr_2S_3$; praseodymium telluride, $Pr_2Te_3$; neodymium sulfide, $Nd_2S_3$; neodymium telluride, $Nd_2Te_3$; samarium(III) sulfide, $Sm_2S_3$; samarium(III) telluride, $Sm_2Te_3$; europium(II) sulfide, EuS; europium(II) selenide, EuSe; europium(II) telluride, EuTe; gadolinium(III) sulfide, $Gd_2S_3$; gadolinium selenide, GdSe; gadolinium(III) telluride, $Gd_2Te_3$; terbium sulfide, $Tb_2S_3$; dysprosium(III) sulfide, $Dy_2S_3$; holmium sulfide, $Ho_2S_3$; erbium sulfide, $Er_2S_3$; erbium telluride, $Er_2Te_3$; thulium sulfide, $Tm_2S_3$; ytterbium sulfide, $Yb_2S_3$; lutetium sulfide, $Lu_2S_3$; lutetium telluride, $Lu_2Te_3$; thorium selenide, $ThSe_2$; thorium sulfide, $ThS_2$.

### 1.2.7.4 Group IVA (4). Titanium, Zirconium, Hafnium

The early transition metals (Groups 4 and 5) form a wide variety of binary chalcogenides, which frequently differ in both stoichiometry and structure from the respective oxides. All the Group 4 dichalcogenides, $MX_2$, occur in layered $CdI_2$-type structures (1T stacking polytype). $TiS_2$, $TiSe_2$, $TiTe_2$, $ZrTe_2$, and $HfTe_2$ compounds may be roughly classified as metallic materials due to an overlap of the chalcogenide $s$ and $p$ states with the metal $d$ states, whereas $ZrS_2$, $ZrSe_2$, $HfS_2$, and $HfSe_2$ are more ionic in nature [68].

Titanium monosulfide, TiS, assumes two forms, both of which are of the NiAs type. In $Ti_3S_4$, the packing of sulfur is of the *ABAC* type, with alternate layers of metal sites being fully occupied but the intermediate sites half filled. A series of intermediate phases $Ti_{2+x}S_4$ ($0.2 < x < 1$) also occurs. The trisulfide $TiS_3$ is best represented as $TiS^{2-}(S_2)^{2-}$. The trichalcogenides of Group IVA elements are typified

---

[8] Ibid., p. 29.

by $ZrSe_3$, which exhibits a monoclinic structure consisting of chains of trigonal prismatic $[ZrSe_6]$ units sharing opposite faces and has semiconducting properties.

In the titanium–selenium system, various stoichiometries such as $Ti_2Se$, $Ti_3Se$, $TiSe_{0.95}$, $TiSe_{1.05}$, $Ti_{0.9}Se$, $Ti_3Se_4$, $Ti_{0.7}Se$, $Ti_5Se_8$, $TiSe_2$, and $TiSe_3$ have been identified. A variety of phases are known also for the titanium–tellurium system, including the compounds $Ti_5Te_4$, $Ti_3Te_4$, $Ti_2Te_3$, $Ti_5Te_8$ (and $TiTe_2$) [69]. Three-dimensional bonded metal arrays are found in the isotypic $Ti_8S_3$ and $Ti_8Se_3$.

In the hafnium–tellurium system, the Te-rich $HfTe_5$, $HfTe_3$, and $HfTe_2$ phases have been identified, as also the Hf-rich $Hf_3Te_2$ with a layered structure that is topologically related to the bcc high-temperature modification of elemental hafnium. The most reduced telluride of the system, i.e., $Hf_2Te$, is a high-temperature phase with a structure isotypic to $Nb_2Se$. It transforms in the solid state into $Hf_3Te_2$ and a solid solution $Hf_{1-x}Te_x$ [70].

The elements Zr and Hf are generally more similar in their chemistry than any other pair of congeneric elements as having nearly identical atomic or ionic radii, electronegativities, and elemental structures (actually, the similarities of Nb and Ta are nearly as close); however, their metal-rich chemistry is often surprising in its structural and physical aspects with fairly sharp distinctions emerging between the two elements [71].

Most commonly available 4–16 binary chalcogenides[9]:

Titanium(II) sulfide, TiS; titanium(III) sulfide, $Ti_2S_3$; titanium(IV) sulfide, $TiS_2$; zirconium sulfide, $ZrS_2$; hafnium selenide, $HfSe_2$; hafnium sulfide, $HfS_2$.

### 1.2.7.5 Group VA (5). Vanadium, Niobium, Tantalum

A plethora of stoichiometries and structural types are found for the chalcogen compounds of the Group 5 metals. Phases approximating to the composition MX have the NiAs-type structure, whereas the $MX_2$ compounds have layer structures related to $MoS_2$, $CdI_2$, or $CdCl_2$ types. Sometimes complex layer sequences occur in which the 6-coordinate metal atom is alternatively octahedral and trigonal prismatic.

The vanadium–chalcogen system comprises metal-rich ($V_3S$, $V_2Se$, $V_5Te_4$) and chalcogen-rich ($VS_4$, $VSe_2$, $VTe_2$) compositions. Many of the relevant compounds exist over wide ranges of composition, on account of the close relation between the NiAs and $CdI_2$ structure types they adopt. Low dimensionality is a common feature of many niobium and tantalum chalcogenides, such as the binary compounds $MX_2$ (M = Nb, Ta; X = S, Se, Te), $MX_3$ (X = S, Se), $MTe_4$, $Nb_3X_4$ (X = S, Se, Te), and $Ta_2X$ (X = S, Se). The dichalcogenides adopt layer structures, whereas chain arrangements are found in tri- and tetrachalcogenides. In the latter case, only telluride chains exist independently; selenide chains have to be stabilized by counter-ions or -chains [72]. The same effect is observed in $NbSe_3$ and $TaSe_3$, which have structures similar to the analogous Group IVA compounds ($ZrSe_3$), but

---

[9] Ibid., p. 29.

the planes of connected chains are somewhat puckered, due to some Se–Se bonding between chains as well as intra-chain diselenide formation.

Particularly spectacular is the metal-rich chemistry of Nb and Ta chalcogenides. Metal-rich compositions, such as the tantalum systems $Ta_6S$, $Ta_2S$, $Ta_3S_2$, $Ta_2Se$, $Ta_6Te_5$, $Ta_2Te_3$, assume unique structures, often departing largely from the sandwich sequence of typical layered solids. For example, the metal frameworks of $Ta_2S$ and $Ta_6S$ consist of distorted, centered $Ta_{13}$ icosahedra, which extend along a "fivefold axis of symmetry" to form chains; or $Ta_2Se$ and the structurally similar ternary compounds $Ta_2(S,Se)$, $Ta_2(Se,Te)$ represent quasi-2D solids, where the layers of metal and chalcogen atoms are arranged in the same way as in the structure of bcc tantalum.

Most of the considered phases exhibit metallic conductivity; magnetic properties range from diamagnetic (e.g., $VS_4$), through paramagnetic (VS, $V_2S_3$), to antiferromagnetic ($V_7S_8$). All the Nb and Ta materials, whether distorted or not, are superconducting, and the truly metallic ones also show band-antiferromagnetism below about 150 K.

Several ternary phases occur, others exhibiting 3D structures (like $BaVS_3$, $BaTaS_3$) and others containing discrete tetrahedral anions, such as the $[VS_4]^{3-}$ unit in $M_3VS_4$ (M = Na, K, Tl, $NH_4$).

Strongly intermetallic bonding in early–late transition metal chalcogenides leads to the formation of an expanding class of ternary compounds with remarkable structural and electronic properties. The considered phases comprise $NbMTe_2$, $TaMTe_2$, $M_2Ta_9S_6$, $M_2Ta_{11}Se_8$ (M = Fe, Co, Ni); $NbMTe_5$ (M = Ni, Pd); $TaMTe_5$ (M = Ni, Pt); $Ta_2Ni_3S_8$, $NiTa_8Se_8$, $Ta_2Pt_3Se_8$, $Ta_3Pd_3Te_{14}$; and $MTa_4Te_4$ (M = Si, Al, Cr, Fe, Co, Ni). Some members of this family are known for their important intercalation chemistry or feature superconductivity, charge density waves, and anisotropic electrical and optical behavior. Band calculations have also revealed a number of interesting features in their electronic structure. For example, both $NbFeTe_2$ and $NbCoTe_2$ crystallize in a layered structure type and are metallic. But, while the temperature-dependent conductivity of $NbCoTe_2$ is typical of that for a metal, it reveals some unusual features for $NbFeTe_2$. Also, $NbCoTe_2$ exhibits Pauli paramagnetic behavior, whereas the magnetic susceptibility data of $NbFeTe_2$ indicate local moment formation on Fe [73, 74].

Related to the above systems are the complex layered tellurides of general composition $[(M_2Te_2)(QTe_2)](MTe_2)_n$ (or $M_nQTe_{2n}$: Q = Ga, Si, Ge; $0 \leq n \leq 1$) that are electronically stabilized by extensive bonding between early transition metals (M) and main group heteroatoms. These compounds have been synthesized and studied as main group counterparts of the layered metal-rich transition metal tellurides. Their special features include the unusual square planar Te-coordination of the main group atoms Ga, Si, and Ge and their modular (tinker toy) structure based on four building blocks. Size effects are important for the structural stability of the modular phases; for instance, attempts to substitute Ga by the group homologues boron or indium lead to the formation of alternate phases such as $Ta_4BTe_8$ containing metal clusters with interstitial atoms or intercalate phases such as $In_xNb_3Te_4$ [75].

Most commonly available 5–16 binary chalcogenides[10]:

Vanadium(III) sulfide, $V_2S_3$; niobium(IV) sulfide, $NbS_2$; niobium(IV) selenide, $NbSe_2$; niobium(IV) telluride, $NbTe_2$; tantalum(IV) sulfide, $TaS_2$; tantalum(IV) selenide, $TaSe_2$; tantalum(IV) telluride, $TaTe_2$.

### 1.2.7.6  Group VIA (6). Chromium, Molybdenum, Tungsten

Along with the Fe–S, Fe–Te, and Co–Te, the chromium–sulfur system provides instances of defect structures intermediate between the NiAs type and the $CdI_2$ one, containing vacant metal sites. The chromium–sulfur system is very complex, with two forms of $Cr_2S_3$ (trigonal and rhombohedral) and several intermediate phases between those and CrS, i.e., the trigonal CrS, $Cr_7S_8$, $Cr_5S_6$, $Cr_3S_4$ phases, related to each other by first-order transitions [76]. Rhombohedral $Cr_2S_3$ has complex electrical and magnetic properties. The monosulfide CrS is formally isotypic with CuO but is best regarded as a unique structure type, intermediate between that of NiAs and PtS. $Cr_3S_4$ is found to have a wide range of homogeneity; deviations from stoichiometry within this range due to point defects have been described with the aid of a Wagner–Schottky model.

Molybdenum and tungsten dichalcogenides $MX_2$ (M = Mo, W) occur in the (hexagonal) 2H stacking polytype, while $MoS_2$, $MoSe_2$, $WS_2$ occur in addition in the (rhombohedral) 3R polytype. Also, tetragonal $1T$-$MoS_2$ has been observed for single layers exfoliated from 2H- or $3R$-$MoS_2$ crystals [77]. The bonding in
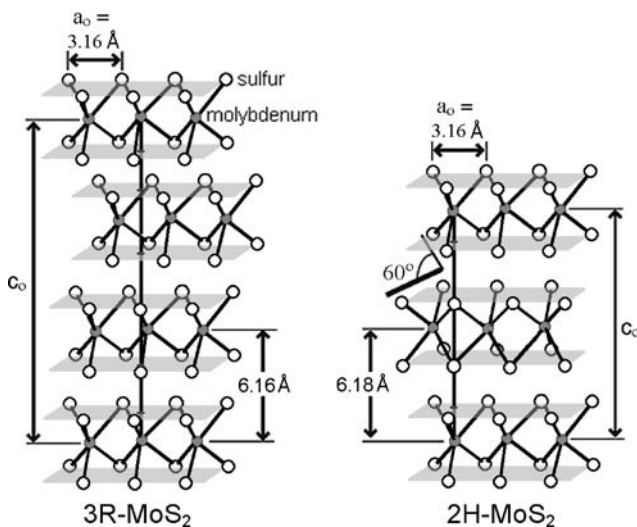


**Fig. 1.5**  The (rhombohedral) 3R and (hexagonal) 2H stacking polytypes of $MoS_2$. Adjacent layers in the 2H polytype are rotated by $60°$, whereas those in the 3R polytype can be superimposed with a translation only. (Reproduced with permission from [77], Copyright 2009, American Chemical Society)

---

[10] Ibid., p. 29.

$MoS_2$, $MoSe_2$, $WS_2$, and $WSe_2$ is predominantly covalent. Both 2H- and 3R-$MX_2$ are composed of covalent X–M–X layers in which a metal atom is located in trigonal prismatic coordination with six chalcogens. The X–M–X layers are stacked in vdW contact with one another along the $c$-axis of the material (Fig. 1.5). Certainly, because of the layered structure, a pronounced anisotropy of electrical conduction is observed, which is considerably (two to three orders of magnitude) larger parallel to the planes. Perpendicular to the planes, conduction occurs by a hopping mechanism.

The layered $MX_2$ compounds have received much attention due to their optical, electrochemical, and mechanical properties, as well as their rich intercalation chemistry. In effect, the preponderate motivation for the study of transition metal sulfides has been associated with the utility of $MoS_2$ and related materials as catalysts for the hydrodesulfurization of petroleum. The $MoX_2$ (X = S, Se, Te) and $WX_2$ (X = S, Se) are all semiconductors ($WTe_2$ is considered rather as a semi-metal) with band gaps well matched to the solar spectrum (e.g., both 3R- and 2H-$MoS_2$ show an indirect transition at 1.2 eV and a direct at 1.95 eV) and inherent corrosion resistance, since their energy gaps are derived from non-bonding molecular orbitals (Chap. 5). Their applications include solid-state and photoelectrochemical solar cells, rechargeable batteries, and solid lubricants.

Let us note in addition that the layered sulfides $MoS_2$ and $WS_2$ have been found to form nanotubes and other fullerene-type structures, on account of their highly folded and distorted nature that favors the formation of "rag" and "tubular" structures. Such materials have 'been synthesized by a variety of methods [78] and exhibit morphologies, which were described as inorganic fullerenes (IF), single sheets, folded sheets, nanocrystals, and nested IFs (also known as "onion crystals" or "Russian dolls").

The structure and chemistry of molybdenum chalcogenide complexes and clusters is remarkably diverse. The trinuclear clusters with $Mo_3X_4^{4+}$ core (X = S, Se), along with the analogous complexes of tungsten, comprise the most studied family of all the early transition metal clusters. Other trinuclear core systems exist such as $Mo_3S_5$, $Mo_3Te_7$, $Mo_3O(S_2)_3$, $Mo_3O(Te_2)_3$, $Mo_3S(Se_2)_3$; also tetranuclear as in $GaMo_4X_8$ (X = S, Se), and the isostructural mixed chalcogenides $GaMo_4(XX')_8$ (X, X' = S, Se, Te); or the hexanuclear $Mo_6X_6$ in $M'_2Mo_6Se_6$ (M'= Na, In, K, Tl), $M'_2Mo_6S_6$ (M' = K, Rb, Cs), and $M'_2Mo_6Te_6$ (M' = In, Tl) [79]. Special reference should be made to the class of ternary molybdenum chalcogenides known as the "Chevrel phases", which are described by the formula $MMo_6X_8$, where M stands for about 40 elements and X = S, Se, Te [80]. These compounds are well-established catalysts for hydro-desulfurization, -nitrogenation, -deoxygenation, and hydrogenation reactions in industrial oil-refining applications [81–83]. Also, their intercalation and conductive properties make them very attractive for energy storage applications (Chap. 6).

Most commonly available Group 6–16 binary chalcogenides[11]:

Chromium(III) sulfide, $Cr_2S_3$; chromium selenide, CrSe; chromium(III) telluride, $Cr_2Te_3$; molybdenum(IV) sulfide, $MoS_2$ (molybdenite); molybdenum(IV) selenide, $MoSe_2$; molybdenum(IV) telluride, $MoTe_2$; tungsten(IV) sulfide,

---

[11] Ibid., p. 29.

$WS_2$ (tungstenite); tungsten(VI) sulfide, $WS_3$; tungsten(IV) selenide, $WSe_2$; tungsten(IV) telluride, $WTe_2$.

### 1.2.7.7 Group VIIA (7). Manganese, Technetium, Rhenium

Manganese dichalcogenides, $MnX_2$ (X = S, Se, Te), adopt pyrite-type structures, with lattice parameters several percent larger than the other transition metal $MX_2$ compounds. These are paramagnetic compounds having five unpaired spins; owing to strong electron correlation, they do not form energy bands and become antiferromagnetic. The Néel temperature,[12] $T_N$, is 48, 47, and 87 K for $MnS_2$, $MnSe_2$, and $MnTe_2$, respectively. The Mn(II) monochalcogenides crystallize in either the rock salt structure (MnS and MnSe) or the NiAs type (MnTe). The stable red sulfide MnS is strongly antiferromagnetic ($T_N$ 121 °C), as also is MnSe ($T_N$ 100 °C). MnTe is a $p$-type semiconductor with a very high density of impurity charge carriers and a direct band gap of 1.3 eV with a potential for photovoltaic applications.

Along with other transition metal elements, manganese is a common contaminant in II–VI semiconductors, like CdTe. The Mn alloys of II–VI compounds ($A_{1-x}^{II}Mn_xB^{VI}$) provide a unique link between impurity and alloy physics in relation to magnetism and semiconductivity. Their role in material properties has been studied in the form of *dilute magnetic semiconductors* (DMS) (or semimagnetic semiconductors), the term commonly referring to alloys which are formed by randomly distributing magnetic ions on the cation sites of a II–VI semiconductor [84]. These systems are distinct from conventional octet isovalent semiconductor alloys (e.g., II–II–VI or III–III–V alloys) in that they include an open shell Mn $d^5$ ion and differ from dilute $d$-electron impurity systems (e.g., 3$d$ impurities in II–VI or III–V semiconductors) in that MnX compounds show considerable solid solubility in common-anion II–VI compounds despite large lattice mismatches and different crystal structures. The $Cd_{1-x}Mn_xTe$ system is probably the most extensively studied member of the $A_{1-x}^{II}Mn_xB^{VI}$ group [41, 85]. It crystallizes in a single-phase zinc blende structure up to a composition $x = 0.7$, above which multiphase structures prevail.

The rhenium chalcogenides $ReS_2$ and $ReSe_2$ are diamagnetic semiconductors (band gaps 1.33, 1.15 eV, respectively) that belong to the family of the layered dichalcogenides. However, unlike most of the latter, $ReS_2$ and $ReSe_2$ adopt a $CdCl_2$-type structure distorted by a Re–Re bonding network, leading to triclinic symmetry that may be described by a unit cell containing four or eight $ReX_2$ formula units. In contrast, crystals of the ditelluride, $ReTe_2$, do not show a plate-like habit, and their structure may be viewed on the basis of an orthorhombic unit cell. The technetium compounds $TcS_2$ and $TcSe_2$ are also semiconductors (band gaps 1.00 and 0.88 eV, respectively), having layer lattices of triclinic symmetry, but their structures are different from those of the corresponding rhenium compounds. Unit cell dimensions of $TcS_2$ indicate that stacking in this compound resembles that of $Cd(OH)_2$ [86].

---

[12] Analogous to the Curie temperature for ferromagnetic materials, the Néel temperature is the one at which an antiferromagnetic material becomes paramagnetic. At $T_N$, the thermal energy becomes large enough to destroy the macroscopic magnetic ordering within the material.

The telluride $TcTe_2$ has been found to crystallize in a monoclinic layer structure. The disulfides of Re and Tc, unlike the pyrite-type $Mn^{II}S_2$, contain monoatomic $S^{2-}$ units.

Technetium and rhenium favor higher oxidation states than manganese in their binary chalcogenides.[13] Both form black diamagnetic heptasulfides, $M_2S_7$, which are isomorphous and decompose to $M^{IV}S_2$ and sulfur on being heated. It has been suggested [87] that $Re_2S_7$ is closely related structurally to the compound $ReS_4$, these two materials being members of a continuum of $Re(S)_{1.5-1}(S_2)_{1-1.5}$ structures that differ in terms of their $S_2^{2-}/S^{2-}$ ratio. Chain structures accommodate these considerations and are consistent with a largely reversible electrochemistry that regenerates $(ReS_4)^-$. Tc and Re have much stronger metallic bonding than Mn and the occurrence of cluster compounds with M–M bonds is a dominant feature of rhenium(III) chemistry. The sulfides of rhenium have attracted attention because Re–S compositions are particularly active hydrodesulfurization and hydrogenation catalysts. $Re_2S_7$ has been used for the hydrogenation of species that poison Pt metal catalysts, e.g., NO and $SO_2$.

Most commonly available 7–16 binary chalcogenides[14]:

Manganese(II) sulfide, MnS (alpha, beta, gamma); manganese sulfide, MnS, cubic; manganese sulfide, MnS, hexagonal; manganese sulfide, MnS (alabandite); manganese sulfide, $MnS_2$ (hauerite); manganese(II) selenide, MnSe, cubic; manganese selenide, MnSe, hexagonal; manganese(II) telluride, MnTe; rhenium(IV) sulfide, $ReS_2$; rhenium(IV) telluride, $ReTe_2$; rhenium(VII) sulfide, $Re_2S_7$.

### 1.2.7.8 Group VIII (8–10). Iron, Cobalt, Nickel

The ferrous sulfide, "FeS", system provides the most renowned example of non-stoichiometric sulfides, involving iron-deficient phases of NiAs structure, in which the framework of S atoms remains intact while some of the lattice iron positions are vacant in a random way. The simple NiAs structure is stable over only a small range of composition, which even if one includes the closely related structures is still a few at.% S. Vacancy compounds that have been identified in this range include $Fe_{1-x}S$ with $x < 0.075$ and $Fe_7S_8$. The magnetic and electrical properties of these materials depend on the type of vacancy order, which varies with temperature as well as with composition. $Fe_{1-x}S$, occurring in mineral pyrrhotite or in magnetic pyrites, is an anti-ferromagnetic compound ($T_N$ 598 K) and an insulator at low temperatures. It undergoes an ($a$-) transition at ca. 420 K (concentration dependent), whereby the lattice parameters, magnetic susceptibility, and electrical resistivity measured along the $c$-axis change very sharply, while the resistivity perpendicular to the $c$-axis does not change significantly. The mechanism responsible for this transition is still not clear.

---

[13] The +2 state is here of little importance. Lower formal oxidation states are stabilized, however, by M–M bonding in ternary chalcogenides containing alkali metals such as $A_4M_6Q_{12 \text{ or } 13}$ (A = alkali metal; M = Re, Tc; Q = S, Se). The structures of such systems are all based on the face-capped, octahedral $M_6X_8$ cluster unit found in Chevrel phases and in the dihalides of Mo and W.

[14] Ibid., p. 29.

The most prevalent modification of the disulfide, $FeS_2$, is pyrite, which may be visualized as a distorted NaCl structure where the Fe atoms occupy sodium positions and $S_2$ groups are placed with their centers at the chloride positions. Pyrite is a largely occurring crystal with semiconductor properties ($E_g = 0.95$ eV). Another modification of $FeS_2$ is the very similar to pyrite but somewhat less regular marcasite structure.

The NiS compound (NiAs structure) shows an insulator to metal transition at 263 K with increasing temperature. The low-temperature phase is anti-ferromagnetic, and the high-temperature phase is paramagnetic. The insulator phase is known to be of a charge transfer type and it is considered to be at the metal–insulator boundary. An energy gap of 0.1 eV has been obtained for NiS. The paramagnetic state of NiS is not considered to be of a usual Pauli type. The disulfide, $NiS_2$, adopts the pyrite structure and is semiconductive and anti-ferromagnetic. Band description for this compound is not relevant as it constitutes a strongly correlated electron system (the band calculations predict $NiS_2$ to be a Mott–Hubbard insulator because of the existence of a half-filled $3d$ band at the Fermi level).

A number of selenium and tellurium compounds of the presently discussed metals show a quite different behavior from the Fe–S system. Iron and selenium form two "compounds": "FeSe" with a broad stoichiometry range and $FeSe_2$ with a much narrower composition field. Below 400 °C, the non-stoichiometric $Fe_{1-x}Se$ exists by creation of iron vacancies and can have compositions lying between $Fe_7Se_8$ and $Fe_3Se_4$. At low temperatures there exist two phases: an α (PbO type) and a β (NiAs type) phase. The crystal structure of the diselenide, $FeSe_2$, is an orthorhombic, C18 (marcasite) type. In the Fe–Te system, the defect NiAs structure is found at a composition close to $FeTe_{1.5}$, as about one-third of the Fe atoms are missing. At compositions around FeTe the behavior is complex, and the β-phase has the PbO structure (like FeSe) but with additional metal atoms (i.e., $Fe_{1.1}Te$).

An even more extreme example of non-stoichiometry is provided by the Co–Te system. Here a phase with the NiAs structure is stable over the entire composition range: CoTe to $CoTe_2$. It is possible to pass continuously from the former to the latter by progressive loss of Co atoms from alternate planes until, at the composition $CoTe_2$, every other plane of Co atoms present in CoTe has completely vanished giving a $CdI_2$-type C6 structure. The same behavior is found in other systems (V–Se, Ti–Se, Ti–Te, and Ni–Te) and is responsible, for example, for the variety of formulae assigned to the mineral melonite, which can have any composition between those corresponding to NiTe and $NiTe_2$.

Both $CoS_2$ and $CoSe_2$ are metallic. The former is ferromagnetic with a Curie temperature of 125 K and the latter appears to be a Curie–Weiss type paramagnet. The solid solutions $Co(S_xSe_{1-x})_2$ in the composition region $0.12 \leq x \leq 0.40$ show a very interesting meta-magnetic transition at 4.2 K, successfully explained on the basis of the energy band structure.

Most commonly available 8–16 binary chalcogenides[15]:

---

[15] Ibid., p. 29.

Iron(II) sulfide, FeS (troilite); iron(II,III) sulfide, $Fe_3S_4$ (greigite); iron disulfide, $FeS_2$ (marcasite); iron disulfide, $FeS_2$ (pyrite); iron sulfide, $Fe_{0.885}S$ (pyrrhotite); iron sulfide, $Fe_{0.980}S$ (pyrrhotite); iron sulfide, $Fe_7S_8$ (pyrrhotite); iron sulfide, FeS (mackinawite); iron(II) selenide, FeSe; iron(II) selenium, $FeSe_2$ (ferroselite); iron(II) telluride, FeTe; iron(II) tellurium, $FeTe_2$ (frohbergite).

Cobalt(II) sulfide, CoS; cobalt disulfide, $CoS_2$; cobalt(III) sulfide, $Co_2S_3$; cobalt(II) selenide, CoSe; cobalt selenium, $CoSe_2$ (trogtalite); cobalt(II) telluride, CoTe.

Nickel(II) sulfide, NiS (millerite); nickel(II, III) sulfide, $Ni_3S_4$ (polymidite); nickel(III) sulfide, $Ni_3S_2$; nickel sulfide, $Ni_3S_2$ (heazelwoodite); nickel sulfide, $NiS_2$ (vaesite); nickel selenide, $NiSe_2$; nickel(II) selenide, NiSe; nickel telluride, $NiTe_2$ (melonite).

## 1.2.7.9  Group VIII (8–10). Platinum Group Metals (Ru, Os, Rh, Ir, Pd, Pt)

The platinum group metals form several binary, pseudo-binary, and ternary chalcogenides. The outstanding features of these compounds as related to catalysis and materials science have been widely reported and reviewed [88].

The disulfides of ruthenium and osmium, $RuS_2$ and $OsS_2$, as well as the ruthenium diselenide and ditelluride compounds, $RuSe_2$ and $RuTe_2$, are known and assume the pyrite structure. Examples of pseudo-binary systems are $Ru_{1-x}Os_xS_2$ and $Ni_xRu_{1-x}S_2$. Examples of ternaries with various structure types are the spinels $M'M_2X_4$ (M' = Cr, Mn, Fe, Co, Ni, Cu; M = Rh, Ir; X = S, Se, Te); $Tl_2Pt_4X_6$ (X = S, Se, Te); MoRuS, etc. Several of these chalcogenides occur in nature as minerals, for instance, laurite (mixed sulfide $(Ru_5Os)S_2$), braggite $(PdPt_3S_4)$, luberoite $(Pt_5Se_4)$, and $Pd_6AgTe_4$.

Rhodium and iridium form a variety of chalcogenide compounds with diverse structural types, which display metallic to semiconducting behavior. They form the monotellurides RhTe and IrTe with a NiAs-type structure and the usual wide range of dichalcogenides, $MX_2$ (M = Rh, Ir; X = S, Se, Te), which adopt pyrite- and $CdI_2$-type structures. Other chalcogenides of these elements include $M_2X_3$ ($Rh_2S_3$, $Rh_2Se_3$, $Ir_2S_3$); $Rh_3X_4$ (X = S, Se, Te); and $M_3X_8$ ($Rh_3Se_8$, $Rh_3Te_8$, $Ir_3Te_8$).

Although it has been reported, rhodium disulfide, $RhS_2$, appears not to exist as a pure compound, since the attempts to prepare it result in formation of $Rh_2S_3$, $RhS_3$, and other phases. The low-temperature modification of $RhSe_2$ is similar to marcasite, as also are the structures of $IrSe_2$ and $IrS_2$. $RhTe_2$ adopts the pyrite structure, but does not exist as a stoichiometric compound above $550\,°C$. The telluride $IrTe_2$ shows polymorphism with three phases: $CdI_2$-type, pyrite type, and monoclinic. The sesquisulfides and selenides $Rh_2S_3$, $Rh_2Se_3$, and $Ir_2S_3$ are isostructural, with the metal atoms in octahedral configuration and octahedron pairs arranged in layers of stacking sequence *ABAB*. The $Rh_3X_4$ compounds (X = S, Te) crystallize in a monoclinic modification of the NiAs structure. The compounds $Rh_3Se_8$, $Rh_3Te_8$, $Ir_3Te_8$ crystallize in a rhombohedral modification of a pyrite type. Other rhodium chalcogenides that have been isolated include $Rh_{17}S_{15}$, $RhSe_{2+x}$, RhTe, and $Rh_3Te_2$.

The binary compounds of palladium and platinum show a higher diversity of structures than found for the Rh–Ir and Ru–Os systems. Aside from several other reported binary phases, four general families can be distinguished:

- MX (PdS, PdSe, PdTe, PtS, PtSe, PtTe);
- $Pd_3X$ (X = S, Se, Te);
- $Pd_4X$ (X = S, Se, Te);
- $MX_2$ ($PdS_2$, $PdSe_2$, $PdTe_2$, $PtS_2$, $PtSe_2$, $PtTe_2$).

PtS and PdS exhibit a square planar coordination of $Pd^{2+}$ and $Pt^{2+}$ (4:4 PdO structure) emphasizing covalent rather than ionic bonding. They are prepared from the bivalent metal cations *in aquo* with $H_2S$ or $Li_2S$, while heating with sulfur results in formation of the disulfides. $PdS_2$ and $PdSe_2$ exist in a deformed pyrite-type structure confirming the preference for the divalent state for palladium, i.e., with a $Pd^{2+}$ ($S_2^{2-}$) formula unit. The remaining $MX_2$ adopt the $CdI_2$ structure. Other phases like $Pd_{2.2}S$, $Pd_3S$, and $Pd_4S$ (the last two both alloy-like) are known. Similarly to Rh and Ir, the tellurides PdTe, PtTe exist and have the NiAs structure.

In the palladium–tellurium system, at least eight binary phases (PdTe, $PdTe_2$, $Pd_3Te_2$, $Pd_7Te_3$, $Pd_8Te_3$, $Pd_9Te_4$, $Pd_{17}Te_4$, and $Pd_{20}Te_7$) have been identified. The platinum–tellurium system exhibits only four binary phases (PtTe, $PtTe_2$, $Pt_2Te_3$, and $Pt_3Te_4$). These compositions are constant and there is no appreciable compositional range. The $Pt_2Te_3$ is stable up to $\sim 675\,°C$ whereas $Pt_3Te_4$ melts above $1,000\,°C$. Semiconducting behavior for some of these compounds has been reported.

Most commonly available platinum group chalcogenides[16]:

Ruthenium(II) sulfide, $RuS_2$ (laurite); iridium(III) sulfide, $Ir_2S_3$; iridium(IV) sulfide, $IrS_2$; palladium(II) sulfide, PdS; platinum(II) sulfide, PtS (braggite, cooperite); platinum(IV) sulfide, $PtS_2$.

### 1.2.7.10  Group IB (11). Copper, Silver, Gold

Various stoichiometries and polymorphs are known for the binary copper chalcogenides, which exhibit defect phases with large ranges of homogeneity. In the copper–sulfur system, at the "copper-rich" side lies chalcocite, $Cu_2S$, and at the "copper-deficient" side the pyrite-type $CuS_2$, with such intermediate phases as $Cu_{2-x}S$ ($Cu_{1.96}S$, $Cu_{1.94}S$, $Cu_{1.8}S$), $Cu_7S_4$, $Cu_9S_8$, and CuS (covellite) [89]. Likewise, the copper–selenium system includes $Cu_2Se$, $Cu_{2-x}Se$, $Cu_7Se_4$, $Cu_3Se_2$, $Cu_5Se_4$, CuSe, and $CuSe_2$ stoichiometries, some of which (in one polymorphic form or another) occur as minerals, e.g., berzelianite ($Cu_{2-x}Se$), umangite ($Cu_3Se_2$), and klockmannite (α-CuSe). Homogeneous, non-stoichiometric phases of the copper–tellurium system have been found for Cu/Te ratios approximating $Cu_2Te$, $Cu_7Te_5$ (rickardite), $Cu_3Te_4$, CuTe, and $CuTe_2$ [90].

Cuprous chalcogenides, $Cu_2X$, are basically dimorphic. The low-chalcocite $Cu_2S$ (an important and widely distributed ore mineral of copper) has a structure

---

[16] Ibid., p. 29.

based on hexagonal close-packed sulfur stacking and a complex arrangement of copper atoms, most having triangular coordination and a few being tetrahedrally coordinated. Above 103 °C, the copper ions disorder to form high chalcocite, a much simpler hexagonal structure. The $Cu_2Se$ is similar, whereas the low-temperature form of $Cu_2Te$ assumes a unique hexagonal structure with mean coordination number seven (7-vertex polyhedra: $Cu:Cu_4Te_3$, $Te_2:Cu_6Te$). The high-temperature modifications of these compounds have defect structures, normally metal-deficient, such as in the (high-digenite) $Cu_{2-x}S$, where the anions together with half of the metal ions form a ZB structure, in the interstices of which copper ions are statistically distributed.

Cupric sulfide, CuS, occurring as the mineral covellite (also known as covelline), exhibits a very unusual structure, in which the Cu is again partly 3-coordinate and partly 4-coordinate, with two-thirds of the sulfur atoms existing as $S_2$ groups like those in pyrites. The low-temperature form of CuSe has also a covellite structure, the high-temperature modification (β-CuSe) being orthorhombic. All $CuX_2$ compounds assume pyrite-type structures.

A few binary chalcogenides of silver and gold are known. $Ag_2S$ is a very insoluble ($k_{sp} \sim 10^{-51}$) black substance exhibiting three polymorphs; 2- and 3-coordination is found in the low-temperature form, while at high temperatures the compound is an ionic conductor due to the mobility of silver atoms within the framework of sulfurs. Interest in $Ag_2S$ has arisen from its use as an ion-specific electrode, its comparatively high electronic and ionic conductivity, the well-known tarnishing of silver in sulfur-containing media, and its uses in the processing of minerals. Gold sulfide $Au_2S$ has the cuprite structure. Little is known about the $Au_2X_3$ (X = S, Se, Te) system. The non-stoichiometric gold tellurides $Au_2Te_3$, $Au_3Te_5$, and $AuTe_2$ have been reported. In $AuTe_2$ "calverite," gold atoms have 4- and 2-coordination by tellurium.

The structural complications with IB-chalcogenides indicate that the apparent simplicity of stoichiometry (and electronic structures) of compounds such as CuX or $CuX_2$ is deceptive. One way to account for the ambiguous valency of the metal and chalcogen atoms in such compounds is by using the concept of mixed valence. Thereby, CuS (covellite), taken as an ionic structure, would be represented as $(Cu^+)_4(Cu^{2+})_2(S^-)_2(S^{2-})_2$, while AuS and AuSe would be of the form $Au^I Au^{III} X_2$, with diagonal gold(I) and square planar gold(III).

Numerous ternary copper chalcogenides are known; for example, the copper–iron sulfides $CuFeS_2$ (chalcopyrite), $CuFe_2S_3$ (cubanite), $Cu_3Fe_4S_6$, $Cu_5FeS_4$ (bornite), and $Cu_5FeS_6$. Most, if not all, of these complex sulfides (and related selenides) have structures in which the metal atoms occupy tetrahedral holes between close-packed chalcogen atoms. Closely associated are quaternary compounds of the stannite ($Cu_2FeSnS_4$) family, such as $Cu_2CdSe_4Sn$, $CoCu_2S_4Sn$, $Cu_2GeHgS_4$, $Cu_2HgS_4Sn$, and $Ag_2FeS_4Sn$, exhibiting superstructures of the ZB type with tetrahedral coordination of all the metal atoms.

Chalcopyrite or copper pyrite, $CuFeS_2$, is one of the major ores of copper, estimated to account for about 50% of all the element's deposits. Compounds of the chalcopyrite type of the general formula $ABC_2$ (with A = Cu, Ag; B = Al, Ga, In;

and C = S, Se, Te) form a large group of semiconducting materials with diverse optical, electrical, and structural properties. These compounds may be regarded as the ternary I–III–VI$_2$ analogues of the Group IVB (Si, Ge) or the isovalent II–VI (or III–V) semiconductors, a view that is supported by the close relationship of the chalcopyrite structure to the diamond and ZB ones, from which it can be derived by simple unit cell doubling because of cation ordering. However, despite the general structural similarity between the I–III–VI$_2$ systems and their binary II–VI analogues, the band gaps of the former are substantially smaller than those of the latter, and some absorb very strongly in the visible. Both copper and silver chalcopyrite semiconductors present band gaps decreasing in the B-component order: Al > Ga > In, for the same chalcogen, and in the C-component order: S > Se > Te, for the same main group B element [91].

Extensive structural, optical, and electronic studies on the chalcopyrite semiconductors have been stimulated by the promising photovoltaic and photoelectrochemical properties of the copper–indium diselenide, CuInSe$_2$, having a direct gap of about 1.0 eV, viz. close to optimal for terrestrial photovoltaics, and a high absorption coefficient which exceeds $10^5$ cm$^{-1}$. The physical properties of this and the other compounds of the family can be modulated to some extent by a slight deviation from stoichiometry. Thus, both anion and cation deficiencies may be tolerated, inducing, respectively, n- and p-type conductivities; a p-type behavior would associate to either selenium excess or copper deficiency.

CuInSe$_2$ has been utilized as the absorber layer in high-efficiency photovoltaic solar cells (e.g., p-CuInSe$_2$/n-CdS) either in single-crystal form or as thin film. The analogous sulfide CuInS$_2$ with an optical band gap of 1.50 eV and an absorption coefficient $10^4$ cm$^{-1}$ at $\lambda = 500$ nm is also suitable for solar cell applications. Copper–aluminum diselenide, CuAlSe$_2$, a wide band gap semiconductor (2.67 eV), has been investigated for blue LED applications and can be thought of as an attractive material to replace CdS (2.4 eV) as window/buffer layer in thin film solar cells, although CuAlSe$_2$ thin films are generally p-type while window/buffer layers like CdS are n-type. The p- to n-type conversion in these ternaries can be managed by varying the Cu/Al ratio or by extrinsic doping by elements like Zn and Cd. The silver–gallium sulfide AgGaS$_2$ is a p-type semiconductor, with a direct band gap of ca. 2.68 eV, while the tellurides AgAlTe$_2$, AgGaTe$_2$, and AgInTe$_2$ have direct energy gaps at 2.35, 1.36, and 1.04 eV, respectively (at 77 K). All three can be made usefully p-type, but only AgInTe$_2$ has been made n-type [92].

The insight and achievements in the chemistry of ternary and quaternary chalcogenides of Group IB elements within the last 20 years are remarkable. The basic reason for this interest is that the crystals containing $X^{2-}$ and/or $X_2^{2-}$ chalcogen "ions" span a broad spectrum of electrical and magnetic properties, ranging from dielectric to superconducting and from diamagnetism to temperature-independent paramagnetism. Most of these crystals are semiconductors, with fast ion-transport properties. Some exhibit (semi)metallic properties and superconductivity at low temperatures (e.g., CuS, CuS$_2$, CuSe$_2$, CuTe$_2$, AgTe$_{\sim 3}$, and Au$_3$Te$_5$) or afford transitions to states with charge density waves (CDW). The metallic state in these systems and the CDW phenomena are closely associated to the variable valence and

charge ordering effects. Notably, it has been observed that thio-, seleno-, and telluro-cuprates provide a substantially wider range of physicochemical properties than the corresponding oxides and have large potential as high-temperature superconductors. The most essential differences with the oxides consist in the higher covalence of the metal–chalcogen bonds, the ability of chalcogen atoms to form bonds with each other resulting in molecular anions, and the higher ability of metal atoms to form metal–metal bonds (due to the lower formal charge) [93, 94].

Most commonly available 11–16 chalcogenides[17]:

Copper(I) sulfide, $Cu_2S$ (chalcocite, high chalcocite, high digenite); copper(I) selenide, $Cu_2Se$ (berzelianite); copper(I) telluride, $Cu_2Te$; copper(II) sulfide, $CuS$ (covellite); copper(II) selenide, $CuSe$ (klockmannite); copper(II) telluride, $CuTe$; copper selenide, $Cu_3Se_2$ (umangite); copper sulfide, $Cu_{1.79}S$ (digenite); copper indium selenide, $CuInSe_2$; copper indium sulfide, $CuInS_2$; copper indium telluride, $CuInTe_2$; copper aluminum sulfide, $CuAlS_2$; copper aluminum selenide, $CuAlSe_2$; copper aluminum telluride, $CuAlTe_2$; copper antimony sulfide, $Cu_3SbS_4$ (famatinite); copper antimony selenide, $Cu_3SbSe_4$; copper arsenic sulfide, $Cu_3AsS_4$ (enargite); copper arsenic selenide, $Cu_3AsSe_4$ (famatinite); copper cadmium tin sulfide, $Cu_2CdSnS_4$; copper gallium selenide, $CuGaSe_2$; copper gallium sulfide, $CuGaS_2$; copper gallium telluride, $CuGaTe_2$; copper germanium selenide, $Cu_2GeSe_3$; copper germanium sulfide, $Cu_2GeS_3$, high-temperature form; copper germanium sulfide, $CuGeS_3$, low-temperature form; copper germanium telluride,; $Cu_2GeTe_3$; copper iron selenide, $CuFeSe_2$; copper iron sulfide, $CuFeS_2$ (chalcopyrite); copper lanthanum sulfide, $CuLaS_2$; copper phosphorus sulfide, $Cu_3PS_4$; copper silicon sulfide, $Cu_2SiS_3$, high-temperature form; copper silicon sulfide, $Cu_2SiS_3$, low-temperature form; copper silicon telluride, $Cu_2SiTe_3$; copper thallium selenide, $CuTlSe_2$, low-temperature form; copper thallium sulfide, $CuTlS_2$; copper tin selenide, $Cu_2SnSe_3$; copper tin sulfide, $Cu_2SnS_3$; copper tin telluride, $Cu_2SnTe_3$.

Silver(I) sulfide, $Ag_2S$ (argentite, high argentite, acanthite); silver(I) selenide, $Ag_2Se$ (high naumanite); silver(I) telluride, $Ag_2Te$ (hessite); silver aluminum selenide, $AgAlSe_2$; silver aluminum sulfide, $AgAlS_2$; silver aluminum telluride, $AgAlTe_2$; silver antimony selenide, $AgSbSe_2$; silver antimony telluride, $AgSbTe_2$; silver bismuth selenide, $AgBiSe_2$, high-temperature form; silver bismuth sulfide, $AgBiS_2$, high-temperature form; silver bismuth telluride, $AgBiTe_2$, high-temperature form; silver gallium selenide, $AgGaSe_2$; silver gallium sulfide, $AgGaS_2$; silver gallium telluride, $AgGaTe_2$; silver germanium selenide, $Ag_2GeSe_3$; silver germanium telluride, $Ag_2GeTe_3$; silver indium selenide, $AgInSe_2$; silver indium sulfide, $AgInS_2$, low-temperature form; silver indium telluride, $AgInTe_2$; silver iron sulfide, $AgFeS_2$; silver tin selenide, $AgSnSe_3$; silver tin telluride, $Ag_2SnTe_3$.

Gold(I) sulfide, $Au_2S$; gold(III) sulfide, $Au_2S_3$; gold(III) selenide, $Au_2Se_3$.

---

[17] Ibid., p. 29.

### 1.2.7.11  Group IIB (12). Zinc, Cadmium, Mercury

All the 12 monochalcogenides of the IIB metals crystallize in the tetrahedral zinc blende (ZB) or wurtzite (W) structures, as shown in the table below, with the exception of HgS that exists also in a distorted rock salt (RS) form.

|     | S     | Se    | Te    |
|-----|-------|-------|-------|
| Zn  | W, ZB | ZB    | W, ZB |
| Cd  | W, ZB | W, ZB | ZB    |
| Hg  | ZB    | ZB    | ZB    |

Zinc blende (ZnS) is the most widespread ore of zinc and the main source of the metal. Zinc sulfide (ZnS) is an industrially important phosphor used in television and X-ray fluorescent screens, as also in scintillation, fluorescent or luminous paints, sensors, and lasers. Under stimulation by cathode rays, X-rays, and radioactivity, ZnS fluoresces in a variety of colors which can be extended by the addition of traces of various metals (activators) or the replacement of Zn by Cd and of S by Se. ZnS activated with silver (ZnS:Ag) is one of the most efficient cathodoluminescent phosphors known, exhibiting a blue luminescence. Changing the activator to copper (ZnS:Cu) and other co-dopants gives a green luminescence. The high-luminescence quantum efficiency obtained from Mn-doped ZnS nanocrystals has stimulated efforts to dope ZnS nanoparticles with rare earth and transition metal ions, from which stable visible light emissions with different colors have been achieved [95]. In addition, ZnS is emerging presently as a potential candidate for replacing CdS window for both CdTe- and $Cu(In,Ga)Se_2$ (CIGS)-based photovoltaic cells. The use of ZnS as a window layer allows a more effective photocurrent generation due to its larger band gap (3.6 eV) compared to that of CdS (2.4 eV) and benefits also for the fabrication of cadmium-free CIGS devices. ZnS is also used as catalyst for the photooxidation and photoreduction of organic groups. Nicolau et al. [96] summarized some important requirements, as regards the microstructure (i.e., crystallinity, morphology, composition) of ZnS and derivative alloy films used in various solid-state applications.

Zinc selenide (ZnSe) is used in conjunction with ZnS as a phosphor. On account of its electronic and structural properties, it appears to be expedient for the fabrication of blue-light photoelectronic diodes. On the basis of band gap energy (direct transition at 2.7 eV), ZnSe can be used as a buffer or window layer in lower gap chalcogenide (CdSe, CdTe, chalcopyrites)-based thin film solar cells. Zinc telluride (ZnTe) has also a high potential for optoelectronic and photovoltaic device applications because of an even lower but still wide 2.26 eV band gap and p-type doping ability. ZnTe ohmic contacts are used in high-efficiency photovoltaic cells like those based on p-type CdTe and GaAs, while polycrystalline thin (<100 nm) ZnTe films serve as passivating layers, instead of CdS, in CdTe- and also in CdSe-based SIS solar cells.

All three zinc chalcogenides are important materials in the fabrication of heteroepitaxial solid-state devices, like those involving ZnSe/GaAs, ZnSe/Ge, ZnS/GaP, ZnS/Si, ZnTe/InAs, and ZnTe/GaSb interfaces. In fact, ZnSe is rather the most extensively investigated wide-gap II–VI compound in heteroepitaxy, in terms of interface chemistry, growth mechanism, and defect generation in epilayers. It constitutes also one of the basic materials for the construction of heterojunction devices under lattice matching conditions by adopting suitable alloy systems of other II–VI compounds.

Cadmium monochalcogenides, with their low energy band gaps (CdS: 2.4 eV, CdSe: 1.7 eV, CdTe: 1.4 eV), have been thoroughly studied both theoretically, as model semiconductor materials, and technologically, for applications ranging from solar photocatalysis to solar photovoltaic (photoelectrochemical) conversion. Activated CdS and CdSe have also been used extensively as phosphors; their application, however, is now limited by the toxicities of cadmium and selenium, although they are still used in radar displays and high-resolution storage tubes. CdSe and CdTe find application in solar cells, thin film transistors, memory as well as magneto-optical and optoelectronic devices, photoelectrochemical cells (CdSe), photoconductors, and γ-ray or infrared (CdTe) detectors. Notably, CdTe has been recognized theoretically (Loferski [97]) as the semiconductor yielding the highest efficiency of photovoltaic solar energy conversion (ca. 24%, defined as the ratio of the maximum electrical power output to the solar power flux incident to the semiconductor surface).

Mercuric sulfide (HgS) is dimorphic. The more common form, cinnabar (red α-form), has a distorted RS, trigonal structure which is unique among the monosulfides, for the crystal is built of helical chains in which Hg has two nearest neighbors at 2.36 Å, two more at 3.10 Å, and two at 3.30 Å. Bulk α-HgS is a large-gap semiconductor (2.1 eV), transparent in the red and near IR bands. The rare, black mineral metacinnabarite is the β-HgS polymorph with a ZB structure, in which $Hg^{(II)}$ forms tetrahedral bonds. Upon heating, β-HgS is converted to the stable α-form. The ZB structure of HgS is stabilized under a few percent admixture of transition metals, which replace Hg ions in the lattice.

The zinc blende mercuric chalcogenide crystals are "zero-gap" degenerate semiconductors with the inverted band structure, hence are of special interest for fundamental studies. The negative energy gap of β-HgS is close to –1.19 eV [98]. HgSe has an inverted bulk gap of − 0.27 eV; recently a direct band gap of 0.81 eV and an indirect of 0.45 eV were reported in epitaxial films [99]. Bulk HgTe exhibits a band overlap of less than $10^{-3}$ eV as was verified by measurements of electrical resistivity and Hall coefficient on crystals grown by the modified Bridgman technique [100]. Seminal studies of the electronic structure of the IIB–VI chalcogenides and their unique features have been carried out by Wei and Zunger [101].

Of particular interest is the fundamental science and technology of the solid solutions between II–VI binary compounds. These isovalent alloys may be classified according to the scheme introduced previously (see Sect. 1.2.3) – a convenient matrix diagram comprising their observed structures can be found in a publication of Wei and Zunger [102].

The "type I" alloys prevail both for pseudobinary (i.e., common anion or common cation), e.g., $ZnS_xSe_{1-x}$, $Cd_xHg_{1-x}Te$, and for pseudoternary (mixed anion and mixed cation quaternary) systems, e.g., $(ZnTe)_x(CdSe)_{1-x}$. The same is true for systems with complete miscibility range, e.g., $ZnSe_xTe_{1-x}$, $HgS_xSe_{1-x}$, as well as for systems exhibiting limited solubility, e.g., $ZnS_xTe_{1-x}$. The pseudobinary $Cd_xHg_{1-x}Te$ alloy exhibits electrical properties ranging from semimetallic for $x = 0$ (HgTe) to semiconducting for $x \geq 0.15$ and has a composition-modulated direct band gap that can be tailored to the desired optoelectronic application. A major part of the research on this system has focused on the narrow band gap, mercury-rich alloys ($0.1 < x < 0.4$), which are important materials in the field of IR detection. Investigations involving cadmium-rich compositions of $Cd_xHg_{1-x}Te$ have shown these alloys to be of value in solar cell technologies. CdTe single crystal is advantageously used as a substrate for HgCdTe epitaxy.

A smaller class of "type II" alloys of II–VI binaries also exists, including the $(CdS)_x(ZnSe)_{1-x}$, $(CdS)_x(ZnTe)_{1-x}$, $(CdSe)_x(ZnSe)_{1-x}$, $(CdS)_x(CdTe)_{1-x}$, $(CdSe)_x(CdTe)_{1-x}$, and $(CdS)_x(ZnS)_{1-x}$ systems, which transform at some critical composition from the W to the ZB structure. Importantly, the transition temperatures are usually well below those required to attain a thermodynamically stable wurtzite form for the binary constituents (e.g., 700–800 °C for pure CdS and > 1,020 °C for pure ZnS). The type II pseudobinary $Cd_xZn_{1-x}Se$ is of considerable interest in thin film form for the development of tandem solar cells as well as for the fabrication of superlattices and phosphor materials for monitors. The $CdSe_xTe_{1-x}$ alloy is one of the most investigated semiconductors in photoelectrochemical applications.

Finally, there exist the rather rare "type III" alloys, which (at "zero" pressure) show structural forms that either are not adopted by the binary constituents for any pressure (e.g., wurtzite HgS, HgSe or NiAs-type ZnTe, CdTe) or exist only at high pressures (e.g., RS CdS and CdSe). To this class belong the $(HgSe)_x(CdSe)_{1-x}$ and $(CdS)_x(CdTe)_{1-x}$ systems (exhibiting a composition range where a single-phase W form exists, whereas HgS and HgSe are not known to have this structural form) and the magnetic semiconductor alloys between MnX (X = S, Se, Te) and a II–VI compound, namely $(MnS)_x(CdS)_{1-x}$ and $(MnSe)_x(CdSe)_{1-x}$ (showing a single-phase RS form which CdS and CdSe do not have) or $(MnTe)_x(ZnTe)_{1-x}$ and $(MnTe)_x(CdTe)_{1-x}$ (showing a single-phase NiAs structure which ZnTe and CdTe do not have, as well as a single-phase ZB structure which MnTe does not have).

Numerous ternary systems are known for II–VI structures incorporating elements from other groups of the Periodic Table. One example is the Zn–Fe–S system: Zn(II) and Fe(II) may substitute each other in chalcogenide structures as both are divalent and have similar radii. The cubic polymorphs of ZnS and FeS have almost identical lattice constant ($a = 5.3$ Å) and form solid solutions in the entire range of composition. The optical band gap of these alloys varies (rather anomalously) within the limits of the ZnS (3.6 eV) and FeS (0.95 eV) values. The properties of $Zn_xFe_{1-x}S$ are well suited for thin film heterojunction-based solar cells as well as for photoluminescent and electroluminescent devices.

Most commonly available 12–16 binary and ternary chalcogenides[18]:

---

[18] Ibid., p. 29.

Zinc sulfide, ZnS, sphalerite (zinc blende); zinc sulfide, ZnS, wurtzite; zinc selenide, ZnSe; zinc telluride, ZnTe, cubic; zinc telluride, ZnTe, hexagonal; zinc polonide, ZnPo; zinc aluminum selenide, $ZnAl_2Se_4$; zinc indium selenide, $ZnIn_2Se_4$; zinc indium telluride, $ZnIn_2Te_4$.

Cadmium sulfide, CdS, cubic (hawleyite); cadmium sulfide, CdS, hexagonal (greenockite); cadmium selenide, CdSe, cubic; cadmium selenide, CdSe, hexagonal (cadmoselite); cadmium telluride, CdTe, cubic; cadmium telluride, CdTe, hexagonal; cadmium polonide, CdPo; cadmium aluminum selenide, $CdAl_2Se_4$; cadmium aluminum sulfide, $CdAl_2S_4$; cadmium gallium selenide, $CdGa_2Se_4$; cadmium gallium sulfide, $CdGa_2S_4$; cadmium gallium telluride, $CdGa_2Te_4$; cadmium indium selenide, $CdIn_2Se_4$.

Mercury(II) sulfide, HgS (black, red, cinnabar, metacinnabarite); mercury(II) selenide, HgSe (tiemannite); mercury(II) telluride, HgTe (coloradoite); mercury aluminum sulfide, $HgAl_2S_4$; mercury aluminum selenide, $HgAl_2Se_4$; mercury gallium sulfide, $HgGa_2S_4$; mercury gallium selenide, $HgGaSe_4$; mercury indium selenide, $HgIn_2Se_4$; mercury indium telluride, $Hg_5In_2Te_8$.

### 1.2.7.12 Group IIIB (13). Boron, Aluminum, Gallium, Indium, Thallium

The Group 13 elements are often designated as poor metals, except boron that is considered as a metalloid. Several boron compounds of the type $(BX_2)_n$ (X = S, Se) have been identified that exhibit layered structures with zigzag chains of interconnected 1,2,4-trithia(selena)-3,5-diborolane rings oriented in a parallel manner within the plane and antiparallel to the strands of neighboring layers. Note that the "normal" boron sulfide $B_2S_3$ (according to the valencies) adopts also a layered structure comprising sheets of interconnected $B_3S_3$ and $B_2S_2$ rings extending throughout the crystal. Molecular cyclic boron–chalcogen compounds with organic or halogen ligands have been characterized, primarily in the gas phase and recently also in the form of single crystals. Structural characterizations have been reported for a variety of thio- and selenoborates, mostly with alkali metals (e.g., $Cs_2B_2S_4$, $Na_3B_3S_6$), but also with alkaline earth and *p*-block metals (e.g., $BaB_2S_4$, $TlBS_2$, $Pb_2B_4S_{10}$), as well as for perchalcogenoborates (e.g., $Li_2B_2S_5$, $K_2B_2S_7$; 1D infinite polymers). Lithium thio- and selenoborates, being ionic conductors in the glassy state, have potential for applications in battery and fuel cell systems. In effect, the boron–sulfur and boron–selenium systems provide an overwhelming number of versatile, chemically, and technologically interesting structures, which call for the development of preparation techniques capable of producing high-purity material in glassy, microcrystalline, and single-crystalline form [103, 104].

The chalcogen compounds of Al, Ga, In, and Tl exhibit intrinsic vacancy structures possessing semiconductor properties. For aluminum, the only stable chalcogenides at normal temperatures are the $Al_2X_3$ with X = S, Se, or Te. The small size of Al relative to the chalcogens dictates tetrahedral coordination and the various $Al_2X_3$ polymorphs are related to wurtzite structure, two-thirds of the available metal sites being occupied in either an ordered (α) or a random (β) fashion. The Ga, In, and Tl chalcogenides are much more numerous and at least a dozen different

structure types have been established. Similar to Al, the $M_2X_3$ crystals (M = Ga, In, Tl; X = S, Se, Te) are mostly based on M-defect tetrahedral structures, namely W ($Ga_2S_3$, $In_2Se_3$) and ZB ($Ga_2Se_3$, $Ga_2Te_3$, $In_2Te_3$). At atmospheric pressure, $In_2S_3$ can be present in three modifications. The low-temperature α-form is a cubic close-packed structure of S atoms, where 70% of the In atoms are randomly distributed on octahedral sites and the rest remain on tetrahedral sites. The β-form is related to the spinel structure, and the γ-modification is hexagonal.

$Al_2Se_3$, with a band gap of 3.1 eV, is of interest for heterostructures with $Ga_2Se_3$, offering potential for a larger band gap analogue to optoelectronic devices based on AlAs, GaAs, and to the band gap engineering provided by $Al_xGa_{1-x}$ As alloys. $Ga_2Se_3$, with its lower band gap of 1.9–2.6 eV [105], has potential for optoelectronic devices, memory switching, and light-emitting diodes in combination with GaP substrate. Both $Ga_2Se_3$ and $Al_2Se_3$ have the advantage of being latticed matched to silicon (0.1 and 1.3% mismatch, respectively) and, therefore, may be readily integrated with silicon-based technologies [106]. $In_2S_3$ is an intrinsic n-type semiconductor with an optical direct band gap of ca. 2 eV. $In_2Te_3$ with its 1 eV band gap has a suitable match to the solar spectrum, while presenting an anomalously high radiation stability and electrical conductivity remarkably insensitive to impurities.

The MX compounds such as GaS, GaSe, GaTe, InS, and InSe are known to form layered semiconductor crystals comprising a regular stacking of X–M–M–X layers, whereas InTe, TlS, and TlSe consist of chains of edge-shared tetrahedra. These systems are not derivatives of M(II), and mixed valence has to be considered to cope with the complexity of their structures. For example, in TlSe half the metal atoms are present as Tl(I) and half as Tl(III); therefore the compound should be formulated as an ionic thallous–thallic selenide, $Tl^I(Tl^{III}Se_2)$. Note also that TlTe is a variant of the complex $W_5Si_3$-type structure, while thallous sulfide, $Tl_2S$, is known to crystallize in a distorted $CdI_2$ layer form, with Tl(I) in trigonal coordination.

Most commonly available 13–16 binary chalcogenides[19]:

Boron sulfide, $B_2S_3$; aluminum sulfide, $Al_2S_3$; aluminum selenide, $Al_2Se_3$; aluminum telluride, $Al_2Te_3$; gallium(II) sulfide, GaS; gallium(III) sulfide, $Ga_2S_3$; gallium(III) selenide, $Ga_2Se_3$; gallium(II) selenide, GaSe; gallium(III) telluride, $Ga_2Te_3$; gallium(II) telluride, GaTe; indium(III) telluride, $In_2Te_3$, high-temperature form; indium(II) sulfide, InS; indium(III) sulfide, $In_2S_3$; indium(III) selenide, $In_2Se_3$; thallium(I) selenide, $Tl_2Se$; thallium(I) sulfide, $Tl_2S$.

### 1.2.7.13  Group IVB (14). Germanium, Tin, Lead

Most metalloid elements form sulfides either of a molecular nature or having polymeric structures involving sulfur bridges. Thus, carbon disulfide, $CS_2$, consists of finite molecules, while silicon disulfide, $SiS_2$, consists of infinite chains of $SiS_4$ tetrahedra sharing opposite edges, the chains being held to one another by vdW forces.

---

[19] Ibid., p. 29.

For the metallic elements of Group 14, all nine MX compounds (M: Ge, Sn, Pb; X: S, Se, Te) are known. Their crystalline structure can be viewed as distortion of the NaCl type to an extent depending on the components. The distortion amplitude is larger for the lighter compounds (GeS, SnS), which exhibit layer structures similar to that of the isoelectronic black phosphorus, and vanishes for the heavier compounds (GeTe, SnTe). The crystal symmetry of the layered structures involves corrugated planes of 3-coordinated covalently bonded atoms. This instability creates a gap at the Fermi energy and is responsible for the semiconducting nature of these compounds.

Various polymorphs have been reported for SnS with band gap widths in the range 1.0–1.5 eV, depending on the preparation method. The α-SnS (herzenbergite) is the most frequently occurring phase and is a p-type semiconductor with a direct optical transition at 1.3 eV and a high absorption coefficient ($> 10^4$ cm$^{-1}$). The orthorhombic δ-SnS phase possesses a direct gap between 1.05 and 1.09 eV.

The lead compounds PbS, PbSe, PbTe are narrow-gap semiconductors that have been widely investigated for infrared detectors, diode lasers, and thermophotovoltaic energy converters. Their photoconductive effect has been utilized in photoelectric cells, e.g., PbS in photographic exposure meters. Integrated photonic devices have been fabricated by their heteroepitaxial growth on Si or III–V semiconductors.

Lead(II) sulfide occurs widely as the black opaque mineral galena, which is the principal ore of lead. The bulk material has a band gap of 0.41 eV, and it is used as a $Pb^{2+}$ ion-selective sensor and IR detector. PbS may become suitable for optoelectronic applications upon tailoring its band gap by alloying with II–VI compounds like ZnS or CdS. Importantly, PbS allows strong size-quantization effects due to a high dielectric constant and small effective mass of electrons and holes. It is considered that its band gap energy should be easily modulated from the bulk value to a few electron volts, solely by changing the material's dimensionality.

PbSe, with a direct gap lower than 0.3 eV, is widely used for manufacturing IR emitters, photodetectors, photoresistors, but also for laser diodes and thermovoltaic energy converters. Great attention has been paid to the investigation of the quantum size dependent properties of PbSe and therefore for production of relevant nanostructures. PbTe, with a similar band gap, makes a good candidate for photodetectors in the mid- and far-IR bands and mid-IR quantum-well laser diodes by providing high quantum efficiency, low noise level, and ability to tune peak wavelength by adjusting alloy composition (e.g., PbSnTe). PbTe and its derivative alloys are among the most efficient materials for thermoelectric power generation in the intermediate range of temperature (500–900 K) as they have high thermoelectric figure of merit combined with favorable material properties. However, the bulk material is not usually commercially available and the conductivity control is not easy.

Other binary metal compounds in this group include $GeS_2$, $GeSe_2$, $SnS_2$, $SnSe_2$, $Sn_2S_3$, and $Sn_3S_4$. Germanium disulfide, $GeS_2$, presents a unique structure consisting of a 3D framework of $GeS_4$ tetrahedra. $SnS_2$ has a $CdI_2$-type (C6) structure characterized by adjoining planes of weakly bound S atoms allowing a cleavage in [001] direction. Nominally it behaves as an n-type semiconductor with an indirect energy gap of 2.2 eV. Solid solutions $SnS_xSe_{2-x}$ are obtained over the entire

composition range from $SnS_2$ to $SnSe_2$. These comprise also $CdI_2$-type layered semiconductors. $Sn_2S_3$ (orthorhombic symmetry) is a semiconductor with an optical band gap at ca. 0.95 eV.

Ternary compounds of the type $MM'S_3$ with M = Sn, Pb and M' = Ge, Sn, i.e., $PbSnS_3$, $SnGeS_3$, and $PbGeS_3$, form two isotypic groups with orthorhombic ($MSnS_3$) and monoclinic ($MGeS_3$) symmetry, respectively. These compounds are semiconductors with optical band gaps ranging from 1.05 eV ($PbSnS_3$) to 2.23 eV ($SnGeS_3$) and 2.40 eV ($PbGeS_3$).

Most commonly available Group 14 (Ge, Sn, Pb)–16 chalcogenides[20]:

Germanium(IV) sulfide, $GeS_2$; germanium(II) sulfide, GeS; germanium(IV) selenide, $GeSe_2$; germanium(II) selenide, GeSe; germanium(II) telluride, GeTe; tin(II) sulfide, SnS (herzenbergite); tin(IV) sulfide, $SnS_2$; tin(II) selenide, SnSe; tin(IV) selenide, $SnSe_2$; tin(II) telluride, SnTe; lead(II) sulfide, PbS (galena); lead(II) selenide, PbSe (clausthalite); lead(II) telluride, PbTe (altaite).

### 1.2.7.14 Group VB (15). Antimony, Bismuth

The binary chalcogenides of antimony and bismuth are highly colored compounds that are readily prepared by direct reaction of the elements at 500–900 °C. They have rather complex ribbon or layer structures and exhibit semiconductor properties.

For the sesquichalcogenides $M_2X_3$ (M = Sb, Bi), the intrinsic band gap energy decreases from Sb to Bi for a given chalcogen and in the sequence S > Se > Te for a given metal. Both n- and p-type materials can be obtained by appropriate doping. Stibnite, $Sb_2S_3$, is regarded as a prospective material for solar energy owing to its direct band gap of 1.8–2.5 eV and finds applications in television cameras and various optoelectronic and switching devices. Bismuth sulfide, $Bi_2S_3$ (of a stibnite structure), with its direct band gap of 1.3 eV has a large potential in optoelectronics and also finds applications in thermoelectric refrigeration. The selenide and telluride semiconductors $Bi_2Se_3$, $Bi_2Te_3$, and $Sb_2Te_3$, along with their solid solutions, are well-known thermoelectric materials.

Bismuth(III) telluride ($Bi_2Te_3$) and its alloys are currently the most widely used thermoelectric materials for room-temperature applications. $Bi_2Te_3$ has a layered, tetradymite structure (rhombohedral) and a narrow band gap of ca. 0.18 eV at 300 K. In the phase diagram of the Bi–Te system, the $Bi_2Te_3$ phase exists within a range of 59.5–60.5 at.% Te. Composition ranges of 59.0–62.6 at.% Te for p-type and 62.6–66.0 at.% Te for n-type semiconducting $Bi_2Te_3$ have been reported. $Bi_2Se_3$, with a similar crystal structure and a band gap of 0.35 eV, is usually used as a dopant in $Bi_2Te_3$ to form $Bi_2Te_{3-y}Se_y$ solid solution. $Sb_2Te_3$ is also used as an isomorphous alloying component to form p-type $(Bi_{1-x}Sb_x)_2Te_3$ solid solution.

Most commonly available Group 15 (Sb, Bi)–16 binary chalcogenides[21]:

Antimony(III) sulfide, $Sb_2S_3$ (stibnite); antimony(V) sulfide, $Sb_2S_5$; antimony(III) selenide, $Sb_2Se_3$; antimony(III) telluride, $Sb_2Te_3$; bismuth(III) selenide,

---

[20] Ibid., p. 29.

[21] Ibid., p. 29.

$Bi_2Se_3$; bismuth selenide, BiSe; bismuth(III) sulfide, $Bi_2S_3$ (bismuthinite); bismuth(III) telluride, $Bi_2Te_3$ (tellurobismuthite); bismuth telluride, BiTe.


# General References

Durrant PJ, Durrant B (1962) Introduction to advanced inorganic chemistry. Longmans, London

Wells AF (1962) Structural inorganic chemistry. 3rd edn. Oxford University Press, London

Schmidt M, Siebert W (1973) Sulphur. In: Trotman-Dickenson AF (ed.) Comprehensive Inorganic Chemistry (Vol 2), Pergamon Press, Oxford

Bagnall KW (1973) Selenium, tellurium and polonium. In: Trotman-Dickenson AF (ed.) Comprehensive inorganic chemistry (Vol 2), Pergamon Press, Oxford

Greenwood NN, Earnshaw A (1984) Chemistry of the elements. Pergamon Press, Oxford.

Cotton FA, Wilkinson G (1988) Advanced inorganic chemistry. 5th edn. John Wiley and Sons, New York

Massey AG (1990) Main group chemistry. Ellis Horwood, Chichester

Rasmussen RL, Morse JG, Morse KW (2004) Main Group elements. In: Meyers RA (ed.) Encyclopedia of Physical Science and Technology – Inorganic Chemistry. Elsevier Science, URL: <http://www.elsevier.com/inca/718245>

Demortier A, Lelieur J-P, Levillain E (2006) Sulfur. In Bard AJ, Stratmann M (eds.) Encyclopedia of electrochemistry, Vol. 7a: Inorganic chemistry, Sholz F, Pickett ChJ (eds.), Wiley-VCH, Weinheim, p 253

2007 Minerals Yearbook. http://minerals.usgs.gov/minerals/pubs/commodity/selenium

 http://www.matweb.com/search/MaterialGroupSearch.aspx

# References

1. Jensen WB (1997) A note on the term "Chalcogen". J Chem Educ 74: 1063–1064
2. Fischer W (2001) A second note on the term "Chalcogen". J Chem Educ 78: 1333
3. Fthenakis V, Wang W, Kim HC (2009) Life cycle inventory analysis of the production of metals used in photovoltaics. Renewable Sustainable Energy Rev 13: 493–517
4. Waitkins GR, Bearse AE, Shutt R (1942) Industrial utilization of selenium and tellurium. Ind Eng Chem 34: 899–910
5. Fischer R (1972) Absorption and electroabsorption of trigonal selenium near the fundamental absorption edge. Phys Rev B 5: 3087–3094
6. Séby F, Potin-Gautier M, Giffaut E, Borge G, Donard OFX (2001) A critical review of thermodynamic data for selenium species at 25 °C. Chem Geol 171: 173–194
7. Ball S, Milne J (1995) Studies on the interaction of selenite and selenium with sulfur donors. Part 3. Sulfite. Can J Chem 73: 716–724
8. Sharp KW, Koehler WH (1977) Synthesis and characterization of sodium polyselenides in liquid ammonia solution. Inorg Chem 16: 2258–2265
9. Sheldrick WS (2007) Polychalcogenides. In Devillanova FA (ed.), Handbook of chalcogen chemistry: New perspectives in sulfur, selenium and tellurium, Royal society of Chemistry: Cambridge, UK
10. Schultz LD, Koehler WH (1987) Synthesis and characterization of sodium polytellurides in liquid ammonia solution. Inorg Chem 26: 1989–1993
11. Schultz LD (1990) Synthesis and characterization of potassium polytellurides in liquid ammonia solution. Inorg Chim Acta 176: 271–275
12. Björgvinsson M, Schrobilgen GJ (1991) Homo- and heteropolychalcogenide anions $Ch^{2-}$, $HCh^-$, $Ch_2{}^{2-}$, $Ch_3{}^{2-}$, and $Ch_4{}^{2-}$ (Ch = Se and/or Te): Solution $^1$H, $^{77}$Se, $^{123}$Te, and $^{125}$Te NMR Study. Inorg Chem 30: 2540–2547

13. Smith DM, Ibers JA (2000) Syntheses and solid-state structural chemistry of polytelluride anions. Coord Chem Rev 200–202: 187–205

14. Kanatzidis MG, Huang SP (1994) Coordination chemistry of heavy polychalcogenide ligands. Coord Chem Rev 130: 509–621

15. Gillespie RJ, Passmore J (1971) Polycations of Group VI. Acc Chem Res 4: 413–419

16. Giggenbach WF (1974) Equilibria involving polysulfide ions in aqueous sulfide solutions up to 240 °C. Inorg Chem 13: 1724–1730

17. Licht S, Hodes G, Manassen J (1986) Numerical analysis of aqueous polysulfide solutions and its application to cadmium chalcogenide/polysulfide photoelectrochemical solar cells. Inorg Chem 25: 2486–2489

18. Dubois P, Lelieur JP, Lepoutre G (1988) Identification and characterization of lithium polysulfides in solution in liquid ammonia. Inorg Chem 27: 73–80

19. Licht S (1995) Electrolyte modified photoelectrochemical solar cells. Sol Energy Mater Sol Cells 38: 305–319

20. Vahrenkamp H (1975) Sulfur atoms as ligands in metal complexes. Angew Chem Int Ed Engl 14: 322–329

21. Draganjac M, Rauchfuss TB (1985) Transition metal polysulfides: Coordination compounds with purely inorganic chelate ligands. Angew Chem Int Ed Engl 24: 742–757

22. DuBois MR (1989) Catalytic applications of transition metal complexes. Chem Rev 89: l–9

23. Ansari MA, Ibers JA (1990) Soluble selenides and tellurides. Coord Chem Rev 100: 223–266

24. Roof LC, Kolis JW (1993) New developments in the coordination chemistry of inorganic selenide and telluride ligands. Chem Rev 93: 1037–1080

25. Kanatzidis MG (1995) From cyclo-$Te_8$ to $Te_x^{n-}$ sheets: Are nonclassical polytellurides more classical than we thought? Angew Chem Int Ed Engl 34: 2109–2111

26. Simon A (1981) Condensed metal clusters. Angew Chem Int Ed Engl 20: 1–21

27. Sokolov MN, Fedin VP, Sykes AG (2003) Chalcogenide-containing metal clusters. In: McCleverty JA, Meyer TJ (ed) The Comprehensive Coordination Chemistry II, 2nd edn., Vol 4. Elsevier Science, URL: <http://www.elsevier.com/inca/702343> pp. 761–823

28. Socolov MN (2007) Metal Chalcogenides: Clusters, layers, nanotubes. In Devillanova FA (ed) Handbook of chalcogen chemistry: New perspectives in sulfur, selenium and tellurium, Royal Society of Chemistry: Cambridge, UK

29. Fedorov VE, Mironov YV, Naumov NG, Sokolov MN, Fedin VP (2007) Chalcogenide clusters of group 5–7 metals. Rus Chem Rev 76: 529–552

30. Kornienko A, Emge TJ, Kumar GA, Riman RE, Brennan JG (2005) Lanthanide clusters with internal Ln ions: Highly emissive molecules with solid-state cores. J Am Chem Soc 127: 3501–3505

31. Kornienko AY, Emge TJ, Brennan JG (2001) Chalcogen-rich lanthanide clusters: Cluster reactivity and the influence of ancillary ligands on structure. J Am Chem Soc 123: 11933–11939

32. Wang Y (1991) Nonlinear optical properties of nanometer-sized semiconductor clusters. Acc Chem Res 24: 133–139

33. Wang Y, Suna A, Mahler W, Kasowki R (1987) PbS in polymers. From molecules to bulk solids. J Chem Phys 87: 7315–7322

34. Hodes G (2007) When small is different: some recent advances in concepts and applications of nanoscale phenomena. Adv Mater 19: 639–655

35. Whittingham MS (1978) Chemistry of intercalation compounds. Prog Solid State Chem 12: 41–99

36. Jobic S, Brec R, Rouxel J (1992) Occurrence and characterization of anionic bondings in transition metal dichalcogenides. J Alloy Compd 178: 253–283

37. Wilson JA, Yoffe AD (1969) The transition metal dichalcogenides. Discussion and interpretation of the observed optical, electrical and structural properties. Adv Phys 18(73): 193–335

38. Iglesias JE, Steinfink H (1973) Crystal chemistry of $AB_2X_4$ (X = S, Se, Te) compounds. J Solid State Chem 6: 119–125

39. Tretyakov YuD, Gordeev IV, Kesler YaA (1977) Investigation of some chalcogenides with spinel structure. J Solid State Chem 20: 345–358

40. Madelung O (1992) Semiconductors – Other than Group IV Elements and II-V Compounds. In: Poerscke R (ed) Data in Science and Technology, Springer-Verlag, Berlin, Heidelberg

41. Wei S-H, Zunger A (1987) Total-energy and band-structure calculations for the semi-magnetic $Cd_{1-x}Mn_xTe$ semiconductor alloy and its binary constituents. Phys Rev B 35: 2340–2365

42. Bruce PG, Irvine JTS (2001) Insertion Compounds. In Encyclopedia of Materials: Science and Technology, Elsevier Science Ltd : Oxford ISBN: 0-08-0431526, pp. 4115–4121

43. Schöllhorn R (1980) Reversible topotactic redox reactions of solids by electron/ion transfer. Angew Chem Int Ed Engl 19: 983–1003

44. Schöllhorn R (1984) Electron/ion-transfer reactions of solids with different lattice dimensionality. Pure Appl Chem 56: 1739–1752

45. Wiegers GA (1996) Misfit Layer Compounds: Structures and Physical Properties. Prog Solid State Chem 24: 1–139

46. Tanaka K (2001) Chalcogenide Glasses. In Encyclopedia of Materials: Science and Technology, Elsevier Science Ltd: Oxford ISBN: 0-08-0431526, pp. 1123–1131

47. Ovshinsky SR (1968) Reversible Electrical Switching Phenomena in Disordered Structures. Phys Rev Lett 21: 1450–1453

48. Sarid D, McCarthy B, Jabbour GE (2004) Nanotechnology for data storage applications. In Bhushan B (ed) Springer Handbook of Nanotechnology – Part E. Springer-Verlag, pp. 899–920

49. Greer AL, Mathur N (2005) Changing face of the chameleon. Nature 437: 1246–1247

50. Kanatzidis MG, Poeppelmeier KR (Organizers) (2007) Report from the third workshop on future directions of solid-state chemistry: The status of solid-state chemistry and its impact in the physical sciences. Prog Solid State Chem 36: 1–133

51. Lu Q, Hu J, Tang K, Qian Y, Zhou G, Liu X (2000) Synthesis of nanocrystalline $CuMS_2$ (M = In or Ga) through a solvothermal process. Inorg Chem 39: 1606–1607

52. Wu C, Yu S-H, Antoniette M (2006) Complex concaved cuboctahedrons of copper sulfide crystals with highly geometrical symmetry created by a solution process. Chem Mater 18: 3599–3601

53. Yamaguchi K, Yoshida T, Sugiura T, Minoura H (1998) A Novel approach for CdS thin-film deposition: electrochemically induced atom-by-atom growth of CdS thin films from acidic chemical bath. J Phys Chem B 102: 9677–9686

54. Yoshimura M, Suchanek W (1997) In situ fabrication of morphology-controlled advanced ceramic materials by Soft Solution Processing. Solid State Ionics 98: 197–208

55. Yu S-H, Yoshimura M (2002) Ferrite/metal composites fabricated by soft solution processing. Adv Funct Mater 12: 9–15

56. Kanatzidis MG, Pottgen R, Jeitschko W (2005) The metal flux: a preparative tool for the exploration of intermetallic compounds. Angew Chem Int Ed 44: 6996–7023

57. Trindade T, O'Brien P, Pickett NL (2001) Nanocrystalline semiconductors: Synthesis, properties, and perspectives. Chem Mater 13: 3843–3858

58. Stöwe K, Appel S (2002) Polymorphic forms of rubidium telluride $Rb_2Te$. Angew Chem Int Ed 41: 2725–2730

59. Sheldrick WS, Wachhold M, Jobic S, Brec R, Canadell E (1997) New low-dimensional solids: tellurium-rich alkali metal tellurides. Adv Mater 9: 669–675

60. Zheng Zh, Greedan JE (2004) Rare earth elements and materials. In Meyers RA (ed) Encyclopedia of Physical Science and Technology – Inorganic Chemistry. Elsevier Science, URL: <http://www.elsevier.com/inca/718245>

61. Chen L, Xia SQ, Corbett JD (2005) Metal-rich chalcogenides. Synthesis, structure, and bonding of the layered $Lu_{11}Te_4$. Comparison with the similar $Sc_8Te_3$ and $Ti_{11}Se_4$. Inorg Chem 44: 30573062

62. Babo JM, Schleid T (2008) Synthesis and crystal structure of the rubidium scandium telluride $RbSc_5Te_8$. Z Anorg Allg Chem 634: 1463–1465

63. Katsuyama S, Tanaka Y, Hashimoto H, Majima K, Nagai H (1997) Effect of substitution of La by alkaline earth metal on the thermoelectric properties and the phase stability of $\gamma$-$La_3S_4$. J Appl Phys 82: 5513–5519

64. Assoud A, Soheilnia N, Kleinke H (2007) Thermoelectric properties of the new tellurides $SrSc_2Te_4$ and $BaSc_2Te_4$ in comparison to $BaY_2Te_4$. Intermetallics 15: 371–376

65. Wu P, Ibers JA (1995) Quaternary chalcogenides containing a rare earth and an alkali- or alkaline-earth metal. J Alloy Compd 229: 206–215

66. Narducci AA, Ibers JA (1998) Ternary and quaternary uranium and thorium chalcogenides. Chem Mater 10: 2811–2823

67. Hübener S (2004) Actinide Elements. In Meyers RA (ed) Encyclopedia of Physical Science and Technology – Inorganic Chemistry. Elsevier Science, URL: <http://www.elsevier.com/inca/718245>

68. Lucovsky G, White RM, Benda JA, Revelli JF (1973) Infrared-reflectance spectra of layered Group-IV and Group-VI transition-metal dichalcogenides. Phys Rev B 7: 3859–3870

69. Cordes H, Schmid-Fetzer R (1994) Phase equilibria in the Ti-Te system. J Alloy Compd 216: 197–206

70. Harbrecht B, Conrad M, Degen T, Herbertz R (1997) Synthesis and crystal structure of $Hf_2Te$. J Alloy Compd 255: 178–182

71. Hughbanks T (1995) Exploring the metal-rich chemistry of the early transition elements. J Alloy Compd 229: 40–53

72. Rouxel J (1992) Low-dimensional solids: An interface between molecular and solid-state chemistry? The example of chainlike niobium and tantalum chalcogenides. Acc Chem Res 25: 328–336

73. Harbrecht B (1989) $Ta_2Se$: A tantalum-rich selenide with a new layer structure. Angew Chem Int Ed Eng 28: 1660–1662

74. Li J, Badding ME, DiSalvo FJ (1992) New layered ternary niobium tellurides: Synthesis, structure, and properties of $NbMTe_2$ (M = Fe, Co). Inorg Chem 31: 1050–1054

75. Tremel W, Kleinke H, Derstroff V, Reisner C (1995) Transition metal chalcogenides: New views on an old topic. J Alloy Compd 219: 73–82

76. Young DJ, Smeltzer WW, Kirkaldy JS (1973) Nonstoichiometry and thermodynamics of chromium sulfides. J Electrochem Soc 120: 1221–1224

77. Li Q, Walter EC, van der Veer WE, Murray BJ, Newberg JT, Bohannan EW, Switzer JA, Hemminger JC, Penner RM (2005) Molybdenum disulfide nanowires and nanoribbons by electrochemical/chemical synthesis. J Phys Chem B 109: 3169–3182

78. Tenne R, Homyonfer M, Feldman Y (1998) Nanoparticles of layered compounds with hollow cage structures (inorganic fullerene-like structures). Chem Mater 10: 3225–3238

79. Shibahara T (1993) Syntheses of sulphur-bridged molybdenum and tungsten coordination compounds. Coord Chem Rev 123: 73–147

80. Chevrel R, Gougeon P, Potel M, Sergent M (1985) Ternary molybdenum chalcogenides: A route to new extended clusters. J Solid State Chem 57: 25–33

81. Harvey G, Matheson TW (1986) Hydroprocessing catalysis by supported ruthenium sulphide. J Catal 101: 253–261

82. Passaretti D, Chianelli RR, Wold A, Dwight K, Covino J (1986) Preparation and properties of the systems $Co_{1-x}Rh_xS_2$, $Co_{1-x}Ru_xS_2$, and $Rh_{1-x}Ru_xS_2$. J Solid State Chem 64: 365–371

83. Riaz U, Curnow OJ, Curtis MD (1994) Desulfurization of organic sulfur compounds mediated by a molybdenum /cobalt /sulfur cluster. J Am Chem Soc 116: 4357–4363

84. Furdyna JK (1988) Dilute magnetic semiconductors. J Appl Phys 64: R29–64

85. Oestreich M, Hübner J, Hägele D, Klar PJ, Heimbrodt W, Rühle WW, Ashenford DE, Lunn B (1999) Spin injection into semiconductors. Appl Phys Lett 74: 1251–1253

86. Lamfers HJ, Meetsma A, Wiegers GA, Boer JL (1996) The crystal structure of some rhenium and technetium dichalcogenides. J Alloy Compd 241: 34–39
87. Schwarz DE, Frenkel AI, Nuzzo RG, Rauchfuss TB, Vairavamurthy A (2004) Electrosynthesis of $ReS_4$. XAS analysis of $ReS_2$, $Re_2S_7$, and $ReS_4$. Chem Mater 16: 151–158
88. Dey S, Jain VK (2004) Platinum group metal chalcogenides. Their syntheses and applications in catalysis and materials science. Platinum Metals Rev 48: 16–29
89. Jiang X, Xie Y, Lu J, He W, Zhu L, Qian Y (2000) Preparation and phase transformation of nanocrystalline copper sulfides ($Cu_9S_8$, $Cu_7S_4$ and CuS) at low temperature. J Mater Chem 10: 2193–2196
90. Blachnik R, Lasocka M, Walbrecht U (1983) The system copper-tellurium. J Solid State Chem 48: 431–438
91. Jaffe JE, Zunger A (1984) Theory of the band-gap anomaly in $ABC_2$ chalcopyrite semiconductors. Phys Rev B. 29: 1882–1906
92. Tell B, Shay JL, Kasper HM (1974) Some properties of $AgAlTe_2$, $AgGaTe_2$, and $AgInTe_2$. Phys Rev B 9: 5203–5208
93. Ouammou A, Mouallem-Bahout M, Peña O, Halet JF, Saillard JY, Carel C (1995) Physical properties and electronic structure of ternary barium copper sulfides. J Solid State Chem 117: 73–79
94. Starodub VA (1999) Ternary and quaternary chalcogenides of Group IB elements. Rus Chem Rev 68: 801–820
95. Davies DA, Vecht A, Silver J, Marsh PJ, Rose JA (2000) A novel method for the preparation of inorganic sulfides and selenides I. Binary materials and Group II–VI phosphors. J Electrochem Soc 147: 765–771
96. Nicolau YF, Dupuy M, Brunel M (1990) ZnS, CdS, and $Zn_{1-x}Cd_xS$ thin films deposited by the successive ionic layer adsorption and reaction process. J Electrochem Soc 137: 2915–2924
97. Loferski JL (1956) Theoretical considerations governing the choice of the optimum semiconductor for photovoltaic solar energy conversion. J Appl Phys 27: 777–784
98. Dybko K, Szuszkiewicz W, Dynowska E, Paszkowicz W, Witkowska B (1998) Band structure of $\beta$-HgS from Shubnikov–de Haas effect. Physica B 256–258: 629–632
99. Mathe MK, Cox SM, Venkatasamy V, Uwe Happek, Stickney JL (2005) Formation of HgSe thin films using electrochemical atomic layer epitaxy. J Electrochem Soc 152: C751–C755
100. Lombos BA, Lee EYM, Kipling AL, Krawczyniuk RW (1975) Mercury Chalcogenides, Zero gap semiconductors. J Phys Chem Solids 36: 1193–1198
101. Wei S-H, Zunger A (1988) Role of metal d-states in II–VI semiconductors. Phys Rev B 37: 8958–8986
102. Wei S-H, Zunger A (1986) Alloy-stabilized semiconducting and magnetic zinc-blende phase of MnTe. Phys Rev Lett 56: 2391–2394
103. Conrad O, Jansen C, Krebs B (1998) Boron – Sulfur and Boron – Selenium compounds – From unique molecular structural principles to novel polymeric materials. Angew Chem Int Ed 37: 3208–3218
104. Takaluoma T, Säkkinen T, Bajorek T, Laitinen RS, Krebs B, Conrad H, Conrad O (2007) Computational study of hybrid chalcogenoborate anions. J Mol Struct (THEOCHEM) 821: 1–8
105. Morley S, Emde von der M, Zahn DRT, Offermann V, Ng TL, Maung N, Wright AC, Fan GH, Poole IB, Williams JO (1996) Optical spectroscopy of epitaxial $Ga_2Se_3$ layers from the far infrared to the ultraviolet. J Appl Phys 79: 3196–3199
106. Lu CY, Adams JA, Yu Q, Ohta T, Olmstead MA, Ohuchi FS (2008) Heteroepitaxial growth of the intrinsic vacancy semiconductor $Al_2Se_3$ on Si(111): Initial structure and morphology. Phys Rev B 78: 075321–075326

# Chapter 2
# Electrochemistry of the Chalcogens

## 2.1 General References

Because of their multiple oxidation states, the chalcogens, particularly sulfur, can engage in numerous redox couples participating in acid–base, oxidation–reduction, precipitation, and complexation equilibria.

In the anion electrochemical series, sulfur, being the less noble element compared to its heavier congeners, occupies an intermediate position between iodine and selenium [(+)F, Cl, Br, I, S, Se, Te(–)]. Selenium, regarded as a metalloid, is a relatively noble element. Tellurium is rather an amphoteric element: it can enter into solution in the form of both cations and anions. Regarded as a metal, i.e., with respect to its cations, tellurium occupies a position between copper and mercury. Regarded as a metalloid, i.e., with respect to its anions, it is located on the extreme right of the above series.

A comprehensive survey of the classical electrochemical facts for sulfur, selenium, and tellurium, as documented until about 1970, can be found in the reviews of Zhdanov [1], wherefrom we cite the lists of standard and formal potentials for aqueous solutions, in Tables 2.1, 2.2, and 2.3, respectively. Many of these potentials have been calculated thermodynamically since the experimental determinations are few. The listed data are largely drawn from the monograph by Pourbaix (below), and the interested reader should validate the measurement conditions for the indicated potentials or the scatter in their values (not given here in detail). In these tables, the redox systems are assorted by decreasing formal valency of chalcogen in the oxidized state, while at a given valency of the oxidized state they appear in the order of decreasing valency of chalcogen in the reduced state. Latimer [2] has compiled useful aqueous redox transition potential diagrams (reproduced also in Zhdanov's monographs) that are convenient as a quick guide in practical problems and for perceiving the oxidation–reduction properties of some chalcogen hydride and oxychalcogenide species. Standard potentials of chalcogens in non-aqueous media are generally not known, at least in a systematic manner.

A standard approach for the theoretical presentation of electrochemical equilibria is the use of Pourbaix, or potential–pH predominance area diagrams, which incorporate chemical and electrochemical thermodynamics simultaneously in a straightforward manner. These diagrams comprise an extremely useful, yet fundamental,

starting point for the study of electrochemical systems. Certainly, the ability to predict, understand, and ultimately control electrochemical reactions requires also knowledge of process kinetics.

Reproduced below are the potential–pH diagrams for the chalcogen–water systems as originally derived and illustrated by Pourbaix [3], along with some accompanying data. These will serve as a guide to all subsequent discussion on aqueous systems used for electrochemical preparations of metal chalcogenides. The reader may take notice of the chalcogen-containing substances that are considered to be present in the electrolytes and their stability domains. The diagrams represent, almost exclusively, the important "valencies" of the chalcogens, namely –2, +4, and +6 (and not effective oxidation states corresponding, e.g., to polysulfides and the like). Still, all known substances for each chalcogen, either stable in water or not, are registered here, in order to serve as a useful basis for the formulae and nomenclature used in the rest of the book. Note that the parts of the Pourbaix diagrams outside the zero activity lines (log $C = 0$) regard ideal solutions containing 1 M of dissolved chalcogen in the forms considered, and the parts inside these lines regard solutions saturated with solid chalcogen (plus $TeO_2$ in the case of tellurium). The diagrams are valid only in the absence of substances with which the respective chalcogen can form soluble complexes or insoluble salts.

It is considered useful to include here the potential–pH diagram for some redox systems related to oxygen (Fig. 2.1) [4]. Lines 11′ and 33′ correspond to the (a) and (b) dashed lines bounding the stability region of water, as depicted in all the subsequent Pourbaix diagrams.
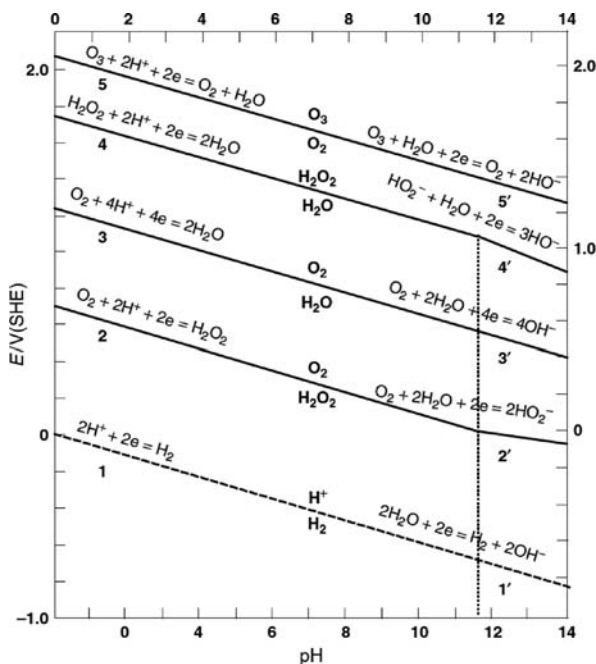


**Fig. 2.1** Potential–pH diagram for oxygen reactions. (L' Her [4] Copyright Wiley-VCH Verlag GmbH & Co. KGaA. Reproduced with permission)

## 2.1.1 Tables of Aqueous Standard and Formal Potentials

**Table 2.1**  Sulfur reactions

| Half-reaction | Standard or formal potential (V vs. SHE at 25 °C) |
|---|---|
| $S_2O_8^{2-} + 2e^- \rightarrow 2SO_4^{2-}$ | +2.01 |
| $S_2O_8^{2-} + 2H^+ + 2e^- \rightarrow 2\,HSO_4^-$ | +2.123 |
| $2SO_4^{2-} + 4H^+ + 2e^- \rightarrow S_2O_6^{2-} + 2H_2O$ | −0.22 |
| $SO_4^{2-} + 4H^+ + 2e^- \rightarrow H_2SO_3 + H_2O$ | +0.17 |
| $SO_4^{2-} + 4H^+ + 2e^- \rightarrow SO_2 + 2H_2O$ | +0.138 |
| $SO_4^{2-} + H_2O + 2e^- \rightarrow SO_3^{2-} + 2OH^-$ | −0.93 |
| $HSO_4^- + 7H^+ + 6e^- \rightarrow S(s) + 4H_2O$ | +0.339 |
| $SO_4^{2-} + 8H^+ + 6e^- \rightarrow S(s) + 4H_2O$ | +0.357 |
| $HSO_4^- + 9H^+ + 8e^- \rightarrow H_2S(aq) + 4H_2O$ | +0.289 |
| $SO_4^{2-} + 10H^+ + 8e^- \rightarrow H_2S(aq) + 4H_2O$ | +0.303 |
| $SO_4^{2-} + 9H^+ + 8e^- \rightarrow HS^- + 4H_2O$ | +0.252 |
| $SO_4^{2-} + 8H^+ + 8e^- \rightarrow S^{2-} + 4H_2O$ | +0.149 |
| $SO_4^{2-} + 10H^+ + 8e^- \rightarrow H_2S(g) + 4H_2O$ | +0.311 |
| $S_2O_6^{2-} + 4H^+ + 2e^- \rightarrow 2H_2SO_3$ | +0.57 |
| $S_2O_6^{2-} + 2H^+ + 2e^- \rightarrow 2HSO_3^-$ | +0.455 |
| $S_2O_6^{2-} + 2e^- \rightarrow 2SO_3^{2-}$ | +0.026 |
| $3H_2SO_3 + 2e^- \rightarrow S_3O_6^{2-} + 3H_2O$ | +0.30 |
| $2H_2SO_3 + H^+ + 2e^- \rightarrow HS_2O_4^- + 2H_2O$ | −0.08, −0.056 |
| $2SO_3^{2-} + 2H_2O + 2e^- \rightarrow S_2O_4^{2-} + 4OH^-$ | −1.12 |
| $2SO_3^{2-} + 4H^+ + 2e^- \rightarrow S_2O_4^{2-} + 2H_2O$ | +0.416 |
| $2HSO_3^- + 3H^+ + 2e^- \rightarrow HS_2O_4^- + 2H_2O$ | +0.060 |
| $2HSO_3^- + 2H^+ + 2e^- \rightarrow S_2O_4^{2-} + 2H_2O$ | −0.013, −0.009 |
| $4H_2SO_3 + 4H^+ + 6e^- \rightarrow S_4O_6^{2-} + 6H_2O$ | +0.51 |
| $4HSO_3^- + 8H^+ + 6e^- \rightarrow S_4O_6^{2-} + 6H_2O$ | +0.581 |
| $4SO_2(g) + 4H^+ + 6e^- \rightarrow S_4O_6^{-2} + 2H_2O$ | +0.510 |
| $2H_2SO_3 + 2H^+ + 4e^- \rightarrow S_2O_3^{2-} + 3H_2O$ | +0.40 |
| $2SO_3^{2-} + 3H_2O + 4e^- \rightarrow S_2O_3^{2-} + 6OH^-$ | −0.58 |
| $2SO_3^{2-} + 6H^+ + 4e^- \rightarrow S_2O_3^{2-} + 3H_2O$ | +0.705 |
| $H_2SO_3 + 2H^+ + 2e^- \rightarrow H_2SO_2 + H_2O$ | < +0.4 |
| $2HSO_3^- + 4H^+ + 4e^- \rightarrow S_2O_3^{2-} + 3H_2O$ | +0.491 |
| $5H_2SO_3 + 8H^+ + 10e^- \rightarrow S_5O_6^{2-} + 9H_2O$ | +0.41 |
| $H_2SO_3 + 4H^+ + 4e^- \rightarrow S(s) + 3H_2O$ | +0.45 |
| $SO_3^{2-} + 3H_2O + 4e^- \rightarrow S(s) + 6OH^-$ | −0.66 |
| $SO_2(g) + 4H^+ + 4e^- \rightarrow S(s) + 2H_2O$ | +0.451, +0.470 |
| $SO_3^{2-} + 6H^+ + 6e^- \rightarrow S^{2-} + 3H_2O$ | +0.231 |
| $S_4O_6^{2-} + 2e^- \rightarrow 2S_2O_3^{2-}$ | +0.08, +0.219, −0.10 |
| $S_4O_6^{2-} + 12H^+ + 10e^- \rightarrow 4S(s) + 6H_2O$ | +0.416 |

**Table 2.1**   (continued)

| Half-reaction | Standard or formal potential (V vs. SHE at 25 °C) |
|---|---|
| $H_2SO_2 + 2H^+ + 2e^- \rightarrow S(s) + 2H_2O$ | $> +0.5$ |
| $S_2O_3^{2-} + 6H^+ + 4e^- \rightarrow 2S(s) + 3H_2O$ | $+0.465$ |
| $S_5O_6^{2-} + 12H^+ + 10e^- \rightarrow 5S(s) + 6H_2O$ | $+0.484$ |
| $SO(g) + 2H^+ + 2e^- \rightarrow S(s) + H_2O$ | $+1.507$ |
| $5S_2O_3^{2-} + 30H^+ + 24e^- \rightarrow 2S_5^{2-} + 15H_2O$ | $+0.331$ |
| $S_2O_3^{2-} + 8H^+ + 8e^- \rightarrow 2HS^- + 3H_2O$ | $+0.200$ |
| $S_2O_3^{2-} + 6H^+ + 8e^- \rightarrow 2S^{2-} + 3H_2O$ | $-0.006$ |
| $S_2Cl_2 + 2e^- \rightarrow 2S(s) + 2Cl^-$ | $+1.23$ |
| $5S(s) + 2e^- \rightarrow S_5^{2-}$ | $-0.340, -0.315$ |
| $4S(s) + 2e^- \rightarrow S_4^{2-}$ | $-0.33$ |
| $S(s) + 2H^+ + 2e^- \rightarrow H_2S(aq)$ | $+0.141$ |
| $S(s) + 2H^+ + 2e^- \rightarrow H_2S(g)$ | $+0.171$ |
| $S(s) + H^+ + 2e^- \rightarrow HS^-$ | $-0.065$ |
| $S(s) + H_2O + 2e^- \rightarrow HS^- + OH^-$ | $-0.52$ |
| $S(s) + 2e^- \rightarrow S^{2-}$ | A large number of measurements and calculated values are available. These vary from $-0.48$ to $-0.58$ V, but most are closer to $-0.48$ V |
| $4S_5^{2-} + 2e^- \rightarrow 5S_4^{2-}$ | $-0.441$ |
| $S_5^{2-} + 5H^+ + 8e^- \rightarrow 5HS^-$ | $+0.003$ |
| $S_5^{2-} + 10H^+ + 8e^- \rightarrow 5H_2S(g)$ | $+0.299$ |
| $3S_4^{2-} + 2e^- \rightarrow 4S_3^{2-}$ | $-0.478$ |
| $S_4^{2-} + 2e^- \rightarrow S^{2-} + S_3^{2-}$ | $-0.52$ |
| $S_4^{2-} + 4H^+ + 6e^- \rightarrow 4HS^-$ | $+0.033$ |
| $2S_3^{2-} + 2e^- \rightarrow 3S_2^{2-}$ | $-0.506$ |
| $S_3^{2-} + 2e^- \rightarrow S^{2-} + S_2^{2-}$ | $-0.49$ |
| $S_3^{2-} + 3H^+ + 4e^- \rightarrow 3HS^-$ | $+0.097$ |
| $S_2^{2-} + 2e^- \rightarrow 2S^{2-}$ | $-0.48, -0.524$ |
| $S_2^{2-} + 2H^+ + 2e^- \rightarrow 2HS^-$ | $+0.298$ |

**Table 2.2**   Selenium reactions

| Half-reaction | Standard or formal potential (V vs. SHE at 25 °C) |
|---|---|
| $HSeO_4^- + 3H^+ + 2e^- \rightarrow H_2SeO_3 + H_2O$ | $+1.090$ |
| $SeO_4^{2-} + 4H^+ + 2e^- \rightarrow H_2SeO_3 + H_2O$ | $+1.15$ |
| $SeO_4^{2-} + 3H^+ + 2e^- \rightarrow HSeO_3^- + H_2O$ | $+1.075$ |
| $SeO_4^{2-} + 2H^+ + 2e^- \rightarrow SeO_3^{2-} + H_2O$ | $+0.880$ |
| $SeO_4^{2-} + 2e^- + H_2O \rightarrow SeO_3^{2-} + 2OH^-$ | $+0.05$ |

**Table 2.2**   (continued)

| Half-reaction | Standard or formal potential (V vs. SHE at 25 °C) |
|---|---|
| $H_2SeO_3 + 4H^+ + 4e^- \rightarrow Se(s) + 3H_2O$ | +0.740 |
| $HSeO_3^- + 5H^+ + 4e^- \rightarrow Se(s) + 3H_2O$ | +0.778 |
| $SeO_3^{2-} + 6H^+ + 4e^- \rightarrow Se(s) + 3H_2O$ | +0.875 |
| $SeO_3^{2-} + 4e^- + 3H_2O \rightarrow Se(s) + 6OH^-$ | −0.366 |
| $Se^{4+} + 4e^- \rightarrow Se(s)$ | +0.846 |
| $H_2SeO_3 + 6H^+ + 6e^- \rightarrow H_2Se + 3H_2O$ | +0.360 |
| $HSeO_3^- + 7H^+ + 6e^- \rightarrow H_2Se + 3H_2O$ | +0.386 |
| $HSeO_3^- + 6H^+ + 6e^- \rightarrow HSe^- + 3H_2O$ | +0.349 |
| $SeO_3^{2-} + 7H^+ + 6e^- \rightarrow HSe^- + 3H_2O$ | +0.414 |
| $SeO_3^{2-} + 6H^+ + 6e^- \rightarrow Se^{2-} + 3H_2O$ | +0.276 |
| $Se_2Cl_2 + 2e^- \rightarrow 2Se(s) + 2Cl^-$ | +1.1 |
| $Se(s) + 2H^+ + 2e^- \rightarrow H_2Se$ | −0.40 |
| $Se(s) + H^+ + 2e^- \rightarrow HSe^-$ | −0.510 |
| $Se(s) + 2e^- \rightarrow Se^{2-}$ | −0.92 |
| $Se(s) + 2H^+ + 2e^- \rightarrow H_2Se(g)$ | −0.369 |

**Table 2.3**   Tellurium reactions [$TeO_2aq(s)$ refers to hydrated $TeO_2$ crystals]

| Half-reaction | Standard or formal potential (V vs. SHE at 25 °C) |
|---|---|
| $H_2TeO_4 + 6H^+ + 2e^- \rightarrow Te^{4+} + 4H_2O$ | +0.920 |
| $H_2TeO_4 + 3H^+ + 2e^- \rightarrow HTeO_2^+ + 2H_2O$ | +0.953 |
| $H_2TeO_4 + H^+ + 2e^- \rightarrow HTeO_3^- + H_2O$ | +0.631 |
| $HTeO_4^- + 2H^+ + 2e^- \rightarrow HTeO_3^- + H_2O$ | +0.813 |
| $HTeO_4^- + H^+ + 2e^- \rightarrow TeO_3^{2-} + H_2O$ | +0.584 |
| $TeO_4^{2-} + 2H^+ + 2e^- \rightarrow TeO_3^{2-} + H_2O$ | +0.892 |
| $H_2TeO_4 + 2H^+ + 2e^- \rightarrow TeO_2(s) + 2H_2O$ | +1.020 |
| $H_2TeO_4 + 2H^+ + 2e^- \rightarrow TeO_2aq(s) + 2H_2O$ | +0.854 |
| $HTeO_4^- + 3H^+ + 2e^- \rightarrow TeO_2(s) + 2H_2O$ | +1.202 |
| $HTeO_4^- + 3H^+ + 2e^- \rightarrow TeO_2aq(s) + 2H_2O$ | +1.036 |
| $TeO_4^{2-} + 4H^+ + 2e^- \rightarrow TeO_2(s) + 2H_2O$ | +1.509 |
| $TeO_4^{2-} + 4H^+ + 2e^- \rightarrow TeO_2aq(s) + 2H_2O$ | +1.343 |
| $TeO_3(s) + 2H^+ + 2e^- \rightarrow TeO_2(s) + H_2O$ | +1.020 |
| $TeO_3(s) + 2H^+ + 2e^- \rightarrow TeO_2aq(s) + H_2O$ | +0.850 |
| $Te^{4+} + 4e^- \rightarrow Te(s)$ | +0.584 (2–3 M HCI), +0.568, +0.556 |
| $HTeO_2^+ + 3H^+ + 4e^- \rightarrow Te(s) + 2H_2O$ | +0.551 |
| $H_2TeO_3 + 4H^+ + 4e^- \rightarrow Te(s) + 3H_2O$ | +0.589 |
| $HTeO_3^- + 5H^+ + 4e^- \rightarrow Te(s) + 3H_2O$ | +0.713 |
| $TeO_3^{2-} + 6H^+ + 4e^- \rightarrow Te(s) + 3H_2O$ | +0.827 |
| $TeO_2(s) + 4H^+ + 4e^- \rightarrow Te(s) + 2H_2O$ | +0.521 |
| $TeO_2aq(s) + 4H^+ + 4e^- \rightarrow Te(s) + 2H_2O$ | +0.604 |

**Table 2.3**  (continued)

| Half-reaction | Standard or formal potential (V vs. SHE at 25 °C) |
|---|---|
| $Te(OH)_6^{2-} + 4e^- \rightarrow Te(s) + 6OH^-$ | $-0.412$ |
| $TeCl_6^{2-} + 4e^- \rightarrow Te(s) + 6Cl^-$ | $+0.55, +0.630$ (2–3 M HCl) |
| $2Te^{4+} + 10e^- \rightarrow Te_2^{2-}$ | $+0.286$ |
| $2HTeO_2^+ + 6H^+ + 10e^- \rightarrow Te_2^{2-} + 4H_2O$ | $+0.273$ |
| $2HTeO_3^- + 10H^+ + 10e^- \rightarrow Te_2^{2-} + 6H_2O$ | $+0.402$ |
| $2TeO_3^{2-} + 12H^+ + 10e^- \rightarrow Te_2^{2-} + 6H_2O$ | $+0.493$ |
| $Te^{4+} + 2H^+ + 6e^- \rightarrow H_2Te$ | $+0.132$ |
| $HTeO_2^+ + 5H^+ + 6e^- \rightarrow H_2Te + 2H_2O$ | $+0.121$ |
| $Te^{2+} + 2e^- \rightarrow Te(s)$ | $+0.40$ |
| $Te_2S + 2e^- \rightarrow 2Te(s) + S^{2-}$ | $-0.90$ |
| $2Te(s) + 2e^- \rightarrow Te_2^{2-}$ | $-0.840, -0.790, -0.74$ |
| $2Te(s) + 2H^+ + 2e^- \rightarrow H_2Te_2$ | $-0.365$ (30 °C) |
| $3Te_2 + 8e^- \rightarrow 2Te_2^{2-} + 2Te^{2-}$ | $-0.92$ |
| $Te(s) + 2H^+ + 2e^- \rightarrow H_2Te$ | $-0.739, -0.50$ (30 °C) |
| $Te(s) + 2H^+ + 2e^- \rightarrow H_2Te(g)$ | $-0.717$ |
| $Te(s) + 2e^- \rightarrow Te^{2-}$ | $-0.913, -1.14$ |
| $Te_2^{2-} + 4H^+ + 2e^- \rightarrow 2H_2Te$ | $-0.638$ |
| $Te_2^{2-} + 2H^+ + 2e^- \rightarrow 2HTe^-$ | $-0.795$ |
| $Te_2^{2-} + 4H^+ + 2e^- \rightarrow 2H_2Te(g)$ | $-0.595$ |
| $Te_2^{2-} + 2e^- \rightarrow 2Te^{2-}$ | $-1.445$ |

## *2.1.2  Pourbaix Diagram for Sulfur–Water*

Solid substances considered: S (sulfur, light yellow, orthorhombic).

Dissolved (*in aquo*) sulfur substances considered:

$H_2S$ (hydrogen sulfide, colorless), $HS^-$ (hydrogen sulfide ion, colorless), $S^{2-}$ (sulfide ion, colorless), $S_2^{2-}$ (disulfide ion, orange), $S_3^{2-}$ (trisulfide ion, orange), $S_4^{2-}$ (tetrasulfide ion, orange), $S_5^{2-}$ (pentasulfide ion, orange), $H_2S_2O_3$ (thiosulfuric acid, colorless), $HS_2O_3^-$ (acid thiosulfate ion, colorless), $S_2O_3^{2-}$ (thiosulfate ion, colorless), $S_5O_6^{2-}$ (pentathionate ion, colorless), $S_4O_6^{2-}$ (tetrathionate ion, colorless), $HS_2O_4^-$ (acid dithionite ion, colorless), $S_2O_4^{2-}$ (dithionite ion, colorless), $S_3O_6^{2-}$ (trithionate ion, colorless), $H_2SO_3$ (sulfurous acid, colorless), $HSO_3^-$ (bisulfite ion, colorless), $SO_3^{2-}$ (sulfite ion, colorless), $S_2O_6^{2-}$ (dithionate ion, colorless), $H_2SO_4$ (sulfuric acid, colorless), $HSO_4^-$ (bisulfate ion, colorless), $SO_4^{2-}$ (sulfate ion, colorless), $S_2O_8^{2-}$ (dipersulfate ion, colorless).

In Fig. 2.2, the potential–pH diagram is represented for the stable equilibria of the system sulfur–water at 25 °C, i.e., equilibria comprising the forms $H_2S$,
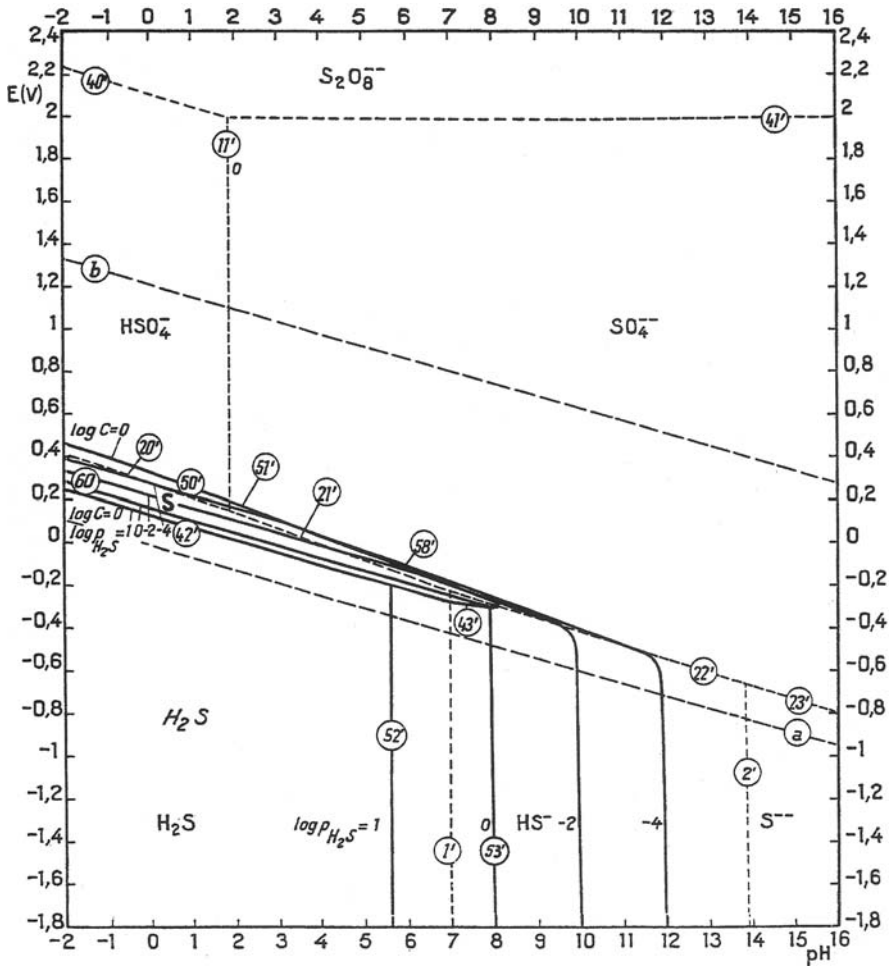
**Fig. 2.2** Potential–pH diagram for the stable equilibria of the system sulfur–water at 25 °C (gaseous hydrogen sulfide is designated in *italic letters*) (Reproduced from [3], Copyright NACE International 2010)

$HS^-$, $S^{2-}$, $S$, $HSO_4^-$, $SO_4^{2-}$, and $S_2O_8^{2-}$, which contain sulfur only in the oxidation states $-2$ and $+6$ (aside from the solid element); other species, such as thiosulfates, dithionites, sulfites, and polythionates are in "false" equilibrium in aqueous solution. Note also that the persulfates ($S_2O_8^{2-}$) are unstable in water, so that if the equilibria were attained, only the remaining six forms would be present in solution. The limits of the domains of relative predominance of the dissolved substances included in the Pourbaix diagram (plus solid sulfur) regard the following homogeneous and heterogeneous (solid/liquid, gas/liquid) equilibria, involving redox and non-redox processes:

| Limits of the domains of relative predominance of dissolved substances | Redox equilibria |
|---|---|
| (**1′**) $H_2S/HS^-$ <br> (**2′**) $HS^-/S^{2-}$ <br> (**52′**) $H_2S(g)/H_2S(aq)$ <br> (**53′**) $H_2S(g)/HS^-$ <br> (**11′**) $HSO_4^-/SO_4^{2-}$ | (**41′**) $S_2O_8^{2-} + 2e^- \rightarrow 2SO_4^{2-}$ <br> (**40′**) $S_2O_8^{2-} + 2H^+ + 2e^- \rightarrow 2HSO_4^-$ <br> (**50′**) $HSO_4^- + 7H^+ + 6e^- \rightarrow S(s) + 4H_2O$ <br> (**51′**) $SO_4^{2-} + 8H^+ + 6e^- \rightarrow S(s) + 4H_2O$ <br> (**20′**) $HSO_4^- + 9H^+ + 8e^- \rightarrow H_2S(aq) + 4H_2O$ <br> (**21′**) $SO_4^{2-} + 10H^+ + 8e^- \rightarrow H_2S(aq) + 4H_2O$ <br> (**22′**) $SO_4^{2-} + 9H^+ + 8e^- \rightarrow HS^- + 4H_2O$ <br> (**23′**) $SO_4^{2-} + 8H^+ + 8e^- \rightarrow S^{2-} + 4H_2O$ <br> (**58′**) $SO_4^{2-} + 10H^+ + 8e^- \rightarrow H_2S(g) + 4H_2O$ <br> (**42′**) $S(s) + 2H^+ + 2e^- \rightarrow H_2S(aq)$ <br> (**60**) $S(s) + 2H^+ + 2e^- \rightarrow H_2S(g)$ <br> (**43′**) $S(s) + H^+ + 2e^- \rightarrow HS^-$ |

## 2.1.3 Pourbaix Diagram for Selenium–Water

Solid substances considered: Se (selenium, gray, trigonal).

Dissolved (*in aquo*) selenium substances considered:

$H_2Se$ (hydrogen selenide, colorless), $HSe^-$ (acid telluride ion, colorless), $Se^{2-}$ (selenide ion, colorless), $H_2SeO_3$ (selenous acid, colorless), $HSeO_3^-$ (acid selenite ion, colorless), $SeO_3^{2-}$ (selenite ion, colorless), $H_2SeO_4$ (selenic acid, colorless), $HSeO_4^-$ (acid selenate ion, colorless), $SeO_4^{2-}$ (selenate ion, colorless).

| Limits of the domains of relative predominance of dissolved substances | Redox equilibria |
|---|---|
| **1′** $HSe^-/H_2Se$ <br> **2′** $Se^{2-}/HSe^-$ <br> **3′** $HSeO_3^-/H_2SeO_3$ <br> **4′** $SeO_3^{2-}/HSeO_3^-$ <br> **6′** $SeO_4^{2-}/HSeO_4^-$ <br> **24** $HSe^-/H_2Se(g)$ | **12′** $HSeO_4^- + 3H^+ + 2e^- \rightarrow H_2SeO_3 + H_2O$ <br> **13′** $SeO_4^{2-} + 4H^+ + 2e^- \rightarrow H_2SeO_3 + H_2O$ <br> **14′** $SeO_4^{2-} + 3H^+ + 2e^- \rightarrow HSeO_3^- + H_2O$ <br> **15′** $SeO_4^{2-} + 2H^+ + 2e^- \rightarrow SeO_3^{2-} + H_2O$ <br> **19** $H_2SeO_3 + 4H^+ + 4e^- \rightarrow Se(s) + 3H_2O$ <br> **20** $HSeO_3^- + 5H^+ + 4e^- \rightarrow Se(s) + 3H_2O$ <br> **21** $SeO_3^{2-} + 6H^+ + 4e^- \rightarrow Se(s) + 3H_2O$ <br> **7′** $H_2SeO_3 + 6H^+ + 6e^- \rightarrow H_2Se + 3H_2O$ <br> **8′** $HSeO_3^- + 7H^+ + 6e^- \rightarrow H_2Se + 3H_2O$ <br> **9′** $HSeO_3^- + 6H^+ + 6e^- \rightarrow HSe^- + 3H_2O$ <br> **10′** $SeO_3^{2-} + 7H^+ + 6e^- \rightarrow HSe^- + 3H_2O$ <br> **11′** $SeO_3^{2-} + 6H^+ + 6e^- \rightarrow Se^{2-} + 3H_2O$ <br> **16** $Se(s) + 2H^+ + 2e^- \rightarrow H_2Se$ <br> **17** $Se(s) + H^+ + 2e^- \rightarrow HSe^-$ <br> **18** $Se(s) + 2e^- \rightarrow Se^{2-}$ <br> **22** $Se(s) + 2H^+ + 2e^- \rightarrow H_2Se(g)$ |
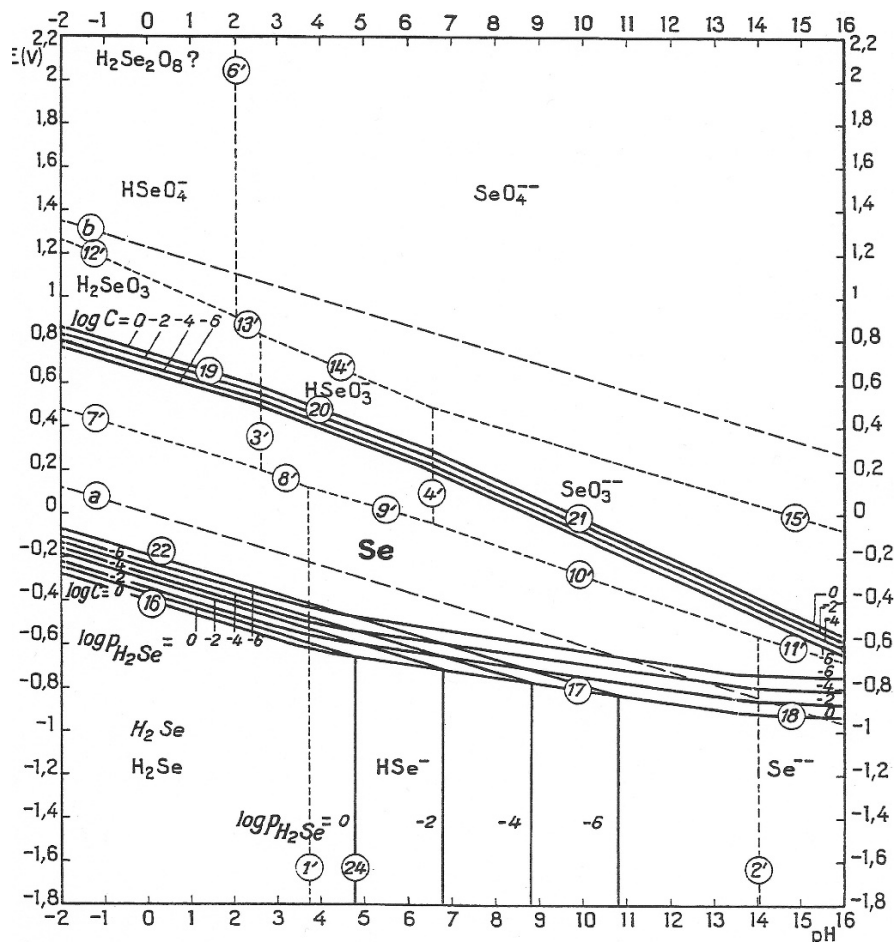
**Fig. 2.3** Potential–pH equilibrium diagram for the system selenium–water, at 25 °C (gaseous hydrogen selenide is designated in *italic letters*) (Reproduced from [3], Copyright NACE International 2010)

The potential–pH diagram for the system selenium–water at 25 °C is given in Fig. 2.3. This diagram was constructed by using the homogeneous and heterogeneous (solid/liquid, gas/liquid) equilibria listed in the previous page, in which all of the above-referred dissolved substances of selenium (as well as solid Se) participate.

## 2.1.4 Pourbaix Diagram for Tellurium–Water

Solid substances considered:

Te (tellurium, brown black, amorphous), $TeO_2$ (tellurous anhydride, white), $TeO_2$ hydr. (tellurous acid, $H_2TeO_3$ or $TeO_2 \cdot H_2O$, white, amorphous), $TeO_3$ hydr. (orthotelluric acid, $H_6TeO_6$ or $TeO_3 \cdot 3H_2O$, colorless, cubic or monoclinic).

Dissolved (*in aquo*) tellurium substances considered:

$H_2Te$ (hydrogen telluride, colorless), $HTe^-$ (hydrogen telluride ion, colorless), $Te^{2-}$ (telluride ion, colorless), $Te_2^{2-}$ (ditelluride ion, red), $Te^{4+}$ (tellurous ion), $HTeO_2^+$ (telluryl ion), $HTeO_3^-$ (acid tellurite ion, colorless), $TeO_3^{2-}$ (tellurite ion, colorless), $H_2TeO_4$ (telluric acid, colorless), $HTeO_4^-$ (acid tellurate ion, colorless), $TeO_4^{2-}$ (tellurate ion, colorless).

The potential–pH diagram for the system tellurium–water at $25\,°C$ is given in Fig. 2.4. It was constructed by using the following homogeneous and heterogeneous (solid/liquid, gas/liquid) equilibria, involving redox and non-redox processes, in which all of the above-referred dissolved substances of tellurium, as well as the solid ones, participate:

| *Limits of the domains of relative predominance of dissolved substances* | *Redox equilibria* |
|---|---|
| $1'$ $H_2Te/HTe^-$ | $17'$ $H_2TeO_4 + 6H^+ + 2e^- \to Te^{4+} + 4H_2O$ |
| $2'$ $HTe^-/Te^{2-}$ | $18'$ $H_2TeO_4 + 3H^+ + 2e^- \to HTeO_2^+ + 2H_2O$ |
| $3'$ $Te^{4+}/HTeO_2^+$ | $19'$ $H_2TeO_4 + H^+ + 2e^- \to HTeO_3^- + H_2O$ |
| $4'$ $HTeO_2^+/HTeO_3^-$ | $20'$ $HTeO_4^- + 2H^+ + 2e^- \to HTeO_3^- + H_2O$ |
| $5'$ $HTeO_3^-/TeO_3^{2-}$ | $21'$ $HTeO_4^- + H^+ + 2e^- \to TeO_3^{2-} + H_2O$ |
| $6'$ $H_2TeO_4/HTeO_4^-$ | $22'$ $TeO_4^{2-} + 2H^+ + 2e^- \to TeO_3^{2-} + H_2O$ |
| $7'$ $HTeO_4^-/TeO_4^{2-}$ | $38'$ $H_2TeO_4 + 2H^+ + 2e^- \to TeO_2(s) + 2H_2O$ |
| | $39'$ $HTeO_4^- + 3H^+ + 2e^- \to TeO_2(s) + 2H_2O$ |
| *Two dissolved substances in the presence of Te (solution saturated with elementary Te)* | $24$ $TeO_3(s) + 2H^+ + 2e^- \to TeO_2(s) + H_2$ |
| | $\qquad TeO_3(s) + 2H^+ + 2e^- \to TeO_2\,aq(s) + H_2O$ |
| | $34'$ $Te^{4+} + 4e^- \to Te(s)$ |
| $8''$ $H_2Te/Te_2^{2-}$ | $35'$ $HTeO_2^+ + 3H^+ + 4e^- \to Te(s) + 2H_2O$ |
| $14''$ $HTeO_2^+/Te_2^{2-}$ | $36'$ $HTeO_3^- + 5H^+ + 4e^- \to Te(s) + 3H_2O$ |
| $15''$ $HTeO_3^-/Te_2^{2-}$ | $37'$ $TeO_3^{2-} + 6H^+ + 4e^- \to Te(s) + 3H_2O$ |
| $16''$ $TeO_3^{2-}/Te_2^{2-}$ | $23$ $TeO_2(s) + 4H^+ + 4e^- \to Te(s) + 2H_2O$ |
| | $11'$ $Te^{4+} + 2H^+ + 6e^- \to H_2Te$ |
| *One solid substance and one dissolved substance* | $12'$ $HTeO_2^+ + 5H^+ + 6e^- \to H_2Te + 2H_2O$ |
| | $33'$ $2Te(s) + 2e^- \to Te_2^{2-}$ |
| | $32'$ $Te(s) + 2H^+ + 2e^- \to H_2Te$ |
| $25'$ $Te^{4+}/TeO_2$ | $45'$ $Te(s) + 2H^+ + 2e^- \to H_2Te(g)$ |
| $26'$ $HTeO_2^+/TeO_2$ | $8'$ $Te_2^{2-} + 4H^+ + 2e^- \to 2H_2Te$ |
| $27'$ $TeO_2/HTeO_3^-$ | $9'$ $Te_2^{2-} + 2H^+ + 2e^- \to 2HTe^-$ |
| $28'$ $TeO_2/TeO_3^{2-}$ | $44'$ $Te_2^{2-} + 4H^+ + 2e^- \to 2H_2Te(g)$ |
| *One gaseous substance and one dissolved substance* | $10'$ $Te_2^{2-} + 2e^- \to 2Te^{2-}$ |
| $42'$ $H_2Te(g)/HTe^-$ | |

**Fig. 2.4** Potential–pH equilibrium diagram for the system tellurium–water, at 25 °C. (The form of TeO$_2$ considered in this diagram is the anhydrous one, which is more stable than the hydrated form TeO$_2$·H$_2$O. Gaseous hydrogen telluride is designated in *italic letters*) (Reproduced from [3], Copyright NACE International 2010)

## 2.2 General Discussion

### 2.2.1 Sulfur

In the Pourbaix diagram, solid sulfur appears to be stable in a very narrow triangular domain, which lies completely within the stability domain of water. Sulfur is therefore stable in the presence of water and in acid solutions free from oxidizing agents. It is unstable, however, in alkaline solutions, in which it tends to disproportionate to give HS$^-$, S$^{2-}$ (and polysulfides), SO$_4^{2-}$, and other oxidation products. In

practice, these reactions are slow and take place only in hot, very alkaline media. The sulfides of the alkali metals and the alkaline earth metals are soluble in water, whereas the other sulfides are insoluble but dissolve in varying degrees in acid solutions.

The various oxidation states of sulfur have been determined by polarography. The electrochemical oxidation of sulfide ions in aqueous solution may lead to the production of elementary sulfur, polysulfides, sulfate, dithionate, and thiosulfate, depending on the experimental conditions. Disulfides, sulfoxides, and sulfones are typical polarographically active organic compounds. It is also found that thiols (mercaptans), thioureas, and thiobarbiturates facilitate oxidation of Hg resulting thus in anodic waves.

The electroreduction behavior of elemental sulfur with formation of polysulfide anions in classical organic solvents (DMF, DMA, DMSO, $CH_3CN$, etc.) as well as in liquid ammonia is well documented [5]. Significant progress has been achieved in the interpretation of this process in dimethylformamide (DMF) [6]. On the other hand, electrooxidation of the element to form polysulfur cations is only known in molten salts and in fluorosulfuric acid [7]. The electrochemical disproportionation of sulfur has been studied in strongly basic media, e.g., in $NaOH+H_2O$ melts [8, 9]. A large number of investigations regard the electrochemical properties of the sulfur–sulfide system in molten mixtures of sulfur and polysulfide [10] or molten chlorides [11, 12] in connection with the production of alkali sulfur batteries (Chap. 6).

The very low solubility of elemental sulfur in water does not allow the study of its electrochemical reduction in aqueous media. Thus, the electrochemical behavior of sulfide ($HS^-$, $S^{2-}$) and polysulfide ions in water is much less documented than for non-aqueous solvents, while the relevant investigations bare often speculative conclusions since the experimental results do not display strong evidence for chemical species involved in the proposed mechanisms. Anyhow, a number of investigations have been carried out on the electrochemical properties of the aqueous sulfur–sulfide system on different substrate electrodes regarding the involved redox behavior, the formation or adsorption of sulfur and sulfur species on the electrodes, and speciation of sulfur species in solution or on the electrode surface. Differences in the method of formation of sulfur layers, stimulated by diverse interests, have led to apparently conflicting observations regarding, for example, the formation or not of polysulfide species as intermediates in the oxidation of sulfide ions to sulfur [13–16]. Analogous dispute is found for the electroreduction of sulfur to sulfide ions [17, 18], since the understanding of these processes requires the unambiguous identification of the reduced forms of sulfur, i.e., polysulfides.

The surface chemistry of sulfur on metals has been intensively studied as being extremely important in several technologies, including metallurgy, metal corrosion, and heterogeneous catalysis. For example, alkali sulfides have been widely used for a long time in the flotation of base metal oxide and sulfide minerals [19, 20]; or well known are the corrosive effects of sulfide ions on iron based alloys during the processing of crude oil and natural gas. The adsorption of sulfur on metal surfaces may have a remarkable effect on the surface reactivity, notably on the electrochemical

properties. Well documented is the effect of sulfur adsorbent layers on the anodic dissolution rate of metals such as copper, silver, gold, nickel or on the conditions for silver electrodeposition, the overvoltage for hydrogen evolution on nickel and iron, etc. (see previous references). The blocking effect of sulfur on hydroxyl adsorption sites of the electrode with subsequent inhibition of the electrochemical oxidation reaction (passivation) is well known, as also is the inhibitory effect of sulfur layers on the electrocatalytic activity of noble metals (especially when the reactants are strongly adsorbed on the electrode). Interestingly, it has been observed that adsorbed sulfur significantly enhances the electrocatalytic activity of some metals causing an increase in the reaction rates. The electroreduction of ferric ions on Pt electrodes in acid media has been used as a model reaction for investigation of the effect of chemisorbed sulfur on the charge transfer across the metal–solution interface. This effect has been interpreted on the basis of the Marcus theory of electron transfer [21, 22].

In the context of environmental chemistry, various polarographic techniques have been successfully used to measure elemental sulfur and sulfide ($H_2S$ and $HS^-$) concentrations in a variety of media, down to nanomolar concentrations.

Redox reactions of sulfur involving reduction–oxidation of sulfate, sulfide, and sulfur species/clusters are of extreme biological, geochemical, and environmental importance. The progress in the electrochemistry of sulfido-clusters is connected with better understanding of the processes that occur in living systems with involvement of transition metals, since at least seven of those (V, Mo, W, Fe, Ni, Cu, and Zn) are bonded quite often to sulfur (and/or selenium) atoms and are vital for various biological functions. For example, the association of sulfur and iron into simple to more complex molecular assemblies allows a great flexibility of electron transfer relays and catalysis in metalloproteins, which play a major role in terminal respiration, photosynthesis, and dinitrogen reduction. Iron–sulfur cluster synthesis in the laboratory and the subsequent study of their electrochemical properties has been stimulated by the occurrence and characterization of such centers in many redox enzymes and provides, in turn, valuable insight into natural reaction mechanisms [23].

## 2.2.2 Selenium

Selenium is stable in water and in aqueous solutions over the entire pH interval in the absence of any oxidizing or reducing agent. Selenium can be electrochemically reduced to hydrogen selenide or to selenides that are unstable in water and aqueous solutions. It can be oxidized to selenous acid or selenites and further (electrolytically) to perselenic acid ($H_2Se_2O_8$). Selenic and selenous acids and their salts are stable in water. The selenides, selenites, and selenates of metals other than the alkali metals are generally insoluble.

The polarographic behavior of selenium in aqueous solutions has been studied in great detail, being in fact far simpler than that of sulfur because the selenium compounds exhibit electrochemical activity essentially in only two different

valent states, i.e., Se(–II) and Se(+IV) [24, 25]. In polarography, the number and shape of the recorded waves as well as the half-wave potential values are influenced considerably by the composition and pH of the solution, mainly through variations in the distribution of the possible solution species ($H_2Se$, $HSe^-$, $Se^{2-}$, $SeO_3^{2-}$, $HSeO_3^-$, $H_2SeO_3$). Quadrivalent selenium exhibits polarographic waves in a number of electrolytes including hydrochloric, sulfuric, nitric, and perchloric acids, potassium nitrate, ammonium acetate, ammonia–ammonium chloride, and orthophosphate buffer solutions [26].

As with sulfur, deposition of Se monolayers tends to passivate electrode surfaces. Selenide compound formation involving the electrode material was evident already from the early studies. Thus, changes in the polarographic waves of Se(IV) upon standing were attributed to the formation of "HgSe" compound [27], while other electrode materials, such as Ag, Cd, Cu, and In, are all known to react chemically with either Se(0) or Se(–II) species. Some electrodes (e.g., Au) promote the UPD of Se(0) via strong metal–Se interactions: Andrews and Johnson [28] reported two waves for the reduction of Se(IV) at an Au electrode in 0.1 M $HClO_4$; the one at the more positive potential was assigned to a UPD process. The authors argued that the electrodeposition of Se(IV) produces Se in three distinct states of activity, one by one corresponding to the three anodic stripping peaks observed for large quantities of deposited Se. The authors claimed that, in effect, approximately a monolayer is initially deposited which is stabilized by 1D interaction with the Au electrode surface. The formation of a bulk deposit produces a large activity gradient which is the driving force for irreversible diffusional transport of Se into the Au electrode forming Au–Se alloy of unknown stoichiometry. Surface-adsorbed selenium and bulk selenium correspond, respectively, to the other two activity states detected by stripping voltammetry.

The mechanism of Se(IV) reduction has been debated a lot in the last four decades. The early polarographic data, as also most recent voltammetric studies, were interpreted in terms of a two-step Se(+IV) $\rightarrow$ Se(0) $\rightarrow$ Se(–II) scheme, where the reduction of Se(0) takes place at the more negative potentials. However, electroreduction of Se(IV), being generally more sluggish than of Te(IV), tends to favor a direct six-electron route at relatively positive potentials. In fact, as first recognized by Skyllas-Kazacos and Miller [29], and emphasized by Wei et al. [30], the $6e^-$ process generating Se(–II) ions, although not recognized in the majority of the earlier studies at least in neutral and acidic media, is considered very likely to occur in competition to the $4e^-$ reduction pathway. Certainly, for a given bath composition, voltammetric or other experiments may reveal which reaction will predominate at any potential.

The observed complexity of the Se(IV) electrochemistry due to adsorption layers, formation of surface compounds, coupled chemical reactions, lack of electroactivity of reduction products, and other interrelated factors has been discussed extensively. Zuman and Somer [31] have provided a thorough literature-based review with almost 170 references on the complex polarographic and voltammetric behavior of Se(+IV) (selenous acid), including the acid–base properties, salt and complex formation, chemical reduction and reaction with organic and inorganic

sulfur compounds, polarographic and stripping analysis in the presence of heavy metal ions, as well as the principles and applications of stripping analyses for determination of ultratraces of Se(IV). Important information was given also on the electroanalytical behavior of Se(IV) on gold, silver, platinum, carbon, copper, titanium, and tin oxide electrodes.

Selenium films have been prepared by electrodeposition via both the cathodic and anodic routes. An informative report embodying findings of early practical work has been given by von Hippel and Bloom [32] who used aqueous selenous/selenic acid mixtures as plating baths. These authors pointed out that the main obstacle in electroplating selenium lies in the polymorphism of the element, and that unless special conditions are chosen the material deposits as a non-conductor and interrupts the current flow. They also reported that the electrodeposition of amorphous selenium practically ceases in the dark but could be continued under strong illumination. Graham et al. [33] described the deposition of thick amorphous Se deposits from $SeO_2$ baths containing a surfactant agent. A serious drawback was the short life of the bath before defective deposits were obtained. The nature of the cathode material was seen to exert a profound influence on the appearance and structure of the deposits. Bright-nickel plating was the best of the substrates examined, which included Pb, Ag, Au, Rh, Cu, dull Ni, bright Cr, black Cr electrodeposits, and Pt sheets. Cattarin et al. [34] studied the Se electrodeposition onto Ti electrodes from acidic selenite baths, as a function of $SeO_2$ concentration, presence of surfactant, electrode illumination, and temperature. Cyclic voltammetry showed a reduction peak followed by a "passive" and then a "transpassive" domain at more negative potentials. Growth of the Se film at potentials within the "reduction" domain stopped at a limiting thickness. The film could be grown further in the "transpassive" potential domain.

Trigonal, "metallic" selenium has been investigated as photoelectrode for solar energy conversion, due to its semiconducting properties. The photoelectrochemistry of the element has been studied in some detail by Gissler [35]. A photodecomposition reaction of Se into hydrogen selenide was observed in acidic solutions. Only redox couples with a relatively anodic standard potential could prevent dissolution of Se crystal.

### 2.2.3 Tellurium

Tellurium is stable in the presence of water and aqueous solutions free from oxidizing agents, except in very alkaline solutions, in which it is possible to dissolve with the simultaneous formation of tellurite, $TeO_3^{2-}$, and ditelluride, $Te_2^{2-}$, ions. In oxygenated water, tellurium becomes covered with the dioxide $TeO_2$, which is non-protective if the tellurium is freshly precipitated, but in the compact state it constitutes a protective film. Tellurium can be cathodically reduced in acid solution to give dissolved and gaseous hydrogen telluride or in alkaline solution to give $Te_2^{2-}$ and possibly $Te^{2-}$ ions. It can be anodically oxidized to tellurous anhydride $TeO_2$ (sparingly soluble at pH around 4–7) or to the telluric oxide (orthotelluric

acid; very soluble), telluric acid, and tellurates. Tellurous ions can be obtained in very acidic solutions. The tellurides, tellurites, and tellurates of metals other than the alkali metals are generally insoluble.

On account of its electrochemically active valent states, tellurium exhibits a very interesting polarographic behavior. Lingane and Niedrach [25], in their fundamental study on dc polarography and controlled potential coulometry in tellurous acid solutions, have shown that, except for strongly alkaline medium, the reduction of Te(+IV) occurs via a four-electron process to tellurium, whereas in sodium hydroxide solutions, $Te^{2-}$ results via a $6e^-$ direct reduction. The presence of a sharp and intense maximum on the wave plateau of acidic or neutral pH media was attributed to the Te/Te(–II) couple, but some difficulties in a correct interpretation arose. Regarding telluride solutions, a practically reversible oxidation of $Te^{2-}$ to the elemental state was noted in the full range of pH [24]. Shinagawa et al. [36, 37] discussed the Te(IV) reduction mechanism in weakly basic solutions, emphasizing that the two-step reduction to Te(0) and further to Te(–II) at the mercury drop electrode is complicated by the adsorption of elemental tellurium at the mercury surface (see also [38–40]). The authors pointed out the influence of UV irradiation on the first reduction step. Panson [41] investigated the polarographic behavior of the ditelluride ion prepared by cathodic dissolution of Te in alkaline solution and noted its disproportionation to Te and $Te^{2-}$.

Lingane and Niedrach have claimed that the +VI states of tellurium (or selenium) are not reduced at the dropping electrode under any of the conditions of their investigation; however, Norton et al. [42] showed that under a variety of conditions, samples of telluric acid prepared by several different procedures do exhibit well-defined (though irreversible) waves, suitable for the analytical determination of the element. The reduction of Te(+VI) at the dropping electrode was found coulometrically to proceed to the –II state (whereas selenate, Se(+VI), was not reduced at the dropping electrode in any of the media reported).

Numerous voltammetric investigations can be found on the electrochemistry of tellurium in aqueous electrolytes and various metals, glassy carbon, or Te electrodes, discussing the mechanism of Te(IV) reduction to Te(0) or the cathodic and anodic stripping of the element (e.g., [43–46]). It is generally accepted that in acid aqueous media the Te(+IV) is present in the form of the telluryl ion $HTeO_2^+$. Experimental data for the solubility and diffusivity of $HTeO_2^+$ have been reported by use of the electrohydrodynamical (EHD) impedance method [47]. In most works, it is assumed that at low pH, the telluryl ion may be electrochemically reduced to give elementary tellurium via a process that takes place in one step with the transfer of four electrons [48]. Further reduction of the formed Te at more negative potentials leads to the $H_2Te$ species and simultaneous hydrogen evolution. In addition, a conproportionation reaction between Te(IV) and Te(–II) appears to give Te(0) deposited on the electrode. Other authors have proposed that the telluryl ion is electrochemically reduced by a direct six-electron transfer to form the $H_2Te$ species, which then reacts chemically with the telluryl ion to give elementary tellurium on the cathode [49, 50]. In any case, using a combination of voltammetry and electrochemical quartz crystal microgravimetry (EQCM), Mori et al. [51] argued that the six-electron reduction

pathway is important and must be considered in the overall mechanistic scheme of electroreduction for both Te(IV) and Se(IV).

The possibility that adsorption reactions play an important role in the reduction of telluryl ions has been discussed in several works (Chap. 3; CdTe). By using various electrochemical techniques in stationary and non-stationary diffusion regimes, such as voltammetry, chronopotentiometry, and pulsed current electrolysis, Montiel-Santillán et al. [52] have shown that the electrochemical reduction of $HTeO_2^+$ in acid sulfate medium (pH 2) on solid tellurium electrodes, generated in situ at $25\,°C$, must be considered as a four-electron process preceded by a slow adsorption step of the telluryl ions; the reduction mechanism was observed to depend on the applied potential, so that at high overpotentials the adsorption step was not significant for the overall process.

Data on the electrochemistry of the telluride ion in alkaline media are relatively limited. Mishra et al. [53] studied the oxidation of $Te^{2-}$ to $Te^0$ at solid electrodes, focusing on the intermediate step(s) of this process, and in particular, the possibility of detecting ditelluride $Te_2^{2-}$ via rotating ring disk electrode (RRDE) methodology. Oxidation beyond the elemental state to $TeO_3^{2-}$ and $TeO_4^{2-}$ was also studied using cyclic and hydrodynamic voltammetry.

Various classes of organotellurium compounds in aprotic solvents have been studied as to their electrochemistry, whereas more limited are the reports on the electrochemistry of tellurium and its inorganic compounds in non-aqueous solvents [54, 55].

# References

1. Zhdanov I (1975) Sulfur. In Bard AJ (ed) Encyclopedia of electrochemistry of the elements, Marcel Dekker, New York (Vol 4, pp. 273–360); Selenium. *Ibid* (pp. 361–392); Tellurium. *Ibid* (pp. 393–443)
2. Latimer WM (1952) The oxidation states of the elements and their potentials in aqueous solutions. 2nd edn. Prentice Hall, New York
3. Pourbaix M (1974) Atlas of electrochemical equilibria in aqueous solutions. National association of corrosion engineers (2nd English Edn.) USA
4. L'Her M (2006) Redox Properties, Electrochemistry of Oxygen. In Bard AJ, Stratmann M (eds) Encyclopedia of Electrochemistry, Vol. 7a: Inorganic Chemistry, Scholz F, Pickett ChJ (eds), Wiley-VCH, Weinheim, p 117
5. Demortier A, Lelieur J-P, Levillain E (2006) Sulfur. In Bard AJ, Stratmann M (eds) Encyclopedia of Electrochemistry, Vol. 7a: Inorganic Chemistry, Scholz F, Pickett ChJ (eds), Wiley-VCH, Weinheim, p 253
6. Levillain E, Gaillard F, Leghie P, Demortier A, Lelieur JP (1997) On the understanding of the reduction of sulfur ($S_8$) in dimethylformamide (DMF). J Electroanal Chem 420: 167–177
7. Fehrmann R, Bjerrum NJ, Poulsen FW (1978) Lower oxidation states of sulfur. 1. Spectrophotometric study of the sulfur-chlorine system in molten sodium chloride-aluminum chloride (37:63 mol%) at $150\,°C$. Inorg Chem 17: 1195–1200
8. Moscardo-Levelut MN, Plichon V (1984) Sulfur chemistry in equimolar NaOH-$H_2O$ melt. I. Electrochemical oxidation of sodium sulfide. J Electrochem Soc 131: 1538–1545
9. Claes P, Dewilde Y, Glibert J (1988) Chemical and electrochemical behaviour in molten alkali hydroxides: Part II. Electrochemistry of chalcogenide ions in the molten NaOH + KOH (49 mol%) eutectic mixture. J Electroanal Chem 250: 327–339

10. Dobson JC, McLarnon FR, Cairns EJ (1986) Voltammetry of sodium polysulfides at metal electrodes. J Electrochem Soc 133: 2069–2076

11. Warin D, Tomczuk Z, Vissers DR (1983) Electrochemical behavior of $Li_2S$ in fused LiCl-KCl electrolytes. J Electrochem Soc 130: 64–70

12. Weaver MJ, Inman D (1975) The sulphur-sulphide electrode in molten salts–I: Chronopotentiometric behaviour in lithium chloride–potassium chloride eutectic. Electrochim Acta 20: 929–936

13. Allen PL, Hickling A (1957) Electrochemistry of sulphur. Part 1 – Overpotential in the discharge of the sulphide ion. Trans Faraday Soc 53: 1626–1635

14. Briceno A, Chander S (1990) Oxidation of hydrosulphide ions on gold – Part I: A cyclic voltammetry study. J Appl Electrochem 20: 506–511

15. Wierse DG, Lohrengel MM, Schultze JW (1978) Electrochemical properties of sulfur adsorbed on gold electrodes. J Electroanal Chem 92: 121–131

16. Van Huong CN, Parsons R, Marcus P, Montes S, Oudar J (1981) Electrochemical behaviour of silver and gold single-crystal surfaces covered with a monolayer of adsorbed sulphur. J Electroanal Chem 119: 137–148

17. Hamilton IC, Woods R (1983) An investigation of the deposition and reactions of sulphur on gold electrodes. J Appl Electrochem 13: 783–794

18. Buckley AN, Hamilton IC, Woods R (1987) An investigation of the sulphur(–II)/sulphur(0) system on gold electrodes. J Electroanal Chem 216: 213–227

19. Hamilton IC, Woods R (1981) An investigation of surface oxidation of pyrite and pyrrhotite by linear potential sweep voltammetry. J Electroanal Chem 118: 327–343

20. Buswell AM, Nicol MJ (2002) Some aspects of the electrochemistry of the flotation of pyrrhotite. J Appl Electrochem 32: 1321–1329

21. Samec Z, Weber J (1972) Reduction of ferric ion on a rotating platinum electrode of the turbulent type in the presence and absence of adsorbed sulfur. J Electroanal Chem Interfacial Electrochem 38: 115–126

22. Samec Z, Weber J (1973) The influence of chemisorbed sulfur on the kinetic parameters of the reduction of $Fe^{3+}$ ions on a platinum electrode on the basis of the Marcus theory of electron transfer. J Electroanal Chem Interfacial Electrochem 44: 229–238

23. Barriére F (2006) Aspects of metallo-sulfur cluster's electrochemistry. In Bard AJ, Stratmann M (eds) Encyclopedia of Electrochemistry, Vol. 7b: Inorganic Chemistry, Scholz F, Pickett ChJ (eds), Wiley-VCH, Weinheim, p 591

24. Lingane JJ, Niedrach LW (1948) Polarography of selenium and tellurium. I. The −2 States. J Am Chem Soc 70: 4115–4120

25. Lingane JJ, Niedrach LW (1949) Polarography of selenium and tellurium. II. The + 4 States. J Am Chem Soc 71: 196–204

26. Christian GD, Knoblock EC, Purdy WC (1963) Polarography of selenium(IV). Anal Chem 35: 1128–1132

27. Christian GD, Knoblock EC, Purdy WC (1965) Use of highly acid supporting electrolytes in polarography. Observed changes in polarographic waves of selenium(IV) upon standing. Anal Chem 37: 425–427

28. Andrews RW, Johnson DC (1975) Voltammetric deposition and stripping of selenium(IV) at a rotating gold-disk electrode in 0.1 M perchloric acid. Anal Chem 47: 294–299

29. Skyllas-Kazacos M, Miller B (1980) Studies in selenous acid reduction and CdSe film deposition. J Electrochem Soc 127: 869–873

30. Wei C, Myung N, Rajeshwar K (1994) A combined voltammetry and electrochemical quartz crystal microgravimetry study of the reduction of aqueous Se(IV) at gold. J Electroanal Chem 375: 109–115

31. Zuman P, Somer G (2000) Polarographic and voltammetric behavior of selenous acid and its use in analysis. Talanta 51: 645–665

32. von Hippel A, Bloom MC (1950) The electroplating of metallic selenium. J Chem Phys 18: 1243–1251

33. Graham AK, Pinkerton HL, Boyd HJ (1959) Electrodeposition of amorphous selenium. J Electrochem Soc 106: 651–654
34. Cattarin S, Furlanetto F, Musiani MM (1996) Cathodic electrodeposition of Se on Ti electrodes. J Electroanal Chem 415: 123–132
35. Gissler W (1980) Photoelectrochemical investigation on trigonal selenium film electrodes. J Electrochem Soc 127: 1713–1716
36. Shinagawa M, Yano N, Kurosu T (1972) Mechanism and analytical aspects of the polarographic maximum wave of tellurium. Talanta 19: 439–450.
37. Shinagawa M, Sorarnasu N, Mori Y, Okuma T (1977) Studies on the prewave of tellurium and its photo-effect. J Electroanal Chem 75: 809–817
38. Volaire M, Vittori O, Porthault M (1974) Determination du tellure (IV) en milieu acide par polarographie à tension alternative impulsionnelle et par voltammétrie à balayage linéaire. Anal Chim Acta 71: 185–191
39. Vittori O (1980) Polarographic study of adsorbed tellurium at the hanging and dropping mercury electrodes in 1 M hydrochloric or perchloric acid solutions. Anal Chim Acta 121: 315–319
40. Sarala Y, Reddy SJ (1986) Electrochemical reduction of tellurium (IV). J Electroanal Chem 214: 179–190
41. Panson AJ (1963) Polarography of the ditelluride ion. J Phys Chem 67: 2177–2180
42. Norton E, Stoenner RW, Medalia AI (1953) Polarography of tellurium (VI). J Am Chem Soc 75: 1827–1830
43. Traore M, Moddo R, Vittori O (1988) Electrochemical behaviour of tellurium and silver telluride at rotating glassy carbon electrode. Electrochim Acta 33: 991–996
44. Ngać N, Vittori O, Quarin G (1984) Voltammetric and chronoamperometric studies of tellurium electrodeposition of glassy carbon and gold electrodes. J Electroanal Chem 167: 227–235
45. Barbier MJ, Becdelievre AM, Becdelievre J (1978) Electrochemical study of tellurium oxidoreduction in aqueous solutions. J Electroanal Chem 94: 47–57
46. Dergacheva MB, Statsyuk VN, Fogel LA (2001) Electroreduction of tellurium (IV) on solid electrodes in neutral solutions. Russ J Electrochem 37: 626–628
47. Deslouis C, Maurin G, Pebere N, Tribollet B (1988) Investigation of tellurium electrocrystallization by EHD impedance technique. J Appl Electrochem 18: 745–750
48. Yagi I, Nakabayashi S, Uosaki K (1998) In situ optical second harmonic rotational anisotropy measurements of an Au(111) electrode during electrochemical deposition of tellurium. J Phys Chem B 102: 2677–2683
49. Gregory WB, Norton ML, Stickney JL (1990) Thin-layer electrochemical studies of the underpotential deposition of cadmium and tellurium on polycrystalline Au, Pt and Cu electrodes. J Electroanal Chem 293: 85–101
50. Dennison S, Webster S (1992) An investigation into the effect of ionic species on the deposition of tellurium and the formation of cadmium telluride. J Electroanal Chem 333: 287–298
51. Mori E, Baker CK, Reynolds JR, Rajeshwar K (1988) Aqueous electrochemistry of tellurium at glassy carbon and gold: A combined voltammetry-oscillating quartz crystal microgravimetry study. J Electroanal Chem 252: 441–451
52. Montiel-Santillán T, Solorza O, Sánchez H (2002) Electrochemical research on tellurium deposition from acid sulfate medium. J Solid State Electrochem 6: 433–442
53. Mishra KK, Ham D, Rajeshwar K (1990) Anodic oxidation of telluride ions in aqueous base: A rotating ring-disk electrode study. J Electrochem Soc 137: 3438–3441
54. Liftman Y, Albeck M, Goldsmidt JME, Yarnitsky Ch (1984) The electrochemistry of tellurium in methylene chloride. Electrochim Acta 29: 1673–1678
55. Jeng EGS, Sun IW (1997) Electrochemistry of tellurium(IV) in the basic aluminum chloride-1-methyl-3-ethylimidazolium chloride room temperature molten salt. J Electrochem Soc 144: 2369–2374

# Chapter 3
# Electrochemical Preparations I (Conventional Coatings and Structures)

## 3.1 Basic Principles and Illustrations

Traditional electrodeposition refers to cathodic formation of bulk metals, preferably in the form of film coatings or electroformed articles, and is concerned with the practical objective of obtaining these materials in a coherent, dense, and macroscopically homogeneous state. Although the majority of plated materials are the (relatively) pure metals, unfavorable chemistry limits the number of metal elements that are capable of being obtained electrochemically from aqueous solutions in an unalloyed state, to only 33 of the about 70 metallic elements in the Periodic Table; and even less are the metals that are deposited to any extent for commercial or technical purposes. Nonetheless, the number of possible alloys which can be made from these metals is very large. Furthermore, immense are the binary or multiple combinations of metals with non-metallic elements; however, electrochemical preparative techniques have not played a significant role in the development of such materials, the reason probably lying in the more complicated character of the relevant processes as compared to electrodeposition of single metal elements or metallic alloys. In any case, the unique feature of electrodeposition being an electrically driven process capable of precise control offers a prospective advantage over thermally driven deposition processes. Further, electrodeposition occurs closer to equilibrium than many vacuum deposition methods; it is more applicable to complex shapes, generally less expensive, and capable of providing very thick coatings.

Efficient methods have been developed to accomplish simultaneous deposition of two or more elements at an electrode, forming an alloy, solid solution, or chemical compound. By far, greater effort has gone into low-temperature processes in aqueous or organic electrolytes, because these systems are simpler to construct, operate, and control. Aqueous electrochemistry is certainly preferred, since certain advantages, such as convenience, longer experience, and soft chemistry, are provided. The large metal plating industry (Cr, Au, Ag, Cu, etc.) is based on aqueous electrochemical techniques and the aqueous solution chemistry is still much better understood than that of non-aqueous system, albeit, in general, the use of water as a solvent is not always possible or even indicated. The choice of solvent or electrolyte depends to a large extent on the ability to put appropriate ions in solution; it may be

crucial in systems where the metal species has a very negative redox potential or the interference of solvent electrochemistry has to be avoided.

The electrochemical preparation of metal chalcogenide compounds has been demonstrated by numerous research groups and reviewed in a number of publications [1–3]. For the most part, the methods that have been used comprise (a) cathodic co-reduction of the metal ion and a chalcogen oxoanion in aqueous solution onto an inert substrate; (b) cathodic deposition from a solvent containing metal ions and the chalcogen in elemental form (the chalcogens are not soluble in water under normal conditions, so these reactions are carried out in non-aqueous solvents); (c) anodic oxidation of the parent metal in a chalconide-containing aqueous electrolyte.

### 3.1.1 Cathodic Electrodeposition

Although similar in some respects to metallic alloy electroplating, as described in the works of Brenner [4], the ionic "alloy" electrodeposition has special features stemming from the particular physical and chemical nature of inorganic (chalcogenide) compounds. The possible semiconducting or insulating nature of such deposits, the large differences in standard reduction potentials between the non-metal (chalcogen) ionic species and most metal ions, the changing nature of the deposit during deposition, and the presence of metastable states present complexities to any theoretical description or practical processing.

In principle, the cathodic deposition of an alloy or chemical compound amounts to a problem of "equilibration" of the Nernst potentials of the constituents to a common (co)deposition potential. Provided that the difference between the standard reduction potentials of the constituents is not too large, this can be achieved by fixing the activities of the electroactive precursors in the solution and near the cathode surface in such a way that the formal reduction potential of the more noble component(s) (N) shifts toward the negative direction, thus approaching that of the less noble component(s) (M). Then the application of an electrode potential slightly more negative than that required to deposit M will form the desired phase on the cathode. In practice though, differences in the individual reduction current densities produce a mixture of the compound and the individual constituents. Fortunately, formation of a pure compound phase may still be achieved by means of "induced" co-deposition, at potentials positive to the Nernst potential of M on account of the chemical interactions between the components of the deposit. In effect, the gain in free energy due to compound formation translates to an anodic shift of the deposition potential, allowing the "underpotential" rather than bulk reduction of the less noble M element. Then, given the proper mass transfer conditions in the cell, a regulated growth of compound film with the correct stoichiometry may be established on the cathode. In order to achieve this goal it is necessary to have one or more hindered steps determining the kinetics of the electrochemical process, such as diffusion of the electroactive species toward the cathode and/or slow surface reactions, i.e., suitably established concentration polarization, possibly along with crystallization

(lattice incorporation) polarization or adsorption effects that may contribute significantly to the whole kinetics. Diffusional transport is important as it also enables oppositely charged ionic species to move in the same direction. Thus, one can perform cathodic electrodeposition with negatively charged ions as well.

From the fundamental point of view, the conditions to be met to achieve cathodic deposition of binary compounds or alloys of well-defined stoichiometry have been discussed in an unprecedented manner by Kröger [5], on the basis of quasi-chemical equilibrium. Kröger treated analytically the "self-regulated" composition observed in binary compound films, by using the Nernst equation as a first approximation. He introduced the concept of quasi-rest potential (QRP) as the physical quantity relevant to a proper description of the deposit bulk, taken as the "equilibrium potential" of the deposit relative to the electrolyte with activities of potential-determining species as they are at the deposit/electrolyte interface during deposition. He argued that the thermodynamic basis of co-deposition can be explained if one takes into account the QRP of the deposit rather than the rest potentials of the individual components, because then one considers inclusively (a) the equilibrium potentials of the components (which may be widely different); (b) the interaction of the components when forming the alloy or compound (this interaction changes the activity of the components in the deposit to an extent depending on the exact deposit composition); (c) the values of the activities of ionic species in the electrolyte at the solid/electrolyte interface during deposition (may be markedly different from those in the bulk); (d) the relative magnitude of the exchange currents of the components in the deposit. Although it was not possible to give exact solutions for the various possible situations, Kröger treated systems in which the rate constants of the exchange currents of individual components were of the same order of magnitude as well as systems in which these rate constants were widely different. In the former case, both species (for a binary deposit) have equal weight in determining the potential and a change between their individual contributions can only occur as a result of a change of the activities of the species in the electrolyte and the corresponding change in the deposit. In the latter case, the exact quantitative treatment of the problem needs a detailed knowledge of the kinetics of processes by which charge transfer for the various components takes place.

Kröger distinguished two cases, according to whether the difference in deposition electrode potential of the individual components is larger (Class I) or smaller (Class II) than the shift in deposition potential of either component as a result of compound or alloy formation. In Class I systems, the deposition potential for a series of alloys is determined by the less noble component. The behavior of Class II systems is more complex, and the potential required to deposit a given composition may be more positive than that of either of the components. Consider for example CdSe and CdTe; both compounds belong to the Class I systems according to Kröger's classification, which means that the less noble component (Cd) remains the potential-determining species over the entire deposition range (for all possible compositions "CdX").

Given the thermodynamic properties of a system, judicious variation of the different plating parameters to assist in manufacturing the desired electrodeposit should be based on an accurate kinetic model. Engelken and Van Doren [6, 7] proposed

a simple kinetic model involving only charge and mass transfer processes, allowing for computer simulation of the electrodeposition process for metal selenides, tellurides, arsenides, and antimonides from respective solutions of the metal and non-metal ions onto bare, inert cathodic substrates. The model was developed in terms of CdTe electrodeposition from acidic solutions of $Cd^{2+}$ and telluryl ions and was based upon a generalized Butler–Volmer equation considering ion transport limitations near the cathode. Effects such as hydrogen generation, ohmic and space charge voltage drops within the deposit, impurity reduction, and possible phase segregation were neglected. The authors argued that despite the simplifying assumptions, their computer simulation of the Cd–Te system may indicate the existence of an underpotential cadmium current density plateau structure, several hundred mV wide, in which Cd should be deposited on a nearly 1:1 basis with Te because of the reduction in cadmium activity associated with compound formation.

Verbrugge and Tobias [8] chose the aqueous Cd–Te system as well, in order to exemplify a mathematical model for a periodic (pulsed current) electrodeposition process, based on their previous work regarding the periodic electrodeposition of multicomponent alloys by an arbitrarily specified current source [9]. These authors argued that pulsing the cell current provides a useful means for improving deposit quality; however, this mode of operation requires a more sophisticated mathematical analysis relative to steady-state processes, to predict deposit composition. They presented an elaborated "engineering" approach to the problem using a multidimensional optimization routine [10] to evaluate physical and chemical parameters from experimental data obtained for the periodic co-electrodeposition of Cd and Te onto a rotating disk electrode (rde). Thermodynamic description of the electrodeposit was coupled with transient convective diffusion equations for the electrolyte species, while the equations describing the solid and electrolyte phases were related by Butler–Volmer expressions for each charge transfer reaction. Transient current–potential relationships, ionic concentration profiles, and deposit compositions, as calculated by the presented model, were in reasonable agreement with the experimental results.

The induced co-deposition concept has been successfully exemplified in the formation of metal selenides and tellurides (sulfur has a different behavior) by a chalcogen ion diffusion-limited process, carried out typically in acidic aqueous solutions of oxochalcogenide species containing quadrivalent selenium or tellurium and metal salts with the metal normally in its highest valence state. This is rather the earliest and most studied method for electrodeposition of compound semiconductors [1]. For MX deposition, a simple $(4+2)e^-$ reduction process may be considered to describe the overall reaction at the cathode, as for example in

$$Cd^{2+} + H_2SeO_3 + 4H^+ + 6e^- \rightarrow CdSe(s) + 3H_2O$$
$$Cd^{2+} + HTeO_2^+ + 3H^+ + 6e^- \rightarrow CdTe(s) + 2H_2O$$
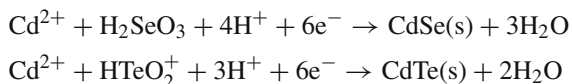
When the diffusion rate of selenite or tellurite species toward the cathode becomes equal to the rate of their discharge, deposition of the chalcogen depletes

its precursor species in the vicinity of the cathode, and a steady-state electrolytic current may be attained for small deviations from the electrode equilibrium potential ensuring a self-regulated induced co-deposition growth by underpotential deposition (UPD) of the metal.

In practical plating situations, complications arise regarding primarily deviations from film stoichiometry by formation of impurity phases, originating from side reactions excluded from self-regulated growth schemes. For the typical baths, the complication may be attributed to the large number of transferred electrons in multiple intermediate steps during the deposition process, as in the scheme $X(+IV)(aq) \rightarrow X^{2-}(aq) \rightarrow X(s)$. Thus, chalcogens in high oxidation states may react homogeneously in solution with electrochemical products of low oxidation state or may redissolve the deposited film producing in both cases a (usually) amorphous elemental chalcogen phase. For example, selenous acid may react (rapidly in acidic and intermediate pH) in the solution phase with selenide ions produced by the six-electron reduction of selenous acid to precipitate elemental Se on the electrode via conproportionation reactions of the type (3.1); or selenous acid may oxidize the selenium in the CdSe phase (3.2):

$$H_2SeO_3 + 2H_2Se \rightarrow 3Se(s) + 3H_2O \tag{3.1}$$

$$2CdSe + H_2SeO_3 + 4H^+ \rightarrow 2Cd^{2+} + 3Se + 3H_2O \tag{3.2}$$
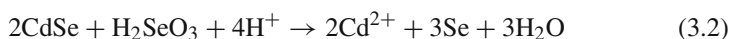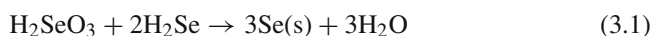
A method to circumvent the problem of chalcogen excess in the solid is to employ low oxidation state precursors in solution, so that the above collateral reactions will not be in favor thermodynamically. Complexation strategies have been used for this purpose [1, 2]. The most established procedure utilizes thiosulfate or selenosulfate ions in aqueous alkaline solutions, as sulfur and selenium precursors, respectively (there is no analogue telluro-complex). The mechanism of deposition in such solutions has been demonstrated primarily from the viewpoint of chemical rather than electrochemical processes (see Sect. 3.3.1). Facts about the (electro)chemistry of thiosulfate will be addressed in following sections for sulfide compounds (mainly CdS). Well documented is the specific redox and solution chemistry involved in the formulation of selenosulfate plating baths and related deposition results [11, 12]. It is convenient to consider some elements of this chemistry in the present section.

In alkaline media, the selenosulfate ions disproportionate to sulfate and highly reactive selenide ions:

$$SeSO_3^{2-} + OH^- \rightleftharpoons HSe^- + SO_4^{2-}$$
$$HSe^- + OH^- \rightleftharpoons Se^{2-} + H_2O$$
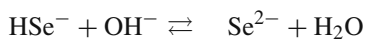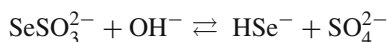
In the presence of a metal ion ($M^{n+}$), a metal chalcogenide phase $M_2Se_n$ will be precipitated upon exceeding the solubility product of $[M^{n+}]$ and $[Se^{2-}]$ (or $[HSe^-]$). The concentration of free metal ions must be controlled by an excess of complexing agent, determining the applicable solubility of the metal and the overall competitive chemical reaction, in order to prevent the formation of sulfite, sulfate, and

hydroxide precipitates in the alkaline media. Then, the overall reaction scheme may be formulated, e.g., for CdSe as

$$Cd(A)_n^{2+} + SeSO_3^{2-} + 2OH^- \rightarrow CdSe + nA + SO_4^{2-} + H_2O$$
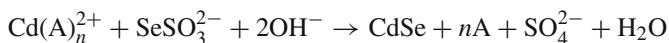
where A is the complexing agent, e.g., $NH_3$, EDTA, or nitrilotriacetate (NTA).

The value of this method lies in the fact that formation of elemental selenium is unlikely to occur since the high-valency species such as Se(IV) that could oxidize the selenide ions are absent from solution. The $SeSO_3^{2-}$ and $SO_3^{2-}$ ions (or their protonated forms) do not oxidize $Se^{2-}$, while any free Se that may be formed would redissolve in sulfite giving selenosulfate again, since the latter is prepared by dissolving Se in excess sulfite.

In the case of electrochemical deposition, several mechanisms have been proposed to account for the formation of the end-product film, the difference among them consisting in the assumed electrochemical step. This may be the reduction of selenosulfate (3.3), inducing deposition of the metal (3.4):

$$SeSO_3^{2-} + 2e^- \rightarrow Se^{2-} + SO_3^{2-} \tag{3.3}$$

$$M^{2+} + Se^{2-} \rightarrow MSe(s) \tag{3.4}$$
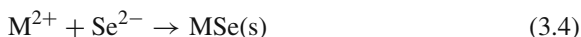
or the electrochemical reduction of the free $M^{2+}$ ions (3.5), followed by a reductive displacement reaction with selenosulfate ions adsorbed at the cathode (3.6):

$$M^{2+} + 2e^- \rightarrow M(s) \tag{3.5}$$

$$M(s) + [SeSO_3^{2-}]_{ads} \rightleftarrows MSe(s) + SO_3^{2-} \tag{3.6}$$
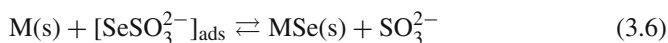
Alternatively, formation of a metal–selenosulfate complex may be assumed to take place in the solution (3.7)):

$$M^{2+} + xSeSO_3^{2-} \rightleftarrows M(SeSO_3)_x^{2-2x}(aq) \tag{3.7}$$
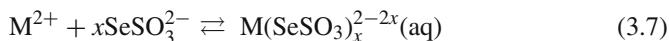
This complex may be reduced either directly to the metal chalcogenide or to the zero-valent metal, which then reacts chemically with selenosulfate adsorbed at the cathode to form MSe.

The detailed mechanism dictating the regulation of the process depends on the specific nature of the system, i.e., on the particular compound to be deposited, complexing agent, solution pH, film thickness, potential, etc. For example, in the case of the Cd–Se system, electroreduction of selenosulfate occurs at more positive potentials for either EDTA–ammonia- or NTA-complexed cadmium [13], whereas for ZnSe, the potential required for the reduction of selenosulfate is already reducing for zinc, implying thus a different mechanism. The metal complex has to be adequately stable and should not interfere with selenosulfate reduction. In these terms,

the process can be regulated so that the chalcogenide film formation will proceed simultaneously with the precipitation of the compound.

Skyllas-Kazacos [14] proposed a different method of cathodic deposition with low-oxidation chalcogen precursors, involving cyanide aqueous solutions of elemental Se and Te, where the chalcogen was presumed to be present as $SeCN^-$ or $TeCN^-$ ions, respectively. Deposition results were only reported for CdSe and CdTe, indicating a nearly amorphous (nanocrystalline) nature of the films, which though did not contain free Se or Te.

Low-temperature, organic electrolyte deposition baths have been used in order to improve the microstructure of the products of simple aqueous cathodic techniques. Aprotic media are effective in avoiding side reactions such as the appearance of hydrogen evolution currents, during the reduction step of the chalcogen precursor, and the formation of various ionic chalcogen complexes resulting from reactions with the solvent and the supporting electrolyte.

Baranski and Fawcett [15] were the first to demonstrate a general method for obtaining stoichiometric metal chalcogenide films by electrodeposition from non-aqueous solutions. The basic idea was to perform cathodic deposition under current control from a suitable aprotic solvent bath containing elemental chalcogen (X) and a salt of the desired metal ion ($M^{n+}$) following, e.g., the route $Me^{2+} + X + 2e^- \rightarrow MX$. As the chalcogen is brought into reaction in non-ionized, molecularly dissolved form, the metal chalcogenide is formed either by a rapid reaction of a freshly deposited metal monolayer with the dissolved X, or by on-site UPD of $M^{n+}$ with electroreduced $X^{2-}$. The technique has proven successful in depositing thin films mostly of binary sulfides (CdS, HgS, PbS, $TI_2S$, $Bi_2S_3$, $Cu_2S$, NiS, CoS) and CdSe. The non-aqueous solvent was usually dimethylsulfoxide (DMSO) while deposits of good quality were also obtained from dimethylformamide (DMF) and ethylene glycol. It must be noted, however, that problems with compositional heterogeneity have been frequently found with this approach too, due to slow kinetics of the M–X reaction and large $M^{n+} \rightarrow M^0$ partial currents leading to metal-rich films. A variant non-aqueous technique comprising a sort of "pulse" deposition that has been proved to ensure better stoichiometry of the deposited compound will be described later in this chapter (Sect. 3.2.16). In addition, there are a few instances of deposition from non-aqueous solvents containing compound rather than elemental chalcogen precursors, such as tri-$n$-butylphosphine selenide or telluride in propylene carbonate and $TeCl_4$ in ethylene glycol (Sects. 3.2.2, 3.2.3, and 3.2.12 (ternaries, $In_2Te_3$); also [1]).

Low-temperature solvents are not readily available for many refractory compounds and semiconductors of interest. Molten salt electrolysis is utilized in many instances, as for the synthesis and deposition of elemental materials such as Al, Si, and also a wide variety of binary and ternary compounds such as borides, carbides, silicides, phosphides, arsenides, and sulfides, and the semiconductors SiC, GaAs, and GaP and InP [16]. A few available reports regarding the metal chalcogenides examined in this chapter will be addressed in the respective sections. Let us note here that halide fluxes provide a good reaction medium for the crystal growth of refractory compounds. A wide spectrum of alkali and alkaline earth halides provides

a sizable temperature window (300–1,000 °C) for synthesis and crystal growth. These fluxes include single salts, such as the monochlorides ACl (with m.p. 605 °C for LiCl up to 801 °C for NaCl), dichlorides $ACl_2$ (m.p. 782 °C for $CaCl_2$ up to 963 °C for $BaCl_2$), and eutectic mixtures such as $CaCl_2/BaCl_2$ (m.p. 450 °C for 43.6/56.4 molar ratio). Recently, a new solvent system, namely room-temperature ionic liquid (RTIL), has attracted much interest [17]. RTILs are organic salts with low melting points that possess a wide range of liquidus temperatures, in some cases in excess of 400 °C, negligible vapor pressure, thermal stability, high ionic conductivity, and a large electrochemical window, making them attractive, novel environmentally friendly solvents for inorganic synthetic procedures [18].

### *3.1.2 Anodization and Other Techniques*

Anodization is facilitated at alkaline pH by the stability of low oxidation state chalcogen species (e.g., $Te^{2-}$) in this range. Thus, intended corrosion of a cadmium electrode in telluride environment may lead to the formation of CdTe:

$$Cd^0 \rightarrow Cd^{2+} + 2e^-$$
$$Cd^{2+} + Te^{2-} \rightarrow CdTe$$
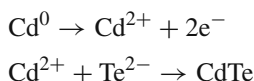
A major disadvantage of the anodic synthesis route is that the thin film growth is self-limiting, so that films thicker than several tens of nm are difficult to attain. On the other hand, much thicker films (several μm) can be realized via the cathodic route. In the latter case, n-type semiconductor compounds will be more likely deposited, since electron transfer is involved – unless light can be used for p-type semiconductors. The opposite is true for anodic formation. It is possible that the originally introduced species in solution or electrogenerated species resulting from the interfacial electrochemical reaction participates in homogeneous chemical reactions (in the electrolyte) whose products may precipitate on the electrode and alter the composition of the deposit. This implication is frequently an important factor in the compositional purity of the end product. Anodic techniques have been originally utilized for the synthesis of binary sulfides, such as CdS, PbS, HgS, and $Bi_2S_3$, by treatment of the parent metal electrode in sulfide solutions.

"Electroless" techniques, that commonly constitute typical galvanic displacement (immersion) processes, have been employed for the formation of some chalcogenide compounds. For instance, electroless anodic chalcogenization of a metal substrate can be conducted by externally coupling this to a reducing chalcogen counter, e.g., a Te rod, when both electrodes are immersed in a suitable electrolyte. During this process (corresponding to corrosion-passivation of valve metals), the cathode material (electron sink) is spontaneously reduced to chalconide ions, which upon releasing in the electrolyte react with the anode material (electron source) to generate the compound. Deposition proceeds as long as oxidized substrate ions are able to permeate through the compound film into solution or until a dielectric layer of oxidized substrate forms, thereby stopping electron transfer. Note that the literature relevant to metal deposition commonly utilizes the term "electroless"

interchangeably to describe three fundamentally different plating mechanisms [19]. Aside from galvanic displacement, these include the so-called autocatalytic and substrate-catalyzed processes, both involving the use of an external reducing agent. These techniques, unlike their "electrolytic" counterparts, do not require instrumentation for potentiostatic or galvanostatic control. Examples of implementation will be discussed in particular in Sect. 3.2.3 and also in Sects. 3.2.10 and 3.2.17.

The virtues of periodic pulse electrolysis (PPE) should be emphasized at this point. The main advantage of the related family of techniques over direct current (dc) electrolysis is that PPE offers more independent variables so that a variety of mass transport situations and electrocrystallization conditions can be created for a given chemical composition of the bath. Pulse plating of metal coatings with improved properties, i.e., reduced porosity and impurity content as well as increased adhesion and uniformity, has been known for some time and widely reported, but the application of PPE for the formation of alloys or binary ceramics is more complicated and remains a relatively unexplored area. Variants of PPE used for the formation of chalcogenides have been shown to promote improved composition control and reduction of film inhomogeneities. Stoichiometric and continuous films of CdTe have been produced by a pulsed potential method [20], while pulsed current methods with and without reversal, or pulsed potential with large pulse to pause ratios, have led to CdTe [21], CdSe [22], $CdSe_xTe_{1-x}$ [23], and ZnSe [24] layers with various microstructural features.

### *3.1.3  Pourbaix Diagrams*

The analysis of thermodynamic data obeying chemical and electrochemical equilibrium is essential in understanding the reactivity of a system to be used for deposition/synthesis of a desired phase prior to moving to experiment and/or implementing complementary kinetic analysis tools. Theoretical and (quasi-)equilibrium data can be summarized in Pourbaix (potential–pH) diagrams, which may provide a comprehensive picture of the electrochemical solution growth system in terms of variables and reaction possibilities under different conditions of pH, redox potential, and/or concentrations of dissolved and electroactive substances.

Primarily connected to corrosion concepts, Pourbaix diagrams may be used within the scope of prediction and understanding of the thermodynamic stability of materials under various conditions. Park and Barber [25] have shown this relevance in examining the thermodynamic stabilities of semiconductor binary compounds such as CdS, CdSe, CdTe, and GaP, in relation to their flat band potentials and under conditions related to photoelectrochemical cell performance with different redox couples in solution.

Pourbaix diagrams for the aqueous Cd–S, Cd–Te, Cd–Se, Cu–In–Se, and Sb–S systems have been compiled and discussed by Savadogo [26] in his review regarding chemically and electrochemically deposited thin films for solar energy materials. Dremlyuzhenko et al. [27] analyzed theoretically the mechanisms of redox reactions in the $Cd_{1-x}Mn_xTe$ and $Cd_{1-x}Zn_xTe$ aqueous systems and evaluated the physicochemical properties of the semiconductor surfaces as a function of pH.

These authors constructed Pourbaix diagrams for the MnTe, ZnTe, $Cd_{1-x}Mn_x$Te, and $Cd_{1-x}Zn_x$Te systems and argued that the related analysis is an effective approach to determine conditions for selective etching, chemical polishing, passivation, and "self-metallization" of ZnTe, MnTe, and their solid solutions.

Equilibria considerations on solution-grown zinc chalcogenide compounds have been put forward by Chaparro [28] who examined the chemical and electrochemical reactivity of solutions appropriate for deposition of ZnS, ZnSe, ZnTe (and the oxide ZnO) in order to explain the results of recipes normally used for the growth of such thin films. The author compared different reaction possibilities and analyzed the composition of solutions containing zinc cations, ammonia, hydrazine, chalcogen anions, and dissolved oxygen, at 25 °C, by means of thermodynamic diagrams, applicable for concentrations usually employed in most studies.

Pourbaix diagrams regarding metal chalcogenides can be retrieved from various resources in the literature, connected to fields ranging from geochemistry and mineral processing to surface treatment and corrosion science. A few diagrams are reproduced in the present chapter for some binary compounds; however, the interested reader should look for the original works including data on the presumed equilibria and redox reactions.

### 3.1.4 Nucleation and Growth

The process of electrolytic growth has been studied intensively in the past decades, both with respect to the phenomenology of the evolving microstructure and in a mechanistic detailed sense. Commonly, the electrocrystallization of a new phase on a foreign substrate may involve in its early stages the nucleation of 3D centers which subsequently grow and overlap to give a continuous deposit. There are two basic mechanisms for formation of a coherent deposit: 2D layer growth and 3D crystallites' growth (or nucleation-coalescence growth). Layer-by-layer deposition proceeds by 2D nucleation and growth of monoatomic layers. A perfect crystal grown (almost) at equilibrium in repeated monoatomic layers will have faces where the energy of incorporation of an adatom at the surface of the face is lowest, because those planes will have sufficient time to develop laterally. When supersaturation increases, more than one step is growing at a time, so that vertical and lateral growth occur simultaneously, and other planes may appear; then the external shape of the crystal becomes round, a dendrite may appear, and 3D nucleation is finally observed. The geometry of a growth center is particularly sensitive to the interaction between the deposit and substrate materials. *Epitaxial growth* refers to the 2D development of monocrystalline deposit layers and can be achieved when there exists an almost exact matching of the lattice parameters between a single-crystal substrate and the deposit (Chap. 4). A parallel concept, *pseudomorphism*, may be thought of as the continuation of grain boundaries and microgeometric features of the cathode substrate into the overlying deposit; or according to an alternative definition, pseudomorphic are the deposits that are stressed to fit upon

a mismatched lattice substrate. The ability to control microstructural features in the produced compounds/films, i.e., crystal form and size in the nanometer scale, spatial distribution on the substrate, etc., has been a crucial development in the field of electrochemical synthesis.

The microstructure of electrodeposits depends on the nature of the target material, the experimental conditions of preparation (electrolyte composition, temperature, current intensity, potential, forced convection, etc.), and also on the substrate and interface properties. Metal chalcogenide films are relatively electrically resistive. As a consequence, the interfacial potential and charge distribution at the working electrode may drastically change after the formation of the first layers. As the electrodeposition proceeds, the resistivity may vary, since it is highly sensitive to defects, orientation, and other factors. For thicker films, this usually leads to severe compositional and morphological changes, but also to complete inhibition of growth, or situations where a non-degenerate semiconductor becomes a degenerate one. Moreover, unlike metal electrodes, space charge layers (SCLs) may play dominant role in the electrochemical growth process. The combined influence of an SCL at the growing film interphase and a high density of intrinsic or extrinsic surface states may exercise controlling effects on the charge transfer reaction. The ohmicity of the junction between the forming material and the conductive electrode substrate is also a significant factor. This junction lies in series with the electrode/electrolyte interface where the electrochemical reaction is taking place. If the contact is such that it allows an electron (in cathodic processes) or a hole (in anodic processes) from the conductive electrode to be replenished in the growing crystal at any polarization, then it comprises an ohmic contact. But it may do so only under forward bias conditions, behaving thus as a rectifying (Schottky) junction. A metal/semiconductor junction will provide a rectifying non-ohmic contact if the work function of the metal is larger than the electron affinity of the semiconductor and if the nature of the contact is determined by the bulk properties of the materials and not by surface states or other imperfections or impurities at the interfaces. Usually, though, the ohmicity of the substrate/semiconductor contact is determined by defects introducing additional levels in the band gap of the semiconductor and, in one way or another, conduction is preserved during the electrochemical process. This means that when the ohmicity is poor, growth may proceed by defects. Most of the electrodeposition work with metal chalcogenides has been implemented using metallic (Ni, Pt, Au, steel, Ti) electrodes as well as tin oxide (TO) or In-doped tin oxide (ITO) covered glass substrates. Hodes [1] has briefly summarized the factors that dictate the choice of a substrate material, yet related mainly to the electrodeposition of II–VI semiconductors.

Conventional electrodeposition from solutions at ambient conditions results typically in the formation of low-grade product with respect to crystallinity, that is, layers with small particle size, largely because it is a low-temperature technique thereby minimizing grain growth. In most cases, the fabricated films are polycrystalline with a grain size typically between 10 and 1,000 nm. The extensive grain boundary networks in such polycrystalline materials may be detrimental to applications; for instance, in semiconductor materials they increase resistivity

and provide recombination centers. Special regard to the crystallinity and purity of the compound deposit is to be implemented; otherwise the deposit may be a spongy, non-adherent mass, contaminated with basic inclusions. In any case, the relatively highly ionic chalcogenide compounds can generally afford larger deviations from stoichiometry without changing their transport electronic properties on account of self-compensation effects, when compared, e.g., to Si and III–V materials. Considering in addition that ionicity of the deposited compound is favorable to the use of electrodeposition, one can see why several electrodeposited chalcogenide semiconductors, particularly from the II–VI family, present sufficient quality for being used in applications.

## 3.2 Binary Compounds and Related Ternaries

In the following, selected results will be presented on the "conventional" electrochemical synthesis of metal chalcogenide binary and ternary systems, conducted by employing variants of the methods outlined in the previous sections. A brief account of chemical bath deposition principles exemplified will be addressed at the end of this chapter, as being closely related to electrochemical deposition of thin films.

### 3.2.1 Cadmium Sulfide (CdS)

Electrodeposition of CdS has been carried out from aqueous and non-aqueous solutions containing precursors of both elements as well as by anodization of cadmium metal in sulfide solutions.

Miller et al. [29, 30] reported the anodic formation of microcrystalline CdS on polycrystalline Cd metal in a strongly alkaline (pH 14) aqueous sulfide–polysulfide solution ($Na_2S$, NaOH). The process could be accomplished both galvanostatically and potentiostatically and resulted typically in the development of a yellowish opaque layer of semiconducting, n-type CdS, which was enriched with electrolysis time by hydroxide or oxide species. The formation and stripping of these films were studied by rotating ring-disk electrode (RRDE) voltammetry, under dark and illuminated conditions. It was concluded that although the as-grown anodic films can hardly show optical absorption efficiencies comparable to CdS single crystals or even polycrystalline pressure-sintered electrodes, they are rather stable in the polysulfide environment, thus operating in a manner appropriate to regenerative photoelectrochemical cells. Better optical results could be obtained with different bath composition, e.g., with buffered $Na_2S$, $NaHCO_3$ solutions of lower pH.

Peter studied in detail the growth of anodic CdS films on the Cd electrode in similar solutions [31], as well as the processes that occur at the Cd/solution and CdS/solution interfaces [32]. According to the linear sweep voltammetry, three characteristic regions could be distinguished revealing the essential features of the anodic passivation of cadmium in alkaline sulfide solutions: (a) the monolayer

region, with a sharp structured current peak corresponding to the passivation of the metal by two or three monolayers of CdS; (b) the plateau region, in which further growth takes place by high field ionic migration until a thickness of some 5 nm is reached; (c) the transpassive region, in which a less compact layer of CdS thickens rapidly to 500 nm or more.

Growth at constant current appeared to be well described in terms of the Cabrera–Mott model of the high-field–assisted formation of insulating rims (in general, the analogy between anodic chalcogenization and corrosion/passivation of valve metals is direct; in fact, both phenomena may be collectively discussed within the framework of well-established semiconductor electrochemistry principles [33]). It was noted that when the potential exceeds a critical value (in constant current or potential sweep experiments) the kinetics abruptly change, and a porous or polycrystalline CdS layer forms over the original barrier layer presumably by a diffusion-controlled process. It was not clear why the growth kinetics and mechanism change abruptly at about 5 nm. Remarkably, however, the growth kinetics at an applied constant potential could be described, not by the inverse logarithmic law as would be required by the Cabrera–Mott model, but rather by the so-called direct logarithmic law, according to which charge density at a constant potential imposed across the electrode increases with the logarithm of time. Peter attempted to reconcile this discrepancy in terms of a Cabrera–Mott model of inverse logarithmic law, modified for the change in potential difference across the inner Helmholtz layer, and hence across the oxide film itself. This attempt, however, did not meet with any success, in contrast, e.g., to the case of oxide growth at Pt electrodes, where an equivalent modification brought the galvanostatic and potentiostatic data into full agreement and proved that the same mechanism controlled the growth under both experimental conditions. It would, therefore, appear that different mechanisms control the formation of the CdS films under galvanostatic and potentiostatic modes of growth.

Since amalgam electrodes are more suitable than polycrystalline metal electrodes for the quantitative study of anodic electrocrystallization phenomena, the anodic formation of CdS has been studied on Cd(Hg) electrode in buffered sodium sulfide solutions by means of potential perturbations and capacitance measurements [34]. Comparison of the experimental data with the predictions of a model known to well describe the growth of multiple layers of Cd(OH) on Cd(Hg) showed a significant lack of agreement. It was suggested that in the present case, during deposition and reduction of CdS films on Cd(Hg), phase transformations or recrystallization processes occur. As an attempt to describe in detail the way in which phase transformations may influence the course of electrocrystallization, a qualitative model was assumed involving changes of the crystal orientation of the deposit during film deposition from (10.0) hexagonal to (110) cubic, transforming again to (10.0) at high overpotentials. This recrystallization could be reversed upon decreasing the overpotential, the film structure changing spontaneously to the (110) texture (Fig. 3.1).

The importance of phase transformations in anodic electrocrystallization processes has been demonstrated for the *mercury/sulfide* system, which exhibits a
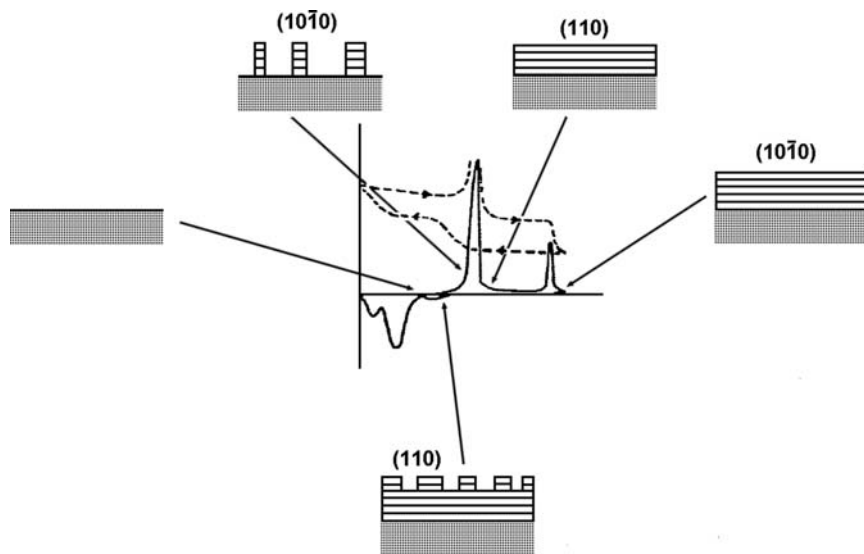
**Fig. 3.1** Model of CdS deposition and recrystallization. The changes in film structure are related to the features of the cyclic voltammogram and the capacitance plot (*broken line*). The interpretation of the capacitance data in this way leads to a mean value of $\varepsilon_{CdS} = 17$ for the relative permittivity of the film. (Reprinted from [34], Copyright 2009, with permission from Elsevier)

number of interesting phenomena in this connection [35]. The oxidative electrochemical growth of mercuric sulfide (HgS) thin films was considered to proceed in three distinct stages along the positive shift of potential. In the first, mercuric sulfide adsorbs over a narrow potential range, at values negative to the reversible potential of the bulk solid, to build up a monomolecular layer exhibiting an isotherm with strong lateral interactions. Subsequently, at a potential close to the reversible potential, the adsorbed layer rearranges in such a way that its packing density is increased. This effect corresponds to a first-order phase transformation, and in this stage there is clear evidence for nucleation of the rearranged phase. Finally the growth of subsequent monolayers of HgS proceeds by the nucleation and expansion of 2D centers on the rearranged first layer, following closely the mechanism discussed by Bewick et al. [36] in the case of calomel ($Hg_2Cl_2$) on mercury.

The authors [35] emphasize that their result regarding the first HgS monolayer, which involves reversible underpotential adsorption, suggests that nucleation cannot be considered as a universal mechanism for the formation of anodic films. Analogous conclusions have been inferred for cathodic HgSe films electrodeposited on mercury electrode by the reduction of selenous acid [37]; the first monolayer appeared to be reversibly adsorbed, while formation of the following two layers was preceded by nucleation.

In fact, monolayer formation has been observed in a number of cases on liquid and solid electrodes when reactive metals are anodized in the presence of ions which

form insoluble salts. The mechanism of these electrocrystallization reactions usually consists of the nucleation of 2D centers which grow by the rate-determining addition of new molecules to the expanding perimeter, until overlap becomes significant. That is actually the case for the first monolayer formation of CdS on Cd(Hg) as manifested by current transients which follow closely the behavior predicted for 2D progressive nucleation. An alternative, to the above two, mechanism involves electrosorption on the uncovered surface with no discernable nucleation stage, as in the case of $Ag_2S$ formation on silver [38].

A kinetic description of the initial stages of CdS growth under potentiodynamic conditions at various sweep rates at room temperature as well as under galvanostatic conditions at different temperatures has been attempted by Damjanovic and co-workers [39, 40]. They showed that the same kinetic equation describes the growth of thin anodic sulfide films at Cd electrodes under both galvanostatic and potentiodynamic conditions. For the growth of films up to about 5 nm, it was confirmed that the kinetics is fully accounted for by the model of high-field–assisted formation of ions at the metal/anodic film interface and their migration through the film.

Anodization generally results in the formation of films with limited thickness, uncertain composition, defects, and small crystallite size. Thus, the barrier nature of the n-type semiconducting CdS film obtained in the previous manner makes it too thin to form the basis of $Cu_2S$/CdS or CdTe/CdS solar cells by the normal dipping process. Heterojunction cells of low efficiency have, however, been made by anodization followed by vacuum deposition of the added layer ($Cu_2S$).

The *cathodic approach* has been investigated actively as a method for the production of thin film CdS, in particular for the fabrication of heterojunction cells. Photoactive CdS films could be grown in alkaline $NH_3$/$NH_4Cl$-buffered aqueous solutions containing thiosulfate as sulfur source and complexed $Cd^{2+}$ ($EDTA+NH_3$), on Ti substrates [41]. The electroreduction of thiosulfate was considered to proceed as

$$S_2O_3^{2-} + 3H_2O + 8e^- \rightarrow 2S^{2-} + 6OH^-$$
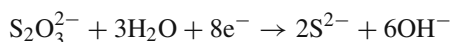
forming CdS in the presence of Cd(II) ions.

In acidic aqueous solutions of thiosulfate and $CdSO_4$, it was suggested [42] that disproportionation of the thiosulfate ions ($S_2O_3^{2-} \rightarrow S + SO_3^{2-}$) is coupled to electrochemical charge transfer to $Cd^{2+}$, according to the overall scheme (3.8) below. In effect, reduction of sulfite is more probable than that of sulfur in the colloidal state, so that considering the disproportionation of thiosulfate in acid solutions may amount to using sulfite, i.e., the anion of sulfurous acid–$SO_2$ in water. Repeated cycling of a Pt rde in this solution yielded a deep yellow, uniform, translucent film on Pt, containing Cd and S in roughly equal amounts with no detectable contaminants (according to microprobe analysis). The produced layers were thin (< 1 $\mu$m) and of poor crystallinity, but photoactive in sulfide, thiosulfate, sulfite, and sulfate solutions.

Dennison [43] studied the cathodic electrodeposition of CdS from similar acidic solutions at 90 °C. Although the reactions involved could not be defined exactly, two alternative overall processes were considered:

$$Cd^{2+} + S_2O_3^{2-} + 2e^- \rightarrow CdS + SO_3^{2-} \tag{3.8}$$

$$2Cd^{2+} + S_2O_3^{2-} + 6H^+ + 8e^- \rightarrow 2CdS + 3H_2O \tag{3.9}$$
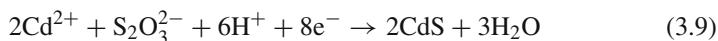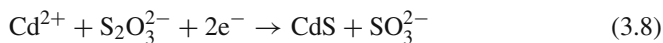
Process (3.8) is a total $2e^-$ per cadmium atom and indicates that CdS formation occurs via a sulfur atom abstraction from $S_2O_3^{2-}$. This reaction was called for in order to suggest that the reduction of $Cd^{2+}$ is the only electrochemical step, whereby charge is consumed, followed by a subsequent chemical step comprising sulfur association to reduced cadmium. Sulfur is generated by the decomposition of thiosulfate. On the other hand, reaction (3.9) corresponds to an overall $4e^-$/Cd process where reduction of $S_2O_3^-$ itself must occur as well as that of $Cd^{2+}$, the former comprising actually the rate-determining step. This route becomes more favorable as pH decreases for it requires additional protons.

Optimum conditions for the formation of CdS by the acidic method on metallic Al substrate at 25 °C have been reported as follows: pH 2.3, potential –1 V vs. SCE, and electrolysis time > 2 h [44]. Thermal treatment improved the characteristics of the films and their photovoltaic properties, which were evaluated by evaporating a $Cu_2S$ layer on the CdS/Al film, to form a heterojunction cell. The influence of the deposition substrate on the formation and morphology of CdS was found to be important. The aluminum substrates gave the best results among Pt, Mo, and Al. In the case of molybdenum, surface blocking by adsorbed sulfur was considered.

Generally, the experimental results on electrodeposition of CdS in acidic solutions of thiosulfate have implied that CdS growth does not involve underpotential deposition of the less noble element (Cd), as would be required by the theoretical treatments of compound semiconductor electrodeposition. Hence, a fundamental difference exists between CdS and the other two cadmium chalcogenides, CdSe and CdTe, for which the UPD model has been fairly successful. Besides, in the present case, colloidal sulfur is generated in the bulk of solution, giving rise to homogeneous precipitation of CdS in the vessel, so that it is quite difficult to obtain a film with an ordered structure. The same is true for the common chemical bath CdS deposition methods.

Yamaguchi et al. [45] suggested specific electrochemical assistance to a chemical deposition process from an acidic aqueous solution of cadmium chloride and thioacetamide, in order to realize film growth only by the heterogeneous reactions at the film/solution interface. The electrochemical reaction, namely electroreduction of protons at small current densities (several tens of $\mu A\ cm^{-2}$), was used in such a way as to maneuver the chemical formation of CdS to take place preferentially at the substrate surface (ITO-glass), while prohibiting the agglomeration of the fine particles formed homogeneously in the solution phase. The film growth was

considered as occurring by an atom-by-atom process generating individual crystallites, so that highly crystallized hexagonal CdS thin films could be developed, consisting of single-crystal CdS particles having hexagonal cylindrical shape. The films could become as thick as 500 nm without suffering from structure disordering. The authors stress in conclusion that an active use of electrochemistry can improve a CBD process drastically. Evidently, their particular approach may be valid also in the deposition of other related compound thin films.

Pulse plating techniques with symmetric or asymmetric waves have been employed for improving the deposition of CdS in acidic aqueous baths of cadmium sulfate and thiosulfate precursors [46, 47]. A better control of sulfur incorporation in the deposits was reported.

To overcome some of the problems associated with aqueous media, non-aqueous systems with cadmium salt and elemental sulfur dissolved in solvents such as DMSO, DMF, and ethylene glycol have been used, following the method of Baranski and Fawcett [48–50]. The study of CdS electrodeposition on Hg and Pt electrodes in DMSO solutions using cyclic voltammetry (at stationary electrodes) and pulse polarography (at dropping Hg electrodes) provided evidence that during deposition sulfur is chemisorbed at these electrodes and that formation of at least a monolayer of metal sulfide is probable. Formation of the initial layer of CdS involved reaction of Cd(II) ions with the chemisorbed sulfur or with a pre-existing layer of metal sulfide.

Actually, it is recognized that two different mechanisms may be involved in the above process. One is related to the reaction of a first deposited metal layer with chalcogen molecules diffusing through the double layer at the interface. The other is related to the precipitation of metal ions on the electrode during the reduction of sulfur. In the first case, after a monolayer of the compound has been plated, the deposition proceeds further according to the second mechanism. However, several factors affect the mechanism of the process, hence the corresponding composition and quality of the produced films. These factors are associated mainly to the complexation effect of the metal ions by the solvent, probable adsorption of electrolyte anions on the electrode surface, and solvent electrolysis.

In practical terms, large-scale cracking in the produced films, detrimental to photoelectric applications, was the main drawback of the above method. In order to prevent the appearance of cracks, propylene carbonate (PC) has been used as a solvent, with encouraging results [51]. The mechanism of electrodeposition of CdS in PC solutions containing Cd(II) ions and elemental sulfur has been studied by performing cyclic voltammetry at stationary Pt and Au electrodes [52].

Recently, a eutectic mixture of choline chloride and urea (commercially known as Reline) was used as a medium from which CdS, as well as CdSe and ZnS, thin films were electrodeposited for the first time [53]. Reline is a conductive room-temperature ionic liquid (RTIL) with a wide electrochemical window. The voltammetric behavior of the Reline–Cd(II)–sulfur system was investigated, while CdS thin films were deposited at constant potential and characterized by photocurrent and electrolyte electroabsorbance spectroscopies.

### 3.2.2 Cadmium Selenide (CdSe)

The interest in CdSe has been generated largely by its potential use in photoelectrochemical cells. Electrochemical deposition/formation of this compound has been widely reported, in all aspects. Gruszecki and Holmström [54] have succinctly reviewed methods of CdSe thin polycrystalline film preparation intended for solar cell applications, up to 1992, laying emphasis on the variants of cathodic electrodeposition, which they considered as being superior to other techniques, in terms of convenience and cost. Electrolytic deposition of CdSe was reported for the first time in 1968 by a Lithuanian group [55] using a very acidic aqueous solution (pH 0) of cadmium sulfate and selenous acid; however, well-defined cathodic formation of CdSe was accomplished primarily by the Weizmann Institute group [56], which obtained layers up to several microns thick on Ti substrate from an acidic aqueous solution of $CdSO_4$ and $SeO_2$. Variants of this method were employed typically in the early and most of the later work, using various cathode substrates such as Ti, Ni, $SnO_2$/glass, C, Ag, Cd, Cu, Au, Pt, and $TiO_2$. In general, the conventional electrodeposits consist of the cubic or hexagonal modification of microcrystalline CdSe with crystal diameters $< 0.1$ $\mu$m, often contaminated by elementary Se or Cd. The implications for cathodic deposition of CdSe have been discussed originally by Skyllas-Kazacos and Miller [57] based on voltammetric and photospectral data. Since then, several mechanisms have been formulated for describing the process in aqueous solutions, most of them implying the induced co-deposition concept leading to self-regulated growth [58].

Loizos et al. [59] proved that the electrolysis potential domain where CdSe can be effectively deposited, from acidic solutions containing a high $[Cd^{2+}]/[H_2SeO_3]$ ratio, corresponds precisely to the selenous acid diffusion plateau of the polarization curve obtained when the mass transfer in the bath is controlled by an rde. Both the limiting current intensity and the lateral extension of the plateau were seen to depend on the chalcogen precursor concentration (Fig. 3.2). A beneficial interface inhibition incurred by the excessive $Cd^{2+}$ ions was considered to largely contribute as a rate-determining step along with diffusion, conditioning thus a slow-rate surface process of crystal growth.

If the electrolysis parameters (precursor concentrations, pH, temperature, current/potential, substrate) be defined in a precise manner, a self-regulated growth of the compound can be established, and highly (111)-oriented zinc blende (ZB) deposits up to several $\mu$m thickness are obtained at potentials lying at the anodic limit of the diffusion range (Fig. 3.3) [60]. Currently, the typical method of cathodic electrodeposition has been developed to yield quite compact and coherent, polycrystalline, ZB n-CdSe films of well-defined stoichiometry. The intensity of the preferred ZB(111) orientation obtained with as-deposited CdSe/Ni samples has been quite high [61].

Alkaline aqueous media containing selenosulfate ions ($SeSO_3^{2-}$) and complexes of $Cd^{2+}$ with EDTA or nitrilotriacetate (NTA) have been successfully utilized to accomplish cathodic electrodeposition of nearly stoichiometric, wurtzite CdSe [62–64]. Similar results have been reported for seleno-cyanate ($SeCN^-$) alkaline baths
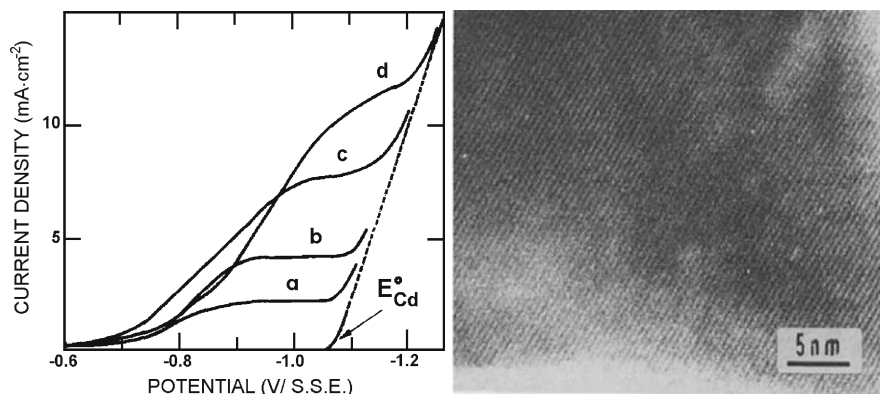
**Fig. 3.2** (*Left*) Current density vs. cathodic potential curves (without ohmic drop correction) of a TO/glass rde in a 0.2 M solution of CdSO$_4$ (pH 2.2) at 85 °C, for various selenous acid concentrations: *a* 0.5; *b* 1.0; *c* 2.0; *d* 3.0 ($\times$ 10$^{-3}$ mol l$^{-1}$). Smooth and crystallized Cd-Se co-deposits can be obtained by electrolysis at a constant potential lying within the observed plateau region of the curves, that is to say, in conditions where normally pure cadmium would be dissolved and pure selenium would form a passivating coating. (*Right*) High-resolution TEM image showing the dense reticular atomic planes within a zinc blende crystallite of an electrodeposited CdSe layer, illustrating the perfect atomic arrangement of the compound. The domains of coherence in the CdSe film are typically 50 nm in diameter. (Reprinted from [59], Copyright 2009, with permission from Elsevier)
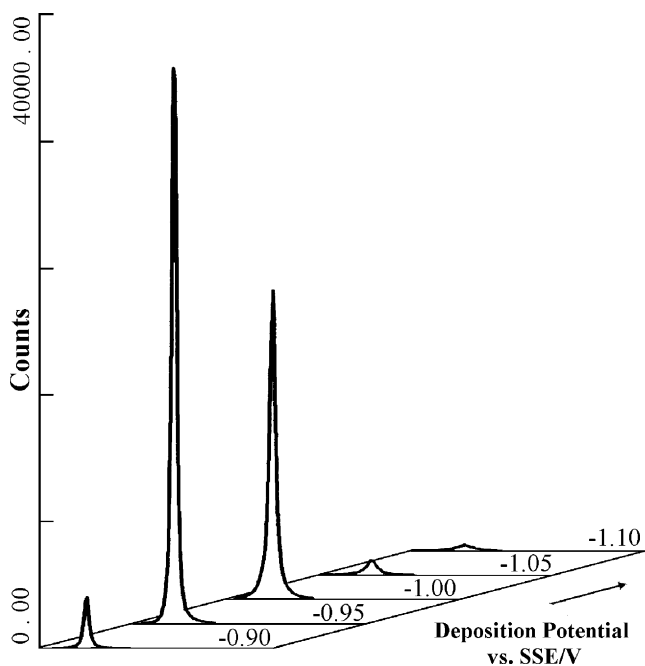


**Fig. 3.3** Zinc blende (111) XRD reflections vs. deposition potential, for 2 μm thick CdSe films electrodeposited from a pH ~2 bath on Ni cathode, at the indicated potentials within the diffusion-limited region. (With kind permission from Springer Science+Business Media [60])

[14]. A quantitative analysis of the kinetics of CdSe deposition from selenosulfate, Cd(II)–EDTA baths in terms of a mechanism involving nucleation and electrode kinetics has been given by Kutzmutz et al. [65]. Note also that selenosulfate-containing baths have been used for the anodic selenization of vacuum-deposited metal films in order to synthesize CdSe and other binary selenide semiconductor thin films such as CuSe and InSe [66].

Other selenium sources that have been used for CdSe deposition include elemental selenium in non-aqueous media [67] and tri-$n$-butylphosphine selenide (BPS) in diethylene glycol (DEG) or propylene carbonate (PC) [68]. The advantages of BPS are the low valency of selenium, the solubility of this compound in organic solvents, and the relative stability of the solution. DEG appeared to be a better solvent than PC for this deposition process. Also, the films deposited from DEG (on Ti) were found to be less dense than those prepared using selenosulfate ion. Cathodic electrodeposition of polycrystalline CdSe and Cd(Se,Te) films was performed also from near boiling water–ethylene glycol solutions of cadmium sulfate and selenous acid, at 110 °C, in a specially designed electrochemical cell [69]. It was shown that by properly adjusting the bath composition and deposition potential, the hexagonal, wurtzite phase of CdSe can be preferably obtained instead of the usual ZB, with the transformation between the two phases occurring within a few mV of deposition potential. In the mixed deposits though, the presence of Te was seen to stabilize the ZB polymorph. Recently, a similar method of CdSe electrodeposition from non-aqueous ethylene glycol solutions of cadmium acetate, selenium dioxide, and EDTA, at room temperature, was reported [70].

A detailed account of the cathodic deposition of CdSe on Ti from typical acidic selenite solutions, in galvanostatic conditions, has been given by Tomkiewicz et al. [71]. The electrodeposition mechanism was described in terms of a competition between chemical reactions that lead to Se formation and electrochemical reduction of Se as polyselenide, at the interfaces between Se and $Se^{2-}$. In particular, it was shown how the mechanism of film growth is responsible for the observed cauliflower morphology (of as-deposited, as well as of annealed at 750 °C in argon, films) – one that is frequently obtained for electrodeposited selenides. This morphology was considered to be well suited for liquid junction solar cells due to the high real-surface area provided. In fact, the authors, based on their characterization results with de-oxygenated sulfide–polysulfide solutions, claimed that their samples had an ideal morphology for this purpose; relatively stable efficiencies as high as 6.4% (under 100 mW cm$^{-2}$ artificial light) were obtained. The performance of the PEC was found to be limited by the dark current and the dielectric properties of the material. Notably, the solid-state properties of the films could be evaluated by capacitance measurements despite their complex morphology. It was concluded that the impedance of the photoelectrode–electrolyte system is not dominated by the solid-state properties of the electrode material (optical, photovoltaic) but rather by disorder-dominated conduction mechanisms created by the convoluted path within the semiconductor–electrolyte interface (Fig. 3.4). The photoelectrodes,
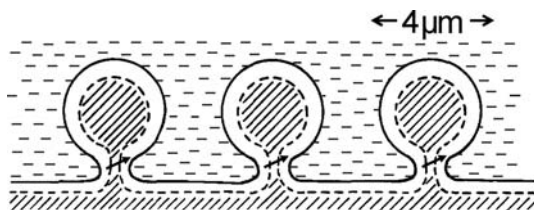
**Fig. 3.4** Schematic representation of the cauliflower structure, showing the space charge layer in relation to the electrolyte and the semiconductor, and the "pinching of cauliflowers", which is believed to be responsible for the disorder-dominated impedance. (Reprinted with permission from [71], Copyright 2009, The Electrochemical Society)

finally, were tested in the presence of surface-bound metal ions such as $Zn^{2+}$, $Ru^{3+}$, and $Ga^{3+}$ (absorbed after treating the electrodeposited films in concentrated solutions of corresponding salts), which were found to strongly influence the dark current, presumably through their catalytic activity in the hydrogen evolution reaction.

The problem of bulk Se formation in CdSe electrodeposition from typical acidic solutions has been dealt with by using a cyclic electrolysis procedure in a single bath [72]. The method involved the electrodeposition of sequential layers of CdSe by sweeping the potential of Ti or Ni substrates continuously between –0.4 and –0.8 V vs. SCE at a scan rate of 10 V $s^{-1}$ in solutions containing Cd(II) and $SeO_2$. The selenium precursor concentration was low enough (0.3 mM) that only sub-monolayer amounts of Se were reduced per cycle, while a large excess of Cd was deposited at the same time and subsequently stripped. The resulting CdSe films were found to have 1:1 stoichiometry and consisted of a dense layer of 100 nm grains beneath micron-size dendritic features, while XRD indicated the existence of both cubic and hexagonal phases of CdSe. The optical properties of the films were reported to be similar to those of previously studied deposits. Although no significant improvements in terms of material properties were attained in the present research, it should be noted that the concept of cycling the deposition potential had an impact in future works and served as a predecessor in recent attempts to develop sophisticated microstructures by cyclic electrodeposition schemes.

Miller et al. [73] put forward an anodic procedure similar to that cited previously for sulfide semiconductors, involving the in situ formation of CdSe photoelectrodes by anodizing Cd metal in a $K_2Se$–KOH solution. The as-produced electrodes presented low efficiency (0.6%) in polysulfide PEC, the most likely reason being the limited thickness of the anodic layer, affording poor light absorption. Ham et al. [33] studied the anodic electrosynthesis of CdSe on Cd electrode in selenide solution by voltammetry, photocurrent spectroscopy, and solid-state characterization techniques and compared the corresponding processes for formation of CdS and CdTe from sulfide and telluride solutions, respectively. In all three cases, the initial peak in the voltammograms was at the same potential and could be correlated with

formation of $Cd(OH)_2$ which subsequently reacted with chalcogenide ions in solution to give CdX. The CdSe growth kinetics in the passive region was found to follow a direct logarithmic rate law (cf. Sect. 3.2.1), while a diffusion mechanism was seen to prevail in the transpassive regime. It was noted that whereas the Cd–S and Cd–Se systems present similar trends, the onset of the transpassive region in the Cd–Te system is not well defined. In the latter case, the monolayer formation feature in the voltammogram preceded two partially resolved peaks, which were ascribed to telluride and tellurium oxidation. The differences in the growth process were discussed and interpreted within the framework of a semiconductor model previously invoked for oxide passivation of metal surfaces. Cyclic photovoltammetry showed an anodic photoeffect already at the monolayer formation stage for both CdSe and CdTe, unlike CdS which lacked this feature. The luminescence response of CdSe suggested a high density of carrier recombination centers located 0.2 eV below the conduction band. The surface semiconductor energy levels in relation to the electrolyte redox positions, the transpassive potential onset (where applicable), and the semiconductor corrosion potentials were estimated and plotted on a common scale, for all three compounds.

### 3.2.3  Cadmium Telluride (CdTe)

Cadmium telluride is the most electrodeposited compound semiconductor, other than oxides. Cathodic electrodeposition of CdTe has been carried out following mainly the pioneering work of Panicker et al. [74] who used aqueous solutions of cadmium sulfate, tellurium dioxide, and sulfuric acid. Deposition with this bath, specifically at low pH (0–2) and with a high $[Cd^{2+}]/[HTeO_2^+]$ ratio, can be made to proceed in an exceptionally self-regulating manner as dominated by the diffusion-limiting current of $HTeO_2^+$ ions, which upon reduction induce UPD of cadmium, leading to the formation of stoichiometric CdTe. Typically, the as-deposited films have crystallite sizes below 0.1 $\mu$m and often contain microcracks, while conditions to obtain both n- and p-type CdTe have been established (see the following discussion). In fact, the deposition potential/current and other parametric variables (solution composition, temperature, illumination, and substrate nature) largely affect the microstructural and solid-state properties of CdTe through their influence on the growing film composition and morphology [75–81].

The thermodynamic principles of the Cd–Te–water system are depicted in the Pourbaix diagram of Fig. 3.5 [82]. The corresponding electrochemical reactions of CdTe reduction and oxidation are shown in Table 3.1.

The work of Verbrugge and Tobias on CdTe [8] comprises a comprehensive source of information about the electrochemistry of the compound and its components. Deposition features are reviewed, and thermodynamic, transport, and kinetic parameters for cadmium and tellurium deposition are reported.

The reaction mechanism in acidic tellurite baths has been the subject of considerable debate in the literature concerning mostly the number of exchanging electrons
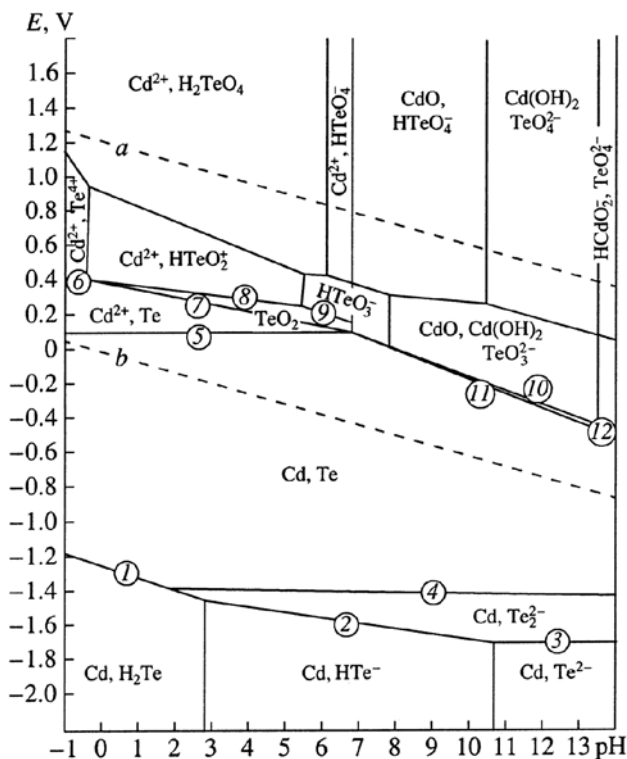
**Fig. 3.5** Potential vs. pH diagram for the CdTe–$H_2O$ system at 25 °C. Solid CdTe is thermodynamically stable over the entire pH range. Consequently, CdTe does not hydrolyze at any $H^+$ and $OH^-$ activities of practical interest. In acidic solutions, the only process accompanying cathodic CdTe polarization is hydrogen release. Therefore, in the region of cathode potentials, CdTe is a sufficiently stable electrode material from the electrochemical point of view. The $-1.35$ V potential is the lowest limit of stability. Below this limit, CdTe corrodes in the whole pH range; e.g., for pH < 2.8, $H_2Te$ vapor is produced at $-1.25$ V. For pH > 2.8, ditelluride or telluride ions are formed with disintegration of the compound. (With kind permission from Springer Science+Business Media [82])

**Table 3.1** Electrochemical reactions in the CdTe–$H_2O$ system

| | |
|---|---|
| 1 | $CdTe + 2H^+ + 2e^- \rightleftarrows Cd + H_2Te$ |
| 2 | $CdTe + H^+ + 2e^- \rightleftarrows Cd + HTe^-$ |
| 3 | $CdTe + 2e^- \rightleftarrows Cd + Te^{2-}$ |
| 4 | $2CdTe + 2e^- \rightleftarrows 2Cd + Te_2^{2-}$ |
| 5 | $CdTe \rightleftarrows Cd^{2+} + Te + 2e^-$ |
| 6 | $CdTe \rightleftarrows Cd^{2+} + Te^{4+} + 6e^-$ |
| 7 | $CdTe + 2H_2O \rightleftarrows Cd^{2+} + TeO_2 + 4H^+ + 6e^-$ |
| 8 | $CdTe + 2H_2O \rightleftarrows Cd^{2+} + HTeO_2^+ + 3H^+ + 6e^-$ |
| 9 | $CdTe + 3H_2O \rightleftarrows Cd^{2+} + HTeO_3^- + 5H^+ + 6e^-$ |
| 10 | $CdTe + 3H_2O \rightleftarrows Cd + TeO_3^{2-} + 6H^+ + 4e^-$ |
| 11 | $CdTe + 5H_2O \rightleftarrows Cd(OH)_2 + TeO_3^{2-} + 8H^+ + 6e^-$ |
| 12 | $CdTe + 5H_2O \rightleftarrows HCdO_2^- + TeO_3^{2-} + 9H^+ + 6e^-$ |

at any potential, that is, the identity of the reduced species and extent of reduction, as well as the possible contribution of surface phenomena. It should be pointed out that for typical acidic baths, CdTe electrocrystallization differs from that of CdSe in important respects. For CdTe, the experimental domain is very narrow, due both to the very weak solubility of $TeO_2$ and to the restricted potential range where CdTe of good quality is obtained (a few tens of mV from the redox potential of cadmium). In contrast, the solubility of $SeO_2$ or $H_2SeO_3$ is much higher and the definite compound can be obtained in a potential range which can be greater than 200 mV. In this connection, the reader will find an extensive parallel discussion of CdSe and CdTe deposition in Hodes [1]. Let us note here that according to the results of Sella et al. [83] and subsequent works [84], the adsorption of $HTeO_2^+$ on the cathode constitutes a critical step in the CdTe deposition process, which thereby, aside from telluryl ion diffusion in the liquid phase, involves the reduction of (weakly) adsorbed telluryl species. It was found that encroaching $Cd^{2+}$ ions from solution – but also other species such as potassium $K^+$ ions – displace the $HTeO_2^+$ from their adsorption sites, causing a shift of the Te(IV) reduction wave and a decrease in the limiting current. Thus, during deposition it is most probable that a competition with specific reaction sites at the surface is quite important in the growth of stoichiometric CdTe films.

Importantly, the doping type of CdTe can be controlled by the electrodeposition potential. Panicker reported a critical value for the quasi-rest potential (QRP) (+340 mV vs. the deposition potential of elemental cadmium, $Cd/Cd^{2+}$), below which n-type CdTe is deposited, while more positive QRPs lead to the formation of p-type CdTe. Kampmann et al. [85] found that a potential of +5 mV vs. $Cd/Cd^{2+}$ leads to the formation of n-type CdTe, while a deposition potential of +250 mV leads directly to the formation of p-type CdTe. The change in semiconductivity type can be rationalized on the basis of the non-stoichiometry and attendant defect chemistry of CdTe. Thus, it could be explained in terms of the electrodeposition mechanism by invoking the hypothesis of intrinsic doping: at the more positive potentials, the incorporation of Te interstitial atoms or cadmium vacancies, which act as acceptors, is enhanced, thus leading to the formation of p-type CdTe, whereas at the more negative but still positive than $Cd/Cd^{2+}$ potentials, the UPD of Cd interstitial atoms, which act as doubly ionized donors in CdTe thereby creating n-type conductivity, becomes competitive to the former action. In fact, observed difficulties in electrodeposition of p-type layers from typical acidic baths have led to the need for post-deposition thermal treatment to induce n- to p-type conversion [86, 87]. Still, evidence has been provided [88, 89] for p-type conductivity in as-deposited, either in situ doped or undoped, CdTe films, which exhibited a satisfactory rectification behavior when fabricated into Schottky barriers (CdTe/In) and heterojunctions (CdS/CdTe). Certainly, whilst electrodeposited CdTe nominally is intrinsically doped as prepared, external dopants can be added to the electrosynthesis medium; for example, As and Cu have been added as acceptor impurities to generate p-type CdTe thin films.

Cathodic photo-currents observed during the deposition of CdTe have been interpreted as evidence for p-type conductivity [90]. Verbrugge and Tobias [91] showed

that significant photoeffects are observed during CdTe deposition, and they implied that illumination affects the composition of the deposit. Sugimoto and Peter [92] investigated the effect of illumination on the deposition of CdTe, using monocrystalline n-type silicon wafers as a substrate, since exceptionally smooth and uniform films of CdTe can be grown on them (at the negative potentials used for CdTe deposition, the n-Si shows no photoeffects since it is in the accumulation region). The results showed that illumination initiates a complex series of reactions that can profoundly influence the electrodeposition process. The consequences for the morphology and composition of the deposit depend on solution composition.

Despite the high solubility of Te(IV) species in alkaline solutions, little is known about the electrodeposition characteristics of CdTe from alkaline media. Ammoniacal aqueous electrolytes prepared by dissolution of $CdSO_4$, $TeO_2$, in an $NH_3/NH_4^+$ buffer (pH 10.7) have been investigated for this purpose [93]. The Cd(II) and Te(IV) species in this electrolyte are dissolved as $Cd(NH_3)_4^{2+}$ and $TeO_3^{2-}$ ions, respectively. Normally, CdTe films prepared under potentiostatic conditions from these solutions contain excessive cadmium, giving rise to dendritic morphology. However, at potentials positive to the reduction potential of $Cd(NH_3)_4^{2+}$ to $Cd^0$, the co-deposition of elemental cadmium could be suppressed and stoichiometric crystalline CdTe films were obtained with flat and smooth surface morphology, on gold-plated copper sheets. The outcome of the method was explained by a cadmium UPD mechanism.

Telluro-cyanide (presumably $TeCN^-$) has been explored as a source of tellurium for electrodeposition of CdTe [14], on account of the possible advantage that this species is less likely than tellurium dioxide to oxidize the cathodically produced telluride ion. Bath solutions were prepared by dissolving powdered Te in a concentrated aqueous solution of KCN and adding $CdCl_2$ and EDTA. Stoichiometric CdTe deposits, free of excess Te, were reported.

Darkowski and Cocivera [94] investigated trialkyl- or triarylphosphine tellurides, as low-valent tellurium sources, soluble in organic solvents. They reported the cathodic electrodeposition of thin film CdTe on titanium from a propylene carbonate solution of tri-$n$-butylphosphine telluride and Cd(II) salt, at about 100 °C. Amorphous, smooth gray films were obtained with thicknesses up to 5.4 μm. The Te/Cd atomic ratio was seen to depend on applied potential and solution composition with values ranging between 0.63 and 1.1. Polycrystalline, cubic CdTe was obtained upon annealing at 400 °C. The as-deposited films could be either p- or n-type, and heat treatment converts p to n (type conversion; cf. Sect. 3.3.2).

The method of Baranski and co-workers enabling deposition to be carried out at much higher temperatures (130–160 °C) than the maximum permissible in aqueous medium has been applied to the electrosynthesis of CdTe. Notably, the deposition of "single-crystal" CdTe films was reported [95], from a DMSO solution of $CdC_2$ and elemental Te, in a galvanostatic regime. The crystalline structure of as-deposited CdTe films was found to depend on the degree of ionic supersaturation at the substrate, as expressed by the current density. Relatively low deposition currents ($\leq 0.25$ mA cm$^{-2}$) were claimed to yield monocrystalline CdTe films (the degree of supersaturation at the interface was below $10^3$). Analysis of variations in the

cathodic overpotentials with current density indicated that the growth of monocrys-
talline CdTe takes place by initial formation of oriented large size ($\geq 2$ nm) nuclei
which grow by surface diffusion of adions. Critical nuclei size reduces and active
growth sites increase rapidly as the deposition current is increased over 0.25 mA
$cm^{-2}$.

Simple *electroless* techniques have been used for the formation of CdTe layers
following an anodic or a cathodic route of deposition. For instance, spontaneous
cathodic formation of CdTe was observed on Ti or glass electrodes short circuited
with a corroding Al contact (electron source) in a solution of $Cd^{2+}$ and $HTeO_2^+$ ions
[96]. After thermal treatment and subsequent growth of an $\alpha$-$PbO_2$ layer on them,
the as-obtained CdTe thin films were found to exhibit n-type behavior in alkaline
polysulfide PEC cells.

A variant involves the short-circuiting of a Te rod and a Cd strip to generate
CdTe on tellurium. Gerritsen [97] demonstrated the formation of CdTe on a tel-
lurium electrode externally connected to a Cd strip, both immersed in 0.1 M $CdSO_4$
neutral aqueous electrolyte, by introducing two different modes of operation. In one,
no bias was applied between the electrodes; in the other, the tellurium electrode was
biased strongly positively. In the first case, Cd and Te electrodes in the electrolyte
solution formed a galvanic cell with a standard open voltage of about 0.63 V (the
actual value depending on the degree of etching previously given to the Te elec-
trode). This Cd/$CdSO_4$(aq.)/Te cell, operated by migration of $Cd^{2+}$ from the Cd to
the Te electrode, discharge to Cd, and subsequent formation of the compound. In
this way, CdTe layers, 0.1–0.2 $\mu$m thick, strongly adhering to the Te substrate were
grown. Interestingly, the layers were reported to consist of single-crystal domains
with areas in the order of $mm^2$. By the second method, CdTe was formed again on
the Te electrode, but this time the electrochemical process involved a tellurite ion
(most likely $HTeO_2^+$) injected into the solution that combined homogeneously with
$Cd^{2+}$ to precipitate the compound. The resultant free positive charge presumably
oxidized water to $O_2$, though the exact mechanism was not studied. Shiny black
layers attached well to the substrate were formed by this method. However, there
were no single-crystal lines observable in the Laue patterns, and the stoichiome-
try of the films was not determined. A telluride film with optimal photosensitivity
was obtained by maintaining a current flow of 5 mA from Te to the metal for about
10 min. This required a bias increase gradually from +1.3 to 4.5 V.

The above methods were used also for the production of ZnTe. Alternatively, the
spontaneous corrosion of a Cd anode in alkaline $Te^{2-}$ solutions may generate CdTe
on the same electrode.

A comprehensive work on the electrodeposition chemistry and characterization
of anodically synthesized CdTe thin films has been presented by Ham et al. [98].
In this work, along with the electrolytic anodic synthesis of CdTe by using Cd
anodes in alkaline solutions of sodium telluride, an electroless route of anodizing
a Cd electrode held at open circuit in the same solution was also introduced. The
anodic method was expected to produce CdTe with little contamination from $Te^0$
on account of the thermodynamic properties of the system; the open-circuit poten-
tial of Cd anodes in the $Te^{2-}$ electrolyte lies negative of the $Te^{2-/0}$ redox point, so

that the oxidation of $Te^{2-}$ to CdTe is more favorable relative to the corresponding $Te^{2-} \rightarrow Te^{0}$ reaction. The virtue of the anodic route in terms of avoiding contamination of CdTe with $Te^{0}$ was clearly seen by surface analytical techniques, especially when the corresponding results obtained for cathodically synthesized thin films were compared. Importantly, anodic CdTe thin films are usually n-type as synthesized, and not p-type as the cathodic CdTe, due to the Cd-rich environment typical of anodic electrosynthesis.

### 3.2.4 Zinc Sulfide (ZnS)

Facts for the electrodeposition of zinc sulfide have been much scarcer than for CdS. Lokhande et al. [99] used aqueous acidic (pH 1–6) solutions of $ZnSO_4$ and thiosulfate ($Na_2S_2O_3$) at room temperature, to electrodeposit the compound on stainless steel and ITO substrates. The deposits were polycrystalline and contained elemental zinc and sulfur phases. By addition of $CdSO_4$ in the bath, mixed $Cd_{1-x}Zn_xS$ alloys were obtained at pH between 2 and 2.5. The band gap of the $Cd_{1-x}Zn_xS$ films was seen to vary in a non-linear manner as Zn content increased in the films, from 2.40 eV (CdS) to the higher energy end (measured 3.55 eV for ZnS). Similar aqueous thiosulfate, acidic (pH 2) baths, containing in addition glycerol, were used by Sanders and Kitai [100], who obtained polycrystalline ZnS films with a predominantly zinc blende $\langle 200 \rangle$ texture on ITO substrate. This preferred growth orientation was unusual and rather unique, considering that conventionally deposited II–VI chalcogenides including ZnS normally adopt a more or less intense ZB $\langle 111 \rangle$ or W (00.2) texture of closest packed planes. A further odd result was the loss of crystallinity of the films upon annealing to either 673 or 973 K in nitrogen as implied by the disappearance of the XRD response. Also, severe cracking of the films was observed after thermal treatment, although annealed ZnS was found to possess a band gap of 3.68 eV, similar to single-crystal ZnS, as estimated from absorption spectra.

Single-phase ZnS films of a fine grain size (no XRD shown) and a band gap of 3.7 eV were electrodeposited from aqueous alkaline (pH 8–10) solutions of zinc complexed with EDTA, and thiosulfate as a sulfur source [101]. The voltammetric data implied that deposition occurred either by S-induced UPD of Zn or by a pathway involving both $Zn^{2+}$ and thiosulfate concurrently.

It should be stressed that the key point in the recent success of ZnS application in thin film solar cells is the use of chemical rather than electrochemical deposition (CBD), which is successfully applied also for obtaining $Cd_{1-x}Zn_xS$ films. Note though that studies on the chemical growth of ZnS are limited compared to CdS, and the level of understanding of the deposition mechanism is inferior.

Amorphous films of the (Zn,Fe)S semiconductor have been obtained by electrodeposition on TO substrates from a diethylene glycol solution containing $S_8$, $FeCl_2$, and $ZnCl_2$ reagents [102]. The films were annealed at 285 °C in argon to give sphalerite and pyrrhotite (Zn,Fe)S phases. A direct relationship was observed

between the Fe and Zn concentration in the electrolytic bath and the Zn/Fe ratio in the deposits. The indirect energy gap transition varied from 0.37 to 3.1 eV, as the Zn/Fe ratio in the solution was increased.

### 3.2.5 Zinc Selenide (ZnSe)

Electrodeposition of zinc selenide from simple (uncomplexed) aqueous acidic solutions of Se(IV) species is quite challenging, since the self-regulating growth manifesting itself in the analogous CdSe and CdTe deposition processes appears not to be functional in the present case, due to the large difference between the redox potentials of zinc and selenium precursors. Various reports on the typical cathodic electrodeposition of ZnSe from aqueous acidic baths of $Zn^{2+}$ and selenous acid have shown that, despite optimization efforts, the method results in the preparation of no better than microcrystalline films suffering from elemental selenium excess (Fig. 3.6) and poor integrity [103–105]. Although removal of free Se can be easily accomplished by annealing at low temperatures, the preparation of qualified, single phase, and uniformly crystalline ZnSe layers is possible only by providing a stoichiometric growth in the first place, since thermal post-treatment hardly ameliorates the structure and morphology of this compound film. Thereupon, efforts have been directed toward the reduction of free Se co-deposition. For this purpose, a fine control of certain variables such as the Se(IV) content in the bath is essential with respect to the typical method [106, 107]; however, a change of the deposition mechanism, e.g., through the use of complexed precursors, should be more effective.

Utilizing low-oxidation selenium precursors appears to be particularly suited for obtaining single-phase ZnSe deposits. Results have been presented of ZnSe electrosynthesis from alkaline selenosulfate solutions of complexed Zn(II) [108].



**Fig. 3.6** XRD patterns (CuK$_\alpha$ source) of equally thick deposits prepared on Ti at –1.2 V/SSE from a 0.5 × $10^{-3}$ M SeO$_2$, 0.2 M ZnSO$_4$, pH 2.5 solution at various temperatures (25–85 °C). Increase of bath temperature promotes the formation of zinc blende ZnSe crystallites, exhibiting a random orientation. The semimetallic, hexagonal phase of Se unavoidably forms together with the selenide compound. (With kind permission from Springer Science+Business Media [105])
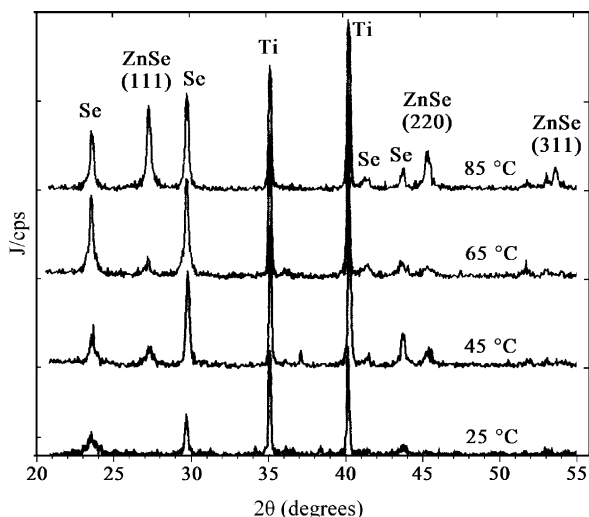
The redox behavior of the $SeSO_3^{2-}$–Zn–EDTA system has been discussed on the basis of Pourbaix and solubility diagrams [11]. Different complexes and substrates have been employed in order to optimize the electrodeposited thin films. By the selenosulfate method it is generally possible to grow ZnSe with an almost stoichiometric composition; however, issues of low faradaic efficiency as well as crystallinity and compactiveness of the product, remain to be solved. Interestingly, in most reports of photoelectrochemically characterized ZnSe electrodeposits, the semiconductor film was found to be p-type under all preparation conditions (ZnSe is normally n-type unless deliberately doped p-type).

Preliminary work on molten salt electrodeposition of ZnSe has been carried out by Cuomo and Gambino [109] who used a KCl solution of $ZnCl_2$ and $SeCl_4$ at 520–550 °C. Improved results were reported later by using ZnO and $Na_2SeO_3$ in KCl/LiCl eutectic at approximately 470 °C [110]. More recently, the semiconductor was deposited at 550 °C from a $CaCl_2$/NaCl eutectic solution of $ZnCl_2$ and $SeO_2$ on TO/glass sheets [111]. Yellow, transparent, and adherent thin films containing up to 90% single-phase ZnSe with a 1 mm grain size were obtained at optimized conditions.

### 3.2.6 Zinc Telluride (ZnTe)

Electrodeposition of ZnTe in aqueous medium has been widely reported [112–115]. Thin films of ZnTe were prepared electrochemically for the first time by Basol in 1988 employing a two-step process, which involved sequential electrodeposition of Te and Zn stacking layers from aqueous electrolytes and subsequent annealing.

Commonly, ZnTe films are prepared using the typical chalcogenides method of electrodeposition from acidic aqueous solutions of Te(IV) and Zn(II) precursors. The cyclic voltammetry of such solutions has been adequately described [116, 90]. It has been demonstrated that ZnTe compound crystallizes in a zinc blende structure, typically with randomly oriented crystallites, although the deposition of [111]-oriented films is possible under conditions that the crystal growth surpasses nucleation. High bath temperatures are necessary for achieving crystalline films, while the nature of the substrate may drastically affect the electrodeposition process and the film properties, principally through its overpotential for hydrogen reduction.

ZnTe, like CdTe, belongs to the Class I in Kröger's classification, and the anticipated potential range for single-step electrodeposition of the compound may be defined by appropriate thermodynamic analysis. An in-depth presentation of the relevant electrochemistry and thermodynamics can be found in the work of Königstein and Neumann-Spallart [116]. The compound is expected to be accessible by electrodeposition from aqueous solutions containing $Zn^{2+}$ and $HTeO_2^+$ ions within a potential range of –0.15 to –0.76 V vs. SHE (calculations concern standard activities). However, in order to obtain compact stoichiometric films of ZnTe, one cannot rely on the theoretical prediction, since adsorption processes and crystallization overpotential play a very significant role. The range of plating conditions leading to stoichiometric ZnTe has been found to be quite narrow compared to that given

on a purely thermodynamic basis, although the latter had some success in the case of CdTe. In fact, just like in the case of ZnSe electrodeposition, no leveling effect, which might be due to $Zn^{2+}$ adsorption, seems to operate with ZnTe. In contrast to Cd-containing systems where a self-regulating process allows fast reduction of $Cd^{2+}$ upon adsorption on the substrate, the formation of zinc chalcogenides is more intricate since $Zn^{2+}$ is not as readily adsorbed, due to its highly negative redox potential. Hence, the deposited Te atoms are not able to immediately trigger the reduction of $Zn^{2+}$ giving rise to stoichiometric ZnTe compound. The recent progress in the field consists of the convenient deposition of single-phase, crystalline ZnTe films of uniform and compact morphology by using citrate as a complexing agent in the typical acidic electrolyte; however, as-obtained deposits are usually contaminated by organic inclusions [117].

Formation of single-phase ZnTe on zinc substrates at 640 K by using electrochemical ion exchange and chemical reaction/alloying with $Te^{4+}$ species, supplied to the substrate as a vapor from $TeCl_4$-containing eutectic LiCl–KCl molten salts, was reported recently [118]. ZnTe films with a smooth dense surface and particle diameters less than about 0.8 $\mu$m were obtained, by properly adjusting the $TeCl_4$ content and the reaction time.

### 3.2.7 Mercury Chalcogenides

Studies of the electrodeposition of mercury chalcogenides are scarce, primarily because of the difference in electrochemical potentials needed to deposit mercury and the chalcogens. Mercury is a noble metal: the standard redox potential for the reduction of $Hg^{2+}$ to $Hg_2^{2+}$ or Hg(0) is 0.670 or 0.613 V vs. SHE, respectively, while for the reduction of $Hg_2^{2+}$ to Hg(0) is 0.555 V. Chalcogenide reduction is much less noble and generally displays slow deposition kinetics, typically depositing below 0.0 V in neutral solutions.

The properties of anodic layers of HgS formed on mercury in sulfide solutions have been investigated in comparison with anodic sulfide layers of cadmium and bismuth. Also, the electrochemistry of mercury electrodes in aqueous selenite solutions has been studied (see Sect. 3.2.1). The problem with the presence of several cathodic stripping peaks for HgSe in acidic Se(IV) solutions has been addressed using various voltammetric techniques at a hanging-mercury-drop electrode [119].

The chemical bath deposition of polycrystalline, zinc blende HgSe thin films on TO glass from aqueous alkaline medium has been reported [120]. Examples of electrodeposited ternary mercury compounds will be discussed in the next section.

### 3.2.8 Pseudobinary $II–VI_x–VI_{1-x}$ and $II_{1-x}–II_x–VI$ Phases

Thin films of ternary *cadmium sulfoselenide* $CdS_xSe_{1-x}$ have been electrodeposited from a non-aqueous organic bath by Baranski et al. [67], as well as by Loutfy and Ng [121], who employed similar principles (deposition from ethylene glycol solution

of $CdCl_2$, S, and $SeO_2$ onto ITO glass under galvanostatic control, at 160 °C). Also, photoactive "$S_xSe_yCd$" thin films were electrodeposited from acidic aqueous solutions of $Na_2SeO_3$, $CdSO_4$, and $Na_2S_2O_3$ at different concentrations, under potentiostatic or galvanostatic control at room temperature on Ti and glass doped with $SnO_2$ [122]. Mahapatra and Roy [123] reported the electrodeposition of $CdS_xSe_{1-x}$ and $CdPb_{1-x}S_x$ from aqueous bath and their electrochemical characterization as photoelectrodes.

An electrophoresis method was presented by Ueno et al. [124] for obtaining homogeneous and optically active films of CdS, CdSe, and $CdS_xSe_{1-x}$, using commercially available CdS and CdSe powders as starting materials. Electrophoretic deposition was performed anodically from suspensions of the semiconductor particles in polar organic media, onto TO/glass substrate by application of dc voltage in the range 30–800 V. The solvents of choice for CdS and CdSe deposition, respectively, were an acetone/isobutyl alcohol equivolume mixture and propylene carbonate. Both these media were employed for the ternary alloy formation. The as-deposited films were thermally treated for 3 h at 400–600 °C in nitrogen atmosphere. An energy conversion efficiency of 2% under white light illumination was attained in polysulfide PEC using CdSe-based films as photoanodes.

Cathodic electrodeposition of microcrystalline *cadmium-zinc selenide* ($Cd_{1-x}Zn_xSe$; CZS) films has been reported from selenite and selenosulfate baths [125, 126]. When applied for CZS, the typical electrocrystallization process from acidic solutions involves the underpotential reduction of at least one of the metal ion species (the less noble zinc). However, the direct formation of the alloy in this manner is problematic, basically due to a large difference between the redox potentials of $Zn^{2+/0}$ and $Cd^{2+/0}$ couples [127]. In solutions containing both zinc and cadmium ions, Cd will deposit preferentially because of its more positive potential, thus leading to free CdSe phase. This is true even if the cations are complexed since the stability constants of cadmium and zinc with various complexants are similar. Notwithstanding, films electrodeposited from typical solutions have been used to study the molar fraction dependence of the CZS band gap energy in the light of photoelectrochemical measurements, along with considerations within the virtual crystal approximation [128].

Gal and Hodes [129] investigated the electrodeposition of the ternary CZS alloy (and ZnSe) in non-aqueous media. Rather nanocrystalline $Cd_{1-x}Zn_xSe$ was electrodeposited galvanostatically on ITO substrates from DMSO containing millimolar concentrations of Se and perchlorates of zinc and cadmium (in lithium perchlorate as supporting electrolyte), maintained at 150 °C. The composition of the mixed selenide could be controlled by variation of the deposition current density, through diffusion control of the low concentrations of $Cd(ClO_4)_2$. The apparent conductivity type of the films was shown to change with the zinc ion concentration in the electrolyte from "n-type" (low Zn) to "p-type" (high Zn). It was noted that in the parallel deposition of CdSe and CdS, the use of chloride rather than perchlorate in the electrolyte resulted in smaller crystal size and pronounced quantum size effects.

An instance of *cadmium-zinc sulfide* ($Cd_xZn_{1-x}S$) cathodic electrodeposition can be found in the work of Morris and Vanderveen [130]. These researchers managed to obtain polycrystalline $Cd_xZn_{1-x}S$ films from stirred aqueous solutions (pH 2,

90 °C) with low concentrations of $Cd^{2+}$ and $S_2O_3{}^{2-}$, and higher concentrations of $Zn^{2+}$, at constant potentials lying between the standard reduction values of the $Cd^{2+/0}$ and $S^{2-/0}$ couples. Film composition was altered by changing the concentration of precursors in solution and by altering the applied potential. The as-deposited $Cd_xZn_{1-x}S$ films with $0.53 < x < 1$ were hexagonal (00.2)-oriented and had a grain size of about 0.16 $\mu$m increased to 0.2 $\mu$m after annealing (300 °C in air). Increasing Cd content in the solid was seen to result in a decrease of resistivity of the as-deposited films. Interestingly, annealing reduced the resistivity of CdS samples by about three orders of magnitude but did not influence the Zn-containing films. A near-linear relationship was observed between the composition of films determined from XPS and their band gaps determined from transmission spectroscopy. Films with composition near $Cd_{0.7}Zn_{0.3}S$ were tested as window layers in solar cells based on the n-$Cd_xZn_{1-x}S$/p-CdTe heterojunction.

Numerous reports have been published on the electrochemical formation of *cadmium selenotelluride,* $CdSe_xTe_{1-x}$. The methods used are similar to those illustrated for the binary end-members of the ternary alloy (i.e., CdTe, CdSe) (Fig. 3.7). The relevant research includes studies on the properties of electroplated alloys [131, 61, 132, 133] on the relationship between crystal structures, photoluminescence behavior, and PEC properties of the alloys [134]; devices and thin film characterization [135, 136]; crystal structure after annealing, and band gap variation with composition [137]; and so on. The $CdSe_xTe_{1-x}$ layers having the wurtzite structure are found to be strongly luminescent both in the red (at a photon energy corresponding to the direct band gap of the alloy) and in the near IR. Much weaker luminescence is shown by layers with the zinc blende structure. Annealing causes recrystallization and cubic-to-hexagonal phase transformation (for CdSe-rich alloys: Fig. 3.8) and is beneficial to the efficiency both of photoluminescence and of photoelectrochemical solar energy conversion.
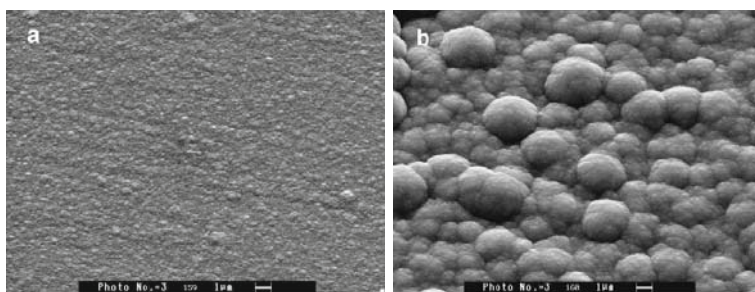


**Fig. 3.7** SEM micrographs of 2 $\mu$m thick films of (**a**) $CdSe_{0.85}Te_{0.15}$/Ni and (**b**) $CdSe_{0.78}Te_{0.22}$/Ti, electrodeposited at similar conditions from typical acidic aqueous selenite–tellurite solutions. The substrate effect on the film morphology is evidently strong. The ternary semiconductor film on Ti consists of spherical grains larger than 1 $\mu$m in diameter, whereas no superficial details larger than a few tens of nm can be observed on the film upon Ni. The morphology is rather independent of the deposition pH and – according to EDX – is not related at all to Se content in the solid film (at least for $x > 0.7$). (Reprinted from [61], Copyright 2009, with permission from Elsevier)

**Fig. 3.8** XRD patterns (CuK$_\alpha$ source) showing a rich in selenium ($x > 0.6$) CdSe$_x$Te$_{1-x}$ electrodeposited film, which adopts the hexagonal CdSe wurtzite structure by annealing at 520 °C (**b**). The as-deposited (from a typical acidic solution) film is rather amorphous (**a**). Segregation of a Te phase is observed in the solid. (Reprinted from: Bouroushian et al. [137], Copyright 2009, with permission from Elsevier)
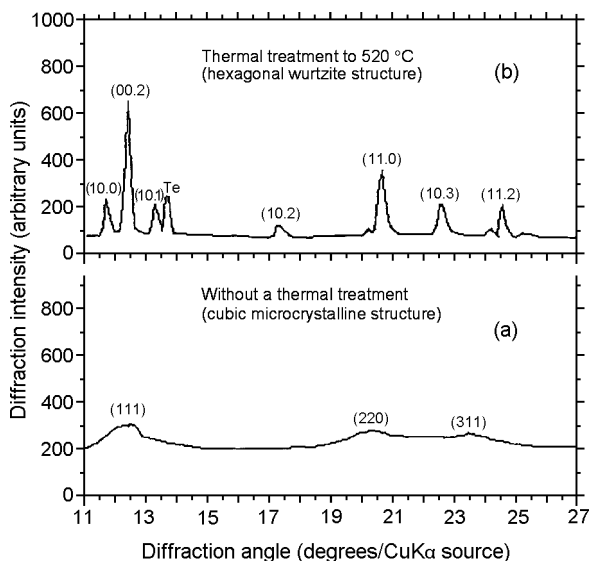


The electrochemical oxidation and reduction of single-crystal mercury tellurides HgTe and Hg$_{0.8}$Cd$_{0.2}$Te have been studied in aqueous buffer solutions of pH 1–13 by potentiodynamic RRDE experiments and XPS analysis [138, 139]. The electrochemical deposition of cadmium-rich Cd$_{1-x}$Hg$_x$Te films from aqueous acidic baths of Cd(II), Hg(II) ions, and tellurite has been reported in several works emphasizing the optical applications of this material [87, 140, 141]. The mechanistic aspects and electrodeposition chemistry of the Cd–Hg–Te system has been studied [142]. Electrodeposition from a non-aqueous bath containing Cd(II), Hg(II), and tri-*n*-butylphosphine telluride in propylene carbonate has also been reported [143]. The obtained films were smooth and adhered well to the ITO-coated glass substrate. The crystallite size was increased by soft heat treatment without substantial loss of Hg. Optical band gaps ranged from 1.03 to 1.32 eV for annealed films with $(1 - x) =$ 0.25–0.07.

Polycrystalline thin films of a single zinc blende phase of *zinc-mercury selenide* Zn$_{1-x}$Hg$_x$Se with $0.2 < x < 1$ were obtained on Ti and FTO/glass substrates by potentiostatic electrodeposition from aqueous baths containing low amounts of HgC1$_2$ and SeO$_2$ and comparatively high concentration of zinc sulfate, at pH 1.7–3.2, and optimally 85 °C [144]. Importantly, in contrast to the case of pure ZnSe deposition where under all deposition conditions an excess of unbound Se was found, this problem did not arise in the present case. Simultaneous formation of HgSe was noticed, when high bath concentrations of SeO$_2$ were used or when the pH was above 3.1 or at low deposition temperatures. The mixed films comprised aggregates of tiny crystallites with XRD-estimated size in the 7–14 nm range. The crystallite size was increasing with the Hg content in the ternary phase, as also did the intensity of the (111) texture; HgSe was almost completely oriented. The photoelectrochemical response of the films in polysulfide solution showed distinct n-type behavior.

### 3.2.9 Molybdenum and Tungsten Chalcogenides

It has been shown that the electrodeposition of molybdenum chalcogenides from high-temperature molten salts can give large, well-defined crystals of these compounds. The preparation of $MoS_2$ as well as $WS_2$ by electrolytic reduction of fused salts was first reported by Weiss [145], who produced small hexagonal blue-gray platelets under drastic conditions of electrolysis. Schneemeyer and Cohen [146] reported the growth of $MoS_2$ single crystals and polycrystalline films by electrodeposition from a sodium tetraborate melt at $T > 800\ °C$ and discussed the physical properties of the deposits and their application as photoanodes for photoelectrochemical cells.

On account of the fact that the electrode potential of molybdenum is more negative than the discharge potential of hydrogen, principle difficulties arise to cathodically electrodeposit molybdenum chalcogenide films from aqueous solutions. Theoretically, the deposition of pure molybdenum by electrolytic reduction of molybdates in acidic aqueous solutions is possible according to the reaction

$$H_2MoO_4(aq) + 6H^+ + 6e^- \rightarrow Mo + 4H_2O$$
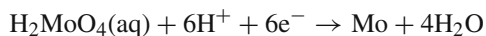
The attempts, however, to obtain pure Mo have been generally unsuccessful. In alkaline solutions, the cathodic process yields oxo-compounds of Mo, such as $MoO_{2-n}(OH)_n$. On the other hand deposition of molybdenum together with iron group metals has been possible, implying that the "induced co-deposition" mechanism should be used as a guiding principle for the electrochemical formation of Mo chalcogenide films from aqueous solutions. Along this line, Chandra and Sahu [147] performed electrodeposition from an ammoniacal solution of $H_2MoO_4$ and $SeO_2$ under galvanostatic conditions, anticipating that the presence of selenium will induce co-deposition of molybdenum with the possibility of obtaining $MoSe_2$. In these experiments it was shown that the first deposited layer consists of $Se^0$, which triggers the co-deposition of Mo, with the result that a phase of approximate $MoSe_2$ stoichiometry is obtained at some intermediate layer thickness. In general, electrodeposition from such "typical" deposition baths of molybdate ($MoO_4^{2-}$) ions and $H_2SeO_3$ has resulted in poorly defined mixtures of Mo and Se compounds.

Potentiostatic electrodeposition of XRD-crystalline $MoSe_2$ in conjunction with $MoO_2$ impurity on TO/glass substrates has been reported from a sulfamatic ($NH_4SO_3NH_2$), slightly acidic (pH 6.5) aqueous solution of $Na_2MoO_4$ and $H_2SeO_3$, at 20–40 °C. Annealing of the as-deposited films led to destruction of the layers [148].

Attempts to electrodeposit $MoS_2$ in a way similar to that used for $MoSe_2$ – in this case from solutions of molybdate and thiosulfate under various conditions of pH and temperature – have been unsuccessful. Instead, thin films of $MoS_2$ were conveniently deposited from tetrathiomolybdate solutions: Ponomarev et al. [149] observed that reduction of $MoO_4^{2-}$ in slightly alkaline solutions results in the formation of an X-ray amorphous film which by annealing at 550 °C in Ar for 1 h

gives crystalline $MoO_2$. By analogy, they expected that the electrolytic reduction of the tetrathiomolybdate ion ($MoS_4^{2-}$) may proceed in a similar way giving $MoS_2$, as $MoS_4^{2-}$ has a similar structure to that of $MoO_4^{2-}$ with the oxygen atoms replaced by sulfur. The corresponding reduction schemes considered were

$$MoO_4^{2-} + 2e^- + 2H_2O \rightarrow MoO_2 + 4OH^-$$
$$MoS_4^{2-} + 2e^- + 2H_2O \rightarrow MoS_2 + 2SH^- + 2OH^-$$
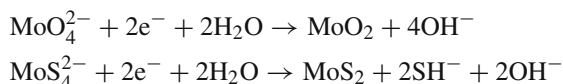
The authors used solutions of freshly prepared tetrathiomolybdate formed by chemical reaction in an aqueous solution of 5 mM $Na_2MoO_4$ and excess $Na_2S$. Hydrochloric acid was added to the stirred solution until a pH of 8.0 was reached. Cathodic deposition on Mo foil and F-doped $SnO_2$ substrates at room temperature resulted in amorphous films composed of Mo and S in an approximately 1:2 atomic ratio. After annealing in argon, highly textured polycrystalline molybdenum sulfide films with the van der Waals planes of the layered structure parallel to the substrate were finally produced. The authors stressed that these films may be useful for both solar cell and lubrication applications, where the high degree of basal plane texture is important. They noticed, however, that both the as-deposited and annealed films contained appreciable amounts of oxygen. In fact, as became clear in later publications, the electrodeposited material was molybdenum oxosulfide. This material, especially in its amorphous form, can serve as an excellent cathode in thin film Li and Li ion cells, taking advantage of the intercalation property. Actually, the lithium diffusion coefficient into amorphous molybdenum sulfide and oxosulfide films has been found to be higher than that in the crystalline structure by several orders of magnitude [150]. Thereby, the previous method was applied to produce amorphous $MoO_yS_z$ films to be used as cathodes in lithium battery cells [151].

Bhattacharya and co-workers [152] demonstrated the electrochemical deposition of amorphous $MoS_3$ (a-$MoS_3$) onto tin oxide-coated glass electrode by anodic oxidation of methanolic and aqueous solutions of ammonium tetrathiomolybdate, $(NH_4)_2MoS_4$, at room temperature. Amorphous $MoS_3$ is a semiconductor with a band gap close to 1 eV and suitable electrochemical properties for fabrication of lithium-active cathodes. Transmission and electroreflectance studies of the as produced a-$MoS_3$ thin films were reported. It was noticed that in general the $MoS_3$ compound (as well as $MoSe_3$, $WS_3$, and $WSe_3$) can be prepared only in the amorphous form; however, this phase readily decomposes to a crystalline form of $MoS_2$ at relatively low temperatures ($\sim350°$ C). Results on the voltammetry, chronoamperometry, and electrodeposition of amorphous $MoS_3$ in aqueous $(NH_4)_2MoS_4$ solutions were given also by Laperriere et al. [153, 154]. Their data analysis indicated that film formation occurs by instantaneous nucleation and 3D growth.

Electrodeposition of polycrystalline tungsten disulfide ($WS_2$) thin films on TO/glass, from an aqueous solution of tungstic acid and $Na_2SO_3$ (pH 7.0–9.5), at different current densities ranging from 20 to 60 mA $cm^{-2}$, and temperatures 40, 60, and 80 °C, has been reported [155]. Both the 2H and 3R phases of $WS_2$ were found

to occur, with XRD-preferred orientation along the (00.4) planes. An indirect optical transition at 1.12 eV was estimated from absorption spectra. Films were found to be p-type.

## 3.2.10 Copper Chalcogenides

The *copper selenide* system differs from the CdTe or CdSe cases, in that several compound phases can be formed by electrodeposition, such as $Cu_2Se$, $Cu_2Se_3$, and CuSe. For the same electrochemical bath composition, the nature of the electrodeposited product depends on the applied potential, i.e., as the potential is made more negative the deposit becomes enriched in copper, going thus from CuSe to $Cu_2Se$. For aqueous acidic deposition baths of copper sulfate and selenous acid, Massaccesi et al. [156] described a model giving the distribution of the formed products on tin oxide/glass as a function of the precursor concentrations and applied potential.

The co-reduction of copper and selenium is considered as an exception to Kröger's theory. Current–potential curves in the literature show that deposition of copper is rather compulsory to make the deposition of selenium possible. In fact, although the standard potential for Se(IV) reduction is more positive than that of copper (0.741 and 0.340 V vs. SHE, for selenous acid and cupric ion, respectively), it turns out that Se(IV) alone is reduced at more negative potentials than Cu(II). In the presence of copper, the order is reversed.

Yang and He [157] developed an electroless method for preparing copper selenide on silicon wafer (p-type) from aqueous solutions of $SeO_2$, $CuSO_4$, and HF, at pH < 1. The deposition occurred via two coupled galvanic displacement reactions at the silicon electrode, namely deposition of copper and subsequent reaction of the latter with selenous acid in the bath. A uniform, adhesive thin film, identified as $Cu_3Se_2$ (umangite) with a band gap of 2.83 eV, was obtained at room temperature. The authors pointed out the promising prospective of their simple technique for the preparation of copper indium selenide films for photovoltaic cells.

Galvanic synthesis of copper selenide was reported also by coupled copper metal oxidation and Se(0) reduction in alkaline selenosulfate ($Na_2SeSO_3$) aqueous bath at room temperature, in a cell comprising externally short-circuited copper foil anode and gold foil or graphite rod cathode electrodes [158]. Spherical nanoparticles of non-stoichiometric $Cu_{2-x}Se$ (clausthalite) and stoichiometric CuSe (hexagonal phase) could be precipitated upon immersing the electrodes in solution, yet only under the catalyzing action of 1-thioglycerol, which acted also as the capping agent of the copper selenide nanoparticles. The TEM diameters of the produced particles were in the range 10–20 and 5–15 nm, respectively, for CuSe and $Cu_{2-x}Se$. The effect of open-circuit potential on the process was investigated.

Works on the electrochemical formation of *copper sulfide* have been reported mainly in connection with the fabrication of $Cu_xS$/CdS junctions for solar cells [159–161].

### *3.2.11 Silver Chalcogenides*

The kinetics and mechanism of the growth of anodic *silver sulfide* films on silver metal in aqueous sulfide solutions has been studied under potentiodynamic conditions [162]. The $Ag_2S$ film formation was presumed to proceed as

$$2Ag + HS^- + OH^- \rightarrow Ag_2S + H_2O + 2e^-$$
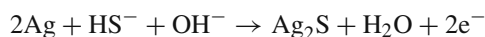
Due to the inherently fast electron transfer reaction between silver and the sulfide ion to form $Ag_2S$, the rate of film growth is limited by processes of nucleation, diffusion, and ion migration, depending on the experimental conditions. In resting solutions, the rate of growth of $Ag_2S$ is controlled by the diffusion of sulfide ions to the electrode surface and their subsequent kinetically irreversible electron transfer reaction with silver. This stage of growth results in the deposition of a filament-like deposit which then becomes crystalline with further film thickening. It has been suggested that, during anodic film growth, prior to the formation of the $Ag_2S$ phase by nucleation steps, a monolayer of the compound forms at a separate stage [38]. The potentiodynamic response for this monolayer was simulated quantitatively on the basis of a mechanism involving the initial adsorption of $HS^-$ on the silver surface in a fast equilibrium step followed by a rate-determining electron transfer step to form AgHS as a surface intermediate; the AgHS species diffuse rapidly on the surface and join a growing 2D silver sulfide monolayer nucleus.

The redox behavior in the silver–selenium–water system at ambient and higher (85 °C) temperatures was studied by Petrov and Belen'kii [163]. According to their voltammetry results, and the presented Pourbaix diagram (Fig. 3.9), the stability
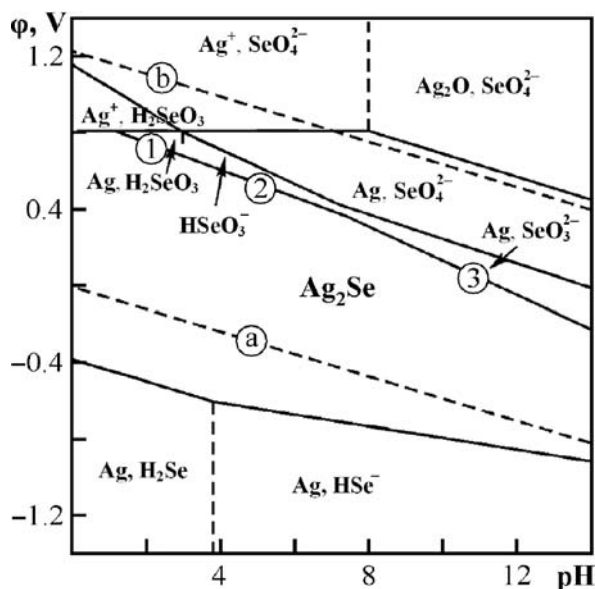


**Fig. 3.9** Potential–pH diagram for the $Ag_2Se–H_2O$ system at 25 °C. (With kind permission from Springer Science+Business Media [163])

region of *silver selenide* $Ag_2Se$ in the whole pH range (except for pH < 1) is bounded at the top by lines 1–3 corresponding to reduction of $Ag^+$ to Ag and oxidation of $Se^{2-}$ to $SeO_3^{2-}$. Selenide ions from the oxidation of silver selenide exist in a narrow potential range, for the entire pH scale. In alkaline solutions, and at redox potentials slightly exceeding this range, $Ag_2Se$ is oxidized to selenate anion which is highly stable and can be reduced to elemental selenium only at a high pressure or in the presence of catalyst. At the bottom limit of the $Ag_2Se$ stability region, the compound is reduced to elemental silver and $Se^{2-}$ in the potential range from –0.4 to –0.8 V. Liberation of $H_2Se$ is possible from the solution with pH < 4.0. In the presence of surfactants (sodium sulfide or ethanol), reduction of silver selenide is accelerated and polyselenide anions are stabilized, which shifts the cathodic potential to the positive direction and suppresses hydrogen evolution.

The electrodeposition of tellurium and silver has been investigated in dilute aqueous solutions of tellurous acid and $Ag^+$ ions (concentrations in the order of $10^{-5}$ to $10^{-4}$ M) in 0.1 M $HClO_4$ [164]. In particular, cyclic voltammetry experiments were conducted with rotating glassy carbon disk electrodes in baths with various concentration ratios of Ag(I) and Te(IV) precursors, and their outcome was discussed in terms of the voltammetric features. For a Ag(I)/Te(IV) ratio close to 0.8, formation of "quasi" pure *silver telluride*, $Ag_2Te$, was reported. The authors, based on their measurements and on account of thermodynamic predictions, assumed that silver is deposited first on the electrode ($Ag^+ + e^- \rightarrow Ag$), and then Te(IV) is reduced on the previous silver deposit with formation of $Ag_2Te$ according to the reaction

$$H_2TeO_3 + 2Ag + 4H^+ + 4e^- \rightarrow Ag_2Te + 3H_2O$$
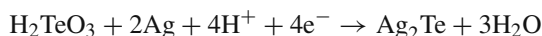
They concluded, thereby, that $Ag_2Te$ formation is governed by the initial amount of silver deposit. It is worth noting that the present method, involving dilute electrolytic baths of the compound precursors, deviates from the typical, initially proposed by Panicker et al., method of employing high concentration ratios of the metal to the chalcogen precursor.

### 3.2.12 Indium Chalcogenides

Reports on electrochemical synthesis of indium chalcogenides have been scarce.

Successive electrodeposition of elemental Se and In layers at respective constant potentials, followed by thermal annealing to obtain *indium selenide*, $In_2Se_3$, has been demonstrated by Herrero and Ortega [165]. An initial layer of metallic gray Se was electrodeposited first on Ti metal at 80 °C from an aqueous solution containing millimolar $SeO_2$, buffered by citrates at pH 4. Then, indium was electroplated over the Se deposit from an aqueous solution of millimolar $InCl_3$, ethanolamine, and $NH_3$ at pH 2 controlled by addition of concentrated HCl. These samples were prepared with a 3/2 Se/In stoichiometry and the estimated thickness of the produced films was 2–5 µm. After annealing at 300–500 °C, the β-$In_2Se_3$ phase was

identified by XRD, while for samples annealed at 600 °C a $\delta$-In$_2$Se$_3$ phase was present; heat treatment at 600 °C produced a noticeable decrease on the selenium content in the samples and the formation of indium–selenium compounds of lower Se stoichiometry. The $\beta$-phase of In$_2$Se$_3$ was found to be photoelectrochemically active as n-type (anodic response) in a sulfite/sulfate cell. The band gap transition of the relevant films was determined to be of a direct nature and 1.68 eV in width.

Wynands and Cocivera [166] reported on the electrodeposition of *indium telluride*, In$_2$Te$_3$, thin films from propylene carbonate solutions containing InCl$_3$ and tri-*n*-butylphosphine telluride. Deposition was carried out under potentiostatic or galvanostatic conditions on Ti and ITO/glass substrates at 90–100 ℃, in illuminated and dark cells. DC polarography studies under conditions that allowed the simultaneous determination of In$^{3+}$ and Te$^{4+}$ indicated a film composition with a slight excess of indium under virtually all deposition conditions. In general, the as-obtained films were adherent, gray-black, and of an amorphous nature. After heat treatment at 250 °C, they showed small diffraction peaks without preferred alignment. Film morphology was found to be dependent on the substrate used, but cracks and pits were always present after heat treatment. The optical band gap of the films was determined by absorption spectroscopy to be 0.96 eV. The photoresponse of thin film In$_2$Te$_3$ was tested in solid-state semiconductor devices.

### *3.2.13  Copper–Indium Dichalcogenides*

*Copper–indium diselenide*, CuInSe$_2$ (CIS), is a widely electrodeposited compound, due to its significance in thin film photovoltaics.

A procedure involving (a) the deposition of nearly stoichiometric films of copper and indium on suitable substrates using vacuum evaporation or electrodeposition and (b) the heat treatment of Cu–In films in a hydrogen–selenium atmosphere at temperatures above 630 °C was reported to yield large grain (several mm in size), stoichiometric thin films of chalcopyrite CIS with a preferred {112} orientation [167].

The first attempt for one-step electrodeposition of CuInSe$_2$ was made by Bhattacharya [168] who used an aqueous, acidic (pH 1) bath containing cuprous ions, In$^{+3}$, and Se(IV) prepared by dissolving CuCl, InCl$_3$, and SeO$_2$, with triethanolamine/ammonia as complexing agent. Since then, several studies concerning CIS monolithic electrodeposition have been reported, using mostly acidic aqueous selenite solutions of chloride, sulfate, or nitrate salts of copper(II) and indium(III) with or without complexing agents, under galvanostatic [169], pulse [170], and potentiostatic [171] plating conditions. Many works have been performed at ambient conditions, but higher temperatures have also been used. The as-deposited films were polycrystalline with varying composition and morphology. Annealing at 300–500 °C was typically applied to improve the microstructure of the deposited films.

Ueno et al. [172] observed that $CuInSe_2/Ti$ with a composition close to the stoichiometric ratio (slight excess of metallic components) could be deposited exclusively at a specific potential value (–0.8 V vs. SCE) from a pH 1 bath of *uncomplexed* precursors at 50–55 °C. A positive shift in the potential was seen to result in the co-deposition of a $Cu_3Se_2$ phase (umangite), while a negative shift led to contamination by metallic indium. On the basis of measured electrolysis charge, the overall reaction of the optimum cathodic process was considered to involve the transfer of 13 electrons per mole of the product:

$$Cu^{2+} + In^{3+} + 2H_2SeO_3 + 8H^+ + 13e^- \rightarrow CuInSe_2 + 6H_2O$$

Mishra and Rajeshwar [173] studied in detail the mechanism of formation of $CuInSe_2$ thin films during voltammetric scanning of a glassy carbon electrode in an acidic solution containing $SeO_2$ and uncomplexed $Cu^{2+}$ and $In^{3+}$ ions, using a combination of Pourbaix analyses, cyclic and hydrodynamic voltammetry of binary In + Se and Cu + Se systems, and cyclic photovoltammetry (CPV), i.e., cyclic voltammetry combined with periodic white light illumination of the electrode, of the ternary Cu + In + Se system. The data on the binary systems were consistent with the facile formation of a $Cu_{2-x}Se$ solid phase in the Cu + Se system and a kinetically sluggish interaction between In and Se in the In+Se case. An internally consistent mechanistic scheme was proposed for the ternary system involving the concurrent formation of the $Cu_{2-x}Se$, its subsequent reduction coupled with the $6e^-$ reduction of $H_2SeO_3$ to $H_2Se$, and finally the underpotential assimilation of In into the solid phase leading to the photoactive chalcopyrite semiconductor CIS. The cathodic decomposition of the initially formed $Cu_{2-x}Se$ was shown to be a key to subsequent assimilation of In and formation of CIS. The photocathodic response observed for the produced CIS films was diagnostic of a Cu-rich ternary composition and consequent p-type behavior.

Guillén et al. [174] remarked that the typical acidic solutions with uncomplexed metals provide high deposition rates; however, the hydrogen evolution reaction leads to poor-quality layers and invokes indium hydroxide precipitation over the working electrode, owing to local pH change near the cathode surface. Complexing and buffer agents have been used to improve the reaction rate control and to avoid pH variation during the process. Among the possible complexing agents that can be used in the electrodeposition of $CuInSe_2$ thin films, carboxylates such as citrate and tartrate anions show some advantages over other candidates. They form complexes with both copper and indium, which are not toxic or hazardous, and they can be used to buffer the pH solution. Citrate anions are generally used in the electrodeposition of alloys of copper and indium with other metals if a large difference exists between the reduction potentials of the ions that are plated. Moreover, the citrate anion correlates to the establishment of a charge transfer reaction in several stages, which lowers the deposition rate and consequently improves the quality of the plated thin films.

Based on voltammetry and solid-state characterization results, Pottier and Maurin [175] defined the electrochemical conditions leading to the formation of smooth crystalline deposits of $CuInSe_2$ and also of the related binary compounds

$Cu_9In_4$ and $Cu_2Se$. They performed electrodeposition potentiostatically at room temperature on Ti or Ni rotating disk electrodes from acidic, citrate-buffered solutions. It was shown that the formation of crystalline definite compounds is correlated with a slow surface process, which induced a plateau on the polarization curves. The use of citrate ions was found to shift the copper deposition potential in the negative direction, lower the plateau current, and slow down the interfacial reactions.

By electrodeposition of $CuInSe_2$ thin films on glassy carbon disk substrates in acidic (pH 2) baths of cupric ions and sodium citrate, under potentiostatic conditions [176], it was established that the formation of tetragonal chalcopyrite CIS is entirely prevalent in the deposition potential interval –0.7 to –0.9 V vs. SCE. Through analysis of potentiostatic current transients, it was concluded that electrocrystallization of the compound proceeds according to a 3D progressive nucleation-growth model with diffusion control.

Electrodeposition has been attempted also on flexible substrates within the scope of fabricating flexible solar cells. Huang et al. [177] investigated the electrodeposition of CIS on Au-coated plastic substrate from aqueous acidic (pH 1.65) solutions of millimolar $CuCl_2$, $InCl_3$, $SeO_2$, containing triethanolamine and sodium citrate. Stoichiometric, semiconductive CIS films ($E_g = 1.18$ eV) were obtained after annealing at 150 °C in nitrogen.

In searching to formulate a mechanism of $CuInSe_2$ phase formation by one-step electrodeposition from acid (pH 1–3) aqueous solutions containing millimolar concentrations of selenous acid and indium and copper sulfates, Kois et al. [178] considered a number of consecutive reactions involving the formation of Se, CuSe, and $Cu_2Se$ phases as a pre-requisite for the formation of CIS (Table 3.2). Thermodynamic and kinetic analyses on this basis were used to calculate a potential–pH diagram (Fig. 3.10) for the aqueous Cu+In+Se system and construct a distribution diagram of the final products in terms of deposition potential and composition ratio of Se(IV)/Cu(II) in solution.

Segregated phases, other than the target material, usually found on the surface of deposited polycrystalline chalcopyrite semiconductor films, such as $CuInSe_2$ and $CuInS_2$, constitute a shortcoming in material quality for solar cell and other applications. In fact, these films are usually prepared purposefully with an excess of

**Table 3.2** Selected reactions in the Cu–In–Se–$H_2O$ system

| | |
|---|---|
| 1 | $Se(IV) + 4e^- \rightleftarrows Se(0)$ |
| 2a | $Se(IV) + Cu(II) + 6e^- \rightleftarrows CuSe$ |
| 2b | $Se(0) + Cu(II) + 2e^- \rightleftarrows CuSe$ |
| 3a | $Se(IV) + 2Cu(II) + 8e^- \rightleftarrows Cu_2Se$ |
| 3b | $Se(0) + 2Cu(II) + 4e^- \rightleftarrows Cu_2Se$ |
| 4 | $2CuSe + 2e^- \rightleftarrows Cu_2Se + Se(-II)$ |
| 5 | $Cu_2Se + 2e^- \rightleftarrows 2Cu(0) + Se(-II)$ |
| 6 | $Se(0) + 2e^- \rightleftarrows Se(-II)$ |
| 7 | $Se(-II) + Cu(II) \rightleftarrows CuSe$ |
| 8 | $3Se(-II) + 2In(III) \rightleftarrows In_2Se_3$ |
| 9 | $2Se(-II) + Se(IV) \rightleftarrows 3Se(0)$ |
| 10 | $Cu_2Se + In_2Se_3 \rightleftarrows 2CuInSe_2$ |

**Fig. 3.10** Pourbaix diagram for the Cu + In + Se + H$_2$O system at 25 °C. The stability fields were drawn for activities of Cu(II), Se(IV), and In(III) reactive species equal to $10^{-2}$ M. The diagram was assembled by using the candidate reactions included in Table 3.2. (Kois et al. [178]. Copyright Wiley-VCH Verlag GmbH & Co. KGaA. Reproduced with permission)
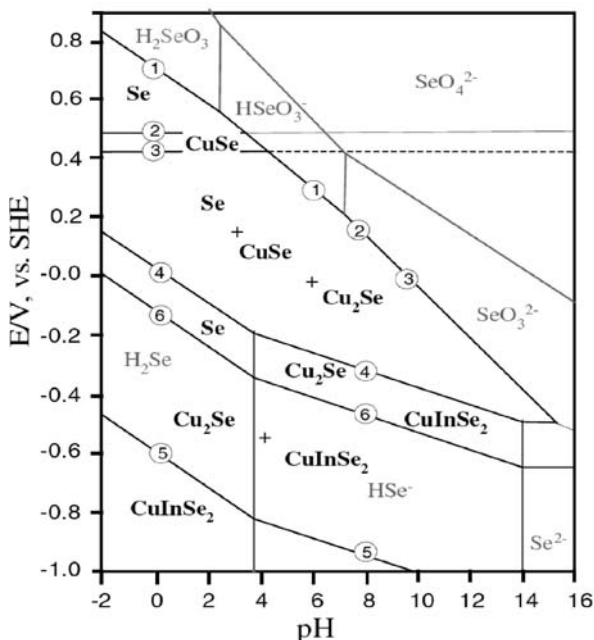


Cu to promote the grain growth; and as a consequence another processing step is needed to remove the segregated separate binary phases of copper. The prevalent method for removing Cu–Se and Cu–S phases is chemical etching in KCN solutions. Alternatively, strong oxidants are utilized, such as Br, H$_2$O$_2$, permanganates, or complexes. In addition, electrochemical oxidation is a useful surface treatment technology and has been employed for surface modification of CuInSe$_2$ and CuInS$_2$ films. Kois et al. [179] investigated and compared the influence of traditional KCN chemical etching and of electrochemical etching on the surface composition and morphology of CuInSe$_2$ thin films electrodeposited on ITO surface (from CuCl$_2$, InCl$_3$, SeO$_2$ solutions) and annealed in hydrogen atmosphere at 400 °C. Electrochemical treatment, performed at various potentials and solution pH (0.8–13), consisted in particular of (a) oxidation of the semiconductor in alkaline solution and (b) electrochemical reduction–oxidation cycling in an acid solution. The influence of both treatments on the surface morphology and elemental composition of thin films as well as on the electrical parameters of fabricated solar cell structures was discussed. Analytical data on the pH–potential behavior of CuInSe$_2$, CuSe, and Se in aqueous medium were compiled in a Pourbaix-like diagram showing the expected immunity, passivity, and corrosion domains relevant to the studied system (Fig. 3.11).

Electrodeposition of *copper indium disulfide* (CuInS$_2$) has been reported [180–182]. In a typical instance, single-phase polycrystalline CuInS$_2$ thin films composed of 1–3 μm sized crystallites were grown on Ti by sulfurization of Cu–In precursors prepared by sequentially electrodeposited Cu and In layers [183]. In this work, solar cells were fabricated by electrodepositing ZnSe on CuInS$_2$. Cyclic
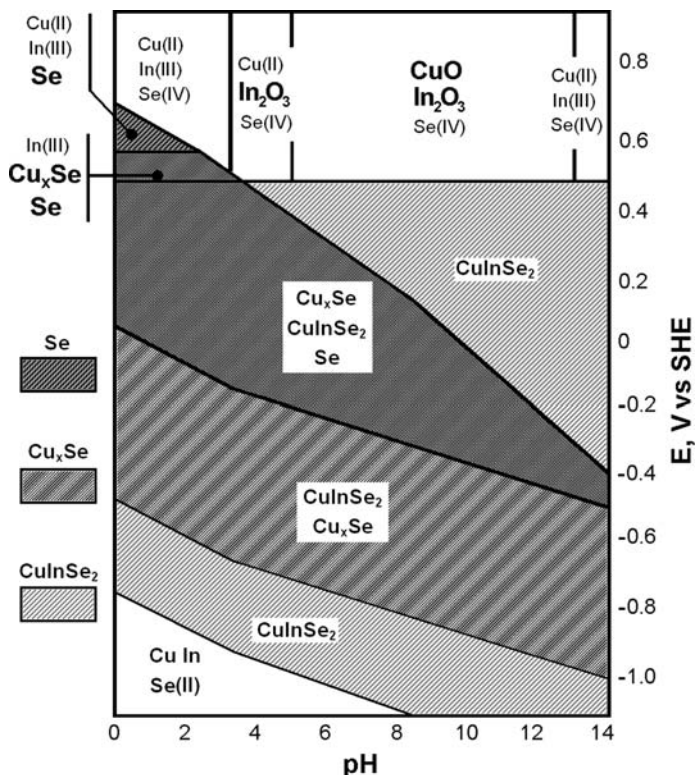
**Fig. 3.11** Theoretical condition of corrosion, immunity, and passivation of $CuInSe_2$, $Cu_xSe$, and Se phases in an aqueous solution. Concentrations of Cu, In, and Se species in the aqueous solution at 25 °C were assumed to be $10^{-4}$ M. (Reproduced from [179], Copyright 2009, with permission from Elsevier)

voltammetry and photovoltaic characteristics established the formation of the $CuInS_2$/ZnSe heterojunction. The mechanistic aspects of the anodic growth of $CuInS_2$ thin films from a sulfide-containing alkaline (KOH) medium have been explored by the combined application of photovoltammetry, electrochemical quartz crystal microbalance (EQCM) technique, coulometry, and potentiometry [184]. Interestingly, Raman spectroscopy evidence was presented in support of a new wurtzite-type structure for the $CuInS_2$ films grown under galvanodynamic conditions. Finally, a few works can be found on the electrodeposition of *copper indium ditelluride* ($CuInTe_2$) [185–187].

### 3.2.14 Manganese and Rhenium Chalcogenides

Manganese is more electropositive than any of its neighbors in the Periodic Table (standard reduction potentials for $Mn^{2+}$(aq) and $Mn^{3+}$(aq) to Mn(s) are –1.185 and –0.283 V vs. SHE, respectively). Thus, electrochemical growth of Mn-chalcogenide

compounds is complicated by the oxidizing nature of the metal in aqueous solutions. Actually, formation of $MnO_2$ impedes the cathodic formation of chalcogenides.

A few recent reports were published on the electrodeposition of manganese tellurides. Polycrystalline thin films of cubic, hexagonal, and orthorhombic mixed MnTe phases have been electrochemically deposited from aqueous acidic solutions (pH ~2), containing a high concentration of $MnSO_4$ (3 M) and millimolar $TeO_2$ at 80 °C [188, 189]. The anodic oxidation of manganese to its hydrated oxide at the counter electrode was controlled using tartaric acid as inhibitive agent. In order to optimize the film stoichiometry, the concentrations of precursors in the solution were chosen so as to provide current diffusion-controlled growth. The adhesion and deposition rates of the telluride films were enhanced by the addition of ammonium sulfate to the electrolytic solution. Compositional analysis showed dependence of the Mn/Te mass ratio on the applied deposition potential. Susceptibility and electrical characterization indicated anti-ferromagnetic behavior of the deposited films.

Schwarz et al. [190] demonstrated the synthesis of a black, amorphous $ReS_4$ film on Pt foil by prolonged oxidation of $MeCN/Bu_4NPF_6$ solutions of $Et_4NReS_4$, at 0.5 V vs. Ag/AgCl. The authors noted that the electropolymerization of a binary metal sulfide as exemplified by the rhenium–sulfur system is a reaction without precedence, although electrochemical methods had been employed with some success in the synthesis of other sulfur-rich transition metal sulfides such as the amorphous $MoS_3$ (above). Reductive depolymerization of $ReS_4$ could be achieved at –0.9 V. The large gap between the deposition and the re-reduction (stripping) potentials for $ReS_4$ suggested that the polymerization entailed a substantial structural rearrangement, a finding that was consistent with XAS characterizations. The oxidative polymerization could also be effected chemically using either $I_2$ or ferrocenium as oxidants.

### 3.2.15  Iron Chalcogenides

Iron sulfide as pyrite ($FeS_2$) has been shown to be a promising photoactive material for photoelectrochemical and photovoltaic solar cells. Whereas a variety of methods have been employed for the preparation of thin films of this material, including CVT, MOCVD, spray-pyrolysis, and sulfidation of either iron oxide or iron, the direct electrodeposition of $FeS_2$ thin films has proven to be problematic.

No attempts had been made to synthesize iron sulfides by electrodeposition until 1991, when Aricò et al. [191] reported a study on the electrochemical mechanism of the compound's formation on a Pt substrate in a diethylene glycol solution containing $FeCl_2$ and sulfur ($S_8$). The potential range at which the iron sulfide cathodic deposition may occur was identified as –0.45 to –0.65 V (SCE). Potentiostatic deposition in this range ensured a suitable composition and good adhesion of the films to the substrate at 120 °C. It was suggested that the deposition mechanism involves at first reduction of the $S_8$ species to $S_n^{2-}$, adsorbing onto the Pt surface, and then diffusion of the $Fe^{2+}$ ions through the double layer at the interface until they precipitate

on the adsorbed sulfide species to form the first nucleation sites for the compound formation. It was considered that the growth of the film proceeds by successive adsorption and reduction of sulfur on these $FeS_x$ sites. If the cathodic potential is not sufficiently large to give rise to a complete reduction, the chemisorbed sulfur preferentially produces –S– chains between the $FeS_x$ sites. A spreading in the film composition was observed by EDAX, accounting for the formation of an amorphous phase.

In general, pure iron disulfide is difficult to obtain by using low-cost, solution growth techniques. An attractive alternative is represented by alloying iron mono-sulfide with zinc sulfide in order to match the energy gap requirements for an efficient solar energy conversion (ternaries; ZnFeS). Some reports are available also on the insertion of Fe in CdS semiconducting thin films. Polycrystalline thin films of *cadmium-iron sulfide* $Cd_{1-x}Fe_xS$ have been prepared on stainless steel and F-doped tin oxide by potentiostatic electrodeposition from cadmium sulfate ($CdSO_4$), ferric chloride, and sodium thiosulfate ($Na_2S_2O_3$) solutions with EDTA as a complexing agent [192]. The composition of the preparation bath was optimized for photoelectrochemical operation of the produced films in a cell containing a typical (0.1 M) polysulfide redox solution. Optical absorption experiments evidenced direct transition. A slightly bowed linear variation of the band gap energy with solid composition was found between the 2.43 and 0.81 eV values corresponding to Fe content from 0 to 1.

The potentiostatic electrodeposition of *iron selenide* thin films has been reported recently in aqueous baths of ferric chloride ($FeCl_3$) and $SeO_2$ onto stainless steel and fluorine-doped TO-glass substrates [193]. The films were characterized as polycrystalline and rich in iron, containing in particular a monoclinic $Fe_3Se_4$ phase. Optical absorption studies showed the presence of direct transition with band gap energy of 1.23 eV.

### *3.2.16 Tin Chalcogenides*

The low-temperature chemical precipitation and vapor deposition of tin sulfide, SnS [194], and the electrodeposition of SnS [195] have been described by Engelken and co-workers, who discussed and compared potentiostatic, galvanostatic, and pulse electrochemical preparation techniques. It was remarked that the electrodeposition of tin sulfide presents problems not normally encountered with other sulfides such as the CdS, $Cu_2S$, $Bi_2S_3$; for instance, the Sn–S reaction rate is about $10^4$ times slower than in the Cu–S case. In their electrochemical work, these authors suggested a room-temperature non-aqueous synthesis technique, which they called "open-circuit voltage-controlled pulse deposition", designed to cope with the usual problems of stoichiometry and sluggish kinetics in such media. The sulfide films were deposited on ITO/glass from a vigorously stirred ethylene glycol solution of anhydrous $SnCl_2$, saturated with elemental sulfur. Incorporation of L-tartaric acid in the bath was found to both increase its longevity and chelate the $Sn^{2+}$ ions, so that the direct $Sn^{2+}$–S reaction was minimized. Further, partial dissociation of this

weak acid enhanced the bath conductivity, while the tartrate anions had a brightening/leveling effect on the deposits. As a first step, the metal was deposited under application of current for a time duration corresponding to the formation of a few monolayers. Subsequently, the circuit was broken and the current interrupted letting thus the open-circuit potential to drift in the positive direction concomitant with the decreased metal activity due to the metal–chalcogen reaction. Finally, the circuit was closed again as soon as the open-circuit potential attained a value corresponding to the desired stoichiometry. The researchers claimed that they achieved better control of the thin film stoichiometry and minimization of metal excess, compared to typical non-aqueous deposition. Anyhow, they experienced poorly adherent films, anion contamination, amorphous materials, and widely ranging Sn/S ratios enriched in tin. The photoactivity of the resulting films was evaluated by photoelectrochemical techniques, and their dark and photocorrosion behavior was discussed with the aid of Pourbaix diagrams.

A brief review of subsequent works on the electrodeposition of SnS has been given by Brownson et al. [196] who recently described a method for aqueous cathodic electrodeposition of tin sulfide. Films deposited from acidic solutions of $SnCl_2$, $Na_2S_2O_3$, and L(+)-tartaric acid on F-doped TO/glass substrate consisted of the orthorhombic polymorph of tin monosulfide, δ-SnS, which could be converted to the α-SnS phase (herzenbergite) by post-annealing at 350 °C in argon gas. The chemistry involved in the formation of δ-SnS by galvanostatic electrodeposition was investigated at pH 1.5 and 2.5 and temperatures of 50, 70, and 90 °C [197]. Uniform films were deposited at both pH values, while the addition of tartaric acid was found to promote the thin film adhesion. UV–vis spectroscopy showed increased disorder in films deposited at 50 °C and a direct optical band gap of lower energy for the δ-SnS phase compared to that of the α-SnS. At 70 °C and pH 2.5, the as-deposited films adopted a distorted herzenbergite structure. Cyclic voltammetry data suggested that tin–tartrate complexes were crucial to attain film electrodeposition and also showed a larger current contribution from the sulfur species than for the tin species, indicating that reduction of the former is favored in the conditions used. Although establishing the α-SnS structure, annealing did not change the film morphology as observed by SEM, indicating pseudomorphic replacement of the δ-SnS phase. Annealed films showed significantly less structural disorder than the as-deposited and a direct allowed optical transition consistent with α-SnS, i.e., 1.22 eV.

A similar method was followed by Switzer and co-workers [198] who demonstrated recently epitaxial electrodeposition of δ-SnS films with a disk-like morphology from an acidic (pH 2.5) solution of $SnCl_2$, $Na_2S_2O_3$, and L-tartaric acid, on a [100]-oriented single-crystal Au substrate, at 70 °C. [Although works relevant to epitaxial deposition are included typically in the next chapter, this work is cited here due to the unusual microstructure involved and the non-quantized nature of the coatings]. It was pointed out that the system under investigation, namely the heterostructure of orthorhombic δ-SnS and face-centered cubic Au, provides fundamental information on the epitaxial growth of high-mismatch systems. The deposits consisted of disks (Fig. 3.12) having a diameter of 300 nm and a thickness of 50 nm
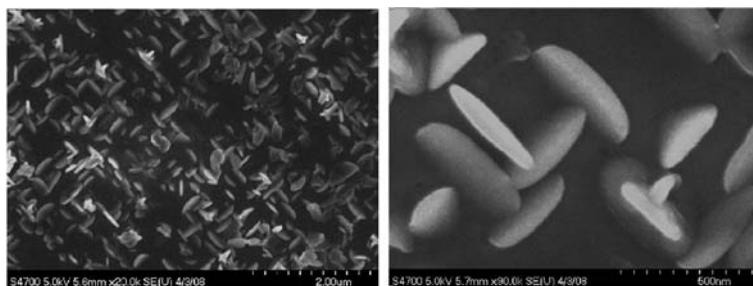
**Fig. 3.12** SEM micrographs of an epitaxial deposit of SnS nanodisks on Au(100), in two different magnifications. (Reprinted with permission from: [198], Copyright 2009, American Chemical Society)

and were found to grow with two different out-of-plane orientations, namely [100] and [301], each having four equivalent in-plane orientations. For the SnS [100], the in-plane mismatch was –2.4% in the [010] direction and 6.1% in the [001] direction. For the [301] orientation, the in-plane mismatch was –2.4% in the [010] direction and alternated between 3.4% and 6.7% in the [10$\bar{3}$]direction. It was shown that mismatch is minimized when the δ-SnS is deposited with its a-axis oriented perpendicular to the surface of the Au(100) substrate. As a matter of fact, semiconductor morphologies comprising forms with high aspect ratios (length/diameter) have attracted much attention lately for fabrication of optical and electronic devices exhibiting superior performance compared to those involving the conventional planar geometry. Thus, the previous high aspect ratio epitaxial SnS deposits may be found useful for photoelectrochemical and photovoltaic applications as their morphology maximizes collection of charge carriers.

The *tin selenide* electrocrystallization process is characterized by the usual drawbacks: solutions are unstable, and properties of coatings are dependent on electrolyte concentration, layer thickness, and conditions of electrolysis. Electrodeposition of SnSe thin films has been described by Engelken and co-workers [199]. Non-stoichiometric, but smooth, uniform and adherent SnSe films were obtained from acidic (pH 3) aqueous solutions of $SnCl_2$ and $SeO_2$ (or $H_2SeO_3$) by the typical cathodic electrodeposition method, as well as from DMF solutions containing $SnCl_2$ and dissolved selenium powder by a method similar to that of Baranski and Fawcett. The as-deposited films ranged from amorphous to polycrystalline and exhibited indirect or non-direct band gaps from 0.85 to 0.95 eV. The appearance and material properties of the films grown by the two techniques were rather similar. In the aqueous solutions, direct reaction between $Sn^{2+}$ and Se(IV) oxoanions yielding a $Se/Sn_xSe$ suspension/precipitate was presumed to occur. This effect, while decreasing the concentration of available species and possibly changing the composition of ions in solution, did not seem to influence the deposition process in any significant degree. Annealing of the deposited films slightly increased the Se/Sn ratio and erased all X-ray diffraction structure. In consistence with the increased Se/Sn ratio, the band gap of the films was shifted from approximately 0.9 to 1.30 eV (indirect

band gaps in the range 0.97–1.16 eV are reported for SnSe single crystals). It is likely that the increased value of the band gap was due to the presence of oxygen in the annealed films, since there have been reported tin–selenium–oxygen compounds such as $Sn_5Se_6O_{22} \cdot xH_2O$, $Sn(SeO_3)_2$, $SnOSeO_4 \cdot xH_2O$, $SnSeO_4$, and $Sn_5Se_4O_6$ with high band gaps (e.g., 1.6 eV for $Sn_5Se_4O_6$).

Electrodeposition of *nanometric* SnSe layers from aqueous and non-aqueous solutions followed by annealing in order to improve their photoelectrical properties has been reported [200].

### 3.2.17 *Lead Chalcogenides*

*Lead sulfide* films have been prepared by various deposition processes like vacuum evaporation and chemical bath deposition. Electrochemical preparation techniques have been used in a few instances. Pourbaix diagrams for all three aqueous lead–chalcogen Pb–S, Pb–Se, and Pb–Te systems, along with experimental results and cited discussion on the chemical etching and electrolytic polishing of lead chalcogenide crystals and films, have been presented by Robozerov et al. [201].

The anodic formation of PbS on polycrystalline Pb has been investigated in aqueous alkaline sulfide solutions [202]. The electrochemical reactions attending the film formation process were discussed on the basis of variations in voltammetric peak potentials with sulfide concentration and pH in the alkaline range. At low polarizations, a (110)-oriented galena (rock salt) structure was obtained, presumably through a 2D nucleation and growth mechanism. Non-linear growth rates were observed though, possibly because of the disordering action of defects originated in the grain structure of the underlying substrate. At higher potentials, thick PbS films could be obtained by high field growth, while dielectric breakdown was observed at fields of ca. $4 \times 10^6$ V cm$^{-1}$.

The anodic electrochemistry of the lead amalgam electrode in alkaline sulfide solutions has been studied by cyclic voltammetry, chronoamperometry, and chronopotentiometry [203]. The first anodic peak in the voltammetric spectra was attributed to the formation of three monolayers (ML) of PbS. Potential step transients, resulting in the formation of this number of ML, showed a non-zero initial current rising to a maximum and then decaying. At low overpotentials, the transients showed evidence of a nucleation and growth mechanism but at higher overpotentials the shapes of the transients were in good agreement with a multilayer adsorption model. After subsequent film thickening to about 10 ML, film breakdown occurred with production of soluble lead species.

Cathodic deposition of lead sulfide from acidic aqueous solutions of Pb(II) ions (nitrate salts mainly) and $Na_2S_2O_3$ on various metallic substrates at room temperature has been reported. Stoichiometric PbS films composed of small crystallites (estimated XRD diameter 13 nm) of RS structure were obtained at constant potential on Ti [204]. Also, single-phase, polycrystalline thin films of RS PbS were electrodeposited potentiostatically on Ti, Al, and stainless steel (SS) [205]. It was found that the Al and Ti substrates promoted growth of PbS with prominent (200) and (111)

orientations, both being of higher intensity on Al than Ti. Only the (200) orientation was found for PbS on the SS substrate. Film thickness and grain size were reported to be of the order of micrometers.

The formation of colloidal sulfur occurring in the aqueous, either alkaline or acidic, solutions comprises a serious drawback for the deposits' quality. Saloniemi et al. [206] attempted to circumvent this problem and to avoid also the use of a lead substrate needed in the case of anodic formation, by devising a cyclic electrochemical technique including alternate cathodic and anodic reactions. Their method was based on fast cycling of the substrate (TO/glass) potential in an alkaline (pH 8.5) solution of sodium sulfide, Pb(II), and EDTA, between two values with a symmetric triangle wave shape. At cathodic potentials, $Pb(EDTA)^{2-}$ reduced to Pb, and at anodic potentials Pb reoxidized and reacted with sulfide instead of EDTA or hydroxide ions. Films electrodeposited in the optimized potential region were stoichiometric and with a random polycrystalline RS structure. The authors noticed that cyclic deposition also occurs from an acidic solution, but the problem of colloidal sulfur formation remains.

Rod-shaped PbS crystals of a rock salt structure, 140–350 nm in diameter and 1–3 $\mu$m in length, were produced in an electroless manner by spontaneous galvanic oxidation of a lead electrode (gold counter) in a sodium thiosulfate solution, in the presence of thioglycerol (TG), at room temperature [207]. The TG additive was found to dramatically catalyze the galvanic reaction. Introduction of butylamine in the electrolyte could lead to the formation of thin crystalline PbS wires with a diameter of ca. 50 nm and length in the range of 1–3 $\mu$m. The morphology of the product layer was variously affected by the concentration of butylamine [208].

Aqueous electrolytes proposed in the literature for cathodic electrodeposition of *lead selenide* are generally composed of dissolved selenous anhydride and a lead salt, such as nitrate or acetate. Polycrystalline PbSe films have been prepared by conventional electrosynthesis from ordinary acidic solutions of this kind on polycrystalline Pt, Au, Ti, and $SnO_2$/glass electrodes. The main problem with these applications was the PbSe dendritic growth. Better controlled deposition has been achieved by using EDTA in order to prevent $PbSeO_3$ precipitation, and also acetic acid to prevent lead salt hydrolysis.

In a voltammetric study [209] with titanium and graphite rde under cathodic polarization in an acidic (pH 3.4) electrolyte containing Pb(II), Se(IV), acetic acid, and EDTA, in room temperature, three characteristic regions were detected in the current–potential traces along the negative shift of potential. PbSe film formation was presumed to be established via "catalytic" reduction of Se(IV), that is, by electrochemical reduction of Pb(II) to metallic Pb with a following "induced" surface chemical reduction of Se(IV). Subsequently, at progressively more cathodic potentials, solid-state reduction of the PbSe film with the production of metallic Pb occurred, followed finally by the formation of elementary Se. It was shown that formation of stoichiometric PbSe with a current efficiency close to 100% takes place in the relevant potential region when the ratio of Se(IV) and Pb(II) concentrations in the electrolyte is equal to 0.5. The PbSe growth rate was observed to be determined by both ion mass transfer of Pb(II) to the electrode and surface Se(IV) reaction with metallic lead.

Streltsov et al. [210] suggested that PbSe electrodeposition from aqueous solutions containing Se(IV) species and Pb(II) ions may proceed "classically" via the chemical interaction between overpotentially deposited Se and underpotentially deposited Pb adatoms. These authors obtained polycrystalline PbSe films of 20–40 nm sized particles, enriched in amorphous Se, on Au and Pt metal substrates. At a potential several mV more positive than the redox value of the $Pb^{2+}/Pb^0$ couple, the surface coverage of adsorbed Pb on Se was seen to reach its maximum value, incurring deposition of Pb and Se atoms in a 1:1 ratio. At potentials 100–300 mV more positive than $Pb^{2+}/Pb^0$, the coverage decreased and the product contained PbSe and a portion of amorphous Se. The investigation of the UPD effect of Pb on chalcogen (Se, Te) enriched electrode surfaces, separately or along with UPD of other metals such as Cd, Bi, In, Cu, and Sn, led this research group to broader considerations regarding exchange processes occurring on the deposition substrate and the mechanism of lead chalcogenide growth; in a subsequent paper [211], they identified an important effect of Cd(II) addition on the PbSe crystallite growth, involving the simultaneous UPD of Cd at the PbSe electrodeposition potentials. Being dependent on Pb(II) and Cd(II) concentrations in solution, the overall surface density of adsorbed Cd on the cathode was found to influence phase composition, grain size, and crystallite orientation of the preparing films. Low densities of Cd adsorbates did not affect PbSe electrosynthesis, while high densities led to the formation of CdSe mainly, or amorphous phases. Intermediate densities induced preferential growth of the PbSe crystallites in the $\langle 100 \rangle$ orientation. It was remarked that the Cd atoms attach practically on all faces of PbSe crystals and cause inhibition of Pb UPD. This effect would prove useful in epitaxial growth of PbSe (Chap. 4).

Li et al. [212] obtained well-crystallized (RS), nearly stoichiometric, and mirror-like PbSe films by potentiostatic electrodeposition on ITO glass at 80 °C using aqueous acidic (pH 4) solutions of lead acetate, selenous anhydride, and disodium EDTA. The effects of deposition time and temperature on the composition of the films were investigated. Two competing processes were considered to take place during electrodeposition: one involving PbSe film growth and a second involving reaction of PbSe with acid in the solution, causing dissolution of the film. A rapid increase of film thickness was observed at the initial stage of deposition, while after a certain electrolysis time the dissolution process predominated over deposition, resulting in decrease of film thickness.

The electrodeposition of *lead telluride* from aqueous tellurite solutions has been reported. Saloniemi et al. [213] fabricated smooth, polycrystalline cubic PbTe thin films with a (200) preferred orientation on Cu and ITO substrates. Given the similar problems as in the PbSe case, EDTA was to be used in the bath electrolyte in order to complex Pb(II) and suppress dendritic growth. However, the tellurium precursor, $TeO_2$, is weakly soluble between pH values of about 2 and 7, while $Pb(EDTA)^{2-}$ is not stable at pH below 2, implying that alkaline solutions should be preferred for carrying out deposition in the present case. The researchers investigated [214] the mechanism of PbTe electrodeposition in solutions of $TeO_2$, $Pb(CH_3COO)_2$, and disodium EDTA at pH 9, using voltammetry combined with the EQCM technique (evaporated gold-covered working electrode and room temperature). In the alkaline working bath, tellurium was expected to be in the form of $TeO_3^{2-}$. The

behavior of Pb and Te precursors was studied separately, and it was suggested that for $Pb(EDTA)^{2-}$ a two-electron reduction with simultaneous adsorption reactions occurs, while tellurium is deposited via a four-electron reduction of $TeO_3^{2-}$. In the latter case, shift of the applied potential to more negative values resulted in increasing degradation of the Te film to powdery morphology, while at the most negative potentials the film was stripped off by reduction to $HTe^-$. The deposition of PbTe in the alkaline bath was considered to take place by an induced co-deposition mechanism, similar to PbSe deposition from the acidic baths described previously. However, the EQCM and EDX results implied that the PbTe films were slightly Te-rich, unlike the stoichiometric PbSe films.

On the other hand, Xiao et al. [215] reported that smooth, dense, and crystalline PbTe films with nearly stoichiometric composition could be obtained by an optimized electrodeposition process from highly acidic (pH 0) tellurite solutions of uncomplexed Pb(II), on Au-coated silicon wafers. The results from electroanalytical studies on Te, Pb, and PbTe deposition with a Pt rde at various temperatures and solution compositions supported the induced co-deposition scheme. The microstructure and preferred orientation of PbTe films was found to change significantly with the deposition potential and electrolyte concentration. At $-0.12$ V vs. Ag/AgCl(sat. KCl), the film was granular and oriented preferentially in the [100] direction. At potentials more negative than $-0.15$ V, the film was dendritic and oriented preferentially in the [211] direction (Fig. 3.13).

It was reported recently [216] that optical-quality PbTe thin films can be directly electrodeposited onto n-type Si(100) substrates, without an intermediate buffer layer, from an acidic (pH 1) lead acetate, tellurite, stirred solution at 20 °C. SEM, EDX, and XRD analyses showed that in optimal deposition conditions the films were uniform, compact, and stoichiometric, made of fine, 50–100 nm in size, crystallites of a polycrystalline cubic structure, with a composition of 51.2 at.% Pb and 48.8 at.% Te. According to optical measurements, the band gap of the films was 0.31 eV and of a direct transition. Cyclic voltammetry indicated that the electrodeposition occurred via an induced co-deposition mechanism.

Being isomorphous, PbSe and PbTe form solid solutions in the whole range of compositions. Cathodic electrodeposition of the $PbSe_xTe_{1-x}$ ternary ($0 \leq x \leq 1$)
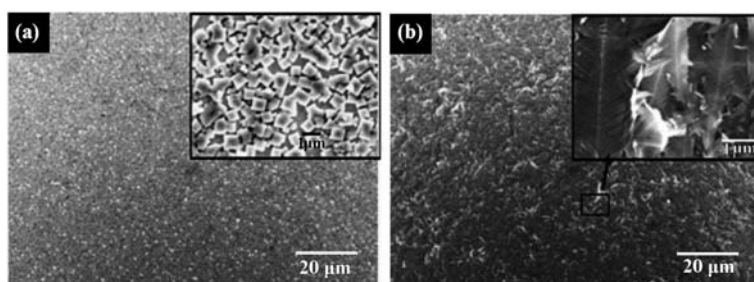


**Fig. 3.13** SEM microstructure of PbTe films electrodeposited at $-0.12$ V (*left*) and $-0.40$ V (*right*) vs. Ag/AgCl. Deposition solution: 0.0001 M $HTeO_2^+$ + 0.05 M $Pb^{2+}$ + 1 M $HNO_3$. (Reprinted from [215], Copyright 2009, with permission from Elsevier)

has been reported from acidic aqueous solutions of selenite, tellurite, and lead(II) salt, through simultaneous reduction of Pb(II), Se(IV), and Te(IV) species [217]. The electrosynthesis involved UPD of lead on chalcogens. The as-obtained films consisted mainly of RS crystalline Pb(Se,Te) phases of varying stoichiometry and also of amorphous chalcogen phases. The composition of the ternary phases was found to depend on the ratio of Se(IV) and Te(IV) concentrations in the electrolyte solution as well as on the electrodeposition potential.

### 3.2.18 Bismuth and Antimony Chalcogenides

In their pioneering work on the formation of photoelectrochemically active metal sulfides by oxidation of the parent metal electrode, Miller and Heller [29] reported the anodic formation of polycrystalline $Bi_2S_3$ on a bismuth metal electrode in a sodium polysulfide cell, wherein this electrode was used in situ as photoanode. When a Bi metal electrode is anodized in aqueous sulfide solutions a surface film is formed by the reaction

$$2Bi + 3HS^- \rightarrow Bi_2S_3 + 3H^+ + 6e^-$$

The electrochemistry of this process and the solid-state properties of the sulfide films developed on polycrystalline Bi have been explored using the ring-disk electrode technique [30] and photocurrent spectroscopy [218]. The kinetics of the anodization reaction has been studied by potential sweep experiments and potential or current transients under conditions of anodic $Bi_2S_3$ monolayer formation on a hanging drop electrode of bismuth amalgam in aqueous $NaHCO_3$ solution containing $HS^-$ at 20 °C [219]. The main conclusion from the kinetic data was that the mechanism for electrocrystallization of a monolayer consists in instantaneous nucleation at a small overpotential followed by rate-controlling growth at the perimeter of expanding 2D centers. Notably, the presumed mechanism is different from that considered to be operative in the case of CdS electrocrystallization on cadmium amalgam. In the latter case, 2D growth of multiple layers with a distinct phase transformation at high coverage was established [34].

Takahashi et al. [220] first reported the formation of Bi–Te alloy films with varying chemical composition by means of cathodic electrodeposition from aqueous nitric acid solutions (pH 1.0–0.7) containing $Bi(NO_3)_3$ and $TeO_2$. The electrodeposition took place on Ti sheets at room temperature under diffusion-limited conditions for both components. In a subsequent work [221], it was noted that the use of the Bi-EDTA complex in the electrolyte would improve the results, since $Bi^{3+}$ is easily converted into the hydrolysis product, $Bi(OH)_3$, a hydrous polymer, thus impairing the reproducibility of electrodeposition. The as-produced films were found to consist of mixtures of Te and several Bi–Te alloy compounds, such as $Bi_2Te_3$, $Bi_{2+x}Te_{3-x}$, $Bi_{14}Te_6$, and BiTe. Preparation of both n- and p-type $Bi_2Te_3$ was reported in this and related works [222].

The electrodeposition of $Bi_2Te_3$ in "typical" acidic solutions can be described by the general reaction

$$3HTeO_2^+ + 2Bi^{3+} + 9H^+ + 18e^- \rightarrow Bi_2Te_3(s) + 6H_2O$$
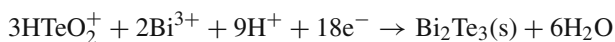
Martin-Gonzales et al. [223] have reported an extensive voltammetric study of nitric acid solutions containing $Bi^{3+}$ and $TeO_2$, individually or as a mixture, with a Pt disk working electrode. They also presented results of potentiostatic electrodeposition on Pt-sputtered quartz slide cathodes. Importantly, possible reactions relating various aqueous bismuth and tellurium species and precipitates thereof were documented and summarized in a Pourbaix diagram (Fig. 3.14), which was calculated according to the experimental conditions selected for electrodeposition. Cyclic voltammetry revealed two different mechanisms underlying the deposition process, depending on the applied potential. One process was considered to involve first the reduction of $HTeO_2^+$ to $Te^0$ and a subsequent interaction between reduced tellurium and $Bi^{3+}$ to form $Bi_2Te_3$. The second, taking place at more negative reduction potentials, involved reduction of the telluryl ions to $H_2Te$ followed by chemical interaction with $Bi^{3+}$. Both electrodeposition processes resulted in the production of crystalline, [11.0]-orientated $Bi_2Te_3$ films in the proper potential range. Deposition at 2 °C appeared to give more homogenous films than those obtained at room temperature. The authors concluded that (only) by changing the potential, the material composition can be manipulated to yield both the p-type (Bi-rich phases) and n-type (stoichiometric $Bi_2Te_3$) branches of a thermoelectric device. It was suggested that multilayers of p- and n-type material can be created by pulsing the potential.

Cathodic deposition of bismuth(III) telluride films has been reported [224] also on copper and nickel foils, from aqueous nitric acid solutions of bismuth oxide and tellurium oxide in molar ratios of Bi:Te = 3:3 and 4:3, at 298 K. The
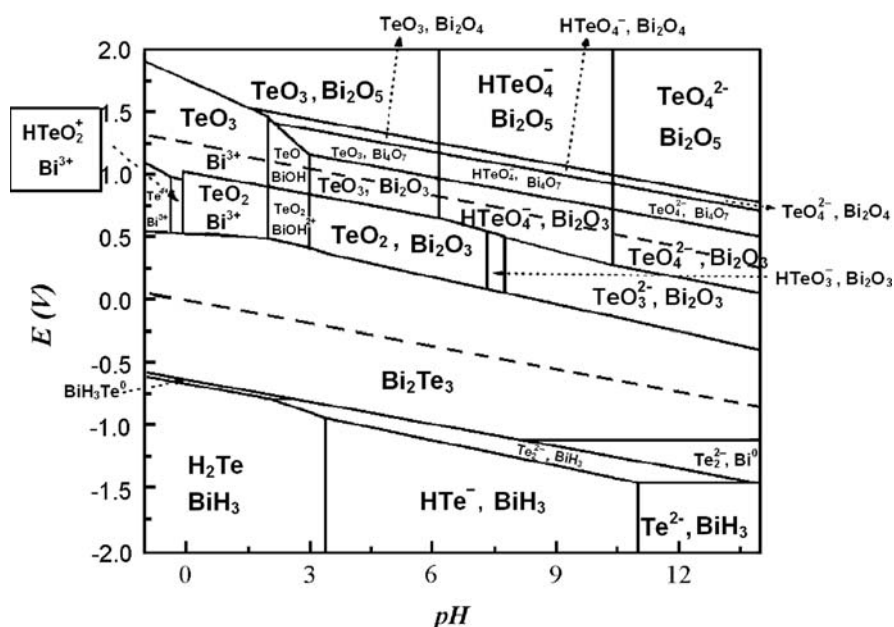


**Fig. 3.14** Potential–pH diagram for the Bi–Te–$H_2O$ system, calculated for dissolved substance concentrations, Bi: $0.75 \times 10^{-2}$ M and Te: $1 \times 10^{-2}$ M in 1 M $HNO_3$ at 25 °C, 1 atm. (Reproduced with permission from [223], Copyright 2009, The Electrochemical Society)

deposits were identified as stoichiometric n-type $Bi_2Te_3$ and could be described as a field-oriented (FT) texture type (Fisher classification). XRD analysis revealed a [11.0] preferred orientation. The thermoelectric properties of the electroplated strips were investigated and shown to yield a much higher thermo-e.m.f. compared to Bi. The authors claimed that the obtained microstructures are suitable for thermoelectric microdevices like batteries or sensors.

Using an approach similar to bismuth telluride, Torane et al. [225] electrodeposited bismuth selenide, $Bi_2Se_3$, potentiostatically, on stainless steel and FTO glass from an acidic nitrate bath at room temperature. The electrolyte was made by first dissolving $Bi(NO_3)_3$ and $SeO_2$ in concentrated nitric acid, followed by proper dilution to the desired concentration. The best samples were obtained from a 7:3 (vol.) mixture of equimolar (0.025 M) stock solutions of $Bi^{3+}$ and $SeO_2$. The as-deposited films were polycrystalline with random orientation. After being annealed at 200 °C in a nitrogen atmosphere for 2 h, the films acquired a (00.6) texture. Based on the optical absorbance variation of $Bi_2Se_3$ with wavelength, the authors estimated a direct band gap at 0.55 eV. Desai [226] used sodium selenosulfate ($Na_2SeSO_3$) as selenium precursor to electrodeposit $Bi_2Se_3$ from an aqueous alkaline bath of bismuth nitrate, containing triethanolamine as complexing agent. The electrodeposition was carried out galvanostatically on Ti or stainless steel substrates, and the as-deposited films were polycrystalline with random orientation. Band gap energy of 0.57 eV was reported.

Michel et al. studied the cathodic electrodeposition of polycrystalline, Bi- or Te-rich $Bi_2Te_3$ [227] and composition-modulated $Bi_2(Te_{1-x}Se_x)_3$ [228] phases on stainless steel substrates at room temperature, under potentiostatic or galvanostatic conditions, using aqueous electrolytes containing $Bi^{3+}$ (nitrate), $HTeO_2^+$, and $H_2SeO_3$, in constant molar proportions 60:36:4, respectively. By controlling the electrode potential or the current density, it was possible to obtain a range of ternary film compositions. Higher cathodic conditions caused bismuth enrichment, while lower cathodic conditions led to chalcogenide (Se+Te)-rich alloys. The electrodeposits consisted of a single phase closer to $Bi_2Te_3$ than to $Bi_2Se_3$. Typically, a fiber texture, with a basal [11.0] preferred orientation, was obtained. The morphology of the samples was rather fixed by their chemical composition. For films presenting a chalcogen excess, a little roughness and a fine granular microstructure were observed, whereas the Bi-rich ternary films presented a coarser granular structure. Electrical and thermoelectric properties were measured for a $Bi_{1.98}Te_{2.67}Se_{0.39}$ sample, which showed n-type behavior.

Electrodeposition of antimony sesquitelluride, $Sb_2Te_3$, or of $(Bi_{1-x}Sb_x)_2Te_3$ alloys from aqueous solutions is challenging because it is difficult to achieve a sufficiently high concentration of antimony. Complexing agents such as tartaric acid, citric acid, or EDTA have been used to solubilize Sb in water.

Successful electrodeposition of $Sb_2Te_3$ has been reported for the first time by Leimkühler et al. [229] who prepared polycrystalline thin films of the material on different transparent conductive oxides, as well as CdTe and Mo, from uncomplexed solutions made by mixing stock solutions of $SbCl_3$, $TeO_2$, and phthalate buffer (pH 4). The electrochemical process was discussed in detail based on results obtained by cyclic voltammetry on ITO/glass. The bath temperature was found to influence

dramatically the crystallinity of the electrodeposits. Films made at room temperature were amorphous, whereas the best crystallinity was obtained at 372 K, almost at the boiling point of the bath. The as-prepared films had a mirror-like appearance up to 500 nm, whereas for larger thickness they became dull.

Tittes and Plieth [230] managed to cathodically deposit ternary Bi–Sb–Te alloys and binary antimony telluride, under potentiostatic conditions, from aqueous alkaline (pH 9), diphosphate ($K_4P_2O_7$) solutions of $BiCl_3$, DTPA, $K_2TeO_3$, and potassium–antimony tartrate, in the temperature range 278–318 K. Alkaline rather than nitric acid electrolytes were employed to circumvent the low solubility of the Sb and Te compounds in the latter as well as the corrosive action of the acidic bath. The kinetics of the process was investigated by cyclic voltammetry with Pt, Cu, and Ni microelectrodes, and the electrodeposited films were characterized by electrochemical impedance spectroscopy. The dependence of layer composition on the electrode potential was determined, but no structural data were given. The authors concluded that nickel substrates are well suited for deposition of ternary alloys, and that the process temperature should not exceed 293 K. Controlled agitation of the electrolyte was found to be quite important for obtaining good films. Both electrodeposited ternary and binary systems were of p-type conductivity. The measured charge carrier concentration of a 6–32–62 at.% Bi–Sb–Te ternary was smaller by a factor of 100 compared to current literature reports.

Wang et al. [231] employed the electrodeposition method to prepare the thermoelectric films directly on Si wafer, suggesting this rather facile route to fabrication of integrated microdevices. The authors investigated the electrochemical deposition and growth mechanisms of $Sb_2Te_3$ on highly doped single-crystal p-type Si(100), at room temperature, from a hydrochloric acid aqueous solution containing $Sb_2O_3$ and $TeO_2$. Electrodeposition on Ag working electrode was also reported for comparison. The Sb/Te ratio of the films deposited at optimal deposition potentials was very close to the stoichiometric ratio in $Sb_2Te_3$, especially for the Si substrate. Preferred orientations for $Sb_2Te_3$ deposited on the Si substrate were given as {015} and {110}, as opposed to the {10$\overline{1}$0} obtained on Ag electrode. The films grown on the Ag substrate were found to consist of about 30 nm grains while the films grown on the Si(100) electrode exhibited a "microbranches" morphology with thickness of about 10 $\mu$m. The morphological distinction could be explained by the different nucleation and subsequent growth of $Sb_2Te_3$ films on the working electrodes.

Further specific information and recent results of the electrodeposition of Bi and Sb binary and ternary systems as well as of other thermoelectric materials can be found in the review of Xiao et al. [232].

### 3.2.19 Rare Earth Chalcogenides

Rare earth sulfides, selenides, and tellurides show semiconducting properties and have potential for application in thermoelectric generation. Thin film chalcogenides of various rare earths have been prepared by multisource evaporator systems [233].

Electrosynthesis of *yttrium chalcogenides* has been attempted by galvanostatic deposition at ambient temperature from non-aqueous, formaldehyde solutions of Y(III) nitrate salt, containing thioacetamide, selenite, and tellurite, respectively, as chalcogen sources and sodium acetate as complexing agent [234]. For the Y–S, and Y–Se systems, single bath deposition was reported to produce polycrystalline thin films of $YS_x$ ($x = 1.71$–$1.76$) and $YSe_2$, while the electrodeposition of Y–Te was carried out in a dual bath, layer-by-layer mode. Stainless steel, Cu, brass, and ITO/glass substrates were used. From optical absorption studies, the band gap energies of Y–S, Y–Se, and Y–Te were estimated as 1.85, 1.6, and 1.7 eV, respectively.

Electrodeposition of *europium selenide* (EuSe) films onto stainless steel (SS), Ti, Cu, and F-doped $SnO_2$/glass substrates, at constant potentials from unstirred aqueous acidic (pH 4) solutions of $Eu_2Cl$, $SeO_2$, and $Na_2EDTA$ as a complexant, at 70 °C, was described [235]. The electrodeposited EuSe films were polycrystalline, with rough surfaces when deposited on Cu, Ti, and SS, but relatively smooth and fine-grained on $F-SnO_2$. According to SEM characterization, spherical particle morphology was observed for the films on Ti and $F-SnO_2$, while for SS and Cu, cauliflower- and leaf-like structures, respectively, were detected. Optical absorption studies of the deposit films revealed a direct transition and band gap energy of 1.75 eV.

## 3.3 Addendum

### 3.3.1 Chemical Bath Deposition

Consideration of the chemistry that implements non-electrochemical solution growth processes along with related mechanistic aspects may be useful to enhance the understanding of electrochemical deposition in similar baths. The chemical deposition of CdS has been chosen as a model for this discussion by reason of the wealth of related publications and the advanced level of knowledge existing for this system (e.g., [45]).

Chemical bath deposition (CBD) can be regarded as an analogue to chemical vapor deposition (CVD), since they rely on the same principle to utilize chemical reaction of the precursor molecules or ions, except that CBD growth takes place in low-temperature (soft-processing) conditions in liquid solution. Advantageously, CBD does not require sophisticated instrumentation like vacuum systems and other costly equipment, so is a relatively inexpensive and simple technique, convenient for large-area deposition of thin films. In the literature, CBD has been also referred to as solution growth, chemical solution deposition, chemical deposition, controlled precipitation, and even electroless plating.

Within the scope of applications in electronics, electrooptics, and photovoltaics, several metal sulfides and selenides, mostly binaries such as CdS, CdSe, $Bi_2S_3$, $Bi_2Se_3$, PbS, PbSe, $Ag_2S$, TlSe, $MoS_2$, ZnSe, ZnS, and $SnS_2$, but also the ternaries

$CuInS_2$, $CuInSe_2$, CdZnS, PbHgS, CdPbSe, have been chemically deposited as thin films, mostly in single bath processes. In addition, compositionally modulated structures have been arranged by dual bath chemical deposition. In the last two decades, CBD attracted renewed attention due to maturing in the perception of the mechanism for solution growth of nanocrystalline, simple or composite materials. Reviews can be found regarding the earlier progress in the field [236] and the initial impetus for such studies [237].

Kitaev and co-workers [238, 239] and Chopra and co-workers [240–242] have illustrated the basic method for deposition of metal chalcogenides by the "homogeneous" precipitation method[1] and discussed the thermodynamic (equilibrium) principles of the process. Alkaline solutions containing chalcogen precursors (e.g., thiourea, or selenosulfate) and the corresponding complexed metal salts were used for the production of thin film sulfides and selenides. It was demonstrated that growth of thin films with thicknesses up to $\sim 1$ $\mu m$ can be attained with this technique [243]. In general, the precipitation process was considered to involve nucleation of molecule clusters undergoing rapid dissociation to form particles/colloids of the new phase, which then coalesced on a substrate. Subsequent works underscored a mechanism involving heterogeneous nucleation and growth directly on the substrate, rather than a net dissociation/precipitation route.

To be specific, let us consider the global reaction between dissolved cadmium ions and thiourea molecules in ammonia solutions, which can be represented as

$$[Cd(NH_3)_4]^{2+} + SC(NH_2)_2 + 2OH^- \rightarrow CdS + CN_2H_2 + 4NH_3 + 2H_2O$$
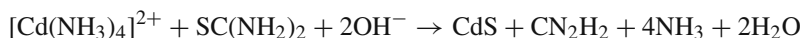
The commonly accepted underlying mechanism involves decomposition (hydrolysis) of thiourea in the alkaline solution to form sulfide ions (3.10), which react with $Cd^{2+}$ ions released by the decomplexation reaction (3.11), with precipitation of cadmium sulfide (3.12) upon exceeding the solubility product of the compound $(= 10^{-25})$:

$$SC(NH_2)_2 + 2OH^- \rightarrow S^- + CN_2H_2 + 2H_2O \qquad (3.10)$$

$$[Cd(NH_3)_4]^{2+} \rightarrow Cd^{2+} + 4NH_3 \qquad (3.11)$$

$$Cd^{2+} + S^{2-} \rightarrow CdS(s) \qquad (3.12)$$

The aqueous decomposition of thiourea to sulfide and cyanamide has been found to be catalyzed by metal hydroxide species and colloidal metal hydroxide precipitates. Kitaev suggested that $Cd(OH)_2$ is actually required for CdS film formation to occur by adsorption of thiourea on the metal hydroxide particles, followed by decomposition of the $Cd(OH)_2$–thiourea complex to CdS. Kaur et al. [241] found

---

[1]The term "homogeneous precipitation" may be misleading. It refers to the method of generating the chalcogenide by reagent decomposition and nucleation in solution as opposed to the "non-homogeneous" method of adding chalcogenide directly to solution as a salt.

solution conditions under which CdS films were formed in the absence of $Cd(OH)_2$ precipitate, albeit these films were much less adherent to the substrate compared to those formed in the presence of hydroxide. In fact, it was concluded already in the early works that the morphology and kinetics of film formation are controlled by the presence or absence of a $Cd(OH)_2$ precipitate in solution or a $Cd(OH)_2$ layer on the substrate surface. The presence of this layer correlated well with the formation of the best quality CdS film.

The role of the distribution of species in solution in determining the CdS film composition and structure was studied by Rieke and Bentjen [244], who performed equilibrium analysis of the cadmium–amine–hydroxide system to predict the speciation in solution. The focus was on the formation of $Cd(OH)_2$ and $Cd(NH_3)^{2+}$ species due to their importance in film growth. It was concluded that for deposition of high-quality, adherent, phase-pure CdS films, a surface catalytically active toward thiourea decomposition is desirable. The $Cd(OH)_2$ film was thought to be responsible for this effect.

Lincot and Ortega-Borges [245] used combined in situ quartz crystal microbalance and electrochemical impedance techniques to study the CBD of CdS in ammonia–thiourea solutions. They observed that a compact, adherent, and homogeneous CdS layer is formed initially by growth, which at longer reaction times transforms abruptly to a porous layer containing large amounts of trapped electrolyte. A possible structure of the duplex layer formed after the transition point is given schematically in Fig. 3.15.

The obtained CdS films were low-doped ($10^{15}$–$10^{16}$ cm$^{-3}$) n-type, thereby fully depleted during the formation process so that their thickness could be monitored in a precise fashion. Three main phases were identified during growth: the induction/coalescence range; the compact layer growth range; and the porous layer growth range. On account of the experimental results, the authors derived a simple columnar growth model describing the film coalescence range, by which they determined the density of nucleation centers for the given process. In a subsequent work [246], an ion-by-ion growth mechanism was proposed in order to interpret quantitatively the experimental results. The formation of CdS was assumed to result



**Fig. 3.15** Representation of the structure of the CdS film. It is suggested that the compact inner layer is deposited by an ion-by-ion mechanism while the porous outer layer is due to a cluster growth. (Reproduced with permission from [245], Copyright 2009, The Electrochemical Society)
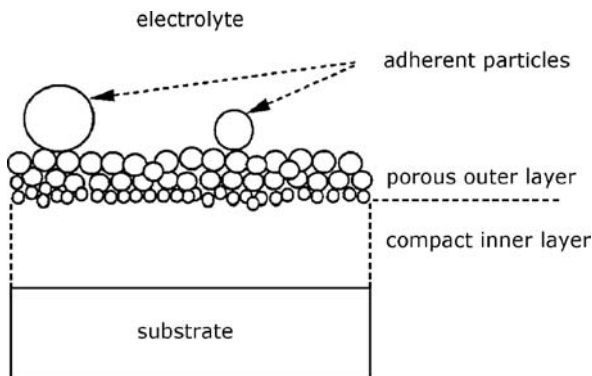
from consecutive surface adsorption/reaction steps comprising decomposition of adsorbed thiourea molecules and the formation of a surface intermediate complex with cadmium hydroxide, as follows:

Reversible adsorption of cadmium hydroxide species:

$$[Cd(NH_3)_4]^{2+} + 2OH^- + Site \rightleftarrows Cd(OH)_{2\ ads} + 4NH_3$$

Formation of a surface complex with thiourea:

$$Cd(OH)_{2\ ads} + S = C(NH_2)_2 \rightarrow [(Cd(S = C(NH_2)_2)(OH)_2]^*_{ads}$$
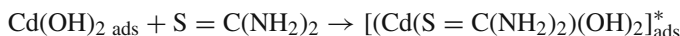
Formation of CdS with site regeneration:

$$[(Cd(S = C(NH_2)_2)(OH)_2]^*_{ads} \rightarrow CdS + CN_2H_2 + 2H_2O + Site$$
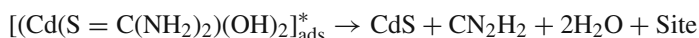
Thus, it was established that adsorption of metal hydroxide species on the surface of the substrate provides a nucleation layer which is chemically converted to the metal chalcogenide. The forming metal chalcogenide layer acts then as a catalytic surface for subsequent anion and cation adsorption.

It is well documented presently that chemical deposition processes occur either by an *ion-by-ion (atom-by-atom) condensation* mechanism, consisting of successive metal and chalcogen ions adsorption on a growing crystal, leading to the growth of a thin film, or a *cluster (colloidal)* mechanism, whereby colloids of the metal chalcogenide formed in solution absorb on the substrate and coagulate to form the film. The actual route of the process, as determined by the competition between these two basic schemes, is a central issue in chemical deposition. Growth mode is highly dependent on solution conditions. The ion-by-ion condensation is promoted through (a) the use of appropriate metal complexing agents so that the availability of free metal ions is controlled through chemical equilibria and (b) the slow hydrolysis of the chalcogen precursor in the presence of hydroxo-ions in the solution. Ideally, the film growth is anticipated to occur only by the heterogeneous chemical reactions at the interface between the substrate and the solution, so that thin films with homogeneous structure and composition can be obtained. However, it is usually difficult to avoid unwanted side reactions in the bulk of the solution that make the product random structured and/or non-stoichiometric. To be sure, a clear understanding of how nucleation and crystal growth can be controlled and how these processes influence film microstructure and properties is of utmost importance.

The different growth modes discussed above have been exemplified also from structural studies. Froment and Lincot [247] used structural characterization methods, such as TEM and HRTEM, to determine the formation mechanisms and habits of chemically deposited CdS, ZnS, and CdSe thin film at the atomic level. These authors formulated reaction schemes for the different deposition mechanisms and considered that these should be distinguished to (a) "atom-by-atom" process, providing autoregulation in normal systems; (b) aggregation of colloids (precipitation);
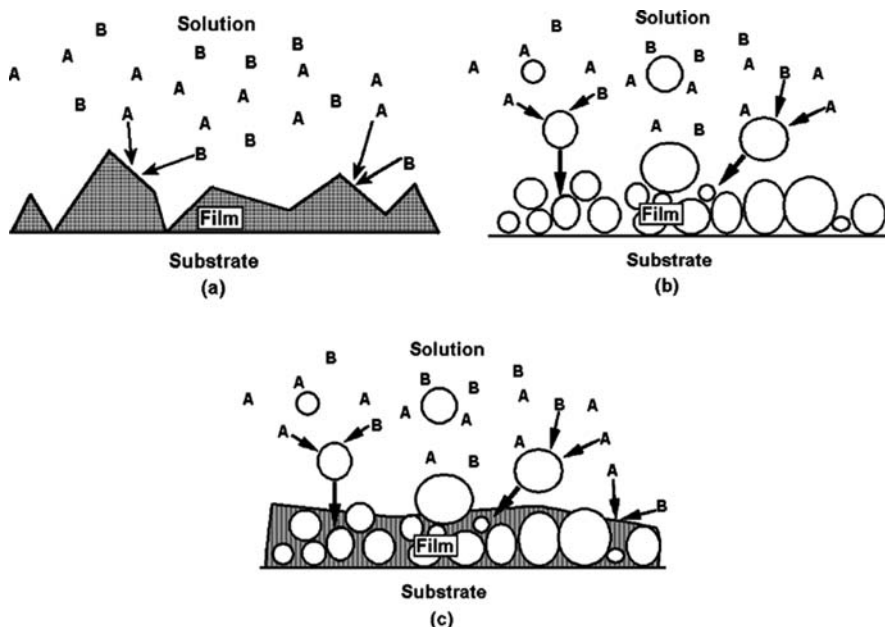
**Fig. 3.16** Reaction schemes of different CBD mechanisms for compound semiconductors: (**a**) atom-by-atom process; (**b**) aggregation of colloids; and (**c**) mixed process. (Reprinted from [247], Copyright 2009, with permission from Elsevier)

and (c) mixed process (Fig. 3.16). The atom-by-atom growth was observed in the case of CdS, leading to good-quality films at near room deposition temperature. Aggregation of colloids formed in the solution was observed for CdSe and ZnS deposition leading to particulate films, with smaller grain sizes.

Important results and a detailed insight into aqueous chemical deposition processes have been reported and discussed elsewhere for CdSe [248, 249] and ZnS [250, 251] target products. We should note also the work of Davies et al. [252] who described an alternative method for the chemical growth of metal sulfides and selenides on the basis of polysulfide or polyselenide solutions (containing hexa- and tetra-chalcogen anions) formed by the dissolution of sulfur or selenium in hydrazine monohydrate.

Epitaxial growth of CdS by CBD technique on $(\overline{111})$InP single-crystal substrate [253] and also on (111)GaP despite a large lattice mismatch (7%) in this case [254] has been demonstrated. It was emphasized that the capability to epitaxially grow a compound film on single-crystal substrate surfaces lends strong support to the model of ion-by-ion condensation. Anyhow, in searching novel ways to realize film growth only by the heterogeneous reactions at the film/solution interface evading any bulk precipitation, Nicolau et al. [255] developed a dual bath method which they called *successive ionic layer adsorption and reaction* (SILAR). By using this technique, CdS thin films were grown by repeating a sequential immersion of the substrate in solutions of Cd salt and $Na_2S$. Further, epitaxial growth of CdS and ZnS on GaAs substrate from aqueous solutions was achieved. The SILAR approach, based on

the successive adsorption of chalcogenide anions and metallic cations in separated baths, is also called "liquid-phase atomic layer epitaxy (LPALE)" analogously to the atomic layer epitaxy (ALE) in the vapor phase [256]. Of course, the mechanistic similarities with ECALE (Chap. 4) are obvious.

### 3.3.2 Electrodeposited CdTe Solar Cells

In 2002, about one-quarter of a century after the pioneering work of Panicker and Kröger on the successful electrodeposition of cadmium telluride and related compounds, CdTe was also the first material to open the age of large-scale industrial applications for semiconductor electroplating, as component of solar cells, underscoring thus the potential of electrodeposition-related technology to become a leading manufacturing process in thin film photovoltaics.

The optical properties of electrodeposited, polycrystalline CdTe have been found to be similar to those of single-crystal CdTe [257]. In 1982, Fulop et al. [258] reported the development of metal junction solar cells of high efficiency using thin film (4 $\mu$m) n-type CdTe as absorber, electrodeposited from a typical acidic aqueous solution on metallic substrate (Cu, steel, Ni) and annealed in air at 300 °C. The cells were constructed using a Schottky barrier rectifying junction at the front surface (vacuum-deposited Au, Ni) and a (electrodeposited) Cd ohmic contact at the back. Passivation of the top surface (treatment with KOH and hydrazine) was seen to improve the photovoltaic properties of the rectifying junction. The best fabricated cell comprised an efficiency of 8.6% (AM1), open-circuit voltage of 0.723 V, short-circuit current of 18.7 mA cm$^2$, and a fill factor of 0.64.

Cadmium telluride solar cells have been manufactured as heterojunctions, homojunctions, buried homojunctions, and metal–insulator–semiconductor (MIS) junctions. In the quest for an all-II–VI solar cell involving CdS as the n-type *window* material, p-CdTe has been an excellent choice for the heterojunction partner, as the band gaps of the two materials are well suited for solar applications. Functional n-CdS/p-CdTe junction devices have been prepared using a variety of preparation techniques; however, in all of the different ways in which heterojunctions involving p-CdTe either in single-crystal or polycrystalline form have been fabricated, three problems appeared to be dominant: recombination losses associated with the junction interface; difficulty in doping the p-CdTe; and the related difficulty in obtaining low-resistance contacts [259]. The work function of p-type CdTe (ca. 5.7 eV) is so high that no metal has a large enough work function to make an ideal ohmic contact. Efforts to make low-resistance contacts to p-type CdTe have involved using p-ZnTe, which has a sufficiently large work function for this purpose.

Aqueous cathodic electrodeposition has been shown to offer a low-cost route for the fabrication of large surface n-CdS/p-CdTe solar cells. In a typical procedure, CdTe films, 1–2 $\mu$m thick, are electrodeposited from common acidic tellurite bath over a thin window layer of a CdS-coated substrate under potential-controlled conditions. The as-deposited CdTe films are stoichiometric, exhibit strong preferential ⟨111⟩ orientation, and have n-type conductivity (doping density typically

**Fig. 3.17.** Structure of the 9.35%-efficient Basol solar cell, with open-circuit voltage 0.73 V, short-circuit current 20 mA cm$^2$, and fill factor 0.64. (Reproduced from [86])
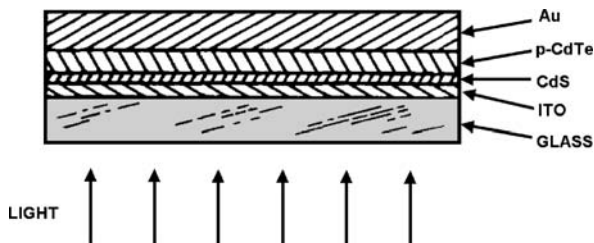


$10^{16}$ cm$^{-3}$). For solar cell fabrication, they are converted to p-type (doping density typically $10^{17}$ cm$^{-3}$) by heating in air at around 420 °C. The CdS sublayers are usually prepared by chemical bath deposition (but also electrodeposition) on (F or In-doped) SnO$_2$-coated glass and they are typically about 80 nm thick [260, 261, 85, 262]. Experimental data have shown that the structure of such cells is p–n rather than p–i–n. By careful design and processing, these cells exhibit efficiency of more than 10%. A cornerstone in this connection was the manufacture, in 1984, of an all-electroplated cell by Basol [86] (Fig. 3.17), with reported efficiency up to 9.35% (AM1.5). [Compare with the 1993 cell of Britt and Ferekides [263] employing chemical bath deposited CdS and close-spaced sublimation deposited p-CdTe, with an AM1.5 efficiency of 15.8%]. Importantly, such n-CdS/p-CdTe cells encapsulated in modules have been shown to provide a high level of confidence for the module reliability according to both outdoor and environmental testing [264].

The use of Hg$_{1-x}$Cd$_x$Te (MCT) alloys in place of p-CdTe in heterojunction solar cells has been proposed in order to partially overcome the high resistivity of p-CdTe. Solar cells using MCT films exhibit, on the average, better fill factors than those using CdTe. Further, the close lattice match and chemical compatibility of Hg$_{1-x}$Cd$_x$Te with CdTe makes the latter an ideal substrate for growth. A review of the pioneering work undertaken up to 1988 by Monosolar Inc. in developing electroplated CdTe and MCT thin film solar cells, especially the CdS/CdTe and CdS/MCT structures, has been given by Basol [87]. Cadmium-rich compositions of Hg$_{1-x}$Cd$_x$Te have been successfully utilized in making high-efficiency thin film solar cells; over 10% solar conversion efficiencies were reported for all-electrodeposited polycrystalline thin film MCT/n-CdS heterojunction cells [265].

Optimizing the properties of these heterojunctions for photovoltaic applications depends critically on a post-deposition heat treatment to improve the interface properties. The key step in obtaining solar cell grade p-type CdTe is the so-called "type conversion junction formation" (TCJF) process, which involves the heat treatment of the as-deposited n-type layers at around 400 °C. This procedure converts the n-type films into high-resistivity p-type and forms a rectifying junction with the underlying n-type window layer. Importantly, experimental evidence has indicated the beneficial effect of a CdS$_{1-x}$Te$_x$ alloy formed at the CdTe/CdS interface due
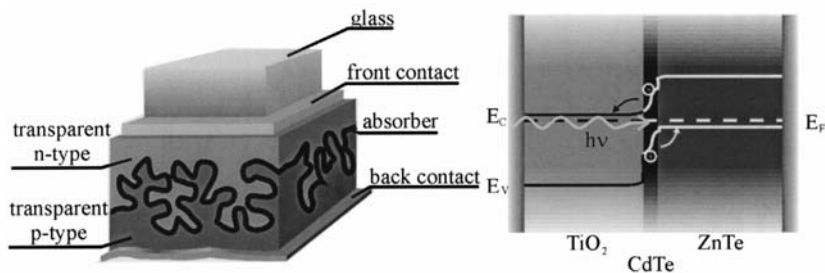
**Fig. 3.18** Schematic outline and ideal band diagram of an "extremely thin absorber" solar cell. The n-TiO$_2$ crystallites are clustered together to form a relatively open, network-like morphology, accommodating a thin layer of CdTe absorber, with p-ZnTe at the back contact. (Reprinted from [270], Copyright 2009, with permission from Elsevier)

to interdiffusion during fabrication. This interfacial layer reduces lattice mismatch-induced structural defects, resulting thus in a lower defect density in the critical region near the interface.

Peter and Wang [266] invented a channel flow cell for rapid growth of CdTe films; they showed that 2 $\mu$m films can be deposited in less than 20 min, as opposed to the 2–3 h normally required in the conventional stirred single batch cells. The as-deposited films were structurally more disordered than the conventional ones, but after annealing and type conversion they became suitable for fabrication of efficient solar cells. A test cell with an AM1.5 efficiency approaching 6% was fabricated using a film prepared in the channel cell.

Electrolyte contacts have been used to characterize as-deposited and annealed CdS/CdTe solar cell structures by photocurrent spectroscopy and electrolyte electroabsorbance/electroreflectance measurements (EEA/EER) [267–269].

Let us note finally that Ernst et al. [270] used electrodeposition to develop all-solid-state solar cells with extremely thin absorber (designated *eta* cells), having as basic components a 100–200 nm thick CdTe layer on n-type nanocrystalline TiO$_2$ substrate and a p-ZnTe layer on top forming an ohmic contact to CdTe (Fig. 3.18). The basic idea was that a highly structured substrate such as the nanocrystalline TiO$_2$ will allow the arrangement of the thin photoactive layer (CdTe) in a multiply folded way in order to allow sufficient absorption. The *eta* cell was prepared by sequential electrodeposition of CdTe and ZnTe from typical acidic aqueous solutions on the TiO$_2$ substrate. Growth from the liquid phase was considered advantageous, since conformal deposition with intimate electrical contact between the different layers could be attained.

# References

1. Hodes G (1995) Electrodeposition of II–VI semiconductors. In: Rubinstein I (ed.) Physical Electrochemistry: Principles, Methods, and Applications. Marcel Dekker, New York

2. Pandey RK, Sahu SN, Chandra S (1996) Handbook of semiconductor electrodeposition. Marcel Dekker, New York

3. Schlesinger TE (2000) Electrodeposition of Semiconductors. In: Schlesinger M, Paunovic M (eds) Modern Electroplating, 4th edn. Wiley, New York

4. Brenner A (1963) Electrodeposition of alloys – Principles and practice. Academic Press, New York

5. Kröger FA (1978) Cathodic deposition and characterization of metallic or semiconducting binary alloys or compounds. J Electrochem Soc 125: 2028–2034

6. Engelken RD, Van Doren TP (1985) Ionic electrodeposition of II–VI and III–V compounds. I. Development of a simple, Butler-Volmer equation-based kinetic model for $M_1X_1$ (CdTe) electrodeposition. J Electrochem Soc 132: 2904–2909

7. Engelken RD, Van Doren TP (1985) Ionic electrodeposition of II–VI and III–V compounds. II. Calculated current density and stoichiometry vs. deposition potential curves for parameter values representative of CdTe and with one partial current density diffusion limited. J Electrochem Soc 132: 2910–2919

8. Verbrugge MW, Tobias CW (1987) The periodic, electrochemical codeposition of cadmium and tellurium. AlChE J 33: 628–641

9. Verbrugge MW, Tobias CW (1985) A mathematical model for the periodic electrodeposition of multicomponent alloys. J Electrochem Soc 132: 1298–1307

10. Verbrugge MW, Tobias CW (1985) Triangular current-sweep chronopotentiometry at rotating disk and stationary, planar electrodes. J Electroanal Chem 196: 243–259

11. Riveros G, Lincot D, Guillemoles JF, Henríquez R, Schrebler R, Cordova R, Gómez H (2003) Redox and solution chemistry of the $SeSO_3{}^{2-}$–Zn–$EDTA^{2-}$ system and electrodeposition behavior of ZnSe from alkaline solutions. J Electroanal Chem 558: 9–17

12. Yochelis S, Hodes G (2004) Nanocrystalline CdSe formation by direct reaction between Cd ions and selenosulfate solution. Chem Mater 16: 2740–2744

13. Szabo JP, Cocivera M (1988) Mechanism of electrodeposition of cadmium selenide from $SeSO_3{}^{2-}$ solution. Can J Chem 66: 1065–1072

14. Skyllas-Kazacos M (1983) Electrodeposition of CdSe and CdSe + CdTe thin films from cyanide solutions. J Electroanal Chem 148: 233–239

15. Baranski AS, Fawcett WR (1980) The electrodeposition of metal chalcogenides. J Electrochem Soc 127: 766–767

16. Elwell D (1981) Electrocrystallization of semiconducting materials from molten salt and organic solutions. J Cryst Growth 52: 741–752

17. Welton T (1999) Room-temperature ionic liquids. Solvents for synthesis and catalysis. Chem Rev 99: 2071–2084

18. Visser AE, Swatloski RP, Reichert WM, Mayton R, Sheff S, Wierzbicki A, Davis JH, Rogers RD (2001) Task-specific ionic liquids for the extraction of metal ions from aqueous solutions. Chem Commun 1: 135–136

19. Porter LA, Choi HC, Ribbe AE, Buriak JM (2002) Controlled electroless deposition of noble metal nanoparticle films on Germanium surfaces. Nano Lett 2: 1067–1071

20. Morris GC, Vanderveen RJ (1993) Cadmium telluride films prepared by pulsed electrodeposition. Sol Energy Mater Sol Cells 30: 339–351

21. Babu SM, Dhanasekaran R, Ramasamy P (1991) Electrodeposition of CdTe by potentiostatic and periodic pulse techniques. Thin Solid Films 202: 67–75

22. Swaminathan V, Murali KR (2000) Influence of pulse reversal on the PEC performance of pulse-plated CdSe films. Sol Energy Mater Sol Cells 63: 207–216

23. Babu SM, Rajalakshmi T, Dhanasekaran R, Ramasamy P (1991) Electrodeposition of $CdSe_xTe_{1-x}$ by periodic pulse technique. J Cryst Growth 110: 423–428

24. Bouroushian M, Kosanovic T, Spyrellis N (2006) A pulse plating method for the electrosynthesis of ZnSe. J Appl Electrochem 36: 821–826

25. Park SM, Barber ME (1979) Thermodynamic stabilities of semiconductor electrodes. Electroanal Chem 99: 67–75

26. Savadogo O (1998) Chemically and electrochemically deposited thin films for solar energy materials. Sol Energy Mater Sol Cells 52: 361–388

27. Dremlyuzhenko SG, Voloshchuk AG, Zakharuk ZI, Yurijchuk IN (2008) Thermodynamic evaluation and potentiometric study of $Cd_{1-x}Mn_xTe$ and $Cd_{1-x}Zn_x$ Te dissolution in acid and alkaline solutions. Inorg Mater 44: 21–29

28. Chaparro AM (2005) Thermodynamic analysis of the deposition of zinc oxide and chalco-genides from aqueous solutions. Chem Mater 17: 4118–4124

29. Miller B, Heller A (1976) Semiconductor liquid junction solar cells based on anodic sulphide films. Nature 262: 680–681

30. Miller B, Menezes S, Heller A (1978) Anodic formation of semiconductive sulfide films at cadmium and bismuth: Rotating ring-disk electrode studies. J Electroanal Chem 94: 85–97

31. Peter LM (1978) The electrocrystallization of cadmium sulphide films on cadmium. Electrochim Acta 23: 165–174.

32. Peter LM (1978) The photoelectrochemical properties of anodic cadmium sulphide films. Electrochim Acta 23: 1073–1080

33. Ham D, Mishra KK, Rajeshwar K (1991) Anodic electrosynthesis of cadmium selenide thin films. Characterization and comparison with the passive/transpassive behavior of the CdX (X = S, Te) counterparts. J Electrochem Soc 138: 100–108; Stimming U (1985) Photoelectrochemical studies of passive films (Review Article). Electrochim Acta 31: 415–429

34. Da Silva Pereira MI, Peter LM (1982) Studies of two-dimensional electrocrystallization: The CdS/Cd(Hg) system. J Electroanal Chem 140: 103–120

35. Peter LM, Reid JD, Scharifker BR (1981) Electrochemical adsorption and phase formation on mercury in sulphide ion solutions. J Electroanal Chem 119: 73–91; Da Silva Pereira MI, Peter LM (1982) Photocurrent spectroscopy of semiconducting anodic films on mercury. J Electroanal Chem 131: 167–179

36. Bewick A, Fleischmann M, Thirsk HR (1962) Kinetics of the electrocrystallization of thin films of calomel. Trans Faraday Soc 58: 2200–2216

37. Mattsson G, Nyholm L, Peter LM (1993) Electrocrystallization, stripping and photoelec-trochemical properties of HgSe/Se films on mercury electrodes. J Electroanal Chem 347: 303–326

38. Birss VI, Wright GA (1982) The potentiodynamic formation and reduction of a silver sulfide monolayer on a silver electrode in aqueous sulfide solutions. Electrochim Acta 27: 1–7

39. Yeh LSR, Hudson PG, Damjanovic A (1982) Anodic formation of thin CdS films. I. Kinetics and mechanisms under galvanostatic and potentiodynamic conditions. J Appl Electrochem 12: 153–162

40. Damjanovic A, Yeh LSR, Hudson PG (1982) Anodic formation of thin CdS films. II. Dependence of the kinetics on $S^{2-}$ concentration. J Appl Electrochem 12: 343–349

41. McCann JF, Skyllas Kazacos M (1981) The Electrochemical deposition and formation of cadmium sulphide thin film electrodes in aqueous electrolytes. J Electroanal Chem 119: 409–412

42. Power GP, Peggs DR, Parker AJ (1981) The Cathodic formation of photoactive cadmium sulfide films from thiosulfate solutions. Electrochim Acta 26: 681–682

43. Dennison S (1993) Studies of the cathodic electrodeposition of CdS from aqueous solution. Electrochim Acta 38: 2395–2403

44. Fatás E, Duo R, Herrasti P, Arjona F, Garcia-Camarero E (1984) Electrochemical deposition of CdS thin films on Mo and Al substrates. J Electrochem Soc 131: 2243–2246

45. Yamaguchi K, Yoshida T, Sugiura T, Minoura H (1998) A novel approach for CdS thin-film deposition: Electrochemically induced atom-by-atom growth of CdS thin films from acidic chemical bath. J Phys Chem B 102: 9677–9686

46. Fatas E, Herrasti P, Arjona F, Garcia Camarero E (1987) Characterization of CdS thin films electrodeposited by an alternating current electrolysis method. J Electrochem Soc 134: 2799–2801

47. Nishino J, Chatani S, Uotani Y, Nosaka Y (1999) Electrodeposition method for controlled formation of CdS films from aqueous solutions. J Electroanal Chem 473: 217–222

48. Baranski AS, Fawcett WR, McDonald AC, Nobriga RM, McDonald JR (1981) The structural characterization of cadmium sulfide films grown by cathodic electrodeposition. J Electrochem Soc 129: 963–968

49. Baranski AS, Fawcett WR (1984) The mechanism of electrodeposition of cadmium sulfide on inert electrodes from diethylene glycol solutions. J Electrochem Soc 131: 2509–2514

50. Baranski AS, Fawcett WR, McDonald AC (1984) The mechanism of electrodeposition of cadmium sulphide on inert metals from dimethylsulphoxide solution. J Electroanal Chem 160: 271–287

51. Fatás E, Herrasti P, Arjona F, Garcia Camarero E, Medina JA (1987) Electrodeposition and characterization of CdS thin films on stainless steel and tin oxide substrates. Electrochim Acta 32: 139–148

52. Fatás E, Herrasti P (1988) Voltammetric study of the electrodeposition of CdS films from propylene carbonate solutions. Electrochim Acta 33: 959–965

53. Dale PJ, Samantilleke AP, Shivagan DD, Peter LM (2007) Synthesis of cadmium and zinc semiconductor compounds from an ionic liquid containing choline chloride and urea. Thin Solid Films 515: 5751–5754

54. Gruszecki T, Holmström B (1993) Preparation of thin films of polycrystalline CdSe for solar energy conversion I. A literature survey. Sol Energy Mater Sol Cells 31: 227–234

55. Patsauskas EI, Yanitskii IV, Saudargaite AI (1968) Proc. 10th Lithuanian conference on electrochemistry, Vilnius, p. 143 (English translation, U.S. Department of Commerce); also Gobrecht HV, Liess HD, Tausend A (1963), Ber Bunsenges Phys Chem 67: 930

56. Hodes G, Manassen J, Cahen D (1976) Photoelectrochemical energy conversion and storage using polycrystalline chalcogenide electrodes. Nature 261: 403–404

57. Skyllas-Kazacos M, Miller B (1980) Studies in selenous acid reduction and CdSe film deposition. J Electrochem Soc 127: 869–873

58. Bouroushian M, Kosanovic T, Loizos Z, Spyrellis N (2000) On a thermodynamic description of Se(IV) electroreduction and CdSe electrolytic formation on Ni, Ti and Pt cathodes in acidic aqueous solution. Electrochem Commun 2: 281–285

59. Loizos Z, Spyrellis N, Maurin G (1991) Electrochemical synthesis of semiconducting CdSe thin films. Thin Solid Films 204: 139–149

60. Bouroushian M, Charoud-Got J, Loizos Z, Spyrellis N (2000) A phase modification of CdSe electrodeposits induced by substrate roughness. J Mater Sci Lett 19: 2201–2203

61. Bouroushian M, Charoud-Got J, Loizos Z, Spyrellis N, Maurin G (2001) Structure and properties of CdSe and $CdSe_xTe_{1-x}$ electrolytic coatings on Ni and Ti cathodes. Influence of the acidic aqueous bath pH. Thin Solid Films 381: 39–47

62. Skyllas-Kazacos M, Miller B (1980) Electrodeposition of CdSe films from selenosulfate solution. J Electrochem Soc 127: 2378–2381

63. Cocivera M, Darkowski A, Love B (1984) Thin film CdSe electrodeposited from selenosulfite solution. J Electrochem Soc 131: 2514–2517

64. Szabo JP, Cocivera M (1986) Composition and performance of thin film CdSe electrodeposited from selenosulfite solution. J Electrochem Soc 133: 1247–1252

65. Kutzmutz St, Lang G, Heusler KE (2001) The electrodeposition of CdSe from alkaline electrolytes. Electrochim Acta 47: 955–965

66. Rastogi AC, Balakrishnan KS, Garg A (1993) A new electrochemical selenization technique for preparation of metal-selenide semiconductor thin films. J Electrochem Soc 140: 2373–2375

67. Baranski AS, Fawcett WR, Gatner K, Mc Donald AC, MacDonald JR, Selen M (1983) Structural and compositional characterization of mixed CdS-CdSe films grown by cathodic electrodeposition. J Electrochem Soc 130: 579–583

68. Sanders BW, Cocivera M (1987) Characterization of cadmium selenide electrodeposited from diethylene glycol solution containing tri-n-butylphosphine selenide. J Electrochem Soc 134: 1075–1080

69. Bouroushian M, Loizos Z, Spyrellis N, Maurin G (1997) Hexagonal cadmium chalcogenide thin films prepared by electrodeposition from near-boiling aqueous solutions. Appl Surf Sci 115: 103–110

70. Pawar SM, Moholkar AV, Shinde PS, Rajpure KY, Bhosale CH (2007) Room temperature electro-crystallization of CdSe thin films from ethylene glycol bath. J Alloy Compd 459: 515–520

71. Tomkiewicz M, Ling I, Parsons WS (1982) Morphology, properties, and performance of electrodeposited n-CdSe in liquid junction solar cells. J Electrochem Soc 129: 2016–2022

72. Kressin AM, Doan VV, Klein JD, Sailor MJ (1991) Synthesis of stoichiometric cadmium selenide films via sequential monolayer electrodeposition. Chem Mater 3: 1015–1020

73. Miller B, Heller A, Robbins M, Menezes S, Chang KC, Thomson JJ (1977) Solar conversion efficiency of pressure sintered cadmium selenide liquid junction cells. J. Electrochem Soc 124: 1019–1021.

74. Panicker MPR, Knaster M, Kröger FA (1978) Cathodic deposition of CdTe from aqueous electrolytes. J Electrochem Soc 125: 566–572

75. Danaher WJ, Lyons LE (1978) Photoelectrochemical cell with cadmium telluride film. Nature 271: 139–139

76. Lyons LE, Morris GC, Horton DH, Keyes JG (1984) Cathodically electrodeposited films of cadmium telluride. J Electroanal Chem 168: 101–116

77. Bhattacharya RN, Rajeshwar K (1984) Electrodeposition of CdTe thin films. J Electrochem Soc 131: 2032–2037

78. Takahashi M, Uosaki K, Kita H (1984) Composition and electronic properties of electro-chemically deposited CdTe films. J Appl Phys 55: 3879–3881

79. Mori E, Rajeshwar K (1989) The kinetics of electrocrystallization of tellurium and cadmium telluride at the glassy carbon surface. J Electroanal Chem 258: 415–429

80. Cowache P, Lincot D, Vedel J (1989) Cathodic codeposition of cadmium telluride on conducting glass. J Electrochem Soc 136: 1646–1650

81. Chen JH, Wan CC (1994) Dependence of the composition of CdTe semiconductor on conditions of electrodeposition. J. Electroanal. Chem 365: 87–95

82. Voloshchuk AG, Tsipishchuk NI (2002) Equilibrium potential–pH diagram of the CdTe–$H_2O$ system. Inorg Mater 38: 1114–1116

83. Sella C, Boncorps P, Vedel J (1986) The electrodeposition mechanism of CdTe from acidic aqueous solutions. J Electrochem Soc 133: 2043–2047

84. Saraby-Reintjes A, Peter LM, Özsan ME, Dennison S, Webster S (1993) On the mechanism of the cathodic electrodeposition of cadmium telluride. J Electrochem Soc 140: 2880–2888

85. Kampmann A, Cowache P, Vedel J, Lincot D (1995) Investigation of the influence of the electrodeposition potential on the optical, photoelectrochemical and structural properties of as-deposited CdTe. J Electroanal Chem 387: 53–64

86. Basol BM (1984) High-efficiency electroplated heterojunction solar cell. J Appl Phys 55: 601–603

87. Basol BB (1988) Electrodeposited CdTe and HgCdTe solar Cells. Sol Cells 23: 69–88

88. Bhattacharya RN, Rajeshwar K, Noufi RN (1985) In situ preparation of p-Type CdTe thin films by cathodic electrodeposition. J Electrochem Soc 132: 732–734

89. Llabres J (1984) In situ preparation of undoped p-Type CdTe by cathodic electrochemical deposition. J Electrochem Soc 131: 464–465

90. Mishra KK, Rajeshwar K (1989) A re-examination of the mechanisms of electrodeposition of CdX and ZnX (X = Se, Te) semiconductors by the cyclic photovoltammetric technique J Electroanal Chem 273: 169–182

91. Verbrugge MW, Tobias CW (1987) Some experimental aspects of the cadmium-tellurium electrochemical codeposition process. J Electrochem Soc 134: 3104–3109

92. Sugimoto Y, Peter LM (1995) Photoeffects during cathodic electrodeposition of CdTe. J Electroanal Chem 386: 183–188

93. Murase K, Uchida H, Hirato T, Awakura YJ (1999) Electrodeposition of CdTe films from ammoniacal alkaline aqueous solution at low cathodic overpotentials. J Electrochem Soc 146: 531–536

94. Darkowski A, Cocivera M (1985) Electrodeposition of cadmium telluride using phosphine telluride. J Electrochem Soc 132: 2768–2771

95. Rastogi AC, Balakrishnan KS (1989) Monocrystalline CdTe thin films by electrochemical deposition from aprotic electrolytes. J Electrochem Soc 136: 1502–1506

96. Bhattacharya RN, Rajeshwar K, Noufi RN (1984) Electroless deposition of CdTe thin films. J Electrochem Soc 131: 939–942

97. Gerritsen HJ (1984) Electrochemical deposition of photosensitive CdTe and ZnTe on tellurium. J Electrochem Soc 131: 136–140

98. Ham D, Mishra KK, Weiss A, Rajeshwar K (1989) Anodic electrosynthesis of CdTe thin films. Chem Mater 1: 619–625

99. Lokhande CD, Yermune VS, Pawar SH (1988) Electrodepositions of CdS, ZnS and Cd$_{1-x}$Zn$_x$S films. Mater Chem Phys 20: 283–292

100. Sanders BW, Kitai AH (1990) The electrodeposition of thin film zinc sulphide from thiosulphate solution. J Cryst Growth 100: 405–410

101. Lokhande CD, Jadhav MS, Pawar SH (1989) Electrodeposition of ZnS films from an alkaline bath. J Electrochem Soc 136: 2756–2757

102. Kashyout AB, Aricò AS, Monforte G, Crea F, Antonucci V, Giordano N (1995) Electrochemical deposition of ZnFeS thin film semiconductors on tin oxide substrates. Sol Energy Mater Sol Cells 37: 43–53

103. Natarajan C, Sharon M, Lévy-Clément C, Neumann-Spallart M (1994) Electrodeposition of zinc selenide. Thin Solid Films 237: 118–123

104. Riveros G, Gómez H, Henríquez R, Schrebler R, Marotti RE, Dalchiele EA (2001) Electrodeposition and characterization of ZnSe semiconductor thin films. Sol Energy Mater Sol Cells 70: 255–268

105. Bouroushian M, Kosanovic T, Loizos Z, Spyrellis N (2002) Electrochemical formation of ZnSe from acidic aqueous solutions. J Solid State Electrochem 6: 272–278

106. Bouroushian M, Kosanovic T, Spyrellis N (2005) Aspects of ZnSe electrosynthesis from selenite and selenosulfate aqueous solutions. J Solid State Electrochem 9: 55–60

107. Kowalik R, Zabinski P, Fitzner K (2008) Electrodeposition of ZnSe. Electrochim Acta 53: 6184–6190

108. Kosanovic T, Bouroushian M, Spyrellis N (2005) Soft growth of the ZnSe compound from alkaline selenosulfate solutions. Mater Chem Phys 90: 148–154

109. Cuomo JJ, Gambino RJ (1968) The synthesis and epitaxial growth of GaP by fused salt electrolysis. J Electrochem Soc 115: 755–759

110. Yamamoto A, Yamaguchi M (1975) Epitaxial growth of ZnSe on Ge by fused salt electrolysis. Japan J Appl Phys 14: 561–562

111. Sanchez S, Lucas C, Picard GS, Bermejo MR, Castrillejo Y (2000) Molten salt route for ZnSe high-temperature electrosynthesis. Thin Solid Films 361–362: 107–112

112. Basol BM, Kapur VK (1988) Preparation of ZnTe thin films using a simple two-stage process. Thin Solid Films 165: 237–241

113. Neumann-Spallart M, Königstein C (1995) Electrodeposition of zinc telluride. Thin Solid Films 265: 33–39

114. Ishizaki T, Ohtomo T, Fuwa A (2004) Electrodeposition of ZnTe film with high current efficiency at low overpotential from a citric acid bath. J Electrochem Soc 151: C161–C167

115. Ishizaki T, Saito N, Takai O, Asakura S, Goto K, Fuwa A (2005) An investigation into the effect of ionic species on the formation of ZnTe from a citric acid electrolyte. Electrochim Acta 50: 3509–3516

116. Königstein C, Neumann-Spallart M (1998) Mechanistic studies on the electrodeposition of zinc telluride. J Electrochem Soc 145: 337–343

117. Bouroushian M, Kosanovic T, Karoussos D, Spyrellis N (2009) Electrodeposition of poly-crystalline ZnTe from simple and citrate-complexed acidic aqueous solutions. Electrochim Acta 54: 2522–2528

118. Kuroda K, Kobayashi T, Sakamoto T, Ichino R, Okido M (2005) Formation of ZnTe compounds by using the electrochemical ion exchange reaction in molten chloride. Thin Solid Films 478: 223–227

119. Mattsson G, Nyholm L, Olin A (1994) Cathodic stripping voltammetry of HgSe. J Electroanal Chem 377: 149–162

120. Hankare PP, Bhuse VM, Garadkar KM, Jadhav AD (2001) A novel method to grow polycrystalline HgSe thin film. Mater Chem Phys 71: 53–57

121. Loutfy RO, Ng DS (1984) Electrodeposited polycrystalline thin films of cadmium chalcogenides for backwall photoelectrochemical cells. Sol Energy Mater 11: 319–328

122. Gonzáles-Velasco J, Rodriguez I (1990) Photoelectrochemical behaviour of $S_xSe_yCd$ electrodes obtained by electrodeposition from aqueous solutions. Sol Energy Mater 20: 167–180

123. Mahapatra PK, Roy CB (1984) Photoelectrochemical cells with mixed polycrystalline n-Type CdS-PbS and CdS-CdSe electrodes. Electrochim Acta 29: 1435–1438

124. Ueno Y, Minoura H, Nishikawa T, Tsuiki M (1983) Electrophoretically deposited CdS and CdSe anodes for photoelectrochemical cells. J Electrochem Soc 130: 43–47

125. Darkowski A, Grabowski A (1991) Electrodeposition of Cd-Zn-Se thin films from seleno-sulphite solutions. Sol Energy Mater 23: 75–82

126. Natarajan C, Nogami G, Sharon M (1995) Electrodeposition of $Zn_{1-x}Cd_xSe$ (x = 0–1) thin films. Thin Solid Films 261: 44–51

127. Bouroushian M, Kosanovic T (2006) Electrochemical formation and composition analysis of $Zn_xCd_{1-x}Se$ solid solutions. J Solid State Electrochem 10: 223–229

128. Bouroushian M, Kosanovic T, Xu HY, Papadimitriou D (2005) Structural and optical investigation of electrosynthesized $Zn_xCd_{1-x}Se$ thin films. J Phys D: Appl Phys 38: 1–6

129. Gal D, Hodes G (2000) Electrochemical deposition of ZnSe and (Zn,Cd)Se films from nonaqueous solutions. J Electrochem Soc 147: 1825–1828

130. Morris GC, Vanderveen R (1992) Electrodeposited cadmium zinc sulphide films for solar cells. Sol Energy Mater Sol Cells 26: 217–228

131. Hodes G, Manassen J, Neagu S, Cahen D, Mirovski Y (1982) Electroplated cadmium chalcogenide layers: Characterization and use in photoelectrochemical solar cells. Thin Solid Films 90: 433–438

132. Mirovsky Y, Tenne R, Hodes G, Cahen D (1982) Photoelectrochemical solar cells: Interpretation of cell performance using electrochemical determination of photoelectrode properties. Thin Solid Films 91: 349–355

133. Loizos Z, Spyrellis N, Maurin G, Pottier D (1989) Semiconducting $CdSe_xTe_{1-x}$ thin films prepared by electrodeposition. J Electroanal Chem 269: 399–410

134. Abramovich M, Brasil MJP, Decker F, Moro JR, Motisuke P, Müller-St N, Salvador P (1985) Crystal structure, luminescence, and photoelectrochemistry of thin electroplated Cd-chalcogenide layers. J Solid State Chem 59: 1–8

135. Rosamilia JM, Miller B (1986) Cathodic generation of $CdSe_xTe_{1-x}$ at Te film electrodes. J Electroanal Chem 215: 249–260

136. Bhattacharya RN (1986) Electrodeposited $CdSe_{0.5}Te_{0.5}$: Photoelectrochemical solar cells. J Appl Electrochem 16: 168–174

137. Bouroushian M, Loizos Z, Spyrellis N, Maurin G (1993) Influence of heat treatment on structure and properties of electrodeposited CdSe or Cd(Se,Te) semiconducting coatings. Thin Solid Films 229: 101–106

138. Sakashita M, Löchel B, Strehblow HH (1982) An examination of the electrode reactions of Te, HgTe and $Cd_{0.2}Hg_{0.8}Te$ with rotating-split-ring-disc electrodes. J Electroanal Chem 140: 75–89

139. Sakashita M, Strehblow HH, Bettini M (1982) Anodic oxide films and electrochemical reactions on $Cd_{0.2}Hg_{0.8}Te$. J Electrochem Soc 129: 1710–1716

140. Neumann-Spallart M, Tamizhmani G, Boutry-Forveille A, Levy-Clement C (1989) Physical properties of electrochemically deposited cadmium mercury telluride films. Thin Solid Films 169: 315–322

141. Neumann-Spallart M, Tamizhmani G, Levy-Clement C (1990) Photoelectrochemical properties of semiconducting cadmium mercury telluride thin films with bandgaps between 1.47 and 1.08 eV. J Electrochem Soc 137: 3434–3437

142. Mori E, Mishra KK, Rajeshwar K (1990) A voltammetric study of compound formation in the Hg-Cd-Te system. J Electrochem Soc 137: 1100–1106

143. Colyer CL, Cocivera M (1992) Thin-film cadmium mercury telluride prepared by nonaqueous electrodeposition. J Electrochem Soc 139: 406–409

144. Natarajan C, Sharon M, Lévy-Clément C, Neumann-Spallart M (1995) Electrochemical deposition of n-zinc mercury selenide thin films. Thin Solid Films 257: 46–53

145. Weiss G (1946) Ann Chim 1: 446.

146. Schneemeyer LF, Cohen U (1983) Electrochemical synthesis of photoactive $MoS_2$. J Electrochem Soc 130: 1536–1539

147. Chandra S, Sahu SNJ (1984) Electrodeposited semiconducting molybdenum selenide films. I. Preparatory technique and structural characterization. J Phys D: Appl Phys 17: 2115–2123

148. Dukstiene N, Kazancev K, Prosicevas I, Guobiene A (2004) Electrodeposition of Mo-Se thin films from a sulfamatic electrolyte. J Solid State Electrochem 8: 330–336

149. Ponomarev EA, Neumann-Spallart M, Hodes G, Levy-Clement C (1996) Electrochemical deposition of $MoS_2$ thin films by reduction of tetrathiomolybdate. Thin Solid Films 280: 86–89

150. Miki Y, Nakazato D, Ikuta H, Uchida T, Wakihara M (1995) Amorphous $MoS_2$ as the cathode of lithium secondary batteries. J Power Sources 54: 508–510

151. Yufit V, Nathan M, Golodnitsky D, Peled E (2003) Thin-film lithium and lithium-ion batteries with electrochemically deposited molybdenum oxysulfide cathodes. J Power Sources 122: 169–173

152. Bhattacharya RN, Lee CY, Pollak FH, Schleich DM (1987) Optical study of amorphous $MoS_3$: Determination of the fundamental energy gap. J Non-Cryst Solids 91: 235–242

153. Laperriere G, Marsan B, Belanger D (1989) Preparation and characterization of electrodeposited amorphous molybdenum sulfide. Synth Metals 29: F201–F206

154. Belanger D, Laperriere G, Marsan B (1993) The electrodeposition of amorphous molybdenum sulfide. J Electroanal Chem 347: 165–183

155. Devadasan JJ, Sanjeeviraja C, Jayachandran M (2001) Electrodeposition of p-$WS_2$ thin film and characterisation. J Cryst Growth 226: 67–72

156. Massaccesi S, Sanchez S, Vedel J (1993) Cathodic deposition of copper selenide films on tin oxide in sulfate solutions. J Electrochem Soc 140: 2540–2546

157. Yang YJ, He LY (2005) Novel electroless deposition of $Cu_3Se_2$ film on silicon substrate by a simple galvanic displacement process. Russ J Electrochem 41: 1241–1243

158. Yang YJ, Hu S (2009) Galvanic synthesis of copper selenides $Cu_{2-x}Se$ and CuSe in alkaline sodium selenosulfate aqueous solution. J Solid State Electrochem (2009) 13: 477–483

159. Vedel J, Cowache P, Soubeyrand M (1984) Electroplating of $Cu_xS$ on CdS. Sol Energy Mater 10: 25–34

160. Al-Dhafiri AM, Pande PC, Russell GJ, Woods J (1988) Electroplated $Cu_xS$-CdS Photovoltaic Cells. J Cryst Growth 86: 900–905

161. Al-Dhafiri AM, Russell GJ, Woods J (1991) Electrochemical control of the $Cu_xS$ phase in $Cu_xS$-CdS photovoltaic cells. Semicond Sci Technol 6: 983–988

162. Birss VI, Wright GA (1981) The kinetics of the anodic formation and reduction of phase silver sulfide films on silver in aqueous sulfide solutions. Electrochim Acta 26: 1809–1817

163. Petrov GV, Belen'kii AM (2005) Interactions in the silver selenide-water system. Russ J Appl Chem 78: 53–56

164. Traore M, Moddo R, Vittori O (1988) Electrochemical behaviour of tellurium and silver telluride at rotating glassy carbon electrode. Electrochim Acta 33: 991–996

165. Herrero J, Ortega J (1987) Electrochemical synthesis of photoactive $In_2Se_3$ thin films. Sol Energy Mater 16: 477–485

166. Wynands H, Cocivera M (1988) Photoelectrodeposition of $In_2Te_3$ using nonaqueous tri-n-butyl phosphine telluride. Sol Energy Mater 17: 185–199

167. Chu TL, Chu SS, Lin SC, Yue J (1984) Large grain copper indium diselenide films. J Electrochem Soc 131: 2182–2185

168. Bhattacharya RN (1983) Solution growth and electrodeposited $CuInSe_2$ thin films. J Electrochem Soc 130: 2040–2042

169. Singh RP, Singh SL, Chandra S (1986) Electrodeposited semiconducting $CuInSe_2$ films. I. Preparation, structural and electrical characterisation. J Phys D: Appl Phys 19: 1299–1309

170. Lokhande CD (1987) Pulse plated electrodeposition of $CuInSe_2$ films. J Electrochem Soc 134: 1727–1729

171. Khare N, Razzini G, Peraldo Bicelli L (1990) Electrodeposition and heat treatment of $CuInSe_2$ films. Thin Solid Films 186: 113–128

172. Ueno Y, Kawai H, Sugiura T, Minoura H (1988) Electrodeposition of $CuInSe_2$ films from a sulphate bath. Thin Solid Films 157: 159–168

173. Mishra KK, Rajeshwar K (1989) A voltammetric study of the electrodeposition chemistry in the Cu + In + Se system. J Electroanal Chem 271: 279–294

174. Guillén C, Galiano E, Herrero J (1991) Cathodic electrodeposition of $CuInSe_2$ Thin Films. Thin Solid Films 195: 137–146

175. Pottier D, Maurin G (1987) Preparation of polycrystalline thin films of $CuInSe_2$ by electrodeposition. J Appl Electrochem 19: 361–367

176. Gomez H, Schrebler R, Cordova R, Ugarte R, Dalchielle EA (1995) Nucleation and growth of $CuInSe_2$ on a glassy carbon electrode. Electrochim Acta 40: 267–269

177. Huang CJ, Meen TH, Lai MY, Chen WR (2004) Formation of $CuInSe_2$ thin films on flexible substrates by electrodeposition (ED) technique. Sol Energy Mater Sol Cells 82: 553–565

178. Kois J, Volobujeva O, Bereznev S (2008) One-step electrochemical deposition of $CuInSe_2$ absorber layers. Phys Status Solidi C 5: 3441–3444

179. Kois J, Bereznev S, Volobujeva O, Mellikov E (2007) Electrochemical etching of copper indium diselenide surface. Thin Solid Films 515: 5871–5875

180. Bhattacharya RN, Cahen D, Hodes G (1984) Electrodeposition of Cu-In-S layers and their photoelectrochemical characterization. Sol Energy Mater 10: 41–45

181. Nakamura S, Yamamoto A (1997) Preparation of $CuInS_2$ films with sufficient sulfur content and excellent morphology by one-step electrodeposition. Sol Energy Mater Sol Cells 49: 415–421

182. Nakamura S, Yamamoto A (2003) Electrodeposited $CuInS_2$-based thin-film solar cells. Sol Energy Mater Sol Cells 75: 81–86

183. Wijesundera RP, Siripala W (2004) Preparation of $CuInS_2$ thin films by electrodeposition and sulphurisation for applications in solar cells. Sol Energy Mater Sol Cells 81: 147–154

184. Schimmel MI, Tacconi NR, Rajeshwar K (1998) Anodic electrosynthesis of $Cu_2S$ and $CuInS_2$ films. J Electroanal Chem 453: 187–195

185. Bhattacharya RN, Rajeshwar K (1986) Electrodeposition of CuInX (X = Se, Te) thin films. Sol Cells 16: 237–243

186. Lokhande CD, Pawar SH (1987) Electrodeposition of $CuInTe_2$ films. J Phys D: Appl Phys 20: 1213–1214

187. Ishizaki T, Saito N, Fuwa A (2004) Electrodeposition of $CuInTe_2$ film from an acidic solution. Surf Coat Techn 182: 156–160

188. Sharma RK, Rastogi AC, Singh G (2004) Electrochemical growth and characterization of manganese telluride thin films. Mater Chem Phys 84: 46–51

189. Sharma RK, Singh G, Shul YG, Kim H (2007) Mechanism of manganese (mono and di) telluride thin-film formation and properties. Physica B 390: 314–319

190. Schwarz DE, Frenkel AI, Nuzzo RG, Rauchfuss TB, Vairavamurthy A (2004) Electro-synthesis of ReS$_4$. XAS Analysis of ReS$_2$, Re$_2$S$_7$, and ReS$_4$. Chem Mater 16: 151–158

191. Aricò AS, Antonucci V, Antonucci PL, Cocke DL, Giordano N (1991) A voltammetric study of the electrodeposition chemistry in the Fe–S system. Electrochim Acta 36: 581–590

192. Deshmukh SK, Kokate AV, Sathe DJ (2005) Studies on electrodeposited Cd$_{1-x}$Fe$_x$S thin films. Mater Sci Eng B 122: 206–210

193. Pawar SM, Moholkar AV, Suryavanshi UB, Rajpure KY, Bhosale CH (2007) Electrosynthesis and characterization of iron selenide thin films. Sol Energy Mater Sol Cells 91: 560–565

194. Engelken RD, McCloud HE, Lee C, Slayton M, Ghoreishi H (1987) Low temperature chemical precipitation and vapor deposition of Sn$_x$S thin films. J Electrochem Soc 134: 2696–2707

195. Mishra K, Rajeshwar K, Weiss A, Murley M, Engelken RD, Slayton M, McCloud HE (1989) Electrodeposition and characterization of SnS thin films J Electrochem Soc 136: 1915–1923

196. Brownson JRS, Georges C, Lévy-Clément C (2006) Synthesis of a δ-SnS polymorph by electrodeposition. Chem Mater 18:6397–6402; correction: (2007) Chem Mater 19: 3080

197. Brownson JRS, Georges C, Larramona G, Jacob A, Delatouche B, Lévy-Clément C (2008) Chemistry of tin monosulfide (δ-SnS) electrodeposition effects of pH and temperature with tartaric acid. J Electrochem Soc 155: D40–D46

198. Boonsalee S, Gudavarthy RV, Bohannan EW, Switzer JA (2008) Epitaxial electrodeposition of Tin(II) sulfide nanodisks on single-crystal Au(100). Chem Mater 20: 5737–5742

199. Engelken RD, Berry AK, Van Doren TP, Boone JL, Shahnazary A (1986) Electrodeposition and analysis of tin selenide films J Electrochem Soc 133: 581–585

200. Lukinskas A, Jasulaitiene V, Lukinskas P, Savickaja I, Kalinauskas P (2006) Electrochemical formation of nanometric layers of tin selenides on Ti surface. Electrochim Acta 51: 6171–6178

201. Robozerov VV, Zykov VA, Gavrikova TA (2000) Chemical etching of lead chalcogenides. Inorg Mater 36: 127–131

202. Scharifker B, Ferreira Z, Mozota J (1985) Electrodeposition of lead sulphide. Electrochim Acta 30: 677–682

203. Totland KM, Harrington DA (1989) Anodic phase formation on lead amalgam electrodes in sodium sulfide solution. J Electroanal Chem 274: 61–80

204. Takahashi M, Ohshima Y, Nagata K, Furuta S (1993) Electrodeposition of PbS films from acidic solution. J Electroanal Chem 359: 281–286

205. Sharon M, Ramaiah KS, Kumar M, Neumann-Spallart M, Levy-Clement C (1997) Electrodeposition of lead sulphide in acidic medium. J Electroanal Chem 436: 49–52

206. Saloniemi H, Ritala M, Leskelä M, Lappalainen R (1999) Cyclic electrodeposition of PbS thin films. J Electrochem Soc 146: 2522–2525

207. Yang YJ, He LY (2006) Dissolution of lead electrode and preparation of rod-shaped PbS crystals in a novel galvanic cell. J Solid State Electrochem 10: 430–433

208. Yang YJ, He LY (2005) A novel galvanic cell and its application in the preparation of lead sulfide nanomaterials. Electrochim Acta 50: 3581–3584

209. Molin AN, Dikusar AI (1995) Electrochemical deposition of PbSe thin films from aqueous solutions. Thin Solid Films 265: 3–9

210. Streltsov EA, Osipovich NP, Ivashkevich LS, Lyakhov AS, Sviridov VV (1998) Electrochemical deposition of PbSe Films. Electrochim Acta 43: 869–873

211. Streltsov EA, Osipovich NP, Ivashkevich LS, Lyakhov AS (1999) Effect of Cd(II) on electrodeposition of textured PbSe. Electrochim Acta 44: 2645–2652

212. Li KW, Meng XT, Liang X, Wang H, Yan H (2006) Electrodeposition and characterization of PbSe films on indium tin oxide glass substrates. J Solid State Electrochem 10: 48–53

213. Saloniemi H, Kanniainen T, Ritala M, Leskelä M (1998) Electrodeposition of PbTe thin films. Thin Solid Films 326: 78–82

214. Saloniemi H, Kemell M, Ritala M, Leskelä M (2000) PbTe electrodeposition studied by combined electrochemical quartz crystal microbalance and cyclic voltammetry. J Electroanal Chem 482: 139–148

215. Xiao F, Yoo B, Ryan MA, Lee KH, Myung NV (2006) Electrodeposition of PbTe thin films from acidic nitrate baths. Electrochim Acta 52: 1101–1107

216. Li X, Nandhakumar IS (2008) Direct electrodeposition of PbTe thin films on *n*-type silicon. Electrochem Commun 10: 363–366

217. Streltsov EA, Osipovich NP, Ivashkevich LS, Lyakhov AS (1998) Electrochemical deposition of PbSe$_{1-x}$Te$_x$ Films. Electrochim Acta 44: 407–413

218. Peter LM (1979) The photoelectrochemical properties of anodic Bi$_2$S$_3$ films. J Electroanal Chem 98: 49–58

219. Peter LM, Wright GA (1987) Electrochemical kinetics of bismuth sulphide formation on bismuth amalgam. Electrochim Acta 32: 1353–1356

220. Takahashi M, Oda Y, Ogino T, Furuta S (1993) Electrodeposition of Bi-Te alloy films. J Electrochem Soc 140: 2550–2553

221. Takahashi M, Muramatsu Y, Suzuki T, Sato S, Watanabe M, Wakita K, Uchida T (2003) Preparation of Bi$_2$Te$_3$ films by electrodeposition from solution containing bi-ethylenediaminetetraacetic acid complex and TeO$_2$. J Electrochem Soc 150: C169–C174

222. Miyazaki Y, Kajitani T (2001) Preparation of Bi$_2$Te$_3$ films by electrodeposition. J Cryst Growth 229: 542–546

223. Martin-Gonzales MS, Prieto AL, Gronsky R, Sands T, Stacy AM (2002) Insights into the electrodeposition of Bi$_2$Te$_3$. J Electrochem Soc 149: C546–C554

224. Tittes K, Bund A, Plieth W, Bentien A, Paschen S, Plöttner M, Gräfe H, Fischer WJ (2003) Electrochemical deposition of Bi$_2$Te$_3$ for thermoelectric microdevices. J Solid State Electrochem 7: 714–723

225. Torane AP, Lokhande CD, Patil PS, Bhosale CH (1998) Preparation and characterization of electrodeposited Bi$_2$Se$_3$ thin films. Mater Chem Phys 55: 51–54

226. Desai JD (1999) Galvanostatic electrodeposition of Bi$_2$Se$_3$ thin films. Bull Electrochem 15: 315–317

227. Michel S, Diliberto S, Boulanger C, Stein N, Lecuire JM (2005) Galvanostatic and potentiostatic deposition of bismuth telluride films from nitric acid solution: effect of chemical and electrochemical parameters. J Cryst Growth 277: 274–283

228. Michel S, Diliberto S, Stein N, Bolle B, Boulanger C (2008) Characterisation of electroplated Bi$_2$(Te$_{1-x}$Se$_x$)$_3$ alloys. J Solid State Electrochem 12: 95–101

229. Leimkühler G, Kerkamm I, Reineke-Koch R (2002) Electrodeposition of antimony telluride. J Electrochem Soc 149: C474–C478

230. Tittes K, Plieth W (2007) Electrochemical deposition of ternary and binary systems from an alkaline electrolyte—a demanding way for manufacturing p-doped bismuth and antimony tellurides for the use in thermoelectric elements. J Solid State Electrochem 11: 155–164

231. Wang CF, Wang Q, Chen LD, Xu XC, Yao Q (2006) Electrodeposition of Sb$_2$Te$_3$ films on Si(100) and Ag substrates. Electrochem Solid State Lett 9: C147–C149

232. Xiao F, Hangarter C, Yoo B, Rheem Y, Lee KH, Myung NV (2008) Recent progress in electrodeposition of thermoelectric thin films and nanostructures. Electrochim Acta 53: 8103–8117

233. Suryanarayanan R, Brun G (1976) A compact multi-source multi-substrate evaporator for thin film studies of rare earth sulphides. Thin Solid Films 35: 263–271

234. Mohite UK, Lokhande CD (1996) Electrosynthesis of yttrium chalcogenides from a non-aqueous bath. Appl Surf Sci 92: 151–154

235. Gaikwad NS, Bhosale CH (2002) Electrodeposition of EuSe thin films onto different substrates. Mater Chem Phys 76: 198–203

236. Lokhande CD (1991) Chemical deposition of metal chalcogenide thin films. Mater Chem Phys 27: 1–43

237. Gorer S, Hodes G (1994) Quantum size effects in the study of chemical solution deposition mechanisms of semiconductor films. J Phys Chem 98: 5338–5346
238. Fofanov GM, Kitaev GA (1969) Analysis of the conditions for the precipitation of metal selenides from aqueous solutions with sodium selenosulphate. Russ J Inorg Chem 14: 322–324
239. Kitaev GA, Terekhova TS (1970) Analysis of the conditions for the precipitation of cadmium selenide from aqueous sodium selenosulphate solutions. Russ J Inorg Chem 15: 25–27
240. Sharma NC Kainthla RC, Pandya DK, Chopra KL (1979) Electroless deposition of semiconductor films. Thin Solid Films 60: 55–59
241. Kaur I, Pandya DK, Chopra KL (1980) Growth kinetics and polymorphism of chemically deposited CdS films. J Electrochem Soc 127: 943–948
242. Kainthla RC, Pandya DK, Chopra KL (1982) Structural and optical properties of solution grown $CdSe_{1-x}S_x$ films. J Electrochem Soc 129: 99–102
243. Pavaskar NR, Menezes CA, Sinha APB (1977) Photoconductive CdS films by a chemical bath deposition process. J Electrochem Soc 124: 743–748
244. Rieke PC, Bentjen SB (1992) Deposition of cadmium sulfide films by decomposition of thiourea in basic solutions. Chem Mater 5: 43–53
245. Lincot D, Ortega-Borges R (1992) Chemical bath deposition of cadmium sulfide thin films. In situ growth and structural studies by Combined Quartz Crystal Microbalance and Electrochemical Impedance techniques. J Electrochem Soc 139: 1880–1889
246. Ortega-Borges R, Lincot D (1993) Mechanism of chemical bath deposition of cadmium sulfide thin films in the ammonia-thiourea system. J Electrochem Soc 140: 3464–3473
247. Froment M, Lincot D (1995) Phase formation processes in solution at the atomic level: Metal chalcogenide semiconductors. Electrochim Acta 40: 1293–1303
248. Hodes G, Albu-Yaron A, Decker F, Motisuke P (1987) Three-dimensional quantum-size effect in chemically deposited cadmium selenide films. Phys Rev B 36: 4215–4222
249. Cachet H, Esaaidi H, Froment M, Maurin G (1995) Chemical bath deposition of CdSe layers from Cd(II)-selenosulfite solutions. J Electroanal Chem 396: 175–182
250. Dona JM, Herrero J (1994) Process and film characterization of chemical-bath-deposited ZnS thin films. J Electrochem Soc 141: 205–210
251. Yamaguchi K, Yoshida T, Lincot D, Minoura H (2003) Mechanistic study of chemical deposition of ZnS thin films from aqueous solutions containing zinc acetate and thioacetamide by comparison with homogeneous precipitation. J Phys Chem B 107: 387–397
252. Davies DA, Vecht A, Silver J, Marsh PJ, Rose JA (2000) A novel method for the preparation of inorganic sulfides and selenides I. Binary materials and group II-VI phosphors. J Electrochem Soc 147: 765–771
253. Froment M, Bernard MC, Cortes R, Makili B, Lincot D (1995) Study of CdS epitaxial films chemically deposited from aqueous solutions on InP single crystals. J Electrochem Soc 142: 2642–2649
254. Lincot D, Mokili B, Cortes R, Froment M (1996) Heteroepitaxy of chemically deposited CdS on mismatched (111) GaP. Microsc Microanal Microstruct 7: 217–224
255. Nicolau YF, Dupuy M, Brunel M (1990) ZnS, CdS, and $Zn_{1-x}Cd_xS$ thin films deposited by the successive ionic layer adsorption and reaction process. J Electrochem Soc 137: 2915–2924
256. Lindroos S, Kanniainen T, Leskelä M (1994) Growth of ZnS thin films by liquid-phase atomic layer epitaxy (LPALE). Appl Surf Sci 75: 70–74
257. Mathew X, Sebastian PJ (1999) Optical properties of electrodeposited CdTe thin films. Sol Energy Mater Sol Cells 59: 85–98
258. Fulop G, Doty M, Meyers P, Betz J, Liu CH (1982) High-efficiency electrodeposited cadmium telluride solar cells. Appl Phys Lett 40: 327–328
259. Bube RH (2001) Cadmium sulfide and telluride. In Encyclopedia of Materials: Science and Technology, Elsevier Science Ltd. ISBN: 0-08-0431526, pp. 873–879

260. McGregor SM, Dharmadasa IM, Wadsworth I, Care CM (1996) Growth of CdS and CdTe by electrochemical technique for utilisation in thin film solar cells. Opt Mater 6: 75–81
261. Morris GC, Das SK (1992) Some fabrication procedures for electrodeposited CdTe solar cells. Int J Sol Energy 12: 95–108
262. Kampmann A, Cowache P, Mokili B, Lincot D, Vedel J (1995) Characterization of (111) cadmium telluride electrodeposited on cadmium sulphide. J Cryst Growth 146: 256–261
263. Britt J, Ferekides C (1993) Thin-film CdS/CdTe solar cell with 15.8% efficiency. Appl Phys Lett 62: 2851–2852
264. Barker J, Binns SP, Johnson DR, Marshall RJ, Oktik S, Ozsan ME, Patterson MN, Ransome SJ, Roberts S, Sadeghi M, Sherborne J, Turner AK, Woodcock JM (1992) Electrodeposited CdTe for thin film solar cells. Int J Sol Energy 12: 79–94
265. Basol BB, Tseng ES (1986) Mercury cadmium telluride solar cell with 10.6% efficiency. Appl Phys Lett 48: 946–948
266. Peter LM, Wang RL (1999) Channel flow cell electrodeposition of CdTe for solar cells. Electrochem Commun 1: 554–558
267. Duffy NW, Lane DW, Özsan ME, Peter LM, Rogers KD, Wang RL (2000) Structural and spectroscopic studies of CdS/CdTe heterojunction cells fabricated by electrodeposition. Thin Solid Films 361: 314–320
268. Duffy NW, Peter LM, Wang RL, Lane DW, Rogers KD (2000) Electrodeposition and characterisation of CdTe films for solar cell applications. Electrochim Acta 45: 3355–3365
269. Duffy NW, Peter LM, Wang RL (2002) Characterisation of CdS/CdTe heterojunctions by photocurrent spectroscopy and electrolyte electroreflectance/absorbance spectroscopy (EEA/EER). J Electroanal Chem 532: 207–214 (see also references therein).
270. Ernst K, Sieber I, Neumann-Spallart M, Lux-Steiner M-Ch, Könenkamp R (2000) Characterization of II–VI compounds on porous substrates Thin Solid Films 361–362: 213–217

# Chapter 4
# Electrochemical Preparations II (Non-conventional)

## 4.1 General

Besides the "conventional" depositions attained by the classical approach, and in addition to epitaxial development issues, products with unusual structures and functionalities mostly related to low-dimensionality phenomena are pursued by electrochemical preparation techniques, which along with purely chemical procedures taking place in low-temperature solutions, bring the advantageous features of soft growth methodology in material science and processing. The character of non-conventional preparations and structures that shall be demonstrated in this chapter is intimately connected to a presumed thorough control over growth, usually in the atomic level, whereby matter of special nature is produced. The major division of substances to be examined can be concisely described by the terms *nanomaterial* or *nanophase* and contextual variants. In fact, the relevant concepts have opened up wide prospects for electrochemistry in newly emerging technologies.

Solid/liquid interfaces provide fundamental advantages for the preparation of well-defined nanostructures with controlled dimensionality. During electrochemical growth, supersaturation can be precisely adjusted (unlike ultrahigh vacuum deposition processes where it is usually a fluctuating parameter) and reaction rates can be readily controlled through the applied potential or current. Importantly, electrochemical nucleation and growth can be performed near thermodynamic equilibrium (unlike most other techniques involving higher energies, e.g., thermal or laser), so that irreversible modifications during the preparation process are suppressed. This is quite relevant to nanotechnology since the properties of nanostructures are determined by their surface and interface atoms and a degradation of the surface by defects or passivation may result in completely different physical or chemical properties.

Electrochemistry provides routes to directly prepare nanostructures both delocalized in a random or organized way and localized at predefined surface sites with adjustable aspect ratios. Purity, monodispersity, ligation, and other chemical properties and treatments are definitely important in most cases. By delocalized electrodeposition it is possible to decorate large areas of metal or semiconductor surfaces with structures of a narrow size distribution; stable nuclei-clusters can be

formed consisting even of only one to a few atoms. In this case, the nucleation centers are randomly dispersed across the surface, following typically a stochastic distribution [1, 2]. On the other hand, patterned electrodeposition or use of sophisticated localization techniques, e.g., scanning probe microscope (SPM) tips as nanoelectrodes [3], have been shown to allow a solely electrochemical bottom-up growth of nanostructures under defined nucleation and growth conditions.

Under the assistance of electrochemistry, materials can be synthesized with various microstructures or existing microstructures can be modified in a chosen manner. Low-dimensional systems prepared at electrochemical interfaces include the so-called zero-dimensional (0D) clusters-dots[1] with diameters in the lower nanometer range (e.g., metal clusters on graphite or silicon surfaces) or "3D" particle aggregates of any form: 1D nanowires a few atomic distances in diameter and up to micrometer lengths; 2D epitaxial films (crystallographically expanded or condensed); adsorbate layers and self-assembled monolayers with structures depending on the substrate; colloid particles in liquid or other media. Growth of nanophase semiconductors/chalcogenides has been accomplished in microstructurally heterogeneous bulk form or in the form of quantum dots, wires, disks, or ribbons, free-standing or in foreign matrices (usually inorganic or organic templates). Deposition of hybrid structures consisting of the semiconductor and organic molecules (e.g., single-crystalline nanoporous ZnO with dye molecules incorporated) has also been demonstrated. Finally, formation of porous semiconductor films by electrochemical etching has long been considered.

The topics that will be discussed in the following sections are categorized, principally, with respect to the dimensionality and morphology of prepared materials. At the same time, special techniques or methodologies are emphasized where appropriate.

## 4.2 Epitaxial Films and Superstructures

Epitaxial growth, considered as the oriented overgrowth of a crystalline phase on the surface of a substrate that is also crystalline, is of great interest for a range of electro-optical, chemical, and catalytic applications due to the significance of interface chemistry in fixing the properties of relevant devices. For instance, in optoelectronic devices (other than cheap solar cells) it is required that the junction between an overlayer and the single-crystal substrate be of excellent quality, bearing an epitaxial relation. Such applications usually involve heteroepitaxial formation of semiconductor films, especially II–VI compounds, on single-crystal semiconductors (typically Si, Ge, or III–V compounds). Clearly, close lattice-matched systems are of great advantage, although various kinds of disparity between the epilayer and the substrate have to be taken into account, such as thermal mismatch due to a difference in thermal expansion coefficient and valence mismatch. Notwithstanding,

---

[1]Designated also as 3D clusters, depending on the number of atoms included, although there is no clear limit for the notation.

latest research shows that crystalline phases can be made to grow on substrates with a rather poor lattice match or even on amorphous substrates. Homoepitaxial growth is of concern also and single-crystal substrates are strongly required in a wide range of applications; those include for example CdTe and CdZnTe for far-infrared HgCdTe photodetectors and radiation detectors, and ZnSe and ZnTe for blue and green light emission (LED) and laser (LD) diodes, respectively.

Variants of vapor-phase deposition techniques, such as molecular beam, chemical beam, hot wall epitaxy, and metal organic chemical vapor deposition, have been utilized in the 300–500 °C temperature range, to grow epitaxial thin films and nanometer-scale artificial multilayers on solid single-crystal surfaces. Epitaxial deposition from liquid solutions at low temperatures can be accomplished by electrodeposition or by a process called liquid-phase epitaxy (LPE), whereby a saturated solution plates out a material on a particular solid substrate. Note that epitaxial effects can be promoted by choosing the appropriate substrate material for the intended deposition, as well as by carefully controlling the growth conditions. Also, a judicious selection of the cleavage face for a monocrystalline substrate electrode may prove essential for determining the properties of the growing phase and modeling the growth process. In chemical or electrochemical deposition studies it is very common to investigate or utilize for epitaxy the low-indexed faces of a substrate as these have the most ordered structures, therefore the lowest energy, and offer the smallest number of sites for adsorption (if adsorption of species is undesirable).

Well-defined structures including oxides and chalcogenides (such as CdS, CdSe, CdTe, ZnSe, ZnO, $PbO_2$, δ-$BiO_3$, $Cu_2O$, $Tl_2O_3$, PbS, PbSe, and $Fe_3O_4$) have been obtained by electrochemical epitaxy on faceted monocrystalline InP, Si, GaN, $TiO_2$, GaAs, or metallic (Au, Pt) substrates.

The single-step heteroepitaxial electrodeposition of chalcogenide semiconductors has been implemented principally by optimal use of generalized Kröger's concepts. For the most part, the related research regards deposition of II–VI semiconductors on III–V semiconductor substrates. Limitations in the one-step process with respect to growth control have been coped with by developing a multistep, cyclic electrodeposition technique called electrochemical atomic layer epitaxy (ECALE). More precise in nature, but more complex in execution, this method has been applied to obtain single-phase films or superlattices of II-VI, III–V, III–VI, IV–VI, and V–VI compounds. As comprising the current state of the art in terms of the dimensional control in the field of electrodeposition, ECALE will be presented comprehensively in a subsequent section. In addition to these main variants of electrochemical epitaxy, other multistep and hybrid techniques have been developed and will be introduced.

### 4.2.1  Single-Step Epitaxy on Semiconductor Substrates

An early attempt for ordered growth of a chalcogenide simple compound has been the cathodic deposition of thin (3 µm) CdTe films on n-type (100) GaAs single crystals from an acidic aqueous electrolyte at 95 °C, which contained Cd(II) and Te traces generated electrolytically in situ by using a pure Te anode [4]. The

produced CdTe film was specular and had predominantly (111) orientation; however, no epitaxy was found.

Electrochemical epitaxial growth of CdTe films in one step has been demonstrated for the first time by Lincot et al. [5], who succeeded in obtaining a (111) CdTe layer in epitaxy with the CdS-coated ($\overline{111}$) face of a InP single crystal, using cathodic electrodeposition from a standard acidic sulfate, tellurite solution at +5 mV vs. Cd/Cd$^{2+}$, i.e., underpotentially for cadmium. Partly epitaxial development was shown to occur on the bare InP substrate in spite of the large crystallographic mismatch (10.5%) between CdTe and InP. Epitaxy, however, was almost complete when the InP substrates were previously covered by a 20–30 nm thick CdS film, epitaxially deposited itself by chemical solution growth from a pH buffered ammonia solution of thiourea. The presence of CdS resulted in a structurally and chemically graded interface that was favorable for the CdTe epitaxial deposition. It was assumed that this intermediate layer enhances chemical bonding and plays the role of a buffer layer which tolerated the misfit between CdTe and InP crystal lattices. It was observed that the epitaxial CdTe films may reach a thickness as large as $\approx$120 nm; thereby probably no critical thickness effect would exist. If so, the growth of thicker epitaxial films should be possible.

To be sure, epitaxial electrodeposition of a II–VI compound on a III–V single crystal with favorable lattice match turns out to be possible without the mediation of a buffer layer. Cachet et al. [6] were able to attain electrochemical epitaxial growth of CdSe directly on InP taking advantage of the relatively low (3.6%) mismatch between the two materials. Stoichiometric, zinc blende, $\langle 111 \rangle$ CdSe layers with a thickness of 30–250 nm were obtained either on the In-rich (111) or the P-rich ($\overline{111}$) face of InP single crystals (Fig. 4.1), from a standard aqueous electrolyte (acidic sulfate solutions of selenite) in conditions identical to those previously identified as optimal for the "conventional" growth of strongly (111)-textured polycrystalline CdSe deposits onto various inactive substrates such as Ti, Ni, or SnO$_2$/glass. Good epitaxy in the present case could be achieved by monitoring the experimental parameters very carefully, in particular the Se(IV) concentration in the electrolyte and the deposition potential, in order to promote the alternate nucleation



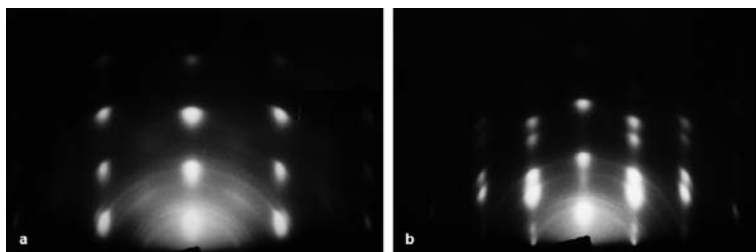**Fig. 4.1** Reflection high-energy electron diffraction (RHEED) patterns corresponding to the best epitaxial conditions of CdSe deposited on a ($\overline{111}$) InP face (thickness 85 nm). (**a**) Observation under the $\langle 112 \rangle$ azimuth; (**b**) observation under the $\langle 1\overline{1}0 \rangle$ azimuth. (With kind permission from Springer Science+Business Media [6])

of 2D monolayers of Se and Cd giving rise to a 2D layer-by-layer growth. Clearly, the single-crystal substrate was mostly favorable for this mechanism. However, as soon as the experimental conditions departed from the optimum, the deviation from stoichiometry appeared to be detrimental to a 2D nucleation/growth process and tended to favor a 3D nucleation of small grains. For optimum conditions, the CdSe layer on InP was nearly stoichiometric, with a carrier density of about $10^{17}$cm$^{-3}$.

Similarly, the $(\overline{111})$ GaAs substrate could be used to achieve epitaxial growth of zinc blende CdSe by electrodeposition from the standard acidic aqueous solution [7]. It was shown that the large lattice mismatch between CdSe and GaAs (7.4%) is accommodated mainly by interfacial dislocations and results in the formation of a high density of twins or stacking faults in the CdSe structure. Epitaxy declined rapidly on increasing the layer thickness or when the experimental parameters were not optimal.

We note that epitaxial deposition of CdTe on single-crystal InP(100) without a buffer intermediate was demonstrated recently [8] using a layer-by-layer growth technique, pertaining to the ECALE methodology, to be discussed in the next section. In situ characterization studies were performed in this work by Auger electron spectroscopy (AES) and low-energy electron diffraction (LEED) following the so-called UHV-EC methodology, which uses an ultrahigh vacuum surface analysis instrument including an antechamber for electrochemical experiments. Thereby, the surface composition and structure of the first few CdTe monolayers could be monitored at the end of each electrochemical deposition cycle, without exposure of the deposit to air.

Froment and co-workers attempted the epitaxial growth of lead selenide, PbSe, on InP(111) single crystals; they perceived, however, that this was not possible by the previously utilized method as it is unable to overcome dendritic growth of PbSe. Lead complexation by EDTA allowed the formation of uniform electrodeposits, but not of epitaxial layers. The researchers then followed another approach, originally introduced by Streltsov et al. [9], involving the addition of cadmium ions in the electrolyte to suppress the dendritic growth of PbSe. It was shown [10] that such an addition allows the formation of epitaxial rock salt PbSe films on (111) InP by electrodeposition at room temperature using the standard aqueous electrolytes containing nitrate salts of the bivalent metals, Pb(II) and Cd(II), and selenite. The epitaxial quality of PbSe films strictly depended on the Cd(II) concentration and the cathodic potential. The conditions for epitaxial growth of PbSe electrodeposits on (111) and (100) InP surfaces were refined and their crystallographic organization was described in subsequent papers, where the role of cadmium additions in the electrolyte has been emphasized [11, 12].

In fact, different techniques revealed cadmium segregation and decrease of the Pb/Se ratio near the InP/PbSe interface, indicating that during the first steps of deposition a CdSe layer is formed on InP prior to the PbSe growth. It was suggested that selective adsorption of Cd(0) on the InP surface gives rise to an epitaxial CdSe monolayer, which facilitates an ordered PbSe growth on account of the small lattice mismatch (0.7%) at the CdSe/(rock salt)PbSe interface. Importantly, it was found

that during electrodeposition continuous cadmium adsorption constantly prevents dendritic growth of PbSe, presumably by inhibiting superficial sites and suppressing the Pb UPD; at the same time Cd incorporation in the PbSe deposits was maintained at a low level due to chemical displacement of the less noble $Cd^0$ by $Pb^{2+}$ (the standard redox potentials of $Cd^{2+/0}$ and $Pb^{2+/0}$ couples being –1.06 and –0.79 V vs. SSE, respectively). The Cd(II) effect turned out to be particularly important in the case of the (111)-textured InP substrate; HREM observations revealed the absence of stacking faults and microtwins in the PbSe structure. On the other hand, poor epitaxy was observed with the (100)-textured InP that could be related to a weak adsorption of cadmium on this crystallographic plane.

Similar to PbSe, the controlled growth of lead telluride, PbTe, on (111) InP was demonstrated from aqueous, acidic solutions of Pb(II) and Cd(II) nitrate salts and tellurite, at room temperature [13]. The poor epitaxy observed, due to the presence of polycrystalline material, was attributed to the existence of a large lattice mismatch between PbTe and InP (9%) compared to the PbSe/InP system (4.4%). The characterization techniques revealed the absence of planar defects in the PbTe structure, like stacking faults or microtwins, in contrast to II–VI chalcogenides like CdSe. This was related to electronic and structural anomalies.

The work on one-step electrochemical epitaxy was extended to zinc selenide, ZnSe [14] – rather the most extensively investigated II–VI compound with respect to atomistic growth techniques. Suitably treated (111) InP wafers with phosphorus-terminated surfaces and (100) GaAs wafers were used as deposition substrates in an electrolyte containing selenosulfate ions as Se precursor, which was previously shown (Chap.3) to prevent the co-deposition of elemental Se, detrimental to the growth of single-phase ZnSe in classical (acidic selenite) plating baths. Epitaxial, stoichiometric deposits were obtained, while it was shown that other than [111] directions of growth are possible, i.e., that the texture of the epitaxial ZnSe layers is not necessarily limited to the ⟨111⟩ one usually obtained by electrodeposition of zinc blende chalcogenides. Following a similar method of employing an electrolyte where elemental Se is soluble, ZnSe has been deposited also from DMSO solutions on $SnO_2$:F/glass, molybdenum, and ($\overline{1}11$), (100) n-InP substrates [15]. According to voltammetry results in the Zn(II)–Se–DMSO system, the mechanism of ZnSe film growth was strongly dependent on the nature of the supporting substrate. Epitaxial growth of ZnSe was attained on the (100) and ($\overline{1}11$) n-InP crystalline planes with good quality as demonstrated by reflection electron diffraction (RHEED) patterns and transmission electron microscopy (TEM).

Epitaxial effects are not limited to single-crystalline substrates. The possibility for substrate-induced epitaxial development in the "difficult" case of ZnSe (cf. conventional electrodeposition) has been established also by using strongly textured, albeit polycrystalline, zinc blende (111) CdSe electrolytic films to sustain monolithic growth of ZnSe in typical acidic selenite baths [16]. Investigation of the structural relations in this all-electrodeposited ZnSe/CdSe bilayer revealed that more than 30-fold intensification of the ⟨111⟩ ZnSe XRD orientation can be obtained on the textured (111) CdSe films, compared to polycrystalline metal substrates (Fig. 4.2). The inherent problems of deposition from the Se(IV) bath, i.e., formation of
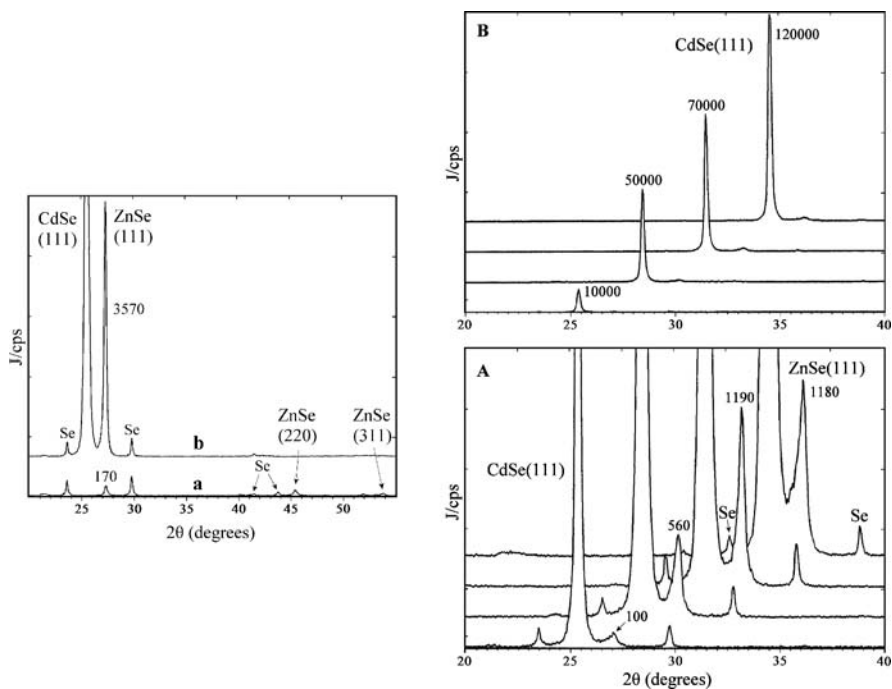
**Fig. 4.2** (*Left*) XRD patterns (CuK$_\alpha$) of equally thick ZnSe (ca. 1 μm) deposits prepared on Ti (**a**) and on CdSe/Ni (**b**), at a deposition potential of –0.7 V vs. SHE from a typical acidic (pH 3) solution. The reflection intensities for ZnSe(111) are denoted in the figure; (*right*) XRD patterns within the low-angle region showing the (111) reflections of ZnSe/CdSe heterostructures (**A**). Overlayers of ZnSe were deposited on CdSe films of various (111) texture intensities. The substrate features are shown in (**B**) in full-intensity scale. Evidently, the preferential orientation of the ZnSe crystallites increases with that of the CdSe substrate, up to a constant limiting value. (Reprinted from [16], Copyright 2009, with permission from Elsevier)

microcrystalline ZnSe together with semimetallic Se, remain; however, epitaxy is observed only for the ZnSe phase, implying the exclusively substrate-related character of the effect. Note that in the ZnSe/CdSe system, a mismatch of 6.3% for zinc blende lattices is found, while valence, chemical, and ionicity mismatches are essentially negligible; still, a rather large thermal expansion coefficient disparity exists (17.3%). The ability to electrochemically grow crystalline ZnSe layers with well-ordered structure on CdSe is important for the fabrication of backwall solar cells with ZnSe window to CdSe absorber.

The fundamental issue of epitaxial growth on polycrystalline substrates has been addressed in a more refined manner in relation to the electrodeposition of CdSe on metals. Polycrystalline, {111}-textured Au surfaces were shown [17] to promote the electrodeposition of coherent, epitaxial CdSe quantum dot films over areas micrometers in size, i.e., much larger than the polycrystalline Au grains, despite the numerous grain boundaries present in the substrate. The Au films (considered as

epitaxial polycrystalline films) were evaporated on freshly cleaved mica and long annealed to obtain an intense {111} texture. The first layer of CdSe Q-dots on Au was shown by high-resolution TEM to form a coherent overlayer, effectively bridging the epitaxial Au grain boundary gaps, while this behavior was not observed with non-epitaxial Au substrates. This coherent QD film serves as a buffer layer, which accommodates the substrate imperfections introduced by the grain boundaries and allows the coherent growth of thicker (e.g., 15 nm) nanocrystalline CdSe films. It was inferred that deposition on a certain grain of a polycrystalline substrate cannot always be treated as an isolated crystal/overgrowth system. That is, interactions with crystallites growing on proximate substrate grains must be considered.

Among possible candidate semiconductors to be used as substrates for epitaxial deposition, silicon is quite appealing because large-area wafers of the highest structural perfection are readily available commercially at a minimal cost, and if practical applications such as optoelectronics are concerned, advantage can be taken of the well-advanced silicon integration technology for fabrication of relevant devices. Heteroepitaxial growth of chalcogenides on silicon substrates by electrochemical methods has been reported in a few works. In particular, the electrodeposition of CdTe onto flat silicon single crystals has been investigated by the Berlouis group [18, 19] and Sugimoto and Peter [20, 21]. Not very satisfactory results were obtained, as the characterization of the electrodeposited films revealed that they do not form either a coherent layer or a preferential crystallographic orientation. In studying the nucleation of CdTe onto three different surface orientations of a Si single crystal by means of a transient analysis technique, Sugimoto and Peter found evidence for a 2D nucleation and growth mechanism, but the formation eventually of an amorphous deposit was not compatible with the desired epitaxial growth. In fact, it is generally difficult to obtain CdTe thin films of good quality onto Si, due to the different nature of the two materials. Most important is the existence of a large lattice mismatch (about 20% at 25 °C, for the cubic lattice parameters of Si 0.543 nm and CdTe 0.648 nm), which may give rise to numerous dislocations at the interface, propagating into the active part of the layer. In high-temperature growth processes (MBE, MOCVD, UHV sublimation, MOVPE, and hot wall epitaxy have been used in this connection) additional strain and dislocations may arise due to the thermal mismatch between CdTe and Si when the layer is cooled down from the growth temperature; therefore, soft solution processing techniques like electrodeposition are highly desirable. In any case, the Si(111) substrate is more pertinent to CdTe deposition than the Si(100) because it has the same symmetry as CdTe(111) and the direct growth of the semiconductor should be possible without the multidomain problem during the nucleation stage that is observed with Si(100).

It appears that a way to efficient electrochemical growth of CdTe and other chalcogenides on silicon crystals is the utilization of light-assisted processes. Works in this direction will be discussed in a subsequent section regarding underpotential deposition studies.

It is worth referring here to a somewhat reverse approach to the problem of an ordered substrate. In the previously reported works, formation of a homogeneous

film has been pursued mainly by employing a flat single-crystal substrate with an energetically uniform surface. However, such an ideal condition is rarely reached in practice. Instead of ensuring the perfection of the substrate phase, an alternative approach has been explored, which consists in using a substrate with a very high density of surface non-uniformities, expected to result in a macroscopic equalization of electronic transfer conditions all along the surface, and therefore a uniform deposit growth [22]. Along this line, the rear side of an n-type (100) Si wafer polished on one side (Fig. 4.3) was successfully employed for the electrodeposition of CdTe [23] (cf. [24] for electrochemical characterization of a Si(111) rough face in $NH_4F$ solutions).

Well-crystallized, stoichiometric (111)-textured CdTe films were grown from a standard acidic plating solution of tellurite, containing $NH_4F$, at 85 °C. The mechanisms related to the initial stages of the CdTe nucleation and growth in this system were investigated [25] in very acidic (pH 0.29) solutions at room temperature. The analysis of potentiostatic current–time transients suggested that at short times a Te–Cd bilayer forms followed by either (a) progressive nucleation and charge transfer – controlled 3D growth or (b) progressive nucleation and diffusion-controlled 3D growth, giving account for the formation of conical and hemispherical nuclei, respectively. Ex situ AFM images of the surface were found to support these assumptions.

The interest in growing CdTe on Si is driven mainly by infrared technology demands (Si is transparent to IR radiation to wavelengths beyond 14 μm), for instance, by its potential use as an alternative substrate for fabricating $Hg_xCd_{1-x}Te$ IR detectors, since selected area $Hg_xCd_{1-x}Te/CdTe/Si$ heteroepitaxy can be combined readily with the Si processing technologies to form monolithic IR detecting systems. In addition, CdTe/Si is now being used for the fabrication of megapixel HgCdTe hybrid infrared focal plane arrays (IRFPAs), intended to be used in very large applications in military, space, and medical imaging areas for IR imaging and low-background detection [23].



**Fig. 4.3** SEM micrograph of the rear side of an n-(100) Si wafer polished on one side. The presence of inverted truncated square pyramidal structures fully covering the surface can be observed. This pyramidal texturing was attributed to the combination of anisotropic etching of the silicon and to hydrogen bubbles evolved during the etching reaction. (Reprinted from [23] Copyright 2009, with permission from Elsevier)

## *4.2.2 Electrochemical Atomic Layer Epitaxy*

ECALE originates from a combination of electrochemical deposition and atomic layer deposition (ALD; or atomic layer epitaxy: ALE [26]) and comprises the solution-phase growth method analogue to ALE epitaxy techniques such as molecular beam epitaxy (MBE) or metal organic vapor-phase epitaxy (MOVPE); the term ALE is formally reserved for vacuum thermal techniques. Unlike conventional chemical vapor deposition, in ALD techniques each precursor is introduced to the substrate separately. The deposition process consists in monolayer stepwise growth that proceeds by exposing the substrate surface alternately to each precursor followed by an inert gas (nitrogen) pulse to remove the excess species and the by-products of the reaction. With this sequential mode, the duration of each exposure is adjusted so that each surface reaction goes to completion before starting the next reaction. The substrate surface temperature is used to ensure specific monolayer adsorption in the absence of multilayer growth. Under properly adjusted experimental conditions, all the surface reactions are saturated making the growth process self-controlled. Therefore, atomic layers of each element making up the compound are alternately deposited by surface-limited reactions, so that ALE offers great control over deposit structure. The film thickness can be determined accurately by the number of deposition cycles.

In a similar way, electrochemistry may provide an atomic level control over the deposit, using electric potential (rather than temperature) to restrict deposition of elements. A surface electrochemical reaction limited in this manner is merely under-potential deposition (UPD; see Sect. 4.3 for a detailed discussion). In ECALE, thin films of chemical compounds are formed, an atomic layer at a time, by using UPD, in a cycle; thus, the formation of a binary compound involves the oxidative UPD of one element and the reductive UPD of another. The potential for the former should be negative of that used for the latter in order for the deposit to remain stable while the other component elements are being deposited. Practically, this sequential deposition is implemented by using a dual bath system or a flow cell, so as to alternately expose an electrode surface to different electrolytes. When conditions are well defined, the electrolytic layers are prone to grow two dimensionally rather than three dimensionally. ECALE requires the definition of precise experimental conditions, such as potentials, reactants, concentration, pH, charge-time, which are strictly dependent on the particular compound one wants to form, and the substrate as well. The problems with this technique are that the electrode is required to be rinsed after each UPD deposition, which may result in loss of potential control, deposit reproducibility problems, and waste of time and solution. Automated deposition systems have been developed as an attempt to overcome these problems.

A variety of compound semiconductors have been successfully prepared by this technique. Much of the work concerning ECALE has been concentrated on the deposition of CdTe on Au substrates. Notwithstanding the inherent problems of the system (for instance, a 10% lattice mismatch), the formation of CdTe epitaxial layers became a model example of ECALE synthesis. In their pioneering studies, Stickney and co-workers [27, 28] have focused on the deposition of the compound on
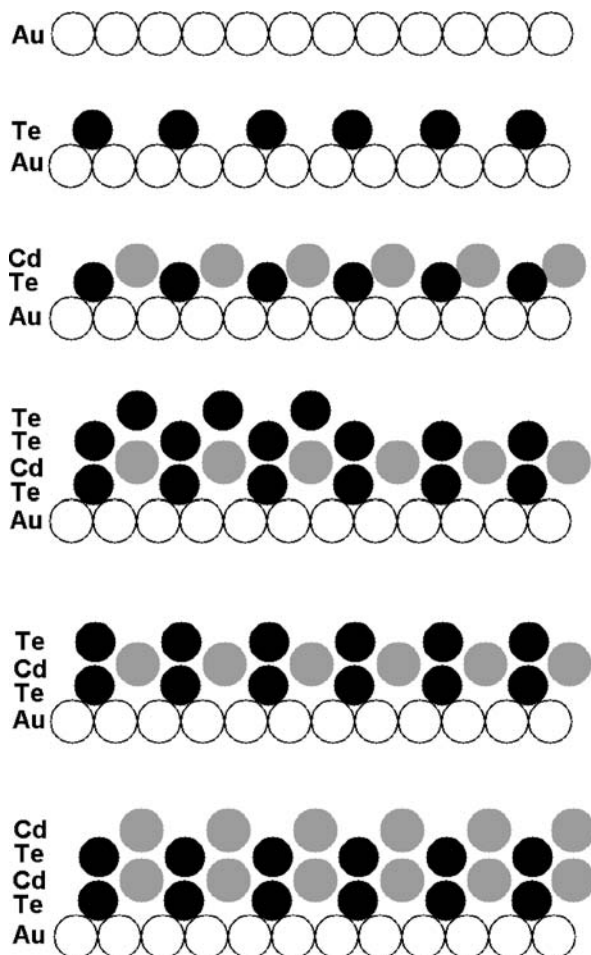
**Fig. 4.4** Atomistic representation of successive steps in the ECALE synthesis of CdTe on an Au substrate. Observe the deposition and stripping of Te for assembling the correct atomic planes of the zinc blende structure. (Adapted from [27])

polycrystalline Pt, Cu, and Au electrodes in thin layer electrochemical cells (TLEs) containing acidic tellurite and Cd(II) ion solutions. UPD layers of Te and Cd were alternatively electrodeposited to build up thin CdTe films (Fig. 4.4). Tellurium deposition on Pt was found to be inhibited by hydrogen co-deposition at low potentials and by surface oxide formation at high potentials, while Cu substrates were found to be unstable at the potentials used to study the reduction of $TeO_2$ to Te(0). From an electrochemical perspective, Au appeared to be the best substrate for UPD of Te and Cd, as presenting a large potential window – Au is generally an excellent electrode material, and its surface chemistry in aqueous solutions is reasonably well understood. However, when performing deposition on single-crystal phase, the

lattice matching turns out to be quite important. As mentioned already, the CdTe lattice matching with Au is far from being ideal [e.g., 11% between CdTe(100) and twice the Au–Au spacing on the Au(100) plane]. Notwithstanding, CdTe formation by ECALE on low-index planes of Au indicated that the structure of the first couple of CdTe monolayers formed on Au(100) resembles the CdTe(100) planes that would be found in a bulk CdTe zinc blende structure, yet with a 10% compression of the CdTe lattice.

In subsequent studies, Suggs and Stickney focused on the structures formed by the underpotential deposition of Te on single-crystal Au surfaces, using a combined UHV-electrochemical instrumentation, and investigated the surface chemistry associated with each step in the ECALE cycle, as well as the microstructures and coverages resulting from the alternated deposition of Te and Cd atomic layers on the low-index planes of Au. Sensitive characterization techniques, such as ex situ LEED, Auger, XPS, and STM were used [29–32]. Several stable Te UPD structures were observed to form on each of the low-index planes of Au as a function of the deposition potential. Subsequent deposition of Cd on the various Te structures gave rise to well-ordered CdTe structures, as observed via LEED and STM, on all three of the Au low-index planes. On the Au(100) surface the structure of the deposit consisted of $c(2\times2)$ unit cells, with $\frac{1}{2}$ coverages of both Te and Cd, requiring a 10% compression of the lattice.

The CdTe bilayers grown by ECALE on the three low-index planes of gold have been successfully imaged by the in situ STM technique, which (similar to in situ AFM) allows to follow the changing surface morphology during the different stages of growth. Hayden and Nandhakumar [33, 34] established a 2D growth mechanism consistent with the observed epitaxial growth of the UPD structures of Te on Au(111) and of Cd on Te-covered Au(111). The Cd/Te bilayer structure formed by Cd UPD on a Au(111)–(12×12) Te surface was found to correspond to Au(111)–(3×3)CdTe. A model was suggested for this structure in which the bilayer corresponds closely to the CdTe(111) plane of the bulk (zinc blende) lattice with an 11% compression. As the bilayer growth is dominated by the requirement to achieve stoichiometry, the initial coverage of the Te UPD layer was emphasized as of overriding importance during the initial growth phase. The researchers showed also that when substantial rearrangement or reconstruction is required of the Te UPD layer, as it is found for the first UPD layer of Te on Au(100), it does not result in 3D growth but in an inhomogeneity in the 2D structure. Stoichiometric CdTe compound deposition by ECALE has been conducted also on Ag(111) [35]. Similar mechanisms for 2D growth were described.

In comparison to CdTe, the heteroepitaxial growth of CdS on gold should be easier to handle since the corresponding lattice mismatch is significantly smaller. Colletti et al. [36] reported preliminary data about this system for ECALE growth of CdS on polycrystalline gold substrates in a thin layer electrochemical flow cell. Aqueous alkaline $Na_2S/NaClO_4$ solution for the deposition of S and aqueous pH 5.9, $CdSO_4$ solution for Cd deposition were used. Nearly stoichiometric CdS films, 50 monolayer (ML) thick, with a distinctly yellow appearance, were grown. Demir and Shannon investigated the kinetics of CdS ML formation [37] on single-crystal

Au and the influence of the Au(111) [38] and Au(100) [39] crystallographic orientations on the structure of the final deposit. Well-defined wurtzite CdS MLs were formed by Cd deposition on S-modified Au (ECALE process took place in aqueous precursors, e.g., $Na_2S$ in $NaOOCCH_3$/KOH for S constituent and $CdSO_4$ in KOH/$CH_3COOH$ for Cd). The researchers examined the structure of the initial CdS ML by µm-scale and atomically resolved STM and found that both S and Cd layers deposit in a layer-by-layer fashion giving atomically flat surfaces. They identified a single sixfold structure for the CdS adlayer and proposed a model to account for these data. In an attempt to improve the overall CdS film quality, the same group investigated the effect of the deposition order on film structure [40]. Interestingly, when S (from aqueous $H_2S$) had been deposited on a Cd-modified Au surface, the characteristic hexagonal structure of wurtzite CdS was not observed until the deposition of the third complete monolayer. The more complex adatom structures associated with this approach were attributed to the strong positive interaction between Cd adatoms and the Au substrate, extending beyond the first monolayer.

Ultrathin films of CdS ranging in coverage from 25 to 200 ML were grown also by the previous method on Au substrates (of non-specified nature) and were characterized by quantitative Raman resonance [41]. It was found that the electronic structure of the films in this coverage regime corresponds to that of bulk CdS. It was concluded also that ECALE does not involve growth by random precipitation of CdS onto the Au surface; the thin deposited layers of the material were contiguous.

Electrochemical epitaxial growth of CdS/HgS heterojunctions onto Au(111) substrates was attempted by Gichuhi et al. [42]. This system was chosen in the first place because of the excellent lattice match between the two materials (CdS 0.4135 nm; HgS 0.4149 nm) and because the band gap of (cinnabar) HgS (2.1 eV) is smaller than that of CdS (2.47 eV). Actually, two methods were used in order to terminate the initially electrodeposited CdS film with a single HgS monolayer. The first involved the chemical exchange of the terminal Cd layer with $Hg^{2+}$, but produced a disordered, highly polycrystalline film, which was dominated by CdS trap luminescence. The second method involved ECALE growth of the HgS monolayer and resulted in the formation of a high-quality heterojunction. Photoluminescence spectroscopy measurements indicated a high degree of electronic coupling between the CdS substrate and the electrochemically deposited HgS layer in this case.

Changing the substrate from gold to silver has been shown to strongly affect the structure of the first few layers of CdS grown by ECALE. STM measurements carried out on the first CdS layer on Ag(111) revealed a much less compact structure than the one found on Au(111). This disparity was tentatively attributed to the different structure of the first S layer on Ag(111), as obtained by oxidative UPD from sulfide ion solutions, due to a higher affinity of sulfur for silver than for gold. The Cd layers were attained on S by reductive UPD from cadmium ion solutions. Precursors for both elements were dissolved in pyrophosphate/NaOH at pH 12 [43–45].

Significant improvements in ECALE deposit morphology and quality were reported as achieved by switching from a thin layer cell to a thick layer H-form cell, integrated in an automated deposition system [46]. Thin epitaxial films of zinc blende CdTe, CdSe, and CdS with predominate (111) orientations were grown.

Films formed with 200 or less cycles generally showed a smooth morphology; however, deposits made with 500 or more cycles showed increased amounts of particulates or crystallites.

Regarding zinc chalcogenides, it has been reported [47] that stable deposits of ZnTe, ZnSe, and ZnS can be electrochemically grown on low-index planes of single-crystal Au. Thermodynamics appeared to play a role in the formation of the initial compound monolayer, as the differences in the UPD potentials of these materials were consistent with their free energies of formation, going like ZnTe > ZnSe > ZnS. Thus, zinc deposition onto Te, Se, and S-coated electrodes occurred at progressively more positive potentials as the stability of the zinc compounds increases. Notwithstanding, Zn was most difficult to deposit on Te and easiest to deposit on S.

Zinc sulfide, ZnS, has been epitaxially deposited by the dual bath approach on Au(111) surface and studied by STM and XPS [48]. The first complete ECALE cycle resulted in the formation of nanocrystallites of ZnS randomly distributed across Au(111) terraces, on account of lattice mismatch induced strain between ZnS and Au(111) – although the mismatch is only 0.13% for ZnS/Au(111). Atomically resolved STM images showed the ZnS/Au(111) monolayer to be sixfold symmetric. The average diameter of the crystallites was $10\pm5$ nm and the apparent coverage 0.38.

Stoichiometric deposits of ZnSe with up to 35 Zn layers and 35 Se layers have been obtained on Ag(111) substrates by automated ECALE in a miniaturized cell; Se precursor was $Na_2SeO_3$ and that of Zn was $ZnSO_4$, both in aqueous pH 9.2 ammonia buffer [49]. The graph of stripping charge suggested that the deposits grew at a rate of only about 0.14 ML per cycle (referred to a monolayer of the Ag(111) substrate). A higher growth rate per cycle was reported recently [50] for 15 Zn and Se manual ECALE deposition cycles in similar solutions (except pH 4 for Se and pH 9 for Zn), with a polycrystalline Au substrate. The deposition program was optimized by adjusting the effects of Zn and Se deposition potentials and the Se stripping potential. Each layer of Se and Zn was found to correspond to the ideal coverage of 0.562 and 0.567 ML – reported as the ratio of deposited atoms per substrate surface atom. The thin ZnSe deposits were single-phase cubic with a strong (220) preferred orientation and consisted of particles with an average size of about 100 nm.

The ECALE deposition of ternary II–VI compound semiconductors such as $Cd_xZn_{1-x}S$, $Cd_xZn_{1-x}Se$, and $CdS_xSe_{1-x}$, on Ag(111), has been reported [51–53]. The compounds were prepared by sequential deposition of the corresponding binaries in submonolayer amounts; for instance, alternate deposition of CdS and ZnS was carried out to form $Cd_xZn_{1-x}S$. The stoichiometry of the ternaries was seen to depend on the deposition sequence in a well-defined and reproducible way, with the limit that only certain discrete $x$ values were attainable, depending on the adopted sequence profile. Photoelectrochemical measurements were consistent with a linear variation of the band gap vs. the composition parameter $x$ of the mixed compounds.

The group of Stickney reported the first deposits of mercury selenide (HgSe) formed via ECALE, using a thin layer flow system [54, 55]. The solutions used were HgO (pH 2) and $SeO_2$ (pH 3) with $Na_2SO_4$ as a supporting electrolyte, and the

electrodeposition was performed on 300 nm thick evaporated gold films, of a (111) habit, on glass. The effect of Hg and Se deposition potentials, and a Se stripping potential, were adjusted to optimize the deposition program. Electron probe micro-analysis (EPMA) and XRD of 100-cycle samples showed a Se/Hg ratio of 1.08 and a zinc blende structure with strong preferential (111) orientation. Ellipsometric measurements indicated a deposit thickness of 19 nm, where 35 nm was expected. Thus, the resulting "optimal" deposits were a little over half of that expected from the ideal model of one compound monolayer for each cycle. FTIR absorption measurements were consistent with the inverted band structure of the compound, expected from the literature, and a negative gap of 0.6 eV.

Torimoto et al. reported quantum confinement in thin films, of CdS [56], ZnS [57], and PbS [58], grown by ECALE. Deposits of these compounds gave anodic photocurrents in aqueous solutions containing triethanolamine (electron donor), i.e., behaved as n-type semiconductor photoelectrodes, and their energy gaps were seen to increase with a decrease in film thickness due to size quantization effects. The critical film thickness at which size quantization effects began to appear was about 4.8 nm for ZnS and 6.8 nm for CdS, as was verified by the analysis of action spectra recorded in the previous solutions. No such threshold could be précised photoelectrochemically for PbS, presumably due to the presence of surface states at the semiconductor film electrodes. Interestingly also, the actual changes in the band gap width of PbS with an increase in film thickness were much smaller than theoretically predicted, whereas the predicted values for CdS and ZnS were in good agreement with those obtained experimentally (at least for films having thicknesses greater than 7.5 and 8.5 layers, respectively). Crystallographic mismatch differences were invoked to explain the observations. The deposited PbS films had the normal rock salt structure, yet with a (200) texture. Hence, whereas a mere mismatch-induced strain was present at the CdS/Au and ZnS/Au interfaces, in the case of PbS the lattices were quite incommensurate, as a PbS(200) plane having a fourfold symmetric structure lay in contact with Au(111) having a sixfold symmetric structure. This complete misfit was responsible for creation of various defects in PbS which would degrade its electronic properties in the observed way.

ECALE has been reported for the fabrication of tin selenide compounds [59] using acidic $Sn^{2+}$ and $H_2SeO_3$ electrolytes at room temperature. Although no structural data could be exhibited, analysis of current–time transients and stripping voltammograms indicated the formation of $SnSe_2$, $SnSe$, and $SnSe_{2-x}$ compounds, the latter probably containing Sn in its two oxidation states. A general reaction scheme was proposed on account of the charges involved in the deposition process.

Vaidyanathan et al. [60] gave a first instance that ECALE can be used to grow PbSe with atomic layer control. A series of stoichiometric rock salt PbSe thin films, with a preferred (200) orientation, were electrodeposited on Au substrates using buffered solutions with millimolar concentrations of $Pb(ClO_4)_2$ (pH 5.5), and $SeO_2$ (pH 5.5). IR adsorption studies, of films grown with 10–50 cycles, showed strong blue shifts of the fundamental absorption edge, which was believed to result from quantum confinement in the thin films. The band gap for the 50-cycle deposit was

greater than that for the bulk compound by a factor of four, while the band gaps for thinner films were even greater, shifted into the visible.

The ECALE synthesis of V–VI (V: Sb, Bi) compounds has been attempted in a few works. Antimony telluride, $Sb_2Te_3$, nanofilms with a homogeneous microstructure and an average size of about 20 nm were formed epitaxially on a Pt substrate [61]. The optical band gap of these films was blue-shifted in comparison with that of the bulk single-crystal $Sb_2Te_3$ compound.

The kinetics and growth mechanism of the first and second monolayers of bismuth sulfide, $Bi_2S_3$, on Au(111) has been studied using voltammetry and chronoamperometry techniques [62]. An adsorption/desorption process governed by Langmuir kinetics and a nucleation/growth process pertinent to ordered $Bi_2S_3$ structures were considered to take place during the formation of the compound. It was indicated that depositing Bi as a first layer results in a more ordered $Bi_2S_3$ layer than the deposition of S as the first atomic layer. The significance of employing a room-temperature process with no complicated precursors or apparatus for preparing V–VI thermoelectric nanomaterials was emphasized. An optimized ECALE program for deposition of bismuth telluride was developed by Yang et al. [63]. Epitaxial 200-cycle thin films of $Bi_2Te_3$ were prepared from buffered solutions of millimolar $Bi(NO_3)_3.5H_2O$ (pH 1.5), and $TeO_2$ (pH 2), on Au-evaporated glass microscope slides. The UPD regions for both the first bismuth cycle on Te-covered Au and the first tellurium cycle on Bi-covered Au were determined on the basis of the integrated faradaic charges of anodic stripping currents. The XRD and EDX results were consistent with the 2:3 compound stoichiometry, while field emission SEM showed that the deposits consisted of 30–100 nm crystallites and were conformal with the Au substrate.

A novel approach proposed by Demir and co-workers to attain growth with good structural control in one step should be included in the present section, as retaining some features of classical ECALE synthesis, while being deprived of the shortcomings of time consumption and production of a large amount of dilute wastewater that characterizes the common (non-automatic) technique. This approach was demonstrated first in preparation of lead sulfide from a single aqueous solution of $Na_2S$, $Pb(CH_3COO)_2$, and EDTA [64]. The idea was to promote an all-UPD atom-by-atom growth of PbS at the substrate, while keeping Pb complexed avoiding thus the formation of PbS particles in the solution phase. In specific, the process involved the co-deposition of Pb and S precursors at a constant potential determined from the UPD potentials of Pb and S. Highly crystalline and stoichiometric deposits of PbS could be grown on Au(111) at a kinetically preferred intense cubic (200) texture. Accordingly [65], monolithic growth of size-quantized ultrathin films of zinc blende ZnS(111) was achieved on single-crystalline Au(111) by electrochemical deposition from an aqueous $Na_2S$, $Zn(CH_3COO)_2$, EDTA solution at pH 4.6.

A similar one-step process was employed successfully [66] to prepare well-crystallized CdS thin films of optical quality on Au(111) from an aqueous solution of $CdSO_4$, EDTA, and $Na_2S$ at room temperature. A phase transition from cubic (zinc blende) to hexagonal (wurtzite) CdS structure was observed with decreasing pH below 5, while highly preferential orientation along [11.0] directions for the

hexagonal crystal and [111] directions for the cubic crystal were identified in the solutions with pH 4 and 5, respectively. UV–visible absorption measurements as a function of deposition time indicated that the band gap of the CdS film increased as the deposition time decreased.

### 4.2.3 Superstructures–Multilayers

Multilayers and superlattices are microstructurally recurrent materials, in the sense that they present periodic modulation of structure or composition or both (Fig. 4.5). Superlattices have the additional constraint that they are crystallographically coherent with respect to atomic planes, i.e., of epitaxial nature. For example, in the CdSe–ZnSe system, a superlattice would comprise periodically alternating epitaxial layers of CdSe and ZnSe, whereas in the absence of crystallographic coherence a bilayer ZnSe/CdSe film or a sequence of multiple layers of ZnSe, CdSe, and/or other compounds would comprise a simple heterojunction or multilayer system. A thoughtful way to figure out such systems of two binary compound phases with a common element is by considering that, as opposed to normal substitutional alloys, where the compositional modulation is uniform along all of the three space directions, in a superlattice or multilayer the composition or structure is modulated along the $z$-direction only, whereas the $x$–$y$ plane is compositionally homogeneous [67] (the equiaxed substitutional alloy of ZnSe and CdSe is the ternary $Cd_{1-x}Zn_xSe$ alloy).

Modern solid-state devices rely on the growth of sequences of many ultrathin epitaxial layers with atomically sharp interfaces and thickness control down to the monolayer level. In most of the technologically relevant cases, the growth of perfectly flat, 2D sheets of material is a stringent requirement for functionality. A typical example is given by quantum well structures where alternating layers of wide band gap and narrow band gap semiconductors are grown to tailor the electronic properties by quantum confinement of charge carriers in the low band gap regions. In such nanomodulated superlattices exhibiting quantization effects, changing the modulation period by even a few atomic layers may change the material's optical and electrical properties. Interfacial sharpness, lattice mismatch, and
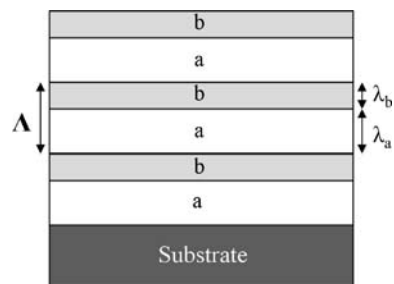


**Fig. 4.5** Superlattices (superstructures) and multilayers are systems composed of alternating layers of, say, phases A and B with a specified AB bilayer thickness, which is called the modulation wavelength ($\Lambda$), or period

stoichiometric modulations through the superlattice period all have substantial effects on these properties.

The primary methodologies for forming superstructures with atomic-level control are MBE, VPE, and a number of other derivative vacuum-based techniques. Electrochemical protocols should in principle be quite effective in assembling superlattices, as the low processing temperatures involved allows growth with minimal interdiffusion across interfaces. Most research on the electrodeposition of superlattices has been on metallic systems; the emphasis has been in growing nanoscale structures with enhanced elastic and plastic properties, improved wear resistance, and magnetic anisotropy. Alternatively, optical and electrical properties have been central in attempts to form nanometer-scale metal oxide and metal chalcogenide compositional superlattices. Electrochemical formation of compound superlattices has been pioneered by Switzer and co-workers [68]. An excellent example of the innovative work done in the 1990s in this direction is the electrodeposition of a lead–thallium–oxygen, Pb–Tl–O, superlattice system with layer thicknesses in the 4–6 nm range from a single aqueous solution by pulsing the applied potential during deposition [69]. In this work, the current–time transients that resulted from the potential steps were monitored to both calculate and tailor the composition profiles of the superlattices during growth. The authors emphasize that the electrochemical method is ideal for both measuring and tailoring the interface symmetry and composition profiles of superlattices in real time on a subnanometer scale. Modulation lengths from 3 to 150 nm were reported for the Pb–Tl–O system, although partial relaxation of coherency was observed for lengths exceeding about 20 nm [70].

Layered structures, in general, can be produced in a variety of ways from the electrochemical environment. The most common approach is to apply an oscillating current or potential function to the working electrode during deposition from a single solution containing precursors for all the elements in a compound. An electrochemically fabricated, band gap engineered system of Cd–Zn–Se has been reported originally by Krishnan et al. [71], being in particular a composition-modulated "superstructure" resulting from the application of electrodeposition cycles. The electrochemical modulation of composition in the ZnSe/CdSe system could be accomplished either by potential or current pulsing between the limits characteristic of CdSe and ZnSe electrolytic deposition. Similarly, simultaneous cathodic deposition of PbSe/PbTe multilayer periodic structures from a single acidic aqueous solution of Pb(II) ions and $XO_2$ (X = Se, Te), on Pt films evaporated on Si(100), has been reported by Streltsov et al. [72]; Pb–Se–Te superlattices with 2.5–10 nm periods (modulation wavelength) were electrodeposited by imposing periodically changing cathodic electrode potential in the single bath. It was not possible to electrodeposit structures with modulation higher than 10 nm as ternary phases ($PbSe_xTe_{1-x}$) were formed instead.

This pulse plating technique has the advantage of simplicity, i.e., application of a simple waveform in current or potential in a single solution. Problems arise, however, because at the more positive potential a pure element or compound is deposited, while during the pulse the second element or compound formed is inevitably contaminated with the first. Switzer et al. [73] reported a variation on

this general theme in which electrochemically driven self-assembly was used to produce periodic $Cu_2O$ superlattices; it was shown that layered nanostructures of copper (Cu) and cuprous oxide ($Cu_2O$) "can be electrochemically self-assembled in a beaker at room temperature". Notwithstanding, the chemical combinations that can be reached are limited and strictly depend on the differences in the redox potentials. It has been already discussed here that a dual bath method like ECALE can be used to overcome some of these limitations. Very few works have been published in this direction.

Well-defined CdS/CdSe superlattices have been formed by means of ECALE [74]. In these structures the CdS component – and not CdSe – suffered from substantial crystallographic strain as was evidenced by surface-enhanced Raman spectroscopy (SERS) – a valuable tool for characterizing the superlattice phonons in electrochemical or other ambient environments. Torimoto et al. reported quantum confinement in superlattices of ZnS/CdS grown by ECALE [75].

Only recently the ECALE formation of PbSe/PbTe superlattice films was reported [76]. An automated electrochemical thin layer flow deposition system was used to grow PbSe/PbTe superlattices with periods of 4:4 and 6:6, on Au evaporated on glass; for instance, for the 4:4 superlattice, each period was formed using four cycles of PbSe followed by four cycles of PbTe (Fig. 4.6). It was concluded that the critical thickness in the system is above 4 nm and below 7 nm, so that by increasing the layer sequence ratio from 4:4 to 6:6, a significant increase in the defect density resulted. The IV–VI compounds PbSe and PbTe have band gaps of 0.26 and 0.29 eV, respectively. Previous studies of lead chalcogenide superlattices have suggested that
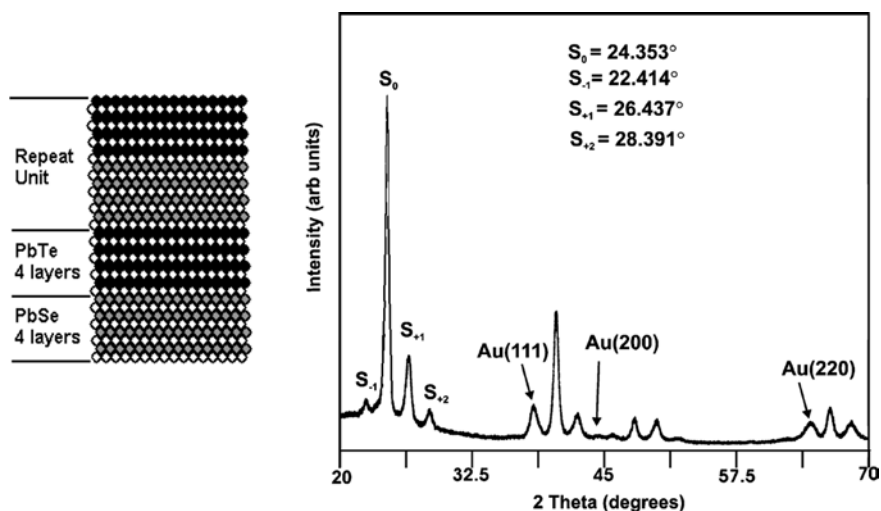


**Fig. 4.6** Layer sequence and X-ray diffraction ($CuK_\alpha$) of 81 period 4PbTe/4PbSe superlattice. Buffer layer is a 10-cycle PbSe. Angle of incidence is 1°. The (111) diffraction peak ($S_0$), along with both ± first-order satellite peaks, and one second-order peak, are evident and indicative of the formation of a superlattice. (The XRD diagram is reprinted with permission from [76], Copyright 2009, American Chemical Society)

they have type II band alignment, which usually results in superlattice band gaps less than either of the constituent semiconducting compounds. However, in this study, the band gaps were blue-shifted from those of the constituent compounds. Note that PbSe and PbTe have a significant lattice mismatch, 6%, and are thus considered to form strained-layer superlattice structures, where dislocations and island growth may occur. Strain builds as a film grows on a mismatched substrate until the critical thickness, at which point the defects result. The principle of a strained-layer super-lattice is that, by switching back to the other compound before the critical thickness, the strain should relax, preventing the formation of the defects.

## 4.3 Atomic Layer Epitaxy and UPD Revisited

Most of the electrochemical syntheses involving epitaxy entail the underpoten-tial deposition of constituent elements as a surface-limited reaction to establish compound growth controlled in an atomic level. Therefore, knowledge of this phe-nomenon is central in performing successful electrochemical epitaxy. UPD results from the free energy given off by surface-binding events leading to formation of adsorbate layers or chemical associations and may involve either an oxidative or a reductive process. Oxidative UPD is the result of the oxidative deposition of an element from a reduced state to form an atomic layer, such as in the deposition of I atoms from an $I^-$ solution. Elements amenable to oxidative UPD include As, Sb, Te, Se, and S. Reductive UPD involves the reductive deposition of an element, usually a metal, from an oxidized form of the element, i.e., deposition of Cu from a $Cu^{2+}$ solu-tion on Au. In any case, the depositing atomic layer is stabilized by interacting with terminal element(s) on the deposit surface. The study of UPD processes presents an exceptional possibility to obtain information on the mechanism of a number of electrochemical phenomena such as adsorption, charge transfer, surface diffusion, double layer changes, and, most relevant here, nucleation and growth. Note that the induced co-deposition concept (Chap. 3) extends the UPD theory from monolayer deposition to bulk growth.

   UPD has been the subject of investigation for over 50 years. Most of the pub-lished works in this connection have been devoted to the investigations of metal adatomic layers on foreign metals, in particular the flat faces of single-crystal Ag, Au, and Pt. The UPD of metals on crystallographically well-defined metal surfaces appears to take place with the formation of regular surface structures at sub- and full-monolayer coverage. In the case of small lattice mismatch between the adsor-bate and the substrate, the resulting structures are often commensurate. In systems with a large lattice mismatch, the deposits are generally incommensurate, espe-cially at monolayer coverage. Recent reviews have emphasized the role of anion co-adsorption during the process [77]; the kinetics of electrodeposition/desorption and the resulting structures are greatly dependent on the nature and concentration of anions in the solution (introducing repulsive interactions with the metal adatom layer [78]). In the presence of weakly adsorbing anions (e.g., perchlorate), the

kinetics of deposition/desorption are typically sluggish. The presence of strongly interacting anions (e.g., halides except fluoride) generally leads to much faster kinetics often ascribed to the formation of co-adsorbed M–X layers (X = halide). The formation of these layers is associated in some cases with phase transitions. As a general mechanism for the monolayer formation one can postulate a sequence of events that involve electrodeposition of the metal coupled with the co-adsorption of anions to form a 2D metal anion layer. Further reduction results in the disruption of these layers with additional electrodeposition leading to the formation of a zero-valent metal adlayer. The presence of surface steps greatly modifies the structure and kinetics by providing sites of enhanced reactivity for adsorption of both metal and anions.

There has been an increasing number of studies of the UPD of main group elements, including S, Se, Te, I, Br, Cl, and As, on metal substrates, whereas studies of UPD processes on the surface of semiconductors and semimetal substrates are significantly less. Presently, most interesting in this connection is the combined use of photoexcitation of a semiconductor substrate and/or an immobilized precursor, and electrodeposition, as will be discussed in a subsequent paragraph.

Definitely, the relevant studies for deposition of chalcogens on metals, or of metals on chalcogens, are substantial in gaining information on the mechanisms of electrodeposition of metal chalcogenides, in particular when employing ECALE. The investigation of the properties of adatomic monolayers (purposely formed or not) on an electrode surface is of fundamental importance also in catalytic processes. Chalcogen layers covering the surface of an electrode typically inhibit catalytic electrode reactions – for instance, sulfur is a well-known catalyst poison [79] – but have been found also to provide in some cases an increased electrocatalytic activity and selectivity. The effect of sulfur and selenium, mostly chemically linked to precious metal clusters, will be discussed in Chap. 6 in connection with electrocatalytic processes of global importance such as the oxygen reduction in fuel cells.

Electrochemical reaction/adsorption effects of sulfur on metal surfaces have been intensively investigated and well documented. Studies of self-assembled monolayers (SAMs) of S (mostly on Au) have increased dramatically in the last few years – such studies on chalcogen adsorption layers are of particular interest as the structures formed generally consist of clusters or chains of atoms, unlike the UPD of transition metals, for example, where close-packed adlayers are normally formed. A detailed insight into the voltammetric behavior of sulfur in the UPD range is provided by Alanyahoğlu et al. [80], who discuss the kinetics of the electrochemical deposition and desorption of S monolayers on highly oriented Au(111) and polycrystalline Au electrodes in aqueous solutions containing sodium sulfide.

Before examining selenium in some detail, as an illustration of the phenomena under consideration, let us note here that although oxidative UPD of sulfur can be achieved from sulfide solutions, the oxidative UPDs of Se and Te are complicated by the fact that, unlike sulfides, the $Se^{2-}$ and $Te^{2-}$ species are not very stable in aqueous solutions; they tend to react with even traces of $O_2$, to form the corresponding element.

The electrochemistry of Se adsorbate and bulk layers has been studied (and debated) by many research groups (e.g., [81, 82]; see also references connected
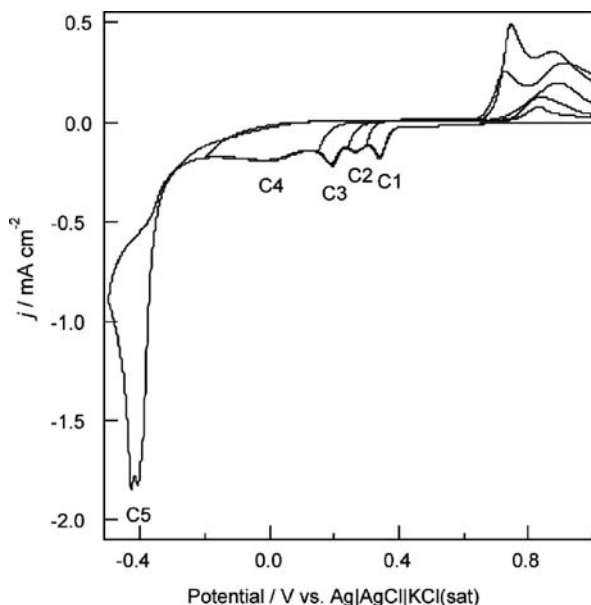
**Fig. 4.7** Voltammetric behavior of a Au(111) electrode immersed in 1 mM $SeO_2$ in 0.100 M $HClO_4$ supporting electrolyte. The five major cathodic waves corresponding to Se deposition are labeled *C1–C5*, respectively. The scan rate was 0.100 V $s^{-1}$. (Reprinted from [82], Copyright 2009, with permission from Elsevier)

to deposition of selenides, specifically CdSe). Following the work of Alanyahoğlu et al. [82] on the voltammetry of Au(111) electrodes in $SeO_2$/$HClO_4$ solutions, one can see that the system is characterized by three voltammetric features preceding the onset of bulk Se deposition (Fig. 4.7). Two of those (peaks C1 and C2) are associated with the conversion of adsorbed selenate species to adsorbed selenite, while only peak C3 is associated with the four-electron, four-proton reduction of adsorbed selenite to Se, i.e., to the formation of atomic layers of elemental Se. These three peaks are surface-limited waves, qualitatively similar to the UPD peaks observed during reduction of metals on high work function substrates. Peak C4 corresponds to the bulk deposition of Se and peak C5 to the reduction of adsorbed Se(0) to Se(–II), which then undergoes a conproportionation reaction with Se(IV) in solution, leading to the chemical formation of Se(0).

In atomistic growth processes of compounds, the first deposited atomic layer is rather the most critical, as that element is depositing on a foreign substrate, and the formation of an adatomic layer partially or wholly covering a foreign surface is the step preceding the nucleation and growth of a new phase. Stickney and coworkers [83], in their study of the Se UPD on Au(100), examined three different methods for forming electrochemically ordered atomic layers of Se, namely (a) the underpotential reduction of Se(IV) species (e.g., $HSeO_3^-$) to elemental Se; (b) the

anodic stripping of a previously deposited thin film of bulk Se, and (c) the cathodic stripping of bulk Se to $Se^{2-}$.

Studies of the adatomic structures resulting from the previous methods revealed four distinctly different stable Se configurations on Au(100), all of which could be considered monolayers, as none was more than a single Se atom thick. The sequence of structures was found to involve the formation of a 1/4 coverage $(2 \times 2)$ followed by a $(2 \times \sqrt{10})$ at 1/3 coverage and then a $c(2 \times 2)$ at 1/2 coverage. In addition, $Se_8$ rings were observed to form, much the same as $S_8$ rings previously observed for sulfur adsorbed on Au surfaces. At coverages near 0.7, these $Se_8$ rings begin to coalesce into a nearly complete monolayer of Se atoms, but with systematic absences, which roughly correspond to the initial holes in the rings. This structure appeared to have an average unit cell which could be described as $(3 \times \sqrt{10})$.

It has been illustrated further [84, 85] that UPD of Se on Au(111) results in a surface composed of domains of two structures: a $(\sqrt{3} \times \sqrt{3})R30°$ structure at 1/3 coverage and a close-packed layer of square $Se_8$ rings (Fig. 4.8). The $Se_8$ ring structure consists of three domains, each rotated by 120°. Formation of a single structure homogeneously covering the whole surface was proven difficult due to the kinetics of the UPD process. Subsequent deposition of a Cd atomic layer resulted in the formation of a CdSe structure with a $(3 \times 3)$ unit cell and 4/9 coverage of both Cd and Se. The unit cell and coverages were accounted for by a slice out of the bulk wurtzite structure for CdSe laid onto the Au(111) substrate, with twice the surface lattice constant for CdSe matching up with three times the Au interatomic spacing.
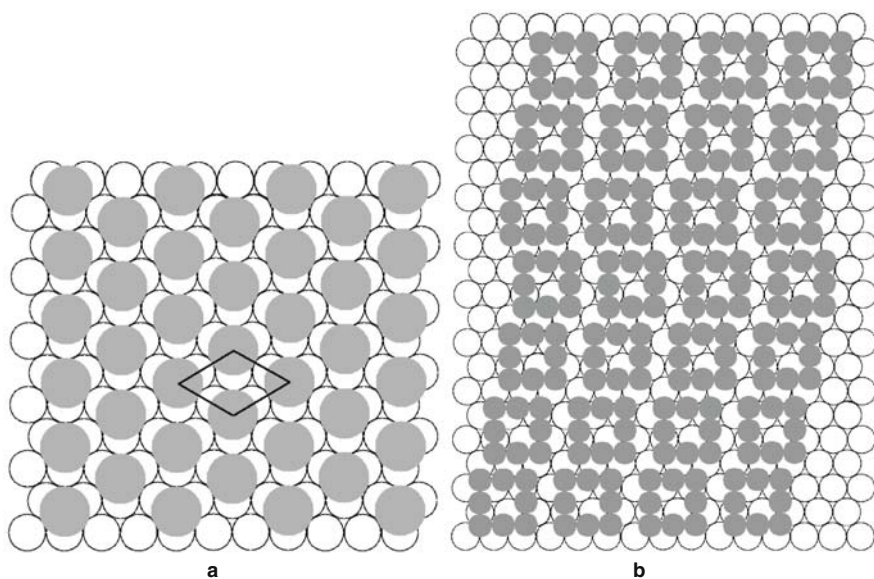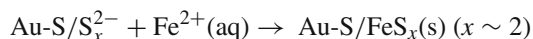


**Fig. 4.8**  Proposed structures for Se, on Au(111): (**a**) $(\sqrt{3} \times \sqrt{3})R30°$ at 1/3 coverage; (**b**) domain structure of $Se_8$ molecules. (Adapted from [85])

STM studies of the Au(110) surface indicated that only the Se $(2 \times 3)$ structure was formed at coverages much below one monolayer and that it was formed homogeneously. At monolayer and higher coverages, a honeycomb structure composed of chains of Se atoms was observed, which at still higher coverages filled in to complete a second Se layer.

UPD of selenium has been studied also on polycrystalline platinum, in aqueous $HClO_4$ solutions of $SeO_2$ by employing cyclic voltammetry, rotating-ring-disk-electrode (RRDE), and electrochemical quartz crystal microbalance (EQCM) techniques [86]. A mechanism for Se monolayer UPD was proposed, consisting in the transfer of four electrons to each Se adatom and the occupation of two active Pt surface sites by each Se. The simultaneous adsorption of non-electroactive molecules such as water and $ClO_4^-$ on the Se monolayer, as well as the formation of platinum oxide, was detected. An older investigation on the voltammetric behavior of selenium in sulfuric and perchloric acid electrolytes on single-crystal Pt basal planes and Pt(332) and Pt(755) stepped surfaces describes the irreversible adsorption of the element [87].

Numerous works have been implemented on tellurium electrochemistry and its adsorption at metal surfaces. The morphological structures of electrodeposited Te layers at various stages of deposition (first UPD, second UPD, and bulk deposition) are now well known [88–93]. As discussed in the previous paragraphs, Stickney and co-workers have carried out detailed characterizations of the first Te monolayer on Au single-crystal surfaces in order to establish the method of electrochemical atomic layer epitaxy of CdTe.

The use of chalcogen-modified surfaces for subsequent deposition of a metal in order to form a metal chalcogenide phase has been addressed by Rajeshwar and co-workers, as exemplified originally by the cathodic reduction of a sulfur-modified polycrystalline Au support for the direct generation of iron sulfide ($FeS_2$) [94]. In this method, the first step was the formation of sulfur adlayers on the Au support surface by potentiodynamically controlled sulfur UPD and stripping, in a sulfide ion solution. Then, in the presence of $Fe^{2+}$ in solution, a thin film of $FeS_2$ was formed in the potential domain of sulfur adlayer electroreduction to polysulfide species. The binary compound (actually two different solid phases of the compound) was seen to precipitate onto the support electrode structure, upon surpassing its solubility product. The overall reaction scheme for this process was considered to comprise the reactions

$$\text{Au-S/S}_n + 2e^- \rightarrow \text{Au-S/S}_x^{2-} \ (x = 2 \text{ to } n)$$

$$\text{Au-S/S}_x^{2-} + Fe^{2+}(aq) \rightarrow \text{Au-S/FeS}_x(s) \ (x \sim 2)$$

As an illustrative example of this method for electrochemical synthesis of sulfide compounds consisted in utilizing a sulfur-modified metal surface as a template for the electrodeposition of metal sulfide films, Tacconi and Rajeshwar described the first attempt to obtain all-electrodeposited *indium sulfide* thin films, by a dual bath procedure [95] (cf. conventional deposition of indium chalcogenides). The
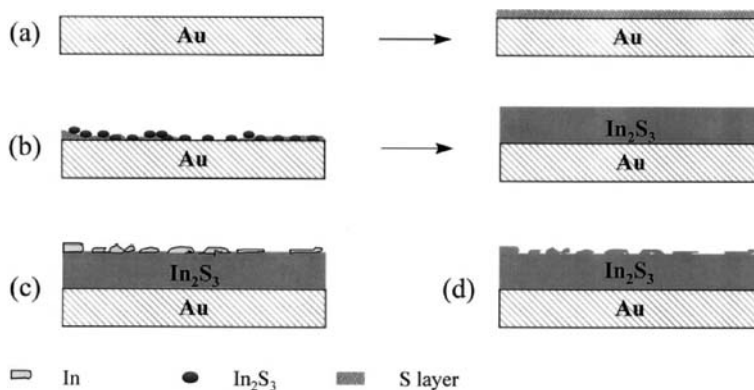
**Fig. 4.9** Schematic illustration of the electrosynthesis procedure using a sulfur-modified gold electrode and alternating exposure to indium- and sulfide ion containing aqueous baths. (**a**) A polycrystalline gold surface is first modified with a sulfur layer. (**b**) Indium is plated onto this layer forming indium sulfide. (**c**) Indium continues to deposit atop the indium sulfide layer. (**d**) Transfer back to a sulfide ion containing bath results in the sulfidization of the residual indium sites. (Reprinted from [95], Copyright 2009, with permission from Elsevier)

method, depicted in Fig. 4.9, was illustrated as follows: multiple (nominally, tens of monolayers) layers of sulfur are first potentiostatically grown on a polycrystalline gold electrode surface from a $Na_2S/Na_2SO_4$ aqueous solution. The electrode is then transferred to an indium ion containing acidic (pH 2.5) $HCl/In_2(SO_4)_3$ electrolyte, where UPD of indium takes place. This results in the formation of an initial indium sulfide layer that has a "catalytic" effect in further deposition of (metallic) indium on the top of it. Finally, the transfer back to the sulfide medium and sulfidization of the incipient indium surface sites yields an indium sulfide film atop the polycrystalline gold support. The product was shown to be photoelectrochemically active n-type indium sulfide, which was assumed to comprise the $\beta$-$In_2S_3$ defect spinel structure.

The UPD of metals onto the surface of chalcogens can be performed not only electrochemically but chemically, i.e., through the use of appropriate redox pairs in solution. Such an approach has been demonstrated by the electroless UPD of bismuth(III) onto the Te surface using the titanium(III)/(IV) redox pair in aqueous solution [96].

Recent considerations of metal UPD on semiconductor surfaces suggest that light-assisted processes gain much significance in the relevant technology. The use of photoinduced UPD as an approach for the preparation of compounds and composite semiconductors either in thin films (layered structures) or in particulate suspensions is a challenging issue that will be outlined promptly.

Rajeshwar and co-workers performed "photocatalytic underpotential deposition" of Cd and Pb onto the surface of Se-modified $TiO_2$ particles to prepare $CdSe/TiO_2$ and $PbSe/TiO_2$ composites [97, 98]. The Se-modified $TiO_2$ particles were prepared themselves by UV illumination of titania particles in a Se(IV)-containing aqueous solution. The photocatalytic UPD of Cd and Pb on the bare $TiO_2$ surface was found

to be either kinetically sluggish (Pb) or thermodynamically unfavorable (Cd), but in the presence of the selenium layer it was made possible. Detailed characterization and model simulations of Se-modified $TiO_2$/electrolyte junctions were also performed [99].

The preparation of immobilized CdTe nanoparticles in the 30–60 nm size range on a Te-modified polycrystalline Au surface was reported recently by a method comprising combination of photocathodic stripping and precipitation [100]. Visible light irradiation of the Te-modified Au surface generated $Te^{2-}$ species in situ, followed by interfacial reaction with added $Cd^{2+}$ ions in a $Na_2SO_4$ electrolyte. The resultant CdTe compound deposited as nanosized particles uniformly dispersed on the Au substrate surface.

The implications of the lead UPD onto chalcogen-modified electrodes have been investigated by Streltsov and co-workers. In one work [101], Pb UPD onto amorphous Se (a-Se) was used to produce nanocomposite films consisting of nanosized PbSe clusters distributed throughout the a-Se matrix. The a-Se sublayer was electrodeposited at constant potential, under illumination, on Au foil electrodes, from acidic $SeO_2$ bath at ambient conditions. Then, lead-doped Se was produced by the metal UPD on the foremost Se layer from a solution containing $Pb(NO_3)_2$. Lead doping resulted in a change of the electronic properties of the Se substrate, manifested by an increase of the charge transfer efficiency both in the film bulk and through the Se/electrolyte interface. This translated to a catalytic effect on Pb UPD in the dark, so that additional submono- and monolayers of PbSe could be readily deposited on the Se(Pb) electrodes. It was argued that modification of the Se surface both with Pb adatoms and PbSe clusters gives rise to electron surface states located in the Se band gap near the valence band edge. Rapid electron exchange between these surface states and the valence band facilitates the dark anodic and cathodic processes that are retarded at the unmodified Se surface due to the presence of a wide space charge region hindering electron transfer. Actually, photoinduced UPD of a Pb monolayer can take place much more readily. Upon illumination of the Se electrode, a significant UPD shift (up to 800 mV) occurs for Pb, while concurrently Se photocorrosion in the Pb(II)-containing solutions results in the formation of PbSe clusters on the Se electrodes [102]. The driving force of both the dark and photoinduced UPD of lead is the formation of strong chemisorption bonds of the Pb adatoms with Se atoms situated at the surface of Se or PbSe particles. The local environment of the Pb adatoms influences their energy state as indicated by the fact that the $Pb_{ad}$ on Se are oxidized at more positive potentials than those on PbSe.

The UPD and anodic oxidation of Pb monolayers on tellurium was investigated also in acidic aqueous solutions of Pb(II) cations and various concentrations of halides (iodide, bromide, and chloride) [103]. The Te substrate was a 0.5 $\mu$m film electrodeposited in a previous step on polycrystalline Au from an acidic $TeO_2$ solution. Particular information on the time–frequency–potential variance of the electrochemical process was obtained by potentiodynamic electrochemical impedance spectroscopy (PDEIS), as it was difficult to apply stationary techniques for accurate characterization, due to a tendency to chemical interaction between the Pb adatoms and the substrate on a time scale of minutes. The impedance

spectroscopy revealed that the Pb UPD on Te comprises an irreversible process, a conclusion supported also by voltammetric measurements. In investigating the effect of halide addition in the electrolyte, the researchers found that iodide has the most pronounced effect as stabilizing the UPD monolayer of Pb against anodic oxidation.

Streltsov and co-workers [104] reported the photoelectrochemical deposition of PbSe and CdTe nanoparticles onto p-type Si(100) wafers or porous $SiO_2$ layers [grown thermally on p-Si(100)] from aqueous solutions containing the bivalent metal cations and the $H_2SeO_3$, $H_2TeO_3$ acids. Deposition was performed at constant cathodic potentials positive to the reversible metal redox values (UPD). It was shown that the UPD of Pb (or Cd) occurs only onto the co-deposited Se (or Te) atoms due to electrons photogenerated in the silicon substrate. Depending on the duration of electrodeposition, distinct chalcogenide particle clusters or polycrystalline film-like layers were obtained on the Si substrates. The PbSe particles formed at ambient conditions were XRD crystalline, whereas crystalline CdTe nanoparticles were obtained only after heating the electrolyte up to 80 °C. The average size of the chalcogenide particles obtained onto p-Si(100) was from 50 to 200 nm for PbSe and 30–80 nm for CdTe. The same group studied the mechanism of PbSe electrocrystallization onto n-type Si(100) wafers from similar baths in terms of the charge transport in the n-Si/PbSe/electrolyte system [105]. Electrocrystallization of PbSe on silicon was observed to occur at more negative potentials than on metal substrates due to the semiconductor nature of Si. According to the researchers, initially 3D Pb and Se nuclei are simultaneously deposited at potentials more negative than the flat band potential of the Si substrate and interact chemically to yield PbSe. Upon formation of the n-Si/PbSe heterostructure, the overvoltage of bulk lead deposition increases, so that further growth of PbSe onto the previously formed nuclei is realized by UPD of Pb and overpotential deposition (OPD) of Se. It was noted that electrodeposition of PbSe on n-Si is irreversible, i.e., anodic stripping does not take place in the dark due to the barrier on the solid interface; oxidation of PbSe on n-Si can be observed only under illumination, when photoholes are generated in the n-Si substrate. We note that PbSe/Si structures have been investigated mostly as produced by MBE, vacuum evaporation, liquid-phase epitaxy (LPE), and pulsed laser deposition. In fact, direct epitaxy of rock salt PbSe on faceted Si substrates is rarely used due to a large lattice mismatch (11.9%) and also thermal expansion mismatch that causes strains in the PbSe layer when the substrate is cooled from the growth temperature down to room temperature. To achieve good epitaxial growth, $CaF_2$ and $BaF_2$ are commonly used as intermediate layers to mitigate the lattice mismatch between PbSe and the Si substrate.

A similar procedure has been used to cathodically deposit lead telluride, PbTe, onto n-Si(100) wafers from an acidic electrolyte containing Pb(II) and Te(IV) species at ambient conditions [106]. Rock salt PbTe particles with size from 80 to 180 nm were obtained, distributed randomly on the Si substrate. The mechanism of PbTe nucleation was considered to involve OPD of 3D islands of tellurium followed by lead UPD. The barrier for anodic current formed at the n-Si/PbTe interface rendered the deposition of PbTe irreversible, although high-efficiency photooxidation

of PbTe could be realized allowing the creation of semiconductor patterns on n-Si by means of selective oxidation at illuminated areas of the electrode surface.

By utilizing the principles of photoelectrochemistry, semiconductor particulate systems, i.e., colloidal semiconductors, have been developed to be used as photocatalysts. In this connection, metal chalcogenides receive considerable attention because of their photocatalytic activity under visible light irradiation. We will refer here to a recent synthesis example involving photodeposition of $In_2Se_3$ and CdSe in a colloidal system using a Se electrode precursor [107]. Nanoparticles of these compounds with average sizes from 40 to 80 nm were synthesized in acidic solutions of the corresponding metal nitrates by a photoelectrochemical technique comprising the illumination of Se electrode at a cathodic potential more positive than the redox potentials of the metals. Selenium film electrodes were prepared by galvanostatic deposition of Se onto suitably treated Au foil from an aqueous solution of selenite. The nanoparticles were obtained both at the Se cathode surface and in the electrolyte bulk as a result of interactions between metal ions ($Me_n^+$) and $H_2Se$ generated photoelectrochemically (Fig. 4.10).

The localization of the chalcogenide nanoparticles was influenced mainly by the concentration of the metal ions in the electrolyte. At metal ion concentrations below 0.01 M, the $In_2Se_3$ and CdSe particles were negatively charged because of $HSe^-$ anion adsorption and repulsed from the electrode surface thus forming colloidal solutions. At metal ion concentration above 0.01 M, selenide particles were positively charged because of $Me_n^+$ adsorption. The positive charge did not allow them to leave the negatively charged electrode surface, which resulted in the formation of $Se/Me_xSe_y$ heterostructures.

A novel method called pulsed light assisted electrodeposition (PLAE), involving the alternate depositions of two elements to form a compound semiconductor, one by electrochemical and the other by photoelectrochemical deposition, should be referred to in this context. Takahashi et al. [108] suggested that high-quality
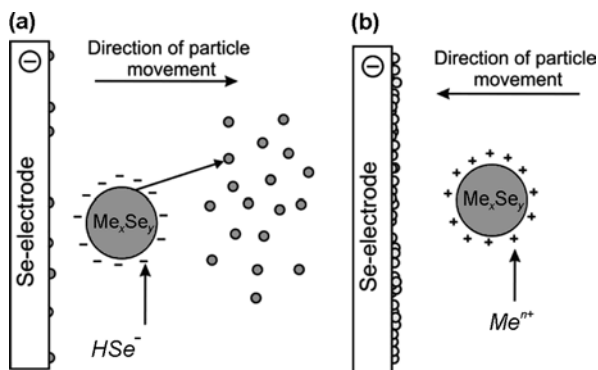


**Fig. 4.10** Scheme of (**a**) colloid solution formation; (**b**) selenides particles deposition onto the electrode surface. (Reproduced from [107], Copyright 2009, with permission from Elsevier)
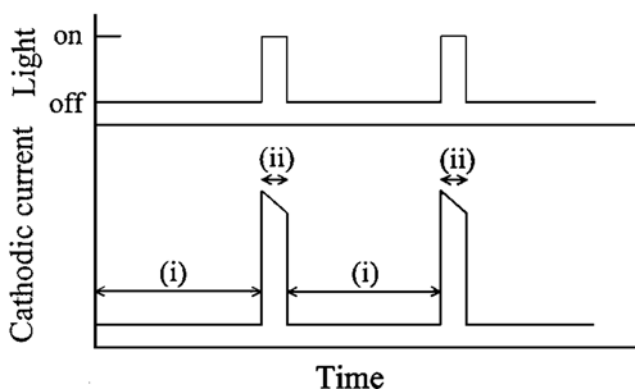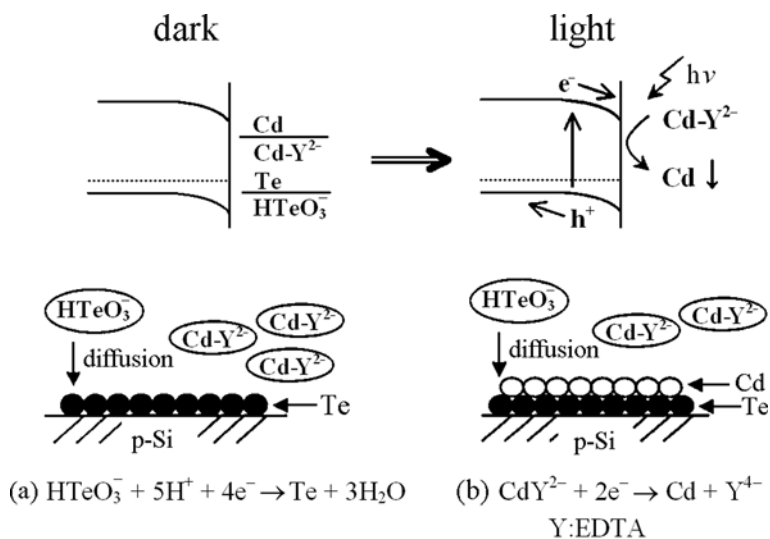
**Fig. 4.11** Schematic representation of the pulsed light assisted electrodeposition of CdTe. (**a**) Deposition of one Te monolayer in the dark; (**b**) deposition of one Cd monolayer under illumination. (Reproduced with permission from [108], Copyright 2009, American Institute of Physics)

and highly oriented epitaxial CdTe films can be grown by electrodeposition onto p-Si(111), assisted by pulsed light, as schematically illustrated in Fig. 4.11.

The deposition takes place from $HTeO_3^{2-}$ and cadmium–EDTA complex solutions at a potential whereat, whilst Te is deposited from $HTeO_3^{2-}$ under a diffusion-limited condition, the Cd–EDTA complex ion is not reduced to metallic Cd. The first step is the "dark" deposition of one monolayer of elemental Te on the p-Si substrate (Fig. 4.11a, i). After completion of this step, as specified by measuring the charge passed, the electrode is illuminated by light with energy higher than the band gap energy of silicon for a limited time. Then conduction band electrons are

generated, which are energetic enough to reduce the Cd–EDTA complex to Cd, so that a cathodic current due to the Cd deposition flows in addition to the cathodic current due to the Te deposition (Fig. 4.11b, ii). The current is controlled by the light intensity and is generally quite higher than for the Te-alone deposition in the dark. Therefore, although Te deposition still takes place under illumination, it can be neglected in comparison with Cd deposition that preferentially occurs on the Te sublayer. The illumination is stopped after the one monolayer of Cd is deposited, which can be determined again by measuring the charge passed. The Te deposition then proceeds on the deposited Cd layer in the dark. These processes should be repeated until the Cd/Te film of the desired thickness is formed. The researchers note that CdTe is expected to be formed by the solid-state reaction.

## 4.4 Electrodeposition of Nanostructures: Size-Quantized Films on Metal Substrates

Thin film coatings of nanocrystalline semiconductors, as collections of quantum dots (QD or Q-dot) attached to a solid surface, resemble in many ways semiconductor colloids dispersed in a liquid or solid phase and can be considered as a subsection of the latter category. The first 3D quantum size effect, on small AgI and CdS colloids, was observed and correctly explained, back in 1967 [109]. However, systematic studies in this field only began in the 1980s.

Size quantization in films of nanocrystalline semiconductors has been demonstrated for many different semiconductors, but a large part of the published work has concentrated, at least originally, on CdSe and CdS. Hodes and co-workers [110, 111] established for the first time a 3D quantum size effect in a coherent film, as exemplified by chemically deposited (CBD) cadmium selenide, and discussed the implications of this effect when found in a thin film as contrasted with colloids and loose aggregates. Size quantization was manifested in the large blue shifts of the optical transmission (absorption) spectra for films with very small crystallites (normally 4–8 nm) due to charge localization in individual crystals; conversely, red shifts of the optical spectra of the films could be correlated with an increase in crystal size. The charge localization clearly implied an electronic isolation between the particles, most probably due to a surface potential arising from a surface insulating layer, unlike the normal intergrain potential barrier between crystallites in a polycrystalline material, resulting from a space charge layer in the crystallites. The CBD CdSe layers, precipitated on glass microscope slide and Ti metal substrates, were compared to CdSe films electrochemically deposited from the same bath [aqueous, alkaline, pH 8–10, solution of $Na_2SeSO_3$, $CdSO_4$, and sodium nitrilotriacetate $N(CH_2COONa)_3$] on $SnO_2$-coated glass. The electrodeposited samples represented "normal" CdSe, possessing properties similar to the large-grained or single-crystal material with a room-temperature band gap of 1.73 eV. However, the chemically deposited layers presented varying blue-shifted band gaps with respect to the normal value, as was established by transmission and photoluminescence spectra. Visually,

a striking difference between CBD and normal CdSe was the change in color of the former and the range of different colors which could be prepared reflecting the varying absorption characteristics. The possibility of direct electrochemical potential and current measurements of (photo) electrochemical reactions on small semiconductor particles was noted in particular.

The same group has investigated all-electrochemical protocols to deposit nanocrystalline semiconductor films exhibiting quantum size effects on noble metal substrates in non-aqueous baths. It was demonstrated originally that wurtzite CdSe nanocrystals can be epitaxially electrodeposited from hot DMSO solutions on a {111}-textured gold substrate [112]. The nanocrystals were shown by TEM to be of ~5 nm in lateral dimensions and of a similar height. Their distribution, i.e., as isolated nanocrystals or aggregates, could be controlled by varying the deposition time, current density, and temperature. A clear ($3 \times 3$) structure was observed (TEM) corresponding to only a –0.6% expansion of the CdSe lattice. The CdSe particles were oriented with their basal, (00.1), plane parallel to the (111)Au surface and possessed a uniform azimuthal orientation on the Au single-crystal grains. Thereby, the epitaxy was attributed to the close lattice match between the relevant spacings, that is $d\{110\}$Au and $a_0$ for wurtzite CdSe, taken in a 3:2 ratio (Fig. 4.12). The epitaxial relationship was investigated and confirmed subsequently by high-resolution electron microscopy imaging and optical diffraction from HREM images [113]. Very few (if any) lattice imperfections were identified in the nanocrystals. Note that in the present case, lattice match is more favorable than for CdS; the previously reported [38] ($3 \times 3$) CdS structure on Au(111) corresponded to a 4% expansion of the CdS lattice. In thicker layers, though, with the CdSe particles not in direct contact with the Au substrate, both the epitaxy and the homogeneous size distribution were lost.

It is well known presently that under certain conditions self-assembled nanocrystal QDs may nucleate spontaneously when a material is grown by an atomistic
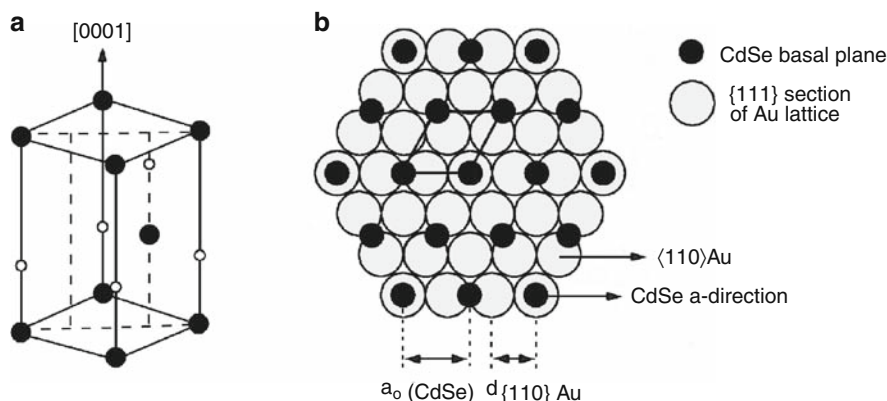


**Fig. 4.12** (**a**) CdSe wurtzite unit cell; (**b**) schematic illustration of a hexagonal (wurtzite) CdSe basal plane on a (111) section of the gold lattice, emphasizing the 2:3 lattice match. Note the [111] Au//(0001)CdSe orientation, with the CdSe a-directions aligned along the (110)Au. The *outlined rhombus* indicates the projection of a CdSe unit cell. (Adapted from [112])

technique (e.g., MBE, MOVPE) on a substrate to which it is not exactly lattice matched. In fact, the resulting strain produces coherently strained islands, usually on top of a 2D "wetting" layer, by a Stranski–Krastanov mode of growth (2D–3D transition). Along this line, Hodes and his group, based on XRD and Raman spectroscopy results, which indicated that epitaxial QDs on Au are coherently strained, suggested that relaxation of mismatch-induced strain energy was the driving force in the CdX/Au system for the transition from 2D heteroepitaxial growth to aggregates of 3D QDs. Experiments on the control of QD size by "misfit tuning" in Cd(Se,Te) QDs on Au supported this finding [114]. The mismatch tuning was accomplished by systematic incorporation of very small amounts of Te into the CdSe QDs, by using a straightforward and easily controlled electrochemical procedure. Thereby, quantum size effects (e.g., variations of the band gap with QD size) could be studied almost independently of chemical composition, since the QD size-control mechanism required only minute changes in their Te/Se content ratio. It was found that increasing the lattice parameter of "CdSe" QDs by incorporation of Te in the lattice led to reduced mismatch with the (111)Au substrate and lower mismatch-induced strain during QD growth, hence to larger QD size. Conversely, partial substitution of Cd by Zn (smaller atomic radius) had the opposite effect, i.e., increased mismatch and larger strain during growth, resulting in smaller QDs. Alternatively, a substrate crystal with larger mismatch was used in order to increase the strain, namely single-crystal {111} Pd, affording a 4.1% mismatch for the 3:2 ratio [115]. In this case, electrodeposition resulted in diffraction-amorphous CdSe (a-CdSe) nanoparticles, with no apparent size limitation, on top of an ultrathin CdSe film, both comprising extremely small (typically 1 nm) ordered CdSe clusters (QDs) in an amorphous CdSe matrix [116]. These "amorphous" CdSe QDs, reported for the first time, were found to exhibit the same short-range order as the crystalline QDs on Au and consisted of < 2.5 nm ordered domains showing a preferred epitaxial relationship with the Pd substrate. Preliminary results of photoelectrochemical measurements indicated that the nanoparticles responded as QDs, showing a blue shift in their energetic gap. It was argued that amorphous QDs are of special interest with respect to the optical and electronic properties expected in highly localized amorphous nanostructures.

    Although lattice mismatch plays a major role in the QD size-control mechanism, deviations of the expected behavior were observed in some cases that were attributed to differences in surface energy and in chemical interactions at the QD/substrate interface. For instance, a rock salt CdSe structure was found to form in the early stages of nanocrystals' electrodeposition from a DMSO solution onto a Cd–Au alloy substrate [117]: this metastable octahedral phase is normally stable only under high pressures, and its lattice parameter, although depending on pressure, is typically 5% smaller than those of the CdSe wurtzite or zinc blende tetrahedral structures. Formation of this phase was thought to be related to the strong interaction between CdSe and Cd–Au and to the compressive surface tension forces of the very thin crystals. Given these complications, and in order to establish the role of the lattice mismatch in determining the QD growth mode, this should be separated from the chemical interaction factor, as any modification adjusting the lattice parameter normally involves a parallel chemical change. This separation was implemented by

mechanically straining the Au substrate via a mica support and depositing CdSe QDs on the strained Au, so that the lattice mismatch between Au and CdSe could be varied without affecting the chemistry at the QD/Au interface [118].

In subsequent works, the nature of the anion of the Cd precursor salt dissolved in the electrolyte was included among the factors that had been identified as controlling the QD size. In particular, the particle dimensions in nanocrystalline CdSe and CdS – electrodeposited galvanostatically from DMSO solutions of elemental Se or S, and a Cd salt, on soda-lime glass coated with conductive tin oxide (NESA glass) – was shown to depend on the anion of the Cd salt [119]. Adsorbing anions resulted in smaller dimensions than non-adsorbing ones. Specifically, the particle size in CdSe and CdS films deposited from baths containing $CdCl_2$ was smaller than that from baths containing $Cd(ClO_2)_4$. Since chloride is a relatively strongly adsorbing anion while perchlorate is a weakly adsorbing one, this suggested that the Cl ions acted as a capping agent on the growing CdSe and CdS. The same effect was obtained if the adsorbing anion was added as a non-Cd salt to the deposition solution. The presence of alkyl phosphine, a strong adsorbent to CdSe and CdS, induced even smaller crystal sizes. The effect was attributed to capping of the growing crystals that prevented their continued growth. Further evidence for this mechanism of size limitation was obtained with electrodeposition of CdTe QDs as will be discussed promptly.

Size quantization of electrochemically or chemically deposited CdTe is more difficult to obtain than for CdS and CdSe due to the lack of suitable tellurium source; hence, few related works have been published. The organic electrodeposition technique used to deposit nanocrystalline CdSe and CdS has not been successful in depositing similar films of CdTe, as it was not possible to dissolve any appreciable amount of elemental Te in DMSO. Most other methods of electroplating CdTe using aqueous $TeO_2$ baths or organic $TeCl_4$ baths result in crystallite sizes of at least 20 nm, hence no size quantization would be expected (the Bohr diameter for CdTe, which indicates this critical size, is ca. 15 nm). However, an older work on CdTe electrodeposition [120], where tri-*n*-butylphosphine (TBP) was used to complex elemental Te in propylene carbonate solution, did suggest smaller crystal sizes; the as-deposited films were reported to be amorphous, and even after annealing at 400 °C, the crystal size was only 50 nm. Using a simplified version of this technique, Mastai and Hodes [121] attempted the electrodeposition of nanocrystalline CdTe films from DMSO solutions containing TBP telluride as a Te source, and cadmium perchlorate, at 100 °C. The phosphine was found to play a double role, enabling dissolution of Te in the organic electrolyte and acting as a capping agent for the CdTe crystals, resulting finally in crystal sizes of few nanometers. The as-obtained films contained about 5–10% Te excess and exhibited small blue shifts (0.1–0.2 eV) in their optical spectra. XRD and SEM characterization suggested a typical crystal size of 8 nm but with a very large size and shape distribution. Pulse reverse plating was used to improve the film stoichiometry, and almost stoichiometric films with average crystal sizes from 4 to 7 nm were obtained, showing even 0.8 eV shifts over the bulk gap, i.e., an energetic band gap of 2.3 eV. Annealing of the films resulted in gradual crystal growth and corresponding spectral red shifts until the bulk band gap was reached. XPS showed phosphorous incorporation in the films. The small crystal size was attributed to capping of the depositing CdTe by strongly adsorbed phosphine groups

and could be controlled by the duty cycle of the plating pulsed current: a longer off-time allowed more efficient capping and therefore smaller nanocrystal size.

For a detailed insight into the work briefly outlined in the last paragraphs, the reader should consult the expert account of Hodes and Rubinstein, concerning research results up to 2000 [122].

A novel, electrochemically assisted method of obtaining semiconductor quantum dots supported on a surface has been introduced by Penner and his group [123]. It comprised a hybrid electrochemical/chemical (E/C) process consisting of electrochemical deposition followed by chemical modification and it was described as a general, rapid, and low-cost solution-phase method for synthesizing supported Q-dots of metal salts.

The E/C synthesis, as exemplified originally for the systems $\beta$-CuI and CdS [124, 125], involved three steps: first, metal nanocrystals (e.g., Cd) of narrow size distribution are electrochemically deposited on a graphite surface from an aqueous solution containing the metal ion ($Cd^{2+}$); second, these particles are oxidized either chemically or electrochemically, thereby transforming, e.g., into $Cd(OH)_2$ particles; and finally, the hydroxyl ($OH^-$) is displaced with another anion (e.g., sulfide, $S^{2-}$) to yield nanoparticles of the compound (CdS). The conversion from metal to metal (hydro-)oxide and then to metal salt occurs on a particle-by-particle basis, so that each metal nanoparticle is converted into a semiconductor nanoparticle. In fact, in a single E/C synthesis operation one metal salt particle is produced for every metal nanoparticle that was formed on the graphite surface during the first step. The procedure is illustrated in the scheme of Fig. 4.13, regarding in particular the preparation of CdS single particle or core–shell nanostructures.
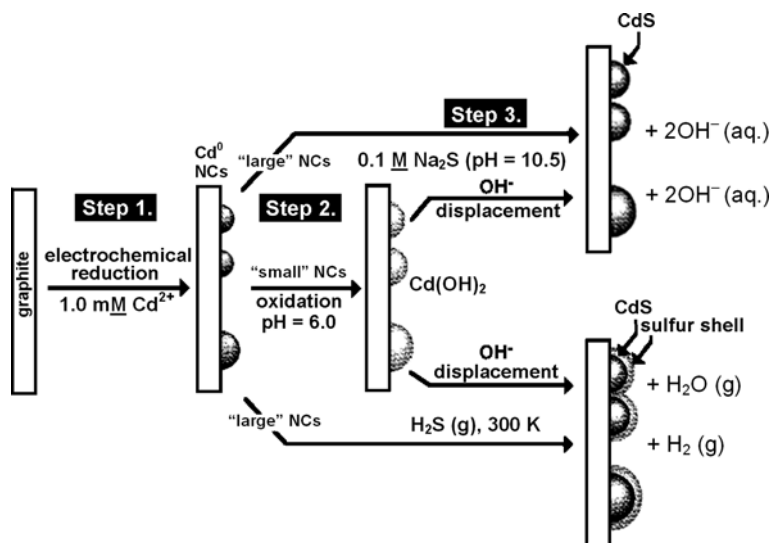


**Fig. 4.13** Electrodeposition of Cd nanoparticles on the graphite surface is followed by electrochemical oxidation and conversion of the oxidized intermediate to CdS or core–shell sulfur–CdS particles. (Reproduced from [125])

   The primary goal of the researchers has been to produce Q-dots possessing all of the attributes of the Q-dots prepared using liquid-phase synthetic methods (that is adjustability of the nanocrystal identity and diameter and size monodispersity) and also the technological utility of Q-dots prepared by MBE (specifically, the deposition of nanocrystals with a defined orientation and an electrical output contact). It was shown that the E/C-synthesized β-CuI and CdS Q-dots were indeed epitaxial with narrow size distribution and strong photoluminescence tunable by the particle size. One of the advantages of the E/C method is that it can be made size selective. The key point is that the size as well as the size dispersion of product nanoparticles are directed actually by the corresponding properties of the metal nanoparticles; therefore the first deposition step assumes special importance.

## 4.5  Directed Electrosynthesis

In the previous two sections, several instances were given of spatially directed or localized growth of semiconductors on metal substrates. Such would be considered, for example, the hybrid E/C synthesis technique of Penner [123], as involving a predetermined distribution of active sites for deposition, or the method of Rajeshwar [97] using Se-modified $TiO_2$ as chemical template for the subsequent photoassisted deposition of metal selenide on the oxide surface. Directed synthesis aims to obtaining materials with prescribed properties and can be attained in effect by using building units with determined characteristics. For example, shape control of nanocrystals may afford efficient 1D electrical transport, which would prove essential for the effectiveness of solar photovoltaic devices built from nanostructured active components (Fig. 4.14); or, fabrication of "core–shell" semiconductor Q-dot structures, with the shell material having a larger band gap, may provide for emission of bright fluorescence at wavelengths determined by the size of the core – such is the case of CdS/ZnS core–shell nanocrystals that can be made to emit in the 460–480 nm range, hence making up blue-light emitters for display applications [126].
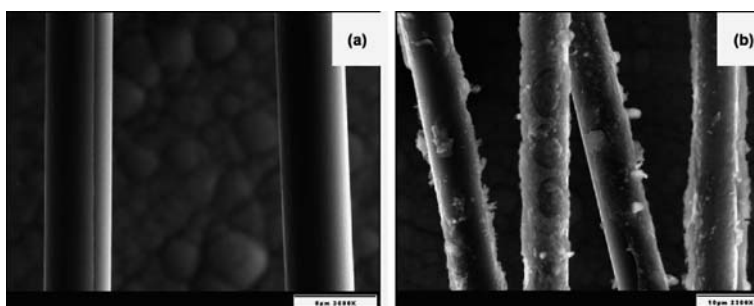


**Fig. 4.14**  SEM micrograph of CVD nickel-coated carbon microfibers (INCOFIBER® 12K20) before (**a**) and after (**b**) the cathodic electrosynthesis of ZnSe on their surfaces (the scale bar is 8 and 10 μm, respectively). Such low-dimensional substrates find application in new-generation photovoltaic solar cells, chemical/biological sensors, and light-emitting devices. (Reprinted from [127], Copyright 2009, with permission from Elsevier)

Spatially directed synthesis implies control of film growth in the lateral dimension and often necessitates the use of an appropriate template defining the areas where nuclei of a new phase can be formed on the substrate surface, inhibiting the rest of the portions of it. Such templates can be either *physical*, e.g., porous alumina membranes (next section) and self-assembled latex sphere arrangements, or *chemical*, e.g., islands of a suitable reagent supported on an electrode, which can be used to direct subsequent growth to targeted areas (often under light assistance), and molecular templates [127].

Colloidal assemblies of monodisperse silica and polystyrene spheres have attracted much attention as physical templates for making photonic materials, because of their size tunability and 3D structure allowing for embedding nanometer-size clusters in such a way as to provide a high density of light-emitting centers [128, 129]. Such template structures can be built up layer by layer through conventional lithography, but processing difficulties limit the formation of more than a few layers. Electrophoretic deposition has been shown to be a suitable method to induce a layer-by-layer aggregation of monodisperse metal and latex particles [130]. Rogach et al. [131] grew colloidal latex crystal layers by electrophoretic deposition on ITO/glass supports from aqueous ethanol emulsions of monodisperse, submicrometer-sized, negatively charged polystyrene spheres. They demonstrated further that electrophoretic deposition can be used as well for the impregnation of these assemblies with luminescent CdTe nanocrystals synthesized chemically in aqueous solution. Such colloidal photonic crystals (artificial opals) present a high refractive index contrast, along with a band gap in the visible/near-infrared spectrum. Promising materials for photonic applications, such as CdS and CdSe, are very reluctant to form 3D microstructures by traditional techniques. Considering that electrodeposition should be an ideal way to fill topologically complex structures (as it starts from deep within the structure and then grows out toward the exposed surfaces, thus filling the interstitial space completely), Braun and Wiltzius [132] showed that these semiconductors can be grown in the form of 3D microporous structures, suitable for photonic applications, by electrochemical deposition within colloidal polystyrene templates.

Molecular templates in the form of self-assembled monolayers (SAMs) are known for their application in molecular recognition of certain sizes, but constitute also an attractive approach to spatially directed semiconductor growth. SAMs formed on electrode surfaces can be used for obtaining highly ordered arrays of Q-dots by electrochemical techniques. A template is created by causing an ionic reaction at an electrolyte–metal interface resulting in the spontaneous assembly of nanostructures on the metal, which then can be used as a mask for mesa-etching or deposition. Choi et al. [133] described electrochemical preparation of CdSe nanoparticles in the cavities of thiolated *b*-cyclodextrin, a template molecule which forms a well-defined SAM on gold electrode surface. A two-step electrosynthesis method was used, similar to that developed earlier by Tacconi and Rajeshwar [95], based on initial deposition of Se on the SAM-modified gold electrode at an appropriate potential, and subsequent reductive stripping of Se to $HSe^-$ in a Se(IV)-free

solution containing $Cd^{2+}$, to produce CdSe. According to SEM imaging, $Se^0$ and CdSe particles of smaller than 60 and 150 nm diameter, respectively, were deposited. Patterned self-assembled monolayers of alkanethiolates on silver have been used also as templates to make ordered 2D arrays of solid CdS nanoclusters [134]. The CdS was grown by ECALE inside the sub-micrometric stripes of hexadecanthiol SAM fabricated by microcontact printing.

### 4.5.1 Porous Templates

Physically templated synthesis on a surface is a method of preparing materials within the pores/voids of a matrix substrate consisting typically of cylindrical tubules of uniform diameter. Organic and inorganic porous matrices in the form of membranes or sheets with various thicknesses, and with pore dimensions in the order of few nm to some hundred nm or a few microns, have been used in order to template the growth of desired structures. Extremely uniform template pores with almost any diameter are obtainable presently, so that highly regular and dimensionally uniform (i.e., monodisperse) structures can be synthesized by deposition of materials in such matrices. In this manner, arrays of, e.g., mesoscopic clusters (2–50 nm) can be fabricated for various purposes. Depending on the filling material and the chemistry of the template pore wall, solid or hollow cylinder arrays may be obtained, e.g., nanofibrils or nanotubules, respectively. After the pore filling/impregnating procedure, the target material may be freed from the template as a stand-alone structure or collected. Alternatively, an ensemble of uniform structures that protrude from a surface may be obtained.

Chemical and electrochemical techniques have been applied for the dimensionally controlled fabrication of a wide variety of materials, such as metals, semiconductors, and conductive polymers, within glass, oxide, and polymer matrices (e.g., [135–137]). Topologically complex structures like zeolites have been used also as 3D matrices [138, 139]. Quantum dots/wires of metals and semiconductors can be grown electrochemically in matrices bound on an electrode surface or being modified electrodes themselves. In these processes, the chemical stability of the template in the working environment, its electronic properties, the uniformity and minimal diameter of the pores, and the pore density are critical factors. Typical templates used in electrochemical synthesis are as follows:

(i) Filtration membranes that have been prepared by the track-etch method [140]. This method entails bombarding a non-porous sheet (standard thickness range from 6 to 20 mm) of the membrane material with nuclear fission fragments to create damaged tracks and then chemically etching these tracks into pores. The resulting membranes contain randomly distributed cylindrical pores of monodispersive dimensions. Commercial membranes are available with pore

diameters as small as 10 nm (pore density ca. $10^9$ pores cm$^{-2}$) and are prepared typically from polycarbonate or polyester.

(ii) Porous aluminum oxide films prepared via the anodization of aluminum metal in strong acids (interchangeably abbreviated as PAA: porous anodic alumina; AAM: anodic alumina membranes; AAO: anodic aluminum oxide). These membranes contain cylindrical pores of uniform diameter, ranging from below 10, to 200 nm, regularly arranged in a hexagonal array. Pore densities as high as $10^{11}$ cm$^{-2}$ can be achieved and typical membrane thickness can range from 10 to 100 mm, with pore lengths from 1 to 50 μm. The pore diameters and densities of AAO films can be easily varied by changing the anodization parameters such as the electrolyte used, its concentration, and the anodizing voltage [141]. Pores in AAMs have been found to be uniform and nearly parallel with respect to the surface normal, unlike the track-etch membranes where the pores are typically tilted. In fact, their isolating, non-connecting pore structure makes the AAO membranes ideal templates for electrochemical deposition of monodispersed nanometer-scale structures. In addition, the optical transparency of the oxide matrix offers the possibility of producing optoelectronic devices based on semiconductor nanostructures. It is now feasible to produce AAMs with pore sizes on the scale of the Bohr diameters of bulk semiconductor excitons, suggesting that quantum confinement effects might be observed in the radial, although not necessarily in the axial, direction; however, such pore sizes are not readily available with commercial AAO membranes.

The main constraint in using AAO sheets directly after anodization for electrochemical purposes is the insulating, dense aluminum oxide barrier layer separating the Al metal substrate and the porous portion of the oxide; this imposes a serious limitation on the use of dc electrodeposition to fill the pores. Further, cracks and defects in the membrane material are detrimental to growth, especially of nanostructures, since deposition primarily occurs in the more accessible cracks, leaving most of the nanopores unfilled. In order to perform electrochemical deposition, the insulating barrier layer is usually removed, and a thin conducting metal film is then evaporated onto the back of the remaining membrane to serve as the cathode for plating. It is possible, however, to employ ac (pulse) electrodeposition without removal of the barrier layer, by utilizing the inherent rectifying properties of the oxide which allow the pores to be filled uniformly without simultaneously depositing material on the surface or into the macroscopic defects of the membrane; since no rectification occurs at defect sites, the deposition and stripping rates are equal, and no material is deposited. Hence, the difficulties associated with cracks are avoided. In this fashion, metals, such as Ag, Co and Fe, and semiconductors, such as CdS, have been deposited into the pores of PAA templates without removing the barrier layer. Surfactants are used when necessary, to facilitate pore filling.

### *4.5.2 Templated and Free-Standing Nanowires and other Forms*

Of the many methods that have been described in the literature for synthesizing nanowires (NWs), there are just three that permit the preparation of free-standing metal NWs with lengths of more than a few microns: (1) template synthesis; (2) fullerene encapsulation; and (3) bulk chemical reduction in micellar solutions. The concept of using a mesoporous membrane as a template for electroplating mesoscopic metal fibrils was first demonstrated in 1970 by Possin [142], who produced metal wires (Sn, In, Zn) with diameters as small as 40 nm and about 15 $\mu$m long in an insulating track-etched mica matrix. Since then, electrochemical methods were utilized broadly to accomplish the formation of highly anisotropic, aligned metal particle/wire arrays into the pores of a template. The unusual optical and magnetic properties of the produced structures motivated further work in the field. Electrodeposition of nanostructures into the pores of nanophase membrane templates has been demonstrated by Martin and co-workers [143, 144] who studied the optical properties of template-synthesized materials and also prepared arrays of micro- and nanoscopic electrodes for fundamental and applied electrochemistry. Chakarvarti and Vetter [145] presented the first templated synthesis of semiconductors, in particular semiconductor–metal heterostructures (Se–Cu) and Se microtubules, by electrodeposition in the etched 2.5 $\mu$m pores of a nuclear track filter.

Patterned arrays/aggregates of semiconductor microcylinders and nanowires have been electrochemically prepared with the prospect of advancing the fabrication of optical, electronic, and electrochemical devices, such as diodes, LEDs, LDs, high-resolution optical detectors, high-definition displays, solar cells, and chemical sensors. In the last 15 years, most of the work in this direction has involved electrodeposition within the pores of porous alumina membranes. The II–VI type compounds, as being especially pertinent to electrodeposition, have been the almost exclusive object of investigation in this field. The key point in the early works was that the restricted dimensions of the membrane templates used are found to eliminate the fractal-like cauliflower morphology often observed in electrodeposited II–VI materials. On these grounds, electrodeposition directly into a suitable template appeared to be a simple and efficient method of producing semiconductor NW arrays with well-controlled crystalline structure.

Nanowires of CdS, CdSe, and CdTe have been prepared either by dc or ac deposition in PAA membranes from aqueous and non-aqueous electrolytes. Klein et al. [146] were the first to demonstrate the electrodeposition of polycrystalline chalcogenide NWs in 1993, by producing cadmium selenide/telluride wires into the 0.2 $\mu$m pores of Anopore AAO membranes (brand name from Anotech Separations, Ltd) (Fig. 4.15). Arrays of diodes in which a CdSe segment was electrochemically grafted onto a gold segment were fabricated. These CdSe/gold NWs showed rectification, qualitatively as expected for Schottky barriers.

In order to perform the electrodeposition, first a 3 nm layer of Au was sputter-coated onto one side of the ca. 50 $\mu$m thick membrane to form a conductive surface. A Ni substrate layer was then electrochemically plated on top of the Au, as to

**Fig. 4.15** SEM image of a CdSe diode array electrodeposited on a Ni substrate, using an Anopore membrane template. (Reprinted with permission from [146], Copyright 2009, American Chemical Society)
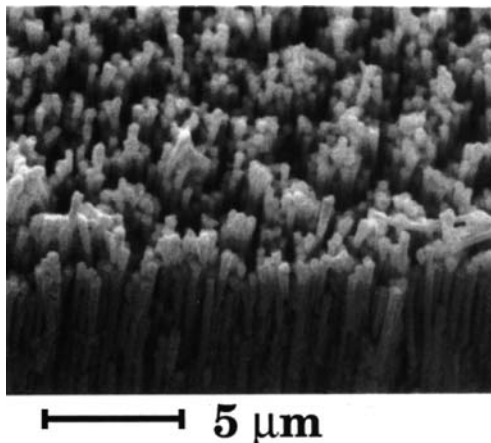


completely cover one side of the membrane and partially fill the pores. Cadmium selenide was deposited using an ac technique from a typical acidic aqueous solution of selenite. The crystal structure of CdSe was found to be primarily zinc blende, with a crystallite size in the order of 200–300 nm. After deposition, the membrane was removed by soaking the electrode in caustic soda. Graded CdSe/CdTe heterojunctions were prepared by initially depositing a predetermined amount of CdSe within the Anopore template and afterward an equal amount (as determined by coulometer) of CdTe from a typical aqueous solution of tellurite. The as-deposited CdTe was non-crystalline. The main conclusion of this work was that template-restricted growth provides an improved morphology of electrodeposited semiconductors, although it did not appear to yield enhanced electronic properties at that point. Pena et al. [147] used a similar approach to synthesize ensembles of gold/CdSe/gold nanowires that showed photoconductivity. Highly ordered polycrystalline CdSe NWs with uniform diameters of about 60 nm were synthesized by dc electrodeposition in PAA membrane from an alkaline (pH 9) aqueous solution containing $CdCl_2$ and $SeO_2$ [148]. The CdSe NWs were stoichiometric and adopted a wurtzite structure after annealing in argon at 400 °C.

Routkevitch et al. [149] described the ac electrodeposition technique for fabricating arrays of uniform CdS NWs with lengths up to 1 $\mu$m and diameters as small as 9 nm, directly into the pores of AAO films, from an electrolyte containing $Cd^{2+}$ and sulfur in DMSO. Although different in execution, the technique was similar in scope to those used by Chakarvarti and Vetter and Klein et al. However, in the present work the employed membranes contained pores of considerably smaller dimensions, close to the Bohr diameter of the 1s exciton in CdS, which is estimated to be approximately 4 nm. The deposited material was found to be hexagonal CdS with the crystallographic $c$-axis preferentially oriented along the length of the pore. On average, the thicker wires (with diameters larger than 12 nm) consisted of a large number of crystallites in the axial direction and rather few in the radial direction,

but the thinner wires (with diameters less than 12 nm) were single-crystal structures. The effects of annealing on the crystallinity of the deposited semiconductor were investigated. Following the previous method, CdS NWs were obtained in PAA templates with 10 nm pore diameter and about 1 $\mu$m pore length, either by direct deposition in the pores or after an initial Ag deposition [150]. It was concluded that CdS grew epitaxially on the silver surface into the pores of the substrate. However, the epitaxial growth did not continue to the same degree over the length of the wire, but rather was most efficient closer to the surface.

Actually, the electrochemical template synthesis of CdS nanowires via PAA membranes is considered to be rather complicated [151], and uniformity of the NWs when transferred away from the templates is hard to control unless special design is integrated [152]. In their investigation on the electrochemical fabrication of low-cost polymer solar cells in ambient environment, Xi et al. [153] showed recently that vertically aligned CdS *nanorods* can be grown in a self-assembling manner by template-free electrochemical deposition. The addition of vertically aligned semiconductor nanorods to polymer solar cells was considered important in terms of improvement of their photovoltaic characteristics, as the interface between a conjugated polymer and semiconductor should provide an efficient charge separation for photogenerated excitons. The nanorods were deposited at constant potential on glass substrates covered by a 1 nm thick titanium layer and a 10 nm thick gold layer, from an acidic aqueous (pH 1.8) solution of cadmium sulfate and potassium thiocyanate, at 70 °C. A yellowish film containing CdS nanorods of a wurtzite structure oriented along the [001] direction was observed after several hours of deposition. The dimension of the nanorods was tailored by experimental conditions with diameter from 20 to 40 nm and height from 100 to 300 nm. To prepare hybrid films for photovoltaic application, the conjugated polymer polybithiophene was deposited into the nanorod arrays by in situ electrochemical polymerization until the total film thickness reached approximately 200 nm. The film was then covered by an evaporated Ca/Al metal layer contact. The nanohybrid films with the Ca/Al cathode and Au anode showed a rectification ratio as high as $10^3$, a large open-circuit voltage of 0.84 V, and a relatively low short-circuit current under white light illumination.

Recently it was reported [154] that CdSe self-assembled nanowires could be grown electrochemically in template-free and surfactant-free conditions, from a classical acidic selenite electrolyte on ITO glass at constant current. The morphology of the CdSe deposit was seen to change during electrodeposition from primarily amorphous spherical grains to web-like and then to nanowire-like structures as the deposition time increased from 500 to 1,000 and then to 1,500 s, respectively. Annealing at 473 K of the 1,500 s samples led to an aggregate of, 20–40 nm in diameter, crystalline NWs randomly distributed on the substrate.

Non-aqueous electrolytes have been used for the preparation of CdS, CdSe, and CdTe nanowire arrays by dc electrodeposition in porous AAO templates of various pore diameters [155, 156]. For instance, CdSe NW arrays with uniform wurtzite crystal structure were fabricated from a non-aqueous DMSO solution containing $CdCl_2$ and elemental Se. The NWs were shown to be of uniform length (2–15 $\mu$m) and diameter (about 20 nm). The *c*-axis, [00.2], of the grown

hexagonal crystals was preferentially aligned along the direction normal to the substrate. The dimension of the as-oriented crystallite domains of the NWs in the radial direction was very close to the pore size of the AAO template used. Both the crystallite dimension along the [00.2] axis and the crystallite orientation were reported to be larger than in the CdS NWs which Routkevitch et al. [149] fabricated by ac electrolysis.

Thin film nanostructures of the III–VI compound $In_2Se_3$ were obtained inside the pores (200 nm) of commercial polycarbonate membrane by automated ECALE methodology at room temperature [157]. Buffered solutions with millimolar concentrations of $In_2(SO_4)_3$ (pH 3.0) and $SeO_2$ (pH 5.5) were used. The atomic ratio of Se/In in the deposited films was found to be 3/2. Band gaps from FTIR reflection absorption measurements were found to be 1.73 eV. AFM imaging showed that the deposits consist of 100 nm crystallites.

There is a growing interest presently in nanostructured thermoelectric materials, such as nanowires, superlattice thin films, and quantum dots, because of the remarkable efficiency improvement that can be achieved as compared to their bulk counterparts, due to quantum confinement effects. Binary and ternary tellurides of Bi and Sb, i.e., $Bi_2Te_3$, $Sb_2Te_3$, and alloys thereof ($Bi_{0.5}Sb_{1.5}Te_3$), are among the preferred thermoelectric materials for applications near room temperature, which makes them best targets for synthesis in nanostructured forms. Martin-Gonzalez et al. [158] managed to fabricate $(Bi_{1-x}Sb_x)_2Te_3$ NWs by electrodeposition on porous AAO from an acidic (1 M $HNO_3$) solution of $TeO_2$, $Bi^{3+}$, and $SbO^+$, in which tartaric acid was introduced as a complexing agent to increase the Sb solubility by forming Sb-tartaric complexes. Optimal deposition conditions for film preparation were determined first with Ag electrodes and used as starting point for deposition of the NWs in the alumina templates. Voltammetric studies showed that the electrodeposition mechanism of the ternary system was similar to that of $Bi_2Te_3$, that is, UPD of both Bi and Sb (Chap. 3). Thick (200 nm) and thinner (40 nm) nanowire arrays with EDAX composition $Bi_{0.7}Sb_{1.4}Te_{2.9}$ and $Bi_{0.6}Sb_{1.6}Te_{2.8}$, respectively, were formed on commercial and laboratory-made AAO porous substrates. Pore filling of approximately 80% was accomplished.

Jin et al. [159] synthesized structurally uniform and single-crystalline $Sb_2Te_3$ nanowires, 50 nm in diameter, by galvanostatic electrodeposition on self-made porous AAO membrane templates, from an acidic nitrate bath of $HTeO_2^+$ and $SbO^+$, with citric acid as a complexing agent. The produced NWs grew highly preferentially along (11.0) planes and the pore filling approached 100%.

Underscoring the theoretical prediction that further enhancement of the thermoelectric figure of merit can be achieved with superlattice nanowires (zero-dimensional) rather than conventional nanowires (1D) or superlattice thin films (2D), Yoo et al. [160] developed a simple electrodeposition technique to synthesize $Bi_2Te_3/(Bi_{1-x}Sb_x)_2Te_3$ superlattice NWs, on a polycarbonate membrane template from a single acidic nitrate solution of $TeO_2$, $Bi^{3+}$, and $SbO^+$ (tartrate). The method was based on the application of a waveform potential profile alternating between $-20$ and $-100$ mV vs. SCE. At $-20$ mV, $Bi_2Te_3$ with a small amount of Sb

incorporation (< 3 at.%) was deposited; at $-100$ mV, $(Bi_{0.3}Sb_{0.7})_2Te_3$ was obtained, which was close to the best bulk composition $Bi_{0.5}Sb_{1.5}Te_3$. The average diameter of the NWs was approximately 50 nm, as predetermined by the pore size of the PC membrane. The composition and length of each nanowire segment were precisely controlled by adjusting deposition potentials and time.

Within the scope of thermoelectric nanostructures, Sima et al. [161] prepared nanorod (fibril) and microtube (tubule) arrays of $PbSe_{1-x}Te_x$ by potentiostatic electrodeposition from nitric acid solutions of $Pb(NO_3)_2$, $H_2SeO_3$, and $TeO_2$, using a ~30 µm thick polycarbonate track-etch membrane, with pores 100–2,000 nm in diameter, as template (Cu supported). After electrodeposition the polymer membrane was dissolved in $CH_2Cl_2$. Solid rods were obtained in membranes with small pores, and hollow tubes in those with large pores. The formation of microtubes rather than nanorods in the larger pores was attributed to the higher deposition current.

Lead sulfide, PbS, nanoparticulate thin films having pancake-like geometry and exhibiting 1D quantum confinement, as controlled by the lowest dimension of the particles, have been synthesized by cathodic electrodeposition on ITO/glass and titanium electrodes from a pH 0.62 solution containing $Pb(NO_3)_2$ and $Na_2S_2O_3$ [162].

Semiconductor *nanoribbons* have attracted much attention ever since the discovery of silicon and oxide nanoribbons. In the past few years, gas sensors, microcavity lasers, field-effect transistors, optical waveguides, resonators, and generators have been fabricated using single nanoribbons as building blocks. Single-crystalline CuTe nanoribbons, which might be used as building blocks for fabricating optoelectronic nanodevices, have been synthesized recently for the first time by a simple electrodeposition method at low temperature (typically 85 °C) on ITO glass substrates, from alkaline (pH 13) aqueous solutions of $TeO_2$, $CuSO_4$, and $NH_3$ [163]. No template or capping agent was used during the growth process. The CuTe nanoribbons were orthorhombic and grew along the [010] direction. It was suggested that the ribbon-like morphology of the CuTe resulted from the synergistic effect of the anisotropic crystal structure of CuTe and the thermodynamics of the crystal growth process, as has been proved in the formation of ZnO nanoribbons [164]. In fact, the arrangement of the atoms in CuTe crystal can be described as a typical layered structure. One Cu atom is distorted and tetrahedrally coordinated to four Te atoms, and one Te atom is one-sided coordinated to four Cu atoms. The Cu–Cu distances are 2.64 Å, which indicates a weak metallic bond between the Cu atoms. Under a suitable temperature and environment, such layered structure of CuTe crystal would prefer growing in a certain plane and finally form a lamelliform morphology.

Electrochemical preparation studies on low-dimensional structures of ternary or higher order compounds have appeared in the last few years. For example, whiskers of the quasi-1D copper(I) sulfide series $KCu_{7-x}S_4$ ($0 \leq x \leq 0.34$) were grown by employing electrochemical methods via anodic dissolution of copper electrodes, at 110 °C in ethylenediamine solution of polysulfide $K_2S_n$ ($n = 5, 6$) electrolytes and, in some cases, CuCl [165].

### *4.5.3 Electrochemical Step Edge Decoration*

The different sites where nuclei are formed on a surface are thermodynamically not equivalent. In fact, the formation of stable nuclei is more favorable at surface inhomogeneities like step edges than on an atomically flat ideal surface. Hence it can be controlled by the adjusted supersaturation, i.e., the electrode potential. This feature is exploited for example in the electrochemical growth of nanoclusters on graphite surfaces [166, 167] or of nanowires with lengths of several micrometers at the step edges of graphite substrates, being decorated at the lowest supersaturation before nuclei are formed at other surface inhomogeneities [168]. A preparation technique utilizing the effect of selective nucleation at the step edges of a surface has been suitably named "electrochemical step edge decoration" (ESED).

Penner and his group [169, 170] managed to produce hemicylindrical in cross section, free-standing molybdenum nanowires with diameters ranging from 10 nm to 1 μm and having lengths of up to 500 μm, by employing an electrochemical/chemical (E/C) two-step process involving the electrodeposition of molybdenum dioxide ($MoO_2$) NWs on a highly oriented pyrolytic graphite (HOPG) surface followed by reduction at 500 °C to form molybdenum metal. On the basis of these results, they reported subsequently the first synthesis of non-fullerene, polycrystalline $MoS_2$ nanowires and nanoribbons [171]. The E/C synthesis relied on the step edge selective electrodeposition of $MoO_x$ to form hemicylindrical nanowires on the basal plane of a HOPG crystal, followed by the conversion of these NWs to $MoS_2$ in $H_2S$ at elevated temperatures.

In the first step, amorphous $MoO_x$ nanowires were electrodeposited by ESED according to the reaction

$$MoO_4^{2-} + (4 - x)\,H_2O + (6 - 2x)e^- \rightarrow MoO_x + (8 - 2x)OH^-$$
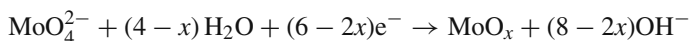
In the second step, these $MoO_x$ NWs were converted to $MoS_2$ by exposure to $H_2S$ within either of two temperature regimes (500–700 °C or 800–1,000 °C) according to the reaction (for $x = 2$)

$$MoO_2 + 2H_2S \rightarrow MoS_2 + 2H_2O$$
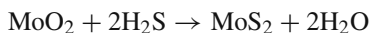
As indicated in Fig. 4.16, conversion from $MoO_x$ to $MoS_2$ within these two temperature regimes produced wires with different morphologies: Conversion of $MoO_x$ wires at 500–700 °C yielded hemicylindrical wires that were nearly identical in diameter to the $MoO_x$ precursor wires. These low-temperature or LT $MoS_2$ wires were composed of multiple, interwoven 2H-structure $MoS_2$ strands with widths of 7–16 nm and lengths of up to hundreds of nanometers. At the higher temperatures (HT) of 800–1,000 °C, conversion to $MoS_2$ was followed by rapid grain growth that produced highly crystalline HT $MoS_2$ wires or "ribbons" that were hundreds of microns in length, 50–800 nm in width, and 3–100 nm in thickness (Fig. 4.17).
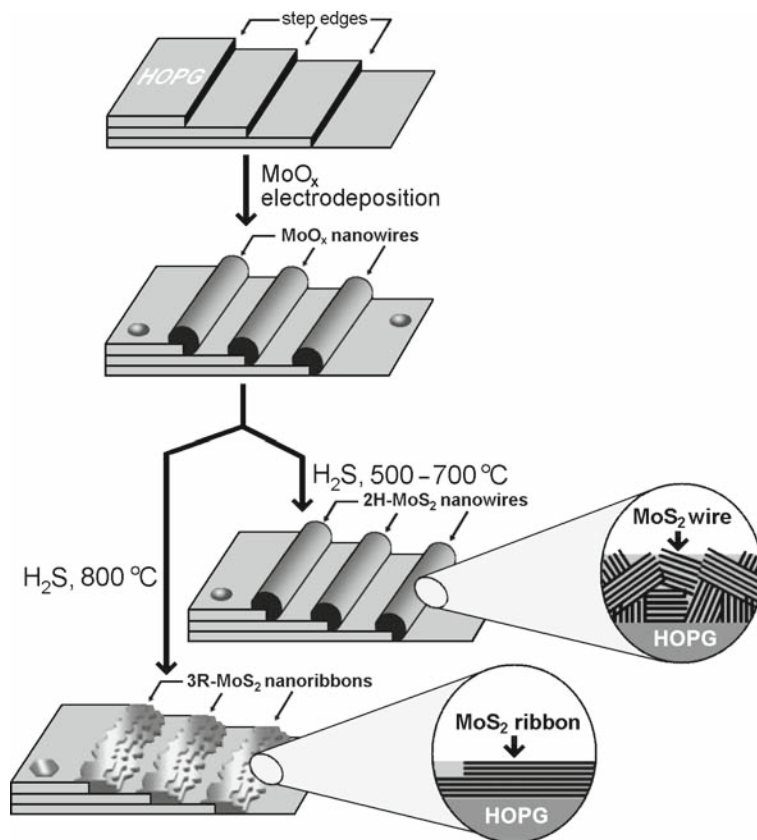
**Fig. 4.16** Schematic representation of the E/C method for synthesizing polycrystalline MoS$_2$ nanowires and nanoribbons on graphite surfaces. (Reproduced in gray scale with permission from [171]. Copyright 2009, American Chemical Society)
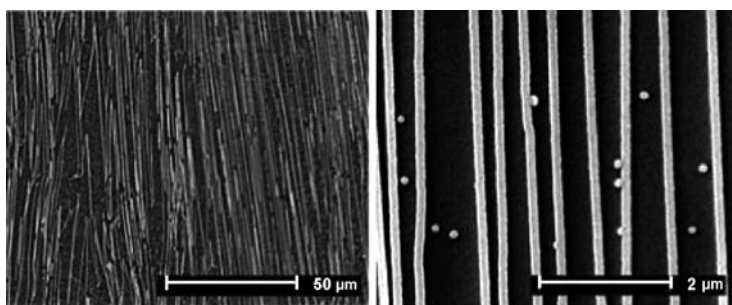


**Fig. 4.17** SEM image of HT (high-temperature) MoS$_2$ nanowire arrays on the adhesive surface at two magnifications. The surface was coated with 10 nm of gold for SEM imaging. (Reprinted with permission from [171], Copyright 2009, American Chemical Society)

According to absorption spectroscopy, these nanoribbons were composed of 3R-$MoS_2$. The E/C synthesis of $MoS_2$ wires and ribbons was size selective: control over the wire or ribbon size was provided by control of the $MoO_x$ nanowire dimensions, which in turn were controlled using the electrodeposition potential and time in the first step of the synthesis.

ESED was used recently in combination with a cyclic electrodeposition/stripping process for the preparation of polycrystalline CdSe NWs composed of many zinc blende CdSe nanocrystallites, on HOPG surfaces, from standard acidic selenite plating baths [172]. The NWs were 30–300 nm in diameter and their length could exceed 100 $\mu$m. They were organized into parallel arrays on the HOPG surface, mimicking the organization of step edges present on these surfaces.

ESED has been applied also to produce polycrystalline nanowires of the thermoelectric material $Bi_2Te_3$ on HOPG electrodes, directly by one-step electrodeposition from an aqueous telluride solution of $Bi^{3+}$ [173]. The NWs were in the 100–300 nm diameter range narrowly dispersed in diameter, more than 100 $\mu$m in length, and organized into parallel arrays containing hundreds of wires. Smaller NWs, with diameters down to 30 nm, with a narrower diameter distribution were obtained by electrooxidation of 150 nm diameter $Bi_2Te_3$ NWs under conditions of kinetic control. These NWs retained a $Bi_2Te_3$ core covered by a thin surface layer composed of Bi and Te oxides. The oxidation process was seen to unexpectedly improve the uniformity of $Bi_2Te_3$ NWs. The researchers noted that in contrast to template synthesis methods, ESED produces nanowires that are much longer – more than 100 $\mu$m in length. This attribute was considered to be essential to the fabrication of high-performance thermoelectric devices, as also was the horizontal orientation of the ESED NWs on the electrode surface and the ease with which they might be transferred to an electrically and thermally insulating surface. After transfer, metal contacts might be readily deposited onto ensembles of these NWs, expediting the measurement of thermal properties. The analogous measurements for template-synthesized nanowires, oriented vertically on the electrode and encapsulated by the template, have proven to be much more difficult.

# References

1. Budevski E, Staikov G, Lorenz WJ (1996) Electrochemical phase formation and growth. Wiley-VCH, Weinheim
2. Obretenov W, Bostanov V, Popov V (1982) Stochastic character of two-dimensional nucleation in the case of electrocrystallization of silver. J Electroanal Chem 132: 273–276
3. Hugelmann M, Hugelmann P, Lorenz WJ, Schindler W (2005) Nanoelectrochemistry and nanophysics at electrochemical interfaces. Surf Sci 597: 156–172
4. Sircar P (1988) Growth of CdTe on GaAs by electrodeposition from an aqueous electrolyte. Appl Phys Lett 53: 1184–1185
5. Lincot D, Kampmann A, Mokili B, Vedel J, Cortes R, Froment M (1995) Epitaxial electrodeposition of CdTe films on InP from aqueous solutions: Role of a chemically deposited CdS intermediate layer. Appl Phys Lett 67: 2355–2357
6. Cachet H, Cortes R, Froment M, Maurin G (1997) Epitaxial electrodeposition of cadmium selenide thin films on indium phosphide single crystal. J Solid State Electrochem 1: 100–107

7. Cachet H, Cortes R, Froment M, Maurin G (1999) Epitaxial growth of electrodeposited cadmium selenide on (111) gallium arsenide. Philos Mag Lett 79/10: 837–840

8. Muthuvel M, Stickney JL (2006) CdTe Electrodeposition on InP(100) via Electrochemical Atomic Layer Epitaxy (EC-ALE): Studies Using UHV-EC. Langmuir 22: 5504–5508

9. Streltsov EA, Osipovich NP, Ivashkevich LS, Lyakhov AS (1999) Effect of Cd(II) on electrodeposition of textured PbSe. Electrochim Acta 44: 2645–2652

10. Beaunier L, Cachet H, Cortes R, Froment M (2000) Electrodeposition of PbSe epitaxial films on (111) InP. Electrochem Commun 2: 508–510

11. Beaunier L, Cachet H, Froment M (2001) Epitaxial electrodeposition of lead selenide films on indium phosphide single crystals. Mater Sci Semicond Process 4: 433–436

12. Froment M, Beaunier L, Cachet H, Etcheberry A (2003) Role of cadmium on epitaxial growth of PbSe on InP single crystals. J Electrochem Soc 150: C89–C94

13. Beaunier L, Cachet H, Cortes R, Froment M (2002) Epitaxial electrodeposition of lead telluride films on indium phosphide single crystals. J Electroanal Chem 532: 215–218

14. Riveros G, Guillemoles JF, Lincot D, Meier HG, Froment M, Bernard MC, Cortes R (2002) Electrodeposition of epitaxial ZnSe films on InP and GaAs from an aqueous zinc-sulfate-selenosulfate solution. Adv Mater 14: 1286–1290

15. Henríquez R, Gómez H, Riveros G, Guillemoles JF, Froment M, Lincot D (2004) Electrochemical deposition of ZnSe from dimethyl sulfoxide solution and characterization of epitaxial growth. J Phys Chem B 108: 13191–13199

16. Bouroushian M, Kosanovic T, Spyrellis N (2005) Oriented [111] ZnSe electrodeposits grown on polycrystalline CdSe substrates. J Cryst Growth 277: 335–344

17. Golan Y, Alperson B, Hutchison JL, Hodes G, Rubinstein I (1997) Electrodeposited quantum dots: Coherent nanocrystalline CdSe on oriented polycrystalline Au films. Adv Mater 9: 236–238

18. Fisher JM, Berlouis LEA, Sawers LJM, MacDonald SM, Affrosman S, Diskett DJ, Astles MG (1994) Growth and characterization of electrodeposited films of cadmium telluride on silicon. J Cryst Growth 138: 86–93

19. Jackson F, Berlouis LEA, Rocabois P (1996) Layer-by-layer electrodeposition of cadmium telluride onto silicon. J Cryst Growth 159: 200–204

20. Sugimoto Y, Peter LM (1995) Cathodic electrodeposition of CdTe on n-type monocrystalline silicon. J Electroanal Chem 381: 251–255

21. Sugimoto Y, Peter LM (1995) Photoeffects during cathodic electrodeposition of CdTe. J Electroanal Chem 386: 183–188

22. Ein-Eli Y, Starosvetsky D (2003) Silicon texturing in alkaline media conducted under extreme negative potentials. Electrochem Solid State Lett 6: C47–C50

23. Gómez H, Henríquez R, Schrebler R, Riveros G, Leinen D, Ramos-Barrado JR, Dalchiele EA (2004) A soft-solution electrochemical processing technique for preparing CdTe/n-Si(100) heterostructures. J Electroanal Chem 574: 113–122

24. Allongue P, Villeneuve De CH, Morin S, Boukherroub R, Wayner DDM (2000) The preparation of flat H–Si(111) surfaces in 40% NH$_4$F revisited. Electrochim Acta 45: 4591–4598

25. Gómez H, Henríquez R, Schrebler R, Córdova R, Ramírez D, Riveros G, Dalchiele EA (2005) Electrodeposition of CdTe thin films onto n-Si(100): nucleation and growth mechanisms. Electrochim Acta 50: 1299–1305

26. Goodman CHL, Pessa MV (1986) Atomic layer epitaxy. J Appl Phys 60: R65–R81

27. Gregory BW, Stickney JL (1991) Electrochemical atomic layer epitaxy (ECALE). J Electroanal Chem 300: 543–561

28. Gregory BW, Suggs DW, Stickney JL (1991) Conditions for the deposition of CdTe by electrochemical atomic layer epitaxy. J Electrochem Soc 138: 1279–1284

29. Suggs DW, Stickney JL (1991) Characterization of atomic layers of tellurium electrodeposited on the low-index planes of gold. J Phys Chem 95: 10056–64

30. Suggs DW, Stickney JL (1993) Studies of the structures formed by the alternated electrodeposition of atomic layers of Cd and Te on the low-index planes of Au. I. LEED and Auger studies. Surf Sci 290: 362–374

31. Suggs DW, Stickney JL (1993) Studies of the surface structures formed by the alternated electrodeposition of Cd and Te on the low-index planes of Au. II. STM studies. Surf Sci 290: 375–387
32. Varazo K, Lay MD, Sorenson TA, Stickney JL (2002) Formation of the first monolayers of CdTe on Au(111) by electrochemical atomic layer epitaxy (EC-ALE): studied by LEED, Auger, XPS, and in-situ STM. J Electroanal Chem 522: 104–114
33. Hayden BE, Nandhakumar I (1997) In-situ STM Study of Te UPD layers on low index planes of gold. J Phys Chem B 101: 7751–7757
34. Hayden BE, Nandhakumar I (1998) In situ STM study of CdTe ECALE bilayers on gold. J Phys Chem B 102: 4897–4905
35. Forni F, Innocenti M, Pezzatini G, Foresti ML (2000) Electrochemical aspects of CdTe growth on the face (111) of silver by ECALE. Electrochim Acta 45: 3225–3231
36. Colletti LP, Teklay D, Stickney JL (1994) Thin-layer electrochemical studies of the oxidative underpotential deposition of sulfur and its application to the electrochemical atomic layer epitaxy deposition of CdS. J Electroanal Chem 369: 145–152
37. Demir U, Shannon C (1996) Electrochemistry of Cd at $(3 \times 3)$R30°-S/Au(111): Kinetics of structural changes in CdS monolayers. Langmuir 12: 6091–6097
38. Demir U, Shannon C (1994) A scanning tunneling microscopy study of electrochemically grown cadmium sulfide monolayers on Au(111). Langmuir 10: 2794–2799
39. Demir U, Shannon C (1996) Reconstruction of cadmium sulfide monolayers on Au(100). Langmuir 12: 594–596
40. Gichuhi A, Boone BE, Demir U, Shannon C (1998) Electrochemistry of S Adlayers at underpotentially deposited Cd on Au(111): Implications for the electrosynthesis of high-quality CdS thin films. J Phys Chem B 102: 6499–6506
41. Boone BE, Shannon C (1996) Optical properties of ultrathin electrodeposited CdS films probed by resonance Raman spectroscopy and photoluminescence. J Phys Chem 100: 9480–9484
42. Gichuhi A, Boone BE, Shannon C (1999) Electrosynthesized CdS/HgS heterojunctions. Langmuir 15: 763–766
43. Foresti ML, Pezzatini G, Cavallini M, Aloisi G, Innocenti M, Guidelli R (1998) Electrochemical atomic layer epitaxy deposition of CdS on Ag(111): An electrochemical and STM investigation. J Phys Chem B 102: 7413–7420
44. Aloisi GD, Cavallini M, Innocenti M, Foresti ML, Pezzatini G, Guidelli R (1997) In situ STM and electrochemical investigation of sulfur oxidative underpotential deposition on Ag(111). J Phys Chem B 101: 4774–4780
45. Innocenti M, Pezzatini G, Forni F, Foresti ML (2001) CdS and ZnS deposition on Ag(111) by electrochemical atomic layer epitaxy. J Electrochem Soc 148: C357–C362
46. Colletti LP, Flowers Jr BH, Stickney JL (1998) Formation of thin films of CdTe, CdSe, and CdS by electrochemical atomic layer epitaxy. J Electrochem Soc 145: 1442–1449
47. Colleti LP, Thomas S, Wilmer EM, Stickney JL (1997) Thin layer electrochemical studies of ZnS, ZnSe, and ZnTe formation by Electrochemical Atomic Layer Epitaxy (ECALE). Mater Res Soc Symp Proc 451: 235.
48. Gichuhi A, Shannon C, Perry SS (1999) A scanning tunneling microscopy and X-ray photoelectron spectroscopy study of electrochemically grown ZnS monolayers on Au(111). Langmuir 15: 5654–5661
49. Pezzatini G, Caporali S, Innocenti M, Foresti ML (1999) Formation of ZnSe on Ag(111) by electrochemical atomic layer epitaxy. J Electroanal Chem 475: 164–170
50. Zhang X, Shi X, Wang C (2009) Optimization of electrochemical aspects for epitaxial depositing nanoscale ZnSe thin films. J Solid State Electrochem 13: 469–475
51. Loglio F, Innocenti M, Pezzatini G, Foresti ML (2004) Ternary cadmium and zinc sulfides and selenides: electrodeposition by ECALE and electrochemical characterization. J Electroanal Chem 562: 117–125

52. Foresti ML, Milani S, Loglio F, Innocenti M, Pezzatini G, Cattarin S (2005) Ternary CdS$_x$Se$_{1-x}$ deposited on Ag(111) by ECALE: Synthesis and characterization. Langmuir 21: 6900–6907

53. Loglio F, Telford AM, Salvietti E, Innocenti M, Pezzatini G, Cammelli S, D'Acapito F, Felici R, Pozzi A, Foresti ML (2008) Ternary Cd$_x$Zn$_{1-x}$Se deposited on Ag (111) by ECALE: Electrochemical and EXAFS characterization. Electrochim Acta 53: 6978–6987

54. Mathe MK, Cox SM, Venkatasamy V, Uwe Happek, Stickney JL (2005) Formation of HgSe thin films using electrochemical atomic layer epitaxy. J Electrochem Soc 152: C751–C755

55. Venkatasamy V, Mathe MK, Cox SM, Happek U, Stickney JL (2006) Optimization studies of HgSe thin film deposition by electrochemical atomic layer epitaxy (EC-ALE). Electrochim Acta 51: 4347–4351

56. Torimoto T, Nagakubo S, Nishizawa M, Yoneyama H (1998) Photoelectrochemical properties of size-quantized CdS thin films prepared by an electrochemical method. Langmuir 14: 7077–7081

57. Torimoto T, Obayashi A, Kuwabata S, Yasuda H, Mori H, Yoneyama H (2000) Preparation of size-quantized ZnS thin films using electrochemical atomic layer epitaxy and their photoelectrochemical properties. Langmuir 16: 5820–5824

58. Torimoto T, Takabayashi S, Mori H, Kuwabata S (2002) Photoelectrochemical activities of ultrathin lead sulfide films prepared by electrochemical atomic layer epitaxy. J Electroanal Chem 522: 33–39

59. Qiao Z, Shang W, Wang C (2005) Fabrication of Sn–Se compounds on a gold electrode by electrochemical atomic layer epitaxy. J Electroanal Chem 576: 171–175

60. Vaidyanathan R, Stickney JL, Happek U (2004) Quantum confinement in PbSe thin films electrodeposited by electrochemical atomic layer epitaxy (EC-ALE). Electrochim Acta 49: 1321–1326

61. Yang J, Zhu W, Gao X, Bao S, Fan X, Duan X, Hou J (2006) Formation and characterization of Sb$_2$Te$_3$ nanofilms on Pt by electrochemical atomic layer epitaxy. J Phys Chem B 110: 4599–4604

62. Öznülüer T, Demir U (2002) Formation of Bi$_2$S$_3$ thin films on Au(111) by electrochemical atomic layer epitaxy: kinetics of structural changes in the initial monolayers. J Electroanal Chem 529: 34–42

63. Zhu W, Yang JY, Hou J, Gao XH, Bao SQ, Fan XA (2005) Optimization of the formation of bismuth telluride thin film by using ECALE. J Electroanal Chem 585: 83–88

64. Öznülüer T, Erdoğan I, Şişman I, Demir U (2005) Electrochemical atom-by-atom growth of PbS by modified ECALE method. Chem Mater 17: 935–937

65. Öznülüer T, Erdoğan I, Demir U (2006) Electrochemically induced atom-by-atom growth of ZnS thin films: A new approach for ZnS co-deposition. Langmuir 22: 4415–4419

66. Şişman I, Alanyahoğlu M, Demir U (2007) Atom-by-atom growth of CdS thin films by an electrochemical co-deposition method: Effects of pH on the growth mechanism and structure. J Phys Chem C 111: 2670–2674

67. Rajeshwar K (1992) Electrosynthesized thin films of group II-VI compound semiconductors, alloys and superstructures. Adv Mater 4: 23–29

68. Switzer JA (2001) Electrodeposition of superlattices and multilayers. In: Hodes G (ed) Electrochemistry of Nanostructures, Wiley-VCH, Weinheim

69. Switzer JA, Phillips RJ, Golden TD (1995) Composition profiles in electrodeposited ceramic superlattices. Appl Phys Lett 66: 819–821

70. Phillips RJ, Golden TD, Shumsky MG, Bohannan EW, Switzer JA (1997) Electrodeposition of textured ceramic superlattices in the Pb–Tl–O system. Chem Mater 9: 1670–1677

71. Krishnan V, Ham D, Mishra KK, Rajeshwar K J (1992) Electrosynthesis of thin films of CdZnSe: Composition modulation and bandgap engineering in the ternary system. J Electrochem Soc 139: 23–27

72. Streltsov EA, Osipovich NP, Ivashkevich LS, Lyakhov AS (1998) Electrochemical deposition of PbSe$_{1-x}$Te$_x$ films. Electrochim Acta 44: 407–413

73. Switzer JA, Hung C-J, Huang L-Y, Switzer ER, Kammler DR, Golden TD, Bohannan EW (1998) Electrochemical self-assembly of copper/cuprous oxide layered nanostructures. J Am Chem Soc 120: 3530–3531

74. Zou S, Weaver MJ (1999) Surface-enhanced Raman spectroscopy of cadmium sulfide/cadmium selenide superlattices formed on gold by electrochemical atomic-layer epitaxy. Chem Phys Lett 312: 101–107

75. Torimoto T, Obayashi A, Kuwabata S, Yoneyama H (2000) Electrochemical preparation of ZnS/CdS superlattice and its photoelectrochemical properties. Electrochem Commun 2: 359–362

76. Vaidyanathan R, Cox SM, Happek U, Banga D, Mathe MK, Stickney JL (2006) Preliminary studies in the electrodeposition of PbSe/PbTe superlattice thin films via electrochemical Atomic Layer Deposition (ALD). Langmuir 22: 10590–10595

77. Herrero E, Buller LJ, Abruna HD (2001) Underpotential deposition at single crystal surfaces of Au, Pt, Ag and other materials. Chem Rev 101: 1897–1830

78. Michaelis R, Zei MS, Zhai RS, Kolb DM (1992) The effect of halides on the structure of copper underpotential-deposited onto Pt(111): a low-energy electron diffraction and X-ray photoelectron spectroscopy study. J Electroanal Chem 339: 299–317

79. Rodriguez JA, Hrbek J (1999) Interaction of sulfur with well-defined metal and oxide surfaces: Unraveling the mysteries behind catalyst poisoning and desulfurization. Acc Chem Res 32: 719–728

80. Alanyahoğlu M, Çakal H, Öztürk AE, Demir U (2001) Electrochemical studies of the effects of pH and the surface structure of gold substrates on the underpotential deposition of sulfur. J Phys Chem B 105: 10588–10593

81. Solaliendres MO, Manzoli A, Salazar-Banda GR, Eguiluz KIB, Tanimoto ST, Machado SAS (2008) The processes involved in the Se electrodeposition and dissolution on Au electrode: the H$_2$Se formation. J Solid State Electrochem 12: 679–686

82. Alanyahoğlu M, Demir U, Shannon C (2004) Electrochemical formation of Se atomic layers on Au(111) surfaces: the role of adsorbed selenate and selenite. J Electroanal Chem 561: 21–27

83. Lister TE, Huang BM, Herrick II RD, Stickney JL (1995) Electrochemical formation of Se atomic layers on Au(100). J Vac Sci Technol B 13: 1268–1273

84. Lister TE, Stickney JL (1996) Formation of the first monolayer of CdSe on Au(111) by electrochemical ALE. Appl Surf Sci 107: 153–160

85. Lister TE, Stickney JL (1996) Atomic level studies of selenium electrodeposition on gold(111) and gold(110). J Phys Chem 100: 19568–19576

86. Santos MC, Machado SAS (2004) Microgravimetric, rotating ring-disc and voltammetric studies of the underpotential deposition of selenium on polycrystalline platinum electrodes. J Electroanal Chem 567: 203–210

87. Feliu JM, Gömez R, Llorca MS, Aldaz A (1993) Electrochemical behavior of irreversibly adsorbed selenium dosed from solution on Pt(h,k,l) single crystal electrodes in sulphuric and perchloric acid media. Surf Sci 289: 152–162

88. Yagi I, Lantz JM, Nakabayashi S, Corn RM, Uosaki K (1996) In situ optical second harmonic generation studies of electrochemical deposition of tellurium on polycrystalline gold electrodes. J Electroanal Chem 401: 95–10

89. Yagi I, Nakabayashi S, Uosaki K (1998) Real time monitoring of electrochemical deposition of tellurium on Au(111) electrode by optical second harmonic generation technique. Surf Sci 406: 1–8

90. Sorenson TA, Lister TE, Huang BM, Stickney JL (1999) A comparison of atomic layers formed by electrodeposition of selenium and tellurium: Scanning tunneling microscopy studies on Au(100) and Au(111). J Electrochem Soc 146: 1019–1027

91. Choong KR, Changhoon J, Bonseong K (2005) 2-Dimensional atomic arrangements of Te on Pt(111) whose coverage is higher than 0.25$^+$. J Solid State Electrochem 9: 247–253

92. Santos MC, Machado SAS (2005) A voltammetric and nanogravimetric study of Te underpotential deposition on Pt in perchloric acid medium. Electrochim Acta 50: 2289–2295

93. Zhu W, Yang JY, Zhou DX, Bao SQ, Fan XA, Duan XK (2007) Electrochemical characterization of the underpotential deposition of tellurium on Au electrode. Electrochim Acta 52: 3660–3666

94. Tacconi NR, Medvedko O, Rajeshwar K (1994) Cathodic electrosynthesis of metal sulphide thin films at a sulphur-modified gold surface: application to the iron sulphide system. J Electroanal Chem 379: 545–547

95. Tacconi NR, Rajeshwar K (1998) Electrosynthesis of indium sulfide on sulfur-modified polycrystalline gold electrodes. J Electroanal Chem 444: 7–10

96. Osipovich NP, Streltsov EA, Susha AS (2000) Bismuth underpotential deposition on tellurium. Electrochem Commun 2: 822–826

97. Chenthamarakshan CR, Ming Y, Rajeshwar K (2000) Underpotential photocatalytic deposition: A new preparative route to composite semiconductors. Chem Mater 12: 3538–3540

98. Somasundaram S, Chenthamarakshan CR, Tacconi NR, Ming Y, Rajeshwar K (2004) Photoassisted deposition of chalcogenide semiconductors on the titanium dioxide surface: Mechanistic and other aspects. Chem Mater 16: 3846–3852

99. Tacconi NR, Chenthamarakshan CR, Rajeshwar K, Tacconi EJ (2005) Selenium-modified titanium dioxide photochemical diode/electrolyte junctions: Photocatalytic and electrochemical preparation, characterization, and model simulations. J Phys Chem B 109:11953–11960

100. Ham S, Choi B, Paeng KJ, Myung N, Rajeshwar K (2007) Photoinduced cathodic deposition of CdTe nanoparticles on polycrystalline gold substrate. Electrochem Commun 9: 1293–1297

101. Ivanov DK, Osipovich NP, Poznyak SK, Streltsov EA (2003) Electrochemical preparation of lead-doped amorphous Se films and underpotential deposition of lead onto these films. Surf Sci 532–535: 1092–1097

102. Streltsov EA, Poznyak SK, Osipovich NP (2002) Photoinduced and dark underpotential deposition of lead on selenium. J Electroanal Chem 518: 103–114

103. Ragoisha GA, Bondarenko AS, Osipovich NP, Streltsov EA (2004) Potentiodynamic electrochemical impedance spectroscopy: Lead underpotential deposition on tellurium. J Electroanal Chem 565: 227–234

104. Ivanou DK, Streltsov EA, Fedotov AK, Mazanik AV, Fink D, Petrov A (2005) Electrochemical deposition of PbSe and CdTe nanoparticles onto p-Si(100) wafers and into nanopores in SiO$_2$/Si(100) structure. Thin Solid Films 490: 154–160

105. Ivanova YA, Ivanou DK, Streltsov EA (2008) Electrodeposition of PbSe onto n-Si(100) wafers. Electrochim Acta 53: 5051–5057

106. Ivanova YA, Ivanou DK, Streltsov EA (2007) Electrodeposition of PbTe onto n-Si(100) wafers. Electrochem Commun 9: 599–604

107. Rabchynski SM, Ivanou DK, Streltsov EA (2004) Photoelectrochemical formation of indium and cadmium selenide nanoparticles through Se electrode precursor. Electrochem Commun 6: 1051–1056

108. Takahashi M, Todorobaru M, Wakita K, Uosaki K (2002) Heteroepitaxial growth of CdTe on a p-Si(111) substrate by pulsed-light-assisted electrodeposition. Appl Phys Lett 80: 2117–2119

109. Berry CR (1967) Structure and optical absorption of AgI microcrystals. Phys Rev 161: 848–851

110. Hodes G, Albu-Yaron A, Decker F, Motisuke P (1987) Three-dimensional quantum-size effect in chemically deposited cadmium selenide films. Phys Rev B 36: 4215–4222

111. Gorer S, Hodes G (1994) Quantum size effects in the study of chemical solution deposition mechanisms of semiconductor films. J Phys Chem 98: 5338–5346

112. Golan Y, Margulis L, Rubinstein I, Hodes G (1992) Epitaxial electrodeposition of cadmium selenide nanocrystals on gold. Langmuir 8: 749–752

113. Golan Y, Margulis L, Hodes G, Rubinstein I, Hutchison JL (1994) Electrodeposited quantum dots II. High resolution electron microscopy of epitaxial CdSe nanocrystals on (111) gold. Surf Sci 311: L633–L640

114. Golan Y, Hutchison JL, Rubinstein I, Hodes G (1996) Epitaxial size control by mismatch tuning in electrodeposited Cd(Se, Te) quantum dots on {111} gold. Adv Mater 8: 631–633

115. Golan Y, Hodes G, Rubinstein I (1996) Electrodeposited quantum dots. 3. Interfacial factors controlling the morphology, size, and epitaxy. J Phys Chem 100: 2220–2228

116. Golan Y, Ter-Ovanesyan E, Manassen Y, Margulis L, Hodes G, Rubinstein I, Bithell EG, Hutchison JL (1996) Electrodeposited quantum dots IV. Epitaxial short-range order in amorphous semiconductor nanostructures. Surf Sci 350: 277–284

117. Zhang Y, Hodes G, Rubinstein I, Grünbaum E, Nayak RR, Hutchison JL (1999) Electrodeposited quantum dots: Metastable rocksalt CdSe nanocrystals on {111} gold alloys. Adv Mater 11: 1437–1441

118. Ruach-Nir I, Wagner HD, Rubinstein I, Hodes G (2003) Structural effects in the electrodeposition of CdSe quantum dots on mechanically strained gold. Adv Funct Mater 13: 159–164

119. Mastai Y, Gal D, Hodes G (2000) Nanocrystal-size control of electrodeposited nanocrystalline semiconductor films by surface capping. J Electrochem Soc 147: 1435–1439

120. Darkowski A, Cocivera M (1985) Electrodeposition of cadmium telluride using phosphine telluride. J Electrochem Soc 132: 2768–2771.

121. Mastai Y, Hodes G (1997) Size quantization in electrodeposited CdTe nanocrystalline films. J Phys Chem B 101: 2685–2690

122. Hodes G, Rubinstein I (2001) Electrodeposition of semiconductor quantum dot films. In: Hodes G (ed) Electrochemistry of Nanostructures, Wiley-VCH, Weinheim

123. Penner RM (2001) Hybrid electrochemical/chemical synthesis of semiconductor nanocrystals on graphite. In: Hodes G (ed) Electrochemistry of Nanostructures, Wiley-VCH, Weinheim

124. Penner RM (2000) Hybrid electrochemical/chemical synthesis of quantum dots. Acc Chem Res 33: 78–86

125. Gorer S, Ganske JA, Hemminger JC, Penner RM (1998) Size-selective and epitaxial electrochemical/chemical synthesis of sulfur-passivated cadmium sulfide nanocrystals on graphite. J Am Chem Soc 120: 9584–9593

126. Steckel JS, Zimmer JP, Coe-Sullivan S, Stott NE, Bulović V, Bawendi MG (2004) Blue luminescence from (CdS)ZnS core–shell nanocrystals. Angew Chem Int Ed 43: 2154–2158

127. Rajeshwar K, de Tacconi NR, Chenthamarakshan CR (2004) Spatially directed electrosynthesis of semiconductors for photoelectrochemical applications. Curr Opin Solid State Mater Sci 8: 173–182

128. Romanov SG, Fokin AV, Tretijakov VV, Butko VY, Alperovich VI, Johnson NP, Sotomayor Torres CM (1996) Optical properties of ordered three-dimensional arrays of structurally confined semiconductors. J Cryst Growth 159: 857–860

129. Vlasov YuA, Luterova K, Pelant I, Hönerlage B, Astratov VN (1997) Enhancement of optical gain of semiconductors embedded in three-dimensional photonic crystals. Appl Phys Lett 71: 1616–1618

130. Böhmer M (1996) In situ observation of 2-dimensional clustering during electrophoretic deposition. Langmuir 12: 547–5750

131. Rogach AL, Kotov NA, Koktysh DS, Ostrander W, Ragoisha GA (2000) Electrophoretic deposition of latex-based 3D colloidal photonic crystals: A technique for rapid production of high-quality opals. Chem Mater 12: 2721–2726

132. Braun PV, Wiltzius P (1999) Microporous materials. Electrochemically grown photonic crystals. Nature 402: 603–604

133. Choi S-J, Woo D-H, Myung N, Kang H, Park S-M (2001) Electrochemical preparation of cadmium selenide nanoparticles by the use of molecular templates. J Electrochem Soc 148: C569–C573

134. Cavallini M, Facchini M, Albonetti C, Biscarini F, Innocenti M, Loglio F, Salvietti E, Pezzatini G, Foresti ML (2007) Two-dimensional self-organization of CdS ultra thin films by confined electrochemical atomic layer epitaxy growth. J Phys Chem C Lett 111: 1061–1064

135. Dresselhaus MS, Lin Y-M, Rabin O, Black MR, Dresselhaus G: (2007) Nanowires. In Bharat Bhushan (ed.), Springer Handbook of Nanotechnology. doi:10.1007/978-3-540-29857-1

136. Van Dyke L S, Martin C R (1990) Fibrillar electronically conductive polymers show enhanced rates of charge transport. Synth Met 36: 275–281

137. Wang Y, Suna A, Mahler W, Kasowki R (1987) PbS in polymers. From molecules to bulk solids. J Chem Phys 87: 7315–7322

138. McMurray L, Holmes AJ, Kuperman A, Ozin GA, Ozkar S (1991) Intrazeolite semiconductors: sodium-23 MAS NMR, thallium(1+) luminescence quenching and far-IR studies of acid-base precursor chemistry in zeolite Y. J Phys Chem 95: 9448–9456

139. Ozin GA (1992) Nanochemistry: Synthesis in diminishing dimensions. Adv Mater 4: 612–649

140. Chakarvarti SK, Vetter J (1991) Morphology of etched pores and microstructures fabricated from nuclear track filters. Nucl Instrum Methods B 62: 109–115

141. Friedman AL, Brittain D, Menon L (2007) Roles of pH and acid type in the anodic growth of porous alumina. J Chem Phys 127: 154717–154723

142. Possin GE (1970) A method for forming very small diameter wires. Rev Sci Instrum 41: 772–774

143. Martin CR (1994) Nanomaterials: A membrane-based synthetic approach. Science 266: 1961–1966

144. Hulteen JC, Martin CR (1997) A general template-based method for the preparation of nanomaterials. J Mater Chem 7: 1075–1087

145. Chakarvarti SK, Vetter J (1993) Microfabrication of metal-semiconductor heterostructures and tubules using nuclear track filters. J Micromech Microeng 3: 57–59

146. Klein JD, Herrick RD, Palmer D, Sailor MJ, Brumlik CJ, Martin CR (1993) Electrochemical fabrication of cadmium chalcogenide microdiode arrays. Chem Mater 5: 902–904

147. Pena DJ, Mbindyo JKN, Carado AJ, Mallouk TE, Keating CD, Razavi B, Mayer TS (2002) Template growth of photoconductive metal-CdSe-metal nanowires. J Phys Chem B 106: 7458–7462

148. Peng XS, Zhang J, Wang XF, Wang YW, Zhao LX, Meng GW, Zhang LD (2001) Synthesis of highly ordered CdSe nanowire arrays embedded in anodic alumina membrane by electrodeposition in ammonia alkaline solution. Chem Phys Lett 343: 470–474

149. Routkevitch D, Bigioni T, Moskovits M, Xu JM (1996) Electrochemical fabrication of CdS nanowire arrays in porous anodic aluminum oxide templates. J Phys Chem 100: 14037–14047

150. Suh JS, Lee JS (1997) Surface enhanced Raman scattering for CdS nanowires deposited in anodic aluminum oxide nanotemplate. Chem Phys Lett 281: 384–388

151. Kang Y, Kim D (2006) Well-aligned CdS nanorod/conjugated polymer solar cells. Sol Energy Mater Sol Cells 90: 166–174

152. Xi D, Pei Q (2007) In situ preparation of free-standing nanoporous alumina template for polybithiophene nanotube arrays with a concourse base. Nanotechnology 18: 095602

153. Xi D, Zhang H, Furst S, Chen B, Pei Q (2008) Electrochemical synthesis and photovoltaic property of cadmium sulfide-polybithiophene interdigitated nanohybrid thin films. J Phys Chem C 112: 19765–69

154. Shaikh AV, Rajaram SM, Pathan HM, Min BK, Joo OS, Han SH (2008) CdSe thin film growth: Primarily amorphous nanograins to self-assembled nanowires. J Electroanal Chem 615: 175–179

155. Xu D, Shi X, Guo G, Gui L, Tang Y (2000) Electrochemical preparation of CdSe nanowire arrays. J Phys Chem B 104: 5061–5063.

156. Xu D, Chen D, Xu Y, Shi X, Guo G, Gui L, Tang Y (2000) Preparation of II-VI group semiconductor nanowire arrays by dc electrochemical deposition in porous aluminum oxide templates. Pure Appl Chem 72: 127–135

157. Vaidyanathan R, Stickney JL, Cox SM, Compton SP, Happek U (2003) Formation of $In_2Se_3$ thin films and nanostructures using electrochemical atomic layer epitaxy. J Electroanal Chem 559: 55–61

158. Martin-Gonzalez M, Prieto AL, Gronsky R, Sands T, Stacy AM (2003) High density 40 nm diameter Sb-rich, $Bi_{2-x}Sb_xTe_3$ nanowire arrays. Adv Mater 15: 1003–1006

159. Jin C, Zhang G, Qian T, Li X, Yao Z (2005) Large-area $Sb_2Te_3$ nanowire arrays. J Phys Chem B 109: 1430–1432

160. Yoo B, Xiao F, Bozhilov KN, Herman J, Ryan MA, Myung NV (2007) Electrodeposition of thermoelectric superlattice nanowires. Adv Mater 19: 296–299

161. Sima M, Enculescu I, Visan T, Spohr R, Trautmann C (2004) Electrochemical deposition of $PbSe_{1-x}Te_x$ nanorod arrays using ion track etched membranes as template. Mol Cryst Liq Cryst 418: 749–755

162. Nanda KK, Sahu SN (2001) One-dimensional quantum confinement in electrodeposited PbS nanocrystalline semiconductors. Adv Mater 13: 280–283

163. She G, Zhang X, Shi W, Cai Y, Wang N, Liu P, Chen D (2008) Template-free electrochemical synthesis of single-crystal CuTe nanoribbons. Cryst Growth Des 8: 1789–1791

164. Fan HJ, Barnard AS, Zacharias M (2007) ZnO nanowires and nanobelts: Shape selection and thermodynamic modeling. Appl Phys Lett 90: 143116–143119

165. Li H, Mackay R, Hwu SJ, Kuo YK, Skove MJ, Yokota Y, Ohtani T (1998) On the electrochemically grown quasi-one-dimensional $KCu_{7-x}S_4$ series ($0 \leq x \leq 0.34$): Nonstoichiometry, superlattice, and unusual phase transitions. Chem Mater 10: 3172–3183

166. Erley G, Gorer S, Penner RM (1998) Transient photocurrent spectroscopy: Electrical detection of optical absorption for supported semiconductor nanocrystals in a simple device geometry. Appl Phys Lett 72: 2301–2303

167. Gorer S, Penner RM (1999) "Multipulse" electrochemical/chemical synthesis of CdS/S core/shell nanocrystals exhibiting ultranarrow photoluminescence emission lines. J Phys Chem B 103: 5750–5753

168. Walter EC, Murray BJ, Favier F, Kaltenpoth G, Grunze M, Penner RM (2002) Noble and coinage metal nanowires by electrochemical step edge decoration. J Phys Chem B 106: 11407–11411

169. Zach MP, Ng KH, Penner RM (2000) Molybdenum nanowires by electrodeposition. Science 290: 2120–2123

170. Zach MP, Inazu K, Ng KH, Hemminger JC, Penner RM (2002) Synthesis of molybdenum nanowires with millimeter-scale lengths using electrochemical step edge decoration. Chem Mater 14: 3206–3216.

171. Li Q, Walter EC, van der Veer WE, Murray BJ, Newberg JT, Bohannan EW, Switzer JA, Hemminger JC, Penner RM (2005) Molybdenum disulfide nanowires and nanoribbons by electrochemical/chemical synthesis. J Phys Chem B 109: 3169–3182

172. Li Q, Brown MA, Hemminger JC, Penner RM (2006) Luminescent polycrystalline cadmium selenide nanowires synthesized by cyclic electrodeposition/stripping coupled with step edge decoration. Chem Mater 18: 3432–3441

173. Menke EJ, Brown MA, Li Q, Hemminger JC, Penner RM (2006) Bismuth telluride ($Bi_2Te_3$) nanowires: Synthesis by cyclic electrodeposition/stripping, thinning by electrooxidation, and electrical power generation. Langmuir 22: 10564–10574

# Chapter 5
# Photoelectrochemistry and Applications

## 5.1 General

In this section, we will be concerned with applications of photoelectrochemical cells (PEC). The term "photoelectrochemical" refers to any situation wherein light is used to augment an electrochemical process; the prefix photo implies in particular radiation of some kind, typically visible light of a continuous frequency range (e.g., solar) or of a single frequency. A photoelectrochemical cell involves photosensitive interphases, at least one of those, formed typically among solids and liquids – generally between electronic and ionic conductors. The radiation absorbed at these junctions stimulates physical and chemical actions, which may be exploited for construction of useful devices. The electrochemical schemes to be described concern mainly PEC applications of inorganic semiconductors in classical (macro) electrode cells. In these cells, semiconductor/liquid junctions are utilized much in the same way as semiconductor solid-state contacts, the essential difference being the nature of the active junction (solid–solid vs. solid–liquid). Related examples and principles of photocatalytic particulate systems will be addressed, whereas photogalvanic and molecular assembly applications, or those encountered in the realm of organic photochemistry, will be excluded from this presentation.

Photoelectrochemical cells are used for versatile light-stimulated or light-sustained or light-assisted processes. An illuminated cell, in which a reversible redox system introducing ionic-type conduction between the electrodes mediates the transfer of electrons in the external circuit may operate as a photovoltaic device; in principle, under light stimulation, the reduced form of the redox system is oxidized at one electrode and is reduced (regenerated) at the counter electrode, so that the cell can continuously convert light energy into electrical, operating in a chemically reversible manner. Such a PEC may be used as a regenerative solar cell. Alternatively, one may achieve direct storage of chemical energy, e.g., by conducting two different reactions in separated half cells of the PEC, which now operates as a reactor producing a storable fuel. The amount of energy stored in this cell is determined by the difference in free energy of the two products.

As a matter of fact, semiconductor/liquid junctions provide the most efficient wet chemical method presently known for converting sunlight into electrical or

chemical energy. Quantum yields for photocurrent production can approach unity for wavelengths of light spanning the near-infrared and visible regions of the spectrum, and the overall solar optical-to-electrical energy conversion efficiencies of such devices can be in excess of 15%. From another respect, electrolyte contacts offer a number of unique opportunities for characterization of crystals and especially thin film structures. Transparent electrolyte contacts can be used for photocurrent and capacitance spectroscopy or electrolyte electroreflectance measurements, which provide valuable insights into basic science of materials and processes. Unfortunately, photoelectrochemical regenerative and synthetic solar cells never met the practical application anticipated in the early days of their development. Presently, in the field of photovoltaics, more than 90% of activities are concentrated on classical crystallized silicon solar cells, and 7.8% are related to thin layer solar cells, which include the not yet satisfactorily stable amorphous silicon cells and also cells made from chalcogenide materials, which, however, include rare and toxic elements like cadmium, tellurium, indium, and gallium [263]. Nonetheless, advances in electrochemistry have opened up new research areas in fields known for many years but which have made remarkable progress only since 1990; that is, dye sensitization and solar detoxification [1, 2].

The study of photoeffects in electrochemical systems can be traced back in 1839 to Becquerel's investigations of the effect of solar illumination on metal electrodes. Becquerel discovered a photovoltaic effect upon illumination of a platinum electrode covered with silver halide in an electrochemical cell, demarcating thus the beginning of photoelectrochemistry. Much later, the discoveries of the p–n junction and the transistor in the mid-1950s led to the understanding that the greatest photoeffects in PEC were to be expected for semiconductor electrodes illuminated with light of an energy exceeding their band gap. It was W. Brattain, coinventor of the transistor, who laid down, in his classical paper with G. C. B. Garrett [3], the foundations of the physics of the illuminated semiconductor electrolyte junction [4]. Fundamental work in the field was contributed by Heinz Gerischer, who formulated an articulated working model for the semiconductor/liquid junction and illustrated the critical dependence of the stability of PEC cells on this interface [5]. General and detailed treatments of semiconductor electrochemistry have been given by Myamlin and Pleskov, Gerischer, and others as well as in numerous publications on the properties of specific semiconductor materials [6–14].

Metal chalcogenides play prominent role in the various aspects of photoelectrochemistry, actually so as by outlining the scientific and technological relevance of these compounds one would unravel in parallel the historical development of the field. Among metal chalcogenides, the most attention from a photoelectrochemical point of view has been gained by the cadmium chalcogenides CdX (X = S, Se, and Te) [15] and the layered transition metal dichalcogenides $MX_2$ (M = Mo, W) [16], basically due to favorable solar conversion features and chemical stability.

## 5.2 Photoelectrochemical Properties

Quantum efficiency and long-term stability are the most essential factors for practical use of PEC. In photovoltaic liquid junction cells, for instance, the primary goal is to utilize semiconductor electrode materials capable of capturing a large fraction of solar spectrum, while at the same time showing sufficient stability when operated in suitable electrolytes. However, these two goals oppose one another, as in most cases the smaller the band gap the higher the susceptibility of the semiconductor to photochemical corrosion. Hence, it is necessary at first to circumvent this problem in order to render the production of electric power or chemical energy in PEC possible. Since the 1970s, considerable efforts have been made to improve chemical stability of semiconductor electrodes for solar energy conversion in liquid junction cells. In the following discussion of publications, it should be kept in mind that the vast majority of photoelectrochemical systems have been assessed under accelerated conditions for limited periods. A prescribed norm [173] defines that if after passage of ca. $2 \times 10^4$ C cm$^{-2}$ of photocharge under at least AM1 illumination, preferably at a potential corresponding to the point of maximum power, no significant change in output stability is observed, then the system in question can be considered "stable". Anyhow, the question of absolute vs. relative stability of these systems remains.

In terms of photoelectrode material quality, single crystals comprise a rational choice since their bulk properties can be controlled better and their influence on cell performance may be evaluated in a rather accurate manner, as being microstructurally well-defined solids. However, the cost and convenience of single-crystal preparation are not suited to the practical requirement of cheap device components. Polycrystalline photoelectrodes are advantageous in terms of fabrication cost, ability to prepare large areas in one operation, and material economy.

The utilization of solid–liquid contacts provides some unique possibilities. In an electrochemical cell, the photosensitive junction is formed spontaneously upon immersing the electrode in the liquid, unlike solid-state processing that requires sophisticated techniques to form rectifying junctions. The resulting liquid contact is extremely abrupt and matched in the atomic scale, compared to a p–n or metal–semiconductor junction. Therefore, lattice mismatch (as for example in CdS/Cu$_2$S) and thermal expansion problems are essentially neglected in liquid junctions. Due to easy construction, barrier height at the interface can in principle be varied conveniently by choosing appropriate match-ups between semiconductors and redox couples in solution. Moreover, since light adsorption and charge transfer to a solution redox couple occurs at the same interface, high efficiency and little effect of grain boundaries are anticipated if the crystallite size is at least comparable to the light absorption depth (this size is of the order of 1 μm for direct band gap semiconductors [5]). Finally, on account of their higher real surface areas, polycrystalline or roughened (e.g., by photoetching) electrodes support larger photocurrents. Thereby, not only is the use of polycrystalline material afforded much more readily in electrochemical than in all-solid-state photocells, but PEC devices may even favor an inhomogeneous electrode surface morphology.

## *5.2.1 Redox and Surface Chemistry vs. Electrode Decomposition*

The basic approach to minimize aqueous-based corrosive decomposition/dissolution or passivation of semiconductor electrodes has been the search for water-soluble molecules that exchange electrons with the photoelectrode more readily than water, i.e., to employ an electrochemically active electrolyte such that its redox chemistry occurs at the expense of the chemistry of the electrode material. For instance, anodic corrosion occurring with n-type semiconductor electrodes may be prevented by using redox species in solution that react with photogenerated holes at the electrode before these holes would set off corrosive action. The oxidized form of the redox couple may be subsequently reduced at the counter electrode and participate again in the anodic process or may provide a useful fuel. In principle, all semiconducting materials of n- or p-type character can be used as photocell electrodes provided that a suitable reversible redox system is found. Relatively stable regenerative cells in the long term (on the months/years timescale) could be constructed in this manner from an otherwise unstable semiconductor electrode, by using suitable redox couple/electrolyte combinations.

This approach has been successfully implemented for n-type electrodes by having chalconide ions in solution to provide an alternative source of reduced chalcogen species to compete with electrode corrosion. Alkaline aqueous sulfide, selenide, and telluride solutions are used in particular, containing polychalcogenide ion species which regenerate the reductants upon reducing at the cathode. Early work with these "polychalcogenide" electrolytes has focused on cadmium chalcogenide electrodes, as will be described in detail for polysulfide solutions, but also on classical III–V semiconductors such as gallium arsenide. Photocorrosion of n-GaAs has been effectively suppressed by use of selenide/polyselenide ($Se^{2-}$, $Se_n^{2-}$) redox couple in alkaline aqueous solutions, and high-efficiency systems have been demonstrated, i.e., the single-crystal n-GaAs/$Se^{2-}$,$Se_n^{2-}$,$OH^-$/C cell with 9% efficiency [17], upgraded to about 12% after etching followed by uptake of $Ru^{3+}$ ions on the surface of the GaAs electrodes [18]; a single-crystal n/n$^+$-GaAs/aqueous polyselenide cell with efficiency 14% (uncorrected) or 19% (corrected for absorption in the solution) [19]; finally, a 15% efficient cell, attained after pretreatment of n-GaAs surface with $Os^{3+}$ [20]. The iodine/iodide or polyiodide redox couple has also given excellent results in many instances such as with transition metal dichalcogenides.

In screening electrolyte redox systems for use in PEC the primary factor is redox kinetics, provided the thermodynamics is not prohibitive, while consideration of properties such as toxicity and optical transparency is important. Facile redox kinetics provided by fast one-electron outer-sphere redox systems might be well suited to regenerative applications and this is indeed the case for well-behaved couples that have yielded satisfactory results for a variety of semiconductors, especially with organic solvents (e.g., [21]). On the other hand, many efficient systems reported in the literature entail a more complicated behaviour, e.g., the above-mentioned polychalcogenide and polyiodide redox couples actually represent sluggish redox systems involving specific interactions with the semiconductor

surface, which undoubtedly play an essential role in insuring good kinetic properties after all. This aspect has been emphasized already in the early works and will be repeatedly encountered in the following sections.

Aqueous electrochemistry is not always fitting to PEC applications. In fact, water has a rather limited thermodynamic (1.23 V) and practical (ca. 1.5 V) stability range for electrochemical applications. This severely limits the potential range of stable redox couples available for electrochemical operation of semiconductor electrodes and increases the probability of undesirable electron transfer reactions between the solvent and the electrode. Besides, the number of simple and reversible redox couples involving soluble reactants and products within the stability range of water are relatively small. In addition, very often, adsorption of impurities even from rigorously purified aqueous systems contaminates the electrode surface, so that reproducible background and faradaic currents may be difficult to obtain, while also surface states may be generated confusing the origin of the observed phenomena. The majority of these problems can be eliminated or at least minimized by using a non-aqueous solvent. Many aprotic solvents have a larger difference between the energies of solvent oxidation and reduction than water (e.g., ca. 5 V for acetonitrile) providing a larger window for electrochemical studies. Numerous reversible redox couples with a wide range of standard potentials (including one-electron transfer reactions without kinetic complications) are available in a number of non-aqueous solvents. Moreover, decomposition of the electrode into its ionic components at anodic potentials and during illumination should be less intense in such solutions, since solvation of the ions comprising the semiconductor lattice, which is a major factor in the dissolution, is usually not as strong as *in aquo*. This permits fundamental study of systems without extensive competition from photocorrosion or passivation processes, if not practical long-term PEC operation. Finally, adsorption of impurities is known to occur to a lesser extent in non-aqueous solvents and fewer difficulties exist with surface phenomena.

In certain cases the use of non-aqueous electrolytes is compulsory as with silicon photoanodes, for which no reagent in aqueous solution has been found that provides stable operation even on the timescale of minutes. Si photoanodes have been operated for months by using methanol or ethanol solvents in the presence of organometallic stabilizing agents. Also, properly prepared GaAs photoanodes have been found capable of sustaining high solar conversion efficiencies in non-aqueous solvents. Probably the first reported PEC using an aprotic solvent was that of Tsubomura and co-workers [22] who described stable n-CdS photocells containing acetonitrile solution of iodide ions. It was noted there that photoanodic dissolution of CdS cannot be fully avoided in organic solvents such as acetonitrile, nitromethane, and dimethylformamide, and the onset potential for the anodic dissolution of CdS was found to change with solvent alkalinity. The photoelectric behavior of classical and III–V semiconductor electrodes in non-aqueous systems, namely acetonitrile solutions containing tetra-*n*-butylammonium perchlorate as supporting electrolyte and redox couples with standard potential varying by more than 1.2 V, has been studied extensively by Bard and co-workers [23–26].

On the other hand, non-aqueous systems suffer from a number of disadvantages such as generally low solubilities of (usually colored) solution redox couples and high solution resistances. For a typical solar cell, a minimum current density of ~10 mA cm$^{-2}$ must be carried with a maximum voltage loss of ~ 0.1 V. But the best of non-aqueous electrolytes have specific conductances of about 0.05 $\Omega^{-1}$ cm$^{-1}$. It results that the effective path length between photo- and counter electrodes in such cells must not exceed ~0.5 cm, even in the most favorable case. This problem may be alleviated by the use of supporting electrolytes coupled with proper attention to cell geometry, i.e., use of thin layer cells. Acetonitrile (ACN) electrolytes have unusually high conductances for aprotic media, higher even than those based on alcohols, so that the resistive losses expected in this case are low. In specific, the ACN/$I_3^-$, $I^-$ system has been found to present several favorable features, including high conductivity for a non-aqueous system, high redox solubility, and electrochemical reversibility. Sustained anodic photocurrents were provided by this electrolyte on n-GaAs electrodes [27]. Notable conversion efficiencies (~10%) of natural light to electricity have been achieved also with n-GaAs/ferrocene/ferricenium in acetonitrile [28].

Aside from conventional organic solvents (e.g., acetonitrile, nitrobenzene, tetrahydrofuran, propylene carbonate, or alcohol solvents), molten salts, liquid ammonia (and ammoniates), and solid electrolytes, may be used as well to prepare non-aqueous redox systems. Molten salts have significantly higher conductivity than organic solvents, so that the need for supporting electrolytes is precluded. However, molten salts possess high viscosity, which leads to low diffusion coefficients of electroactive species. Again, thin layer cell design is a way to partially overcome this problem. Let us note finally, that a restricting feature of the non-aqueous PECs in general is that they can operate only as regenerative cells, since the reduced and/or oxidized forms of the stabilizing couples are rarely useful fuels.

An alternative line of attack against photocorrosion is the modification of the electrode surface in order to afford desired electrochemical behavior. This modification may be carried out prior to operation or in situ. For instance, the semiconductor electrode surface may be deliberately passivated provided that its charge transfer properties are retained. A straightforward way to protect the electrode surface is to apply some sort of coating to prevent electrolyte attack. The coating may be either a noble-metal layer deposited onto the electrode or a wide band gap semiconductor, a polymer, or even an organic dye. In general, the optimal characteristics which a coating material must have for PEC applications are high optical transparency over the solar spectrum and good electrical conductivity. Chemical inertness is quite desirable also, especially since electrolytes for PEC applications span a wide range of reactivity.

Besides improving stability, a practical goal of surface modification has been to utilize redox reactions, otherwise not applicable, to yield better electrical characteristics such as higher open-circuit photovoltage, and to promote high conversion efficiencies.

Derivatized semiconductor photoelectrodes offer a way to design photosensitive interfaces for effecting virtually any redox process. Manipulation of interfacial charge transfer processes has been demonstrated using hydrolytically unstable redox

reagents invoking chemical derivatization of photoelectrode surfaces [29, 9]. One of the first illustrations as given by Wrighton et al. [30, 31] regarded surface derivatization of single-crystal n-type silicon using hydrolytically unstable silanes in order to suppress photoanodic decomposition of the electrode. The initial derivatization was accomplished by dipping the electrode in dry isooctane solution of a ferrocene derivative, generating a ferrocene layer covalently attached to the surface. The derivatized surface aside from protecting Si to a substantial extent from $SiO_2$ anodic formation was found to be photoelectrochemically active. On the contrary, non-derivatized n-type Si was too susceptible to photoanodic $SiO_2$ growth to allow any sustained, or even reproducible, photoelectrochemistry.

Aromatic compounds which undergo both facile oxidation and electrophilic substitution reactions have been investigated as precursors to electrochemically active protecting films on semiconductive electrodes. For example, polyaniline films on Pt electrodes have been found to be electroactive for both anodic and cathodic reactions in ACN solutions [32], therefore they should afford also electrochemical oxidation and reduction at photoelectrodes. Noufi et al. [33] described the electrochemical properties of semiconductor electrodes (Cd-chalcogenides, Si, GaAs, GaP), on which polyaniline was directly formed by electrodeposition from an acidic aqueous solution of aniline. The coated electrodes were examined by cyclic voltammetry in aqueous and non-aqueous solutions of various redox couples and good conduction properties were substantiated. In addition, more stable photocurrents were attained in comparison with non-coated electrodes. This fact was attributed to the improved kinetics of the photocharge transfer to solution species, mediated by the polymer film, compared to the reaction with the electrode material or to recombination. A shortcoming in the process was the permeability of the polymer film due to poor integrity or less than perfect adhesion. As well, the electrodeposition of polypyrrole films on the surface of semiconductor photoanodes (Cd-chalcogenides, Si, GaAs) from ACN solutions of pyrrole has been shown to decrease photocorrosion [34]. Polypyrrole films were considered to act as barriers to ion/solvent transport, thus suppressing photodegradation of the electrode, while allowing efficient electron exchange with the electrolyte. Furthermore, the rate of certain reactions could be increased by incorporating catalysts or sensitizers into the polymer film.

Organic dyes, aside from their role as sensitization agents for wide band gap semiconductors have been employed also for stabilization of narrow band gap semiconductors. The majority of such studies have considered metal or metal-free phthalocyanine films for both sensitization and electrode protection purposes [35].

## 5.2.2 Energetic Considerations

The prediction of which semiconductor materials are suitable as electrodes for a given photoelectrolysis reaction would be straightforward if the energy position of the bands at the electrode surface remained fixed with respect to the solution redox levels and independent of the redox species in the solution. Gerischer

[36] as well as Bard and Wrighton [37] formulated thermodynamic criteria for the stability of semiconductor electrodes, based on the oxidative and reductive decomposition potentials, and the quasi-Fermi levels of holes and electrons at the surface of the electrode. The simple model suggests that an n-type semiconductor undergoes oxidative dissolution in contact with the electrolyte if its formal oxidation potential, $U_{decomp}$, is more negative than the edge of the valence band at the surface of the electrode. In the presence of a redox couple with a formal reversible potential $U_{rdx}$, spontaneous oxidation of the semiconductor by the electrolyte solution is possible in the dark if $U_{decomp} < U_{rdx}$. Accordingly, only redox couples should be selected for which $U_{rdx} < U_{decomp}$. Such thermodynamic predictions, however, are only of limited value because the electrode reactions are controlled by the kinetics and the detailed relative position of energy states on both sides of the interface. The most efficient electron transfer is expected from occupied states of the redox system to the valence band of the semiconductor if these energy states show a good overlap.

At any rate, the knowledge of energetic factors such as the decomposition potentials and doping density of the semiconductor electrode, the band edge potentials, and the formal redox potentials of the electrolyte is essential in understanding charge transfer kinetics and can be summarized in diagrams of so-called "interfacial energetics" relating characteristic energies of the electrode with those associated to solution redox couples. Such data have been collected for a variety of semiconductor/redox systems (e.g., Fig. 5.1). Seminal illustrations in this connection are the investigations carried out by Wrighton and co-workers (e.g., [70, 137]) on the interface energetics of single-crystal n-type cadmium and molybdenum chalcogenide electrodes. These authors distinguished summarizing classes of electrochemical behavior, which may be established as a general classification scheme in discussing the redox behavior of fast, one-electron, redox couples at n-type semiconductor electrodes.

Understanding of the band energetics of a semiconductor is associated with an accurate knowledge of the flat band potential, $U_{FB}$, which is mainly determined by the intrinsic solid-state properties, but it is affected also by (1) the potential drop at the interface between the electrode and the electrolyte, (2) illumination, and (3) the existence of surface states at the semiconductor/electrolyte interface. For a given redox system, the maximum efficiency for photovoltaic conversion in a regenerating manner depends upon the $U_{FB}$ of the photoactive electrode. For a cell with an n-type photoanode and in the so-called ideal conditions (band edge pinning), the more negative the value of $U_{FB}$, which is approximately equal to the conduction band edge level at the surface of the electrode ($-eE_{CB}$), the greater the possible output voltage (which has a maximum value $U_{rdx}-U_{FB}$) and the larger the maximum photoconversion efficiency that can be attained. Equivalently, for invariant flat band conditions (for the same electrode), a more positive redox couple would correlate to a larger photovoltage. However, for effective defense against photoanodic decomposition less positive redox potentials are needed, i.e., at a low energy for photogenerated holes.

In an electrolyte medium containing ions that strongly interact with the electrode, the $U_{FB}$ is shifted according to the concentration of the ions, "equilibrating"
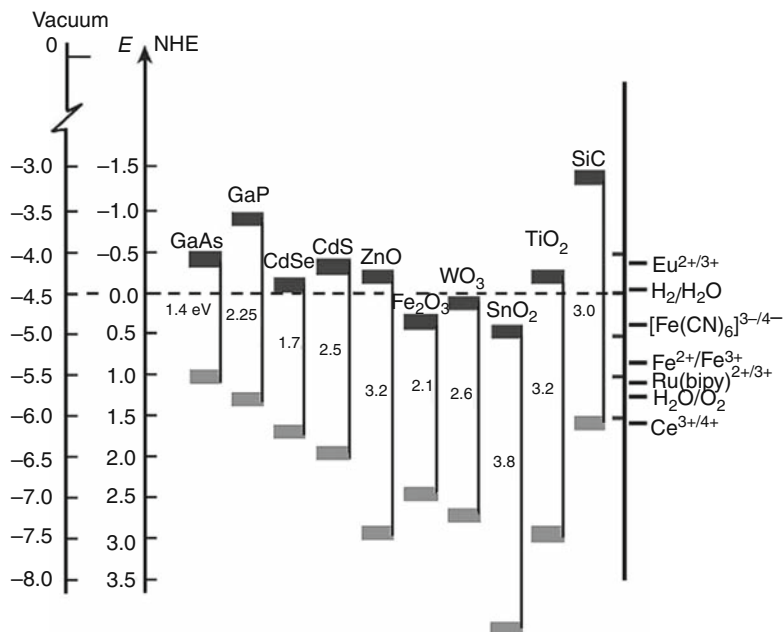
**Fig. 5.1** Position of energy bands at the surface of various semiconductors at pH 1 and redox potentials of the indicated couples. In liquid junctions, in order to achieve a large band bending at the semiconductor electrode, an n-type semiconductor should be combined with a redox system whose formal potential ("Fermi level" in solution) is close to the valence band of the semiconductor. It is evident from the diagram, that an ideal combination would be n-CdSe with $Ce^{4+}/Ce^{3+}$ as a redox system. A large band bending, however, of opposite sign can also be obtained on combining a p-type semiconductor with a redox couple whose energy is close to the conduction band. An example is p-GaAs and $Eu^{2+}/Eu^{3+}$. These ideal electrodes might be used to construct PEC such as n-CdSe/$Ce^{4+/3+}$/metal and p-GaAs/$Eu^{2+/3+}$/metal. However, the first cell does not work at all because of the anodic dissolution of CdSe, and the other cell does so only under certain limitations. (Adapted from [4], Copyright 2010, with permission from Elsevier)

thus with the electrolyte solution rather than remaining fixed by the solid-state property. For example, $U_{FB}$ of metal oxide semiconductor electrodes has been frequently found to shift 60 mV negatively per pH unit increase [38], while $U_{FB}$ of n-CdX electrodes is relatively unaffected by pH, but shifts negatively in electrolytes containing sulfide, polysulfide, or organic thiolates. The $U_{FB}$ of molybdenum and tungsten dichalcogenide electrodes shifts negatively in electrolytes containing iodide. Importantly, a sufficiently large density of surface states may "pin" the Fermi level of the semiconductor at a fixed value, so that photovoltage becomes insensitive to the contacting solution. Specific adsorption, surface charging effects, and Fermi level pinning are rather preponderant in most systems studied, and such effects appear often to be a prerequisite for good photoresponse [39]. The important concept of Fermi level pinning in connection with liquid junctions was introduced and investigated for several semiconductors and redox couples by Bard, Wrighton, and

co-workers [40, 41]. Aspects of the above-mentioned effects will be encountered in the following discussions.

The theoretical solar energy conversion efficiency maximizes at about 30% for a single photoelectrode-based cell with an optimum band gap of ~1.4 eV. Measurements of photoconversion efficiency in PEC are performed under solar irradiation or more frequently under illumination by artificial light sources (e.g., a xenon arc lamp). The comparison of figures obtained for different semiconductor materials requires that these efficiencies are presented for a standard solar spectrum; this is usually the AM1.5 global spectrum, although artificial light sources do not accurately replicate such spectra, and it is likely that the recording efficiencies are higher than those that would be obtained by sunlight. Attention should be paid in comparing efficiencies from different sources as in most of the literature reports, the photoconversion efficiency values are photoelectrode efficiencies representing potentiostatic control of the semiconductor electrode relative to the reference and cannot be directly compared to solar cell efficiencies in a two-electrode configuration without actual fabrication of such devices.

### 5.2.3 Cadmium Chalcogenides

The cadmium compounds CdS, CdSe, and CdTe absorb an appreciable fraction of the visible spectrum even in thin layers (in the $\mu$m order) due to direct band gaps of ca. 2.4, 1.7, and 1.4 eV, respectively, and high absorption coefficients. To be sure, as demonstrated by Gerischer [42] in one of his pioneering contributions in the field of photoelectrochemistry, even cadmium sulfide could yield initial conversion efficiency greater than 5% for sunlight to electric power in a liquid junction cell configuration, despite its narrow absorption range limited in wavelengths lower than 550 nm. But, irreversible decomposition of CdX electrodes under illumination in PEC is a serious obstacle in practice.

#### 5.2.3.1 Single-Crystal Photoelectrodes – PEC Fabrication and Properties

In one of the pioneering works, Williams [43], using single-crystal photoelectrodes of various, mostly chalcogenide, binary compounds (CdS, CdSe, ZnS, ZnO, ZnTe, CuI, and GaAs), illustrated the electrochemical reactions that take place at the illuminated interphase of a semiconductor/electrolyte system as being either of a corrosion nature or interfacial charge transfer without corrosion. In the former case, the observed photovoltaic effects were attributed to a chemical reaction in which the material of the illuminated electrode itself is consumed and in the latter case to an electron exchange process with an oxidation–reduction couple in the solution. For a corroding CdS crystal, the "photovoltaic" effect was shown to be accompanied by a reaction in which $Cd^{2+}$ ions go into solution and free sulfur is left behind on the crystal. Two electrons are liberated in this process, which can be written as
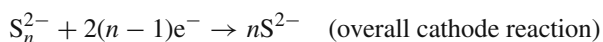
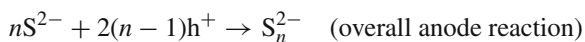$$CdS + 2\,h\nu \rightarrow Cd^{2+}(aq) + S + 2e^-$$
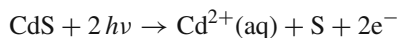
By this reaction the semiconductor becomes negatively charged with respect to the solution as long as the electrons are not led away from the CdS electrode. Anodic polarization in a closed circuit causes an anodic current to flow through the electrode. At sufficiently high polarization this current saturates at a value proportional to the light intensity [44]. Since holes are the minority charge carriers in n-type semiconductors, this saturation current represents the point at which holes are used up in the anodic dissolution reaction as fast as they are made available at the electrode surface [3]. Reverse effects are observed with illuminated p-type semiconductors, i.e., positive charging of the electrode and cathodic currents of minority carrier electrons. In this case, photocorrosion is less severe than in the anode case.

In fact, all n-type CdX electrodes suffer from aqueous photoanodic dissolution producing $Cd^{2+}$ and elemental chalcogen. Early attempts to stabilize such photoelectrodes by the use of redox couples yielded diverse results. Fujishima et al. [46] found that although oxidation of iodide ions occurs at an irradiated CdS anode, electrode decomposition proceeds at an appreciable rate even at high concentrations of $I^-$. Others suggested that the anodic dissolution of CdX could be effectively suppressed by the use of $Fe(CN)_6^{4-/3-}$, which provides rapid annihilation of photogenerated holes. Nonetheless, no stable systems were unequivocally established. Inoue et al. [47] investigated the stabilization of CdS single-crystal photoanodes by addition of suitable reducing agents to the electrolyte solution. Measurements of the percentage of dissolution suppression were carried out for eight reducing agents differing widely in their redox potentials. It was seen that reducing agents with more negative redox potential suppress more effectively the dissolution of the CdS surface. Gerischer and Gobrecht [42] studied the power characteristics of single-crystal n-CdS electrochemical photocells containing aqueous $Fe(CN)_6^{4-/3-}$ and $S_2O_3^{2-}/S_4O_6^{2-}$. They found a smaller photopotential for the latter redox couple and explained this result on the basis of the difference between the formal redox potential of the couple and the Fermi level of CdS. It was pointed out that the major problem with such cells was that oxidation of CdS competes with the desired hole capture by the reducing agent in solution and leads to rapid surface disintegration, the resulting elemental sulfur giving rise to an insulating layer covering the surface of the photoanode and stopping it from functioning.

The first effective photoelectrochemical conversion of low-energy (visible) light to electrical energy in a "regenerative" or "self-sustained" cell has been reported by Ellis et al. [48] for CdSe and CdS single-crystal electrodes.[1] An alkaline sulfide/polysulfide aqueous solution (1 M $Na_2S$, 1 M S, and 1 M NaOH) was employed, where the photooxidation product on the n-CdX (X = S, Se) anode was reduced at the dark cathode to complete a cycle whereby input light resulted in current flow with no net chemical change in the system. Passing by the complicated equilibria existing in aqueous solutions of $Na_2S$ and S (Sect. 1.1.4.4), the reversible chemistry occurring in the cell could be synopsized by the two half cell reactions:
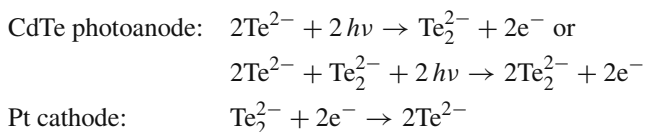
---

[1] Actually, G. C. Barker was the first to suggest the idea of stabilizing the n-CdS photoanode by a sulfide solution – see discussion in Gerischer [44].

$$nS^{2-} + 2(n-1)h^+ \rightarrow S_n^{2-} \quad \text{(overall anode reaction)}$$

$$S_n^{2-} + 2(n-1)e^- \rightarrow nS^{2-} \quad \text{(overall cathode reaction)}$$

The reaction occurring at the photoanode (CdS or CdSe) is the oxidation of sulfide or polysulfide, while at the cathode (Pt) some polysulfide species are reduced, so that the electrolyte undergoes no net chemical change. Here, the previous problem of poor stability in $Fe(CN)_6^{4-}$ solutions could be minimized, at the expense of lowering the driving potential (and thus the conversion efficiency), by using the $S^{2-}/S_n^{2-}$ redox couple (standard potentials $+0.36$ V vs. SHE, for $Fe(CN)_6^{3-/4-}$, and $-0.71$ V vs. SHE for $S_2^{2-}/S^{2-}$). The measured power conversion efficiency with an un-optimized cell under monochromatic illumination was lower than 1%. It was shown though that conversion efficiency depends strongly on the properties of the interface as controlled by prior chemical etching of the single-crystal electrodes. Efficiencies were found to vary by as much as three orders of magnitude with the method of crystal preparation, and optimization led to significantly improved values while stability was still maintained. For given semiconductor–redox electrolyte combinations, spectral photoresponse characterization provided a sensitive indicator for optimizing surface preparation conditions [49].

The data presented in an associated publication [50] confirmed that both CdS and CdSe can be stabilized to photoanodic dissolution in electrolytes containing sulfide or polysulfide. Importantly, large open-circuit photopotentials were found possible, up to 0.8 V for CdS and 0.65 V for CdSe-based cells, and high quantum yields for electron flow could be obtained under conditions of actual solar conversion. Overall optical-to-electrical energy conversion under monochromatic illumination was ~7% for CdS at 500 nm and ~9% for CdSe at 632.8 nm while an output voltage of ~0.3 V could be realized at low light intensity. On the other hand, solar energy conversion efficiency for CdSe was estimated as ~2%. In any case, the key finding was the suppressing of photoanodic dissolution. The promising properties of CdS and CdSe/polysulfide cells were found to be offset by several facts including photocurrent instability at high light intensities reflecting surface structural changes for etched surfaces in these conditions and loss of a substantial fraction of the high energy portion of the visible spectrum due to absorption in the polysulfide electrolyte.

After demonstrating the stabilization of CdS- and CdSe-based PEC, using sulfide- or polysulfide-containing electrolytes, Ellis et al. [51] proceeded to show that the photoanodic dissolution of single-crystal n-type CdTe, which was found to be unstable in a polysulfide electrolyte, could be completely quenched by adding $Na_2Te$ in the alkaline solution of NaOH. The photoelectrochemistry in their cell was considered to be consisting of the reactions

$$\text{CdTe photoanode:} \quad 2Te^{2-} + 2\,h\nu \rightarrow Te_2^{2-} + 2e^- \text{ or}$$

$$2Te^{2-} + Te_2^{2-} + 2\,h\nu \rightarrow 2Te_2^{2-} + 2e^-$$

$$\text{Pt cathode:} \quad Te_2^{2-} + 2e^- \rightarrow 2Te^{2-}$$

Visible light irradiation of $Te_2^{2-}$ did not cause any detectable change in the $Te^{2-}/Te_2^{2-}$ solution. Open-circuit photopotentials of up to –0.7 V were generated in this cell. The measured maximum overall optical-to-electrical energy conversion was 10.7% at 633 nm (0.079 mW cm$^{-2}$ irradiation), while efficiencies of 14 and 7% at 800 and 400 nm, respectively, were calculated from wavelength response data at the same light intensity. The maximum power output occurred at –0.45 V, and the quantum efficiency for electron flow at short-circuit was ~0.6. Similar to CdS- and CdSe-based cells, the efficiency suffered at higher light intensities.

The same research group [52] gave a general experimental account on CdX-based PEC in $X^{2-}/X_n^{2-}$ electrolytes for X = S, Se, and Te. For eight of the nine electrode/electrolyte combinations they found that the n-type single-crystal CdX photoelectrodes were stable to anodic dissolution. CdTe in $S^{2-}/S_n^{2-}$ was the only combination where the added chalcogenide did not quench the decomposition of the electrode. For all nine combinations as well as for CdX in alkaline $H_2O$, the redox level associated with the oxidation of $X^{2-}$ or with $O_2$ evolution was between the valence and conduction band positions at the semiconductor–electrolyte interface. Thus, energetic requirements for $X^{2-}$ oxidation or $O_2$ evolution from $H_2O$ were met in all cases, but kinetic factors controlled whether oxidation of $X^{2-}$ or of $H_2O$ will be fast compared to anodic dissolution, which was also energetically feasible. For the stable electrode/electrolyte systems, conversion of optical to electrical energy could be accomplished with efficiencies > 10% for monochromatic visible light. For CdTe or CdSe in the $Te^{2-}/Te_n^{2-}$ electrolyte, input power densities > 500 mW cm$^{-2}$ were converted with a few percent efficiency and no deterioration of properties. Output voltages at maximum power conversion efficiency were of the order of 0.4 V.

In searching for ways to upgrade the polysulfide PEC, Hodes and co-workers [53] focused attention on the counter electrode of the cell. In fact, since the discovery that polysulfide electrolytes could stabilize various semiconductors against photocorrosion, the need for a cheap, inert, and efficient counter electrode with a minimal overpotential for sulfur or polysulfide reduction (in the case of an n-type photoelectrode) or for sulfide oxidation (for a p-type photoelectrode) had arisen, since electrodes of carbon and platinum, usually employed for this purpose, were not very active for the polysulfide redox system. The effect of different electrode materials on the overpotential of sulfur/sulfide reduction and oxidation had been studied in the past, and typical overpotentials of 100–200 mV at 10 mA cm$^{-2}$ were reported. These overpotentials would lead to an intolerably high loss of efficiency in a practical PEC, since any overpotential at the counter electrode is reflected in a decrease in output voltage of the cell under load. The authors noted that unlike the usual laboratory cells that use very small photoelectrodes together with counter electrodes of much larger areas, in a practical cell the counter electrode would preferably be of the same size as the photoelectrode so that its electrocatalytic properties become of the highest importance.

In their earlier work, Hodes et al. [53] described low polarization electrodes composed of Teflon-bonded high surface area carbon, loaded with different electrocatalysts (Pt, platinized Pt, Co, Ni). The best results were obtained by using cobalt

which yielded overpotentials of less than 25 mV at current densities of 10 mA cm$^{-2}$ for both the anodic and the cathodic reaction in aqueous electrolyte of NaOH, S, and Na$_2$S (each 1 M) without stirring. Later experiments showed that the electrocatalytically active species actually were the corresponding sulfides formed upon immersing the electrode in the sulfide electrolyte. Of the several metal sulfides that were shown to act as good electrocatalysts for the polysulfide redox reactions, PbS, Cu$_2$S, and CoS electrodes were mainly considered for examination [54]. The effect of electrolyte composition and temperature on the activity of these electrodes was measured, enabling a choice of electrolyte for polysulfide PEC to be made on the basis of the counter electrode. It was suggested that at normal temperatures, the optimum electrolyte was ~2 M S and 2 M S$^{2-}$; the concentration of OH$^-$ was of secondary importance for the counter electrode, although there was a slight improvement in performance with higher [OH$^-$], particularly at low total ionic concentrations. The best choice for long-term operation, CoS, was found to remain stable after 7 months operation in a PEC, both in electrocatalytic activity and physically, and without having any adverse effect on the photoelectrode (CdSe).

The importance of controlling the operating temperatures of single-crystal and polycrystalline n-CdSe/polysulfide/CoS liquid junction cells to obtain the maximum possible photoconversion has been emphasized [55]. In fact, a dramatic effect of temperature was established on the power output of the cells, particularly those based on thin film electrodes.

Licht et al. investigated the effect of alkali cations in the electrolyte solution on CdX/S$_n^{2-}$ PEC performance [56, 57] and found that the conductivity of cesium polysulfide solutions is higher than that of equivalent sodium solutions. Also, superior charge transfer kinetics was established for metal (and metal-like) electrodes in various cesium solutions, compared to equivalent lithium, sodium, and potassium solutions. The nature of the polysulfide electrolyte, based on cesium polysulfide without excess hydroxide and containing small amounts of copper ions, was shown to be of particular importance in determining the PEC efficiency. Interestingly, alkali hydroxide, which had always been added in the preparation of the alkali polysulfide electrolyte in n-CdX/S$_n^{2-}$ PECs, was considered to be detrimental to cell performance [58]. Removal of the alkali hydroxide was shown to (1) decrease the solution absorbance of light, (2) positively shift the redox potential, and (3) increase the calculated disproportionation-limited lifetime of the solution. The researchers concluded that if alkali hydroxide is not added to the polysulfide electrolyte, improvements in PEC current, voltage, and efficiency are observed. These improvements were shown to be related to calculated changes in distribution of the species in the solution. It was noted that in the absence of hydroxide, the reduction of ion pairing due to an overall decrease in ionic concentration results in substantially increased polysulfide activity.

The findings of this investigation, along with optimization of the sulfur-to-sulfide ratio in the polysulfide electrolyte, led to the achievement of one of the highest sustained solar-to-electrical conversion efficiencies reported for a PEC: a 12.7% conversion efficiency was demonstrated for a chemically and photoelectrochemically etched CdSe$_{0.65}$Te$_{0.35}$ single-crystal photoelectrode in 1.8 M Cs$_2$S, 3.0 M

sulfur, and 0.5 mM $CuSO_4$ [59] electrolyte. Solar efficiency was measured outdoors, under 93.7 mW $cm^{-2}$ insolation, in a potentiostatically controlled cell (Pt counter and Pt reference) (open-circuit potential 0.78 V, short-circuit current 22 mA $cm^{-2}$). The same efficiency was obtained indoors, using an ELH lamp to provide simulated AM1 light intensity, in a solution without added copper salts. Output stability was satisfactory after the passage of 6040 C $cm^{-2}$; the current at maximum power conditions dropped from 44.9 to 37.0 mA $cm^{-2}$. The improved performance was considered to be principally due to the choice of cation and hydroxide-related effects. Copper ion treatment had a beneficial effect on efficiency that was ascribed to blocking (passivation) of defect sites at the semiconductor surface by $Cu_xS$ deposits. Let us remind here (cf. Chap. 1) that mixtures between two isomorphous binary chalcogenides with common metal or common chalcogen are ternary "compounds" or alloys with composition-dependent properties; solid solutions of CdSe and CdTe, denoted $CdSe_xTe_{1-x}$, are characterized by band gap energy whose value varies with composition between those of the end members. In the present case, for $x < 1$, the photoelectrode absorbs longer wavelengths than CdSe, since for $x = 0.35$ the band gap is ca. 1.4 eV; however, since CdSe is much more stable than CdTe in polysulfide solutions (CdTe is characterized by extreme susceptibility to PEC corrosion in aqueous electrolytes especially in the form of thin polycrystalline films) the beneficial increase in this respect of the Te content might adversely affect the output stability of this electrode. Notwithstanding, fixing the Te content at $x = 0.35$ gave a better compromise between the competing factors. Actually, it was found that $CdSe_{0.65}Te_{0.35}$ in the cesium polysulfide was more stable than CdSe in the sodium-rich solutions.

Taking advantage of the fact that their high-efficiency $CdSe_{0.65}Te_{0.35}$ cell with modified polysulfide electrolyte was capable of delivering sufficient voltage (–1.1 V vs. SHE) to drive a storage component directly, Licht et al. [60] developed a PEC with in situ electrochemical storage, by adding a single Sn/SnS/alkaline sulfide half cell (Fig. 5.2). The stannous sulfide reduction was driven with a redox potential of –1.0 V (SHE), and the combined system operated at 11.3% overall solar to electrical conversion efficiency, with a generated power insensitive to daily fluctuations in solar radiation. Following their previous innovation, the researchers used a thin film CoS counter electrode, electrocatalytic to the polysulfide redox reaction (prepared by electrodeposition of cobalt onto brass with subsequent electrochemical oxidation to CoS in polysulfide solution). The authors underscored their invention of an autonomous chalcogenide cell with sufficient voltage to allow electrochemical storage induced by a single photoelectrode and with a high continuous output, unlike previously presented bipolar dual photoelectrode systems combining solar conversion with electrochemical storage with maximum efficiencies not more than 3%.

A comprehensive survey of solar rechargeable PEC batteries, up to 1991, along with the historical development of photoelectrochemical cells has been given by Sharon et al. [61]. The principles and performance of solar PEC batteries with or without a membrane, with an aqueous solution or with solid-state electrolytes, are discussed there.
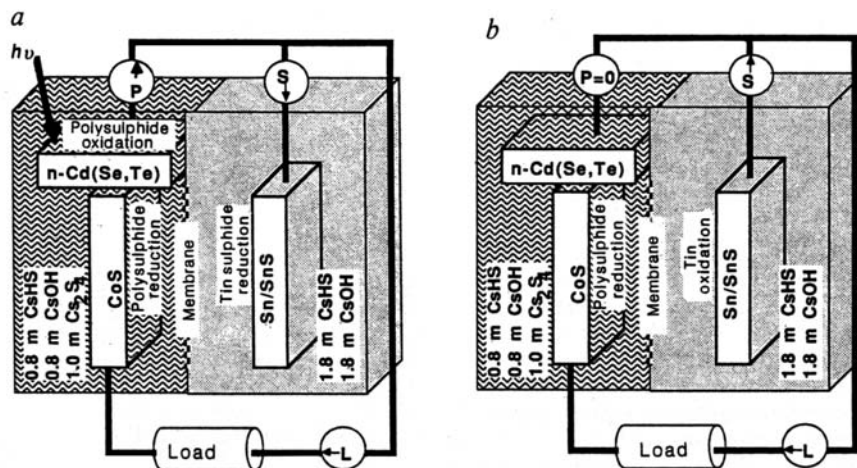
**Fig. 5.2** The n-Cd(Se,Te)/aqueous $Cs_2S_x$/SnS solar cell. *P*, *S*, and *L* indicate the direction of electron flow through the photoelectrode, tin electrode, and external load, respectively; (**a**) in an illuminated cell and (**b**) in the dark. For electrolytes, *m* represents molal. Electron transfer is driven both through an external load and also into electrochemical storage by reduction of SnS to metallic tin. In the dark, the potential drop below that of tin sulfide reduction induces spontaneous oxidation of tin and electron flow through the external load. Independent of illumination conditions, electrons are driven through the load in the same direction, ensuring continuous power output. (Reproduced with permission from Macmillan Publishers Ltd [Nature] [60], Copyright 2009)

No other Cd-chalcogenide based PEC with solar conversion efficiency greater than 8% had been reported at that time (1985), except for the highly unstable CdSe/basic ferri-ferrocyanide system (although higher efficiency cells based on other semiconductors had been described). In specific, the highest conversion efficiencies in aqueous n-CdSe/$Fe(CN)_6^{4-/3-}$ solar cells, i.e., 12–14%, were reported using electrolytes containing a 1:1 ratio of $Fe(CN)_6^{4-}$ to $Fe(CN)_6^{3-}$ salts in a highly alkaline environment [62, 63] albeit the observed photo-currents decayed within hours. Attempts to enhance the photoconversion stability of these systems have been made by means of cationic surface modification of the n-CdSe photoelectrode [64] and isolation of the wavelength dependence of the surface instability [65]. Note that $CdSe_{0.65}Te_{0.35}$ single-crystal photoelectrodes have shown high conversion efficiencies also in basic ferri-ferrocyanide solution; however, both the photoelectrode and electrolyte were unstable.
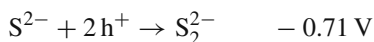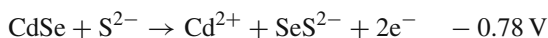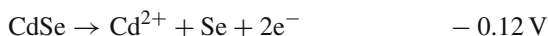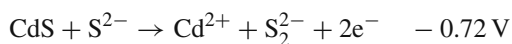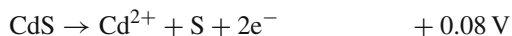
Remarkably, Licht and Peramunage [66] reported in 1990 the highest efficiency (16.4%) single band gap PEC based on CdSe single-crystal photoelectrode in modified ferri-ferrocyanide electrolyte affording a 100-fold improvement in photocurrent lifetime compared to previous works. Although this figure is short of the best values reported to date for Si-based photovoltaic cells, ca. 25 and 20%, for specially designed textured single-crystal and polycrystalline Si, respectively, it compares

favorably with most practical Si solar cells, which are in the 12–16% efficiency range. In specific, the single-crystal (11.0 face exposed) n-CdSe/Fe(CN)$_6^{4-/3-}$/Pt-mesh solar cell with an optimized alkaline electrolyte showed, outdoors, a stable (for charge passage > 5 kC cm$^{-2}$) conversion efficiency > 16% with an open circuit 1.20 V and short circuit 18 mA cm$^{-2}$ (fill factor 0.63) and quantum yield approaching unity. This highest recorded for any wide band gap (1.7 eV) solar cell (solid state or photoelectrochemical) efficiency was achieved by optimization of the distribution of species in solution and addition of cyanide (KCN), which enhanced the available voltage and ease of charge transfer and suppressed the formation of decomposition products.

### 5.2.3.2 Single-Crystal Photoelectrodes – A Closer Look into Interfacial Electrochemistry

The optimism in the 1970 decade for the future of regenerative PEC was over as soon as it became evident that long-term stability with liquid junction cells, which ran at current densities in excess of 10 mA cm$^{-2}$ (that are typical of efficient solar-irradiated photovoltaic cells), was not as practical as expected originally. The photocurrents with the supposed stable CdX electrodes in polysulfide electrolytes were seen to deteriorate slowly with time, especially at high light intensities, by a process involving chalcogenide exchange between the electrolyte and the electrode surface via photooxidation followed by reprecipitation. Heller et al. [67] indicated a catastrophic reduction in the short-circuit current supplied by single-crystal CdSe in an unstirred 1 M S, 1 M Na$_2$S, 1 M NaOH electrolyte after passing a charge of 200 C cm$^{-2}$. Formation of a CdS-enriched film was detected on the CdSe photoelectrode, acting as a barrier against the flow of holes to the surface. Nonetheless, addition of small amounts of elemental Se to the solution was found to substantially improve the stability by preventing excessive sulfide enrichment of the surface. With 0.5 M Se added, the output of <11.0> electrodes operated at 35 mA cm$^{-2}$ remained essentially unchanged beyond $2 \times 10^4$ C cm$^{-2}$ charge passage. It was presumed that in the presence of the SeS$_n^{2-}$ ions, the S-enriched surface retains a sufficient selenide concentration (consisting thus of CdSe$_x$S$_{1-x}$) to avoid the barrier problem. Importantly, the stabilization experiments led to an efficient (i.e., 7%) cell that operated for months without change in its electrical characteristic.

It was concluded from this and related works that suppression of the photodissolution of n-CdX anodes in aqueous systems by X$^{2-}$ ions results primarily from specific adsorption of X$^{2-}$ at the electrode surface and concomitant shielding of the lattice ions from the solvent molecules, rather than from rapid annihilation of photogenerated holes. The prominent role of adsorbed species could be illustrated, by invoking thermodynamics, in the dramatic shift in CdX dissolution potentials for electrolytes containing sulfide ions. The standard potentials of the relevant reactions for CdS and CdSe, as well as of the sulfide oxidation, are compared as follows (vs. SCE) [68]:

$$CdS \rightarrow Cd^{2+} + S + 2e^- \qquad\qquad + 0.08 \text{ V}$$
$$CdS + S^{2-} \rightarrow Cd^{2+} + S_2^{2-} + 2e^- \quad - 0.72 \text{ V}$$

$$CdSe \rightarrow Cd^{2+} + Se + 2e^- \qquad\qquad - 0.12 \text{ V}$$
$$CdSe + S^{2-} \rightarrow Cd^{2+} + SeS^{2-} + 2e^- \quad - 0.78 \text{ V}$$

$$S^{2-} + 2\,h^+ \rightarrow S_2^{2-} \qquad - 0.71 \text{ V}$$

In principle, the oxidation of $S^{2-}$ proceeds at an electrode potential that is more negative by about 0.7 V than the anodic decomposition paths in the above cases; however, because of the $S^{2-}$ adsorption shift, it is readily seen that practically there is no energetic advantage compared to CdX dissolution in competing for photo-generated holes. Similar effects are observed with $Se^{2-}$ and $Te^{2-}$ electrolytes. As a consequence of $X^{2-}$ specific adsorption and the fact that the $X^{2-}/X_n^{2-}$ couples involve a two-electron transfer, the overall redox process (adsorption/electron transfer/desorption) is also slow, which limits the degree of stabilization that can be attained in such systems. In addition, the type of interaction of the $X^{2-}$ ions with the electrode surface which produces the shifts in the decomposition potentials also favors anion substitution in the lattice and the concomitant degradation of the photoresponse.

On the basis of these remarks, it may be considered that fast one-electron redox couples which do not involve strong specific adsorption on the electrode surface should represent best candidates for "clean" stabilization of n-CdX electrodes against photodissolution, given that some interaction between the redox species and the electrode surface would be desirable if it resulted in a negative shift in the flat band potential (so that the open-circuit voltage of the cell be increased). In effect, the importance of kinetics in the competition for photogenerated holes had been already evident from the fact that the one-electron $Fe(CN)_6^{4-/3-}$ couple partially quenches the photodissolution of n-CdS in water even though its redox reaction is thermodynamically unfavorable compared to dissolution as having a more positive standard potential (+0.12 V vs. + 0.08 V vs. SCE) [5, 47]. On the other hand, the $Fe(CN)_6^{4-/3-}$ example illustrates that fast electron transfer by itself is not sufficient to ensure stabilization, at least in aqueous electrolytes.

Added stability in PEC can be attained through the use of non-aqueous solvents. Noufi et al. [68] systematically evaluated various non-aqueous ferro-ferricyanide electrolytes (DMF, acetonitrile, PC, alcohols) for use in stabilizing n-CdSe photoanodes. Selection of the solvent was discussed in terms of inherent stability provided, the rate of the redox reaction, the tendency toward specific adsorption of the redox species, and the formal potential of the redox couple with respect to the flat band potential (attainable open-circuit voltage). On the basis of these data, the methanol/$Fe(CN)_6^{3-/4-}$ system (transparent below 2.6 eV) was chosen as providing complete stabilization of CdSe. Results were presented for cells of the type

n-CdSe/methanol, $Fe(CN)_6^{3-/4-}$/Pt, operated for up to 700 h at 6 mA cm$^{-2}$ with no detectable degradation in either the electrode surface or the photoresponse.

In a series of detailed investigations, Wrighton and co-workers illustrated the photoelectrochemistry and interface energetics of single-crystal cadmium chalcogenide electrodes in $CH_3CN/[n\text{-}Bu_4N]ClO_4$ solutions containing low concentrations of fast, outer-sphere, one-electron redox reagents having a wide range of redox potentials [69, 70]. For each semiconductor electrode, the photovoltage, $E_V$, was measured by cyclic voltammetry as the difference between the photoanodic current peak and that of a Pt electrode, and was taken to approximate the barrier height, $E_B$. In the case of single-crystal n-CdSe photoanodes, it was observed that the electrochemical response was fairly reversible at both dark and illuminated (632.8 nm light) electrodes for couples such as $Ru(bpy)_3^{2+/+/0/-}$ having (formal) redox potentials, $U_{rdx}$, more negative than the flat band potential, –1.2 V vs. SCE. For couples with $U_{rdx}$ more positive than –1.2 V, CdSe was blocking to the oxidation of the reduced form in the dark, but not so under illumination. In the $U_{rdx}$ range –1.2 to –0.1 V, the photovoltage was found to increase with $U_{rdx}$ in a nearly ideal manner. Thus, $E_B$ was seen to increase nearly linearly as $U_{rdx}$ moved positive of –1.2 V vs. SCE. For $U_{rdx} > -0.1$ V vs. SCE, $E_V$ was constant, independent of redox potentials. The effect of a number of different etches on the interface energetics of CdSe was investigated including oxidizing ($K_2Cr_2O_7/HNO_3$, $Br_2/CH_3OH$) and reducing ($Na_2S_2O_4/NaOH$) treatments. These did not give significantly different results with respect to $E_B$ vs. $U_{rdx}$, despite large variation in the electrode's surface composition deduced from Auger and XPS spectra. The highest $E_V$ obtained was ~0.8 V using the $Fe(C_5Me_5)_2^{+/0}$ (formal $U_{rdx} = +0.43$ V vs. SCE) and more positive redox couples.

Cadmium sulfide was found to nearly fit the ideal model of a semiconductor/liquid electrolyte interface that follows from the considerations for an ideal semiconductor/metal interface, unlike n-CdTe that was found to behave quite differently. A significant and essentially constant photovoltage at –0.6 V (SCE) for a range of redox couples having $U_{rdx}$ spanning –2.0 to +0.7 V vs. SCE (a range of potential greater than the separation of the valence and conduction band of CdTe) was found for the CdTe liquid junctions. This value of photovoltage was about the same as previously reported for n-type CdTe/metal Schottky barriers. In agreement with the solid-state theoretical description, it was established that "Fermi level pinning" (FLP) occurs in the present case, implying that no effect appears on barrier energetics from contacting the surface of the semiconductor with different $CH_3CN/0.1$ M $[n\text{-}Bu_4N]ClO_4$ redox electrolyte solutions, much like contacting the surface with metals. The authors remarked that the CdTe photovoltage is comparable to that for n-type GaAs, also a direct, 1.4 eV, gap semiconductor that exhibits FLP. Thus, the n-type CdTe would appear, in terms of photovoltage alone, to be as good a candidate material in solar conversion devices as is n-type GaAs. Comparatively, the CdS photoanode did not exhibit FLP over the measured range of redox systems; photovoltage did depend on the $U_{rdx}$ of the contacting couple, except that it varied less than would be expected. Only values of $U_{rdx}$ positive of the flat-band potential, $U_{FB} \approx -1.0$ V vs. SCE, gave a photovoltage. However, at potentials positive to $U_{FB}$,

surface states did appear to play a role in facilitating reduction of the oxidized form of a couple. The maximum photovoltage observed by CdS was ~0.9 V. Note that with respect to $E_B$ vs. $U_{rdx}$, n-type CdSe more closely resembled the behavior of CdS than CdTe, despite the fact that the band gap of CdSe (1.7 eV) is closer to that of CdTe (1.4 eV) than to CdS (2.4 eV).

Studies of the flat band potential as influenced by redox couples and corrosion layers, as well as information on energy band levels, and interface (surface) state densities have been reported a lot in the literature. The classical methods typically used for such determinations are based on interface capacity measurements (Mott–Schottky plots), photovoltammetric data combined with measurements of the open-circuit photovoltage and the photocurrent onset potential [7, 8, 71], or more sophisticated techniques such as electrolyte-electroreflectance measurements (for direct gap semiconductors) [72]. In fact, differing methods and electrode types have led to very different values for the flat band potential and surface energetics of CdX electrodes. This is only part of the problem, as – alleged to be precise – capacity measurements are extremely sensitive to surface layers such as those formed by corrosion processes, e.g., sulfur on the CdS surface [73], or even to the perturbation frequency – although the latter effect can be attributed once more to the formation of surface forms or layers, i.e., extrinsic surface states. Hence, the assignment of the flat band potential in semiconductor/liquid interfaces is generally very difficult.

The influence of corrosion on the capacitance vs. voltage characteristics was pointed out as early as 1971 by Tyagai and Kolbasov [74] in their investigation on single-crystal CdS or CdSe liquid junctions using the aqueous redox couples $Fe^{+2}/Fe^{+3}$ and $Fe(CN)_6^{4-/3-}$. Importantly, it was claimed that electron transfer processes across the interface were contributed significantly by surface states acting as mediators to redox processes. A first detailed look at the electrochemistry of the single-crystal n-CdS/alkaline aqueous sulfide–polysulfide/Pt system was given by Ginley and Butler [75], who were able to predict the flat band potential of the CdS anode from the atomic electronegativities of the constituent atoms and then compare it with experiment. The calculated value (–0.83 V vs. SCE), corrected for the potential across the Helmholtz layer due to specific ion adsorption as evaluated using well-established procedures, was found to be in excellent agreement with the experimentally measured value corrected to the point of zero zeta potential, PZZP (–0.84 V vs. SCE); note that in these systems, the crucial influence of the adsorbed ions brings up the requirement that flat band measurements are referenced to the appropriate PZZP, i.e., with zero net adsorbed surface charge, otherwise the magnitude of the potential across the Helmholtz layer remains unknown and the value of the intrinsic flat band cannot be determined. By examining the behavior of the $U_{FB}$ with $S^{2-}$ and $OH^-$ concentration, it was identified also that the potential-determining species on the cadmium sulfide electrode are $HS^-$ and $H^+$, and not $S^{2-}$; the latter, contrary to previous ideas, seemed to play no direct role.

Meissner et al. [76] proposed a detailed reaction mechanism for the photocorrosion of n-CdS, based on experimental data in indifferent solutions (i.e., without intentionally added redox couples) of KCl, $Na_2SO_4$, or $NaClO_4$ and in accordance with results reported in the literature. They suggested that illumination of

the electrode leads to surface-state charging due to formation of the radical $S^{\bullet-}$, presumed to be intermediate in the formation of both possible photooxidation products, i.e., $S^0$ in the absence of oxygen or $SO_4^{2-}$ in the presence of oxygen. The understanding of the central role of the surface state $S^{\bullet-}$ in both charge transfer and corrosion processes was considered crucial for the analysis of the CdS photoelectrochemistry. Measurements on clean surfaces as prepared by pre-polarizing the electrode at about $-1.1$ V (SCE) in the presence of oxygen revealed that the true flat band potential of the wurtzite CdS–(0001)Cd face is $-1.8$ V (SCE), about 1 V more negative than previously thought. The opposite (0001)S surface was assumed to have a considerably more anodic flat band potential of about $-0.9$ V (SCE), though definitive results were not obtained. In a subsequent related work [77], regarding investigations on a number of typical redox systems, it was shown that the energy bands at the surface of clean CdS become unpinned upon illumination and are shifted in the anodic direction by several hundred millivolts. The same effect occurred in the dark after addition of the oxidized species of certain redox systems whose standard potentials were located in the band gap of CdS. According to the model developed by the authors, this band movement was due to the positive charging of surface states: in the case of light excitation this is done by capture of a hole from the valence band, while in the presence of a suitable oxidizing agent in the dark the surface state is charged by direct electron transfer to the acceptor in the electrolyte (Fig. 5.3). The potential dependence of photocurrents and dark currents could be explained semi-quantitatively in terms of charge transfer via surface states. Both minority carrier (anodic photocurrent) and majority carrier transfer (cathodic dark current) was assumed to occur via these states. Note that a somewhat similar model has been formulated for $RuS_2$ electrodes as will be cited later in this chapter.

The previous authors gave an inclusive list of reported $U_{FB}$ values as measured by different techniques, until 1988, for single-crystal or polycrystalline CdS electrodes in various electrolytes.

In a series of detailed studies on the photoelectrochemistry of CdSe [78, 79] Frese reported on the anodic behavior of n-CdSe($11\bar{2}0$) crystals in various aqueous electrolytes, focusing on the role of the Se corrosion layer. He observed that the flat band potential, as determined by capacitance/voltage measurements, was dominated by the redox potential of the electroactive couple present. $U_{FB}$ shifted in the same direction with the latter, the slope being unity in a rather wide potential window. This result suggested the existence of a metal-like surface due to a high density of surface states. Evidence was given that the $U_{FB}$ shifts were due to carrier exchange at the interface leading to variable surface state charge. The author observed also that very little frequency dispersion was found with an intentionally anodized CdSe($11\bar{2}0$) face (in $Na_2SO_4$, pH 7 solution), in contrast to previous results of impedance analysis regarding faceted crystals of CdSe in inert[2] electrolytes. The anodically produced Se layer was amorphous, and its structure resembled evaporated Se layers made up of polymer chains and possibly rings; it was a good hole-conductor but not an active component of the CdSe/Se/liquid junction under illumination, since all the anodic

---

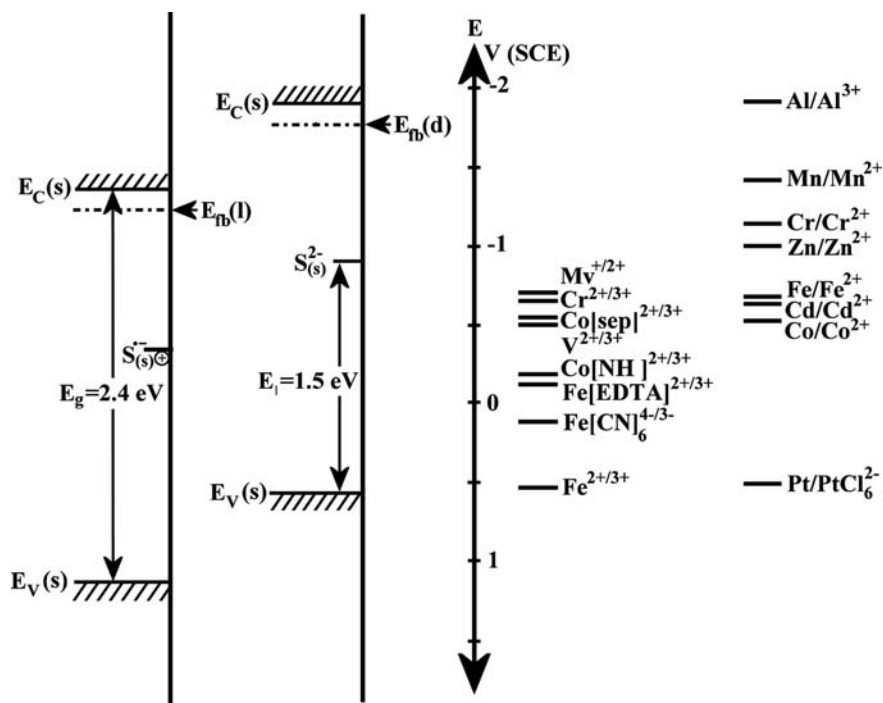[2] i.e., indifferent: without intentionally added redox couples.

**Fig. 5.3** Comparison between positions of the energy band edges at the surface of clean CdS–(0001)Cd with positively charged surface states ($S^{\bullet -}$ – formed, $E_{fb} = E_{fb}(l)$, *left*) and with uncharged surface states ($S^{\bullet -}$, $E_{fb} = E_{fb}(d)$, *right*), with formal potentials of various redox couples. At potentials near $E_{fb}(d)$, the number of electrons getting trapped in surface states reaches its highest value and the electroluminescence intensity coming from these states saturates. Yet, at even more negative potentials the number of electrons in the conduction band at the surface will further increase. On the other hand, the number of holes trapped at the surface by the band bending decreases as $E_{fb}(d)$ is approached, so that no further increase of the band-to-band transition can be expected negative of $E_{fb}(d)$. The luminescence intensity saturates at –1.8 V (SCE). (Reproduced with permission from [76], Copyright 2010, American Chemical Society)

photocurrent was generated in CdSe. Frese concluded that the relevant phenomena should be related to the general problem of surface passivation in PEC cells using conducting polymer layers. Let us note that, elsewhere [80], the Se corrosion layer was considered to be responsible for the observation of cathodic photoeffects.

As providing valuable information about excited states, the photoluminescence (PL) and electroluminescence (EL) of semiconductor electrodes comprise a unique probe for gaining an insight into various processes occurring in PEC, such as the electron–hole recombination, which can be investigated through the quenching features of emission bands. Hence, PL and EL of CdX electrodes have been the subject of a number of studies, e.g., regarding single-crystal, n-type, Te-doped CdS [81] or single-crystal CdSe [82] used as photo- or dark anodes in aqueous PEC employing sulfide and polychalcogenide electrolytes, respectively.

A thorough insight into the comparative photoelectrochemical–photocorrosion behavior of CdX crystals has been motivated by the study of an unusual phenomenon consisting of oscillation of photocurrent with a period of about 1 Hz, which was observed at an n-type CdTe semiconductor electrode in a cesium sulfide solution [83]. The oscillating behavior lasted for about 2 h and could be explained by the existence of a Te layer of variable width. The dependence of the oscillation features on potential, temperature, and light intensity was reported. Most striking was the non-linear behavior of the system as a function of light intensity. A comparison of CdTe to other related systems (CdS, CdSe) and solution compositions was performed.

### 5.2.3.3  Polycrystalline Photoelectrodes

It might be argued that thin film polycrystalline photoelectrodes should be more stable than comparable single-crystal ones, owing to the lower microscopic current densities flowing through a higher surface area. However, performance degradation mechanisms counteract and typically predominate over such an advantage, with the result that the materials inhomogeneous in a microstructural level are always more susceptible to corrosion than flat single crystals, unless special designs are employed. Microstructural and (photo)electrochemical properties of Cd-chalcogenide binary and ternary compound films have been shown to depend strongly on the film preparation and post-treatment process.

It has been illustrated that polycrystalline materials can be operated in regenerative electrolytic solar cells yielding substantial fractions of the respectable energy conversion efficiency obtained by using single crystals. Pressure-sintered electrodes of CdSe subsequently doped with Cd vapor have presented solar conversion efficiencies approaching 3/4 of those exhibited by single-crystal CdSe electrodes in alkaline polysulfide PEC [84].

In 1976, Hodes et al. [85] reported the stabilization of polycrystalline CdSe photoelectrodes (prepared by electrodeposition and subsequent heat treatment) in de-aerated alkaline aqueous or organic (not specified) solution of $S^{2-}$, in which some elemental sulfur was dissolved. It was claimed that besides CdSe, other semiconductors such as CdS, CdTe (n- and p-types), ZnSe, or $Bi_2S_3$ are also stable as photoelectrodes in a polycrystalline form in the sulfide solution, and that such cells under AM1 sunlight are stable over periods of months, a rather exaggerated claim. It was described in addition how a part or all of the converted energy could be stored in a controlled way in the system by the introduction of an electrode of porous silver.

An interesting idea has been to prepare the photosensitive electrode "on site" having the liquid play the dual role of a medium for anodic film growth on a metal electrode and a potential-determining redox electrolyte in the electrochemical solar cell. Such integration of the preparation process with PEC realization was demonstrated initially by Miller and Heller [86], who showed that photosensitive sulfide layers could be grown on bismuth and cadmium electrodes in solutions of sodium polysulfide and then used in situ as photoanodes driving the $S^{2-}/S_n^{2-}$

redox couple when connected to a suitable cathode. Two cells were considered, namely $Cd/CdS/Na_2S–Na_2S_x(aq)/C$ and $Bi/Bi_2S_3/Na_2S–Na_2S_x(aq)/C$. In this and other works, however, the power efficiency of liquid junction cells using anodically formed CdS to drive a polysulfide reaction was found to be substantially lower than for cells with single-crystal CdS under comparable conditions. The diverging stoichiometry of the anodic polycrystalline films and charge carrier recombination were denoted as the main limiting factors of performance. In fact, the anodic films retained typically about 25% of the single-crystal efficiency, according to the results of Peter [87], who measured the relative power output of polycrystalline CdS/Cd and single-crystal CdS cells, under typical conditions of solar irradiation (Fig. 5.4).

The lower efficiency of the polycrystalline CdS/Cd electrode compared to the single crystal reflected the measured primary photocurrent quantum yields, being about 0.3 and close to unity, respectively. Upholding the polycrystalline character of the CdS/Cd photoelectrode, Peter argued that although the efficiency of devices employing anodic films is lower by a factor of three to four than comparable single-crystal arrangements, this reduction of efficiency may well be offset by the ease with which large-area thin film photoanodes can be prepared electrochemically.

Differences in behavior between polycrystalline and single-crystal CdSe electrodes in polysulfide PEC involving the short- and long-term changes in photovoltage and photocurrents have been discussed by Cahen et al. [88], on the basis of XPS studies, which verified the occurrence of S/Se substitution in these electrodes when immersed in polysulfide solution, especially under illumination. The presence of a thin (several nanometers) layer of CdS on top of the CdSe was shown to influence
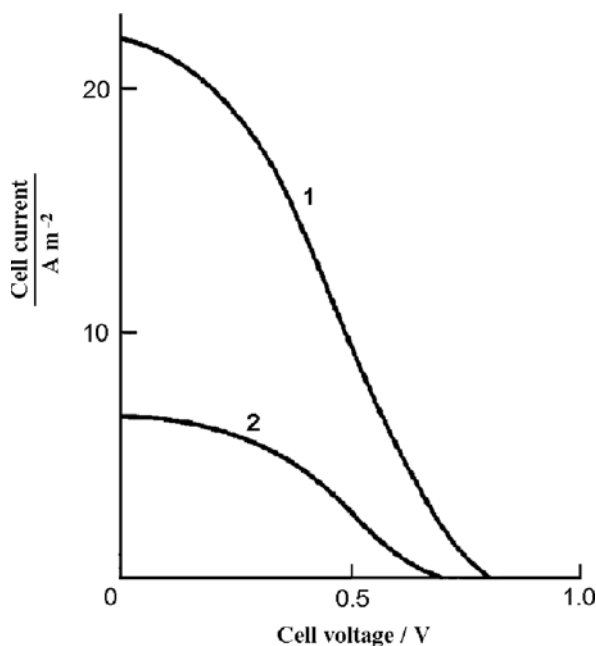


**Fig. 5.4** Power characteristics of CdS/sodium polysulfide solar cells. Solution composition is 0.1 M $Na_2S$ + 0.01 M S + 0.01 M NaOH. (*1*) Single-crystal photoanode; (2) $10^{-6}$ m thick CdS film grown at 20 A $m^{-2}$ in 0.1 M $Na_2S$ and etched in 1 M HCl. (Reproduced from [87], Copyright 2009, with permission from Elsevier)

the photovoltage and, to a lesser extent, the photocurrent obtainable from this kind of PEC. The slow deactivation of highly crystalline CdSe photoelectrodes by the formation of this sulfide layer was also discussed.

In attempting to preserve the stability of CdS while improving its absorption in the visible, Noufi et al. [89] constructed solar cells using sintered pellet sulfoselenide $CdS_xSe_{1-x}$ polycrystalline electrodes, configured as $CdS_xSe_{1-x}$/1 M $Na_2S$, 0.2 M S, 0.1 M NaOH/Pt. For a composition $x = 0.9$, a 9% power efficiency was obtained at a cell voltage of 202 mV, under 1 mW cm$^{-2}$ irradiation with 577 nm light. Studies of the photoassisted oxidation of sulfide (in 1 M $Na_2S$, 0.1 M NaOH) showed that the flat band potential of $CdS_xSe_{1-x}$ was more negative with respect to pure CdS and CdSe. Along this line instead of another chalcogen, mercury may be added in CdS to decrease the band gap width. Indeed, polycrystalline thin film $Cd_{1-x}Hg_xS$ electrodes were prepared by chemical co-deposition on Ti and tested in polysulfide solution [90]. A stable output current for a period of over 16 h was reported for a $Cd_{0.86}Hg_{0.14}S$ photoanode having a 1.88 eV gap (illumination 75 mW cm$^{-2}$).

Russak et al. [91] estimated carrier densities ($N_D$) and minority carrier diffusion lengths ($L_P$) for polycrystalline hexagonal (00.1)-textured CdSe thin film photoanodes (prepared by co-evaporation) in polysulfide solutions and correlated the latter with measured photovoltaic efficiency, by applying simple depletion layer theory to monochromatic photocurrent curves. The $N_D$ and $L_P$ values for the thin films were found to be in the range $6 \times 10^{16}$–$1 \times 10^{18}$ cm$^{-3}$ and 0.400–0.006 µm, respectively, while measurements on single-crystal CdSe gave $N_D = 8 \times 10^{16}$ cm$^{-3}$ and $L_P = 1.46$ µm. Conversion efficiencies (AM1) in excess of 5% were found for optimized cells. Analysis of action spectra indicated that the films were defective, as evidenced by the reduction of photoresponse at shorter wavelengths, as well as the presence of sub-band gap energy photocurrents. According to the experimental data, the conversion efficiency was more sensitive to $L_P$ than $N_D$, as expected for defective polycrystalline semiconductors. It was remarked that the simple depletion layer model was not adequate to predict completely the current–potential behavior of the liquid-junction devices, particularly under forward bias, due to the inherent assumption that recombinations within the space charge region can be neglected. However, within the limits defined (i.e., reverse bias and a wavelength that minimizes surface recombination effects), the model was found to yield very useful information in terms of sample-to-sample variation for the thin film electrodes, allowing the correlation of voltammetric performance with donor density and minority carrier diffusion length.

Lyden et al. [92] used in situ electrical impedance measurements to investigate the role of disorder in polysulfide PEC with electrodeposited, polycrystalline CdSe photoanodes. Their results were consistent with disorder-dominated percolation conduction and independent of any CdS formed on the anode surface (as verified by measurements in sulfide-free electrolyte). The source of the observed frequency dispersion was located at the polycrystalline electrode/electrolyte interface.

Effects due to grain boundaries have been discussed by Chartier et al. [93] with respect to the CdS/polysulfide junction. The photoelectrochemical behavior of polycrystalline CdS layers obtained by the spraying technique was found to be

compatible with a carrier density of $10^{16}$–$10^{17}$ cm$^{-3}$ and a minority carrier (hole) diffusion length $L_p < 0.01$ μm. The latter was rather low compared to the values quoted for CdS crystal ($L_p \sim 4$ μm) or evaporated CdS layers (0.1 μm < $L_p < 0.3$ μm). The authors underscored that the inconsistencies follow from the application, to polycrystalline layers, of the theories pertaining to the single crystal.

Advantages of the standard electrodeposition method (acidic aqueous solutions), attainable goals, and result of annealing, etching, and double-sided illumination of CdSe electrodes in PEC have been discussed [94]. The performance of electrodeposited CdSe electrodes could be improved by immersion and/or potential cycling in the polysulfide electrolyte [95]. Application of different annealing conditions in order to yield optimal solar cell performance with electrodeposited films has been reported [96, 97]. Besides thermal treatment, the influence of chemical- and photoetching treatments on the physical parameters determining the photoelectrochemical behavior of electrodeposited CdSe thin films in contact with polysulfide electrolytes has been systematically studied [98].

The strong photocorrosion effect on an electrodeposited CdSe film treated near short-circuit conditions (positive to the flat band potential) in a polysulfide media under intense illumination is shown in Fig. 5.5, as manifested by the formation of numerous, regularly arranged pinholes often reaching the substrate surface [99].

Photovoltaic response parameters for electrodeposited (polycrystalline) CdTe thin film electrodes in sulfide–polysulfide or alkaline sodium telluride PEC have been reported, primarily with no reference to the stability of the cells [100]. In view of the instability of CdTe in aqueous solutions, Bhattacharya and Rajeshwar [101] employed two methods for the characterization of their electrodeposited CdTe-based PEC. In the first one, a coating of PbO$_2$ (~100 nm thick) was deposited on the CdTe film surface by electroless deposition, and the coated films
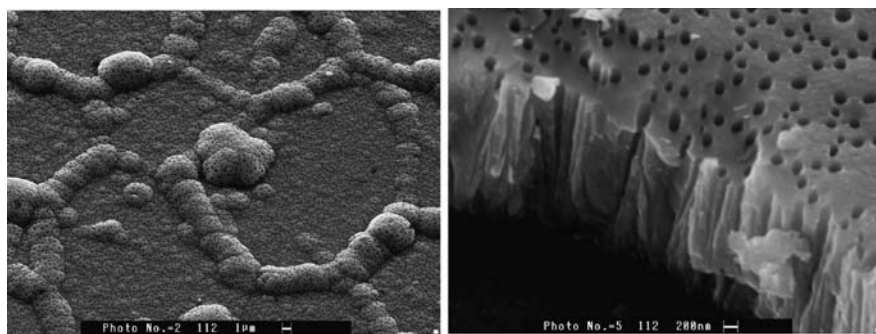


**Fig. 5.5** SEM surface view and cross section of an electrodeposited, ca. 1 μm thick, CdSe/Ti film subjected to accelerated photocorrosion by the application of –0.1 V vs. Pt bias in polysulfide solution under a focused, high-power (1 W cm$^2$) solar illumination for 30 min. The coherence of the as-deposited film morphology is evident. The authors emphasize that, even in this situation, the liquid junction nature prevents the flow of high leakage currents during the process (as it might be the case with a solid junction). (Reprinted from [99], Copyright 2009, with permission from Elsevier)

were tested in alkaline polysulfide electrolyte. In the second approach, a non-aqueous methanol/[$n$-Bu$_4$N]ClO$_4$ solution of ferrocene/ferrocenium redox species was employed and found to be effective in suppressing PEC corrosion; the fill factor, though, was much inferior to the single-crystal case, indicating substantial degradation in cell efficiency through carrier recombination.

The particular advantages of using spectral response measurements to characterize the optical, electrical, and morphological properties of polycrystalline thin film photoelectrodes in PEC have been emphasized by Mirovsky et al. [102], in view of the fact that conventional methods such as Hall or differential capacitance measurements are not easily applicable to systems constructed of a polycrystalline material. Their work regarded polycrystalline n-CdSe$_{0.65}$Te$_{0.35}$ electrodes prepared either by electroplating or by slurry pasting. Hole-diffusion lengths in the range of 0.1–0.5 μm and typical efficiencies of 2–5% were determined. High quantum efficiencies also were proclaimed which were attributed to the rather low doping of about $10^{15}$ cm$^{-3}$, a result that was reflected in the moderate open-circuit voltages and fill factors obtained with the alloy photoelectrode. Elsewhere [103], electrode-posited isomolar mixtures of CdTe with CdSe (CdSe$_{0.5}$Te$_{0.5}$) were reported to show an efficiency of 4.9% in polysulfide solution, for photoetched and annealed films.

Importantly, Licht [104], using the optimized polysulfide electrolytes developed for CdX PEC (described in a preceding paragraph), was able to demonstrate true long-term stability for a polycrystalline pasted thin film Cd(Se,Te)/aqueous polysulfide system. In specific, complete stability was exhibited for an 8-month outdoors operation at 4.1% conversion efficiency.

In any case, it is perceived from the above discussion that the problem of long-term chemical stability of polycrystalline semiconductor liquid junction solar cells is far from being solved. Still, as already pointed out in the early research, any practical photovoltaic and PEC device would have to be based on polycrystalline photoelectrodes. Novel approaches mostly involving specially designed PEC systems with alternative solid or gel electrolytes and, most importantly, hybrid/sensitized electrodes with properties dictated by nanophase structuring – to be discussed at the end of this chapter – promise new advances in the field.

Let us add here that the fabrication of polycrystalline semiconductive films with enhanced photoresponse and increased resistance to electrochemical corrosion has been attempted by introducing semiconductor particles of colloidal dimensions to bulk deposited films, following the well-developed practice of producing composite metal and alloy deposits with improved thermal, mechanical, or anti-corrosion properties. For instance, it has been reported that colloidal cadmium sulfide [105] or mercuric sulfide [106] inclusions significantly improve photoactivity and corrosion resistance of electrodeposited cadmium selenide.

## 5.2.4 A Note on Multilayer Structures

Junctions involving a bilayer (two-semiconductor) electrode and a liquid have been investigated as to their photoelectrochemical properties primarily in works which

were mostly concerned with the possibility of stabilizing low band gap semiconductors against photocorrosion, by covering them with a larger band gap material. Titanium oxide has been a favorite cover material for both p- and n-type single-crystal and polycrystalline semiconductor substrates [107, 108]. In most cases the photoresponse of such structures is dominated by the top layer and in general, stabilization of the bottom material could not be obtained because the top layer was porous.

Protective and properties-modifying barrier films, such as intentionally grown elemental chalcogen or II–VI material epilayers, have been applied on CdX electrodes in order to stabilize and upgrade their performance in PEC. The work of Frese on CdSe/Se/liquid junctions under illumination has been addressed in a preceding section. Let us note that n-CdSe/p-Se diode structures have been used for rectifiers and photosensitive elements for many decades, and possible application as low-cost solar cells has been discussed. Kampmann et al. [109] developed CdSe/Se junctions by electrodeposition of Se layers on n-CdSe single crystal from buffered selenite solutions in the dark or by photocorroding CdSe crystals in a partially stabilizing solution containing various amounts of ferrocyanide. The photoelectrochemical behavior of these n-CdSe/p-Se structures was examined in phthalate buffer (pH 5) with and without redox species.

The influence of ZnSe on the photoelectrochemical properties of CdSe has been investigated in a few works. Zinc selenide is a wide gap (2.7 eV) semiconductor comprising, along with CdTe, the only II–VI obtainable in both n- and p-type forms. Its integration in CdSe-based diodes as an interface layer may provide a barrier to electrochemical corrosion and enhance the conversion efficiency of solar cells with CdSe absorber electrode through its influence on open-circuit voltage [110]. A similar result can be obtained by zinc ion treatment of CdSe photoanodes, as the incorporation of zinc induces a Fermi level shift in a direction to enhance the barrier height, while also stabilizing the semiconductor surface against dissolution [111].

The photoelectrochemical behavior of ZnSe-coated CdSe thin films (both deposited by vacuum evaporation on Ti) in polysulfide solution has been described by Russak and Reichman [112] and was reported to be similar to MIS-type devices. Specifically, Auger depth profiling showed the ZnSe component of the (ZnSe)CdSe heterostructures to convert to ZnO after heat treatment in air, thus forming a (ZnO)CdSe structure, while the ZnO surface layer was further converted to a ZnS layer by cycling the electrode in polysulfide electrolyte. This electrochemically generated ZnS layer provided an enhanced open-circuit potential compared to CdSe alone. Efficiencies as high as 5.4% under simulated AM2 conditions were recorded for these electrodes.

More recently, the photovoltaic and chemical behavior of electrochemically prepared, single- and double-layer structures of microcrystalline CdSe and ZnSe were investigated in PEC with sulfide–polysulfide and (non-optimized) ferro-ferricyanide redox electrolytes [113]. A reproducible rectifying behavior could be determined in polysulfide solution, where the CdSe(ZnSe) electrodes showed higher photovoltage and improved chemical stability with respect to single layer CdSe. The pH-neutral $Fe(CN)_6^{3-/4-}$ electrolyte provided in general the expected enhanced charge transfer

kinetics, invalidated though by the irreversible formation of insoluble salts causing severe deterioration of the photoanodes. A more stable operation could be established with alkaline (pH 12) $Fe(CN)_6^{3-/4-}$ electrolyte.

Presently, laboratory solar cells such as those of crystalline silicon have reached photovoltaic conversion efficiencies of 25%, which for a semiconductor with an energy gap of 1.1 eV is close to the thermodynamic optimum. On the other hand, photovoltaic conversion efficiencies between 30 and 40% have been reached or are feasible if several solar cells are arranged in series to form a stack [114]. The idea of using multiple band gap cells in order to capture a greater fraction of the solar spectrum has motivated much work in the area of solid-state photovoltaic solar cells and, as a result, has stimulated also photoelectrochemical research. In a series of seminal works in this connection, Licht and co-workers [115–118] undertook the investigation of several, distinct, multiple band gap PEC configurations (MPEC) providing either regenerative or energy storage photoelectrochemistry. These authors developed a useful classification scheme for MPEC based on whether the solid-state p–n junctions are arranged in a bipolar (e.g., pnpn) or inverted (e.g., pnnp) fashion. Notably, a solar-to-electrical efficiency of 19.2% using an AlGaAs (wide band gap)–Si (narrow band gap) bilayer was achieved. Most of the work thus far has involved ohmic rather than Schottky-type semiconductor–electrolyte junctions, which unfortunately negates one of the inherent advantages of the photoelectrochemical approach.

We note finally that the development of multilayer, band gap systems with variable width by (electro)chemical soft preparation methods provides opportunities for low-cost structures with high efficiency in solar cell devices. Examples of such devices are given elsewhere in this book.

### 5.2.5 Zinc Chalcogenides

The zinc chalcogenides, ZnX, comprise another class of II–VI compounds that have been investigated as to their photoelectrochemical performance, albeit much less than their CdX counterparts, as being more ionic compounds with larger band gaps (ca. 3.7 eV for ZnS, 2.7 eV for ZnSe, and 2.3 eV for ZnTe), hence having less motivating electrochemistry under low-energy irradiation. Besides, all these compounds are more or less susceptible to PEC corrosion. We will focus here on some reference works on zinc selenide (ZnSe) electrodes.

Efficient photoelectrochemical decomposition of ZnSe electrodes has been observed in aqueous (indifferent) electrolytes of various pHs, despite the wide band gap of the semiconductor [119, 120]. On the other hand, ZnSe has been found to exhibit better dark electrochemical stability compared to the CdX compounds. Large dark potential ranges of stability (at least 3 V) were determined for I-doped ZnSe electrodes in aqueous media of pH 0, 6.3, and 14, by Gautron et al. [121], who presented also a detailed discussion of the flat band potential behavior on the basis of the Gärtner model. Interestingly, a Nernstian pH dependence was found for

$U_{FB}$ estimated by both electrical (Mott–Schottky) and optical (photocurrent voltammetry) methods in the media studied, for (111)-oriented ZnSe electrode surfaces. A different variation was observed for the (110) orientation at pH > 6. At pH 0, for both (110) or (111)-oriented electrode surface, the flat band potential value was –1.65 V (SHE) and the measured potential stability range (no detected current) was –0.35 to +2.65 V (SHE). A comparison of band levels with the other II–VI compounds as well as decomposition levels of ZnSe is given in Fig. 5.6.

The dark stability of ZnSe, in addition to its very negative flat band potential, was found to be connected with interesting interfacial behavior in electrolyte solutions. The above researchers [122] studied the electrochemical decomposition of n-ZnSe single crystals [(111) face exposed, and free carrier concentration of $10^{18}$ cm$^{-3}$] in connection with the chemisorption of OH$^-$ groups onto the semiconductor surface. The influence of oxidizing agents such as the illumination of the electrode or/and the presence of ferricyanide ions in solution, leading to injection of holes into the valence band, was also investigated. A complex and multistep corrosion mechanism, as opposed to the usual rather simple decomposition models, was proposed in order to account for the different observations made on the ZnSe electrodes, comprising the formation of triangular decomposition pits, a deep red layer of amorphous selenium, and a bright gray layer of zinc oxide. From a fundamental viewpoint, it was considered that the electrolyte action by means of its OH$^-$ groups was controlled by the band bending in the semiconductor space charge region. Injection of electrons from OH$^-$ groups into the conduction band was claimed to invoke the formation of
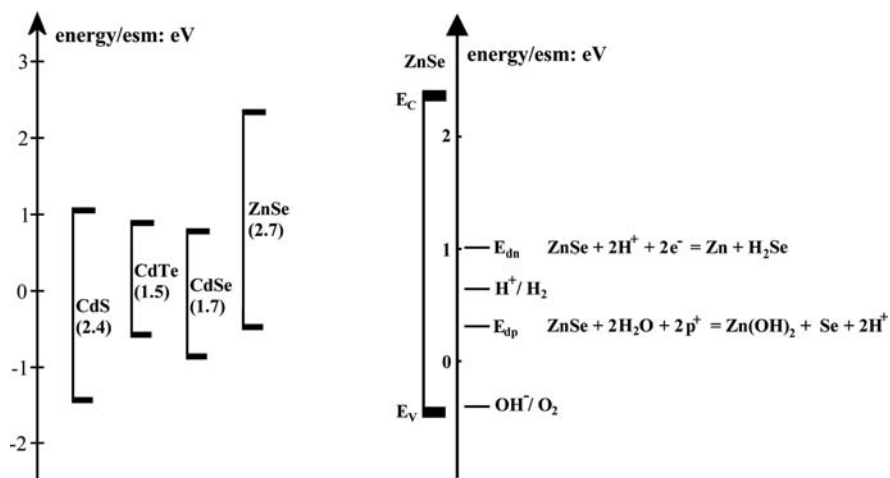


**Fig. 5.6** (*Left*) Comparison of band energy levels for different II–VI compounds. Note the high-energy levels of ZnSe. Representation is made here for electrodes in contact with 1 M HClO$_4$. The reference is a saturated mercury–mercurous sulfate electrode, denoted as esm (0 V/esm = +0.65 V vs. SHE). (*Right*) Anodic and cathodic decomposition reactions for ZnSe at their respective potentials ($E_{dp}$, $E_{dn}$) and water redox levels in the electrolytic medium of pH 0. (Adapted from [121])

soluble zinc and selenium species. Imposing large (anodic) potential values to the electrode, in the presence of an oxidizing agent injecting holes in the valence band, the sensitization of selenide species was found to give rise to the formation of an amorphous selenium layer, the products of zinc dissolution remaining soluble.

Having investigated the electrochemical behavior of ZnSe, and in view of the well-known blue luminescence of the compound, the previous authors extended their work to study electroluminescence from I-doped n-ZnSe crystals under anodic polarization in aqueous media containing metal ions such as Cu(II) and Sn(II) [123].

It was observed in other works that in sulfide electrolyte, decomposition of ZnSe was still obtained; stable PECs could be constructed though from single-crystal, n-type, Al-doped ZnSe electrodes and aqueous diselenide or ditelluride electrolytes [124]. Long-term experiments in these electrolytes were accompanied by little electrode weight loss, while relatively constant photocurrents and lack of surface damage were obtained, as well as competitive electrolyte oxidation. Photoluminescence and electroluminescence from the n-ZnSe:Al electrodes were investigated.

Photoelectrochemical studies with ternary chalcogenide systems containing zinc as one of the components have been published; however, such investigations on bulk or thin film binary ZnS and ZnTe electrodes are practically absent from the literature or may be found fragmentary in electrosynthesis-oriented works. ZnTe has been studied as a possible candidate for a photocathode in the photoelectrochemical production of hydrogen. Related information will be given in the relevant section.

Photoelectrochemical techniques have been utilized to determine the minority (electron) diffusion length ($L$) and other electrical parameters of p-ZnTe [125] and p-type $Cd_{1-x}Zn_xTe$ alloys [126]. In the latter case, the results for a series of single crystals with free carrier concentration in the range $10^{14}$–$10^{15}$ cm$^{-3}$ ($L = 2$–$4$ μm, constant Urbach's parameter at ca. 125 eV$^{-1}$) were considered encouraging for the production of optical and electro-optical devices based on heterojunctions of these alloys.

Zinc sulfide, with its wide band gap of 3.66 eV, has been considered as an excellent electroluminescent (EL) material. The electroluminescence of ZnS has been used as a probe for unraveling the energetics at the ZnS/electrolyte interface and for possible application to display devices. Fan and Bard [127] examined the effect of temperature on EL of Al-doped self-activated ZnS single crystals in a persulfate–butyronitrile solution, as well as the time-resolved photoluminescence (PL) of the compound. Further [128], they investigated the PL and EL from single-crystal Mn-doped ZnS (ZnS:Mn) centered at 580 nm. The PL was quenched by surface modification with $I_2$-treated poly(vinylferrocene). The effect of pH and temperature on the EL of ZnS:Mn in aqueous and butyronitrile solutions upon reduction of peroxydisulfate ion was also studied. EL of polycrystalline chemical vapor deposited (CVD) ZnS doped with Al, Cu–Al, and Mn was also observed with peaks at 430, 475, and 565 nm, respectively. High EL efficiency, comparable to that of single-crystal ZnS, was found for the doped CVD polycrystalline ZnS. In all cases, the EL efficiency was about 0.2–0.3%.

## *5.2.6 Layered Transition Metal Chalcogenides*

Along with the CdX compounds, the layered (van der Waals: vdW) transition metal dichalcogenide (TMD) semiconductors, specifically those of Mo and W, have been thoroughly studied with respect to their photoelectrochemical properties. The salient structural features of the $CdI_2$-type TMD $MX_2$ compounds are blocks of two hexagonally close-packed chalcogen layers between which the transition metals reside in either prismatic or octahedral coordination of six chalcogens (Chap. 1). The vdW character of bonding between chalcogen atomic layers as opposed to the strict polar covalent sequence of layers in CdX endows the TMDs with unique electronic properties that will be discussed presently in connection with photoelectrochemistry.

Layered TMDs include metal components belonging to the Groups IVA (4), VA (5), VIA (6), VIIA (7), and VIII (in particular 10). Among them the most interesting semiconductor compounds comprise metals of the Groups 4, 6, and 10. Specifically, Mo, W, Zr, and Hf sulfides and selenides show optical band gaps between 1 and 2 eV. Transition from non-metallic to metallic affinities occurs from sulfur to tellurium compounds. The $TiS_2$, although theoretically a semiconductor, has experimentally been found to be semimetallic due to an excess of titanium metal whose electrons partially fill the $d$-type conduction band. Established intercalation applications of this compound will be discussed elsewhere. Platinum dichalcogenides are of little practical interest, since they would be expensive and have small energy gaps (< 1 eV). Zirconium and hafnium sulfides and selenides have been examined, particularly with reference to their applicability to photointercalation processes as having the electrochemical property of forming energy-storing insertion compounds at low electrode potentials (Chap. 6).

Interest in the layered TMD semiconductors originated primarily from their potential for solar energy conversion, since they present particularly fitting properties for both Schottky and liquid junction solar cells, namely band gap energies in the optimum range for terrestrial energy conversion and high absorption coefficients, while being composed of readily available non-precious constituents. Further, and most important for liquid junctions, is that, unlike most of the non-oxide semiconductors, these materials show good photoanode stability in relatively oxidizing solutions. This has been suggested to be a result of the fact that the optical absorption near the band edge is dominated by direct transitions between hybridized metal $d$-bands and not between metal $d$- and chalcogen $p$-bands as in the polar metal–chalcogen compounds; these almost intrametallic transitions leave the bonding of the TMD semiconductor largely unaffected, so that its susceptibility to photocorrosion is low. In other words, holes photogenerated in $d$-bands of covalent TMD-layered compounds react electrochemically differently from holes generated in semiconductors with valence bands based on $p$-orbitals (e.g., CdS, ZnO, CdSe, GaAs). They do not constitute broken crystal bonds and therefore do not lead directly to anodic photodecomposition of the electrode. On the other hand, the chemical character of these holes as missing $d$-electrons, which is associated to an increased oxidation state of the transition metal, has the consequence that surface-positioned transition metal atoms will interact with the electrolyte and change their

ligand composition, giving rise to specific electrochemical surface reactions with electron donors such as $I^-$, $Br^-$, and $OH^-$, as will be discussed shortly.

Typical results and applications of TMD compounds in PEC systems, up to 1985, are summarized by Rajeshwar [129]. Tributsch [130] was the first to introduce the concept of using layered TMD as electrodes in PEC applications. In searching for a method to attack the problem of corrosion of polar metal chalcogenides in aqueous media he suggested that instead of trying to evade bond dissociation upon electron excitation or to prevent transport of reaction products, materials should be used that provide favorable optical transitions between non-bonding orbitals; these transitions would therefore not affect the original bonding in the semiconductor surface. On account of a detailed theoretical analysis, mostly based on energetic and kinetic considerations, Tributsch reached the conclusion that the most promising electrode materials would be transition metal chalcogenides. Upon inspection of some basic solid-state properties as, for instance, the metal–metal distance which determines the $d$–$d$ interaction and hence also the $d$–$d$ splitting, $MX_2$ compounds with M $=$ W, Mo, and X $=$ S, Se were identified as the theoretically most promising.

The experimental investigation [131] of the photoelectrochemical behavior of $MoS_2$ electrodes (with vdW surface exposed) in neutral and alkaline indifferent aqueous electrolytes (0.1 M KCl) showed that upon illumination with visible light, the semiconductor (which occurs as p-, n-, or intrinsic type, with a direct band gap of ~1.7 eV) reacts with water instead of anodically decomposing into metal ions and molecular sulfur. Evidence was given that the oxidation of water is initiated by a hole-mediated transition of Mo from the four-valent to the five-valent state, creating an additional bonding possibility for $OH^-$ ions from which electrons can subsequently be transferred to recombine with holes in the low-lying $d_{z^2}$-band of $MoS_2$ (Fig. 5.7). Actually, the main anodic product was sulfate, produced from the oxidation of the sulfide sulfur via a reaction involving radicals, with an overall scheme

$$MoS_2 + 8H_2O + 18\,h^+ + h\nu \rightarrow Mo(VI) + 2SO_4^{2-} + 16H^+$$
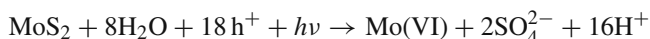
At low anodic potentials a parallel photochemical liberation of small quantities of oxygen (formed via the $2h^+$ oxidation of $H_2O$) could be traced on freshly prepared surfaces by polarographic techniques. Interestingly, the flat band potential of $MoS_2$ was found remarkably far in the anodic range, so that it was possible also to construct a regenerative solar cell with p-$MoS_2$ as a photocathode, at which a suitable oxidizing agent of a redox couple was reduced.

Comparison of the previous findings to the behavior of zirconium disulfide, $ZrS_2$, is revealing about the nature of photoelectrochemical mechanisms involving holes on $d$-orbitals of TMD compounds. Although $ZrS_2$ ($E_g = 1.68$ eV) has a layer-type structure very similar to that of $MoS_2$ (the only difference is that the cations in $ZrS_2$ have an octahedral arrangement and not a trigonal prismatic one as in $MoS_2$), its anodic photoproducts are very different. In fact, sulfur and not sulfate is formed; further, at the $ZrS_2$ interfaces, unlike $MoS_2$, there is neither a specific interaction with $OH^-$ or $I^-$ ions, which would decrease the activation energy for oxidation, nor is there a kinetic inhibition for the anodic release of metal ions, which
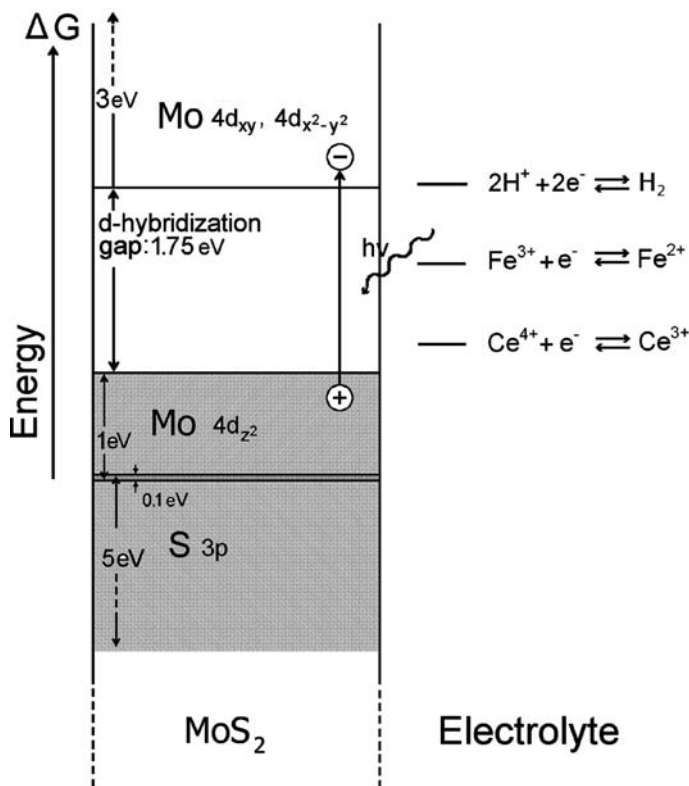
**Fig. 5.7** The band structure of $MoS_2$ is very unusual for a sulfide semiconductor. The conduction band is about 3 eV wide and based on four of the six Mo $4d$ orbitals ($4d_{xy}$, $4d_{x^2-y^2}$), with anti-bonding admixtures of sulfur $3p$ orbitals. Somewhat less than 2 eV below (the absorption edge for direct optical transitions in these experiments was at 1.75 eV) there is the non-bonding Mo $4d_{z^2}$ orbital (approximately l eV wide) holding two electrons per $MoS_2$. Below and slightly overlapping (0.1 eV) with the Mo $4d_{z^2}$ band is the principal S $3p$ valence band. Thus, a Mo $d$-band overlapping the sulfur valence band appears. The relative energy levels of one-electron transfer agents ($Fe^{2+}$, $Ce^{3+}$) able to supply electrons into the valence band of $MoS_2$ are depicted. (Reproduced from [131], Copyright 2009, with permission from Elsevier)

would prevent corrosion. In this aspect, $ZrS_2$ behaves similarly to CdS and appears not to be especially interesting for conventional electrochemical solar cells [132]. On the other hand, zirconium sulfides and selenides present a great potential for photo-intercalation applications, as already mentioned. The key point here, which underscores the advantage of having holes in $d$-bands in accomplishing energetically demanding oxidation reactions, is that despite the close similarity of the crystal structures of $ZrS_2$ and $MoS_2$, and in combination with a similar chemical behavior of Zr and Mo, the valence band of $ZrS_2$ derives from sulfur $3p$ orbitals and not metal $d$-states. The discrepancies therefore are attributed in principle to this pronounced difference of the respective electronic structures. Similarly, the layer-type $HfSe_2$ ($E_g$ = 1.13 eV) photocorrodes anodically to Hf(IV) and selenium since its valence band is not derived from $d$-states but from selenium $p$-states, as in CdSe [133].

In general, layered transition metal sulfides and selenides can only be stabilized kinetically in contrast to the large band gap oxides like $TiO_2$ and $SrTiO_3$, which appear to be thermodynamically stable in water-oxidizing conditions. Thus, the photooxidation of iodide ions ($I^-$) to $I_3^-$ or $I_2$ in aqueous solutions is quite efficient at $MoS_2$, $MoSe_2$, or $WSe_2$ photoanodes, as being kinetically more favorable than the semiconductor decomposition. Solar cells with such electrodes in iodide solutions have been reported to reach conversion efficiencies similar to the CdS or CdSe-based cells operating in the polysulfide and polyselenide redox systems, yet easily stabilized against photodecomposition [134]. The most efficient systems comprised the lower band gap selenides $n$-$MoSe_2$ or $n$-$WSe_2$ (both direct, $E_g = 1.4$ eV). Long-term stability was demonstrated for an $n$-$MoSe_2/I^-$, $I_2/Pt$ solar cell operating for 9 months at a photocurrent density of 10 mA cm$^{-2}$. Importantly, an unexpectedly large photovoltage was measured in the cell, despite the relatively reducing redox potential of the $I_2/I^-$ couple (reported formal potential 0.28 V vs. SCE; standard 0.5355 V vs. SHE for $I_2/I^-$, and 0.5360 V vs. SHE for $I_3^-/I^-$). This was considered to reflect a shift of the flat band potential of the electrode to several hundred mV more negative values than in indifferent solutions, due to a strong interaction of the $I^-$ ions with the $MoSe_2$ surface. At any rate, the results were very sensitive to crystal selection and orientation.

At this stage, it was clear that the increased stability of TMD toward anodic decomposition permits use of redox systems with more positive potentials than those of the specific redox systems used previously for the more difficult to stabilize Cd-chalcogenides invoking increased light absorption in the electrolyte, toxicity, and air sensitivity. The inherently stable TMD semiconductors would afford a wider range of redox couples with less limited properties, provided that their flat band positions were also advantageous. Important results in this connection were established by Menezes et al. [135] who investigated the photoelectrochemical compatibility of $n$-$WSe_2$ and $n$-$MoSe_2$ with several redox systems. Unlike $I_2/I^-$ systems, a specific surface interaction which would lead to a large negative flat band shift was absent in the $Br_2/Br^-$ case, hence the redox potential of the latter turned out to be too positive (standard: +1.065 V vs. SHE) to restrain photocorrosion. Then again, such surface interactions could occur with the larger, multiply charged $Fe(CN)_6^{3-/4-}$ ions which have redox potential close to that of the $I^-/I_2$ couple and also a well-defined oxidation step, but less of a flat band potential shift. Qualitatively similar results were reported for $n$-type $MoS_2$.

Thus, a good PEC behavior could be established for $WSe_2$, $MoSe_2$, and $MoS_2$ photoelectrodes in aqueous solutions containing redox couples with reasonably positive redox potentials such as $I^-/I_3^-$. In principle, the oxidizing power of the photogenerated holes in these electrodes is positive enough to effect $Cl_2$ or $Br_2$ generation; however, in the presence of $Br^-$ or $Cl^-$ [standard aqueous ($Cl_2/Cl^-$): 1.3583 vs. SHE], photoanodic corrosion has been the dominant process. Notwithstanding, Wrighton and co-workers [136] demonstrated that $MoSe_2$ and $MoS_2$ can effectively photooxidize aqueous bromide and chloride, if highly concentrated solutions were used. Their strategy has been to employ super high concentrations of these ions by using aqueous solutions of LiCl (15 M) or LiBr (12 M). The rationale was twofold: (i) the effective activity of $X^-$ can be much higher than the concentration (the $Cl^-$

activity of 15 M LiCl is 480 M and the $Br^-$ activity of 12 M LiBr is 560 M) to provide the kinetic advantage for productive photooxidation of $X^-$ and (ii) the activity of $H_2O$ can be reduced significantly by the high ionic strength to reduce the efficiency for photocorrosion.

Schneemeyer and Wrighton [137, 138] studied the interface energetics of n-type $MoS_2$ and $MoSe_2$ by means of cyclic voltammetry at dark and illuminated (laser 632.8 nm at ~50 mW $cm^{-2}$) single-crystal electrodes, at 25 °C, in aprotic $CH_3CN/0.1$ M [$n$-$Bu_4N$]$ClO_4$ solutions of various reversible (at Pt) redox couples with formal potentials spanning a range –0.8 to +1.5 V vs. SCE (Fig. 5.8). All couples were fast, one-electron, outer-sphere systems so that kinetics for heterogeneous electron transfer was not expected to differ significantly. Thus, differences in performance could be attributed to those in redox potential. An exceptionally well-defined flat band potential was reported for n-type $MoS_2$, based on voltammetric measurements with biferrocene (BF) and $N,N,N',N'$-tetramethyl-$p$-phenylenediamine (TMPD) redox couples, each having two, reversible, one-electron waves at Pt electrode. At the $MoS_2$, the first oxidation was reversible in the dark, whereas the second oxidation was observed only upon illumination. The dark oxidation
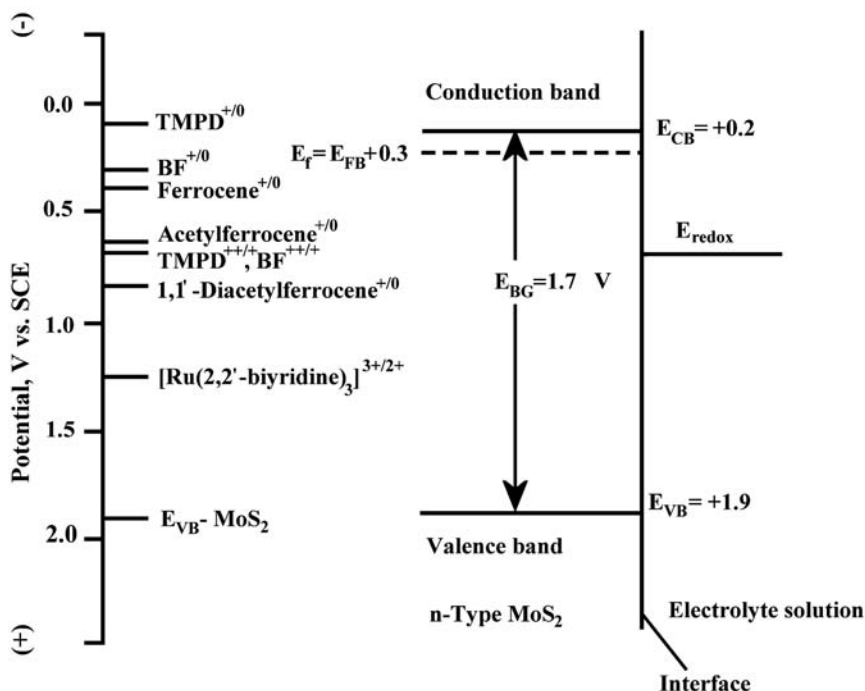


**Fig. 5.8** The energy levels of n-type $MoS_2$ at the flat band potential relative to the positions of various redox couples in $CH_3CN/[n$-$Bu_4N]ClO_4$ solution. The valence band edge of the semiconductor as revealed by accurate flat band potential measurement is at ca. +1.9 V vs. SCE implying that photooxidations workable at $TiO_2$ are thermodynamically possible at illuminated $MoS_2$ as well. (Reproduced with permission from [137], Copyright 2010, American Chemical Society)

$BF \rightarrow BF^+$ and the photoanodic $BF^+ \rightarrow BF^{2+}$ were separated by only $-150$ mV, allowing the authors to assign an accurate flat band potential of $+0.30$ ($+0.05$) V vs. SCE to $MoS_2$.

Quite interesting results were drawn regarding the photoelectrochemical behavior of $MoSe_2$ in acetonitrile and aqueous solutions of $X_n^-/X^-$ couples (X = Cl, Br, I) along with comparative data for the $MoS_2$-based cells. The onset potential of $MoSe_2$ photoanodic decomposition in aqueous electrolyte solutions ($\sim +0.5$ V vs. SCE) was reported to be less positive than the formal potential of $Br_2/Br^-$ and $Cl_2/Cl^-$,[3] so that stabilization should be ruled out with these couples *in aquo* (their reducing forms being at a high energy for photogenerated holes). A reverse order was true for the $CH_3CN$ medium, i.e., the onset potential for photoanodic decomposition was less negative than the redox potentials of these couples. Thus, the use of $CH_3CN$ solvent allowed the study of both $Br^-$ and $Cl^-$ oxidations at the illuminated photoanodes. In $CH_3CN$ solutions, where n-type $MoSe_2$ could be used as a stable photoanode, sustainable conversion of $\geq E_g$ light to electricity was obtained with efficiency ordered as Cl > Br > I. Specifically, conversion of 632.8 nm light to electricity was found to have an efficiency up to 7.5% for $Cl_2/Cl^-$, 1.4% for $Br_2/Br^-$, and 0.14% for $I_2/I^-$. This large variation reflected the differences among the halide redox systems in terms of PEC output voltage and short-circuit current, as related to increasing formal potentials in the same order. In aqueous solution, only the $I_3^-/I^-$ couple yielded a stable n-type $MoSe_2$-based PEC, one with efficiency a little lower than that for the $CH_3CN/Cl_2$, $Cl^-$ system, implying thus the important role of the solvent in the thermodynamics of electrode decomposition. For the sulfide n-$MoS_2/X_n^-$, $X^-$ cell, the results for acetonitrile and aqueous solutions were qualitatively similar to the $MoSe_2$ case. In conclusion, both $MoSe_2$ and $MoS_2$ could be used as stable photoanodes in acetonitrile solutions even for the oxidation of chloride. The ability to effect $Cl^-$ oxidation in $CH_3CN$ is considered important, in part because the formal potential of the $Cl_2/Cl^-$ couple in $CH_3CN$ is quite positive, thus inducing high photovoltage, and further because the $Cl_2/Cl^-$ solution is optically transparent over most of the visible spectrum, providing a non-absorptive path for the light.

Several behavior classes were established for the investigated redox couples, as already mentioned here in a preceding section. Importantly, the ability to observe photoeffects within the whole range of formal potentials, and in particular the observation of a constant photovoltage for formal potentials more positive than $\sim +0.7$ V vs. SCE (indicating a constant barrier height in this range) implied pinning of the Fermi level at the semiconductor/electrolyte interface. Either the existence of a significant density of surface states at energies lying in the band gap of the semiconductor or carrier inversion (such that a "p-type" near-surface region develops at the n-type material as the Fermi level in this region becomes closer to the top of the valence band) was considered to account for these observations. The authors consented to the former explanation, claiming an important role for "extrinsic" surface states, created from oxide or other impurity material on the $MoSe_2$ surface; intrinsic

---

[3] The reported values in 0.9 M $I^-$, 1 M $Br^-$, and 1 M $Cl^-$ solutions, for the respective couples, were $+0.3$, $+0.7$, and $+1.1$ V vs. SCE.

surface states were ruled out on the basis of earlier results indicating that layered Mo compounds are relatively free of them. Whatever the origin of the Fermi level pinning, the fact was that the $MoSe_2$ "pinned" photoanodes could attain oxidations that would be regarded as impossible within the ideal model where the band edges remain fixed. Similar observations made in related systems have been attributed to charging effects at the semiconductor surface produced by the redox species in the electrolyte. In their work on the energetics of p/n photoelectrochemical cells, comprising simultaneously illuminated p-type photocathodes and n-type photoanodes, namely n-$WSe_2$, n-$MoSe_2$, n-$WS_2$, n-$TiO_2$, p-InP, p-GaP, and p-Si electrode combinations, Parkinson et al. [139] suggested that the advantage of charge trapping in surface states without concomitant anodic corrosion is that the flat band potential does not have to be adjusted to the desired redox reaction. In this situation, the obtainable photovoltage remains constant for all redox couples of comparable charge transfer kinetics and is available to drive photoelectrolytic processes.

Fan and Bard [140] employed capacitance and voltammetric measurements to investigate the photoelectrochemical behavior of n-$WSe_2$, p-$WSe_2$, and n-$MoSe_2$ single-crystal electrodes in aqueous solutions containing various redox couples, namely $Br^-/Br_2$, $I^-/I_3^-$, $Fe(CN)_6^{4-}/Fe(CN)_6^{3-}$, $Fe^{2+}/Fe^{3+}$, $HV^+/HV^{2+}$, and $MV^+/MV^{2+}$ (HV is heptyl viologen and MV is methyl viologen). The specific effects of iodide on the electrochemical behavior of the layer-type compounds were compared, and the characteristics of several PEC cells were described. The interface energies for n-$MoSe_2$ in contact with various redox couples were given as in Fig. 5.9.

The interfacial energetics of $MoTe_2$ (n- and p-type, $E_g \approx 1.0$ eV) electrodes in solutions containing various redox couples have also been characterized [141]. The compound showed behavior qualitatively similar to the other layered semiconductors in terms of the sensitivity of their properties to growth conditions and surface imperfections. PEC cells based on n-$MoTe_2$ with $I^-/I_3^-$ as a redox couple reached monochromatic light (He/Ne laser) to electrical conversion efficiencies of over 8%. Koval and Olson [142] described the interface energetics of n-$WSe_2$ single-crystal electrodes (with a doping density of $2.8 \times 10^{17}$ cm$^{-3}$) in dry acetonitrile–tetrabutylammonium fluoroborate solutions containing acetylferrocene, ferrocene, or decamethylferrocene redox couples. Based on their simultaneous voltammetric and impedance (Mott–Schottky) analysis, the authors claimed that $WSe_2$ represents an ideal material for fundamental investigations of the electrochemistry of narrow band gap semiconductors.

A common conclusion in the aforementioned and other works, as already stated, has been that the flat band potential ($U_{FB}$) of molybdenum or tungsten dichalcogenide electrodes in contact with iodide solutions is shifted to the cathodic direction. Further, this negative $U_{FB}$ shift has been found to increase significantly upon addition of $I_2$ to the $I^-$ solution forming $I_3^-$. By measuring $U_{FB}$ variations for n-$WS_2$ electrodes in electrolyte media containing $I^-$ or $I_3^-$, Huang and Wrighton [143] found that the magnitude of the shift depended on the concentration of these species, the dependence fitting a Langmuir adsorption isotherm. The researchers tried to investigate further the nature of the flat band potential shift of metal dichalcogenides in
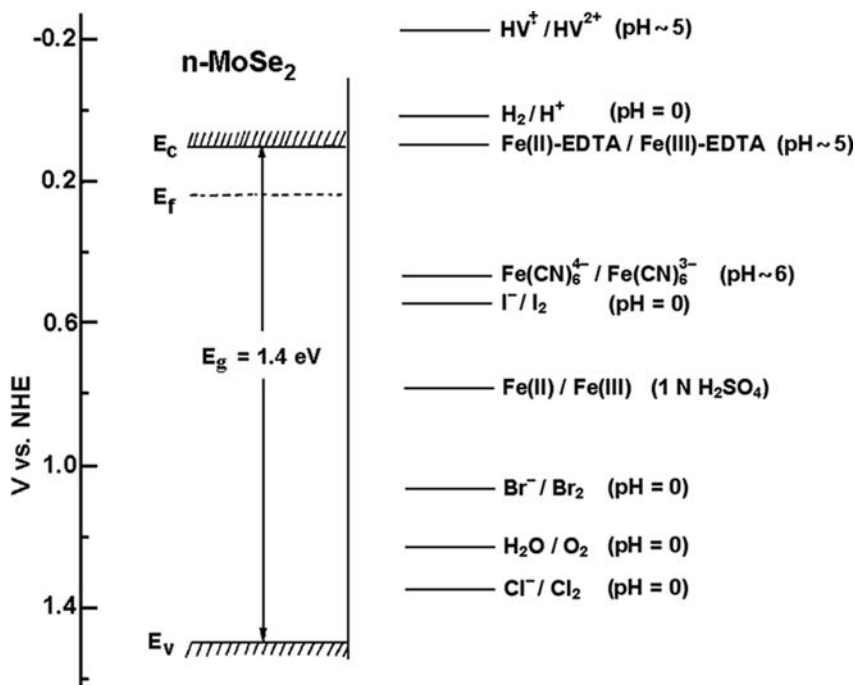
**Fig. 5.9** Schematic representation of the energetic situation at the n-MoSe$_2$/solution interface. (Reproduced from [140])

I$^-$ or I$_3^-$ electrolytes by modifying the electrode with a derivative which concentrates I$^-$ from dilute solutions. In particular they employed differential interfacial capacitance measurements to determine the $U_{FB}$ of naked and cationic viologen (BPQ$^{2+}$)$_n$-modified n-WS$_2$ electrodes in KI and KI$_3$ solutions. Because of the high concentration of anions in the cationic viologen polymer due to electrostatic forces, the polymer-modified n-WS$_2$ surface was in contact with a high concentration of I$^-$ or I$_3^-$ even in dilute solutions. However, the $U_{FB}$ shifts were found to be about the same for both naked and polymer-modified electrodes in a wide range of concentrations of I$^-$ or I$_3^-$ solutions. This result was explained on the basis of thermodynamic equilibria: the fact that the polycation concentrates I$^-$ or I$_3^-$ from dilute solutions only means that the concentration in the polymer is increased; the activity of I$^-$ or I$_3^-$ at the WS$_2$ surface is essentially unaffected, resulting in $U_{FB}$ shifts of the same magnitudes and concentration dependencies for naked WS$_2$ and polycation-coated WS$_2$. Thus, the surface energetics of WS$_2$ are unaffected by the polycation in dilute I$^-$ or I$_3^-$ solutions, though the higher concentrations of anion in the polymer may be important in acceleration of the redox reactions of the anion by the polycation-modified electrode.

The rhenium dichalcogenides, ReS$_2$ and ReSe$_2$, have a distorted CdCl$_2$ layered structure leading to triclinic symmetry, with the Re $d$-states forming the top of the

valence band. $ReS_2$ and $ReSe_2$ single crystals of the n-type have been found to exhibit enhanced stability against photocorrosion in aqueous solutions of $I_3^-/I^-$ with respect to other semiconductors such as CdS and GaAs [144]. Photoelectrochemical spectral response measurements gave an indirect optical band gap of 1.4 eV for $ReS_2$, while analysis of optical absorption spectra resulted in lowest-energy indirect optical band gaps of 1.32 eV for $ReS_2$ and 1.17 eV for $ReSe_2$. Considering that p-type materials can be useful in photosynthetic applications, Wheeler et al. [145] described the growth of p-$ReS_2$ and p-$ReSe_2$ crystals and their PEC behavior in aqueous solutions. The determined band gaps agreed well with the previously specified values for the n-type compounds. Open-circuit photovoltage values of ca. 400 mV were obtained from both crystals in Fe(II/III), EDTA solution. It was stated that the conduction band edges of the compounds are too positive to photoreduce $CO_2$, but might be able to produce $H_2$ with a suitable catalyst. Presently, considerable attention had been focused on rhenium sulfides because of potential applications as sulfur-tolerant hydrogenation and hydrodesulfurization catalysts [146, 147].

Layered crystals of *chalcogenophosphates* ($MPX_3$, with X = S, Se) have been evaluated for use as photoelectrodes in photoelectrochemical cells. The structure of these compounds, typified by $FePS_3$, is closely related to the dichalcogenides. In specific, the iron atoms and pairs of phosphorus atoms, in the form of dumbbells, take up the positions of the titanium atoms in $TiS_2$. Frequently, and in particular for the sulfides, the $MPX_3$ structure is monoclinically distorted; the selenides are more likely to be found in the rhombohedral modification. A wide range of metal atoms can take up the iron positions including V, Cr, Mn, Ni, Zn, Sn, and 2/3 In (below); however, the electronic properties of the $MPX_3$ compounds are different from those of the layered $MX_2$, as the fundamental transition in this case occurs between bands related to anion or phosphorus levels and localized *d*-states. The reported values of their optical absorption edges indicate that these compounds can be used, in principle, as solar cell materials. Three compounds in the thiophosphates series, namely, $SnPS_3$, $FePS_3$, and $NiPS_3$, were reported to yield clear photoresponse and low dark currents in aqueous pH 2 ($H_2SO_4$) solutions. $SnPS_3$ as grown by iodine vapor transport was found to be n-type whereas the other two compounds were p-type [148].

The photovoltammetry and capacitance–voltage characteristics of p-type (as-grown) single-crystal electrodes of $FePS_3$ and $FePSe_3$ have been studied in acid ($H_2SO_4$) solutions. The quantum efficiencies were low in most of the visible spectrum in agreement with the nature of the *d*-levels and low carrier mobilities. The current–voltage and flat band potential measurements indicated significant surface recombination, due to the presence of surface states. Interpretation of the measured quantum efficiencies in PEC was proposed in terms of two indirect optical transitions at 1.62 and 2.3 eV for $FePS_3$ and at 1.3 and 1.83 eV for $FePSe_3$ [149]. The energy band schemes of these compounds were discussed in relation to the electronic properties of other layered chalcogenophosphates including those of Zn, Cd, In, Mn, and Ni.

### 5.2.6.1 Surface Anisotropy Effect

The attractive features of layered TMD for PEC applications are counterbalanced with anisotropic effects and difficulties of fabrication in polycrystalline form. Similar to other systems (CdX), a wide variance in measured electrochemical parameters (e.g., flat band potential) in PEC has been reported from different laboratories for layered TMD electrodes, mostly due to the significant sample-to-sample variations in the morphology of utilized crystals. Clearly, with polycrystalline electrodes, the extensive anisotropy and the multitude of extrinsic surface states, such as those due to surface complexes with redox species from solution, are usually responsible for degraded performance; for instance, the heterogeneity of electrodeposited molybdenum selenide films accompanied by a high density of surface states and deep level traps contributing significantly to the interfacial charge transfer has been invoked to explain the low efficiencies of as-fabricated n-$MoSe_2$/I$^-$, $I_2$ solar cells [150]. However, the problem is not limited to poorly defined crystallinity as the one found in polycrystalline surfaces. The electrochemical response may depend considerably on the crystallographic orientation that is exposed to the electrolyte, and this is particularly evident in the case of layered-type semiconductors, where steps are present at their vdW surface. In fact, it has been suggested that cleavage steps in single-crystal TMD electrodes are associated with a high density of recombination surface states.

Experimentally, the presence of exposed edges in the vdW surfaces has been connected to high dark anodic currents at n-type electrodes limiting thus their photocurrent efficiencies. The first investigation of $WSe_2$ in an electrochemical environment [151] revealed that the photovoltage and photocurrent were significantly reduced on account of recombination losses. The solar energy conversion efficiency for a p-$WSe_2$ photocathode was only 2% and the fill factor did not exceed 0.25. Still, conversion efficiencies in excess of 10% were achieved after a careful cleavage of the vdW face of $WSe_2$ [152]. In an early work, Lewerenz et al. [153] established a correlation between photovoltaic parameters and surface perfection, by investigating the performance of n-$WSe_2$ photoanodes of different surface morphology, in an aqueous $I_3^-$/I$^-$ cell. According to their results, surface damage is of extreme importance in layered semiconductors for any type of solar cell, including liquid junction devices. On the basis of a developed model, it was predicted that the efficiency obtained with flat single-crystalline surfaces will be markedly enhanced compared to ill-defined surfaces. $WSe_2$ was found to exhibit various types of recombination sites. Besides those frequently found in layered semiconductors (i.e., bulk dislocations, growth irregularities, and occlusions), steps were considered to be the most commonly encountered recombination sites and their presence was shown to be particularly deleterious for solar energy conversion devices [154]. An illustrative mechanism involving a very effective deflection of minority carriers toward the edge of a step was proposed to explain this fact. It was considered that an electric field acting parallel to the layered structure, on account of its highly anisotropic nature, deflects the holes to recombination sites at the edges of steps. That is, holes, on their

way to the interface find themselves in essentially "dead" regions with respect to photoresponse.

Hence, the properties of PEC with single-crystal layered TMD absorber electrodes may depend strongly on the nature of the electrode surface. Highly efficient and stable PEC can be constructed provided the bulk and surface properties of single crystals can be sufficiently optimized. For this purpose, either an improved growth process leading to large-area smooth samples or the invention of a method to suppress the disadvantageous effects of steps on layered semiconductors is needed. In fact, it has been shown [155] that careful photoetching of n-WSe$_2$ as a pretreatment leads to a large improvement in photoresponse, yielding conversion efficiencies above 14%, rather the highest achieved to date.

Nonetheless, it has been stated that a simple differentiation between smooth and corrugated vdW surfaces is not sufficient for evaluating the photoelectrochemical behavior of layered TMD materials. In fact [156, 157], the kinetics of iodide photooxidation on an n-WSe$_2$ electrode are more favored at corrugated zones where there are plenty of steps than at smooth vdW surfaces free of defects, as a consequence of the better interaction of I$_3^-$ electrolyte ions with tungsten $d_{z^2}$ valence band orbitals. Likewise, structural and kinetic information obtained by photocurrent and electrolyte electroreflectance (EER) imaging techniques, for the characterization of the photoelectrochemical behavior of an n-MoSe$_2$ single crystal to the iodide reaction, as a function of its surface morphology, showed that the photooxidation kinetics is enhanced in those areas of a fresh single-crystal surface where a high density of surface defects (steps) is generated [158].

### 5.2.7   Iron Sulfides

Pyrite, FeS$_2$, is an abundant, low-cost, non-toxic material, which crystallizes in the cubic system, in a rock salt type structure with iron as Fe$^{2+}$ and sulfur as S$_2^{2-}$. It possesses most of the main requirements for efficient solar energy conversion, in particular a low, although indirect, energy gap (0.95 eV) close to that of silicon and an extremely high absorption coefficient ($6 \times 10^5$ cm$^{-1}$ for $hv \geq 1.3$ eV); optical measurements have shown that visible light is absorbed in an extremely thin layer (16 nm) of the material, in spite of the indirect gap. The electronic structure of FeS$_2$ resembles that of Mo and W dichalcogenides, as both the valence and conduction band states derive from $d$-orbitals of the metal atom. A survey on the properties of iron disulfide in relation to solar energy conversion has been given by Ennaoui et al. [159].

The electrochemistry of single-crystal and polycrystalline pyrite electrodes in acidic and alkaline aqueous solutions has been investigated extensively. Emphasis has been laid on the complex anodic oxidation process of pyrite and its products, which appears to proceed via an autocatalytic pathway [160]. A number of investigations and reviews have been published on this subject [161]. Electrochemical corrosion has been observed in the dark on single crystals and, more drastically, on polycrystalline pyrite [162]. Overall, the electrochemical path for the corrosion of n-FeS$_2$ pyrite in water under illumination has been described as a 15 h$^+$ reaction:

$$FeS_2 + 8H_2O + 15\,h^+ \rightarrow Fe^{3+} + 2SO_4^{2-} + 16H^+$$
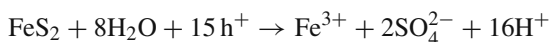
Hence, in the absence of a redox system in solution the anodic reaction of $FeS_2$ yields iron oxide/hydroxide and water-soluble sulfate ions. The compound does not undergo non-oxidative dissolution.

In photoelectrochemical applications, attempts have been made to minimize pyrite anodic corrosion by using suitable redox equilibria as well as proper preparation and assembling procedures of the photoelectrodes. Similar to the layered TMD case, one of the best redox systems for pyrite photoelectrodes has been the aqueous iodide/iodine. In fact, Ennaoui et al. [163], in a detailed investigation on the influence of various redox systems, organic electrolytes, and etching treatments on the photochemistry of pyrite, reported an "extraordinary" stability for the $FeS_2$–iodide/iodine system that was superior to all classical semiconductors (e.g., CdS, GaAs) and in line with the high stability found with TMD compounds. In particular, monocrystalline n-$FeS_2$ electrodes in aqueous $I^-/I_3^-$ were found to give very high photocurrents ($1$–$2$ A cm$^{-2}$) under intensive illumination ($4$–$5$ W cm$^{-2}$) without evidence of photocorrosion after passage of electrolysis charge as high as $623$ kC cm$^{-2}$. Proper control of the solid-state and interfacial chemistry was considered crucial for the high photocurrent quantum efficiency ($> 90\%$) and stability recorded. The superior interfacial properties of the $FeS_2$ photoelectrodes were tentatively attributed to the formation of iron–sulfur–iodine cluster compounds, suggesting thus an explanation of the results on the basis of charge transfer catalyst action. It was noted that such surface clusters are discussed as model compounds of the ferrodoxin charge transfer "catalysts" in biological systems. But, poor current–voltage characteristics involving a large dark current and a small fill factor were obtained from the PEC, and thus too low an output energy ($2.8\%$). A small photopotential not exceeding $200$ mV ($500$ mV is theoretically possible) was invariably found associated to a strong pinning of the Fermi level by surface states. The fact that a very high photocurrent density was observed simultaneously with a high dark current density was considered to indicate that the solid-state properties of pyrite are more complicated than those of conventional semiconductors and need special attention.

In effect, improved pyrite photoelectrode performances have been reported in the presence of oxide film on their surface [164]. The oxides were formed by thermal treatment in air of electrodes prepared by screen printing a paste consisting of a mixture of $FeS_2$ powder (natural iron sulfide from ore deposits) and polytetrafluoroethylene (PTFE) as a binder, dispersed in a Triton X-114 aqueous solution. The photoelectrochemistry of variously thermally activated samples were investigated in $I^-/I_3^-$ solutions and the results were discussed on the basis of the electronic structure of the compounds involved in the interfacial chemistry [165]. The oxides were found to improve the semiconducting behavior, in terms of either absorption or surface charge transfer, and to provide a good rectifying behavior toward semiconductor dissolution. In particular, the heterostructure based on $FeS_2/\gamma$-$Fe_2O_3$ was claimed as a promising system for matching optimal photoconversion efficiency values with low cost. An air-hydrogen activated electrode gave the best performance (efficiency $5.52\%$) as showing optimal combination of the optical absorption characteristics and charge transfer properties. It is noteworthy that the iron oxides $Fe_2O_3$

and $Fe_3O_4$, with band gap energies 2.2 and 3.0 eV, respectively, have never shown photocurrents with high quantum efficiency due to low mobility of holes (however, although not being suitable for the direct conversion of light into electricity, they have been extensively investigated for water splitting in photoelectrolysis cells).

Treatment by cathodic hydrogen evolution has been observed to improve the current–voltage characteristic of pyrite photoelectrodes. In investigating the influence of molecular and atomic hydrogen on the interfacial properties of pyrite, Alonso-Vante et al. [166] found that molecular hydrogen selectively converts $FeS_2$ surfaces other than the {100} to FeS, producing defect levels in the band gap, while atomic hydrogen generated by electrochemical and chemical treatments significantly improves the photocurrent to dark current ratio, presumably due to the passivation of these FeS centers. It was suggested that atomic hydrogen increases the barrier height at the solid–electrolyte junction and decreases the concentration of electronic states within the forbidden energy region, which assist dark or photogenerated electronic charge carriers in bypassing and penetrating the interfacial barrier. It was considered that atomic hydrogen associates itself to sulfur atoms adjacent to sulfur vacancies, thereby attracting negative charges from iron, transforming thus the electronically unfavorable FeS states, into more favorable FeSH centers.

A reasonably stable behavior under illumination has been observed for polycrystalline layers of As-doped $FeS_2$ in iodide electrolyte, although the photoelectric properties were poor [167].

The energetics of the pyrite interface/electrolyte as given by Ennaoui et al. [159] for indifferent acid electrolyte as well as with redox couples in solution is shown in Fig. 5.10.

Iron monosulfide exists in nature mainly as non-stoichiometric $Fe_{1-x}S$ (pyrrhotite) with hexagonal crystal structure (similar to that of NiAs), where octahedral coordination of iron by sulfur atoms occurs. The extent of $x$ in the pyrrhotite formula ranges typically between 0 and 0.2; when $x$ is greater than 0.07, the compound shows ferromagnetic behavior. $Fe_{0.9}S$ pyrrhotite is considered a promising low-cost semiconductor for solar energy conversion. According to its bulk solid-state characteristics, it should exhibit p-type conduction and an energy gap not exceeding 0.2 eV. Aricò et al. [168] reported on the photoelectrochemical behavior of polycrystalline layers of pyrrhotite ($Fe_{0.9}S$) mixed with organic binders (PTFE, Triton X-114) produced through a screen-printing method, followed by pressure and thermal ($N_2$) treatments. These electrodes showed behavior as photoactive n-type semiconductors giving rise to a photopotential of about 200 mV in $I^-$- and $Fe^{2+}$-containing solutions. Although electrochemical corrosion was greatly inhibited by PTFE, photocorrosion was observed at the illuminated $Fe_{0.9}S$ electrode in the presence of redox electrolytes. The electrode behavior was discussed in relation to its structure. To explain the discrepancy of finding an n-type conductivity, the observed results could be interpreted asserting that pressure and heat treatments in the course of the preparation procedure may have caused significant modifications in the actual crystal lattice, in such a way as to increase the crystal field by sulfur atoms and/or spin pairing of the $d$-electrons.
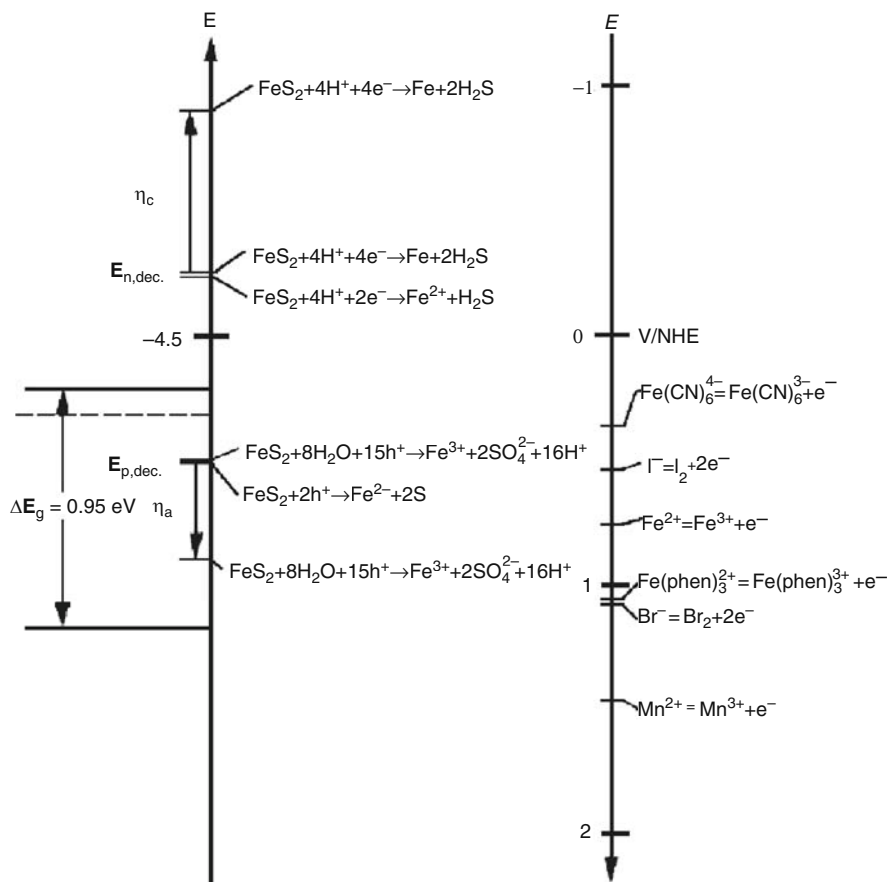
**Fig. 5.10** Relative band edge diagram for $FeS_2$ and the energy position of some electron donor species. The thermodynamic reactions corresponding to corrosion processes at the anodic and cathodic sides are indicated as decomposition potentials due to holes, $E_{p,dec}$, and to electrons, $E_{n,dec}$, respectively. $\eta_c$ and $\eta_a$ are the cathodic and anodic overpotentials, respectively, for the decomposition reaction of pyrite crystals in acid medium. (Reproduced from [159], Copyright 2009, with permission from Elsevier)

## 5.2.8 Chalcopyrites

The photovoltaic implications of the solid-state chemistry of $CuInSe_2$, particularly where deviations from the 1:1:2 stoichiometry along the $Cu_2Se$–$In_2Se_3$ tie line are concerned, have been studied, and results of measurements of some photoelectrochemical properties along this tie line (e.g., for $In_2S_3$) have been given [169].

An early discovery about n-$CuInSe_2$ and n-$CuInS_2$ semiconductor crystals was that they are extremely stable when used as photoanodes in aqueous polysulfide
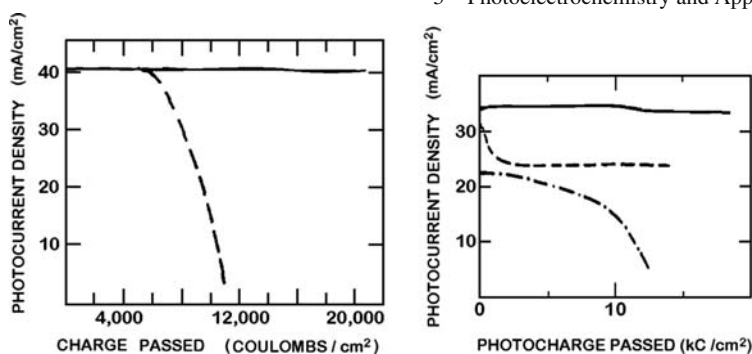
**Fig. 5.11** (*Left*) Short-circuit current as a function of total charge passed. The *full line* shows the behavior of a CuInSe$_2$(112) single crystal and the *dotted line* shows that of a CdSe(11.0) single crystal etched and photoetched. The experiment was under potentiostatic control at 50 °C. The solution contained 3 M each of KOH and Na$_2$S and 4 M of S. The (11.0) face is the more stable face of CdSe, and etching in aqua regia followed by photoetching results in the best possible output stability characteristics. (Reproduced with permission from [171], Copyright 2009, American Institute of Physics). (*Right*) Comparison of the output stability (under load conditions) of CdSe and CuInX$_2$ photoanodes in polysulfide electrolyte: *solid curve*, n-CuInSe$_2$ at −100 mV vs. polysulfide solution potential, in 3/3/4 (KOH/Na$_2$S/S) solution; *dashed curve*, n-CuInS$_2$ at −200 mV, in 1/1/1 solution; *dash-dot curve*, n-CdSe at −200 mV, in 3/3/4 solution. (Reproduced with permission from [173], Copyright 2009, American Chemical Society)

electrolyte. Robbins et al. [170], having assessed single-crystal and pressure-sintered polycrystalline n-CuInS$_2$ electrodes in PEC with aqueous l–2 M Na$_2$S, 1–3 M S, 0–2 M NaOH electrolyte, point out that while solar conversion efficiencies were reasonable (a few percent), by far the most outstanding feature of this system was its remarkable output stability. No detectable weight loss or visible alteration of electrodes was observed in the above cells after the application of extended runs to 20 kC cm$^{-2}$ charge passage. Additionally, the current output at short circuit or resistive load has been essentially constant for the same level of charge passage throughout test periods approximating 1.5 months of 8 h/day sun.

Results on the n-CuInSe$_2$/aqueous polyiodide system show that this, too, can be stabilized after suitable preparation of the solution and surface modifications. Mirovsky and Cahen [171] stated that the n-CuInSe$_2$ electrode shows a notable stability in operation with a redox couple which does not contain its anion element, i.e., Se. In this respect, it does not resemble the n-CdSe electrode, although the latter has almost twice as large a band gap as CuInSe$_2$. On the basis of this observation, the ternary selenide appears to be an exception to the often stated generalization that the most stable semiconductors are necessarily those that have the largest band gaps. According to surface XPS analysis, no evidence was found for an exchange of Se by S on electrodes operated in polysulfide solutions even after the passage of > 17 kC cm$^{-2}$ charge, in contrast to what has been observed for CdSe [88], where such an exchange was believed to be an important factor involved in deactivation of the CdSe electrode. Difference in output stability between CdSe and CuInX$_2$ photoanodes in aqueous polysulfide solutions are illustrated in Fig. 5.11.

Notwithstanding the excellent output stability of the $CuInX_2$ photoanodes, scanning electron micrographs revealed that some surface restructuring occurs during their use in polysulfide electrolyte [172]. In order to reach some understanding of the causes for their resistance to photocorrosion, n-$CuInS_2$ and n-$CuInSe_2$ crystals operated as photoanodes in polysulfide solutions were subjected to surface analyses by XPS and AES. Characterization results were given referring, for comparison, to data on binary Cu and In chalcogenides. On the surface of $CuInS_2$, rich indium heterogeneous patches were found containing mainly oxidized In. Some Cu compounds, such as $Cu_xS$, $Cu_2O$, and $CuO$, were claimed to be present as well. The surface of $CuInSe_2$ electrodes was depleted in Cu while most of the remaining In appeared to occur as indium oxide and/or indium selenide. On the basis of such findings, Cahen and Mirovsky [173] attempted a thermodynamic analysis of possible decomposition pathways in their fundamental study on the photoelectrochemistry of $CuInX_2$. Using literature thermodynamic data, they estimated the Gibbs free energy changes for several decomposition and exchange reactions for $CuInS_2$ and $CuInSe_2$ in aqueous polysulfide and aqueous polyiodide solution and calculated the corresponding electrode potentials. Thereof, with the aid of measured flat band potentials they determined the band edges of the semiconductors (or semiconductor/surface oxide systems, since $In_2O_3$ was believed to be the native oxide on these semiconductors) and estimated the quasi-Fermi levels from literature data. Combining these with the calculated decomposition potentials and the measured redox potentials, the authors could construct (in)stability electron energy diagrams that were strictly valid near open circuit. Notwithstanding the necessary assumptions and limitations of the approach, a thorough insight was provided in this manner to the stabilization of $CuInX_2$ photoanodes. By the developed model, the authors were able to explain several observations, such as (1) the absence of oxidative Se/S exchange in the n-$CuInSe_2/S_n^{2-}$ system; (2) the difference between $CuInS_2$ and $CuInSe_2$, in terms of indium oxide/indium sulfide surface coverage, in polysulfide solution; (3) the different probabilities for oxidative decomposition of $CuInS_2$ and $CuInSe_2$ in polysulfide; (4) the protective function of an indium oxide surface layer for $CuInSe_2$ in polyiodide; (5) the stabilizing effect of addition of copper ions to polyiodide solution, for $CuInSe_2$ photoanodes; (6) stability of $CuInSe_2$ against reductive decomposition; (7) the photoanodic decomposition of $CuInSe_2$ in acetonitrile; and (8) the possibility of $CuInS_2$ and, especially, $CuInSe_2$ formation on the surface of $In_2S_3$ and $In_2Se_3$, immersed in cuprous ion containing solutions.

On the other hand, several observations could not be explained by the collected and elaborated data: (1) the difference between CdSe and $CuInSe_2$ with respect to chemical Se/S exchange; (2) the absence of chemical oxygen/iodine exchange for $In_2O_3$, i.e., the lack of $InI_3$ formation, in polyiodide; (3) the absence of appreciable photoanodic decomposition of $CuInX_2$ into $Cu_2S$ and $In_2S_3$ in polysulfide (although consideration of possible first steps could provide part of the answer); and (4) the lack of $Cu_2Se$ formation from photoanodic decomposition of $CuInSe_2$ in polyiodide, viz. why $Cu^+(aq)$, rather than $Cu_2Se$, together with $InI_3$, would be formed upon decomposition of the unprotected chalcopyrite. In these latter

cases, kinetic factors, related to the large number of reactants and charge carriers involved in some of the suggested decomposition reactions, were considered to be dominant. Importantly, the authors noted that the initial oxidative (reductive) decomposition potentials could be shifted sufficiently negatively (positively), because of negligible initial activities of decomposition products, rendering a clean semiconductor surface thermodynamically unstable with respect to initial decomposition. This implies that thermodynamic reasons can be invoked for assuming that "no ideal semiconductor/electrolyte interface can exist".

Intentional restructuring of the chalcopyrite electrodes surface led to outstanding results regarding the performance of relevant liquid junctions. According to Menezes and Lewerenz [174], chemical reactions of illuminated $CuInSe_2$ with a polyiodide/CuI electrolyte transform the semiconductor surface to generate the $CuISe_3$–$Se^0$ phase; this in situ formation of a new phase was considered to be pivotal to stable and efficient operation of the n-$CuInSe_2$/$I^-$–$I_2$–$Cu^+$–HI solar cell. Although the p-type semiconducting $CuISe_3$ film was thought to serve primarily as a window mate of the heterojunction, its band gap of 2 eV suggested partial contribution to photogeneration of charge carriers. By modifying the growth conditions of the p-$CuISe_3$ phase, Menezes [175] was able to increase the solar energy conversion efficiency of the n-$CuInSe_2$/p-$CuISe_3$/$I^-$–$I_2$–$Cu^+$–HI cell from 9.5 to 12.2% (open circuit 0.49 V, short circuit 39.4 mA cm$^{-2}$). Growth conditions included the use of pre-polished n-$CuInSe_2$(110) surfaces, higher concentrations of HI and $Cu^+$, and an air anneal at 200 °C. XRF in conjunction with SEM characterization of the new interphase gave evidence of further transformation of $CuISe_3$ to $CuIn_2Se_3I$. Correlation of the energy bands and the Fermi levels of the resulting three-phase n-$CuInSe_2$/p-$CuISe_3$–$Se^0$/liquid contact showed that the principal barrier is located in the solid p–n heterojunction, with the redox electrolyte providing the front ohmic contact.

Only a few photoelectrochemical results have been published with p-type $CuInSe_2$. Recently, Djellal et al. [176] investigated the bulk and photoelectrochemical properties of p-$CuInSe_2$ ingots of lamellar crystallization, prepared by the fusion technique. The compound was found to exhibit an excellent chemical stability in KCl media, with a corrosion rate of only 8 μmol cm$^{-2}$ month$^{-1}$. From capacitance measurements, the flat band potential and the holes density were determined as –0.62 V vs. SCE and $4 \times 10^{17}$ cm$^{-3}$, respectively. A variation in the flat band potential with the electrolyte pH was observed, indicating strong $OH^-$ adsorption. The chalcopyrite ingots were tested for hydrogen generation process as will be discussed in a later paragraph.

Silver–indium diselenide, $AgInSe_2$, has been studied at a lesser extent than its parent compound $CuInSe_2$. Following the method developed by Cahen and Mirovsky, of deducing the energy diagram of the semiconductor from experimental as well as calculated data, Bicelli [177] has given an excellent illustration of the thermodynamic stability of n-$AgInSe_2$ electrodes in aqueous PEC cells containing different redox couples. In his paper, the standard free energy changes and decomposition potentials of all the possible bond cleavage and decomposition photoreactions in the polyiodide and polysulfide electrolyte were evaluated by thermodynamic principles. In addition, the possible chemical and electrochemical

Se/S exchange reactions in the polysulfide electrolyte were considered. A model was developed accounting for the electrode stability, on the basis of the relative position of the hole quasi-Fermi level under open-circuit conditions, the photodecomposition potentials, and the energy level of the redox couple in the electrolyte. It could be established thus that n-$AgInSe_2$ is more prone to hole attack than its copper analogue. The results were in accordance with previous experimental evidence of substantial instability of the n-$AgInSe_2$ photoanode in the considered electrolytes, even after coating its surface with an artificially formed indium oxide layer. Instability of the compound has been observed to be more pronounced in the polyiodide than in the polysulfide solution since $Se^0$ rapidly dissolves in the latter electrolyte, $Se^0$ being the main corrosion product well known to depress the PEC performance.

Becker et al. [178] studied the photoelectrochemistry of p-$HgIn_2Te_4$, p-$CdIn_2Te_4$, and n-$CdIn_2Te_4$ in a variety of aqueous redox couples (both $HgIn_2Te_4$ and $CdIn_2Te_4$ are ordered vacancy compounds crystallizing in defect tetrahedral structures of the chalcopyrite type). Regarding the p-type semiconductors, good results were obtained in terms of stability and performance with two very different pH redox couples both having significantly negative redox potentials: chromium(III)EDTA complex [pH 4.5, $U_{rdx} = -1.24$ V (SCE)] and Fe(III)TEA complex [pH 13, $U_{rdx} = -1.09$ V (SCE)]. For p-$HgIn_2Te_4$, quantum efficiencies of carrier collection higher than 90% were measured even at short circuit in either redox couple; the monochromatic and polychromatic power efficiencies based on three electrode cell experiments were found to be up to ~10 and ~3%, respectively. In either couple, the flat band potential was –0.70 V (SCE), indicating no preferential absorption of $H^+$ or $OH^-$ on the semiconductor surface. Indirect and direct gap transitions were determined at 0.88 and 1.04 eV, respectively. In the Fe(TEA) complex couple, it appeared that the semiconductor approaches 100% stability to photocorrosion. For p-$CdIn_2Te_4$, the quantum efficiencies of carrier collection were equally high even at short circuit in either redox couple. Monochromatic power efficiency was even higher (11%) than for p-$HgIn_2Te_4$, while the polychromatic was somewhat lower (2%), both calculated from three electrode cell experiments. It was noted that the power efficiencies would show significant improvement, provided that the relatively low fill factor (0.24–0.3) would increase. The flat band potential was near –0.55 V (SCE) and largely independent of the nature of the two couples considered. Both an indirect (1.16 eV) and a direct (1.24 eV) transition could be determined. Data for both semiconductors in a polysulfide solution indicated considerably poorer PEC characteristics than for the other redox solutions.

### 5.2.9 *Some Chalcogenides of p-Block Metals*

Interesting systems, mainly with respect to solid-state optoelectronics and chalcogenide glass sensors (due to ionic conductivity effects) are found among the Group IIIB (13) and IVB (14) chalcogenides, such as the p-type semiconductors MSe (M = Ga, In, Sn), SnS, and GeX (X = S, Se, Te). Some of the IIIB compounds,

such as p-GaSe ($E_g = 2.0$ eV) as well as n- and p-InSe ($E_g = 1.3$ eV), crystallize in layered vdW structures and have been the subject of recent electrochemical studies. Several ternary chalcogenide crystals of the composition I–III–VI$_2$ such as LiInS$_2$ and the chalcopyrite-type CuGaS$_2$, AgGaS$_2$, and AgGaSe$_2$, as well as the cation-deficient I–III$_5$–VI$_8$ chalcogenides CuGa$_5$S$_8$, CuGa$_5$Se$_8$, and AgGa$_5$S$_8$, present ionic conductivity [179]. The latter class of compounds is closely related to the well-known solid electrolytes α-Cu$_2$HgI$_4$ and α-Ag$_2$HgI$_4$. The bismuth and antimony tellurides and selenides and their mutual alloys are important for their thermoelectric applications.

### 5.2.9.1 Gallium and Indium Chalcogenides

The flat band potential of n- and p-InSe and p-GaSe single crystals as determined by rectified alternating photocurrent voltammetry (RAPV) in 1 M NaOH solution has been discussed in comparison with determinations carried out by direct current photovoltammetry and capacitance voltage measurements [180]. Anodic–cathodic photocurrent transitions were observed for the p-type semiconductors examined, unlike the n-type InSe. The origin of the n-type behavior for p-type materials was attributed to their possible doping with some n-type impurities during crystal growth.

Indium monoselenide, InSe, is a semiconductor with a weakly allowed direct band gap transition at 1.3 eV and an indirect at 1.2 eV, having a strongly anisotropic layered structure that consists of covalent bonded units (Se–In–In–Se) held together by vdW forces. The cleavage surface, the (00.1) plane, is perpendicular to the $c$-axis (vdW plane) and is made of Se atoms bonded together with covalent forces. The interface energetics of InSe single-crystal electrodes having their vdW cleavage surfaces exposed in indifferent aqueous acidic (0.1 M H$_2$SO$_4$) solutions has been described by Levy-Clement et al. [181]. The crystals were synthesized by the non-stoichiometric Bridgman technique either as n-type (Cl- or Ga-doped) or p-type (Zn-doped). The photoelectrochemical measurements showed rectifying behavior in the dark for both n- and p-InSe electrodes. Observed anodic and cathodic photocurrents under white light upon applying a positive bias to n-InSe and a negative bias to p-InSe, respectively, were ascribed to photoelectrochemical effects, whereas observed cathodic photocurrents for the n-type and anodic photocurrents for the p-type were explained invoking a bulk photoconductive effect corresponding to an increase in carriers or of their mobility by the absorption of light. The flat band potential of the electrodes was found to be pH independent. Photocurrent spectra indicated a 1.2 eV band gap. It was concluded from the experimental results that InSe should comprise good hydrogen-evolving semiconductor photocathode if a suitable metal catalyst was plated at the surface. Further, it was stressed that, as a p-type lamellar semiconductor, InSe should be used to study photointercalation, preferably of copper(I) ions due to its redox potential situated between the band energy levels of InSe.

In a subsequent work [182], it was shown that the photoelectrochemical performance of InSe can be considerably improved by means of selective (photo)electrochemical etching. Interestingly, whereas the cleavage vdW plane showed little improvement, the photocurrent in the face parallel to the $c$-axis was doubled. Note that, in contrast to InSe crystals cleaved in the plane perpendicular to the $c$-axis that are almost defect free, the crystals cut in the plane parallel to the $c$-axis contain a high density of defects on their surface which leads to a high rate of electron–hole recombinations and inferior quantum efficiency. The asymmetry in the role of electrons and holes, as manifested, e.g., in the fact that surface holes carry out the selective corrosion of the semiconductor surface in both cleavage orientations, was discussed.

The (photo)electrochemical behavior of p-InSe single-crystal vdW surface was studied in 0.5 M $H_2SO_4$ and 1.0 M NaOH solutions, in relation to the effect of surface steps on the crystal [183]. The pH–potential diagram was constructed, in order to examine the thermodynamic stability of the InSe crystals (Fig. 5.12). The mechanism of photoelectrochemical hydrogen evolution in 0.5 M $H_2SO_4$ and the effect of Pt modification were discussed. A several hundred mV anodic shift of the photocurrent onset potential was observed by depositing Pt on the semiconductor electrode.

Hyposelenophosphate $In_{2/3}PSe_3$, a layered compound of the $MPX_3$ series containing indium vacancies, has been considered potentially interesting for solar energy conversion. Photoelectrochemical measurements on $In_{2/3}PSe_3$ single crystals evidenced an indirect transition at 1.55 eV and a direct one at 1.80 eV. Interestingly, a hole diffusion length of 4 μm was evaluated and a very negative flat band potential of about −1.4 V (SHE) at pH 1 ($H_2SO_4/H_2O$). However, the electron mobility and concentration were low [184].

Polycrystalline thin films of gallium-containing CdSe, i.e., (CdGa)Se of variable composition, have been synthesized by electrochemical co-deposition and characterized by photovoltammetry, photocurrent spectroscopy, and electrochemical
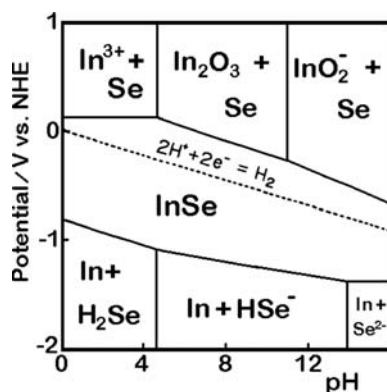


**Fig. 5.12** Potential–pH diagram for the In–Se–water system at 25 °C. *Each line* represents the equilibrium reaction with activity of dissolved substance $10^{-6}$. (Reproduced from [183])

impedance measurements [185]. The effect of progressive inclusion of Ga on the corrosion behavior of the electrodeposits was examined.

Recently, 1D quantum dots of gallium selenide with average diameter 8–10 nm, connected in the form of chains of average length 50–60 nm, were synthesized on ITO substrates by cathodic electrodeposition from acidic aqueous solutions of gallium(III) nitrate and selenious acid [186]. The structural analysis from XRD patterns revealed the formation of $Ga_2Se_3$/GaSe composition. The films were found to be photoactive in aqueous sodium thiosulfate solution and showed p-type conductivity.

Photoconductivity and photoelectrochemical studies have been reported for $In_2S_3$ in the form of single crystals, polycrystalline thin films, and colloids. It has been shown that $\beta$-$In_2S_3$ crystals (defect spinel structure), with a band gap of 1.97 eV, can be made to have high dark conductivity either by incorporation of halogen donors, as from $CdCl_2$ or $NH_4Cl$, or by heating the pure material in nitrogen to temperatures above 800 °C [187]. Studies of the conduction mechanism in pure single crystals of $\beta$-$In_2S_3$ showed that the conductivity is always n-type, and no p-type conductivity is observed when the samples are doped with copper or cadmium [188]. Becker et al. [189] studied extensively the photoelectrochemical properties of $\beta$-$In_2S_3$ synthesized in a variety of manners and with various dopants and evidenced the unsatisfactory output stability of the material. A p-response was obtained when the single crystals were prepared with an excess of sulfur or InP, but an n-type response was also present. Thermodynamic analyses of the photoelectrochemical behavior of $In_2S_3$ are available. The work of Bicelli [190], following previous analysis on $CuInS_2$ and related binaries [173], gives valuable information as to the evaluated thermodynamic stability of n-$In_2S_3$ in relation to the experimental results obtained with neutral polysulfide, hexacyanoferrate, and polyiodide electrolytes.

$In_2S_3$ polycrystalline thin films obtained by chalcogenization of electroplated metallic indium films on Ti substrates with a flowing stream of $H_2S$ gas have been examined as to their PEC behavior [191]. The variation of their flat band potential with different redox couples, solution concentration, and pH values has also been studied [192]. Sulfide, sulfate, and hexacyanoferrate reducing agents were found to interact strongly with the $In_2S_3$ electrode surface, shifting the $U_{FB}$ to the cathodic direction. The magnitude of this interaction was in the order $S^{2-} > SO_4^{2-} > Fe(CN)_6^{4-}$. Also, a linear variation of $U_{FB}$ with pH was observed, indicating a varying surface chemical composition, which was claimed to involve a partial hydroxylation. Photoelectrochemical characterization in aqueous polysulfide solutions showed a direct allowed transition at 2.06 eV for the electrodes, according to the Gärtner–Butler model.

The photoelectrochemical properties of $In_2S_3$ colloids prepared by chemical solution growth [193] have been demonstrated by carrying out oxidation and reduction processes under visible light irradiation. Charged stabilizers such as Nafion were found to provide an effective microenvironment for controlling charge transfer between the semiconductor colloid and the redox relay.

### 5.2.9.2  Tin Sulfides

Photoelectrochemical studies on phosphorus-doped n-type $SnS_2$ single crystals (layered structure, first indirect transition at 2.21 eV) in contact with aqueous electrolytes containing various redox couples have been reported [194]. Under illumination, the electrode was unstable in both acidic and alkaline media and the photocurrents were mostly due to the decomposition of the semiconductor. In fact, the electrode could be stabilized only in acidic solutions containing iodide. The influence of redox reagents on the flat band position of the n-type $SnS_2$ crystals in aqueous solutions of different pH values has also been investigated [195]. Decomposition of $SnS_2$ was attributed to the existence of surface states at the semiconductor/electrolyte interface consisting primarily of negatively charged surface sulfur atoms. It was established that in sufficiently alkaline solutions, the oxidized form of redox reagents such as $Fe(CN)_6^{3-}$ and $I_3^-$ reacts with these states and leads to anodic decomposition of the electrode in the dark, accompanied by a positive flat band shift. On the contrary, in acidic solutions the $Fe(CN)_6^{3-}$, $I_3^-$, and $Fe^{3+}$ reagents do not contribute to the electrode decomposition reaction due to the positive shift in flat band potential with decreasing pH. Only couples with more positive redox potential ($Br_3^-$ and $Ce^{4+}$) react then with these states and decompose the electrode. A diode-like behavior has been shown also for SnSSe, a layered-type semiconductor with an energy gap of 1.53 eV [196]. In this case also, the light-driven reactions were of a corrosive nature, but the stability could be improved substantially in the presence of an acidic solution containing potassium iodide.

Hüsser et al. [197] used $SnS_2$ crystals to illustrate an interesting experimental technique allowing photoelectrochemical studies of nearly intrinsic, highly resistant semiconductors. This technique consisted in using sub-band gap illumination to make the bulk material photoconductive. It was claimed that, with the aid of a corresponding model explaining the photoelectrochemical behavior in terms of a potential distribution similar to that of a doped semiconductor, this method allows one to predict whether the time-consuming process of chemical doping, for applications such as photoelectrolysis, is worth undertaking. Based on these considerations, the authors compared the photoelectrochemistry of undoped $SnS_2$ to chemically doped $SnS_2$. Furthermore, they found that the response at high photon energies caused by the sub-band gap illumination scales with the photoconductivity of highly resistant semiconductors, lending additional support for the model. The effect was observed on a number of single crystals of very poor photoconductors, such as the layered chalcogenides $SnS_2$, $Sn(Se_{0.1}S_{0.9})_2$, $MPSe_3$ (M = Cd, Mn). The validity of the proposed model relied heavily on the photoconductivity of the insulator.

Mishra et al. [198] discussed in an exemplary way the dark and photocorrosion behavior of their SnS-electrodeposited polycrystalline films on the basis of Pourbaix diagrams, by performing photoelectrochemical studies in aqueous electrolytes with various redox couples. Polarization curves for the SnS samples in a $Fe(CN)_6^{4-/3-}$ redox electrolyte revealed partial rectification for cathodic current flow in the dark, establishing the SnS as p-type. The incomplete rectification was

attributed to defects (e.g., grain boundaries) in the polycrystalline films. The flat band location of the SnS surface, i.e., the apparent flat band potential of the electrode, was taken as the onset of the cathodic photocurrent, which was observed at $0.40 \pm 0.05$ V (SCE) regardless of the redox potential of the electrolyte. Attempts to measure this surface energy level via impedance experiments were unsuccessful because of the severe frequency dispersion of the impedance parameters. An indirect band gap of 1.1 eV was obtained by photocurrent spectra. The authors correlated the surface energy levels of SnS, as estimated from the flat band potential, and the band gap information from photocurrent spectra to the known Pourbaix equilibria of the $Sn–S–H_2O$ system, in order to perform a corrosion analysis of the semiconductor electrode. The surface energy levels in SnS and the energies corresponding to selected redox couples and corrosion reactions were superimposed as presented in Fig. 5.13. As can be seen in this comprehensive diagram, the conduction and valence band levels in SnS encompass all the corrosion reaction candidates. Thus, since the corresponding decomposition potentials were found to lie within the band gap region, it was concluded that both electrons and holes can corrode SnS, the relative dominance of these reactions depending on kinetic factors.
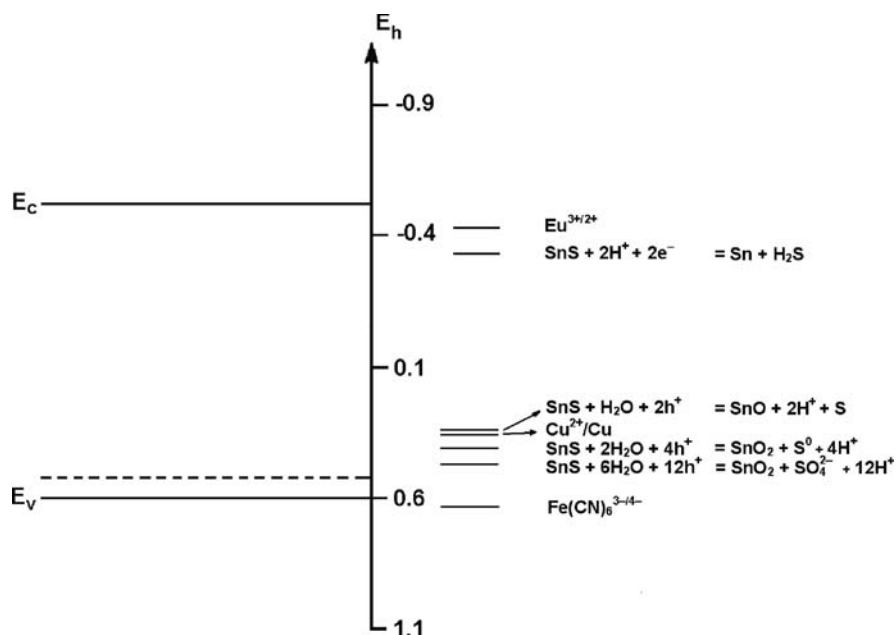


**Fig. 5.13** Energy level diagram comparing the surface band edge positions of SnS and the energies corresponding to selected redox couples and corrosion reactions involving the semiconductor. (Reproduced from [198])

### 5.2.9.3  Lead Chalcogenides

The metallic or semi-metallic character of many common sulfides implies the significance of electrochemical factors in the study of their oxidation, which is relevant to environmental, energy, and metallurgical issues, e.g., in connection with the direct electrochemical conversion of sulfide ores to metals, the pressure leaching of ore materials, or flotation processes.

Photoelectrochemical techniques have been used to characterize the bulk semiconducting properties of cleaved or abraded surfaces of natural galena (PbS) in order to elucidate the surface oxidation of the mineral relevant to industrial flotation processing [199]. Natural galena samples from the same cluster of crystals were found to range from highly n-type, probably degenerate, to slightly p-type; most of the samples were highly n-type and exhibited only anodic photocurrents in mildly acid solutions. Oxidation has been postulated in general to change the semiconducting properties of sulfide minerals in such a way as to facilitate collector adsorption during flotation. For n-type galena, it was suggested that oxygen chemisorption localizes conduction band electrons at the surface and gives rise to an underlying depletion layer (positive space charge layer) that facilitates oxidation reactions involving xanthate collectors [200].[4] For cleaved surfaces, the potential dependence of the characteristics of photocurrent transients and photocurrents was interpreted in terms of both light-induced acceleration of anodic oxidation and corresponding cathodic reduction process, the former removing lead ions ($Pb^{2+}$) and leaving lead vacancies in the lattice and the latter resulting in sulfur vacancies. Rotating ring-disk electrode studies confirmed that anodic and cathodic processes leading to dissolved $Pb^{2+}$ or $H_2S$ occur at all potentials. Abrading the samples under water in equilibrium with air greatly reduced the magnitude of the photoresponse and changed the photoelectrochemical features. The results indicated that abrasion produces a thick p-type layer at the galena surface.

Lead selenide (PbSe) finds applications in infrared emitting and detecting devices, whose performance depends strongly on surface properties. Detrimental charge carrier recombination at the surface of PbSe can be reduced by passivation, e.g., involving formation of $PbSeO_3$. Anodic oxidation and photoelectrochemical properties of p-doped PbSe single vapor-phase grown crystals have been investigated in alkaline solutions [201, 202]. Depending on the pretreatment of the PbSe crystal surface, two different types of oxide formation were identified. In the case of freshly polished surfaces, a passivating and polycrystalline oxide film was formed following an island growth. At pre-oxidized samples, a uniform oxidation of the entire surface was observed implying homogeneous formation of anodic oxide film by a high field growth mechanism. The electronic properties of the anodic oxides

---

[4] Xanthate compounds are widely used as collectors in flotation. Their function is to render the mineral surface hydrophobic and thus facilitate bubble attachment. The adsorption of xanthates onto sulfide minerals occurs via an electrochemical mechanism involving the reduction of oxygen and the anodic adsorption of xanthate.

on PbSe were determined by photocurrent spectroscopy in the alkaline solutions. A direct transition at 2.4 eV and an indirect at 1.8 eV were reported for both types of anodic oxide. The potential dependence of the oxide thickness for the presumed high field growth mechanism was confirmed by the concomitant weakening of the photocurrent generated in the bulk of the electrodes (i.e., in PbSe phase) due to scattering or absorption within the oxide.

The electrochemical behavior of single-crystal ⟨100⟩ lead telluride, PbTe, has been studied in acetate buffer pH 4.9 or HClO$_4$ (pH 1.1) and KOH (pH 12.9) solutions by potentiodynamic techniques with an RRDE setup and compared to the properties of pure Pb and Te [203]. Preferential oxidation, reduction, growth, and dissolution processes were investigated. The composition of surface products was examined by XPS analysis. It was concluded that the use of electrochemical processes on PbTe for forming well-passivating or insulating surface layers is rather limited.

Significant size quantization phenomena with lead chalcogenide layers/ nanoparticles have directed the modern relevant research, including electrochemical studies, to applications related to optoelectronics (e.g., PbS [204], PbSe [205]). (Photo)electrochemical aspects of lead chalcogenide layers/films/nanophases regarding mainly their electrochemical growth, and Q-dot sensitizing of oxide electrodes, may be encountered throughout this book.

### 5.2.9.4  Bismuth Sulfide

With a band gap of about 1.2 eV at room temperature, Bi$_2$S$_3$ has been investigated for optical device applications, such as photoconductors and solar cells. Conventional single crystals of the compound are found to be n-type, with a donor density in the order of $10^{17}$ cm$^{-3}$. Miller and Heller [86] demonstrated the feasibility of using anodic Bi$_2$S$_3$ films grown in situ in a polysulfide liquid junction solar cell. The preparation of photosensitive anodic Bi$_2$S$_3$ films and their photoelectrochemistry were described by Peter [206], who measured the quantum yield of the photocurrent as a function of the wavelength of excitation and determined the absorption spectrum of Bi$_2$S$_3$. The spectrum showed an indirect transition at 1.25 eV and possibly a direct transition at ca. 1.7 eV. In contrast to Miller and Heller who reported that Bi$_2$S$_3$ films were not as efficient as the CdS layers grown under similar conditions, Peter established that Bi$_2$S$_3$ formed on bismuth anodes can exhibit photocurrent quantum yields close to unity over a wide spectral range. In this respect, he concluded that sulfide films on bismuth are superior to anodic CdS films. In this work, the photodecomposition and thermodynamic stability of Bi$_2$S$_3$ were compared to CdS in an energy level scheme. Calculations showed that illuminated Bi$_2$S$_3$ should be stable in sodium polysulfide solution, while it was argued that if the surface concentration of sulfide ions is small, the anodic photodecomposition of Bi$_2$S$_3$ may take place as

$$Bi_2S_3 + 6\,h^+ + 6OH^- \rightarrow Bi_2O_3 + 3H_2O + 3S$$
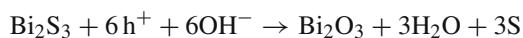
The cathodic decomposition of $Bi_2S_3$ by electrons in the conduction band occurs at the standard potential of the $Bi_2S_3$ electrode by the reaction

$$Bi_2S_3 + 6e^- \rightarrow 2Bi + 3S^{2-}$$
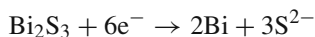
## 5.3 Semiconductor Photocatalysis

Besides requiring noble metal electrodes, the ability to generate useful chemical products by electrolysis often suffers from high overvoltage. Chemical reactions may be advantageously carried out, though, in photocatalytic electrochemical cells with photosensitive semiconductor electrodes, where the light energy is used to reduce the required bias. Likewise, particulate (heterogeneous) systems consisting of powder suspensions may afford various photochemical processes and actually have found important applications in xerography, photography, chemical synthesis, conversion/storage of solar energy, and degradation of pollutants. The following discussion is considered as an introduction to metal chalcogenide related aspects of the photocatalytic decomposition of water, and solar energy conversion with sensitized electrodes that will be addressed in subsequent sections. A brief outline of colloid photochemistry is also given here, mostly based on several pioneering works that outline the main features of interest.

The term "photocatalysis" implies the acceleration of a photoreaction (referred also as photoinduced or photoactivated reaction) by the presence of a catalyst. In "heterogeneous photocatalysis" the rate of a thermodynamically favorable reaction ($\Delta G < 0$) is increased by the presence of an illuminated solid catalyst. On the other hand, in "heterogeneous photosynthesis" a thermodynamically unfavorable reaction ($\Delta G > 0$) is caused to occur by the presence of an illuminated solid, with the conversion of radiant to chemical energy. Examples of photocatalytic reactions are deposition of precious metals, methanol mineralization, oxidation of hydrocarbons at an illuminated n-semiconductor/solution interface in an oxygenated medium, and biomass conversion to hydrogen. Examples of photosynthetic reactions are water splitting, photoreduction of $N_2$ or $CO_2$, and organic photosynthetic processes. The above definition of photocatalysis includes the process of "photosensitization," i.e., a process by which a photochemical alteration occurs in one chemical species as a result of the initial absorption of radiation by another chemical species called the "photosensitizer." Heterogeneous photocatalysis involves photoreactions which occur at the surface of a catalyst. Semiconductors (e.g., $TiO_2$, $ZnO$, $Fe_2O_3$, $CdS$, and $ZnS$) can act as sensitizers for light-induced redox processes due to their electronic structure which is characterized by a filled valence band and an empty conduction band. The valence band holes are powerful oxidants while the conduction band electrons are good reductants; an energetic range of +1.0 to +3.5 V vs. SHE may be provided for holes, and a corresponding range of +0.5 to –1.5 V vs. SHE for electrons, depending on the semiconductor and solution properties (e.g., pH).

Photoelectrosynthetic processes can be regarded as photocatalytic inasmuch as a photosensitizer is used to accomplish the (photo)reaction. The term "photoassisted reaction" should be relevant when the excitation light energy only partially furnishes the voltage needed for the electrolysis process, the rest being accommodated by an applied external bias. Of course, photosynthetic/photocatalytic reactions may be catalyzed by also suitable redox catalysts. Thus, although an n-type semiconductor is able to photosensitize the reduction, oxidation, or cleavage of water, a platinum-group metal redox catalyst, such as Pt, deposited on the surface of the semiconductor, is invariably used to facilitate the reduction of water by the photogenerated electrons. In fact, very efficient as well as selective heterogeneous catalysts assisting the generation of multielectron transfer oxidation–reduction products are needed for practical applications (Chap. 6). As dictated by the principles of electrocatalysis, in the choice of materials for photocatalysis those catalytic materials are used for which the overvoltage requirements for the desired reactions are low. Examples are the Pt group metals for the hydrogen evolution reaction and the so-called "dimensionally stable anodes" composed of $RuO_2$ supported on Ti (or $TiO_2$) for the oxygen and chlorine evolution reactions [207, 208].

In most studies, heterogeneous photocatalysis refers to semiconductor photocatalysis or semiconductor-sensitized photoreactions, especially if there is no evidence of a marked loss in semiconductor photoactivity with extended use. It is meant here that the initial photoexcitation takes place in the semiconductor catalyst substrate and the photoexcited catalyst then interacts with the ground state adsorbate molecule [209].

Semiconductor-sensitized photoprocesses may take place on (macro) electrodes of a typical cell or in dispersed particle systems (powders, sols, colloids). In the latter case, any individual particle may be considered as a "microelectrode" at which electrons are transferred across the solution interface in an electrochemical manner. Thereby, extension of photoelectrochemical principles and techniques to such systems is straightforward. Let us note though that, whereas only one carrier species (either the hole or the electron) is normally available for reaction at the surface of a bulk semiconductor electrode due to band bending, both species may be present on the surface of a small particle, so that each particle in a single sol may be considered as a short-circuited (photo)anode and (photo)cathode, providing both the oxidizing and reducing sites for the reaction. Different types of particulate photoreactive systems can be envisaged in this respect: with an n-type powder, photooxidation occurs and reduction comprises the "dark site" reaction, while the converse is true with a p-type powder. Thus, the photocatalytic oxidation of cyanide, sulfide, and other pollutants can be carried out on $n$-$TiO_2$, n-ZnO, and n-CdS, the cathodic process in these reactions being the reduction of oxygen. Further, one may use composite p–n particles, each of those operating as a photochemical diode active toward both oxidation and reduction. These composites may provide an efficient electron–hole separation that minimizes the energy wasteful recombination.

One advantage with semiconductor particulate systems is that light-induced oxidation/reduction is very often irreversible, unlike homogeneous solutions of

photoredox species, such as transition metal polypyridine complexes, metalloporphyrins, and organic dyes, for which the lifetime of photogenerated species is restricted to a few microseconds due to reverse electron transfer. On the other hand, the "dark site" reactions on a single semiconductor sol may not occur with as high an efficiency (e.g., with as low an overpotential) as on a metallic or electrocatalytic site, therefore a portion of the particle surface may be modified by deposition of metal or electrocatalyst in order to obtain better performance. This is often a necessity, especially for multielectron reactions, for most of the known semiconductors are inherently poor catalyst materials for the overall photoredox process. For this reason, similar to macro-electrodes or homogeneous dye-based systems, the semiconductor dispersions are "loaded" with suitable redox catalysts to facilitate the generation of multielectron transfer products.

The primary target of studies on photocatalytic semiconductor suspensions has been water cleavage by visible light. Suspension-based photocatalytic processes are also useful for the removal of inorganic (metal ions) and organic pollutants, the reduction of $CO_2$, the photodestruction of bacteria and viruses, and various organic reactions; an example is the use of Pt-loaded CdS for the photocatalytic racemization of L-lysine [210].

## 5.3.1 Colloidal Systems

Following the initial work on ultrafine Pt and $RuO_2$ sols as mediators for the reduction and oxidation of water, a great deal of research has been conducted for the exploration of colloidal suspensions providing extremely high surface area catalysts with regard to photochemical applications. Selected topics in the early research on very small metal and semiconductor particles in solution (or in the solid state after removal of the solvent) have been discussed by Henglein [211], one of the pioneers in the field; this author identifies the term "small particle" with a cluster of atoms or molecules ranging in size from < 1 nm to almost 10 nm or having agglomeration numbers from < 10 up to a few hundred.

A major part of the early bibliography up to 1990 on the field of semiconductor suspensions can be found in the publication of Kamat and Dimitrijević [212]. Most of the semiconductor colloids that have been produced for photocatalytic studies are metal oxides such as $TiO_2$, $WO_3$, ZnO, CdO, and $In_2O_3$ and metal chalcogenides such as CdS, CdSe, $MoS_2$, and $WS_2$. Their "classical" synthesis mostly involves precipitation from homogeneous solution via the controlled release of anions (or cations) or forced hydrolysis. Stabilizing polymers are often used in these preparations. For example, metal sulfide colloids have been obtained by the reaction between metal perchlorate and $H_2S$ or $Na_2S$ in the presence of sodium metaphosphate, silicon sol, or Nafion [213, 214]. Phase transformations and reactions with aerosols have also been employed for colloidal synthesis. Simple dissolution of crystalline powder in acetonitrile has been used to produce suspensions of crystalline $MoS_2$ and $WS_2$ small (1–3 nm) particles [215].

A seminal review illustrating the principles of semiconductor photocatalysis, and the results in the field, until 1997, focusing on $TiO_2$, has been given by Mills and Le Hunte [209]. We may briefly indicate that colloidal semiconductor (photo)redox systems offer a number of very desirable properties, such as high extinction coefficients, fast carrier diffusion to the interface, and suitable positioning of valence and conduction bands to achieve high efficiencies in photoconversion processes. A detailed account of the mechanistic and kinetic aspects of surface photochemical processes in sols can be found in the review of Kamat [216]. A proper understanding of the behavior of such sols lies heavily on the elucidation of interfacial charge transfer processes. Techniques used for this purpose include electron spin resonance, photoelectrophoresis, laser photolysis, and luminescence measurements.

Importantly, the transparent nature of colloid suspensions, owing to the fact that small particles usually exhibit much less scattering and reflection of light than macro-particles, allows detection of short-lived intermediates by fast kinetic spectroscopy, thus rendering possible the direct monitoring of the kinetics of heterogeneous electron transfer reactions with redox species present in the solution. With finely dispersed semiconductors, it is also possible to monitor photoluminescence readily, and this greatly enhances the ability to monitor photo-processes following band gap excitation. In this connection, electrochemical measurements such as photocoulometry, involving collection of the charge photogenerated at the semiconductor particles at an inert metal electrode immersed in the irradiated suspension, have been applied with success [217]. Using this technique in CdS suspensions, White and Bard [218] observed enhanced photocurrent on addition of small quantities of electron-trapping agents such as $Fe^{3+}$, $Cu^{2+}$, or methyl viologen ($MV^{2+}$). From measurements of photocurrent of the order of $\mu A$, they determined the position of the quasi-Fermi level of electrons for CdS, and for CdS modified with Pt and $RuO_2$, as a function of pH.

Cadmium sulfide colloids and dispersions have received considerable attention, because of their photocatalytic activity under visible light irradiation [219]. In fact, the first direct observation of the dynamics of interfacial electron- and hole-transfer processes from colloidal semiconductors to electron donors and acceptors in solution was carried out by Duonghung et al. [220] in transparent aqueous dispersions of colloidal $TiO_2$ and CdS particles. These authors reported a method for the determination of the flat band potential of ultrafine colloidal particles using a laser flash photolysis technique. Roy et al. [221] indicated that application of this technique to macro-dispersions of semiconductor powders is not possible because of the high turbidity of these systems. They introduced, instead, another approach in order to determine the flat band potential of CdS as well as of $CdS/Ag_2S$ particles in suspension, based on the measurement of the photovoltage developed on irradiating the suspension with visible light in the presence of an electron acceptor ($MV^{2+}$). Their results were in reasonable agreement with those of White and Bard.

An important aspect of semiconductor photochemistry is the retardation of the electron–hole recombination process through charge carrier trapping. Such phenomena are common in colloidal semiconductor particles and can greatly influence surface corrosion processes occurring particularly in small band gap materials, such

as metal sulfides [193]. Laser flash photolysis and pulse radiolysis techniques have proved quite useful for the characterization of trapped charge carriers. Both methods complement each other in investigating fast processes in the internal and on the surface of colloidal particles. For example, laser flash photolysis has been used for the investigation of the photochemical behavior of colloidal CdSe with diameter smaller than 5 nm, in particular to clarify the mechanism of CdSe anodic photocorrosion with various hole and electron scavengers [222]. The reactions of hydroxyl radicals with colloidal CdS and ZnS have also been studied by pulse radiolysis [223].

The observation of photophysical and photochemical effects in *ultrafine* semiconductor particle assemblies is of particular interest, as these systems give striking examples of size quantization effects [224]. When the size of a particle becomes comparable to the de Broglie wavelength of the charge carriers (2.5–25 nm), the band model breaks down and the energy of electrons becomes quantized. Thus, small particles of PbS, stabilized in a suspension containing sodium polyphosphate or poly(vinyl alcohol), have been shown to have an onset of absorption lying in the visible, instead of in IR as dictated by the bulk phase band gap of 0.41 eV [211]. More recently, nanoclusters of $PtS_2$ synthesized from $PtCl_4$ and $(NH_4)_2S$ in inverse micelles were shown to have an indirect band gap of 1.58 eV as compared to 0.87 eV for bulk $PtS_2$ [225]. Several investigators have also shown that size quantization can enhance photoredox chemistry in suspensions, although a large increase in the effective band gap, i.e., by several eV, can also lead to inherent instability of the particles, since cathodic and anodic corrosion potentials acquire new positions against band edges.

The shift of the absorption threshold with particle size has been studied primarily in most detail with CdS, ZnO, and PbS. The problem of how the ionization potential and electron affinity of small, singly charged, inorganic semiconductor crystallites varies with size, as well as the related question regarding the size dependence of hole and electron redox potentials for surface chemical reactions in aqueous colloidal solutions, has been treated theoretically by Brus [226–229] using CdS as a model semiconductor. In these works, the onset of quantum size effects was located at a characteristic crystal dimension of about 8 unit cells, that is, about 5 nm. Let us note that, until recently, the inferred exact dependence of redox potential on particle size for CdS was not assessed by actual electrochemical measurements in solution, largely because of the limited solvent window of many solvent/electrolyte systems and the instability of the particles. Bard et al. [230] considered this question showing a direct correlation between the electrochemical band gap and the electronic spectra of CdS nanoparticles in DMF. Further, emission from CdS colloids has served as an excellent probe of the free hole and electron surface chemistry and physics [231]. Henglein, Weller, and co-workers [232] described blue or green luminescing sols of CdS with a mean particle diameter between 4 and 6 nm and a narrow size distribution. Emission occurred close to the band gap energy, which depended on the size of the particles. Fluorescence quantum yields greater than 50% were obtained upon activation of the particles by a cadmium hydroxide precipitate. Violet fluorescing samples of activated ZnS–CdS co-colloids were also prepared and evaluated. The stability of these colloids was tested in photoanodic dissolution experiments with

continuous illumination and high laser intensity irradiation. It was shown that the activated CdS colloid was 2,000 times more stable than the non-activated one.

Importantly, rapid developments have taken place in recent years in the area of preparation and characterization of particles of mesoscopic dimensions with narrow size distribution, which appear to benefit largely the construction of novel solar cells. In parallel, remarkable complex core/shell II–VI heterostructures entailing the coating of nanocrystallites (or nanowires) with a shell of another semiconductor to enhance emission quantum yields and/or charge separation capabilities have been engineered using solution chemistry [233–236]. Finally, tailored semiconductor–receptor systems with chalcogenides coupled to enzymes and organic linkers have been shown to provide unique opportunities for designing integrated chemical systems for photoelectrosynthetic and photocatalytic reactions. An important type of a relevant electrochemical device, the sensitized solar cell, will be dealt with in a next section.

## 5.3.2 Solar Detoxification – $CO_2$ Photoreduction

It has been emphasized [14] that during the 1990s, part of the tremendous momentum that was built up during the 1970s and 1980s in the field of photo-electrochemistry was channeled into the closely related area of photocatalysis, and in particular environmental photocatalysis. Along with the realization that semiconductor electrodes or sols could be used for the photo(electro)catalytic generation of useful chemical products, it was conceived that they could also be employed for destruction of pollutants. The first such reports were those of Frank and Bard in 1977, who described the decomposition of cyanide in the presence of aqueous $TiO_2$ suspensions [219]. The use of $TiO_2$ particle photocatalysts enables solar detoxification of polluted wastewaters, by producing oxidizing agents in water that react with the contaminants. The hazardous chemicals are oxidatively converted to compounds such as water, carbon dioxide, and dilute acids that are easily neutralized. Certainly, in order to maintain electrical neutrality, a reduction process has to occur in addition, in most cases the reduction of oxygen.

The oxidative degradation of organic pollutants in water and air streams is considered as one of the so-called *advanced oxidation processes*. Photocatalytic decomposition of organics found widespread industrial interest for air purification (e.g., decomposition of aldehydes, removal of $NO_x$), deodorization, sterilization, and disinfection. Domestic applications based on $TiO_2$ photocatalysts such as window self-cleaning, bathroom paints that work under illumination with room light, or filters for air conditioners operating under UV lamp illumination have already been commercialized. Literature-based information on the multidisciplinary field of photocatalytic anti-pollutant systems can be found in a number of publications, such as Bahnemann's [237, 238] (and references therein).

In particular, the photo(electro)chemical reduction of carbon dioxide is connected to one of the most important environmental problems necessitating an urgent solution, that is, the fixation of $CO_2$ in the atmosphere. The feasibility of $CO_2$
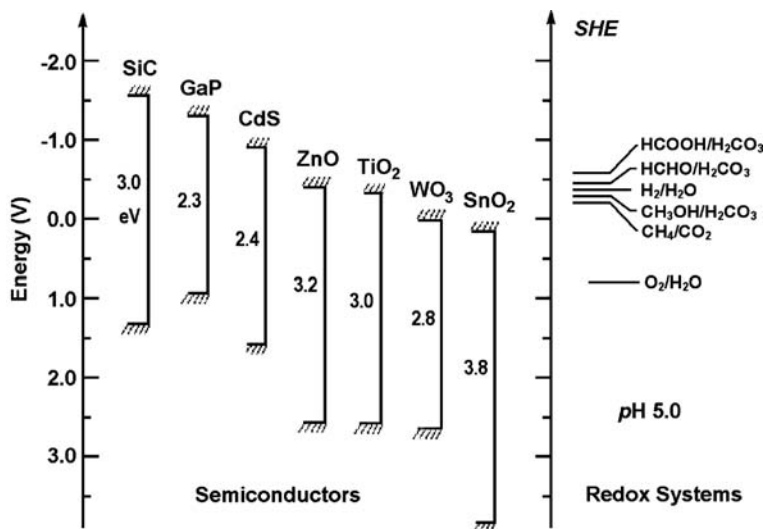
**Fig. 5.14** Inoue et al. carried out a systematic study of the photocatalytic reduction of $CO_2$ by different semiconductor powders in aqueous suspensions. Shown here is the energy correlation between semiconductor catalysts and redox couples in water, as presented in their paper. In principle, the solution species with more positive redox potential with respect to the conduction band level of the semiconductor is preferably reduced at the electrode. Photoexcited electrons in the more negative conduction band certainly have greater ability to reduce $CO_2$ in the solution. (Reproduced from [240])

photoreduction processes has been demonstrated either by homogeneous photore-actions in electronic relay systems ([239] and references therein) and heterogeneous colloidal semiconductor photocatalytic systems [240] (Fig. 5.14) or by photoelec-trochemical systems with semiconductor electrodes such as phosphides [241] and oxides [242]. Actually, a variety of p-type semiconductor electrodes such as CdTe, GaP, GaAs, InP, Si, and SiC has been examined for this purpose [14].

Reduction of $CO_2$ is an endothermic process, so that it is advantageous to carry out the artificial reaction with a very low consumption of energy or with the use of a renewable energy source, or ideally with both. Electrochemical reduction at metal electrodes requires highly negative potentials; hence catalysts are needed to make the process practical. For this reason, photo-aided reduction of $CO_2$ at a semi-conductor electrode without catalysts has been highly desirable. In 1983, Taniguchi et al. [243] proposed CdTe as the most effective electrode for this purpose. They reported the first example of photoelectrochemical reduction of $CO_2$ to monoxide, CO, at a p-type CdTe electrode, at potentials at least 0.7 V less negative than at metal electrodes. The experiments were conducted in a gas-tight cell containing a DMF–TBAP–$H_2O$ solution under a $CO_2$ atmosphere. The effect of various sol-vents, supporting electrolytes (different tetraalkyl ammonium salts), temperature, partial pressure of $CO_2$, and presence of thin metal coatings on CdTe, was exam-ined and also compared to several other p-type semiconductor electrodes and metals

as well [244]. A few years later, Bockris and Wass [245] established that crown ethers were the best catalysts to use with CdTe in order to increase further the efficiency of $CO_2$ photoreduction. In particular, they investigated the kinetics of the photoreduction in non-aqueous solutions containing tetraalkyl ammonium cations with special reference to the effects of surface decoration of p-CdTe with metals, organic complexes, and crown ethers. The principal product throughout was CO, although small amounts of formate and methanol were observed. Apart from the crown ethers, the other catalysts were seen to produce a 100–200 mV anodic shift in the current–potential curves, equivalent to ~10 times increase in the rate constant. The efficiency of the conversion of light to CO was ~5%.

One attractive approach to photochemical conversion and storage of solar energy is photofixation of carbon dioxide to C–1 organic compounds (formic acid, formaldehyde, methanol, and methane). Photoreduction of $CO_2$ to formic acid and formaldehyde has been demonstrated by using n-type $Bi_2S_3$ and CdS semiconductor powders (particle size 300–400 mesh) as photoelectrocatalysts in emulsions [246]. Addition of hydrogen sulfide in solution was found to enhance the rate of this process albeit the efficiencies were generally low, partly due to concomitant precipitation of elemental sulfur during the photolytic experiments. The effects of reaction temperature, light intensity, and pH of the electrolyte were studied, and the photocatalytic mechanism was discussed with reference to the theory of charge transfer at photoexcited metal sulfide semiconductors.

Photoreduction of $CO_2$ to formate in metal sulfide colloids has been reported to provide a novel photosynthetic route for production of methanol as the end-product [247]. Photoreduction of formate to methanol was achieved using ZnS colloid suspension containing formate, 2-propanol, and methanol dehydrogenase (MDH) with a quinone (PQQ) electron mediator. For the overall reduction of $CO_2$ to methanol, a quantum efficiency of 5.9%, at 280 nm, was obtained, which was referred to as the highest value ever reported for this process. Formate photodecomposition has been carried out also in CdS suspensions, assisted by the coupled action of cadmium metal and hydrogenase catalysts [248]. This investigation regarded in specific the effect of Cd metal (photo-formed on the surface of CdS particles) as well as the influence of the enzyme hydrogenase from *Thiocapsa roseopersicina*, on the CdS-photosensitized formate decomposition under anaerobic conditions.

### 5.3.3  Photocatalytic Decomposition of Water

Solar energy cannot be utilized for the direct photodecomposition of water into gaseous $H_2$ and $O_2$, although the free energy required for this reaction is only 1.23 eV and the peak of the solar spectrum occurs at a photon energy of about 2.4 eV, because the threshold energy for decomposition is about 6.5 eV. However, this activation energy can be greatly reduced by means of a suitable photocatalytic material in, say, a photochemical reactor. The ability of an irradiated single semiconductor particle system for photochemical activity depends upon the relative positions of the energy levels of the semiconductor valence and conduction bands

with respect to $H_2O/H_2$ and $O_2/H_2O$ redox levels. In an ideal system, which would accomplish photo-cleavage of water, the conduction band edge should be well above (more negative than) the electrochemical potential of hydrogen reduction, and the valence band edge should be well below (more positive than) that of water oxidation; that implies of course that the band gap width should be greater than the difference between the above formal potentials. Some materials satisfying both the above conditions are $SrTiO_3$, $Nb_2O_5$, SiC, CdS, and GaP.

Decomposition of water can be accomplished also by means of photoelectrolysis in a suitable cell with the reduction and oxidation occurring on different electrodes. Such a system can be constructed using an n-type semiconductor photoelectrode as an anode for oxygen evolution reaction (OER) with a counter electrode catalytic for hydrogen evolution reaction (HER), e.g., Pt black. Alternatively, the HER can be photodriven on a p-type semiconductor electrode with the OER occurring at a "dark" anode. In the former configuration, the n-type photoanode must be stable with respect to photooxidation while evolving oxygen and must also have a flat band potential more negative than the formal potential of the $H^+/H_2$ couple in the working medium plus any overpotential required to drive the "dark" HER at the counter electrode. The use of wide-gap semiconductors (typically oxides) is a prerequisite in order to defend stability of the anodic photoelectrode. Leading works demonstrating photoelectrolysis of water with oxide semiconductor photoanodes have been those of Fujishima and Honda [249], who used an n-(rutile)$TiO_2$-anode/Pt-cathode cell, and Wrighton et al. [250] who used an n-$SrTiO_3$-anode/Pt-cathode, bias-free, cell. A straightforward explanation of water electrolysis in such cells in terms of the energy levels of the electrodes and the electrolyte has been given by Mavroides et al. [251]. These authors showed that an illuminated aqueous cell with n-(rutile)$TiO_2$ and a platinized Pt cathode operates either in the "photogalvanic" mode (no $H_2$ evolved) or in the "photoelectrolytic" mode ($H_2$ evolved at the cathode by decomposition of water), depending on whether or not the electrolyte surrounding the cathode contains dissolved oxygen. In both cases, current flows through the external circuit and $O_2$ is evolved at the anode.

In practice, any photosensitizing semiconductor surface has to be made catalytically active toward OER or HER due to kinetic hindrance producing overpotentials. Be that as it may, no stable, un-assisted, single photoelectrode cell has been reported capable of water splitting by solar light without the application of either an external bias or a pH gradient. A method, though, for augmenting the effective voltage of the photoelectrolysis cell may be to simultaneously illuminate two ohmically connected p- and n-type photoelectrodes. Upon illumination, the minority carriers are available at the conduction band edge of the p-type electrode and at the valence band edge of the n-type electrode, while the majority carriers recombine at the ohmic contact. The usable photopotential of this dual-type cell is increased compared to a single photoelectrode cell, so that smaller band gap semiconductors can be used to drive more energetic electrode reactions, but at the expense of halving the maximum quantum yield for current flow due to annihilation of the majority carriers at the ohmic contact. Such a p/n cell requires two photons per separated electron–hole pair and is roughly analogous to photosynthesis in green plants, where both

the oxidation of water and the reduction of $CO_2$ are also photo-driven at two physically distinct sites. The photovoltages produced by the individual electrodes are additive.

Bockris and co-workers [252, 253] considered p-type ZnTe, CdTe, and other elemental and III–V semiconductors as possible candidates for a photocathode in the electrochemical production of hydrogen and studied in detail the current–voltage characteristics, quantum efficiency–wavelength dependence, flat band potentials, and stability in p/n cells containing alkaline (1 N NaOH) or acidic (1 N $H_2SO_4$) solutions. Critical preconditions for successful application were that the semiconductor photocathode must exhibit sufficient light absorption > 20% of the solar spectrum, while the cathodic photocurrent must start at as positive a potential as possible and be more positive than the potential from which the anodic photocurrent is observed in the n-type photoanode. Both CdTe and ZnTe electrodes were found to satisfy the first condition. However, for ZnTe the photocurrent was observed at a potential more negative than –0.85 V (SHE), far more cathodic than the potential from which the anodic photocurrent was observed with any reasonably absorbing n-type semiconductor. On the other hand, the photocurrent for CdTe was observed at a potential more negative than –0.5 V (SHE), i.e., more positive than the value of the potential from which the anodic photocurrent was observed on a $TiO_2$ electrode (–0.65 V vs. SHE). Further, the photocurrent of ZnTe decreased constantly as a function of time, but that of CdTe was quite constant over several hours. It was concluded that CdTe is a p-type semiconductor which can be used as a stable photocathode for a photodriven cell (CdTe/NaOH/$TiO_2$), unlike ZnTe. The researchers suggested [254] the combination of n-$TiO_2$ and n-$SrTiO_3$ anodes with p-CdTe and p-GaP cathodes to form the cells: n-$TiO_2$//p-CdTe, n-$TiO_2$//p-GaP, n-$SrTiO_3$//p-CdTe, and n-$SrTiO_3$//p-GaP. Results in 1 M NaOH solutions under 0.05 W $cm^{-2}$ xenon light showed self-driven water photoelectrolysis albeit with very low efficiencies of hydrogen production due to the wide gaps of the oxide photoanodes. Results on dual photoelectrode cells with microscopically smooth n-$MoSe_2$ or n-$WSe_2$ photoanodes and p-InP photocathodes with noble metal catalyst islands on the surface have been reported as well [255]. Spontaneous photoelectrolysis of HBr and HI into hydrogen and bromine or iodine, respectively, was demonstrated. The efficiency of the HBr photoelectrolysis by 632.8 nm light based on the stored free energy was 7.8%.

Tien and co-workers [256, 257] proposed a novel type of PEC using a semiconductor/metal septum (SC-SEP) as the active electrode in a two-compartment cell, modeled after the natural photosynthetic systems containing a bilayer lipid membrane. The SC-SEP PEC was illustrated originally with polycrystalline n-CdSe/metal as the septum (bipolar) electrode separating two aqueous solutions; the one exposed to light and in contact with the n-CdSe side consisted of polysulfide or ferro-ferricyanide solution, and the other, not illuminated but in contact with the metal surface, was either a strongly acidic ($H_2SO_4$) solution or artificial seawater. A variety of metal foils or sheets were tested for the CdSe support, including Pt, Ti, Ni, and brass. Irradiation of the first chamber with visible light ($\lambda$ > 390 nm) was reported to evolve hydrogen at the metal surface without any externally applied

voltage. These cells were claimed as being able to deliver enhanced photovoltage and efficient hydrogen production in comparison with conventionally designed PEC, provided that two different redox couples having standard potentials sufficiently wide apart from each other are used in the working electrolytes. However, a simple electric circuit analysis shows that the SC-SEP arrangements are equivalent to a conventional dark galvanic or electrolytic cell wired in series with a conventional PEC cell. By analyzing the performance of these devices in terms of three possible modes of operation of the dark cell, i.e., regenerative, sacrificial, and storage, Bard and Mallouk [258] showed that no special advantages or higher power conversion efficiencies were provided compared to conventional, two-electrode PEC cells. They argued that claims of attaining efficient visible light water photolysis with the CdSe-based SEP cells need to be reconsidered, in view of the fact that in these cases a galvanic cell (which one should think of as a battery or sacrificial anode) is used to drive the photoproduction of hydrogen; in conclusion, such cells can run only as long as the battery is charged and therefore should be considered as photocatalytic rather than photosynthetic devices.

Anyhow, various SEP PEC have been demonstrated using a variety of classical chalcogenide or oxide semiconductors for the septum component (e.g., CdS, CdSe, CdTe, $TiO_2$, $Fe_2O_3$) along with different electrolyte combinations; an example is the work of the group of Srivastava [259, 260] discussing characteristics of these designs. Polycrystalline n-$Sb_2S_3$ thin film electrodes were used also for storage of chemical energy using the configuration |C|polyiodide|n-$Sb_2S_3$|Ti||ferri-ferrocyanide|C| [261], while a solar rechargeable SC-SEP storage cell constructed as |C|polysulfide|n-Fe:CdSe|stainless steel||$FeCl_3$ or $K_4Fe(CN)_6$|C|, using Fe:CdSe thin films electrodeposited onto stainless steel substrates, was reported recently [262].

Intensive research for almost four decades has shown that photoanodic corrosion and lack of suitable materials pose a serious limitation on efficient production of both oxygen and hydrogen from water by means of an unassisted, photoelectrochemical process using solar energy. Most of the overpotentials and losses in any water splitting system are associated with the oxygen reaction, basically because four electrons need to be transferred before OER can occur, whereas $H_2$ production requires only a two-electron transfer. Certainly, the oxidation of water may be "bypassed" by adding a more reducing species in solution, such as methanol, formaldehyde, or sulfite. Then hydrogen can be photogenerated using most semiconductors. But, only if such an oxidative process takes place, which liberates oxygen from water in one electrode, it makes sense to use the separated electron for hydrogen evolution at the counter electrode; if electrons would be donated from other molecular species than water, the process would be "sacrificial" and typically not sustainable [263]. Of course, when sacrificial agents are present the overall water splitting reaction may be rendered photocatalytic in the exact sense.

The detailed mechanism of forming $O_2$ from water involves a number of elementary reaction steps, so that photoinduced interfacial coordination reactions are needed that may induce water species to form metal complexes, which are gradually oxidized and may, thereby, liberate oxygen. This may be done by introducing

specific catalysts into the semiconductor electrode interphace, which would be able to accumulate holes for inducing a multielectron transfer oxidation of water at a favorable thermodynamic potential. Therefore, identification of catalytically active and stable anodes for the photoelectrolysis of water is of considerable importance. Transition metal oxides have been and are still being assessed as catalysts for OER from water. Presently, metal oxides, such as $RuO_2$, $IrO_2$, and $NiO$, are the most well-known catalysts for this process. These oxides are chemically stable; however, their conduction band typically cannot be sufficiently negative to generate hydrogen with useful rates, at least for narrow band gaps, because of a deep valence band of oxygen of $2p$ character lying at 7.2 eV below vacuum [269]. Sensitization of oxide semiconductors (e.g., n-$TiO_2$, n-$SrTiO_3$) with various types of organic dyes, as well as other inorganic semiconductors such as CdSe, CdS, GaAs, GaP, have been used to extend the limited light absorption of oxides (for improving the wide band gap problem). Another strategy is to use photocatalysts whose electronic bands derive from metal character with less stable orbital, i.e., with strong reducing power. Notwithstanding the toxicity of the elements, metal sulfides, which have narrow band gaps and band edge levels at relatively negative potentials compared to oxides, are alternative candidates for visible light-driven decomposition of water. However, the stabilization of sulfide semiconductors is a critical factor in their recycling efficiency and activity. Polymeric material coatings, hole-scavenger sacrificial species, such as sulfide/sulfite/sulfate salts or aliphatic carboxylic acids, and electron mediators such as organic dyes have played an important role in this connection. Moreover, modified photocatalytic semiconductor particles or (macro)electrodes, loaded with metals (especially the transition series) or other semiconductors with a different band gap, have been shown to increase photocatalytic efficiency compared to naked semiconductors, due to the influence of the additive on the optical absorption and charge transfer characteristics.

Literature-based information on the early research on photocatalytic hydrogen production can be found in the critical survey of Getoff [264]. Results regarding semiconductor particulate systems, up to 1998 – specifically, experimental techniques, mechanistic aspects, and a summary of factors which influence the hydrogen production efficiency of semiconductor particles – are presented in the overview of Ashokkumar [265]. Recent reviews on hydrogen generation with irradiated semiconductors have been given by Rajeshwar [266] (a survey focused on oxide photocatalysts with almost 400 references) and Tributsch [263]. Presently, oxide semiconductors, in particular $TiO_2$, $WO_3$, and $Fe_2O_3$, are the photocatalyst materials of choice for the hydrogen generation application, Pt being an excellent (co)electrocatalyst. Photocathodic hydrogen evolution has been studied also on p-type Si [267]; reduction of water to $H_2$ by visible light was achieved by using the Si electrode modified with Pt catalysts with significant photoefficiency [268].

In any case, no electrode material or approach fulfills the requirements for a successful photoelectrochemical process in all respects, i.e., for routine practical use; hence novel materials and approaches are constantly pursued. Note that beside the robust performance needed, the most important figure of merit for a semiconductor photoelectrode used for water splitting is the photoconversion efficiency, which is

defined as the ratio of the chemical potential energy stored in the form of hydrogen molecules to the incident radiative energy. The benchmark efficiency is 10%, which is generally considered to be required for commercial implementation [269].

### 5.3.3.1  Cadmium Sulfide and Related Photocatalysts

Among the available sulfide semiconductors, cadmium sulfide has a prestigious position as one of the best characterized semiconductors for use in solar-energy conversion systems. The main reason for this interest is the interface energetics of CdS in aqueous solution, believed to be more suitable than nearly all other known semiconductors for the direct splitting of water by solar energy [4]. The position of the conduction band at the surface of CdS is located at a sufficiently cathodic potential to reduce water if a catalyst is used to decrease the overpotential of this reaction. Furthermore, the reported flat band position of CdS indicates that there should be a sufficient overpotential for holes in the valence band to oxidize water. In fact, the maximum thermodynamically achievable photoconversion efficiency for CdS under AM1.5 global solar illumination has been estimated as 9.1% [270]. However, in practice, studies on CdS photoelectrochemical and photocatalytic systems have shown that the better understanding of this material seems to make it less attractive for application-oriented photoelectrochemistry [76]. In particular, the claims that CdS can be used as a sensitizer for the photo-cleavage of water have been considered highly uncertain given the tendency of the semiconductor to undergo photoanodic corrosion [209]. Thus, although the production of stoichiometric hydrogen and oxygen on irradiation of catalyst (Pt, $RuO_2$)-loaded CdS particles by visible light was reported already in the early 1980s [271, 272], photoanodic instability of the semiconductor severely limited the effectiveness of the process.

Nevertheless, there have been strategies for reducing photocorrosion and increasing the photocatalyst efficiency of CdS toward hydrogen production, relying on the general methods mentioned above. Commonly, suitable sacrificial reagents may be used; for example, the addition of a sulfide–sulfite mixture (e.g., $Na_2S/Na_2SO_3$) to CdS-based catalyst water suspensions led to a considerable reduction of photocorrosion [47]. Other routes to improve the photocatalytic properties of CdS included changes in the structural characteristics of the semiconductor, use of protective coatings, and combination of CdS with different elements or semiconductors (co-catalysts) to form mixed photocatalysts.

All of the above factors have been considered in the pioneering work of Bard and co-workers [273], who prepared CdS particles of ca. 20 nm diameter, embedded in a polymer (Nafion) matrix containing Pt as a $H_2$-evolution catalyst, and evaluated them for photocatalytic hydrogen production in water–sulfide media. Flocculation was avoided with these CdS/Nafion particles, while the polymer matrix was observed to play a role in the operation of the system by its ion-exchange properties. The crystal structure of the CdS particle was found to greatly influence the yield of hydrogen, with cubic β-CdS acting as a more active catalyst than hexagonal α-CdS. The optimal hydrogen production rate (4.2 $\mu$mol cm$^{-2}$ h$^{-1}$) obtained by the integrated chemical system was found to be comparable to the best colloidal

or powdered CdS preparations that had been reported at the time, under the same experimental conditions. Although the rate of hydrogen production was diminished with irradiation time after about 2 h, it was claimed that no extensive oxidation of the CdS itself occurred during operation.

Addition of small amounts of group VIIIA metals like Pt and Rh/Ru was shown to enhance the activity of CdS photocatalyst [274]. Such enhancement was explained in terms of a photoelectrochemical mechanism in which the electrons generated by light irradiation in the semiconductor are transferred to the loaded metal particles unlike the photogenerated holes, resulting in a decrease in electron–hole recombination. The same mechanism was invoked to explain changes in the photoactivity of CdS that could be achieved by combining the CdS semiconductor with other semiconductors with different energy levels, such as noble metal oxides ($RuO_2$, $Rh_2O_3$), noble metal sulfides ($RuS_2$, $Rh_2S_3$), ZnS, ZnO, $TiO_2$, and others. Photogenerated electrons in these composite systems move from CdS to the attached semiconductor, while photogenerated holes remain in CdS, this charge-carrier separation preventing charge recombination.

Reber and Rusek [275] investigated suspensions of platinized CdS in solutions of $S^{2-}$ and/or $SO_3^{2-}$ ions and pointed out that hydrogen production efficiency of CdS particles can be considerably increased by different methods of photoplatinization. The authors reported that co-precipitation of CdS with 0.5–3 wt% $Ag_2S$, or surface modification of CdS (with a large specific surface area) by silver ions, permitted preparation of very active platinized photocatalysts for the photochemical $H_2$ production from solutions containing $S^{2-}$ as hole-scavenger. The enhancement of activity was not limited to the own absorption range of CdS, but also resulted from a significant extension of the spectral response up to about 620 nm. Further improvement of the photoactivity could be achieved by doping the $Ag_2S$-activated CdS powders with ZnS. The rate of hydrogen formation in solutions containing $S^{2-}$ ions was seen to decrease with irradiation time due to the formation of disulfide ions which competed with the proton reduction. Addition of sulfite ions allowed hydrogen to evolve at a higher rate, as efficiently suppressing the disulfide formation. In solutions containing both $S^{2-}$ and $SO_3^{2-}$ ions, hydrogen was generated concomitantly with thiosulfate ($S_2O_3^{2-}$) ions. A quantum yield of 0.37 was estimated for the most active photocatalyst (Zn:CdS containing $Ag_2S$). However, these photocatalysts were less stable than platinized powders of pure CdS of low specific surface area.

The ZnS–CdS catalyst has been reported to exhibit activity similar to Pt/CdS for $H_2$ generation under visible light [276]. Nafion- or silica-supported, co-precipitated ZnS–CdS catalysts have well been used for photocatalysis of hydrogen production in aqueous sulfide solution. Sobczynski et al. [277] studied the visible light photoassisted production of hydrogen from methanol–water solutions containing mixtures of small particles consisting of $CdS/SiO_2$ and a platinized wide-gap oxide separately supported on silica ($TiO_2$, ZnO, $SnO_2$, or $WO_3$ /$SiO_2$). The activity was observed to be higher for the separately supported particles than for samples prepared by depositing the active materials together on the silica particles. The efficiency of $H_2$ production did not depend on the conduction band energy of the wide band gap metal oxide. Hence, it was concluded that electron injection from the conduction

band of CdS into the conduction band of the metal oxide does not comprise an important pathway for charge transport to the Pt particles.

Suspensions of semiconductors with heterojunctions formed by CdS or solid solution $Zn_yCd_{1-y}S$ and $Cu_xS$ have been prepared and tested as photocatalysts for photochemical hydrogen production [278]. With platinized powders of $Zn_{0.17}Cd_{0.83}S/Cu_xS$ in solution containing both $S^{2-}$ and $SO_3^{2-}$ ions, hydrogen was generated concomitantly with thiosulfate ions with quantum yield of about 0.5.

By coating an n-CdS photoanode with a polymer-pendant $Ru(bpy)_3^{2+}$ film containing $RuO_2$ catalyst, simultaneous formation of $H_2$ and $O_2$ from water by visible light was reported, but with quite low efficiency [279]. Sabaté et al. [280] tested different semiconductor photocatalytic systems to produce $H_2$ by visible light, including (1) $Pt/TiO_2$ plus sensitizers like $Ru(bipy)_3^{2+}$ and $RuL_3^{2+}$ (L = 2,2′-bipyridine-4,4′-dicarboxylate), (2) naked CdS, Pt/CdS, and $RuO_2/CdS$, and (3) mixtures of CdS + $Pt/TiO_2$, and CdS + ZnS co-precipitated on $\gamma$-$Al_2O_3$. EDTA, isopropanol, sulfide, and sulfide/sulfite mixtures were used as sacrificial agents. The photocatalytic systems which used sensitizers showed a poor stability and they only produced $H_2$ when EDTA was used as sacrificial agent. The mixture CdS + $Pt/TiO_2$ gave the highest reaction rates for $H_2$ production in isopropanol medium, and CdS, naked or with Pt deposits, produced the best results when sulfide or sulfide/sulfite was used as sacrificial agents. The addition of sulfite to a sulfide aqueous solution increased the $H_2$ production rate about four times with respect to the case when only sulfide was employed. The maximum photochemical and energy efficiencies obtained were 13.2 and 5.0%, respectively, with reference to the wavelength range 300–520 nm. The same group [281], in investigating different types of CdS-based photocatalysts (added semiconductors $Cu_xS$, $TiO_2$, and catalytic materials Pt or $RuO_x$) for hydrogen evolution from a sulfide + sulfite solution, emphasized the benefit of the thermal treatment of CdS in air, argon, hydrogen sulfide, or hydrogen atmospheres, as well as that of etching its surface. The best results were obtained using particles of CdS of 1.4 $\mu$m diameter, treated at 400 °C in air and etched with concentrated $HNO_3$, and on which 0.4% by weight of Pt was deposited.

Studies performed on CdS [282, 283] have revealed the importance of the microstructure, i.e., crystal structure, crystallite size, and geometrical surface area, in both the control of band structure and the concentration and mobility of charges, in relation to the photocatalytic performance of the photocatalyst. It has been shown also that the solubility product of CdS colloids prepared from acetate buffer aqueous solutions of suitable precursors increases from $7.2 \times 10^{-27}$ for large particles to about $10^{-15}$ for small (< 2.5 nm) particle colloids, this increase invoking a positive shift on the cathodic corrosion potential [284].

In situ metallization has been claimed to provide a convenient method for the preparation of metal-deposited and metal sulfide deposited CdS during photocatalytic decomposition of aqueous sulfide. As-prepared MS/CdS and M/CdS bifunctional photocatalysts (MS = Pt or Ir sulfide; M = Pt or Ir) were reported to be more active photocatalysts than CdS and ex-situ metallized CdS [285].

Recently, Navarro et al. [286] prompted the combination of ZnO and CdO with CdS to improve its photoabsorption ability: CdO exhibits a band gap in the interval 2.2–2.4 eV with high transmittance and very low resistance, while ZnO has

a wide band gap of 3.2 eV. A CdS–CdO–ZnO mixture annealed at different temperatures and loaded with Ru or Pt co-catalysts was tested in the production of hydrogen from aqueous solutions containing $SO_3^{2-} + S^{2-}$ as sacrificial reagents under visible light. The physicochemical characterization of the CdS–CdO–ZnO catalyst revealed significant changes in crystalline structure and visible light absorption capacity as a result of thermal treatments, hence also catalytic activity was found to be strongly dependent on thermal annealing. Hydrogen evolution over the CdS–CdO–ZnO catalyst was enhanced in the sample annealed at 773 K due to a better contact between the CdS and CdO–ZnO phases, which improved charge separation. The catalyst activity was significantly improved further by the addition of Pt or Ru co-catalysts. Activity promotion was higher for the sample loaded with Ru, this effect being associated to a better suppress of electron–hole recombination due to effective interaction between Ru oxide particles and CdS.

In the last 10 years, new photocatalytic sulfides which oxidize water by visible light with a sacrificial electron donor have been developed [287, 288]. For instance, $AgInZn_7S_9$, a solid solution of $AgInS_2$ and ZnS, with a 2.3 eV band gap, showed photocatalytic activity for $H_2$ evolution from an aqueous solution containing sacrificial reagents $SO_3^{2-}$ and $S^{2-}$ under visible light irradiation, even though $AgInS_2$ and ZnS separately hardly possessed any activity under the same conditions; loading of Pt co-catalyst improved the photocatalytic performance. However, the light conversion efficiency of these materials for water oxidation is very low at present.

The fabrication of p–n composite semiconductor particulate systems has been proposed as a generic strategy to develop highly active photocatalysts under visible light. Jang et al. [289] demonstrated that a non-oxide nano-bulk composite structure, in which nanoparticles of a semiconductor lie in contact with highly crystalline bulky particles of an other semiconductor, is particularly promising for hydrogen generation. A p-type semiconductor, $AgGaS_2$ (AGS), was prepared by conventional solid-state reaction and heat treated at various temperatures under He and $H_2S$ gas flow to eliminate vacancies or interstitial defects and to improve crystallinity. The AGS surface was decorated then with nanoparticles of n-CdS by hydrothermal treatment, so that a p–n diode, n-CdS/p-$AgGaS_2$, was formed (Fig. 5.15). Efficient rectification of photo-electrons and holes was observed with this diode system, which exhibited a high rate of hydrogen production under visible light irradiation from water containing sulfide and sulfite as hole scavengers. Importantly, the single component AGS photocatalyst showed high activity for hydrogen production in the same electrolyte whereas nanosized CdS photocatalyst produced only small amount of $H_2$ (13 $\mu$mol h$^{-1}$). The rates observed for AGS and CdS/AGS (heat treated at 423 K for 1 day), both loaded with 1 wt% Pt, were 296 $\mu$mol h$^{-1}$ and 473 $\mu$mol h$^{-1}$, respectively, i.e., representing ca. 12.4 and 19.7% of the quantum yields (100 $\times$ hydrogen atoms produced per absorbed photon).

On account of the reported photocatalytic activity of titania nanosheets in the oxidation of water [290], Yamada et al. [291] attempted to fabricate photoelectrodes responsive to visible light by coating CdS electrodes with titania nanosheets. It was considered that since the thickness of a nanosheet is as small as two atomic layers of

**Fig. 5.15** A configuration model consisting of bulky p-AgGaS$_2$ decorated with nanosized n-CdS particles. The *inset* shows the TEM image that supports the structure model. (Reprinted from [289], Copyright 2009, with permission from Elsevier)
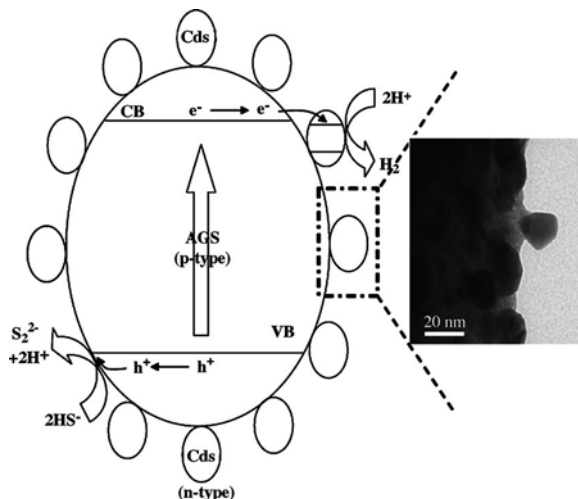


titanium, holes produced in the excited CdS electrodes may oxidize water through the sheet, the latter playing a protective or other active role. Further, cationic metal complexes, which were previously found [292] to give photocurrents on layered titania by visible light excitation, were intercalated between the titania sheets. The results indicated that the catalytic active site for water oxidation did not occur on the surface of titania nanosheet or that there was a barrier to hole transfer across the nanosheet.

### 5.3.3.2 Transition Metal Dichalcogenides and Related Photocatalysts

Semiconducting transition metal chalcogenides which provide sufficient high densities of *d*-metal states at the band edges have proven to be very promising catalytic materials for generation of chemical fuels in photoelectrochemical solar cells, as inducing favorable coordination chemistry at the electrode interface during multi-electron transfer reactions. The surface metal atoms of such a compound may attach OH$^-$ groups from water in order to compensate arriving photogenerated holes, thus forming hydroxide, oxide, and peroxide complexes; if the formation of peroxo-complexes with oxygen as intermediate states is sufficiently favorable, molecular oxygen may be liberated.

Dichalcogenides such as those of Mo, W, Re, Fe, Pt, and Ru photoreact with water, albeit with various products depending on material parameters; we have already referred to the preference of layered compounds such as MoS$_2$ to oxidize water instead of anodically decomposing themselves into metal ions and molecular sulfur. In fact, only dichalcogenides which are able to reach high oxidation states are able to photoevolve molecular oxygen from water [293]. MoS$_2$ and WS$_2$ show this property, as long as their vdW surface is quite perfect; however, when edge sites are present the oxidation complexes tend to involve also the sulfur species and

to generate sulfate. This process leads to the photodegradation of the metal sulfide. Rhenium sulfide, $ReS_2$, a layered triclinic compound, is also able to reach reasonably high Re oxidation states and can, in principle, photooxidize water to molecular oxygen under assistance of an external potential. However, because of an unfavorable interfacial chemistry, photodegradation takes place owing to oxidation of the material. It has been suggested that oxidized intermediate rhenium complexes are too stable for oxygen to be liberated [294]. On the other hand, transition metal atoms which cannot reach sufficiently high oxidation states, e.g., Fe, react with $OH^-$ but instead of forming peroxo-complexes, they directly transfer the bound oxygen to the chalcogenide ligands, e.g., sulfur, forming $SO_4^{2-}$.

Platinum disulfide ($PtS_2$), a layer-type semiconductor with $E_g \approx 0.95$ eV, is able to reach high Pt oxidation states, and it has the advantage over Mo and W sulfides, of containing a cation which is a noble metal [295]. That means that platinum cannot easily leave the electrode surface as a positive ion, so that in addition to resisting anodic photocorrosion leading to molecular sulfur, conversion of $PtS_2$ to platinum sulfate by the photoreaction involving the oxidation of water is inhibited. In order to solubilize platinum, a complex of this metal has to be formed with suitable ligands; experimental indications for such a corrosion mechanism have been reported indeed, but the principal photoreaction is the discharge of $OH^-$ ions and of other electron donating species. $PtS_2$ is therefore a photoelectrode which can utilize low-energy holes, generated by visible and near-infrared light, for photoassisted electrolysis of water. Notwithstanding, unfavorable catalytic behavior, connected to formation of platinum oxide, and non-ideal surface properties have been addressed.

Ruthenium disulfide ($RuS_2$), with $E_g \approx 1.9$ eV, and of a non-layered structure, has the same crystalline and an electronic structure similar to pyrite. The interfacial processes involved in the anodic reactions at $RuS_2$ and $FeS_2$ electrodes have been correlated to the percentage of metal $d$-character in the valence band, the chemistry of the metal ion, and the kinetic steps involved in the light-induced electron transfer [296]. Importantly, $RuS_2$, similar to $PtS_2$, is able to evolve oxygen as the principal oxidation product from water (with quantum efficiency up to 60% in the near UV region), with only marginal evidence of corrosion. It has even been referred to as one of the most efficient catalytic electrodes for (potential-assisted) photoevolution of oxygen (and chlorine) from water.

The implications of dark- and photo-evolution of oxygen or hydrogen on sintered (polycrystalline) and single-crystal $RuS_2$ have been discussed in the early 1980s [297–298]. By their results, at first on Fe-doped $RuS_2$ [299], and then on single-crystalline n-type $RuS_2$ grown from powder of the compound in bismuth melt [300], Kühne and Tributsch confirmed the original proposition of Tributsch that photoelectrolysis of water should be possible by developing a photoelectrochemistry based on transition metal $d$-states. It is noteworthy that a decrease of ability for oxygen evolution was observed in the series $RuS_2$, $RuSe_2$, $RuTe_2$, accompanied with a simultaneous increase of corrosion, connected to the parallel increase of mixing between Ru electronic states at the edge of the valence band and the lower

chalcogen states. This finding emphasized the role of $d$-states in the multielectron reaction leading to the evolution of molecular oxygen [301]. Interestingly, the photocurrent spectral sensitivity of the Bi-grown n-RuS$_2$ single crystals was observed to extend into the infrared part of the solar spectrum; an indirect energy gap of about 1.3 eV was determined (cf. the 1.37 eV gap of indirect transition, inferred from electrolyte electroreflectance data [302]). On the basis of these results, RuS$_2$ was considered a very attractive model system for research on low photon energy photooxidation of water. In fact, it was the first oxygen evolving photoelectrode to be described utilizing photons of the entire visible and near IR solar spectrum, while remaining reasonably stable.

The authors underscored the central importance of surface state complexes on the RuS$_2$ electrode in promoting its ability to react with water molecules by inducing interfacial coordination bonding. According to their model (cf. description of CdS surface states in [76]), a high density of Ru-based surface states exists situated in the forbidden energy gap of the semiconductor rendering the surface of RuS$_2$ positively charged during electrochemical polarization due to minority carrier (hole) trapping. The average positive charge accumulated in the surface complexes determines the energetic position of the (unpinned) energy band edges of the semiconductor, which upon application of an electrode potential are shifted until their position becomes stabilized by electron injection from the electrolyte. Although favorable for charge transfer catalysis, the overall mechanism was seen to induce considerable potential losses at the RuS$_2$/electrolyte interface as specified in various redox electrolytes, hence limiting the obtainable photovoltage and solar conversion efficiency in the respective cells. This limitation was mainly due to the small surface barrier height brought about by the position of the surface states being too high above the edge of the valence band.

On the basis of the existing knowledge, Salvador et al. [303] performed an electrolyte electroreflectance and photocurrent transient study of the single-crystal RuS$_2$/water interface with the aim of obtaining fundamental information on the catalytic reactivity of RuS$_2$, in particular to understand the dynamics of photocurrent flow through the oxygen-evolving interface. Contributions in water oxidation overpotential, charge transfer kinetics, the mechanism of oxygen evolution, and the factors affecting photoelectrocatalytic activity such as temperature dependence of surface reactions were examined. The authors stated that the main factor defining the catalytic activity of RuS$_2$ for water oxidation, both in the dark and under illumination, is a low overpotential (~0.3 V), which is comparable to that of the RuO$_2$ catalyst for oxygen evolution at darkness.

The layered thiophosphates n-SnPS$_3$, p-FePS$_3$, and p-NiPS$_3$, with measured indirect band gaps in the vicinity of 2 eV, have shown ability to photoelectrolyze water in acid solutions, with onset potentials which were observed to change in a Nernstian manner with the solution pH [304]. At n-type crystals, oxygen could be evolved upon irradiation at underpotentials of 850 mV, while at p-type crystals, hydrogen could be evolved at underpotentials of 400 mV, indicating a net gain in energy conversion.

Unbiased photocatalytic reduction of water has been pursued by employing p-type semiconductor photocathodes, on account of the advantageous combination they typically provide of a small band gap energy and positive flat band potential. Unfortunately, p-type semiconductors are much rarer in nature than the n-type, their band gaps are usually too small, and most suffer serious stability problems, so that they are rarely used in semiconductor photocatalysis. The case of $CuInSe_2$ chalcopyrite, with an optical gap of 0.95 eV, that can be obtained with p-type conductivity (e.g., due to copper deficiency) is very interesting in this connection. The energetic position of its conduction band appropriately matches the $H_2O/H_2$ level to reduce spontaneously water into hydrogen even in strongly alkaline solutions. Besides, $CuInSe_2$ crystals possess appreciable electrical conductivity and have shown a long-term chemical stability over the whole pH range. Notwithstanding, decomposition of water does not occur over narrow band gap semiconductors since the sum of overpotentials generally exceeds 1 V; therefore water reduction with such a photocathode should be combined to the oxidation of suitable hole scavengers.

Thin films of p-type $CuInSe_2$, prepared on Mo-covered glass substrates by coevaporation of the elements, have been characterized photoelectrochemically in aqueous acidic solutions [305]. In electrolyte without added redox species, the films showed a poor photoresponse, which was attributed to slow interfacial kinetics for the reduction of protons. Addition of $Eu^{3+}$ ions in the electrolyte was observed to allow an efficient collection of the generated photocurrent on bare surfaces. The effect of surface modifications by metal deposition was investigated: in acidic electrolytes with no redox species, the deposition of noble metals (Pt, Pd, Ru) was found to catalyze the hydrogen evolution reaction. However, the photocurrent onset potential remained very negative compared to the values of other p-type semiconductors such as InP, evidently due to the comparatively more negative value of the flat band potential of p-$CuInSe_2$.

Djellal et al. reported recently [306] on the PEC characterization of p-$CuInSe_2$ ingots of lamellar morphology synthesized by fusion technique, focusing on the capability for unbiased hydrogen production under visible light in aqueous solutions containing various redox couples with negative redox potentials. Capacity measurements with the p-type crystals gave a hole density of $5.9 \times 10^{18}$ cm$^{-3}$ and a flat band potential of $-0.36$ V (SCE). Hence, the conduction band, located at $-1.29$ V (SCE), should allow a spontaneous $H_2$ liberation upon visible light (Fig. 5.16). The semiconductor electrode could be almost completely stabilized by hole consumption involving $S^{2-}$ and $SO_3^{2-}$ species, both inducing a large band bending. However, the best photoactivity for $H_2$ formation was obtained in alkaline thiosulfate electrolyte. A two-step mechanism was considered for the light-induced oxidation of $S_2O_3^{2-}$ to $SO_3^{2-}$ and $SO_4^{2-}$, successively. In $S^{2-}$ and $SO_3^{2-}$ solutions, a tendency toward saturation was observed for prolonged irradiation, which was attributed to competitive (to water) reductions of the oxidation end-products $S_n^{2-}$ and $S_2O_6^{2-}$, as well as the generation of yellow polysulfide ($S_n^{2-}$) in solution. Almost complete regeneration of the photoactivity was achieved by evacuation of hydrogen and reactivation of the catalytic sites through nitrogen bubbling.
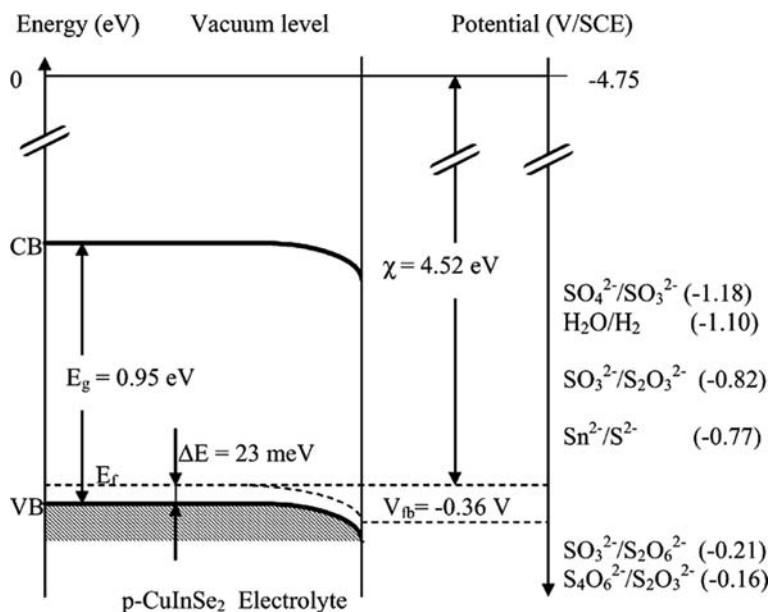
**Fig. 5.16** Energy-level diagram of p-CuInSe$_2$/electrolyte junction. (Reprinted from [306], Copyright 2009, with permission from Elsevier)

## 5.4 Sensitized Solar Cells

Wide-gap semiconductor electrodes can be sensitized with respect to light absorption by surface modification with a luminescent species injecting carriers to their conduction levels. In photoelectrochemical research, a variety of sensitizing dyes have been examined in order to improve the characteristics of semiconductor (macro) photoelectrodes or of dispersed semiconductor particle photochemical systems. Inception of this research has been assisted by the vast information accumulated over the years in the field of photographic science [307], since dye-sensitized electron injection is the basis of color photography, while dye-sensitized hole injection has been used in photography and in electrophotography (e.g., photocopying). Studies carried out during the early period of research (up to 1985) regarding mostly photo-sensitization of oxide substrates by covalently anchored or simply adsorbed dye molecules have been summarized by Rajeshwar [129].

The usefulness of electrochemical methods for the investigation of sensitization effects at different semiconductor surfaces has been examined originally by Gerischer and co-workers [308, 309] using zinc oxide as a typical n-type inorganic semiconductor and the hydrocarbon perylene as a typical p-type organic semiconductor. It was underscored that the well-known methods of electrochemical kinetics, including the dynamical ones, can be applied in the field, as indeed has been done extensively in subsequent work. Adding redox systems or changing other chemical conditions of the electrolyte solution was considered as a fruitful way to promote or

inhibit the electrochemically studied sensitization process. Light to energy conversion via photoelectrochemical reactions of organic dyes adsorbed on semiconductor electrodes has been demonstrated by Tributsch [310], who investigated excited chlorophyll molecules and applied electrochemical kinetics for the elucidation of chlorophyll-sensitized reactions in photosynthetic membranes. Aspects of these processes were discussed by Calvin [311]. Already in 1975, Gerischer remarked [5] that the quantum efficiency in such systems was limited by the fact that only monolayers of dyes are active for electron transfer to the semiconductor in the excited state, since thicker films of the sensitizer increase the resistance of the cell, acting as a filter, without adding to the current generation; thereby, a restriction of light absorption to the order of 1–2% was envisaged. In effect, it turned out later that a massive expansion of the dye–photoelectrode interfacial area could offer a viable solution to this problem as it enhances the light absorption to such level that even a 1000-fold increase could be obtained in the cell photocurrent compared with a dye-sensitized electrode having a flat surface morphology.

O'Regan and Grätzel [312] were the first to report remarkably high photon-to-current conversion efficiencies from dye-sensitized $TiO_2$ cells, using microheterogeneous film electrodes in combination with stable Ru-bipyridine sensitizers. The nanocrystalline, porous nature of the semiconductor electrode allowed a long optical path length for the dye molecules attached to the $TiO_2$ film while maintaining contact with the electrolyte. Importantly, surface and bulk recombination losses due to lattice defects, normally encountered in conventional photovoltaic cells, were minimized in this device, despite the disordered structure of the absorber film. The reason was simply that no minority carriers were involved in the photoconversion process, since the role of the semiconductor in a dye-sensitized device is merely to conduct the injected majority charge carriers. An important consequence was that the materials' purity requirements could be relaxed relative to conventional solar cells, thus allowing a low cost of fabrication. The "Grätzel" cell based on a mesoscopic semiconductor affording a so-called "bulk" junction, named after its 3D structure, comprised a cornerstone in the field and conduced to render photoelectrochemistry of the last 15 years synonymous to the science and technology of dye-sensitized cells (DSC). The relatively high solar efficiencies combined with very cheap preparation techniques could eventually make DSC superior to conventional solar cells. Since 1990, the efficiency of DSC in the conversion of light to electricity has been continuously improved. Grätzel and co-workers constructed cells with dye-modified $TiO_2$ film electrodes with solar conversion efficiency exceeding 10% and quantum current efficiency reaching practically unity [313]. Presently, DS $TiO_2$ nanostructured electrodes are used in state-of-the-art solar cells with high energy conversion efficiency (11%), long time stability, and low-cost production.

The prototype DSCs used liquid electrolytes, typically $I^-/I_2$ in an organic solvent such as propylene carbonate. The electron generation/collection problem in this cell has been discussed analytically with the help of intensity-modulated photocurrent and photovoltage spectroscopy [314]. A particularly challenging issue has been the replacement of the liquid electrolyte with a solid charge-transport material

in order to develop all-solid-state versions of DSCs, to benefit from the ease of manufacturing and robustness. Organic materials such as ionic conducting polymer solids [315] or gels [316] and inorganic p-type semiconductors [317] have been assessed as electrolytes in this regard, to build the so-called *dye-sensitized heterojunctions* (DSH). O'Regan and Schwartz [318] reported the fabrication of a dye-sensitized p–n heterojunction formed from a planar interface between n-$TiO_2$ and p-CuSCN, containing an intervening monolayer of a sulforhodamine-B dye. The CuSCN layer could be electrodeposited from solution without disturbing the dye/$TiO_2$ interaction. It was found that when exposed to visible light, the photoexcited dye molecules transferred electrons to the n-$TiO_2$ and holes to the p-CuSCN. The absorbed-photon-to-current efficiency was $\geq$ 70%. Later, a solar cell based on DSH $TiO_2$ with an amorphous organic hole-transport material (OMeTAD) was described [319] with a photon-to-current yield of 33%. p-Type conductive polypyrrole has been used also as a hole-transport layer in $TiO_2$ heterojunctions sensitized by Ru-bipyridyl and Ru-pyrrole complexes [320]. Improvement of the cell characteristics with the latter dye was explained by invoking direct molecular wiring of the polymer chain to the excited metal center of the complex. Dye molecules were considered to chemically bind not only with $TiO_2$ but also with the hole transport phase. Other strategies employed ionic liquids, blends of organic materials, such as polymeric or molecular semiconductors as well as hybrid cells using a p-type semiconducting polymer, in conjunction with a fullerene, or CdSe nanorods [321].

Organic dyes usually have a strong absorption over a discrete and relatively narrow band in the visible followed by a broad spectral region of very weak absorbance at shorter wavelengths. For efficient solar energy conversion, however, materials are needed which exhibit high absorption coefficients over the whole spectral region from near IR to UV. It has been recognized that the ideal sensitizer, a 1.5 eV edge absorber, is well approximated by a narrow band gap semiconductor. Along with the continual progress in nanoscience, it was conceived also that inorganic nanocrystals are superior to conventional organic dyes in several respects and offer the potential of higher efficiency as well as longer operational life for sensitized systems. That is because, apart from absorbing strongly all ultraband gap light thus rendering available a larger energy for conversion, nanocrystals may be very stable in the sensitizing role if properly prepared with a protective shell, unlike organic dyes, which tend to photobleach over a relatively short amount of time. A unique capability of the nanocrystal-sensitized solar cell is the production of quantum yields greater than unity by multiple exciton generation in Q-dots [322], as well as other opportunities offered by optical quantization effects.

Harvesting visible light energy in DSC-like systems by chalcogenide semiconductors has been pioneered in the 1980s. Gerischer and Lübke [323] were the first to suggest the use of a low-gap inorganic semiconductor (CdS) as an alternative to organic dye sensitizers on $TiO_2$. Thin films of CdS (up to 300 monolayers) were chemically deposited on n-$TiO_2$ crystal expecting that electrons would pass easily from the conduction band of CdS into the $TiO_2$ phase, on account of the favorable band edge relative positions in the two semiconductors. Indeed, sensitization currents were observed, whose spectral range was shifted to shorter wavelengths

compared to the single-crystal CdS, due to size quantization effects. However, holes generated by the light absorption in CdS accumulated in the CdS phase and caused anodic decomposition, as not being able to enter the $TiO_2$ phase because of too high an energetic position of the CdS valence band. Further, the photocurrent obtained was low, owing to the restraint of electron harvesting by fast charge recombination. Ennaoui et al. [159] fabricated a p–i–n like structure by grafting an ultrathin (10–20 nm) layer of pyrite ($E_g = 0.95$ eV) between larger-gap p-type and n-type materials. In this "sandwich" system, which was defined as a "sensitization solar cell", the pyrite layer only acted as photon absorber and mediated injection of excited electrons. In a related work, transparent, nanocrystalline $TiO_2$/CdS and CdS/$TiO_2$, "sandwich" bilayer electrodes were prepared by electrodeposition on conductive (F-doped TO) glass and characterized in aqueous electrolyte solution of varying pH, by potential-dependent spectroscopy [324]. Interface energetics on these electrodes was compared to that on bare $TiO_2$ or CdS electrolytic layers. Implications of the band-to-band charge transfer in the composite electrodes were discussed, considering potential applications in regenerative photoelectrochemical cells. Kohtani et al. [325] employed a sublimation flow method to prepare microcrystalline CdS-sensitized $TiO_2$ and ZnO electrodes which were assessed as to their photoelectrochemical properties in polysulfide solution.

During the 1990s, sensitization of (macro) electrodes by inorganic semiconductors was rather of marginal importance in view of the spectacular progress in dye-sensitized cells. On the other hand, since the 1980s, several studies appeared regarding surface-modified colloids in solution, which were denoted by such names as sensitized particles, p/n diodes, bifunctional catalysts, etc., usually all to the same effect of photoinduced electron transfer capability between different semiconductors. Interestingly, these systems were seen to offer enhanced photochemical activity and/or stability compared to single sols. Merging of the colloid and electrochemistry research communities led finally to appealing innovations comprising the development of specially designed electrodes with tailored surfaces, e.g., with specifically linked semiconductor Q-dots in an orderly fashion on oxide substrates, or nanocrystals embedded in nanotube arrays.

In the early studies on semiconductor sols, luminescence quenching and other experiments implied that CdS or CdSe nanocrystallites chemically deposited on $TiO_2$, $SnO_2$, and ZnO particles were capable of injecting excited electrons to the substrate. In studying mixed CdS/$TiO_2$ or CdS/ZnO suspensions, Henglein et al. [326] were able to show that chemical reactions induced by light absorption in the CdS part of the "sandwich" colloids occurred with much higher quantum yield than in the case of simple CdS catalyst particles, due to efficient primary charge separation. The composite particles were considered to act as small diodes of almost molecular dimensions or like p/n junctions; however, the authors made the judicious remark that the typical machinery involving a depletion layer, which in compact semiconductors produces useful potential gradients, was practically not operative in this case. Small colloidal particles with dimensions much smaller than the several tenths of nm of a depletion layer were definitely expected to afford a different mechanism of charge separation.

The utilization of the properties of quantum-sized particles (Q-dots) for typical semiconductor applications was emphasized in the pioneering work of Weller and co-workers [327] who used a film of CdS nanocrystallites to sensitize a transparent nanocrystalline $TiO_2$ foil electrode. The CdS coating was prepared by repeatedly dipping and washing the $TiO_2$ foil in $Cd(ClO_4)_2$ and $Na_2S$ solutions. The photocurrent quantum yield of the CdS-sensitized electrodes under visible light reached values of more than 70%. In a subsequent comprehensive study, the group of Weller [328] investigated the sensitization of nanoporous $TiO_2$, ZnO, $SnO_2$, $Nb_2O_5$, and $Ta_2O_5$ by in situ grown quantum-sized metal sulfides CdS, PbS, $Ag_2S$, $Sb_2S_3$, and $Bi_2S_3$. Substrate electrodes were prepared by spin coating ITO-glasses with concentrated colloidal solutions of the oxides, which then were dipped first into saturated nitrate solutions of $Cd^{2+}$, $Pb^{2+}$, $Ag^+$, $SbO^+$, and $BiO^+$, respectively, followed by dipping in solutions of $Na_2S$. The authors described the process of particle formation at the surface of the substrate electrodes as determined by the interplay of the lattice energy of the particles and a strong adsorption of metal ions at the surface, prior to the reaction with $S^{2-}$. Photoelectrochemical characterization, performed mostly in sulfide–sulfite solutions, showed that for any particular material combination the energetics at the interface between the sensitizing particles and the oxide substrate could be optimized in terms of electron injection by utilizing the size-quantization effect. Photocurrent quantum yields of up to nearly 80% and open-circuit voltages up to the 1 V range were measured. The best photostability of sensitized electrodes was achieved with CdS on $TiO_2$, while surface modification of the particles significantly enhanced the stability of the electrodes in corrosive conditions. In the same direction, the effect of PbS Q-dots in a porous $TiO_2$ solar cell structure was studied further by Hoyer and Konenkamp [329]. Seminal illustrations describing the sensitization of nanocrystalline $SnO_2$, ZnO, and $TiO_2$ electrodes by CdS [330, 331] and CdSe [332, 333] have been presented by Kamat and co-workers. The principles of charge injection and recombination suppress are drawn schematically in Figs. 5.17 and 5.18.

The photosensitization of various $TiO_2$ morphologies, from polycrystalline to nanostructured powder and thin films, has been undertaken by embedding chalcogenide particles, commonly by employing variants of chemical bath deposition (CBD) comprising in situ growth of the nanoparticles onto the substrate. The advantages of nanoporous substrates in enhancing light harvesting efficiency by folding the sensitizing semiconductor, by preventing particle growth and by inhibiting particle detachment, have been emphasized [334]. Hodes and co-workers [335] presented an investigation on CBD deposition mechanisms of CdSe into nanoporous $TiO_2$ films, along with correlation to the properties of as-fabricated liquid junction solar cells. Ion-by-ion and cluster mechanisms were invoked to illustrate the employed deposition process. Modes of preparation included CdSe deposition on a Cd-rich CdS film coated first on $TiO_2$ or selenization of the Cd-rich CdS layer with selenosulfate solution. The CdSe layers obtained by an ion-by-ion process were found to give superior cell performance compared to those deposited by a cluster process. Photocurrent spectroscopy measurements showed strong spectral dependence on illumination intensity indicating photocurrent losses due to poor
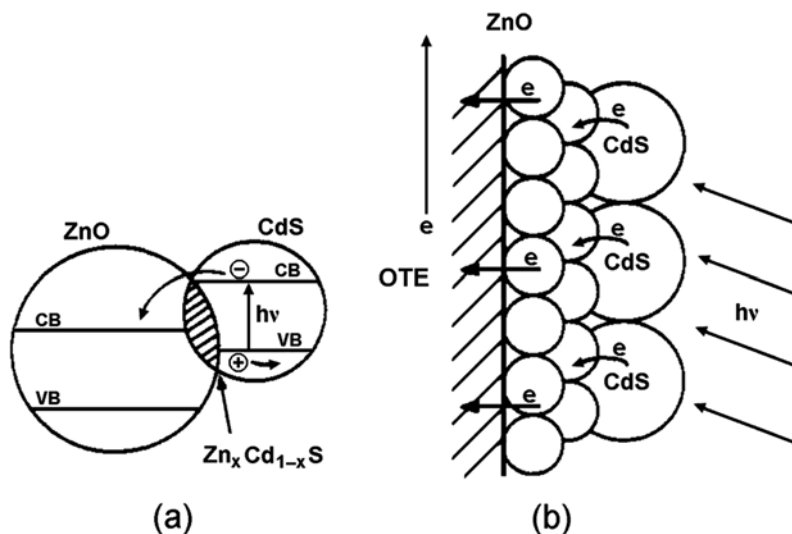
**Fig. 5.17** CdS–ZnO coupled semiconductor system: (**a**) interaction between two colloidal particles showing the principle of the charge injection process and (**b**) light absorption and electron transfer on an electrode surface leading to the generation of photocurrent. (Reproduced from [330])
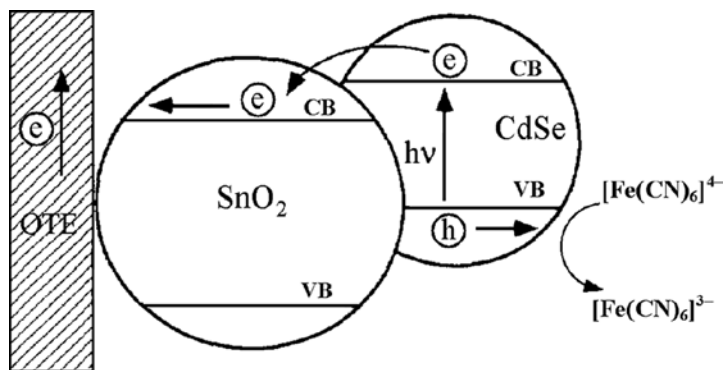


**Fig. 5.18** Suppression of charge recombination in coupled $SnO_2$/CdSe system. The photogenerated electrons in CdSe quickly migrate to the lower lying conduction band of $SnO_2$. As a result, they escape recombination with photogenerated holes in CdSe and are collected in greater number at the back contact OTE producing a larger photocurrent. (Reproduced from [333])

collection efficiencies. Stabilized solar efficiencies up to 2.8% were reported for cells using a polysulfide electrolyte. In their related work, Toyoda et al. [336–338] employed a photoacoustic technique to characterize optical absorption spectra in order to study the crystal growth and sensitizing properties of CdSe Q-dots chemically deposited on nanostructured $TiO_2$ foil electrodes with different rutile/anatase ratios.

Degradation problems typically encountered with the Q-dot sensitized PECs substantiated the need to explore alternative approaches toward improving photostability. Solid-state photovoltaic cells, providing inhibition of interfacial charge recombination by introducing an organic hole conductor on dye-sensitized mesoporous films of $TiO_2$ [339], have been considered to provide suitable conditions for the application of inorganic Q-dots as optical sensitizers. Along this line, Plass et al. [340] studied the excitation dynamics and the absorption features of an all-solid sandwich-type system involving a p–n heterojunction between $TiO_2$ and an organic hole conductor (spiro-OMeTAD), sensitized to the visible light by PbS Q-dots formed in situ on $TiO_2$ using CBD. During operation, the organic material was oxidized instead of PbS, due to the transfer of holes from PbS particles to spiro-OMeTAD molecules providing thus regeneration of the PbS particles. Ultrafast laser photolysis experiments suggested the initial charge separation to proceed in the subpicosecond time range. Transient absorption laser spectroscopy showed that recombination of the initially formed charges (injected electrons in $TiO_2$ and holes in spiro-OMeTAD) was much faster than in comparable dye-sensitized systems. The heterojunction showed incident photon-to-electron conversion efficiencies of up to 45% and energy conversion efficiencies under simulated sunlight AM1.5 (10 mW $cm^2$) of 0.49%.

The sensitized electrode preparation method is of major importance for the properties of the resulting assembly. The successful incorporation of the semiconductor particles by in situ CBD growth onto a mesoporous oxide substrate is counterbalanced by a broad size distribution of the produced particles; the consequent variation in the energy level alignment may lead to an energy barrier to electrons (rather than a favorable energetic pathway) in a significant fraction of the Q-dots. Hence, size control which would allow selection of the Q-dots that optimize the energy-level alignment with the various metal oxide electrode materials is indispensable in these systems. Modern colloidal syntheses, employing high-boiling solvents in conjunction with coordinating/non-coordinating surfactants, have been shown to produce semiconductor nanoparticles with monodisperse size distributions, clear and discrete optical transitions, and high fluorescence quantum yields [341–343]. These processes offer the possibility to create high-quality surfaces with optimized Q-dot coverage that maximizes light harvesting and energy conversion efficiency in solar cells. Further in the direction of system optimization, functionalized surfaces can be conveniently prepared by tethering nanoparticles to substrates through *bifunctional molecular linkers* [344], whose affinity for surfaces is dictated by coordinate covalent bonding interactions. For example, thiols and thiolates bind strongly to gold, silver, and metal chalcogenides; isocyanides bind to platinum; carboxylic acids and carboxylates bind to metal oxides; and silanes and siloxanes bind to silicon and silica. Bifunctional linker molecules such as MPA (HOOC-$CH_2$-$CH_2$-SH), which have both carboxylate and thiol functional groups, facilitate binding between chalcogenide Q-dots and $TiO_2$ surfaces and ensure monolayer coverage of the sensitizing film within the substrate network.

Application of the above techniques has enabled the synthesis of a range of nanostructured materials with tunable composition, physical properties, and

chemical reactivity. Examples illustrating the underlying potential and perspectives of this approach follow.

Hyun et al. [345] prepared PbS Q-dots in a suspension and tethered them to $TiO_2$ nanoparticles with a bifunctional thiol–carboxyl linker molecule. Strong size dependence due to quantum confinement was inferred from cyclic voltammetry measurements, for the electron affinity and ionization potential of the attached Q-dots. On the basis of the measured energy levels, the authors claimed that photoexcited electrons should transfer efficiently from PbS into $TiO_2$ only for dot diameters below ~ 4.3 nm. Continuous-wave fluorescence spectra and fluorescence transients of the PbS/$TiO_2$ assembly were consistent with electron transfer from small Q-dots. The measured charge transfer time was surprisingly slow (~100 ns). Implications of this fact for future photovoltaics were discussed, while initial results from as-fabricated sensitized solar cells were presented.

Peter and co-workers, after demonstrating a photosensitization effect using size-selected CdS Q-dots, prepared by arrested precipitation and self-assembly on nanocrystalline $TiO_2$ electrodes [346], presented a related study on the incorporation and properties of $Bi_2S_3$ Q-dots into nanocrystalline $TiO_2$ [347]. The bismuth sulfide semiconductor was chosen as complying with the requirement for a Q-dot sensitizer to have an absorption onset at around 1.4 eV, in order to optimize power output under solar illumination. $Bi_2S_3$ nanoparticles were prepared and self-assembled on the oxide electrodes by arrested precipitation, using 3-mercapto-propionic acid (3-MPA) as the stabilizer in order to facilitate assembly on the $TiO_2$ substrate via a carboxylate linkage. In evaluating the modified electrodes in a cell arrangement, the authors observed a band-edge tuning effect for the bismuth sulfide particles, which was associated with the adsorption of sulfide ($HS^-$) ions from the electrolyte solution. According to the derived interface energetics, in the absence of sulfide ions only the smaller $Bi_2S_3$ particles could inject electrons into the $TiO_2$ phase, due to their effectively larger band gap. But, progressive addition of sulfide ions to the electrolyte induced an upward shift of the $Bi_2S_3$ conduction band level (toward more negative potentials), so that larger nanoparticles became able to inject carriers and the long wavelength component of the photocurrent response from the cell increased. This quite interesting phenomenon was connected to the well-known fact that the flat band potential of chalcogenide semiconductors shifts to more negative potentials in the presence of $HS^-$ in the electrolyte solution, an effect explained by the change in surface dipole caused by adsorbed $HS^-$ ions.

Kamat and co-workers [348] used MPA bifunctional surface modifiers to assemble CdSe Q-dots onto mesoscopic $TiO_2$ films (Fig. 5.19). The injection of electrons from the conduction band of CdSe into $TiO_2$, upon visible light excitation was confirmed by femtosecond transient absorption and emission-quenching experiments. The injected charge carriers could be collected at a conducting electrode to generate a photocurrent. A photon-to-charge carrier generation efficiency of 12% was obtained from the $TiO_2$/CdSe composite electrode photoanodes. Significant loss of electrons was seen to occur due to scattering as well as charge recombination at the $TiO_2$/CdSe interfaces and internal $TiO_2$ grain boundaries.
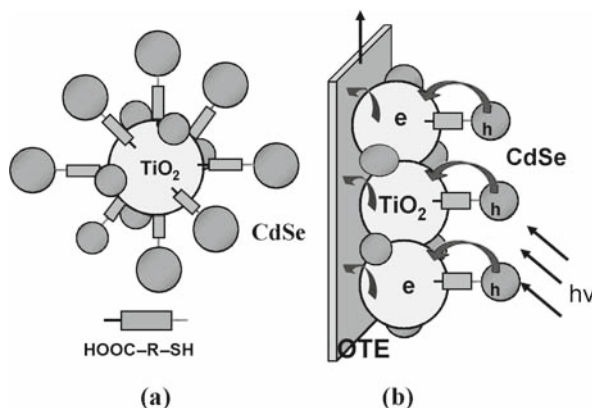
**Fig. 5.19** (**a**) Linking CdSe quantum dots to TiO$_2$ particle with bifunctional surface modifier; (**b**) light harvesting assembly composed of TiO$_2$ film functionalized with CdSe Q-dots on optically transparent electrode (OTE). [Adapted (in gray scale) from [348]]

Zhang and co-workers [349] investigated the sensitizing effect of CdSe Q-dots on highly ordered TiO$_2$ nanotube arrays, which were fabricated on Ti substrates by self-organized anodic oxidation. The CdSe colloids were prepared ex situ by a one-pot synthesis, known to give high-quality monodisperse quantum-confined dots and rods [350]. Air annealing pretreatment of the TiO$_2$ nanotubes was considered to be essential for better performance of the final composite system as increasing the anatase phase. Attachment of the CdSe crystallites was found to significantly extend the photocurrent of TiO$_2$ nanotubes in the visible region. The photoresponse showed strong dependence on the Q-dots size.

Recently, size-dependent charge injection into TiO$_2$ from different-sized CdSe Q-dots, assembled via a bifunctional linker molecule (MPA) on TiO$_2$ films composed of particle and nanotube morphologies, was demonstrated by using spectroscopic and photoelectrochemical techniques [351]. The presented results highlighted the ability to tune the photoelectrochemical response via size control of CdSe Q-dots and the improvement in photoconversion efficiency by facilitating the charge transport through a TiO$_2$ nanotube architecture. It was shown in particular that smaller-sized CdSe Q-dots allow greater charge injection rates and also higher photon-to-electron conversion efficiencies at the excitonic band (Fig. 5.20). Larger particles, although absorbing better in the visible region, could not inject electrons into TiO$_2$ as effectively as the smaller CdSe Q-dots. The maximum power-conversion efficiency ($\leq 1\%$) was observed for the 3 nm in-diameter dots.

The authors claimed that although the net power-conversion efficiency of their Q-dot solar cells was significantly lower than of DSC or organic solar cells, the results are quite encouraging toward demonstrating the effectiveness of quantum dots as sensitizers for the next-generation solar cells. The performance of such devices might be improved by optimizing the cell configuration and improving the light absorption properties of the electrodes. According to the authors this can be done
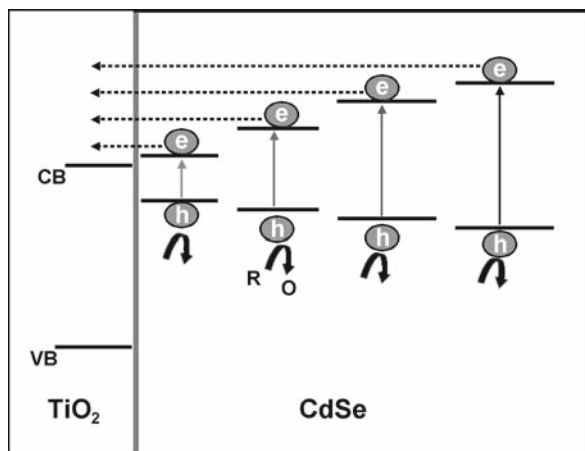
**Fig. 5.20** Schematic diagram illustrating the energy levels of different-sized CdSe quantum dots and $TiO_2$ (band positions are not drawn to scale). The injection of electrons from CdSe into $TiO_2$ is influenced by the energy difference between the two conduction bands. [Adapted (in gray scale) from [351]]

by the construction of a "rainbow solar cell", which employs an ordered assembly of CdSe nanoparticles of different diameters absorbing and transmitting different wavelength regions. Essentially, this cell consists in creating an orderly gradient of band gap energy, rendering it possible to maximize the capture of the incident light while collecting and transmitting electrons through the $TiO_2$ tube network. Such a cell configuration allows one to couple the faster electron injection rate of small-sized particles and greater absorption range of large particles effectively.

# References

1. Meissner D (2002) Photoelectrochemical solar energy conversion. In Luther J, Nast M, Norbert Fisch M, Christoffers D, Pfisterer F, Meissner D, Nitsch J (Article) Solar Technology. Ullmanns Encyclopedia of Industrial Chemistry, Wiley VCH (electronic release)
2. Grätzel M (2007) Photovoltaic and photoelectrochemical conversion of solar energy. Phil Trans R Soc A 365: 993–1005
3. Brattain WH, Garrett CGB (1955) Experiments on the interface between Germanium and an Electrolyte. Bell Syst Tech J 34: 129–176
4. Memming R (1980) Solar energy conversion by photoelectrochemical processes. Electrochim Acta 25: 77–88
5. Gerischer H (1975) Electrochemical photo and solar cells. Principles and some experiments. Electroanal Chem Interfacial Electrochem 58: 263–274
6. Boddy PJ (1965) The structure of the semiconductor-electrolyte interface. J Electroanal Chem 10: 199–244
7. Gerischer H (1970) Semiconductor Electrochemistry. In: Eyring H (ed) Physical Chemistry – An advanced treatise Vol IXA, Academic Press, New York

8. Pleskov YV, Gurevich YY (1986) Semiconductor Photoelectrochemistry. Consultants Bureau, New York

9. Wrighton MS (1979) Photoelectrochemical conversion of optical energy to electricity and fuels. Acc Chem Res 12: 303–310

10. Rajeshwar K, Singh P, Dubow J (1978) Energy conversion in photoelectrochemical systems – A review. Electrochim Acta 23: 1117–1144

11. Heller A (1981) Conversion of sunlight into electrical power and photoassisted electrolysis of water in photoelectrochemical cells. Acc Chem Res 14: 154–162

12. Koval CA, Howard JN (1992) Electron transfer at semiconductor electrode-liquid electrolyte interfaces. Chem Rev 92: 411–433

13. Lewis NS (1998) Progress in understanding electron-transfer reactions at semiconductor/liquid interfaces. J Phys Chem B 102: 4843–4855

14. Tryk DA, Fujishima A, Honda K (2000) Recent topics in photoelectrochemistry: achievements and future prospects. Electrochim Acta 45: 2363–2376

15. Rauh RD (1988) Cadmium Chalcogenides (CdS, CdSe, CdTe). In: Finklea HO (ed) Semiconductor Electrodes (Studies in Physical and Theoretical Chemistry 55) Elsevier

16. Scrosati B (1988) Molybdenum and Tungsten Dichalcogenides ($MoX_2$ and $WX_2$). In: Finklea HO (ed) Semiconductor Electrodes (Studies in Physical and Theoretical Chemistry 55) Elsevier

17. Chang KC, Heller A, Schwartz B, Menezes S, Miller B (1977) Stable semiconductor liquid junction cell with 9 percent solar-to-electrical conversion efficiency. Science 196: 1097–1099

18. Parkinson BA, Heller A, Miller B (1978) Enhanced photoelectrochemical solar-energy conversion by gallium arsenide surface modification. Appl Phys Lett 33: 521–523

19. Noufi R, Tench D (1980) High-efficiency GaAs photoanodes. J Electrochem Soc 127: 188–190

20. Tufts BJ, Abrahams IL, Santangelo PG, Ryba GN, Casagrande LG, Lewis NS (1987) Chemical modification of n-GaAs electrodes with $Os^{3+}$ gives a 15% efficient solar cell. Nature 326: 861–863

21. Gronet C, Lewis NS (1983) Design of a 13% efficient n-GaAs$_{1-x}$P$_x$ semiconductor-liquid junction solar cell. Nature 300: 733–735

22. Nakatani K, Matsudaiva S, Tsubomura H (1978) Photoanodic behavior of n-type cadmium sulfide in acetonitrile solutions containing iodide ion. J Electrochem Soc 125: 406–409

23. Frank SN, Bard AJ (1975) Semiconductor Electrodes. II. Electrochemistry at n-type $TiO_2$ electrodes in acetonitrile solutions. J Am Chem Soc 97: 7427–7433

24. Laser D, Bard AJ (1976) Semiconductor Electrodes. IV. Electrochemical behavior of n- and p-type silicon electrodes in acetonitrile solutions. J Phys Chem 80: 459–466

25. Kohl PA, Bard AJ (1979) XVII. Electrochemical behavior of n- and p-type InP electrodes in acetonitrile solutions. J Electrochem Soc 126: 598–603

26. Kohl PA, Bard AJ (1979) XVIII. Liquid junction photovoltaic cells based on n-GaAs electrodes and acetonitrile solutions. J Electrochem Soc 126: 603–608

27. Langmuir ME, Parker MA, Rauh MD (1982) Electrochemical photovoltaic cells based on n-GaAs and the triiodide/iodide redox couple in acetonitrile. J Electrochem Soc 129: 1705–1710

28. Gronet CM, Lewis NS (1983) n-type GaAs photoanodes in acetonitrile: Design of a 10.0% efficient photoelectrode. Appl Phys Lett 43: 115–117

29. Bolts JM, Wrighton MS (1978) Chemically derivatized n-type semiconducting germanium photoelectrodes. Persistent attachment and photoelectrochemical activity of ferrocene derivatives. J Am Chem Soc 100: 5257–5262

30. Bocarsly AB, Walton EG, Wrighton MS (1980) Use of chemically derivatized n-type silicon photoelectrodes in aqueous media. Photooxidation of iodide, hexacyanoiron(II), and hexaammineruthenium(II) at ferrocene-derivatized photoanodes. J Am Chem Soc 102: 3390–3398

31. Wrighton MS, Austin RC, Bocarsly AB, Bolts JM, Haas O, Legg KD, Nadjo L, Palazzotto MC (1978) Design and study of a photosensitive interface: A derivatized n-type silicon photoelectrode. J Am Chem Soc 100: 1602–1603

32. Diaz AF, Logan JA (1980) Electroactive polyaniline films. J Electroanal Chem 111: 111–114

33. Noufi R, Nozik AJ, White J, Warren LF (1982) Enhanced stability of photoelectrodes with electrogenerated polyaniline films. J Electrochem Soc 129: 2261–2265

34. Noufi R, Tench D, Warren LF (1981) Protection of semiconductor photoanodes with photoelectrochemically generated polypyrrole films. J Electrochem Soc 128: 2596–2599

35. Jaeger CD, Fan FRF, Bard AJ (1980) Semiconductor electrodes. 26. Spectral sensitization of semiconductors with phthalocyanine. J Am Chem Soc 102: 2592–2598

36. Gerischer H (1977) On the stability of semiconductor electrodes against photodecomposition. J Electroanal Chem 82: 133–143

37. Bard AJ, Wrighton MS (1977) Thermodynamic potential for the anodic dissolution of n-type semiconductors – A crucial factor controlling durability and efficiency in photoelectrochemical cells and an important criterion in the selection of new electrode/electrolyte systems. J Electrochem Soc 124: 1706–1710

38. Gerischer H (1989) Neglected problems in the pH dependence of the flatband potential of semiconducting oxides and semiconductors covered with oxide layers. Electrochim Acta 34: 1005–1009

39. Singh P, Singh R, Gale R, Rajeshwar K, DuBow J (1980) Surface charge and specific ion adsorption effects in photoelectrochemical devices. J Appl Phys 51: 6286–6291

40. Bard AJ, Bocarsly AB, Fan FRF, Walton EG, Wrighton MS (1980) The concept of Fermi level pinning at semiconductor/liquid junctions. Consequences for energy conversion efficiency and selection of useful solution redox couples in solar devices. J Am Chem Soc 102: 3671–3677

41. Bocarsly AB, Bookbinder DS, Dominey RN, Lewis NS, Wrighton MS (1980) Photoreduction at illuminated p-type semiconducting silicon photoelectrodes. Evidence for Fermi level pinning. J Am Chem Soc 102: 3683–3688

42. Gerischer H, Gobrecht J (1976) On the power characteristics of electrochemical solar cells. Ber Bunsenges Phys Chem 80: 327–333

43. Williams R (1960) Becquerel photovoltaic effect in binary compounds. J Chem Phys 32: 1505–1514

44. Gerischer H (1966) Electrochemical behavior of semiconductors under illumination. J Electrochem Soc 113: 1174–1182

45. Turner DRJ (1961) Saturation currents at n-type silicon and germanium electrodes in chemical etching solutions. Electrochem Soc 108: 561–563

46. Fujishima A, Sugiyama E, Honda K (1971) Photosensitized electrolytic oxidation of iodide ions on cadmium sulfide single crystal electrode. Bull Chem Soc Japan 44: 304

47. Inoue T, Watanabe T, Fujishima A, Honda K, Kohayakawa K (1977) Suppression of surface dissolution of CdS photoanode by reducing agents. J Electrochem Soc 124: 719–722

48. Ellis AB, Kaiser SW, Wrighton MS (1976) Visible light to electrical energy conversion. Stable cadmium sulfide and cadmium selenide photoelectrodes in aqueous electrolytes. J Am Chem Soc 98: 1635–1637

49. Heller A, Chang KC, Miller B (1977) Spectral response and efficiency relations in semiconductor liquid junction solar cells. J Electrochem Soc 124: 697–700

50. Ellis AB, Kaiser SW, Wrighton MS (1976) Optical to electrical energy conversion. Characterization of cadmium sulfide and cadmium selenide based photoelectrochemical cells. J Am Chem Soc 98: 6855–6866

51. Ellis AB, Kaiser SW, Wrighton MS (1976) Optical to electrical energy conversion: Cadmium telluride-based photoelectrochemical cells employing telluride/ditelluride electrolytes. J Am Chem Soc 98: 6418–6420

52. Ellis AB, Kaiser SW, Bolts JM, Wrighton MS (1977) Study of n-type semiconducting cadmium chalcogenide-based photoelectrochemical cells employing polychalcogenide electrolytes. J Am Chem Soc 99: 2839–2848

53. Hodes G, Manassen J, Cahen D (1977) Photo-electrochemical energy conversion: electro-catalytic sulphur electrodes. J Appl Electrochem 7: 181–182

54. Hodes G, Manassen J, Cahen D (1980) Electrocatalytic electrodes for the polysulfide redox system. J Electrochem Soc 127: 544–549

55. McCann JF, Skyllas-Kazacos M, Haneman D (1981) Temperature dependence for the power outputs of n-CdSe liquid junction cells. Nature 289: 780–782

56. Licht S, Tenne R, Flaisher H, Manassen J (1984) A pronounced cation effect on performance and stability of Cd- chalcogenide/polysulfide photoelectrochemical cells. J Electrochem Soc 131: 950–951

57. Licht S, Tenne R, Flaisher H, Manassen J (1986) Cation effects on the electrochemistry of anions in polysulfide photoelectrochemical cells. J Electrochem Soc 133: 52–59

58. Licht S, Manassen J (1985) The effect of hydroxide ion on Cd-chalcogenide/aqueous polysulfide photoelectrochemical cells. J Electrochem Soc 132: 1076–1081

59. Licht S, Tenne R, Dagan G, Manassen J, Hodes G, Cahen D, Triboulet R, Rioux J, Levy-Clement C (1985) High efficiency n-Cd(Se,Te)/S$^=$ photoelectrochemical cell resulting from solution chemistry control. Appl Phys Lett 46: 608–610

60. Licht S, Hodes G, Tenne R, Manassen J (1987) A light-variation insensitive high efficiency solar cell. Nature 326: 863–864

61. Sharon M, P Veluchamy P, Natarajan C, Kumar D (1991) Solar rechargeable battery-principle and materials. Electrochim Acta 36: 1107–1126

62. Frese KW Jr (1982) A high efficiency single-crystal CdSe photoelectrochemical solar cell and an associated loss mechanism. Appl Phys Lett 40: 275–277

63. Reichman J, Russak MA (1984) I-V Behavior of the CdSe/sulfide-polysulfide and CdSe/ferro-ferricyanide photoelectrochemical systems. J Electrochem Soc 131: 796–798

64. Rubin HD, Humphrey BD, Bocarsly AB (1984) Role of surface reactions in the stabilization of n-CdS-based photoelectrochemical cells. Nature 308: 339–341

65. Rubin HD, Arent DJ, Bocarsly AB (1985) The n-CdSe photoelectrochemical cell: Wavelength-dependent photostability. J Electrochem Soc 132: 523–524

66. Licht S, Peramunage D (1990) Efficient photoelectrochemical solar cells from electrolyte modification. Nature 345: 330–333

67. Heller A, Schwartz GP, Vadimsky RG, Menezes S, Miller B (1978) Output stability of n-CdSe/Na$_2$S-S-NaOH/C solar cells. J Electrochem Soc 125: 1156–1160

68. Noufi R, Tench D, Warren LF (1980) Stabilization of n-CdSe photoanodes in nonaqueous Fe(CN)$_6$$^{3-/4-}$ electrolytes. J Electrochem Soc 127: 2709–2713

69. Aruchamy A, Wrighton MS (1980) Comparison of the interface energetics for n-type cadmium sulfide/ and cadmium telluride/nonaqueous electrolyte junctions. J Phys Chem 84: 2848–2854

70. Aruchamy A, Bruce JA, Tanaka S, Wrighton MS (1983) Characterization of the interface energetics for n-type cadmium selenide/nonaqueous electrolyte junctions. J Electrochem Soc 130: 359–364

71. Finklea HO (1988) Semiconductor electrode concepts and terminology. In: Finklea HO (ed) Semiconductor Electrodes (Studies in Physical and Theoretical Chemistry 55) Elsevier

72. Lemasson P, Dalbera JP, Gautron J (1981) Flat band potential determination of an electrolyte/semiconductor junction by an electro-optical method. J Appl Phys 52: 6296–6300

73. Reeves JH, Cocivera M (1984) Comparison of behavior of single-crystal and polycrystalline CdS in photoelectrochemical cells. J Electrochem Soc 131: 2042–2047

74. Tyagai VA, Kolbasov GY (1971) The contribution of surface states to the charge transport process across CdS, CdSe–electrolyte interface. Surf Sci 28: 423–436

75. Ginley DS, Butler MA (1978) Flatband potential of cadmium sulfide (CdS) photoanodes and its dependence on surface ion effects. J Electrochem Soc 125: 1968–1974

76. Meissner D, Memming R, Kastening B (1988) Photoelectrochemistry of cadmium sulfide. 1. Reanalysis of photocorrosion and flat-band potential. J Phys Chem 92: 3476–3483

77. Meissner D, Lauermann I, Memming R, Kastening B (1988) Photoelectrochemistry of cadmium sulfide. 2. Influence of surface-state charging. J Phys Chem 92: 3484–3488

78. Frese Jr KW (1982) Capacitance/voltage studies on etched and anodized single-crystal n-CdSe. J Appl Phys 53: 1571–1576

79. Frese Jr KW (1983) Electrochemical studies of photocorrosion of n-CdSe. J Electrochem Soc 130: 28–33

80. Tenne R, Giriat W (1985) Controlled photoelectrochemical etching of CdSe and observation of a photocathodic effect. J Electroanal Chem 186: 127–137

81. Karas BR, Strickert HH, Schreiner R, Ellis AB (1981) Luminescent photoelectrochemical cells. 5. Multiple emission from tellurium-doped cadmium sulfide photoelectrodes and implications regarding excited-state communication. J Am Chem Soc 103: 1648–1651

82. Strickert HH, Tong JR, Ellis AB (1982) Luminescent photoelectrochemical cells. 6. Spatial aspects of the photoluminescence and electroluminescence of cadmium selenide electrodes. J Am Chem Soc 104: 581–588

83. Marcu V, Tenne R (1988) Photocurrent oscillations in the CdTe electrolyte systems. J Phys Chem 92: 7089–7092

84. Miller B, Heller A, Robbins M, Menezes S, Chang KC, Thomson JJ (1977) Solar conversion efficiency of pressure sintered cadmium selenide liquid junction cells. J Electrochem Soc 124: 1019–1021

85. Hodes G, Manassen J, Cahen D (1976) Photoelectrochemical energy conversion and storage using polycrystalline chalcogenide electrodes. Nature 261: 403–404

86. Miller B, Heller A (1976) Semiconductor liquid junction solar cells based on anodic sulphide films. Nature 262: 680–681

87. Peter LM (1978) The photoelectrochemical properties of anodic cadmium sulphide films. Electrochim Acta 23: 1073–1080

88. Cahen D, Hodes G, Manassen J (1978) S/Se Substitution in polycrystalline CdSe photoelectrodes photoelectrochemical energy conversion. J Electrochem Soc 125: 1623–1628

89. Noufi RN, Kohl PA, Bard AJ (1978) Semiconductor Electrodes XV. Photoelectrochemical cells with mixed polycrystalline n-type CdS-CdSe electrodes. J Electrochem Soc 125: 375–379

90. McCann JF, Kainthla RC, Skyllas-Kazacos M (1983) Chemical deposition of $Cd_{1-x}Hg_xS$ thin film electrodes for liquid-junction solar cells. Sol Energy Mater Sol Cells 9: 247–251

91. Russak MA, Reichman J, Witzke H, Deb SK, Chen SN (1980) Thin film CdSe photoanodes for electrochemical photovoltaic cells. J Electrochem Soc 127: 725–733

92. Lyden JK, Cohen MH, Tomkiewicz M (1981) Role of disorder in photoelectrochemical solar cells with polycrystalline photoanodes. Phys Rev Lett 47: 961–963

93. Chartier P, Ba B, Ebothe J, Alonso Vante N, Nguyen Cong H (1982) Photoassisted interfacial charge transfers at inhomogeneous semiconducting film-electrolyte junction in photoelectrochemical cells: Case of CdS and CdS(Al) sprayed films on to conductive glass. J Electroanal Chem 138: 381–394

94. Miller DJ, Haneman D (1981) Preparation of stable efficient CdSe films for solar PEC cells. Sol Energy Mater 4: 223–231

95. Houston GJ, McCann JF, Haneman D (1982) Optimising the photoelectrochemical performance of electrodeposited CdSe semiconductor electrodes. J Electroanal Chem 134: 37–47

96. Hodes G, Manassen J, Neagu S, Cahen D, Mirovski Y (1982) Electroplated cadmium chalcogenide layers: Characterization and use in photoelectrochemical solar cells. Thin Solid Films 90: 433–438

97. Bouroushian M, Loizos Z, Spyrellis N, Maurin G (1993) Influence of heat treatment on structure and properties of electrodeposited CdSe or Cd(Se,Te) semiconducting coatings. Thin Solid Films 229: 101–106

98. Gutierrez MT, Salvador P (1987) Photoelectrochemical characterization and optimization of a liquid-junction photovoltaic cell based on electrodeposited CdSe thin films: Influence of annealing and photoetching on the physical parameters determining the cell performance. Sol Energy Mater 15: 99–113

99. Bouroushian M, Charoud-Got J, Loizos Z, Spyrellis N, Maurin G (2001) Structure and properties of CdSe and CdSe$_x$Te$_{1-x}$ electrolytic coatings on Ni and Ti cathodes. Influence of the acidic aqueous bath pH. Thin Solid Films 381: 39–47

100. Danaher WJ, Lyons LE (1978) Photoelectrochemical cell with cadmium telluride film. Nature 271: 139

101. Bhattacharya RN, Rajeshwar K (1984) Electrodeposition of CdTe thin films. J Electrochem Soc 131: 2032–2037

102. Mirovsky Y, Tenne R, Hodes G, Cahen D (1982) Photoelectrochemical solar cells: Interpretation of cell performance using electrochemical determination of photoelectrode properties. Thin Solid Films 91: 349–355

103. Bhattacharya RN (1986) Electrodeposited CdSe$_{0.5}$Te$_{0.5}$: photoelectrochemical solar cells. J Appl Electrochem 16: 168–174

104. Licht S (1986) Combined solution effects yield stable thin-film Cd(Se,Te)/polysulfide photoelectrochemical solar cells. J Phys Chem 90: 1096–1099

105. Singh K, Mishra SSD (2004) Photoelectrochemical studies on colloidal cadmium sulfide containing cadmium selenide electrodeposits. Electrochem Solid State Lettate 7: A185–A186

106. Singh K, Srivastava ML, Mishra SSD (2006) Electrochemical deposition and photoelectrochemical characterization of colloidal HgS containing CdSe composites. Sol Energy Mater Sol Cells 90: 923–932

107. Kohl PA, Frank SN, Bard AJ (1977) Semiconductor electrodes XI. behavior of n- and p-type single crystal semiconductors covered with thin n-TiO$_2$ films. J Electrochem Soc 124: 225–229

108. Tomkiewicz M, Woodall J (1979) Photoelectrolysis of water with semiconductor materials. J Electrochem Soc 124: 1436–1440

109. Kampmann A, Marcu V, Strehblow HH (1990) Production and characterization of diodes made in thin p-Se layers on top of n-CdSe. J Electroanal Chem 280: 91–103

110. Singh K, Mishra SS (2002) Photoelectrochemical studies on galvanostatically formed multiple band gap materials based on CdSe and ZnSe. Sol Energy Mater Sol Cells 71: 115–129

111. Mandal KC (1990) Fermi level shift with photovoltages at zinc modified CdSe surfaces. J Mater Sci Lett 9: 1203–1204

112. Russak MA, Reichman J (1982) Photoelectrochemical performance of ZnSe/CdSe thin film electrodes in aqueous polysulfide electrolyte. J Electrochem Soc 129: 542–545

113. Bouroushian M, Karoussos D, Kosanovic T (2006) Photoelectrochemical properties of electrodeposited CdSe and CdSe/ZnSe thin films in sulphide-polysulphide and ferro-ferricyanide redox systems. Solid State Ionics 177: 1855–1859

114. Green MA (2007) Third generation photovoltaics – Advanced solar energy conversion. Springer, Berlin

115. Licht S, Khaselev O, Ramakrishnan PA, Soga T, Umeno M (1998) Multiple-bandgap photoelectrochemistry: Bipolar semiconductor ohmic regenerative electrochemistry. J Phys Chem B 102: 2536–2545

116. Licht S, Khaselev O, Ramakrishnan PA, Soga T, Umeno M (1998) Multiple-bandgap photoelectrochemistry: Inverted semiconductor ohmic regenerative electrochemistry. J Phys Chem B 102: 2546–2554

117. Licht S, Khaselev O, Soga T, Umeno M (1998) Multiple bandgap photoelectrochemistry: Energetic configurations for solar energy conversion. Electrochem Solid State Lett 1: 20–23

118. Licht S, Wang B, Soga T, Umeno M (1999) Light invariant, efficient, multiple band gap AlGaAs/Si/metal hydride solar cell. Appl Phys Lett 74: 4055–4057

119. Williams R (1967) Chemistry and electrical properties of the interface between ZnSe and an electrolyte. J Electrochem Soc 114: 1173–1179

120. Lemasson P, Etcheberry A, Gautron J (1982) Analysis of photocurrents at the semiconductor-electrolyte junction. Electrochim Acta 27: 607–614

121. Gautron J, Lemasson P, Rabago P, Triboulet R (1979) Electrochemical behavior of an aqueous electrolyte/I-doped ZnSe junction in the dark and under illumination. J Electrochem Soc 126: 1868–1875

122. P. Lemasson and J. Gautron (1981) On the anodic decomposition of the zinc selenide electrode. J Electroanal Chem 119: 289–299

123. Gautron J, Dalbera JP, Lemasson P (1980) Electroluminescence of the electrolyte/n-ZnSe junction under anodic polarization. Surf Sci 99: 300–308

124. Smiley M, Biagioni RN, Ellis AB (1984) Zinc selenide photoelectrodes. J Electrochem Soc 131: 1068–1073

125. Gautron J, Lemasson P (1982) Photoelectrochemical determination of minority carrier diffusion length in II-VI compounds. J Cryst Growth 59: 332–337

126. Lemasson P, Boutry AF, Triboulet R (1984) The semiconductor-electrolyte junction: Physical parameters determination by photocurrent measurement throughout the $Cd_{1-x}Zn_xTe$ alloy series. J Appl Phys 55: 592–594

127. Fan FRF, Bard AJ (1985) Semiconductor Electrodes. 58. The effect of temperature on photo- and electroluminescence in Al-doped self-activated ZnS crystals. J Phys Chem 89: 1232–1236

128. Ouyang J, Fan FRF, Bard AJ (1989) Semiconductor Electrodes, 62. Photoluminescence and electroluminescence from manganese-doped ZnS and CVD ZnS electrodes. J Electrochem Soc 136: 1033–1039

129. Rajeshwar K (1985) Materials aspects of photoelectrochemical energy conversion. J Appl Electrochem 15: 1–22

130. Tributsch H (1978) Hole reactions from d-energy bands of layer type group VI transition metal dichalcogenides: New perspectives for electrochemical solar energy conversion. J Electrochem Soc 125: 1086–1093

131. Tributsch H, Bennett JC (1977) Electrochemistry and photochemistry of $MoS_2$ layer crystals. I. J Electroanal Chem 81: 97–111

132. Tributsch H (1981) Photoelectrochemistry of layer-type zirconium disulfide. J Electrochem Soc 128: 1261–1269

133. Abramovich M, Tributsch H (1982) Photoelectrochemistry of $HfSe_2$ involving two conduction bands. J Electroanal Chem 138: 121–129

134. Gobrecht J, Tributsch H, Gerischer H (1978) Performance of synthetical n-$MoSe_2$ in electrochemical solar cells. J Electrochem Soc 125: 2085–2086

135. Menezes S, DiSalvo FJ, Miller B (1980) Photoelectrochemical compatibility of n-$WSe_2$ and n-$MoSe_2$ with various redox systems. J Electrochem Soc 127: 1751–1758

136. Kubiak CP, Schneemeyer LF, Wrighton MS (1980) Visible light driven generation of chlorine and bromine. Photooxidation of chloride and bromide in aqueous solution at illuminated n-type semiconducting molybdenum diselenide and molybdenum disulfide electrodes. J Am Chem Soc 102: 6898–6900

137. Schneemeyer LF, Wrighton MS (1979) Flat-band potential of n-type semiconducting molybdenum disulfide by cyclic voltammetry of two-electron reductants: Interface energetics and the sustained photooxidation of chloride. J Am Chem Soc 101: 6496–6500

138. Schneemeyer LF, Wrighton MS (1980) n-Type molybdenum diselenide-based photoelectrochemical cells: Evidence for Fermi level pinning and comparison of the efficiency for conversion of light to electricity with various solvent/halogen/halide combinations. J Am Chem Soc 102: 6964–6971

139. Fornarini L, Nozik AJ, Parkinson BA (1984) The energetics of p/n photoelectrolysis cells. J Phys Chem 88: 3238–3243

140. Fan FF, Bard AJ (1981) Semiconductor electrodes XXXVI. Characteristics of n-$MoSe_2$, n- and p-$WSe_2$ electrodes in aqueous solution. J Electrochem Soc 128: 945–952

141. Abruna HD, Hope GA, Bard AJ (1982) Semiconductor electrodes XLV. Photoelectrochemistry of n- and p-Type $MoTe_2$ in aqueous solutions. J Electrochem Soc 129: 2224–2228

142. Koval CA, Olson JB (1988) Simultaneous determination of interfacial energetics and kinetic currents at the $WSe_2$/acetonitrile interface. J Phys Chem 92: 6726–6732

143. Huang J, Wrighton MS (1994) Flat band potential measurements of naked and viologen-modified n-$WS_2$ electrodes in aqueous iodide and triiodide solutions. J Phys Chem 98: 9097–9101

144. Marzik JV, Kershaw R, Dwight K, Wold A (1984) Photoelectronic properties of $ReS_2$ and $ReSe_2$ single crystals. J Solid State Chem 51: 170–175

145. Wheeler BL, Leland JK, Bard AJ (1986) Semiconductor Electrodes LX. Photoelectrochemistry of p-$ReS_2$ and p-$ReSe_2$ in aqueous solutions. J Electrochem Soc 133: 358–361

146. Schwarz DE, Frenkel AI, Nuzzo RG, Rauchfuss TB, Vairavamurthy A (2004) Electrosynthesis of $ReS_4$. XAS analysis of $ReS_2$, $Re_2S_7$, and $ReS_4$. Chem Mater 16: 151–158

147. Escalona N, Gil Llambias FJ, Vrinat M, Nguyen TS, Laurenti D, López Agudo A (2007) Highly active $ReS_2/\gamma$-$Al_2O_3$ catalysts: Effect of calcination and activation over thiophene hydrodesulfurization. Catal Commun 8: 285–288

148. Byvik CE, Reichman B, Coleman DW (1982) Photoelectrochemical response of some layered chalcogenophosphate compounds ($MPX_3$). J Electrochem Soc 129: 237–238

149. Aruchamy A, Berger H, Levy F (1988) Photoelectronic properties of the p-type layered trichalcogenophosphates $FePS_3$ and $FePSe_3$. J Solid State Chem 72: 316–323

150. Chandra S, Singh DP, Srivastava PC, Sahu SN (1984) Electrodeposited semiconducting molybdenum selenide films: II. Optical, electrical, electrochemical and photoelectrochemical solar cell studies. J Phys D: Appl Phys 17: 2125–2138

151. Gobrecht J, Gerischer H, Tributsch H (1978) Electrochemical solar cell based on the d-band semiconductor tungsten-diselenide. Ber Bunsenges Phys Chem 82: 1331–1335

152. Kline G, Kam K, Canfield D, Parkinson BA (1981) Efficient and stable photoelectrochemical cells constructed with $WSe_2$ and $MoSe_2$ photoanodes. Sol Energy Mater 4: 301–308

153. Lewerenz HJ, Heller A, DiSalvo FJ (1980) Relationship between surface morphology and solar conversion efficiency of $WSe_2$ photoanodes. J Am Chem Soc 102: 1877–1880

154. Lewerenz HJ, Ferris SD, Doherty CJ, Leamy HJ (1982) Charge collection microscopy on p-$WSe_2$: Recombination sites and minority carrier diffusion length. J Electrochem Soc 129: 418–423

155. Tenne R, Wold A (1985) Passivation of recombination centers in n-$WSe_2$ yields high efficiency (>14%) photoelectrochemical cell. Appl Phys Lett 47: 707–709

156. Chaparro AM, Salvador P, Peter LM (1995) The role of surface defects in the photooxidation of iodide at n-$MoSe_2$: evidence for a local "autocatalytic" effect. J Phys Chem 99: 6677–6683

157. Salvador P, Chaparro AM, Mir A (1996) Digital imaging of the effect of photoetching on the photoresponse of n-type tungsten diselenide and molybdenum diselenide single crystal electrodes. J Phys Chem 100: 760–768

158. Chaparro AM, Salvador P, Mir A (1996) The scanning microscope for semiconductor characterization (SMSC): Study of the influence of surface morphology on the photoelectrochemical behavior of an n-$MoSe_2$ single crystal electrode by photocurrent and electrolyte electroreflectance imaging. J Electroanal Chem 418: 175–183

159. Ennaoui A, Fiechter S, Pettenkofer N, Alonso-Vante N, Büker K, Bronold M, Höpfner C, Tributsch H (1993) Iron disulfide for solar energy conversion. Sol Energy Mater Sol Cells 29: 289–370

160. Lalvani SB, Shami M (1986) Electrochemical oxidation of pyrite slurries. J Electrochem Soc 133: 1364–1368

161. Lowson RT (1982) Aqueous oxidation of pyrite by molecular oxygen. Chem Rev 82: 461–497

162. Meyer RE (1979) Electrochemistry of $FeS_2$. J Electroanal Chem 101: 59–71

163. Ennaoui A, Fiechter S, Jaegermann W, Tributsch H (1986) Photoelectrochemistry of highly quantum efficient single-crystalline n-$FeS_2$ (pyrite). J Electrochem Soc 133: 97–106

164. Aricó AS, Antonucci V, Giordano N, Crea F, Antonucci PL (1991) Photoelectrochemical behavior of thermally activated natural pyrite-based photoelectrodes. Mater Chem Phys 28: 75–87

165. Antonucci V, Aricò AS, Giordano N, Antonucci PL, Russo U, Cocke DL, Crea F (1991) Photoactive screen-printed pyrite anodes for electrochemical photovoltaic cells. Sol Cells 31: 119–141

166. Alonso-Vante N, Chatzitheodorou G, Fiechter S, Mgoduka N, Poulios I, Tributsch H (1988) Interfacial behavior of hydrogen-treated sulphur deficient pyrite ($FeS_{2-x}$). Sol Energy Mater 18: 9–21

167. Ennaoui A, Fiechter S, Goslowsky H, Tributsch H (1985) Photoactive synthetic polycrystalline pyrite ($FeS_2$). J Electrochem Soc 132: 1579–1582

168. Aricò AS, Antonucci V, Antonucci PL, Cocke DL, Russo U, Giordano N (1990) Photoeffects at the polycrystalline pyrrhotite-electrolyte interface. Sol Energy Mater 20: 323–340

169. Folmer JC, Turner JA, Noufi R, Cahen D (1985) Structural and solar conversion characteristics of the $(Cu_2Se)_x(In_2Se_3)_{1-x}$ system. J Electrochem 132: 1319–1327

170. Robbins M, Bachmann KJ, Lambrecht VG, Thiel FA, Thomson J Jr., Vadimsky RG, Menezes S, Heller A, Miller B (1978) CuInS$_2$ liquid junction solar cells. J Electrochem Soc 125: 831–832

171. Mirovsky Y, Cahen D (1982) n-CuInSe$_2$/polysulfide photoelectrochemical solar cells. Appl Phys Lett 40: 727–728

172. Mirovsky Y, Tenne R, Cahen D, Sawatzky G, Polak M (1985) Ternary chalcogenide-based photoelectrochemical cells V. Surface Analyses of the CuInX$_2$/aqueous polysulfide interface (X = S, Se) by X-ray photoelectron spectroscopy; Absence of Se/S exchange in the CuInSe$_2$/S$_n$= system. J Electrochem Soc 132: 1070–1076

173. Cahen D, Mirovsky Y (1985) Ternary Chalcogenide-Based Photoelectrochemical cells. 6. Is There a Thermodynamic Explanation for the Output Stability of CuInS$_2$ and CuInSe$_2$ Photoanodes? J Phys Chem 89: 2818–2827

174. Menezes S, Lewerenz HJ (1984) Heterojunction by photoelectrochemical surface transformation: n-CuInSe$_2$/p-CuSe$_3$Se$^o$. J Electrochem Soc 131: 2462–2463

175. Menezes S (1984) 12% solar conversion efficiency by interface restructuring. Appl Phys Lett 45: 148–149

176. Djellal L, Bouguelia A, Kadi-Hanifi M, Trari M (2008) Bulk p-CuInSe$_2$ photoelectrochemical solar cells. Sol Energy Mater Sol Cells 92: 594–600

177. Bicelli LP (1988) Thermodynamic stability of n-AgInSe$_2$ in photoelectrochemical cells. J Phys Chem 92: 6991–6997

178. Becker RS, Zhou GD, Elton J (1986) Preparation and photoelectrochemistry of p-HgIn$_2$Te$_4$ and p- and n- CdIn$_2$Te$_4$. J Phys Chem 90: 5866–5870

179. Tell B, Wagner S, Kasper HM (1977) Ionic conduction in ternary chalcogenides. J Electrochem Soc 124: 536–537

180. McCann JF, Pezy J (1981) The measurement of the flatband potentials of n-type and p-type semiconductors by rectified alternating photocurrent voltammetry. J Electrochem Soc 128: 1735–1740

181. Levy-Clement C, Le Nagard N, Gorochov O, Chevy A (1984) Photoelectrochemistry of lamellar n- and p-type InSe in aqueous solution. J Electrochem Soc 131: 790–796

182. Tenne R, Theys B, Rioux J, Clement CL (1985) Improved performance of InSe-based photoelectrochemical cells by means of a selective (photoelectrochemical) etching. J Appl Phys 57: 141–145

183. Uosaki K, Kaneko S, Kita H, Chevy A (1986) Electrochemical behavior of p-type indium selenide single crystal electrodes in dark and under illumination. Bull Chem Soc Jpn 59: 599–605

184. Etman M, Katty A, Levy-Clement C, Lemasson P (1982) Photoelectrochemical study of the layered compound In$_{2/3}$PSe$_3$. Mater Res Bull 17: 579–584

185. Singh K, Rashid Tanveer MD (1995) Photoelectrochemical and impedance spectral studies on electrodeposited (CdGa)Se films. Sol Energy Mater Sol Cells 36: 409–420

186. Gujar TP, Shinde VR, Park JW, Lee HK, Jung KD, Joo OS (2008) Electrodeposition of photoactive 1D gallium selenide quantum dots. Electrochim Acta 54: 829–834

187. Bube RH, McCarroll WH (1959) Photoconductivity in indium sulfide powders and crystals. J Phys Chem Solids 10: 333–335

188. Rehwald W, Harbeke G (1965) On the conduction mechanism in single crystal β-indium sulfide $In_2S_3$. J Phys Chem Solids 26: 1309–1318

189. Becker RS, Zheng T, Elton J, Saeki M (1986) Synthesis and photoelectrochemistry of $In_2S_3$. Sol Energy Mater 13: 97–107

190. Bicelli LP (1987) Thermodynamic stability of n-$In_2S_3$ photoelectrodes. Electrochim Acta 32: 777–783

191. Herrero J, Ortega J (1988) n-Type $In_2S_3$ thin films prepared by gas chalcogenization of metallic electroplated indium: Photoelectrochemical characterization. Sol Energy Mater 17: 357–368

192. Herrasti P, Fatas E, Herrero J, Ortega J (1990) Determination of the flat band potential for $In_2S_3$/electrolyte interfaces. Electrochim Acta 35: 345–349

193. Kamat PV, Dimitrijević NM, Fessenden RW (1988) Photoelectrochemistry in particulate systems. 7. Electron-transfer reactions of indium sulfide semiconductor colloids. J Phys Chem 92: 2324–2329

194. Katty A, Fotouhi B, Gorochov O (1984) Photoelectrochemical study of $SnS_2$ in aqueous solution. J Electrochem Soc 131: 2806–2810

195. Fotouhi B, Katty A, Parsons R, (1985) Current-voltage and capacitance-voltage characteristics of n-$SnS_2$ single crystals in aqueous solutions containing different redox reagents. J EIectroanal Chem 183: 303–314

196. Fotouhi B, Katty A, Gorochov O (1985) Photoelectrochemical and corrosion study of n-type SnSSe. J Electrochem Soc 132: 2181–2184

197. Hüsser OE, von Känel H, Lévy F (1985) Photoelectrochemistry of doped and undoped semiconductors: A comparison. J Electrochem Soc 132: 810–814

198. Mishra K, Rajeshwar K, Weiss A, Murley M, Engelken RD, Slayton M, McCloud HE (1989) Electrodeposition and characterization of SnS thin films J Electrochem Soc 136: 1915–1923

199. Richardson PE, Yoon R-H, Woods R, Buckley AN (1994) The photoelectrochemistry of galena. Int J Mineral Proc 41: 77–97

200. Richardson PE, O'Dell CS (1985) Semiconducting characteristics of galena electrodes. J Electrochem Soc 132: 1350–1356

201. Meincke H, Ebling DG, Heinze J, Tacke M, Böttner H (1998) Potentiostatic oxide formation on lead selenide single crystals in alkaline solutions. J Electrochem Soc 145: 2806–2812

202. Meincke H, Ebling DG, Heinze J, Tacke M, Böttner H (1999) A photoelectrochemical study of anodic oxides on lead selenide surfaces in alkaline solutions. Fresenius J Anal Chem 365: 147–149

203. Strehblow HH, Bettini M (1980) Electrochemical surface reactions on PbTe. J Electrochem Soc 127: 847–855

204. Chen S, Truax LA, Sommers JM (2000) Alkanethiolate-protected PbS nanoclusters: Synthesis, spectroscopic and electrochemical studies. Chem Mater 12: 3864–3870

205. Wehrenberg BL, Guyot-Sionnest P (2003) Electron and hole injection in PbSe quantum dot films. J Am Chem Soc 125: 7806–7807

206. Peter LM (1979) The photoelectrochemical properties of anodic $Bi_2S_3$ films. J Electroanal Chem 98: 49–58

207. Bard AJ (1979) Photoelectrochemistry and heterogeneous photocatalysis at semiconductors. J Photochem 10: 59–75

208. Kalyanasundaram K, Grätzel M, Pelizzetti E (1986) Interfacial electron transfer in colloidal metal and semiconductor dispersions and photodecomposition of water. Coord Chem Rev 69: 57–125

209. Mills A, Le Hunte S (1997) An overview of semiconductor photocatalysis. J Photochem Photobiol A 108: 1–35

210. Ohtani B, Kawaguchi J, Kozawa M, Nishimoto S, Inui T, Izawa K (1995) Photocatalytic racemization of amino acids in aqueous polycrystalline cadmium(II) sulfide dispersions. J Chem Soc Faraday Trans 91: 1103–1109

211. Henglein A (1989) Small-particle research: Physicochemical properties of extremely small colloidal metal and semiconductor particles. Chem Rev 89: 1861–1873

212. Kamat PV, Dimitrijević NM (1990) Colloidal semiconductors as photocatalysts for solar energy conversion. Sol Energy 44: 83–98

213. Becker WG, Bard AJ (1983) Photoluminescence and photoinduced oxygen adsorption of colloidal zinc sulfide dispersions. J Phys Chem 87: 4888–4893

214. Kamat PV, Dimitrijević NM, Fessenden RW (1987) Photoelectrochemistry in particulate systems. 6. Electron-transfer reactions of small cadmium sulfide colloids in acetonitrile. J Phys Chem 91: 396–401

215. Peterson MW, Nenadovic MT, Rajh T, Herak R, Micid OI, Goral JP, Nozik AJ (1988) Quantized colloids produced by dissolution of layered semiconductors in acetonitrile. J Phys Chem 92: 1400–1402

216. Kamat PV (1993) Photochemistry on nonreactive (semiconductor) surfaces. Chem Rev 93: 267–300

217. Ward MD, White JR, Bard AJ (1983) Electrochemical investigation of the energetics of particulate titanium dioxide photocatalysts. The methyl viologen-acetate system. J Am Chem Soc 105: 27–31

218. White JR, Bard AJ (1985) Electrochemical investigation of photocatalysis at CdS suspensions in the presence of methylviologen. J Phys Chem 89: 1947–1954

219. Frank SN, Bard AJ (1977) Heterogeneous photocatalytic oxidation of cyanide and sulfite in aqueous solutions at semiconductor powders. J Phys Chem 81: 1484–1488

220. Duonghung D, Ramsden J, Grätzel M (1982) Dynamics of interfacial electron-transfer processes in colloidal semiconductor systems. J Am Chem Soc 104: 2977–2985

221. Roy AM, De GC, Sasmal N, Bhattacharyya SS (1995) Determination of the flatband potential of semiconductor particles in suspension by photovoltage measurement. J Hydrogen Energy 20: 627–630

222. Dimitrijević NM, Kamat PV (1987) Transient photobleaching of small CdSe colloids in acetonitrile. anodic decomposition. J Phys Chem 91: 2096–2099

223. Baral S, Fojtik A, Weller H, Henglein A (1986) Photochemistry and radiation chemistry of colloidal semiconductors. 12. Intermediates of the oxidation of extremely small particles of cadmium sulfide, zinc sulfide, and tricadmium diphosphide and size quantization effects (a pulse radiolysis study). J Am Chem Soc 108: 375–378

224. Katsikas L, Eychmüller A, Giersig M, Weller H (1990) Discrete excitonic transitions in quantum-sized CdS particles. Chem Phys Lett 172: 201–204

225. Parsapour F, Kelley DF, Williams RS (1998) Spectroscopy of $Eu^{3+}$-doped $PtS_2$ nanoclusters. J Phys Chem B 102: 7971–7977

226. Rossetti R, Nakahara S, Brus LE (1983) Quantum size effects in the redox potentials, resonance Raman spectra, and electronic spectra of CdS crystallites in aqueous solutions. J Chem Phys 79: 1086–1088

227. Brus LE (1983) A simple model for the ionization potential, electron affinity, and aqueous redox potentials of small semiconductor crystallites. J Chem Phys 79: 5566–5571

228. Brus LE (1984) Electron-electron and electron-hole interactions in small semiconductor crystallites: The size dependence of the lowest excited electronic state. J Chem Phys 80: 4403–4409

229. Rossetti R, Ellison JL, Gibson JM, Brus LE (1984) Size effects in the excited electronic states of small colloidal CdS crystallites J Chem Phys 80: 4464–4469

230. Haram SK, Quinn BM, Bard AJ (2001) Electrochemistry of CdS nanoparticles: A correlation between optical and electrochemical band gaps. J Am Chem Soc 123: 8860–8861

231. Kamat PV, Dimitrijević NM, Fessenden RW (1987) Photoelectrochemistry in particulate systems. 6. Electron-transfer reactions of small cadmium sulfide colloids in acetonitrile. J Phys Chem 91: 396–401

232. Spanhel L, Haase M, Weller H, Henglein A (1987) Photochemistry of colloidal semiconductors. 20. Surface modification and stability of strong luminescing CdS particles. J Am Chem Soc 109: 5649–5655

233. Hines MA, Guyot-Sionnest P (1996) Synthesis and characterization of strongly luminescing ZnS-capped CdSe nanocrystals. J Phys Chem 100: 468–471

234. Kim S, Fisher B, Eisler HJ, Bawendi M (2003) Type-II Quantum Dots: CdTe/CdSe (core/shell) and CdSe/ZnTe(core/shell) heterostructures. J Am Chem Soc 125: 11466–11467

235. Aharoni A, Mokari T, Popov I, Banin U (2006) Synthesis of InAs/CdSe/ZnSe core/shell1/shell2 structures with bright and stable near-infrared fluorescence. J Am Chem Soc 128: 257–264

236. Goebl JA, Black RW, Puthussery J, Giblin J, Kosel TH, Kuno M (2008) Solution-based II-VI core/shell nanowire heterostructures. J Am Chem Soc 130: 14822–14833

237. Hoffmann MR, Martin ST, Choi W, Bahnemann DW (1995) Environmental applications of semiconductor photocatalysis. Chem Rev 95: 69–96

238. Bahnemann D (2004) Photocatalytic water treatment: solar energy applications. Sol Energy 77: 445–459

239. Benniston AC, Harriman A (2008) Artificial photosynthesis. Materials Today 11: 26–34

240. Inoue T, Fujishima A, Konishi S, Honda K (1979) Photoelectrocatalytic reduction of carbon dioxide in aqueous suspensions of semiconductor powders. Nature 277: 637–638

241. Halmann M (1978) Photoelectrochemical reduction of aqueous carbon dioxide on p-type gallium phosphide in liquid junction solar cells. Nature 275: 115–116

242. Heminger JC, Carr R, Somorjai GA (1987) The photoassisted reaction of gaseous water and carbon dioxide adsorbed on the $SrTiO_3$ (111) crystal face to form methane. Chem Phys Lett 57: 100–104

243. Taniguchi I, Aurian-Blajeni B, Bockris O'MJ (1983) Photo-aided reduction of carbon dioxide to carbon monoxide. J Electroanal Chem 157: 179–182

244. Taniguchi I, Aurian-Blajeni B, Bockris O'MJ (1984) The reduction of carbon dioxide at illuminated p-type semiconductor electrodes in nonaqueous media. Electrochim Acta 29: 923–932

245. Bockris O'MJ, Wass JC (1989) The photoelectrocatalytic reduction of carbon dioxide. J Electrochem Soc 136: 2521–2528

246. Aliwi SM, Al-Jubori KF (1989) Photoreduction of $CO_2$ by metal sulphide semiconductors. Sol Energy Mater 18: 223–229

247. Kuwabata S, Nishida K, Tsuda R, Inoue H, Yoneyama H (1994) Photochemical reduction of carbon dioxide to methanol using ZnS microcrystallite as a photocatalyst in the presence of methanol dehydrogenase. J Electrochem Soc 141: 1498–1503

248. Nedoluzhko AI, Shumilin IA, Nikandrov VV (1996) Coupled action of cadmium metal and hydrogenase in formate photodecomposition sensitized by CdS. J Phys Chem 100: 17544–17550

249. Fujishima A, Honda K (1972) Electrochemical photolysis of water at a semiconductor electrode. Nature 238: 37–38

250. Wrighton MS, Ellis AB, Wolczanski PT, Morse DL, Abrahamson HB, Ginley DS (1976) Strontium titanate photoelectrodes. Efficient photoassisted electrolysis of water at zero Applied Potential. J Am Chem Soc 98: 2774–2779

251. Mavroides JG, Tchernev DI, Kafalas JA, Kolesar DF (1975) Photoelectrolysis of water in cells with $TiO_2$ anodes. Mater Res Bull 10: 1023–1030

252. Ohashi K, Uosaki K, Bockris JO'M (1977) Cathodes for photodriven hydrogen generators: ZnTe and CdTe. Energy Res 1: 25–30

253. Bockris JO'M, Uosaki K (1977) The rate of the photoelectrochemical generation of hydrogen at p-type semiconductors. J Electrochem Soc 124: 1348–1355

254. Ohashi K, McCann J, Bockris JO'M (1977) Stable photoelectrochemical cells for the splitting of water. Nature 266: 610–611

255. Levy-Clement C, Heller A, Bonner WA, Parkinson BA (1982) Spontaneous photo-electrolysis of HBr and HI. J Electrochem Soc 129: 1701–1705

256. Tien HT, Chen JW (1989) Hydrogen generation from artificial sea water in a semiconductor septum electrochemical photovoltaic cell. Photochem Photobiol 49: 527–530

257. Tien HT, Chen JW (1990) Hydrogen production from water by semiconductor septum electrochemical photovoltaic cell using visible light. Int J Hydrogen Energy 15: 563–568

258. Bard AJ, Mallouk TE (1993) On septum-based photoelectrochemical cells. J Phys Chem 97: 7127–7128

259. Pandey RN, Misra M, Srivastava ON (1998) Solar hydrogen production using semiconductor septum (n-CdSe/Ti and n-TiO$_2$/Ti) electrode based photoelectrochemical solar cells. Int J Hydrogen Energy 23: 861–865

260. Chandra Babu KS, Pandey RN, Srivastava ON (1995) Photoelectrochemical semiconductor septum (CdSe/Ti and TiO$_2$/Ti) solar cells in relation to hydrogen production. Int J Hydrogen Energy 20: 771–775

261. Rajpure KY, Bhosale CH (2000) Sb$_2$S$_3$ semiconductor-septum rechargeable storage cell. Mater Chem Phys 64: 70–74

262. Pawar SM, Moholkar AV, Rajpure KY, Kim JH, Lokhande CD, Bhosale CH (2009) Fabrication of Fe:CdSe solar rechargeable (semiconductor–septum) storage cells. Curr Appl Phys 9: 1122–1124

263. Tributsch H (2008) Photovoltaic hydrogen generation. Int J Hydrogen Energy 33: 5911–5930

264. Getoff N (1990) Photoelectrochemical and photocatalytic methods of hydrogen production: A short review. Int J Hydrogen Energy 15: 407–417

265. Ashokkumar M (1998) An overview on semiconductor particulate systems for photoproduction of hydrogen. Int J Hydrogen Energy 23: 427–438

266. Rajeshwar K (2007) Hydrogen generation at irradiated oxide semiconductor–solution interfaces. J Appl Electrochem 37: 765–787

267. Dominey RN, Lewis NS, Bruce JA, Bookbinder DC, Wrighton MS (1982) Improvement of photoelectrochemical hydrogen generation by surface modification of p-type silicon semiconductor photo-cathodes. J Am Chem Soc 104: 467–482

268. Nakato K, Takabayashi S, Imanishi A, Murakoshi K, Nakato Y (2004) Stabilization of n-Si electrodes by surface alkylation and metal nano-dot coating for use in efficient photoelectrochemical solar cells. Sol Energy Mater Sol Cells 83: 323–330

269. Bard AJ, Fox MA (1995) Artificial photosynthesis: solar splitting of water to hydrogen and oxygen. Acc Chem Res 28: 141–145

270. Murphy AB, Barnes PRF, Randeniya LK, Plumb IC, Grey IE, Horne MD, Glasscock JA (2006) Efficiency of solar water splitting using semiconductor electrodes. Int J Hydrogen Energy 31: 1999–2017

271. Kalyanasundaram K, Borgarello E, Grätzel M (1981) Visible light induced water cleavage in CdS dispersions loaded with Pt and RuO$_2$. Hole scavenging by RuO$_2$. Helv Chim Acta 64: 362–366

272. Kalyanasundaram K, Borgarello E, Duonghong D, Grätzel M (1981) Cleavage of water by visible-light irradiation of colloidal CdS solutions: Inhibition of photocorrosion by RuO$_2$. Angew Chem Int Ed 20: 987–988

273. Mau AWH, Huang CB, Kakuta N, Bard AJ, Campion A, Fox MA, White JM, Webber SE (1984) Hydrogen photoproduction by Nafion/cadmium sulfide/platinum films in water/sulfide ion solutions. J Am Chem Soc 106: 6537–6542

274. Bühler N, Meier K, Reber JF (1984) Photochemical hydrogen production with cadmium sulfide suspensions. J Phys Chem 88: 3261–3268

275. Reber JF, Rusek M (1986) Photochemical hydrogen production with platinized suspensions of cadmium sulfide and cadmium zinc sulfide modified by silver sulfide. J Phys Chem 90: 824–834

276. Kakuta N, Park KH, Finlayson MF, Ueno A, Bard AJ, Campion A, Fox MA, Webber SE, White JM (1985) Photoassisted hydrogen production using visible light and coprecipitated ZnS-CdS without a noble metal. J Phys Chem 89: 732–734

277. Sobczynski A, Bard AJ, Campion A, Fox MA, Mallouk T, Webber SE, White JM (1987) Photoassisted hydrogen generation: platinum and cadmium sulfide supported on separate particles. J Phys Chem 91: 3316–3320

278. Savinov EN, Gruzdkov YA, Parmon VN (1989) Suspensions of semiconductors with micro-heterojunctions — A new type of highly efficient photocatalyst for dihydrogen production from solution of hydrogen sulfide and sulfide ions. Int J Hydrogen Energy 14: 1–9

279. Kaneko M, Okada T, Teratani S, Taya K (1987) Visible light cleavage of water by CdS photoanode coated with polymer-pendant $Ru(bpy)_3^{2+}$ film containing $RuO_2$ dispersions. Electrochim Acta 32: 1405–1407

280. Sabaté J, Cervera-March S, Simarro R, Giménez J (1990) A comparative study of semi-conductor photocatalysts for hydrogen production by visible light using different sacrificial substrates in aqueous media. Int J Hydrogen Energy 15: 115–124

281. Borrell L, Cervera-March S, Giménez J, Simarro R, Andújar JM (1992) A comparative study of CdS-based semiconductor photocatalysts for solar hydrogen production from sulphide + sulphite substrates. Sol Energy Mater Sol Cells 25: 25–39

282. Sathish M, Viswanathan B, Viwanath RP (2006) Alternate synthetic strategy for the preparation of CdS nanoparticles and its exploitation for water splitting. Int J Hydrogen Energy 31: 891–898

283. Pal B, Torimoto T, Iwasaki K, Shibayama T, Takahashi H, Ohtani B (2004) Size and structure-dependent photocatalytic activity of jingle-bell-shaped silica-coated cadmium sulfide nanoparticles for methanol dehydrogenation. J Phys Chem B 108: 18670–18674

284. Vučemilović MI, Vukelić N, Rajh T (1988) Solubility and photocorrosion of small CdS particles. J Photochem Photobiol 42: 157–167

285. Rufus IB, Viswanathan B, Ramakrishnan V, Kuriacose JC (1995) Cadmium sulfide with iridium sulfide and platinum sulfide deposits as a photocatalyst for the decomposition of aqueous sulfide. J Photochem Photobiol A 91: 63–66

286. Navarro RM, Valle F, Fierro JLG (2008) Photocatalytic hydrogen evolution from CdS–ZnO–CdO systems under visible light irradiation: Effect of thermal treatment and presence of Pt and Ru cocatalysts. Int J Hydrogen Energy 33: 4265–4273

287. Kudo A, Tsuji I, Kato H (2002) $AgInZn_7S_9$ solid solution photocatalyst for $H_2$ evolution from aqueous solution sunder visible light irradiation. Chem Commun 17: 1958–1959

288. Tsuji I, Kato H, Kobayashi H, Kudo A (2004) Photocatalytic $H_2$ evolution reaction from aqueous solutions over band structure-controlled $(AgIn)_xZn_{2(1-x)}S_2$ solid solution photocatalysts with visible-light response and their surface nanostructures. J Am Chem Soc 126: 13406–13413

289. Jang JS, Huang DW, Lee JS (2007) $CdS$–$AgGaS_2$ photocatalytic diodes for hydrogen production from aqueous $Na_2S$/$Na_2SO_3$ electrolyte solution under visible light ($\lambda \geq 420$ nm). Catal Today 120: 174–181

290. Sakai N, Ebina Y, Takada K, Sasaki T (2004) Electronic band structure of titania semi-conductor nanosheets revealed by electrochemical and photoelectrochemical studies. J Am Chem Soc 126: 5851–5858

291. Yamada S, Nosaka AY, Nosaka Y (2005) Fabrication of CdS photoelectrodes coated with titania nanosheets for water splitting with visible light. J Electroanal Chem 585: 105–112

292. Unal U, Matsumoto Y, Tanaka N, Kimura Y, Tamoto N (2003) Electrostatic self-assembly deposition of Titanate(IV) layered oxides intercalated with transition metal complexes and their electrochemical properties. J Phys Chem B 107: 12680–12689

293. Alonso Vante N, Jaegermann W, Tributsch H, Hoenle W, Yvon K (1987) Electrocatalysis of oxygen reduction by chalcogenides containing mixed transition metal clusters. J Am Chem Soc 109: 3251–3257

294. Tributsch H (1985) Interfacial processes involving strong electronic interactions in solar energy conversion and storage. J Photochem 29: 89–113

295. Tributsch H, Gorochov O (1981) Photoelectrochemical reaction behaviour of platinum disulphide with water and reducing agents. Electrochim Acta 27: 215–221

296. Ennaoui A, Tributsch H (1986) Light-induced electron transfer and photoelectrocatalysis of chlorine evolution at $FeS_2$ electrodes. J Electroanal Chem 204: 185–195

297. Heindl R, Parsons R, Redon AM, Tributsch H, Vigneron J (1982) Photoelectrochemical behaviour of ruthenium disulphide electrodes in contact with aqueous electrolytes. Surf Sci 115: 91–103

298. Ezzaouia H, Heindl R, Parsons R, Tributsch H (1983) Visible light photo-oxidation of water with single-crystal $RuS_2$ electrodes. J Electroanal Chem 145: 279–292

299. Kühne HM, Tributsch H (1983) Oxygen evolution from water mediated by infrared light on iron doped $RuS_2$ electrodes. J Electrochem Soc 130: 1448–1450

300. Kühne HM, Tributsch H (1986) Energetics and dynamics of the interface of $RuS_2$ and implications for photoelectrolysis of water. J Electroanal Chem 201: 263–282

301. Kühne HM, Jaegermann W, Tributsch H (1984) The electronic band character of Ru dichalcogenides and its significance for the photoelectrolysis of water. Chem Phys Lett 112: 160–164

302. Huang YS, Chen YF (1988) Electronic-structure study of $RuS_2$. Phys Rev B 38: 7997–8002

303. Salvador P, Alonso-Vante N, Tributsch H (1998) Photoelectrocatalytic study of water oxidation at n-$RuS_2$ electrodes. J Electrochem Soc 145: 216–225

304. Byvik CE, Smith BT, Reichman B (1982) Layered transition metal thiophosphates ($MPX_3$) as photoelectrodes in photoelectrochemical cells. Sol Energy Mater 7: 213–223

305. Lincot D, Gomez Meier H, Kessler J, Vedel J, Dimmler B, Schock HW (1990) Photoelectrochemical study of p-type copper indium diselenide thin films for photovoltaic applications. Sol Energy Mater 20: 67–79

306. Djellal L, Omeiri S, Bouguelia A, Trari M (2009) Photoelectrochemical hydrogen-evolution over p-type chalcopyrite $CuInSe_2$. J Alloys Compd 476: 584–589

307. McEvoy AJ, Grätzel M (1994) Sensitization in photochemistry and photovoltaics. Sol Energy Mater Sol Cells 32: 221–227

308. Gerischer H, Michel-Beyerle ME, Rebentrost F, Tributsch H (1968) Sensitization of charge injection into semiconductors with large band gap. Electrochim Acta 13: 1509–1515

309. Gerischer H (1972) Electrochemical techniques for the study of photosensitization. Photochem Photobiol 16: 243–260

310. Tributsch H (1972) Reaction of excited chlorophyll molecules at electrodes and in photosynthesis. Photochem Photobiol 16: 261–269

311. Calvin M (1974) Solar Energy by Photosynthesis. Science 184: 375–381

312. O'Regan B, Grätzel M (1991) A low-cost, high-efficiency solar cell based on dye-sensitized colloidal $TiO_2$ films. Nature 353: 737–740

313. Grätzel M (1994) Nanocrystalline solar cells. Renew Energy 5: 118–133

314. Peter LM, Ponomarev EA, Franco G, Shaw NJ (1999) Aspects of the photoelectrochemistry of nanocrystalline systems. Electrochim Acta 45: 549–560; Peter L (2007) Transport, trapping and interfacial transfer of electrons in dye-sensitized nanocrystalline solar cells. J Electroanal Chem 599: 233–240

315. Matsumoto M, Miyazaki H, Matsuhiro K, Kumashiro Y, Takaoka Y (1996) A dye sensitized $TiO_2$ photoelectrochemical cell constructed with polymer solid electrolyte. Solid State Ionics 89: 263–267

316. Cao F, Oskam G, Searson PC (1995) A solid state, dye sensitized photoelectrochemical cell. J Phys Chem 99: 17071–17073

317. O'Regan B, Schwartz DT (1995) Efficient photo-hole injection from adsorbed cyanine dyes into electrodeposited copper(I) thiocyanate thin films p-type semiconductors. Chem Mater 7: 1349–1354

318. O'Regan B, Schwartz DT (1996) Efficient dye-sensitized charge separation in a wide-bandgap p-n heterojunction. J Appl Phys 80: 4749–4754

319. Bach U, Lupo D, Comte P, Moser JE, Weissörtel F, Salbeck J, Spreitzer H, Grätzel M (1998) Solid-state dye-sensitized mesoporous $TiO_2$ solar cells with high photon-to-electron conversion efficiencies. Nature 395: 583–585

320. Murakoshi K, Kogure R, Wada Y, Yanagida S (1998) Fabrication of solid-state dye-sensitized $TiO_2$ solar cells combined with polypyrrole. Sol Energy Mater Sol Cells 55: 113–125

321. Huynh WU, Dittmer JJ, Alivisatos AP (2002) Hybrid nanorod-polymer solar cells. Science 295: 2425–2427

322. Nozik AJ (2008) Multiple exciton generation in semiconductor quantum dots. Chem Phys Lett 457: 3–11

323. Gerischer H, Lübke M (1986) A particle size effect in the sensitization of $TiO_2$ electrodes by a CdS deposit. J Electroanal Chem 204: 225–227

324. Flood R, Enright B, Allen M, Barry S, Dalton A, Doyle H, Tynan D, Fitzmaurice D (1995) Determination of band edge energies for transparent nanocrystalline $TiO_2$–CdS sandwich electrodes prepared by electrodeposition. Sol Energy Mater Sol Cells 39: 83–98

325. Kohtani S, Kudo A, Sakata T (1993) Spectral sensitization of a $TiO_2$ semiconductor electrode by CdS microcrystals and its photoelectrochemical properties. Chem Phys Lett 206: 166–170

326. Spanhel L, Weller H, Henglein A (1987) Photochemistry of semiconductor colloids. 22. Electron injection from illuminated CdS into attached $TiO_2$ and ZnO particles. J Am Chem Soc 109: 6632–6635

327. Vogel R, Pohl K, Weller H (1990) Sensitization of highly porous, polycrystalline $TiO_2$ electrodes by quantum sized CdS. Chem Phys Lett 174: 241–246

328. Vogel R, Hoyer P, Weller H (1994) Quantum-sized PbS, CdS, $Ag_2S$, $Sb_2S_3$, and $Bi_2S_3$ particles as sensitizers for various nanoporous wide-bandgap semiconductors. J Phys Chem 98: 3183–3188

329. Hoyer P, Konenkamp R (1995) Photoconduction in porous $TiO_2$ sensitized by PbS quantum dots. Appl Phys Lett 66: 349–351

330. Hotchandani S, Kamat P (1992) Charge-transfer processes in coupled semiconductor systems. Photochemistry and photoelectrochemistry of the colloidal cadmium sulfide-zinc oxide system. J Phys Chem 96: 6834–6839

331. Nasr C, Hotchandani S, Kim WY, Schmehl RH, Kamat PV (1997) Photoelectrochemistry of composite semiconductor thin films. Photosensitization of $SnO_2$/CdS coupled nanocrystallites with a ruthenium polypyridyl complex. J Phys Chem B 101: 7480–7487

332. Liu D, Kamat P (1993) Photoelectrochemical behavior of thin cadmium selenide and coupled titania/cadmium selenide semiconductor films. J Phys Chem 97: 10769–10773

333. Nasr C, Kamat PV, Hotchandani S (1997) Photoelectrochemical behavior of coupled $SnO_2$/CdSe nanocrystalline semiconductor films. J Electroanal Chem 420: 201–207

334. Mane RS, Roh SJ, Joo O-S, Lokhande CD, Han S-H (2005) Improved performance of dense $TiO_2$/CdSe coupled thin films by low temperature process. Electrochim Acta 50: 2453–2459

335. Niitsoo O, Sarkar SK, Pejoux C, Rühle S, Cahen D, Hodes G (2006) Chemical bath deposited CdS/CdSe-sensitized porous $TiO_2$ solar cells. J Photoch Photobio A 181: 306–313

336. Toyoda T, Tsuboya I, Shen Q (2005) Effect of rutile-type content on nanostructured anatase-type $TiO_2$ electrode sensitized with CdSe quantum dots characterized with photoacoustic and photoelectrochemical current spectroscopies. Mater Sci Eng C 25: 853–857

337. Toyoda T, Kobayashi J, Shen Q (2008) Correlation between crystal growth and photosensitization of nanostructured $TiO_2$ electrodes using supporting Ti substrates by self-assembled CdSe quantum dots. Thin Solid Films 516: 2426–2431

338. Shen Q, Arae D, Toyoda T (2004) Photosensitization of nanostructured $TiO_2$ with CdSe quantum dots: effects of microstructure and electron transport in $TiO_2$ substrates. J Photoch Photobio A 164: 75–80

339. Krüger J, Bach U, Plass R, Cevey L, Piccirelli M, Grätzel M (2001) High efficiency solid-state photovoltaic device due to inhibition of interface charge recombination. Appl Phys Lett 79: 2085–2087

340. Plass R, Pelet S, Krueger J, Grätzel M, Bach U (2002) Quantum dot sensitization of organic-inorganic hybrid solar cells. J Phys Chem B 106: 7578–7580

341. Murray CB, Norris DJ, Bawendi MG (1993) Synthesis and characterization of nearly monodisperse CdE (E = sulfur, selenium, tellurium) semiconductor nanocrystallites. J Am Chem Soc 115: 8706–8715

342. Peng X, Wickham J, Alivisatos AP (1998) Kinetics of II-VI and III-V colloidal semiconductor nanocrystal growth: "Focusing" of size distributions. J Am Chem Soc 120: 5343–5344

343. Peng ZA, Peng XG (2001) Formation of high-quality CdTe, CdSe, and CdS nanocrystals using CdO as precursor. J Am Chem Soc 123: 183–184

344. Mann JR, Watson DF (2007) Adsorption of CdSe nanoparticles to thiolated $TiO_2$ surfaces: Influence of intralayer disulfide formation on CdSe surface coverage. Langmuir 23: 10924–10928

345. Hyun BR, Zhong YW, Bartnik AC, Sun L, Abruña AD, Wise FW, Goodreau JD, Matthews JR, Leslie TM, Borrelli NF (2008) Electron injection from colloidal PbS quantum dots into titanium dioxide nanoparticles. ACS Nano 2: 2206–2212

346. Peter LM, Riley DJ, Tull EJ, Wijayantha KGU (2002) Photosensitization of nanocrystalline $TiO_2$ by self-assembled layers of CdS quantum dots. Chem Commun 10: 1030–1031

347. Peter LM, Wijayantha KGU, Riley DJ, Waggett JP (2003) Band-Edge Tuning in Self-Assembled Layers of $Bi_2S_3$ Nanoparticles Used To Photosensitize Nanocrystalline $TiO_2$. J Phys Chem B 107: 8378–8381

348. Robel I, Subramanian V, Kuno M, Kamat PV (2006) Quantum dot solar cells. Harvesting light energy with CdSe nanocrystals molecularly linked to mesoscopic $TiO_2$ films. J Am Chem Soc 128: 2385–2393

349. Si H-Y, Sun Z-H, Zhang H-L (2008) Photoelectrochemical response from CdSe-sensitized anodic oxidation $TiO_2$ nanotubes. Colloids Surf A 313–314: 604–607

350. Peng ZA, Peng X (2001) Nearly monodisperse and shape-controlled CdSe nanocrystals via alternative routes: Nucleation and growth. J Am Chem Soc 124: 3343–3353

351. Kongkanand A, Tvrdy K, Takechi K, Kuno M, Kamat PV (2008) Quantum dot solar cells. Tuning photoresponse through size and shape control of CdSe-$TiO_2$ architecture. J Am Chem Soc 130: 4007–4015

# Chapter 6
# Electrochemical Processes and Technology

## 6.1 Oxygen Reduction Reaction – ORR

### 6.1.1 General

Electrode processes that involve the transfer of several electrons, usually accompanied by the breaking and creation of bonds, commonly proceed slowly or not at all in the absence of electrocatalysts, in contrast to most simple electrode processes that involve the transfer of a single electron without associated ion/atom transfer. Such complex electrode processes, an example of which is the reduction of molecular oxygen by a four-electron process to water or by a two-electron process to hydrogen peroxide (Chap. 2), often involve high-energy intermediates that must be stabilized by interactions with suitable molecules or complexes if the electrode reactions are to proceed at reasonable rates. These intermediate-stabilizing species are the electrocatalysts [1, 2]. In electrocatalysis, multifunctionality is obligatory: for obtaining high performance, some combination of surface reactivity, electronic and ionic conductivity, separation of electron–hole pairs, or facile mass transport of molecules must be provided to enhance the molecular conversion. Electrocatalyzed reactions range from synthetic (often using a molecular electron transfer reactant) and destructive (in which pollutants are detoxified or mineralized) to energy conversion (converting fuel and oxidant to electricity, as in fuel cells) [3]. Continuing interest in the electrochemical reduction of molecular oxygen in the fuel cell technology and for electrocatalytic oxidations in mild conditions is associated with a vital need for materials able to actively catalyze these processes.

The development of new electrocatalysts for fuel cells is a priority for materials' research. The *anodic reaction* in fuel cells is either the direct oxidation of hydrogen or the oxidation of methanol (excluding indirect oxidations via a reformating step). The *cathodic reaction* is usually oxygen reduction [4]. Already by the early 1960s it was realized that the principal difficulty of commercializing fuel cells would be the effectiveness of the *oxygen reduction reaction* (ORR), and that the way to solve this problem was electrocatalysis. Presently, the catalysis necessary to generate

electricity in fuel cells is analogous to bifunctional heterogeneous catalysis, in that catalytic particles are highly dispersed on a functional support such as electronically conductive carbon to achieve the desired rates of reaction. Platinum catalyst has been recognized as being the most effective toward ORR, especially in the low to medium temperature range acidic environments of proton exchange membrane (PEM) fuel cells and electrolyzers. Cathode electrodes based on dispersions of Pt nanoparticles in carbon are now in practical use for these applications.

However, in addition to the high cost of the metal, Pt-based cathodes in low-temperature fuel cells suffer from unfavorable overpotentials toward ORR, as well as poor methanol tolerance (in methanol fuel cells). Intensive research has been directed to the utilization of Pt-alloys or other noble metals of the Pt group (and their alloys) for cathodic electrocatalysis. Pt-based bimetallic alloys explored as electrocatalysts for reduction of oxygen (primarily $Pt_xCr_y$ or $Pt_xRu_y$) and oxidation of methanol (primarily $Pt_xRu_y$) have proved to be more active in both bulk and nanoparticulate form for the respective fuel cell reactions than is pure Pt. Marković and Ross [5] have presented an extensive discussion on electrocatalysis for fuel cells regarding pure Pt and Pt-based bimetallic alloy electrocatalysts, studying model systems by surface spectroscopy techniques. Note that the goals posed by the US Department of Energy for 2010 require electrocatalysts for ORR that are stable during 5,000 h of operation and use 0.2 g of precious metal per rated kW of power.

Perspectives for fabrication of improved oxygen electrodes at a low cost have been offered by non-noble, transition metal catalysts, although their intrinsic catalytic activity and stability are lower in comparison with those of Pt and Pt-alloys. The vast majority of these materials comprise (1) macrocyclic metal transition complexes of the $N_4$-type having Fe or Co as the central metal ion, i.e., porphyrins, phthalocyanines, and tetraazaannulenes [6–8]; (2) transition metal carbides, nitrides, and oxides (e.g., $FeC_x$, $TaO_xN_y$, $MnO_x$); and (3) transition metal chalcogenide cluster compounds based on Chevrel phases, and Ru-based cluster/amorphous systems that contain chalcogen elements, mostly selenium.

The above classes (1) and (2) are unlikely to meet the requirements of cathode catalysts in fuel cells in comparison to the state-of-the-art Pt-based catalysts. They show a low catalytic selectivity toward the four-electron reduction of oxygen to water, producing a large amount of $H_2O_2$ (typically higher than 10%), and exhibit very low electrochemical stability in acidic environments. For example, pyrochlore oxides although being extremely active in alkaline solution are not stable in acid; even in alkaline medium, slow dissolution of "B"-metal components of the oxide and their redeposition at the anode cause severe cumulative poisoning problems. In the case of metal–nitrogen chelate catalysts, $H_2O_2$ is responsible for the deterioration of electrode performance over time, as it destroys the active reaction sites by the oxidation of nitrogen ligands and hence accelerates the dissolution of transition metals. The promising catalytic properties of class (3) compounds, which show high catalytic activity and selectivity for oxygen reduction, will be the topic of the following section.

### *6.1.2 Pt-Free Chalcogenide Catalysts*

The transition metal chalcogenides known as Chevrel phases [9] have attracted much attention since the mid-1980s, with respect to their significant capacity for interfacial coordination chemistry favoring multielectron electrocatalysis. A Chevrel phase denotes a type of structure that is characterized by a central quasi-octahedral (or trigonal prismatic) metal cluster $M_6X_8$ (M = high-valent transition metal, usually Mo, and X = S, Se, Te), where the metal atoms are coordinated in a fcc cell with the respective chalcogenide atoms located at the periphery, forming a $M_6X_8$ pseudo-cube (Fig. 6.1); in this structure of "$M_6$" clusters, delocalization of electrons leads to high electron conductivity [10].

Chevrel-phase clusters including inserted guest atoms M in a composition $M_xMo_6X_8$ (i.e., M intercalated in the 3D channels running along the chains of weakly coupled $Mo_6X_8$ clusters), come under the heading of *ternary cluster materials*. In contrast, compounds of formula $M_xMo_{6-x}X_8$, where one or more Mo atoms in the binary $Mo_6X_8$ are replaced by other metals (such as Re, Ry, Rh), while the channels remain unoccupied, are named *pseudoternary clusters* [11].

In searching to identify stoichiometries which provide high interfacial electrochemical stability and active catalysis of ORR, considerable potential has been ascribed to pseudoternary Chevrel phases, such as those of $M_xMo_{6-x}X_8$ with M = Ru, Re, for example $Ru_2Mo_4Se_8$ and $Re_4Mo_2Se_8$. Capacity of such cluster materials in acid medium was first reported by Alonso-Vante and Tributsch [12, 13] who demonstrated that $Mo_{4.2}Ru_{1.8}Se_8$ (a p-type semiconductor with energy gap 1.3 eV, containing octahedra statistically composed of 4.2 molybdenum and 1.8 ruthenium atoms) could in principle compete with Pt as a catalyst in acid fuel cells at a considerable cost reduction. The catalytic activity of $Mo_{4.2}Ru_{1.8}Se_8$ was found
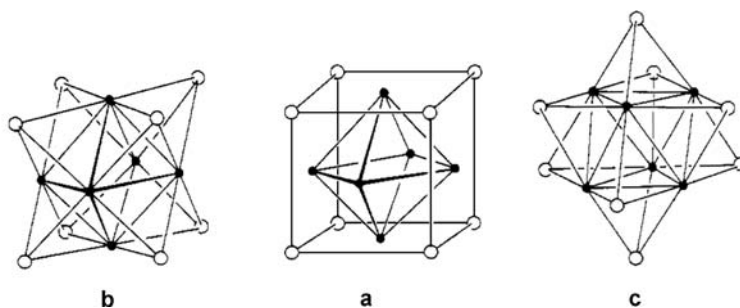


**Fig. 6.1**   The fundamental structural unit found in the Chevrel phases (cluster $Mo_6X_8$; *full circles*: Mo atoms) displayed in three ways to emphasize different views of the connectivity. In (**a**) an octahedron of molybdenums (Mo–Mo = 2.7 Å) is encased in a cube of chalcogens (Mo–S 2.45 or Mo–Se 2.6 Å). Scheme (**b**) exhibits the same cluster as consisting of an octahedron with its triangular faces capped by chalcogenides. In (**c**), the cluster has been reoriented so that a threefold axis is vertical. (Reproduced from [10])

to increase from samples containing non-substituted Mo octahedra showing metallic behavior to samples containing Ru-substituted Mo octahedra showing semiconducting behavior. Important features for the cluster moiety were considered to be its capacity (1) to act as a reservoir for electronic charge carriers while maintaining a stable electrochemical potential; (2) to provide neighboring binding sites for reactants and intermediates; and (3) to change its volume and bonding distances in the course of electron transfer.

Ensuing electrocatalytic studies on oxygen reduction and hydrogen evolution with Chevrel-type cluster compounds have indicated their remarkable catalytic nature. Oxygen reduction with these materials has been observed to occur directly to $H_2O$ in a four-electron process, owing to the coordination of oxygen to the transition metal complexes [14, 1] and bimetallic interactions giving rise to catalytic processes [15]. A limiting factor is the interfacial instability of the clusters prior to reaching the thermodynamic redox potential of the reaction to be catalyzed – a typical key problem in heterogeneous catalysis. Issues related to the chemical structure of the pseudoternary clusters and the catalytic centers of these complexes have been addressed widely, and conflicting opinions have been presented.

Notwithstanding their potential, one of the major downsides of the bimetallic pseudoternary cluster compounds lies in the fact that their synthesis is quite challenging and difficult to control. For example, Ru-based chalcogenides of the Chevrel-phase type are typically prepared by solid-state reaction of pure elements at elevated temperatures (1,200–1,700 °C) and pressures (0.7 GPa), which makes the synthesis procedure very complicated and costly. To circumvent this problem, low-temperature methodologies have been developed, involving either *thermolysis of metal carbonyls* or *colloid precipitation*. In effect, these methods were found to produce non-Chevrel phases, designated loosely as "amorphous phases," but some of these materials proved to be quite active toward ORR electrocatalysis in acid electrolyte. Gradually, the interest shifted to tailoring metal nanoparticles via surface modification with chalcogens as a means to influence their structure, electronic properties, and catalytic activity.

Alonso-Vante and co-workers [16] synthesized amorphous Mo–Ru–Se phases adsorbed on active carbons, by reacting metal carbonyls and selenium powder in xylene under refluxing conditions, at the boiling point of the solvent (140 °C) in an inert atmosphere. The produced compounds were initially thought to relate to Chevrel phases, but actually were not. Related studies on the Mo–Ru–S system [17] showed evidence for the formation of a stable $RuS_x$ phase together with an initially unstable $MoO_y$ phase. An approximate (non-Chevrel) composition $Mo_2Ru_5S_5$ was identified for the phase with the highest oxygen reduction activity. Thus, it was found that the reaction of carbonyl clusters with elemental chalcogen generates a variety of polynuclear compounds with *d*-state coordination centers. These polynuclear moieties are small enough to be considered as quasi-molecular metal clusters rather than metallic particles, and their catalytic properties are distinct from those of metallic particles.
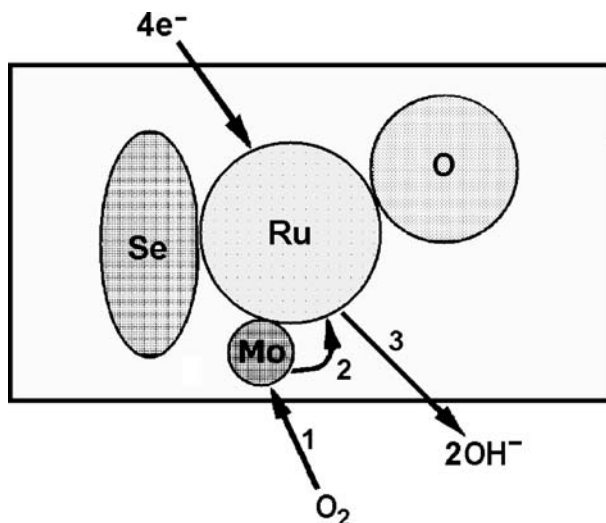
**Fig. 6.2**  Schematic representation of a Mo-containing ruthenium-clustered material. The indicated reaction paths represent (1) adsorption, (2) electrocatalysis, (3) desorption. (Adapted from [18])

Chemically prepared polynuclear Se-containing compounds of the type $(Ru_{1-x}Mo_x)_ySeO_z$, with stoichiometry corresponding to $0.02 < x < 0.04$, $1 < y < 3$ and $z \approx 2y$, were found to permit multielectron charge transfer affording effective oxygen reduction mostly via a four-electron transfer reaction to water (efficiency 96%) [18]. Compared to previous work with Mo–Ru electrocatalysts, the decrease of molybdenum content to a ratio in the range Mo:Ru = 1:25–50 was found to improve electrocatalytic properties by reducing the overpotential of the performed reaction. In this essentially Ru-cluster material, the low concentrated Mo was considered to act as an adsorption site for molecular oxygen (Fig. 6.2).

Reeve et al. [19] prepared a range of transition metal (Mo, Rh, W, Ru, Os, Re) sulfide electrocatalysts in high surface area form by direct chemical synthesis, consisting of refluxing the respective carbonyls together with sulfur and carbon black in xylene, onto various surface-functionalized carbon blacks, and tested them as fuel cell cathodes. Catalysts based on Re–Ru–S and Mo–Ru–S were found to give the best oxygen reduction activities. In addition, significant increases in performance were observed upon employing sulfur-functionalized carbon black, attributed to the preferential deposition of active Ru sites in the catalyst preparation process. In the case of the Mo–Ru–S catalyst, the electrochemical response was complicated by the oxidation and partial dissolution of Mo. Although the presence of a Mo-based oxidation reaction was observed to decrease the rest potential of the oxygenated system, the catalytic output increased due to the active nature of Mo in providing favorable oxygen adsorption sites. Analogous investigations have concerned

selenide compounds. The high catalytic activity of chemically synthesized carbon-supported Mo–Ru–Se cluster systems was found to reduce appreciably after heat treatment due to the loss of Se from the compound [20].

Polyaniline-modified, polynuclear Ru–Mo–Se catalysts were shown to have a good performance for ORR in acid media [21]. The so-called nanostructured $Ru_xMo_ySe_z$ compounds were prepared by thermolysis of their carbonyl compounds in organic solvents and were evaluated with respect to their catalytic activity, either directly on carbon paper as-prepared or on carbon paper modified by polyaniline (PA) deposition. An important increase in the ORR rate was observed using PA-coated carbon black matrix. In the presence of methanol, the activity of these electrodes was better than that of non-modified carbon-supported, as polyaniline modification was seen to decrease the poisoning of the surface and probably increase the matrix conductivity. The oxygen reduction activity and methanol tolerance of both electrodes were compared with those of commercial E-TEK (20% Pt on Vulcan XC-72 carbon black) electrodes prepared under identical experimental conditions either by PA modification or without. The activity of the PA-modified Ru chalcogenide catalysts was found to be superior to that of PA-modified E-TEK electrodes even in the presence of methanol. In the latter case, the number of electrons transferred was higher when using PA-modified E-TEK electrodes, indicating thus the selectivity of Ru chalcogenide electrodes toward oxygen reduction.

Binary systems of ruthenium sulfide or selenide nanoparticles ($Ru_xS_y$, $Ru_xSe_y$) are considered as the state-of-the-art ORR electrocatalysts in the class of non-Chevrel amorphous transition metal chalcogenides. Notably, in contrast to pyrite-type $MS_2$ varieties (typically $RuS_2$) utilized in industrial catalysis as effective cathodes for the molecular oxygen reduction in acid medium, these Ru-based cluster materials exhibit a fairly robust activity even in high methanol content environments of fuel cells.

Alonso-Vante and co-workers [22] first developed a series of ruthenium chalcogenide cluster materials, $Ru_xX_y$ (X = S, Se, and Te) by utilizing a preparation procedure similar to that used to synthesize the mixed polynuclear complexes, i.e., reaction of metal carbonyls with elemental chalcogen in xylenes, and examined their performance in methanol-containing acidic media. The $Ru_xSe_y$ complex was proved to be the most active catalyst among these materials, exhibiting also remarkable stability against oxidation by virtue of selenium atoms coordinated onto the catalytic center (as clarified later). In the first attempts to explain the influence of Se it was suggested that a ruthenium core, which acts as an electron reservoir, is surrounded by an amorphous Se shell, which catalyzes the electroreduction of oxygen [23]. Subsequently [24], structural and stability studies of $Ru_x$ and $Ru_xSe_y$ cluster-like particles having similar sizes (1.4–1.6 nm) in the reduced state revealed that, whereas $Ru_x$ particles were rather sensitive to oxygen from air, they were chemically stabilized against oxidation by the coordination of Se atoms. It was established that besides the chemical effect, selenium stabilizes also the nanostructural nature of the compound (geometric effect), as demonstrated by temperature measurements (up to 300 °C) in the gas phase, and provides the electronic effect for electrocatalysis. The structure of $Ru_xSe_y$ was investigated with special attention to the distribution
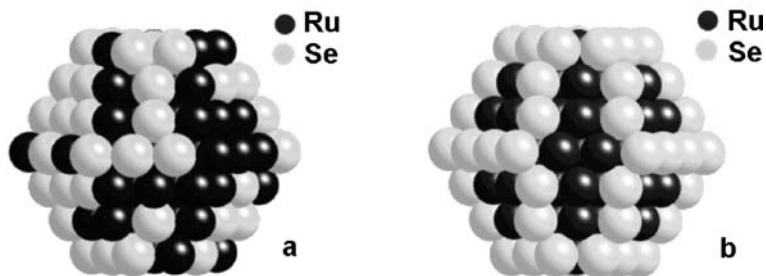
**Fig. 6.3** Cluster model structure for $Ru_{99}Se_{54}$ showing the selenium bonding onto the ruthenium clusters (**a**) with a statistical distribution; (**b**) with an ordered positioning. (Adapted with permission from [24]. Copyright 2009, American Chemical Society)

of the Se atoms in the particles. On account of the characterization results and the increased disorder deduced from extended X-ray absorption fine structure (EXAFS) calculations, it was suggested that the Se atoms are mainly coordinated to surface sites of the ruthenium clusters in a statistical manner. Figure 6.3 depicts such an hcp cluster model $Ru_{99}Se_{54}$, with (a) all 54 Se atoms replacing surface Ru atoms at random and (b) all 54 Se atoms replacing surface Ru atoms in a regular way, i.e., those that are five-, six-, and sevenfold coordinated. Note that the coverage of the Ru-cluster surface by selenium atoms allows enough free active sites for an efficient electrocatalysis or coordination with oxygen/water.

The $Ru_xSe_y$ catalysts have been prepared also through the thermochemical treatment of colloidal Ru particles in Se-saturated xylene solvent under refluxing conditions. In this method, the first step is to produce nanosized Ru clusters (Ru black), which is accomplished by chemical reduction of a ruthenium salt ($RuCl_3$) dissolved usually in tetrahydrofuran (THF), on a suitable substrate. Cao et al. [25] obtained the as-denoted Ru/Se catalyst particles immobilized on an electrode (e.g., gold) surface. Tests toward ORR in acid solutions provided evidence for similar reactivity functions between the Ru/Se and the $Ru_xSe_y$ catalysts, obtained by the colloid and carbonyl-thermolysis methods, respectively, while full methanol tolerance was established for the range of investigated methanol concentrations (0.1–5 M). The high catalytic activity of Ru/Se was attributed to a similar surface structure to $Ru_xSe_y$, involving active Ru metallic sites embedded in a Se matrix. Similarly prepared sulfide, Ru/S, catalysts were found to be methanol-tolerant at 0.1 M methanol concentration but much less active than Ru/Se and $Ru_xSe_y$ toward ORR, although slightly more active than hydrogen-reduced (chalcogen-free) Ru black. Note that analogous experiments with rhodium nanoparticles indicated a decrease in ORR rates for both Se and S additives. Ensuing XPS studies [26] on Ru, Ru/Se, and Ru/S nanoparticle samples immobilized on gold, either as prepared or electrochemically processed, confirmed that the Se and S additives protect Ru against oxidation. Exceptional chemical stability in acidic media, even at high positive potentials, was reported for the Se-modified Ru samples. Interestingly, the performance of the investigated catalysts was correlated to their chemical state with respect to oxygen

uptake, which was seen to be suppressed in the order Ru/Se > Ru/S > Ru black, in accordance with the ORR activity. It should be noted that unlike the cluster-type $Ru_xSe_y$ and Ru/Se materials, surface modification of bulk polycrystalline Ru with Se did not lead to comparable enhancement of the ORR activity.

The previous conclusions were strengthened in subsequent works aimed at the understanding of the role of Se in promoting the electrocatalytic activity of Ru for the ORR. The transformation of Ru nanoparticles upon introduction of increasing amounts of Se was systematically investigated [27]. Se-modified Ru/C samples with Se:Ru ratio from 0 to 1 were prepared by reacting carbon-supported Ru nanoparticles with $SeO_2$ in water/THF solution, followed by evaporation of the solvent and reductive annealing. The characterization results suggested a strong chemical bonding interaction between Se and Ru, which was considered to be essential for the catalytic activity. For Se:Ru = 1, high-resolution electron microscopy (HREM) showed evidence of formation of core–shell particles, comprising a hexagonally packed Ru core and a Ru selenide shell with lamellar morphology. For low Se content, the core of the selenide clusters could be described as $Ru_2Se_2O_{0.5}$ (taking into account also earlier considerations implying that molecular oxygen binds to Ru centers [22]). The main conclusion was that Se strongly influences the susceptibility of Ru nanoparticles to oxidation: the higher the amount of Se, the lower the extent of Ru oxidation. Apparently, for obtaining good results toward ORR a compromise should be attained between inhibition of surface oxidation and blocking of the surface; a sufficiently thin selenide layer allowed the access of oxygen molecules to Ru centers, whereas this condition was not fulfilled for the samples with the high (1:1) Se content.

The change in the electronic properties of Ru particles upon modification with Se was investigated recently by electrochemical nuclear magnetic resonance (EC-NMR) and XPS [28]. In this work, it was established for the first time that Se, which is a p-type semiconductor in elemental form, becomes metallic when interacting with Ru, due to charge transfer from Ru to Se. On the basis of this and previous results, the authors emphasized that the combination of two or more elements to induce electronic alterations on a major catalytic component, as exemplified by Se addition on Ru, is quite a promising method to design stable and potent fuel cell electrocatalysts.

The different classes of Ru-based catalysts, including crystalline Chevrel-phase chalcogenides, nanostructured Ru, and Ru–Se clusters, and also Ru–N chelate compounds ($RuN_x$), have been reviewed recently by Lee and Popov [29] in terms of the activity and selectivity toward the four-electron oxygen reduction to water. The conclusion was drawn that selenium is a critical element controlling the catalytic properties of Ru clusters as it directly modifies the electronic structure of the catalytic reaction center and increases the resistance to electrochemical oxidation of interfacial Ru atoms in acidic environments.

With respect to non-noble and non-Ru catalysts, transition metal chalcogenides with spinel and pyrite structures have been investigated and shown that these can also be active to oxygen reduction processes. The motivation in the present case is that chalcogen addition might enhance the stability and activity toward the ORR

of otherwise inactive and unstable in an acidic medium metals, such as W and Co. Behret et al. [30] synthesized several cobalt (Co)-based catalysts such as $Co_3S_4$. Sidik and Anderson [31] proved that the partially –OH covered (202) surface of a $Co_9S_8$ chalcogenide is an active site for oxygen reduction. In terms of the ORR overpotential, this surface was reported to have a similar behavior to that of a Pt surface. $CoS_2$, $NiS_2$, and ternary $(Co,Ni)S_2$ thin films, prepared by magnetron sputtering on glassy carbon substrates, were shown recently [32] to have significant ORR catalytic activity, increasing in the order $NiS_2 < CoS_2 < (Co,Ni)S_2$, with that of the ternary film being paramount in terms of both open-circuit potential (OCP) and current density. The OCP value of 0.89 V vs. SHE was claimed to show closer approach to values for Pt than have been obtained to date for other transition metal chalcogenides. According to XRD characterization the films were nanocrystalline with a pyrite structure. The mixed-metal sulfide involved a solid solution, probably with some amorphous material. XPS and AES showed that each metal is in a single chemical state, and that there is no detectable elemental sulfur even though the surfaces are sulfur-rich. These surfaces did not appear to bind oxygen tightly, but they maintained sufficient electronic conductivity to remain active without the passivation that can occur with an insulating oxide on a metal. However, while the film formed from $CoS_2$ was stable for several hours under oxygen reduction conditions, the mixed-metal film degraded, as a consequence of the spinodal decomposition observed.

Susac et al. [33] showed that the cobalt–selenium (Co–Se) system prepared by sputtering and chemical methods was catalytically active toward the ORR in an acidic medium. Lee et al. [34] synthesized ternary non-noble selenides based on W and Co by the reaction of the metal carbonyls and elemental Se in xylenes. These W–Co–Se systems showed catalytic activity toward ORR in acidic media, albeit lower than with Pt/C and seemingly proceeding as a two-electron process. It was pointed out that non-noble metals too can serve as active sites for catalysis, in fact generating sufficient activity to be comparable to that of a noble metal, provided that electronic effects have been induced by the chalcogen modification.

### 6.1.3 Methanol Oxidation

The electrocatalytic oxidation of methanol has been widely investigated for exploitation in the so-called direct methanol fuel cell (DMFC). The most likely type of DMFC to be commercialized in the near future seems to be the polymer electrolyte membrane DMFC using proton exchange membrane, a special form of low-temperature fuel cell based on PEM technology. In this cell, methanol (a liquid fuel available at low cost, easily handled, stored, and transported) is dissolved in an acid electrolyte and burned directly by air to carbon dioxide. The prominence of the DMFCs with respect to safety, simple device fabrication, and low cost has rendered them promising candidates for applications ranging from portable power sources to secondary cells for prospective electric vehicles. Notwithstanding, DMFCs were

long being considered as the most difficult fuel cell technology due to catalytic inefficiency and methanol crossover (see following discussion).

The problems of the oxygen (cathode) electrode are common to almost all acid electrolyte fuel cells whereas those concerning the fuel electrode catalysts are peculiar to the particular fuel. Very few electrode materials have been shown to be capable of oxidizing methanol in acidic media at low enough potentials. This reaction, similarly to hydrogen oxidation, is actively catalyzed by platinum, but catalytic activity of this metal decays rapidly with time in the acid solution environment owing to poisoning by a strongly adsorbed dehydrogenated methanolic residue [35]. Methanol oxidation at a Pt electrode is known to proceed by the consecutive, dissociative electrosorption of methanol leading to "multibonded" carbon monoxide ($Pt_xCO$) via dehydrogenation of $Pt_{3-x}CH_x$–OH intermediates [36].

In order to cope with the deactivating effect of CO groups on the Pt surface and enhance the catalytic activity of Pt, several CO-tolerant electrocatalysts have been developed based on Pt–M alloy (M = Mo, Sn, Ge, Sb, Rh, Ru, W, Os) or bimetallic electrodes. The activity of such catalysts is due to the capacity of the metal partner to deliver oxygenated species that lead to oxidation of CO to $CO_2$ at low overpotentials. Compared to pure Pt, the most active electrocatalysts known to date, exhibiting low overpotentials and extended lifetimes, are Pt and Ru alloys supported on carbon. High surface area catalysts prepared by dispersion of Pt or other noble metals in inorganic oxides are also of particular interest [37]. Recently, Petrii [38] presented a step-by-step historical account of the progress in design and characterization of Pt–Ru based electrocatalysts in connection with DMFC and thoroughly reviewed (523 references) the material, mechanistic, and applied aspects of these electrocatalysts.

Layered materials such as Mo and W sulfides and selenides have been combined with platinum black and tested as anodes for methanol oxidation. The advantage of using a support such as $MoSe_2$ is that it can be electrochemically oxidized to produce an oxide layer on the film. This oxide surface will serve as a source of –OH groups necessary for the removal of adsorbed CO on platinum. $Pt/MoO_x/MoSe_2$ electrodes consisting of a $MoO_x/MoSe_2$ surface covered with highly dispersed Pt microparticles have been reported to exhibit high stability under continuous use for methanol oxidation [39, 40]. The electrodes were prepared by electrochemical formation of $MoO_x$ and subsequent deposition of Pt (from sulfuric acid potassium hexachloroplatinate solution) on Li-intercalated and -exfoliated $MoSe_2$/Ti thin films. In particular, the $MoO_x/MoSe_2$ surface was used as a support for electrodeposition of Pt to take advantage of its high surface area and its stability in acid solution, combined with the enhanced catalytic activity of Pt in the presence of Mo oxide species. It was found that the adsorption of oxygen-containing species on the $Pt/MoO_x/MoSe_2$ electrodes commences at lower potentials compared with the pure Pt electrode indicating thus an improved electrocatalytic activity for methanol oxidation.

Although ORR catalysts for DMFCs are mostly identical to those for the PEM fuel cell, one additional and serious drawback in the DMFC case is the *methanol crossover* from the anode to the cathode compartment of the membrane electrode assembly, giving rise to simultaneous methanol oxidation at the cathode. The

concomitant depolarization, i.e., the drop in cathode potential, leads to an over-all efficiency loss of the cell. A practical way to alleviate this problem, in the current DMFC designs using Nafion polymer membranes, is the development of oxygen reduction catalysts which are inactive toward methanol oxidation, thereby preventing the establishment of a mixed potential at the cathode.

Different methanol-tolerant cathode catalysts have been investigated. Most promising among such materials are the dispersed sulfides. The composition of these catalysts is a controllable variable, and their interaction with the carbon support surface can be modulated by controlling the sulfur content.[1] Alonso-Vante and co-workers reported [41] on the performance of platinum sulfide, $Pt_xS_y$, electro-catalyst synthesized under mild conditions in the nano-length scale. The catalyst supported on carbon ($Pt_xS_y$/C) was obtained by thermal treatment (350 °C) of the chemical precursor, which was generated by reacting sulfur and salts of platinum at room temperature. Cyclic voltammetry and rotating disk electrode measurements in methanol-containing acid electrolyte revealed that the chalcogenide material is 95% selective, as compared to commercial Pt/C, for the ORR and that the depolarization effect was minor for the former catalyst. It was explained that, in the final form of the catalyst, sulfur atoms interact with surface platinum atoms in a chemical way such as to avoid to a great extent the methanol interaction. Further, the ORR kinet-ics was not perturbed, indicating that sulfur atoms and methanol have a little effect on the molecular oxygen adsorption.

Grinberg et al. [42] fabricated carbon-supported catalysts based on chalcogenide clusters of the Pt–M–X type (M = Fe, Mn; X = S, Se, Te) and used them as cathodes (in gas diffusion electrode configuration; see below) in methanol–oxygen fuel cells. The preparation procedure involved the impregnation of highly dispersed carbon (Ketjen Black) by solutions of organometallic clusters in organic solvents, followed by drying in vacuum at 100 °C, and thermal treatment in argon atmosphere at 250–500 °C for 1 h. The authors pointed out that their approach in producing metal chalcogenide cluster catalysts enables one to obtain the chalcogenide coating directly on the support surface, thereby allowing ready permutation of the com-ponent metals and chalcogenides as well as wide variation of their quantitative ratio in the precursor skeleton. They claimed also that this method provides higher reproducibility of composition than those using reactions of metal carbonyls with elemental chalcogen in xylenes. All catalysts were reported to be highly tolerant to methanol; the $PtMn_2S_2$/C system appeared to be most active, its current response in oxygen reduction being equal to that given by the commercial Pt–C E-TEK catalyst.

We have already referred to the Mo/Ru/S Chevrel phases and related catalysts which have long been under investigation for their oxygen reduction properties. Reeve et al. [19] evaluated the methanol tolerance, along with oxygen reduction activity, of a range of transition metal sulfide electrocatalysts, in a liquid-feed solid-polymer-electrolyte DMFC. The catalysts were prepared in high surface area by direct synthesis onto various surface-functionalized carbon blacks. The intrinsic

---

[1]It is well known that surface functionality can be introduced onto carbons and that such functionalities can have a profound impact on the carbon surface chemistry.

activity of the best material tested, namely $Mo_2Ru_5S_5$ on sulfur-treated XC-72, was lower than of platinum (by ca. 155 mV throughout the entire polarization curve); however, in methanol-contaminated electrolytes, $Mo_2Ru_5S_5$ presented better figures than Pt, since the net activity of the latter was reduced due to methanol oxidation side reactions, especially at low overpotentials. With regard to the overall performance of the DMFC, it appeared that the $RhRu_5S_5$:Ketjen EC-600JD system could prove a suitable alternative to Pt [43].

Since the introduction of Chevrel phases and polynuclear transition metal chalcogenide catalysts, the development of novel, Pt-free cathode catalysts with high methanol tolerance has been an important goal of broad general interest and significance. The Ru-based systems are promising alternatives to Pt, since, unlike Pt, they lack available surface sites for methanol adsorption because of the strongly adsorbed oxygenated species. It has been shown that a full tolerance of methanol can be obtained for the ORR by means of ruthenium chalcogenide systems [21]. Optimized operating conditions in a DMFC single cell of methanol-tolerant RuSe/C as well as alternative carbon-supported platinum-alloy catalysts have been determined [44].

### 6.1.4 ODP Applications (Oxygen-Depolarized Electrolysis of HCl)

Electrodes in electrolyzers and fuel cells have to be porous to gas diffusion in order to ensure the supply of the reactant gases to the active zones where the metal catalyst lies in contact with the ionic and electronic conductor. A remarkable efficiency gain has been achieved in important electrolytic processes by replacing the standard cathode where ORR takes place by an oxygen-consuming *gas diffusion electrode* (GDE) operating as the so-called *oxygen-depolarized cathode* (ODC), mainly due to the associated decrease in energy consumption needed to operate the system, corresponding to a lowering of overpotential even by as much as 1 V.

The electrolysis of aqueous HCl solutions is a widely used industrial method for the recovery of high-value chlorine gas from the anodic compartment of the electrolyzer, according to the reaction $2HCl \rightarrow Cl_2 + 2H^+ + 2e^-$. At the cathode, oxygen is reduced to hydrogen peroxide or water. The successful operation of a GDE in the environment of the HCl electrolyzer is solely dependent on the stability and activity toward ORR of the electrocatalyst material utilized. Platinum-based catalysts have been typically used, however, with serious drawbacks, as Pt is severely depolarized primarily due to chloride anion adsorption and to a lesser extent by the surface reactions of omnipresent dissolved organic compounds. In the past years, these problems have been partially addressed with the development of rhodium-based catalysts (e.g., Rh/C), which despite their lower activity for oxygen reduction relative to Pt-based electrocatalysts have exhibited significantly higher oxygen depolarization and good performance in the presence of chloride ions and other organics. Studies on the capacity of transition metal cluster chalcogenides for oxygen-depolarized chlorine-saturated electrolyzer applications only very recently appeared in the literature, despite the promising performance of these compounds

in PEM and DM fuel cell applications. It seems though that their use will constitute a major advancement in the commercialization and implementation of the novel oxygen-consuming GDE technology.

At any rate, noble metal chalcogenides are the preferred choice of electrocatalysts for GDE over pure metals and metal alloys in industrial processes involving operation in highly corrosive environment. Pioneered by E-TEK Inc. in early 2000, various kinds of rhodium sulfide ($Rh_xS_y$) have been developed as catalysts for the depolarized electrolysis of hydrochloric acid, where rhodium/sulfur is incorporated into a GDE structure for use as oxygen-consuming cathode. Highly active catalyst systems are obtained by increased dispersion of the $Rh_xS_y$ in carbon support. Recently, the $Rh_xS_y$ loading on Vulcan XC72-R carbon was studied in terms of morphological characteristics and ORR activity in the oxygen-depolarized electrolysis of HCl [45]. Physicochemical characterization suggested that the preparation methodology of such chalcogens plays a fundamental role in terms of chemical structure since loading affects the nature of the chalcogen surface and the statistics of active reaction centers. Enhanced catalytic activity was reported for relatively low-loaded $Rh_xS_y$/C samples. ORR kinetics was addressed using a series of rde experiments in 1 M HCl electrolyte, in which the optimal $Rh_xS_y$ loading was found to be at 15 wt%, a value two times lower with respect to the commercially available 30 wt% material. It was claimed that it is possible to efficiently and effectively reduce the precious metal loading in the ODC by as much as three times without any detrimental effect in terms of cell performance and catalyst durability.

In contrary to a simple rhodium-based catalyst, the $Rh_xS_y$ does not require any conditioning step to survive in the highly corrosive operational environment of HCl electrolysis. In general, these catalysts show very good performance both in terms of activity and chemical resistance; however, their price and availability is a difficult issue to overcome inasmuch as large commercial applications are concerned. Rhodium is one of the most expensive noble metals with a price exceeding that of osmium and being several orders of magnitude higher compared to the price of ruthenium and iridium.

Recently, rhodium and ruthenium-based carbon-supported sulfide electrocatalysts were synthesized by different established methods and evaluated as ODP cathodic catalysts in a chlorine-saturated hydrochloric acid environment with respect to both economic and industrial considerations [46]. In particular, patented E-TEK methods as well as a non-aqueous method were used to produce "binary" $Rh_xS_y$ and $Ru_xS_y$; in addition, some of the more popular Mo, Co, Rh, and Re-doped $Ru_xS_y$ catalysts for acid electrolyte fuel cell ORR applications were also prepared. The roles of both crystallinity and morphology of the electrocatalysts were investigated. Their activity for ORR was compared to state-of-the-art Pt/C and Rh/C systems. The $Rh_xS_y$/C, $Co_xRu_yS_z$/C, and $Ru_xS_y$/C materials synthesized by the E-TEK methods exhibited appreciable stability and activity for ORR under these conditions. The Ru-based materials showed good depolarizing behavior. Considering that ruthenium is about seven times less expensive than rhodium, these Ru-based electrocatalysts may prove to be a viable low-cost alternative to $Rh_xS_y$ systems for the ODC HCl electrolysis industry.

## 6.2 Electrochemical Energy Storage

### 6.2.1 Intercalation in Chalcogenides

Solid electrolytes involve various chemical structure types and mechanisms of conduction, well studied being those related to point defects [47]. A special class of solid electrolytes is based on intercalation mechanisms consisting of the reversible insertion of an atomic or molecular guest species into a host crystal lattice at low temperature while the structure of the host is preserved. A reaction that leads to an intercalated substance is a special case of a topochemical process and such reactions are classified as reversible, topotactic solid-state reactions. Solids forming intercalation compounds contain structural elements like frameworks, layers, or chains with channels and cavities. Insertion of mobile guest species may occur into an empty host lattice that provides adequate free volume and appropriate geometry or by exchange reactions with a host that already contains a guest. Many common solid materials including clays, graphite, transition metal oxides, and chalcogenides possess the property of intercalation. By far the most common class of intercalation compounds is that of the layered structure type, which provides relatively easy access to the interlayer space, as well as stability of the final products [48]. Applications of intercalates have been numerous. Sorption and ion exchange by zeolites and related substances, catalysis by layered compounds, and (photo) electrochemical energy storage in cells with intercalation-active electrodes may be regarded under this heading.

Intercalation carried out by electrochemical electron transfer has received much attention since the 1970s, once the concept and its potential use were clearly defined. A major impetus to studies of both intercalation compounds and batteries was the finding that layered disulfides exhibit high electrochemical activity and reversibility as cathodes in alkali metal cells. Following the first successful electro-intercalation reactions in layered dichalcogenides [49–51] it was recognized that such compounds exhibiting both ion transport and electronic conductivity (as being also semiconductors) would be appropriate for the fabrication of secondary cells, provided that the intercalation effect is highly reversible and continuous over the entire composition range of the electrode material. Let us note here that reversibility is of major importance in battery utilization since there is no need to expend energy in nucleating a new phase either on the initial reaction or on the reverse (recharge reaction) [52]. To obtain a battery system that is highly reversible preferably at ambient temperatures one possibility for the cathode is to be in the liquid state so that reactions can readily take place (but then the active material must be kept away from the anode, otherwise self-discharge will occur) or to employ a solid cathode that would react by formation/deformation of a new phase upon cell operation.

Layered dichalcogenides, such as sulfides or selenides of Ti, Mo, W, Zr, Ta, Nb, V, and Cr, are able to dissolve certain alkali metal ions and in some cases post-transition (pseudo-alkali) metal ions ($Cu^I$, $Ag^I$), via a mechanism in which the guest is inserted between the dichalcogenide layers. Lithium ion intercalation into $TiS_2$, which among layered dichalcogenides has been one of the most prominent cathode

**Fig. 6.4** Layered structure of $Li_xTiS_2$, showing the lithium ions between the $TiS_2$ sheets. This is an anion close-packed lattice in which alternate layers between the anion sheets are occupied by a redox-active titanium atom. Lithium inserts itself into the empty remaining layers. (Adapted from [68])
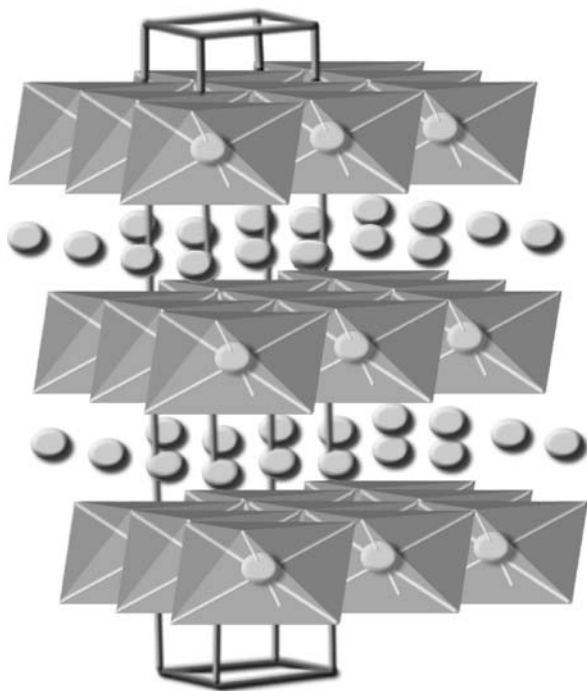
materials for Li batteries, illustrates the basic features of the process. By insertion of one lithium ion, a complete charge transfer occurs that involves the reduction of $Ti^{IV+}$ to $Ti^{III+}$ and the diffusion of $Li^+$ into the van der Waals (vdW) gaps of the host structure, according to Scheme 6.1, and Fig. 6.4.

$$x\text{Li} + \text{TiS}_2 \rightleftarrows \text{Li}_x\text{TiS}_2 \qquad 0 \leq x \leq 1 \qquad (6.1)$$

Available for intercalation are the octahedral and tetrahedral interstitial sites of the chalcogenide structure; generally, the octahedral sites are energetically more favored leading to the maximum possible intercalation level of one guest atom per formula unit, while diffusion proceeds via the tetrahedral sites. The weak vdW forces between the $TiS_2$ layers are thereby replaced by coulombic interactions, with the guest insertion resulting possibly in lattice expansion along the crystallographic $c$-direction. In fact, intercalation of lithium in $TiS_2$ is accompanied by minimal structural change and is consequently readily reversed either chemically or electrochemically. This property together with high lithium diffusivity and a high free energy of reaction makes systems such as $Li/TiS_2$ attractive for rechargeable (secondary) batteries.

A critical review on the foundation and earlier results on metal intercalates of the transition metal dichalcogenides and related host materials can be found in the seminal paper of Whittingham [53]. The electrochemical and transport properties

of lithium and sodium intercalation have been studied with a variety of chalcogenide hosts, e.g., metal-rich pseudo-2D compounds, such as the tantalum selenides and tellurides $Ta_2Se$, $Ta_2Te_3$ [54], or "misfit" layer compounds of general formula $(MX)_{1+x}(TX_2)_n$ (M = Sn, Pb, Bi, rare earth; T = V, Cr, Ti, Nb, Ta; X = mainly S, Se; $n = 1$–3) produced by reaction of main group metals with early transition metal dichalcogenides. The structures of these solids contain NaCl-type MX slabs alternating with $(TX_2)_n$ sandwiches; well-known examples are the lead compounds $(PbS)_{1.14}(TS_2)_2$ (T = Ti, Nb, Ta) [55, 56].

Layered indium selenide compounds have been investigated also for lithium intercalation. In an early work, chemical diffusivity of the alkali metal in single-crystal annealed $\alpha$-$In_2Se_3$ was shown to reach ca. $5 \times 10^{-10}$ cm$^2$ s$^{-1}$ [57], the values in the transition metal dichalcogenides being in the order of $10^{-9}$–$10^{-8}$ cm$^2$ s$^{-1}$. Further, the electrical conductivity of Li-intercalated single crystals of InSe and $\alpha$-$In_2Se_3$ was found to change by three orders of magnitude with respect to non-intercalated samples, while an interesting time-dependent anisotropy was noted during intercalation, associated to an initial non-uniform Li distribution and movement of Li concentration kinks [58].

In addition, a variety of systems have been shown to afford insertion of multi-valent metals. Boulanger and Lequir [59] used potentiodynamic methods to study the redox behavior of $Cd^{2+}$ insertion in molybdenum cluster chalcogenide hosts with the general formula $Mo_yX_z$, namely Chevrel phases with $X_z = S_8$, $Se_8$, $Te_8$, and $S_xSe_{8-x}$, and condensed cluster phases such as $Mo_9S_{11}$, $Mo_6Se_6$, and $Mo_{15}S_{19}$. Intercalation activity of divalent $Mg^{2+}$, $Ca^{2+}$, $Zn^{2+}$, and trivalent $Y^{3+}$ ions in $TiS_2$ [as well as a number of transition metal oxides and phosphates such as $Co_3O_4$, $V_2O_5$, and $Mg_{0.5}Ti_2(PO_4)_3$] has been reported; however, all these cases feature slow kinetics, as well as low intercalation level [60]. The reason for this relates to the multivalency of the above cations that result in high energetic barriers for solid-state ion diffusion, along with difficulty in the redistribution of the electronic charge in the host, in the vicinity of the ion-residing site.

Photoinduced intercalation and deintercalation cathode reactions with chalcogenide materials have been considered as a possible route to develop solar-powered intercalation batteries as well as for optical information storage. A detailed theoretical analysis of this possibility supported by experimental data obtained with p-$ZrSe_2$ has been provided originally by Tributsch [61]. The author has discussed various aspects of photoinduced ionic mechanisms on the basis of selected experimental results obtained with host materials of the composition MX, $MX_2$, $MPX_3$, $M_3PX_4$, $M_6PX_5Y$, $MO_2$, and $(CH)_n$ (M = metal, X = S, Se; Y = halogen) [62].

## 6.2.2 Principles of the (Thin Film) Rechargeable Lithium Battery

Main electrode features, which determine the energy density of an electrochemical storage cell, are the *volumetric* or *specific capacity*, i.e., the electric charge that electrodes can store per unit volume or weight, respectively, and the electrochemical potential they produce. Considering thermodynamic reasons, lithium, as being the most electropositive (–3.04 V vs. SHE) metal, is exceptional for use as

an anode in high-energy/power batteries. Also, lithium is the lightest alkali metal with very high thermal and electrical conductivity and largest specific heat of any solid element, thus facilitating the design of storage systems with high energy density. Various types of cells using lithium in different states/phases at the negative electrode have been devised and developed. Primary, i.e., non-rechargeable, lithium batteries that operate at room temperature have been in existence since the 1970s for powering small devices such as watches and cameras, while high-temperature types like those using liquid sulfur cathode have been investigated since the 1960s for power applications (next section).

Secondary cells using metallic lithium (or a Li-intercalating material) at the anode and Li-intercalating material at the cathode have been intensively studied for producing thin film or flat batteries. It was the introduction of the lithium ion ($Li^+$) transfer cell ($LiCoO_2$/graphite) by Sony Corporation in 1990 that brought about a revolution in the rechargeable battery industry and is considered as one of the great successes of modern materials electrochemistry. The $Li^+$ battery satisfies demands for high specific energy and high power supply for portable applications, especially for cellular phones and portable computers. In effect, the Li-based rechargeable cell technologies -although compared to mature battery technologies, such as Pb-acid or Ni–Cd, are still in their infancy- presently dominate development in the field of flat batteries [63].

The principal concept of operation for both Li metal and Li ion cells is based on the intercalation reaction and is rather different from conventional secondary batteries which are based on chemical reactions. In both Li-based types, the alkali ions swing between a suitable anode and an oxidizing cathode through a concentrated liquid organic solution of an inorganic lithium salt (e.g., liquid carbonates or esters of simple alcohols and glycols dissolving $LiPF_6$) or an appropriate solid electrolyte.[2] The Li metal cells use metallic Li as an anode, whereas in Li ion cells, the anode contains no Li and is typically a carbon-based electrode. The choice of the cathode depends on the cell type; unlike Li metal batteries, the Li ion systems must incorporate a cathode which acts as a source of lithium because the carbon anode is initially empty, i.e., contains no Li, so the cathode needs to be lithiated before cell assembly. For both types, energy is delivered during discharge by the transfer of lithium ions from the anode through the electrolyte into the cathode, owing to the difference in chemical potential of lithium in the two electrodes; during charging, the reverse lithium transfer consumes energy. The cathode materials suitable for the Li ion cell are highly oxidizing compounds which may compensate for the loss in cell potential at the (non-Li) anode.

State-of-the-art thin film $Li^+$ cells comprise carbon-based anodes (non-graphitic or graphite), solid polymer electrolytes (such as those formed by solvent-free membranes, for example, polyethylene oxide, PEO, and a lithium salt like $LiPF_6$ or $LiCF_3SO_3$), and metal oxide based cathodes, in particular mixed or doped oxides

---

[2] The electrolyte used in lithium cells, i.e., for all lithium couples, must be completely anhydrous (< 20 ppm $H_2O$); alkali metals in general are compatible with neutral salt solutions in aprotic solvents or neutral molten salts or solid ion-conductors.

such as $LiCoO_2$, $LiNiO_2$, $LiMn_2O_4$, and $V_2O_5$[64]. Typically, the electrodes are fabricated from small particle size (5–20 $\mu$m) electroactive materials. At present, the main deposition techniques for making thin film cathodes are those used in microelectronics industry including chemical vapor deposition (CVD), sputtering, spray pyrolysis and evaporation, and, to a lesser degree, electrochemical methods.

An account of developments in thin film lithium batteries over the past 30 years can be found in the recent review of Patil et al. [65]. The concept of the thin film lithium battery is to construct solid films of anode, solid/gel (polymer) electrolyte, and cathode sequentially on a substrate, both electrodes being capable of reversible lithium insertion. In terms of specific volumetric and gravimetric capacity, Li or Li ion based batteries are most attractive for the construction of miniaturized power sources or "microbatteries", required in modern microelectronic and MEMS devices [66]. Presently, two kinds of lithium batteries are complementing each other to satisfy the need for such devices. One type utilizes polymer films as electrolytes or separators; the second type, usually denoted as *thin film microgenerators*, comprises solid-state cells with glassy electrolytes. Typically, these microgenerators have a total thickness of around 10 $\mu$m including the protective package, that is, one order of magnitude lower than that of the usual polymer electrolytes, allowing thus the use of poor conductive electrolytes like oxide glasses, which have the great advantage to have a pure $Li^+$ conductivity. Consequently, the redox stability range is very large and allows the use of very oxidizing species. The keys to making such microbatteries viable in performance/cost terms are new thin film materials for cathodes and low-cost preparation methods of these films [67].

With the appropriate choice of electrode material, lithium batteries can be tailored to almost any application requiring cell voltages in the range of 1–3 V and current densities from a few $\mu$A to tens of mA per $cm^2$. In addition, the change of potential with state of charge can be controlled from almost 0 V in the case of $VSe_2$ to more than a volt for $TaS_2$.

### 6.2.3 Chalcogenide Cathodes for Rechargeable Lithium Cells

The key requirements for an intercalating cathode material in rechargeable cell include high diffusivity and reversibility of the intercalation reaction without structure degradation, a high free energy of reaction, good electronic conductivity, no solubility in the electrolyte, and certainly long cycle life, availability, and low cost of the compound. A seminal review focused on cathode materials for lithium batteries has been given by Whittingham [68], who notes that almost all of the relevant research and commercialization has centered on two classes of materials. The first comprises layered compounds with an anion close-packed or almost close-packed structure in which alternate layers between the anion sheets are occupied by a redox-active transition metal (as in Fig. 6.4) and is exemplified by $TiS_2$, $CoO_2$, $NiO_2$, and $Ni_yMn_yCo_{1-2y}O_2$. The second group comprises materials having more open structures, like many of the vanadium oxides, the tunnel compounds of $MnO_2$, and most recently the transition metal phosphates, such as the olivine $LiFePO_4$.

Although oxides and phosphates are currently the state-of-the-art cathode materials for lithium rechargeable batteries, metal chalcogenides have been quite relevant to the development of this technology. Actually, the practical thin film battery started in 1982, when a solid-state cell comprising a $TiS_2$ cathode prepared by low-pressure CVD, a $Li_{3.6}Si_{0.6}P_{0.4}O_4$ glass electrolyte, and metallic lithium as the anode was announced by Hitachi Co., Japan [69]. Titanium disulfide is a light material of low cost and satisfies the criteria for a good rechargeable electrode, as exhibiting a high free energy for the lithium intercalation reaction, a single homogeneous phase of intercalation with only 10% lattice expansion in the entire intercalation range of up to $x = 1$ in $Li_xTiS_2$, a good electronic conductivity in both the non-intercalated and lithiated state, and a fast Li diffusion with a coefficient of about $10^{-12}$ $m^2s^{-1}$ at room temperature leading to high rate capability. Its conductivity increases on intercalation and there is no evidence of solubility in the organic electrolytes commonly used, so there is no self-discharge due to reaction of dissolved species with the lithium anode. An average discharge voltage of 2.1 V and an almost 100% $TiS_2$ utilization result in a specific energy of about 450 W h $kg^{-1}$ for a secondary cell with metallic Li anode. The ready reversibility of lithium in $TiS_2$ has permitted deep cycling for close to 1,000 cycles with minimal capacity loss, less than 0.05% per cycle, with excess lithium anodes.

Most of the other layered dichalcogenides are also electrochemically active with respect to lithium intercalation, afford good energy densities in general, and many show a similar single-phase behavior like $TiS_2$ although poor reversibility is a frequent problem (e.g., for the group VIA layered disulfides). Molybdenum disulfide, in particular, which abundantly occurs in nature as molybdenite, is a good candidate for cathode active material needing a minimum amount of processing. It is found, however, that crystalline (molybdenite) $MoS_2$ is stable only at low discharge depths of about 10%, since a higher degree of lithium intercalation leads to the formation of $Li_2S$ and Mo metal, due to the low free energy of formation of the host sulfide itself. Despite this shortcoming, the development of $MoS_2$ as a cathode material for lithium cells was greatly assisted by the discovery of a new crystalline phase stabilized by the presence of lithium within the crystal lattice. Py and Haering [70] showed that upon intercalation, the naturally occurring 2H-$MoS_2$ host lattice may undergo a first-order phase transition in which the Mo coordination changes from trigonal prismatic to octahedral (1T structure). This change shifts the equilibrium potential of the material so that it becomes considerably more electropositive for a wide range of Li concentrations in $Li_xMoS_2$. The transformation could be accomplished by inserting one lithium per $MoS_2$ into the lattice and then letting it convert to the new phase. This system formed the foundation of a commercial battery developed by MoliEnergy in British Columbia.

Layered dichalcogenides of transition metals are limited by the fact that only one alkali metal per $MX_2$ can be incorporated in a useful voltage range. Attempts have been made to increase the energy storage capacity by using other low-dimensional materials such as the trichalcogenides $MX_3$ (with M = transition metal of the IVA or VA groups, and X = S, Se), following the original innovation due to Trumbore and co-workers [71] with their research on the electrochemical behavior of $NbSe_3$,

which was found to react reversibly with three lithium ions to form $Li_3NbSe_3$ in a single phase; other trichalcogenides were found also to readily react with lithium but not in such a reversible manner. In this connection, materials such as $MoO_3$, $V_2O_5$, and $NbSe_4$, where either the metal is in a high formal oxidation state, e.g., $Mo^{VI}O_3$, or there exist polychalcogen bonds, have been shown in principle to give increased capacity for reaction with alkali metals. Also, layered chalcogenophosphates of the general formula $MPX_3$ (M = transition metal; X = S, Se) have been considered for use as cathode materials in room-temperature lithium batteries [72]. In most systems studied, however, substantial structural rearrangements occur, which limit reversibility at ambient temperature, and the compounds are inferior in performance to the layered dichalcogenides.

Amorphous materials with low densities often show better properties as the cathode and/or anode in lithium secondary cells than the corresponding crystalline compounds. This is because they may possess a wider space for $Li^+$ diffusion, while also the absence of long range order in their structure leads to improvement of cycle life. Miki et al. [73] synthesized an amorphous $MoS_2$ powder and found that the lithium diffusion coefficient into this material was higher by several orders of magnitude than in the crystalline structure. Amorphous $MoS_2$ has been shown to afford a high degree of reversibility and a continuous discharge profile when used as the cathode active material in lithium batteries. It has been claimed by the group of Whittingham [74] that of all possible candidates for a lithium-active cathode, the amorphous trisulfide $MoS_3$ offers perhaps the best possibilities. This compound, as prepared by chemical or thermal decomposition of $(NH_4)_2MoS_4$, was found to react readily with $n$-butyl lithium and sodium or potassium naphthalides to give compositions $M_xMOS_3$ ($0 < x \leq 4$, M = Li, Na, K). Electrochemically, $MoS_3$ cathodes in lithium cells reacted with up to 3.8 Li per $MoS_3$ under constant current conditions ($0.5$ mA $cm^{-2}$) above 1.40 V. The mean discharge voltage of $Li/MoS_3$ was close to 2.0 V which together with the high coulombic capacity gave rise to a high theoretical energy density for the resulting cell. On recharge at constant current the system showed good reversibility.

Amorphous titanium and molybdenum oxysulfide ($TiO_yS_z$ and $MoO_yS_z$) thin films deposited by reactive radio-frequency magnetron sputtering have been used as active materials in lithium cells. The operation of such cells is based on reversible $Li^+$ insertion into the single-phase host material (producing, e.g., $Li_xMoO_yS_z$). The all-solid-state thin film lithium generators known as *microbatteries* appeared for the first time in the 1989 work of Meunier et al. [75], using RF-sputtered $TiO_yS_z$ films as cathodes, oxide glass electrolyte, and an evaporated lithium anode. More than 50 cycles were readily obtained in the Meunier cells for current densities up to 62 $\mu$A $cm^{-2}$. The wide composition range accessible for the amorphous $TiO_yS_z$ and the large electrochemical stability window of the cell components were emphasized [76]. Later electrochemical studies on sputtered, amorphous $MoO_yS_z$ films showed that the Li intercalation process strongly depends on the composition of these films [77]. In specific, it was found that up to 3.5 mole lithium per mole molybdenum can be intercalated in films with high oxygen content and 1.7 in the others. The Li diffusion coefficient was found equal to $10^{-13}$ $cm^2$ $s^{-1}$ at the beginning of the intercalation. It was noted that intercalation of the first Li is never reversible.

Thin film lithium batteries using sputtered $TiO_{0.2}S_{1.4}$ or $MoO_{1.6}S_{1.8}$ have reached the pre-industrial level of realization. These cells use glassy oxide-based electrolyte film with a thickness similar to the cathode, deposited by the same technique, and negative lithium electrode (4–5 $\mu$m thick) obtained by vacuum evaporation [67]. Alternative electrolytes and/or preparation methods have been tested also for implementing novel layouts. One example is the cells of Yufit et al. [78] comprising hybrid gel electrolyte (HPE) or composite solid polymer electrolyte (SPE), and molybdenum oxysulfides as cathodes. In this work, $MoO_yS_z$ films of sub-micron thickness and stoichiometry varying with depth were prepared on nickel foils or nickel-coated silicon substrates by the Ponomarev's electrodeposition technique. The charge/discharge cycling of the lithium cells indicated a satisfactory behavior both at room and at high temperatures. A Li/HPE/$MoO_yS_z$-on-nickel cell ran at discharge and charge currents of 100 $\mu$A cm$^{-2}$ and room temperature for 1,000 charge/discharge cycles with 0.05% per cycle capacity loss and 100% faradaic efficiency. The cell with the cathode deposited on nickel-coated silicon showed similar capacity loss and efficiency under the same operating conditions. Cells with SPE, cycled at 125 °C, showed a higher per cycle capacity loss of 0.5%. In a related work [79], the physicochemical and structural attributes of electrolytic molybdenum hydroxydisulfide compounds deposited from aqueous molybdate, thiosulfate solutions were investigated. Thin layer electrodes, prepared from as-grown molybdenum oxydisulfides, were tested in a laboratory lithium cell configuration.

Further, tungsten oxysulfide films, $WO_yS_z$, have shown promising behavior as positive electrodes in microbatteries, unlike $WS_2$ that is not suitable as cathode in lithium cells. Using amorphous thin films of $WO_{1.05}S_2$ and $WO_{1.35}S_{2.2}$ in the cell Li/LiAsF$_6$, 1 M ethyl-methyl sulfone (EMS)/$WO_yS_z$, Martin-Litas et al. [80] obtained current densities up to 37 $\mu$A cm$^{-2}$ between 1.6 and 3 V. In these cathode materials, 0.6 and 0.8 lithium per formula unit, respectively, could be intercalated and de-intercalated reversibly.

## 6.2.4  Mg-Ion Intercalation

In order to increase battery capacity, materials are needed in which the electrochemically active ions undergo redox changes of more than one electron (e.g., $Ni^{2+}$–$Ni^{4+}$, $V^{3+}$–$V^{5+}$) in a narrow voltage window, maintaining capacity at high charge/discharge rates.

The thermodynamic properties of magnesium make it a natural choice for use as an anode material in rechargeable batteries, as it may provide a considerably higher energy density than the commonly used lead-acid and nickel–cadmium systems, while in contrast to Pb and Cd, magnesium is inexpensive, environmentally friendly, and safe to handle. However, the development of Mg-ion batteries has so far been limited by the kinetics of $Mg^{2+}$ diffusion and the lack of suitable electrolytes. Actually, in spite of an expected general similarity between the processes of Li and Mg ion insertion into inorganic host materials, most of the compounds that exhibit fast and reversible Li ion insertion perform very poorly in $Mg^{2+}$ ions. Hence, there

is only very limited selection of intercalation materials for cathodes of rechargeable Mg batteries, and it is considered that chemistry in this area may be enabled only by moving away from the oxide systems relevant to lithium cell technology. In addition, the chemical activity of Mg constrains the possible Mg-conducting electrolytes only to solutions that neither donate nor accept protons; but most of these solutions allow the growth of passivating surface films, which inhibit any electrochemical reaction.

Following their investigations on the electrochemistry of Mg electrodes in various non-aqueous solutions and a variety of intercalation electrodes, Aurbach and co-workers [12–83] developed promising rechargeable Mg battery systems with specific capacity around 90–100 mA h g$^{-1}$(based on the active components), reasonable rates, and good cyclability. These researchers utilized composite cathodes comprising Chevrel-phase $Mo_6S_8$ as the active mass together with carbon and a polymeric binder, Mg-foil anodes, and electrolytes based on Mg organohaloaluminate salts, namely solutions of complexes of the stoichiometric formulae $Mg(AlCl_2R_2)_2$, R = $-CH_3$, $C_2H_5$, $C_4H_9$ (Me, Et, Bu) in ether solvents such as THF. These authors have concluded that the pure Chevrel framework, $Mo_6X_8$ (X = S, Se), is a unique cathode material for secondary Mg batteries. In contrast to many other known intercalation compounds that show excellent activity with Li$^+$, but extremely poor activity with Mg$^{2+}$ ions, $Mo_6X_8$ inserts two Mg$^{2+}$ ions per formula unit reversibly and relatively rapidly. In effect, up to now, only the Chevrel-phase cathodes exhibit sufficiently fast and reversible Mg$^{2+}$ insertion, for the development of practical rechargeable batteries. Further improvements in the energy density might render these batteries a viable alternative to existing systems.

### 6.2.5 High-Power Batteries and Related Types

#### 6.2.5.1 Sulfur-based Cathode

A rational candidate for high-energy/power secondary battery applications has been the non-aqueous lithium/(elemental)sulfur (Li/S) system, since for all the redox couples enabling for rechargeable batteries the Li–S couple has almost the highest theoretical specific energy of 2,600 W h kg$^{-1}$ (assuming complete reaction to the product $Li_2S$ upon discharge). That is because the theoretical capacity of sulfur is highest (1,672 mA h g$^{-1}$) among solid compounds known for primary and rechargeable cathodes [84], not to mention the advantages of its natural abundance, low cost, and low toxicity. Solid sulfur is both ionically and electronically resistive ($\sim 5 \times 10^{-30}$ S cm$^{-1}$ at 25 °C), so that high temperatures are required to operate a Li/S cell with a 100% sulfur cathode. Rechargeable Li/S batteries operating at around 450 °C, with two liquid active electrodes and a liquid molten salt electrolyte such as the LiCl–KCl eutectic, have been developed and tested since the early 1970s. However, the problems with electrode containment proved insurmountable. The discharge reaction of sulfur involves stepwise reduction processes and generates various forms of soluble intermediate polysulfides, which can dissolve in liquid electrolytes and cause

a rapid irreversible fading of capacity at repeated cycles [85]. Further, deprivation of the Li electrode in the molten salt and dendrite formation limits the cell performance. A practical Li/S cell must therefore incorporate a robust anode in a suitable electrolyte as well as well-distributed electronically and $Li^+$-conducting phases in the positive "sulfur" electrode. Workable batteries were developed by alloying Li with Al or Si and by replacing elemental S by metal sulfides of high sulfur activity to yield solid active materials at the typical operating temperature of the cells. A variety of metal sulfides were examined for this purpose including those of copper, iron, nickel, chromium, and cobalt. Cost considerations led to the selection of FeS and $FeS_2$ for commercial applications; prismatic Li–Al/LiCl–KCl/FeS or bipolar Li–Al/LiCl–LiBr–KBr/FeS(or $FeS_2$) cells and batteries operating in the range of 450–500 and 400–450 °C, respectively, were manufactured for electric van and stationary energy storage applications [86–88]; however, these designs turned out to be unpractical, and development ceased around 1990 when corrosion, temperature, and other issues overwhelmed the advantages of the system.

Obviously, solid electrolytes with high ionic conductivity below the melting temperatures of the electrode elements would allow the development of all-solid-state Li/S batteries and are highly desirable. Efficient performance at lower operation temperatures, with suppression of intermediate polysulfide dissolution, has been pursued by using organosulfur compounds, carbon–sulfur composites, and conductive polymer–sulfur composites instead of elemental sulfur. The influence of solid polymer electrolytes on the discharge performance of sulfur cathodes at temperatures ranging from ambient to about 100 °C has been discussed [89]. Interestingly, a novel room-temperature ionic liquid imide (PP14-RTIL) was synthesized recently [90] and found to be an electrochemically stable and workable electrolyte for lithium and sulfur electrodes, presenting a wide potential window of 5.2 to –0.15 V (vs. $Li/Li^+$). Charge–discharge experiments with the Li/RTIL/S cells showed that the sulfur cathode could achieve a high initial capacity of 1,055 mA h $g^{-1}$ maintaining a reversible capacity of ca. 750 mA h $g^{-1}$ after a few cycles. Improved performance was claimed as compared to the sulfur cathodes cycled in organic liquid or polymer electrolytes.

The most successfully developed high-temperature rechargeable cell with a sulfur cathode is the *sodium/sulfur* cell. The use of sodium metal as the negative electrode instead of lithium in high-power sources is quite attractive, on account of its highly negative reduction potential (–2.71 V vs. SHE), its low weight, non-toxic nature, relative abundance, and low cost. Thereby, much development work has been undertaken since the mid-1960s on batteries using sodium as an anode. However, in order to construct practical sodium-based batteries the metal must be used in liquid form, and since its melting point is 98 °C, they must operate at high temperatures, typically in excess of 270 °C. The relevant research in conjunction with the progress in solid electrolytes led to the invention of the high-power sodium/sulfur secondary battery, which typically uses molten sodium at the anode, liquid (molten) sodium polysulfide and sulfur inserted in porous graphite at the cathode, and beta alumina solid electrolyte ($\beta$-$Al_2O_3$) as a $Na^+$ ion conductor. The Na/S battery together with the *solid oxide fuel cells* (SOFC) using oxide ion conductors [91] comprises

actually the two presently most well-established types of high-power batteries that use ion-conducting ceramic electrolytes.

Upon discharge of the Na/S cell, the sodium level at the anode drops and sodium ions move to the cathode producing polysulfides (e.g., $Na_2S_4$). The beta alumina electrolyte is a good conductor for $Na^+$ but a poor one for electrons, preventing thus self-discharge. The normal discharge process, however, is reversible as charging causes sodium polysulfides to release the $Na^+$ back through the electrolyte to recombine as elemental Na. Once running, the heat produced by charging and discharging cycles is sufficient to maintain operating temperatures (300–350 °C) and usually no external thermal source is required. Na/S batteries based on these cells afford large-scale energy storage at low material cost, long cycle life, and high specific energy and power. They have a typical life of ~2,500 cycles, and their typical energy and power density are in the range of 150–240 and 150–230 W kg$^{-1}$, respectively. The energy density is many times greater than that of the customary lead batteries, and the materials needed for the electrolytes and electrodes are available in large quantities [92].

However, the realization of Na/S battery has a number of difficulties to overcome. One of the severe problems has been its high operating temperature, above 300 °C, which could induce explosions, corrosion, and power consumption to maintain heating at the working condition. Based on the successful development of Li-ion batteries, several groups have tried to develop room-temperature sodium ion batteries, which are considered as promising substitutes for the former in various application areas. In a low-temperature Na/S battery, the sulfur cathode will incur the same problems as in Li/S batteries: mainly, low utilization of active material, poor rechargeability, and dissolution of polysulfides into the electrolyte. Several kinds of polymer electrolytes have been studied to serve as sodium ion conducting electrolytes at low temperatures. Examples are polyethylene oxide (PEO) with sodium trifluoromethane sulfonate ($NaCF_3SO_3$) and sodium nitrate ($NaNO_3$), poly(ethylene glycol) dimethyl ethers (PEGDME), or polyvinylidene fluoride-hexafluoropropene (PVDF) [93].

Recently, Park et al. [94] examined the possibility to fabricate an all-solid-state sodium/sulfur cell operating at room temperature, using the PVDF gel polymer electrolyte, and compared their results to the high-temperature Na/S battery. The cell showed a high initial discharge capacity of 489 mA h g$^{-1}$ sulfur at room temperature with two plateau potential regions at 2.28 and 1.28 V. According to XRD results and thermodynamic considerations the authors concluded that the lower plateau region should be due to the formation of $Na_2S_2$ and $Na_2S_3$. The discharge capacity of the cell decreased continuously during repeated charge–discharge cycling and remained at 40 mA h g$^{-1}$ after 20 cycles, i.e., the cell had a much shorter cycle life than the high-temperature Na/S battery. It was noted though that the theoretical specific energy of the Na/S cell operating at room temperature is 954 W h kg$^{-1}$, i.e., higher than that of the high-temperature cell. The same group reported the electrochemical properties of an all-solid Na/S battery composed of a solid sulfur electrode, a sodium metal electrode, and a solid PEO polymer electrolyte, operated at 90 °C [95]. During the first discharge, the battery showed plateau potentials at 2.27 and 1.76 V. The first

discharge capacity was 505 mA h g$^{-1}$ sulfur at 90 °C. From thermodynamic considerations, the authors claimed that the lower plateau region should originate from the formation of Na$_2$S, Na$_2$S$_2$, and Na$_2$S$_3$ and the upper plateau region from Na$_2$S$_4$ and Na$_2$S$_5$. The discharge capacity decreased continuously during repeated charge–discharge cycling and remained at 166 mA h g$^{-1}$ sulfur after 10 cycles. The latter value was higher than the previously reported value for the Na/PVDF/S battery at room temperature.

Wang et al. [96] constructed a Na/S battery with a sodium metal anode, liquid electrolyte, and a sulfur (dispersed in polyacrylonitrile) composite cathode and tested its electrochemical characteristics at room temperature. The charge/discharge curves indicated that sodium could reversibly react with the composite cathode at room temperature. Average charge and discharge voltage was 1.8 and 1.4 V, respectively. Similar to lithium batteries, dendrite formation was noted as a critical problem for these cells.

Cuprous sulfide (Cu$_2$S) is one of the potential candidates for cathode materials of sodium batteries, as it has high theoretical capacity and low material cost due to occurrence of chalcocite ore in nature. A Na/Cu$_2$S rechargeable cell of a high coulombic efficiency, using NaCF$_3$SO$_3$-TEGDME (tetra ethylene glycol dimethyl ether) liquid electrolyte at room temperature was reported recently [97]. Cell operation showed a discharge curve representing a slope-shape profile without distinct plateau potential regions. The first discharge capacity was 294 mA h g$^{-1}$ at room temperature, which decreased to 220 mA h g$^{-1}$ after the 20th cycle. The discharge process could be illustrated by intercalation of sodium into the Cu$_2$S phase without phase separation of Cu$_2$S, according to the scheme

$$Cu_2S + xNa \rightarrow Na_xCu_2S \qquad (x < 2)$$

The results implied a maximum intercalation of 1.75 sodium atoms into the Cu$_2$S.

Other metal sulfides such as Na/Ni$_3$S$_2$, Na/FeS$_2$ have been reported to exhibit good electrochemical properties as cathodes in the Na/S battery at room temperature [98].

An alternative ambient temperature design based on sodium ion reaction refers to the domain of the so-called *flow batteries*. The polysulfide bromide cell (PSB) provides a reversible electrochemical reaction between two salt solution electrolytes (sodium bromide and sodium polysulfide), according to the scheme

$$3NaBr + Na_2S_4 \rightleftarrows 2Na_2S_2 + NaBr_3$$
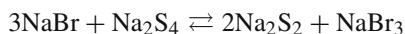
PSB electrolytes are brought close together in the battery cells where they are separated by a polymer membrane that only allows Na$^+$ ions to go through, producing about 1.5 V across the membrane. Cells are electrically connected in series and parallel to obtain the desired voltage and current levels. The net efficiency of this battery working at room temperature is about 75%. It has been verified in the laboratory and demonstrated at multi-kW scale in the UK [92].

### 6.2.5.2 Se- and Te-based Cathodes

Tellurium has been tested as a cathode material for use in conjunction with an anode made of alkali metal, primarily lithium, in power sources with a high specific energy and power [99]. The theoretical specific energy for Li/Te pair is 612 W h $kg^{-1}$. High-temperature (470 °C) cells with Li, Te, and eutectic (LiF–LiCl–LiI) electrolyte in the molten state, or with more convenient, albeit more resistive, paste-type electrolytes, have been tested in the laboratory. Similar layouts have been proposed for utilizing the Li/Se pair (theoretic cal specific energy 1,210 W h $kg^{-1}$) with the cell ingredients in the molten state (365 °C) or with paste electrolyte at a lower temperature.

Since the inception of the solid-state ionics field, there have been also a few early attempts to utilize elemental tellurium and selenium or their compounds as the oxidizing electrode in thin film cell configurations with a solid electrolyte. A general review covering the early literature, up to 1976, on the fabrication and properties of thin film solid electrolyte materials, including silver compounds, lithium iodide, metal fluorides, metal oxides, and metal chlorides, and their use in electrochemical cells, has been given by Kennedy [100]. The use of some chalcogen-containing cathode electrodes or solid electrolytes in thin film cells can be traced in those early works. Solid-state battery systems based on inorganic materials have been discussed by Linford [101] with emphasis on room-temperature applications.

Takahashi and Yamamoto [102] demonstrated solid cells of the type Ag/RbAg$_4$I$_5$/X (X = Te, Se), where silver was used as the anode, the solid electrolyte RbAg$_4$I$_5$ being a good Ag$^+$ ionic conductor even at room temperature. The cells with Te cathode showed open-circuit voltages around 0.22 V, while the corresponding Se-cathode cells gave values around 0.27 V (at 20–100 °C). The maintenance of a low discharge plateau voltage provided by these layouts using chalcogen cathodes was suggested by the low decomposition potential (0.68 V) of the silver iodide electrolyte severely limiting the number of available cathode materials for practical operation. The primary advantage of Te over Se (and also over iodine or TeI$_4$) was its higher electronic conductivity, thereby leading to realization of cells with better discharge characteristics; vacuum-deposited tellurium cathodes 10 μm thick could support currents of 2 mA $cm^{-2}$. Aside from elemental chalcogens, compounds with low free energies of formation such as Ag$_2$Se and Ag$_2$Te could be conveniently used as cathodes for solid-state batteries using Ag$^+$ ionic conductors. Further, pressed powder thin films of β-Ag$_2$Se and β-Ag$_2$Te have been proposed as electrode materials in Ag/RbAg$_4$I$_5$/Ag$_2$Te or Ag/Ag$_6$I$_4$WO$_4$/Ag$_2$Se cells serving as memory devices, variable resistors, or switching cell-timers [103, 101]. Such electrochemical units are often called *chemotronic components*, this term connoting galvanic cells containing solid electrolytes, which find use in electrical circuits.

Let us note finally, that tellurium has been considered as an appropriate component for the lead grid alloy in lead-acid batteries, as improving its durability, mechanical strength, and anti-corrosive ability. In investigating Pb–Te binary alloys with different contents of Te (0.01–1.0 wt%) in sulfuric acid solution it was shown recently [104] that the introduction of Te can inhibit the growth of PbO$_2$ and increase corrosion resistance of the positive grid alloy of a lead-acid battery. By the

introduction of Te to lead, and irrespective of the Te content, oxygen evolution was found to be accelerated in these experiments.

### 6.2.5.3  Thermal Batteries

Thermal batteries are high-temperature power sources of the primary cell type, operating typically between 350 and 550 °C, that use an ionically conducting molten salt in the separator between the anode and the cathode. A typical cell uses lithium as the negative electrode and a metal sulfide as the positive electrode, the primary compounds in use today being (pyrite) $FeS_2$ and synthetic $CoS_2$ (for high-rate applications). Typically, the cell parts are pressed from powdered mixtures. The usual electrolytes melt between 319 and 436 °C, with the LiCl–KCl eutectic being the most common. Thermal batteries are commonly used in military applications that require a burst of power for a short time (a few seconds to a few minutes). They usually are application specific and have high labor costs which tend to make them somewhat expensive.

An overview of the history of thermally activated batteries, and a description of the mechanisms of discharge of the currently prevailing Li-alloy/$FeS_2$ and Li-alloy/$CoS_2$ chemistries, can be found in the work of Guidotti and Masset [105–107]. In the second of these papers, the authors examine the physicochemical properties and electrochemical performance of the pyrite $FeS_2$ cathode, including the discharge mechanisms, self-discharge phenomena, and recent developments. In the third paper, an overview is presented of, other than $FeS_2$, materials that have been used or evaluated for use as thermal-battery cathodes. Typically, these are thermally stable at the battery operation temperatures (up to 600 °C) and are mainly sulfides ($FeS$, $NiS_2$, $NiS$, $Fe_{0.2}Co_{0.8}S_2$) and, to lesser extent, oxides. The use of $CoS_2$ is preferred over $FeS_2$ for high-power and high-rate application because of the higher electrical conductivity and greater thermal stability of $CoS_2$.

## 6.3  Ion-Selective Electrodes

Devices called sensors, which are sensitive to physical influences other than electricity and light, like pressure, temperature, chemical concentrations, or magnetic fields, can convert non-electric signals into electrical ones (see, e.g., the review of Janata [108] for chemical sensors).

Electrochemical sensors play a crucial role in environmental and industrial monitoring, as well as in medical and clinical analysis. The common feature of all electroanalytical sensors is that they rely on the detection of an electrical property (i.e., potential, resistance, current) so that they are normally classified according to the mode of measurement (i.e., potentiometric, conductometric, amperometric). A number of surveys have been published on this immense field. The reader may find the major part of the older and recent bibliography in the comprehensive reviews of Bakker et al. [109–111]. Pejcic and De Marco have presented an interesting survey

on electrochemical sensors in connection with the use of electrochemical impedance spectroscopy (EIS) as a characterization technique [112].

Potentiometric sensors comprise the oldest and largest electrochemical sensor field and one of the best described. In many ways, it serves as a role model for other sensor areas [113]. Also known as ion-selective electrodes (ISEs), potentiometric sensors encompass a large subset of electrochemical sensors, which comprise an ion-conducting membrane that can be either a solid (i.e., glass, inorganic crystal) or a plasticized polymer, in many cases with a unique composition chosen in order to impart a potential that is primarily associated with the ion of interest via a selective binding process at the membrane–electrolyte interface. The magnitude of the surface potential is directly related to the activity or number of primary ions in solution according to the Nernst equation. It has been suggested that the selective response mechanism of potentiometric sensors involves chemisorption [114] and/or phase-boundary potential model [115]. By far, the most widely used and successful potentiometric sensor is the pH glass electrode. Most commercial ISEs are typically configured as self-supporting disk-type membranes with liquid or solid internal contact. If there are no free-flowing liquids used in the electrode construction, then one refers to all-solid-state electrodes.

Crystalline-based ISEs comprise a large family of inorganic materials that act as ionic conductors at room temperature and which undergo ion exchange reactions at the membrane/solution interface. Membranes of these sensors may be classified primarily as (1) pressed powder pellets, (2) single crystals, and (3) powdered salts held together by an inert binder. The crystalline material may be a single compound (e.g., $Ag_2S$) or a homogeneous mixture of compounds (e.g., $AgI$–$Ag_2S$); if the mechanical properties of the pressed pellet are unsatisfactory it may be advantageous to embed the crystals into an inert polymer matrix, such as silicone rubber, to make the so-called heterogeneous membranes. Further, polycrystalline thin layers, typically deposited on a metal surface by electrolysis or by vacuum deposition techniques, may be used as electrodes. Note also that amorphous or glassy solids are used successfully as membrane materials in ISEs; amorphous membranes, with the exception of silicate-type glasses, are conventionally regarded as solid electrodes; however, the term "glass electrode" is retained also for electrodes with membranes composed of different vitreous materials as with chalcogenide glasses, to be discussed next.

Polycrystalline metal chalcogenides, e.g., insoluble pressed sulfides and selenides, are broadly used as membrane materials. Silver sulfide ($Ag_2S$) is an excellent material for a solid-state electrode, responding to both silver and sulfide ions with good practical detection limits ($10^{-8}$–$10^{-7}$ mol l$^{-1}$) in Nernstian manner. Important applications of this electrode are the direct determination of sulfide (or other sulfur-containing species converted to sulfide) in aqueous solutions [116] and as an indicator electrode in argentometric titrations. The electrode has a very low solubility and only few potentiometric interferences ($CN^-$, $Hg^{2+}$). It can be easily compressed into mechanically stable pellets and it is also accessible as single crystal for electrodes. At ambient conditions (below 176 °C), its monoclinic modification, acanthite, is stable and shows high ionic conductivity due to silver ions.

There has been a great deal of work reported in the literature on the analysis of copper(II) in various systems using a pressed pellet of $CuS–Ag_2S$ [117]. It has been shown that a ternary sulfide called jalpaite (i.e., $Ag_{1.5}Cu_{0.5}S$) leads to desirable electrochemical and electroanalytical properties for the detection of Cu(II) in natural waters [118].

## 6.3.1 Chalcogenide Glass Sensors

Because of their high chemical stability and appropriate analytical characteristics, vitreous materials can be used in cases where potentiometry could not previously have been used. Chalcogenide glass sensors (CGS) are already known for three decades and have been applied successfully for the detection of various metal ions in aqueous media. The membrane probe of these sensors is composed of amorphous solids that are binary, ternary, or multicomponent compounds/alloys of IIIB, IVB, or VB (Groups 13–15) elements (i.e., boron, aluminum, gallium, germanium, phosphorus, arsenic, antimony) with sulfur, selenium, or tellurium. These systems can be both stoichiometric (e.g., $As_2S_3$, $GeS_2$) and non-stoichiometric (e.g., $As_xSe_{1-x}$), and they are often doped with transition metals and alkali metals. Oxychalcogenide and chalcohalide glasses can also be synthesized. A variety of stable chalcogenide glasses can be prepared in bulk, fiber, thin film, and multilayer forms using melt quenching, vacuum deposition, and other less common techniques, such as spin coating and mechanical amorphization [119]. Typical glass membranes are obtained by melting the components and forming the membrane proper from the homogeneous melt. A CG membrane is obtained as a disk cut from the solidified melt, and after polishing it is pasted into the plastic body in a way similar to that for crystalline ion-selective electrodes.

Most CGs possess electrical and optical band gaps of 1–3 eV and accordingly they can be regarded as amorphous semiconductors. The gap decreases in the sequence of sulfur, selenium, and tellurium compounds, reflecting the increasing metallic character in this direction. The electronic structure of a chalcogenide glass is essentially the same as that of the corresponding crystal; however, glasses exhibit smaller electrical conductivities than the latter, because the electronic mobility is suppressed by band-tail and gap states, which are manifestations of disordered structures; thereby, sulfide glasses such as $As_2S_3$ and $GeS_2$ behave as insulators. On the other hand, the carrier density of intrinsic semiconductor glasses is similar to that in the corresponding crystal as governed by the band gap energy, which is not more than $\sim \pm10\%$ different. Hole conduction in CGs is greater than electron conduction; therefore these glasses can be regarded as p-type semiconductors. Further, some CGs behave as (super)ionic conductors, exhibiting thus a mixed ionic or electronic conductance. In effect, the way that a CG functions is not yet clear. It may be sensitive to powerful redox systems, its characteristics may be influenced by doping, and its behavior is often non-Nernstian.

Compared to the corresponding polycrystalline metal chalcogenides, chalcogenide glasses exhibit better chemical stability in acidic and redox media and often

possess better selectivity and reproducibility of analytical characteristics and longer life time. For instance, the CG Cu(II)-ISEs are 10–30 times more sensitive in strong acidic solutions than the polycrystalline $Cu_{18}Se$ and $CuS + Ag_2S$ membranes. Due to these advantages, the CG have become preferred membrane materials in ISEs for determination of $Ag^+$, $Cd^{2+}$, $Pb^{2+}$, and $Cu^{2+}$ ions, instead of their crystalline analogues.

Initial data on the manufacture of CG sensor elements have been reported in the period 1971–1974. Trachtenberg and co-workers were the first to use CG membranes as potentiometric sensors for determination of metal ions in aqueous solution. In 1971 [120], they reported the development of ISE with active material prepared from Fe-, Co-, and Ni-doped chalcogenide glasses (28% Ge, 60% Se, 12% Sb), which responded to $Fe^{+3}$ and $Cu^{+2}$ at concentrations as low as $10^{-6}$ M. Later, it was shown that properly prepared and activated $Fe_nSe_{60}Ge_{28}Sb_{12}$ electrodes ($1.3 < n < 2$) respond to changes in ferric ion concentration in perchlorate, chloride, and nitrate solutions and information was presented on the ferric ion sensing mechanism of the chalcogenide glass [121]. Further, electrodes formed from the chalcogenide glass $Cu–As_2S_3$, whose active component was considered to be a "sinnerite" ($Cu_6As_4S_9$) phase, were described as being selective to cupric copper in concentrated solutions of chloride, bromide, nitrate, and acetate [122].

Early results on CG all-solid-state sensor compositions and characteristics, for selective sensing of Cu(II), Fe(III), Cr(VI), Cd(II), Hg(II) ions in solution, have been surveyed by Vlasov et al. [123]. Presently, multicomponent CGs are investigated as membranes in potentiometric, single or multisensor systems, directed for use in process control, environmental management, and seawater analyses (for example, consider the work of Vassilev and co-workers on the glass formation in the three-component systems $Ag_2Te–As_2Se_3–CdTe$ [124], and $GeSe_2–Sb_2Se_3–PbSe$ [125], $GeSe_2–PbSe–PbTe$ [126], for Cd(II)- and Pb(II)-ISE applications, respectively). Importantly, the introduction of halogen atoms in the chalcogenide glass-former network, giving rise to chalcohalide glasses, enhances the defectiveness and flexibility of the structure, facilitating ion mobility and exchange between the membrane surface layer and the investigated solution [127]. Hence, chalcohalide glasses may be advantageously used for ISE. Preponderate chalcogenide and chalcohalide glass-forming systems investigated as membrane materials for chemical sensors, microsensors, and multisensor systems have been summarized in the review of Vassilev and Boycheva [128].

Regarding the probe form, considerable interest exists today for the construction of thin film chemical microsensors, following the trends for device miniaturization, raw materials economy, and ecologic production considerations [129]. A wide range of CG alloys meet the requirements of such devices. Further, it has been demonstrated that the problem of insufficient selectivity of single sensors can be surmounted by using arrays based on chalcogenide thin film chemical sensors, so-called "electronic tongues," which exhibit wide cross sensitivity to a number of cations combined with good chemical durability [130]. Thereby, different chalcogenide glass materials have been used to make arrays of miniaturized ISEs. The use of such sensor arrays or multisensor systems is a promising way to cope with the complications of on-site measurements, i.e., continuous

application directly in the analyzing media, which is quite desirable for environmental pollution control [131]. Along this line, CG multisensor systems based on arrays of non-specific CG sensors have been used in combination with processing of their complex signals by pattern recognition methods, for determination of inorganic pollutants in river, ground, sea and waste waters, for corrosion process monitoring of technological equipment, technological electrolyses process control, beverages and foodstuffs control ([128] and references therein).

Perhaps the most innovative research direction in potentiometric sensors has been and continues to be the remarkable improvement of lower detection limit, which has been accomplished by novel CG-ISEs. As an illustration, we should refer to the monitoring of trace metals in natural waters; this is an important task since the speciation/distribution along with the biological and geochemical cycling of various elements in the ocean is of significant interest in environment safety issues. A characteristic example is the potentiometric detection of mercury(II) by chalcogenide glass ISE. The effectiveness of a CG-based Hg(II) sensor (membrane composition not reported) in various media was first demonstrated by Vlasov et al. [123]. De Marco and Shackleton [132] investigated the ability of a similar commercial chalcogenide Hg(II) ISE of unknown membrane composition in measuring free Hg(II) levels in seawater. The researchers obtained a near-Nernstian response over 19 orders of magnitude (i.e., $10^{-20}$–$10^{-1}$ M Hg$^{2+}$) in chloride-free unbuffered and saline-buffered standards. It was shown that chloride does not interfere with the Hg(II) ISE response; however, when the electrode was exposed to seawater the formation of a passive film was observed. Extended aging in seawater induced a memory effect causing the electrode to respond in a sub-Nernstian fashion. The group studied the constituents of the commercial ISE using a range of analytical techniques and fabricated a comparable sensor with a AgBr–Ag$_2$S–As$_2$S$_3$–HgI$_2$ membrane, which behaved in a similar fashion to the commercial electrode. By using a range of surface analysis techniques it was shown that the fouling of the fabricated electrode upon prolonged contact in saline solution was linked to the poisoning by silver salts [133]. A combination of XPS, SEM, and electrochemical impedance analysis revealed photooxidation, hydration, and arsenic depletion of the CG membrane as well as surface adsorption of mercury and variety of halides [134].

The development of a chalcogenide membrane to selectively probe the free Fe(III) concentration in seawater has also been undertaken by the group of De Marco. Detection limits were reported to be drastically lowered in the case of Fe$_{2.5}$Se$_{58.5}$Ge$_{27.3}$Sb$_{11.7}$ ISE [135]. Note that this and previous papers were disputed by van den Berg [136] who argued that the response obtained is not due to the ionic iron in the water, but due to the kinetics of iron diffusing away from the electrode or being complexed by ligands.

### 6.3.2 Biosensors

Biosensors play a significant role in the monitoring of a wide range of diseases and pathogens. A biosensor is an analytical device, which incorporates a biological recognition element or bioreceptor which is capable of sensing the presence,

activity, or concentration of a chemical analyte in solution. Recognition elements include enzymes as biocatalytic units, immuno-agents and DNA segments as affinity ligand recognition elements, coupled to electrochemical and optical modes of transduction. It is stated recently, in the survey of D' Orazio [137], that more than half of the biosensors reported in the literature involve the electrochemical detection method (i.e., amperometric; potentiometric; capacitive; conductometric sensor-based). A striking example is the glucose sensor, widely used for the diagnoses and management of diabetes. The construction of biological assemblies on various conductive and semiconductive surfaces forms the basis of most electrochemical-based biosensors. Several reviews have been published discussing the relative merits of electrochemical-based biosensors [138, 139].

Enzyme sensors are based primarily on the immobilization of an enzyme onto an electrode, either a metallic electrode used in amperometry (e.g., detection of the enzyme-catalyzed oxidation of glucose) or an ISE employed in potentiometry (e.g., detection of the enzyme-catalyzed liberation of hydronium or ammonium ions). The first potentiometric enzyme electrode, which appeared in 1969 due to Guilbault and Montalvo [140], was a probe for urea with immobilized urease on a glass electrode. Hill and co-workers [141] described in 1986 the second-generation biosensor using ferrocene as a mediator. This device was later marketed as the "glucose pen". The development of enzyme-based sensors for the detection of glucose in blood represents a major area of biosensor research.

Particularly attractive for numerous bioanalytical applications are colloidal metal (e.g., gold) and semiconductor quantum dot nanoparticles. The conductivity and catalytic properties of such systems have been employed for developing electrochemical gas sensors, electrochemical sensors based on molecular- or polymer-functionalized nanoparticle sensing interfaces, and for the construction of different biosensors including enzyme-based electrodes, immunosensors, and DNA sensors. Advances in the application of molecular and biomolecular functionalized metal, semiconductor, and magnetic particles for electroanalytical and bio-electroanalytical applications have been reviewed by Katz et al. [142].

A semiconductor nanoparticle/enzyme hybrid system for photocurrent generation and biosensor applications has been demonstrated [143] by tailoring an acetylcholine esterase (AChE)-CdS nanoparticle hybrid monolayer on an Au electrode. AChE is a central neurotransmitter that activates the synapse and the neural response. CdS nanoparticles (3 nm) were capped with a protecting monolayer of cysteamine and mercaptoethane sulfonic acid, and the capped nanoparticles were covalently linked to a functionalized Au electrode. The AChE was then covalently linked to the CdS nanoparticles. The hybrid CdS/AChE system provided a functional interface for sensing of the AChE inhibitors by means of photocurrent measurements. The driving force for the formation of the photocurrent was the biocatalyzed formation of thiocholine that scavenges the photogenerated valence-band holes. A similar hybrid system composed of CdS nanoparticles and co-immobilized formaldehyde dehydrogenase that utilized formaldehyde as an electron donor (converting to formic acid) has been reported [144]. In this system direct electron transfer was achieved from the enzyme active center to the CdS photogenerated

holes. The steady-state photocurrent signal was reported to be directly related to the substrate concentration. The results suggested that the CdS nanocrystal system may comprise an effective photoactive material to replace the $NAD^+/NADH$ role as charge transfer in the enzymatic reaction.

The development of DNA sensors and high-density DNA arrays has been prompted by the tremendous demands for innovative analytical tools capable of delivering the genetic information in a faster, simpler, and cheaper manner at the sample source, compared to traditional nucleic acid assays. Nanoparticle–biopolymer conjugates offer great potential for DNA diagnostics and can have a profound impact upon bioanalytical chemistry. Nanoparticle/polynucleotide assemblies for advanced electrical detection of DNA sequences have been reviewed by Wang [145].

Photoelectrochemical transduction of DNA recognition processes has been demonstrated by using CdS nanoparticles modified with nucleic acids [146]. Wang et al. [147] demonstrated the use of CdS colloids for electrochemical monitoring of DNA hybridization. Their basic analytical protocol (Fig. 6.5) included the binding of a biotinylated target to streptavidin-coated magnetic beads, followed by hybridization to a CdS-labeled probe, dissolution of the CdS tag, and stripping potentiometric detection of the dissolved cadmium ion. Nanoparticle-promoted cadmium precipitation was used to enlarge the nanoparticle tag and amplify the stripping DNA hybridization signal. Further, solid-state detection of cadmium could be accomplished through "magnetic" collection of the DNA-linked nanoparticle network onto a thick-film electrode transducer.

This protocol was extended to other inorganic colloids (e.g., ZnS, PbS), and it was pointed out that such extension paves the way to an electrochemical coding technology for the simultaneous detection of multiple DNA targets based on nanocrystal tags with diverse redox potentials [148].

Electrogenerated chemiluminescence (ECL) has proved to be useful for analytical applications including organic analysis, ECL-based immunosensors, DNA probe assays, and enzymatic biosensors. In the last few years, the electrochemistry and ECL of compound semiconductor nanocrystallites have attracted much attention due to their potential applications in analytical chemistry (ECL sensors).
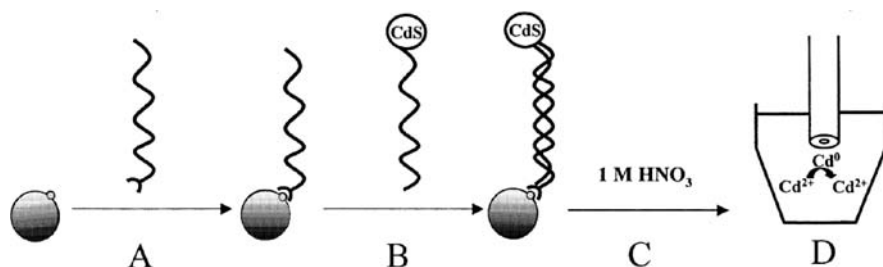


**Fig. 6.5**  Schematic representation of a bioelectronic protocol for detection of DNA hybridization: (**A**) binding of the target to magnetic beads; (**B**) hybridization with CdS-labeled probe; (**C**) dissolution of CdS tag; (**D**) potentiometric stripping detection at a mercury-film electrode. (Reprinted from [136], Copyright 2009, with permission from Elsevier)

In 2004, Poznyak et al. [149] first observed band gap chemiluminescence from CdSe and CdSe/CdS core–shell nanocrystals (Q-dots) in aqueous solution and in nanoparticulate layers. Efficient and stable electrogenerated chemiluminescence could be obtained by applying a cathodic potential to the nanocrystal films. Zou and Ju [150] studied the ECL of CdSe Q-dots deposited on a paraffin-impregnated graphite electrode (PIGE) and its first sensing application toward $H_2O_2$ detection in aqueous solution. Since then, the analytes detected by CdSe (or CdTe) nanocrystallites have been extended to catechol derivatives, scavengers of hydroxyl radical, glucose, tyrosine, and dopamine. In 2005, Ren et al. [151] observed ECL phenomena with CdS spherical assemblies consisting of CdS nanocrystals about 5 nm in diameter in both non-aqueous and aqueous solutions. The morphology of the spherical assemblies turned out to play an important role in maintaining the stability of partial electrogenerated species to generate the ECL light. In subsequent works, different morphologies of CdS nanomaterials with ECL properties were synthesized and further applied to the detection of $H_2O_2$ and low-density lipoprotein (LDL) [152]. The detection of LDL is of particular importance, as LDL is most closely associated with heart disease. Recently, Fang et al. [153] investigated the electrochemical and ECL properties of a glassy carbon electrode (CGC) modified with CdS nanotubes, in neutral aqueous media. The CdS nanotubes were immobilized on the GCE with Nafion, allowing a large number of them to be exposed to the solution. Stable ECL produced by a catalytic mechanism at the modified electrode was observed, and a detailed mechanism was discussed. Also, a strong catalytic current in the presence of nitrate with good linear correlation to concentration was observed, suggesting the potential applications of the CdS-CGE system in nitrate determination.

# References

1. Shi C, Steiger B, Anson FC (1995) Coordination chemistry in electrocatalysis. Pure Appl Chem 67: 319–322
2. Bockris JM, Minevski ZS (1994) Electrocatalysis: Past, Present and Future. Electrochim Acta 39: 1471–1479
3. Rolison DR (2003) Catalytic nanoarchitectures—the importance of nothing and the unimportance of periodicity. Science 299: 1698–1701
4. Carrete L, Friedrich KA, Stimming U (2000) Fuel cells: Principles, types, fuels, and applications. Chem Phys Chem 1: 162–193
5. Marković NM, Ross PN (2002) Surface science studies of model fuel cell electrocatalysts. Surf Sci Rep 45: 117–229
6. Alt H, Binder H, Sandstete G (1973) Mechanism of the electrocatalytic reduction of oxygen on metal chelates. J Catal 28: 8–19
7. Dodolet JP, Cote R, Faubert G, Denes G, Guay D, Bertrand P (1998) Iron catalysts prepared by high-temperature pyrolysis of tetraphenylporphyrins adsorbed on carbon black for oxygen reduction in polymer electrolyte fuel cells. Electrochim Acta 43: 341–353
8. Convert P, Countanceau C, Crouïgneau P, Gloaguen F, Lamy C (2001) Electrodes modified by electrodeposition of CoTAA complexes as selective oxygen cathodes in a direct methanol fuel cell. J Appl Electrochem 31: 945–952
9. Chevrel R, Sergent M, Prigent J (1971) Sur de nouvelles phases sulfurées ternaires du molybdène. J Solid State Chem 3: 515–519

10. Hughbanks T, Hoffmann R (1983) Molybdenum chalcogenides: Clusters, chains, and extended solids. The approach to bonding in three dimensions. J Am Chem Soc 105: 1150–1162

11. Alonso-Vante N, Schubert B, Tributsch H (1989) Transition metal cluster materials for multi-electron transfer catalysis. Mater Chem Phys 22: 281–307

12. Alonso-Vante N, Tributsch H (1986) Energy conversion catalysis using semiconducting transition metal cluster compounds. Nature 323: 431–432

13. Alonso-Vante N, Jaegermann W, Tributsch H, Hoenle W, Yvon K (1987) Electrocatalysis of oxygen reduction by chalcogenides containing mixed transition metal clusters. J Am Chem Soc 109: 3251–3257

14. Tavagnaco C, Moszner M, Cozzi S, Peressini S, Costa G (1998) Electrocatalytic dioxygen reduction in the presence of a rhodoxime. J Electroanal Chem 448: 41–50

15. Gates BC (1995) Supported metal clusters: Synthesis, structure, and catalysis. Chem Rev 95: 511–522

16. Solorza-Feria O, Ellmer K, Giersig M, Alonso-Vante N (1994) Novel low-temperature synthesis of semiconducting transition metal chalcogenide electrocatalyst for multielectron charge transfer: Molecular oxygen reduction. Electrochim Acta 39: 1647–1653

17. Trapp V, Christensen PA, Hamnett A (1996) New catalysts for oxygen reduction based on transition-metal sulfides. J Chem Soc Faraday Trans 92: 4311–4319

18. Alonso-Vante N, Tributsch H, Solorza-Feria O (1995) Kinetics studies of oxygen reduction in acid medium on novel semiconducting transition metal chalcogenides. Electrochim Acta 40: 567–576

19. Reeve RW, Christensen PA, Hamnett A, Haydock SA, Roy SC (1998) Methanol tolerant oxygen reduction catalysts based on transition metal sulfides. J Electrochem Soc 145: 3463–3471

20. Rodríguez FJ, Sebastian PJ, Solorza O, Pérez R (1998) Mo–Ru–W chalcogenide electrodes prepared by chemical synthesis and screen printing for fuel cell applications. Int J Hydrogen Energy 23: 1031–1035

21. Ozenler SS, Kadirgan F (2006) The effect of the matrix on the electro-catalytic properties of methanol tolerant oxygen reduction catalysts based on ruthenium-chalcogenides. J Power Sources 154: 364–369

22. Alonso-Vante N, Malakhov IV, Nikitenko SG, Savinova ER, Kochubey DI (2002) The structure analysis of the active centers of Ru-containing electrocatalysts for the oxygen reduction. An in situ EXAFS study. Electrochim Acta 47: 3807–3814

23. Bron M, Bogdanoff P, Fiechter S, Hilgendorff M, Radnik J, Dorbandt I, Schulenburg H, Tributsch HJ (2001) Carbon supported catalysts for oxygen reduction in acidic media prepared by thermolysis of $Ru_3(CO)_{12}$. Electroanal Chem 517: 85–94

24. Dassenoy F, Vogel W, Alonso-Vante N (2002) Structural Studies and Stability of Cluster-like $Ru_xSe_y$ Electrocatalysts. J Phys Chem B 106: 12152–12157

25. Cao D, Wieckowski A, Inukai J, Alonso-Vante N (2006) Oxygen reduction reaction on ruthenium and rhodium nanoparticles modified with selenium and sulfur. J Electrochem Soc 153: A869–A874

26. Lewera A, Inukai J, Zhou WP, Cao D, Duong HT, Alonso-Vante N, Wieckowski A (2007) Chalcogenide oxygen reduction reaction catalysis: X-ray photoelectron spectroscopy with Ru, Ru/Se and Ru/S samples emersed from aqueous media. Electrochim Acta 52: 5759–5765

27. Zaikovskii VI, Nagabhushana KS, Kriventsov VV, Loponov KN, Cherepanova SV, Kvon RI, Bönnemann H, Kochubey DI, Savinova ER (2006) Synthesis and structural characterization of Se-modified carbon-supported Ru nanoparticles for the oxygen reduction reaction. J Phys Chem B 110: 6881–6890

28. Babu PK, Lewera A, Chung JH, Hunger R, Jaegermann W, Alonso-Vante N, Wieckowski A, Oldfield E (2007) Selenium becomes metallic in Ru-Se fuel cell catalysts: An EC-NMR and XPS investigation. J Am Chem Soc 129: 15140–15141

29. Lee JW, Popov BN (2007) Ruthenium-based electrocatalysts for oxygen reduction reaction—a review. J Solid State Electrochem 11: 1355–1364
30. Behret H, Binder H, Sandstede G (1975) Electrocatalytic oxygen reduction with thiospinels and other sulphides of transition metals. Electrochim Acta 20: 111–117
31. Sidik RA, Anderson AB (2006) $Co_9S_8$ as a catalyst for electroreduction of $O_2$: Quantum chemistry predictions. J Phys Chem B 110: 936–941
32. Zhu L, Susac D, Teo M, Wong KC, Wong PC, Parsons RR, Bizzotto D, Mitchell KAR, Campbell SA (2008) Investigation of $CoS_2$-based thin films as model catalysts for the oxygen reduction reaction. J Catal 258: 235–242
33. Susac D, Sode A, Zhu L, Wong PC, Teo M, Bizzotto D, Mitchell KAR, Parsons RR, Campbell SA (2006) A methodology for investigating new nonprecious metal catalysts for PEM fuel cells. J Phys Chem B 110: 10762–10770
34. Lee K, Zhang L, Zhang J (2007) Ternary non-noble metal chalcogenide (W–Co–Se) as electrocatalyst for oxygen reduction reaction. Electrochem Commun 9: 1704–1708
35. Mc Nicol BD (1981) Electrocatalytic problems associated with the development of direct methanol-air fuel cells. J Electroanal Chem 118: 71–87
36. Wasmus S, Küver A (1999) Methanol oxidation and direct methanol fuel cells: a selective review. J Electroanal Chem 461: 14–31
37. Lasch K, Hayn G, Jörissen L, Garche J, Besenhardt O (2002) Mixed conducting catalyst support materials for the direct methanol fuel cell. J Power Sources 105: 305–310
38. Petrii OA (2008) Pt–Ru electrocatalysts for fuel cells: a representative review. J Solid State Electrochem 12: 609–642
39. Castro RJ, Cabrera CR (1997) Photovoltammetry and surface analysis of $MoSe_2$ thin films prepared by an intercalation-exfoliation method. J Electrochem Soc 144: 3135–3140
40. Bolivar H, Izquierdo S, Tremont R, Cabrera CR (2003) Methanol oxidation at $Pt/MoO_x$/$MoSe_2$ thin film electrodes prepared with exfoliated $MoSe_2$. J Appl Electrochem 33: 1191–1198
41. Gochi-Ponce Y, Alonso-Nuñez G, Alonso-Vante N (2006) Synthesis and electrochemical characterization of a novel platinum chalcogenide electrocatalyst with an enhanced tolerance to methanol in the oxygen reduction reaction. Electrochem Commun 8: 1487–1491
42. Grinberg VA, Pasynskii AA, Kulova TL, Maiorova NA, Skundin AM, Khazova OA, Law CG (2008) Tolerant-to-methanol cathodic electrocatalysts based on organometallic clusters. Russ J Electrochem 44: 187–197
43. Reeve RW, Christensen PA, Dickinson AJ, Hamnett A, Scott K (2000) Methanol-tolerant oxygen reduction catalysts based on transition metal sulfides and their application to the study of methanol permeation. Electrochim Acta 45: 4237–4250
44. Christenn C, Steinhilber G, Schulze M, Friedrich KA (2007) Physical and electrochemical characterization of catalysts for oxygen reduction in fuel cells. J Appl Electrochem 37: 1463–1474
45. Gullá AF, Gancs L, Allen RJ, Mukerjee S (2007) Carbon-supported low-loading rhodium sulfide electrocatalysts for oxygen depolarized cathode applications. Appl Catal A 326: 227–235
46. Ziegelbauer JM, Gullá AF, O' Laoire C, Urgeghe C, Allen RJ, Mukerjee S (2007) Chalcogenide electrocatalysts for oxygen-depolarized aqueous hydrochloric acid electrolysis. Electrochim Acta 52: 6282–6294
47. Maier J (2004) Transport in electroceramics: micro- and nano-structural aspects. J Eur Ceram Soc 24: 1251–1257
48. Lerf A (2004) Different modes and consequences of electron transfer in intercalation compounds. J Phys Chem Sol 65: 553–563
49. Whittingham MS (1974) Electrointercalation in transition-metal disulphides. J Chem Soc Chem Commun 9: 328–329
50. Schöllhorn R, Meyer H (1974) Cathodic reduction of layered transition metal chalcogenides. Mater Res Bull 9: 1237–1245

51. Subba Rao GV, Tsang JC (1974) Electrolysis method of intercalation of layered transition metal dichalcogenides. Mater Res Bull 9: 921–926
52. Whittingham MS (1979) Intercalation chemistry and energy storage. J Solid State Chem 29: 303–310
53. Whittingham MS (1978) Chemistry of intercalation compounds. Prog Solid State Chem 12: 41–99
54. Lavela P, Conrad M, Mrotzek A, Harbrecht B, Tirado JL (1999) Electrochemical lithium and sodium intercalation into the tantalum-rich layered chalcogenides $Ta_2Se$ and $Ta_2Te_3$. J Alloy Compd 282: 93–100
55. Hernán L, Morales J, Sánchez L, Tirado JL (1993) Kinetics of intercalation of Lithium and Sodium into $(PbS)_{1.14}(NbS_2)_2$. Chem Mater 5: 1167–1173
56. Lavela P, Morales J, Sánchez L, Tirado JL (1997) Novel layered chalcogenides as electrode materials for lithium-ion batteries. J Power Sources 68: 704–707
57. Balkanski M, Kambas K, Julien C, Hammerberg J, Schleich D (1981) Optical and transport measurements on Lithium intercalated $\alpha$-$In_2Se_3$ layered compounds. Solid State Ionics 5: 387–390
58. Julien C, Hatzikraniotis E, Chevy A, Kambas K (1985) Electrical behavior of Lithium intercalated layered In-Se compounds. Mater Res Bull 20: 287–292
59. Boulanger C, Lequir JM (1988) Molybdenum cluster chalcogenide electrochemistry–III. Study of cadmium insertion into the host-lattices $Mo_yX_z$. Electrochim Acta 33: 1573–1579
60. Amatucci GG, Badway F, Singhal A, Beaudoin B, Skandan G, Bowmer T, Plitz I, Pereira N, Chapman T, Jaworski R (2001) Investigation of Yttrium and polyvalent ion intercalation into nanocrystalline Vanadium Oxide. J Electrochem Soc 4148: A940–A950
61. Tributsch H (1980) Photo-intercalation: Possible application in solar energy devices. Appl Phys 23: 61–71
62. Tributsch H (1983) Photo-electrochemical studies on intercalation and semiconducting intercalation compounds. Solid State Ionics 9–10: 41–58
63. Takamura T (2002) Trends in advanced batteries and key materials in the new century. Solid State Ionics 152–153: 19–34
64. Thackery MM (1999) Materials for alkali metal batteries. In: Besenhard JO (ed) Handbook of battery materials. Wiley-VCH, New York
65. Patil A, Patil V, Shin DW, Choi JW, Paik DS, Yoon SJ (2008) Issue and challenges facing rechargeable thin film lithium batteries. Mater Res Bull 43: 1913–1942
66. Jones SD, Akridge JR (1996) A microfabricated solid-state secondary Li battery. Solid State Ionics 86–88: 1291–1294
67. Souquet JL, Duclot M (2002) Thin film lithium batteries. Solid State Ionics 148: 375–379
68. Whittingham MS (2004) Lithium batteries and cathode materials. Chem Rev 104: 4271–4301
69. Kanehori K, Matsumoto K, Miyauchi K, Kudo T (1983) Thin film solid electrolyte and its application to secondary Lithium cell. Solid State Ionics 9–10: 1445–1448
70. Py MA, Haering RR (1983) Structural destabilization induced by lithium intercalation in $MoS_2$ and related compounds. Can J Phys 61: 76–84
71. Murphy DW, Trumbore FA (1976) The Chemistry of $TiS_3$ and $NbSe_3$ cathodes. J Electrochem Soc 123: 960–964
72. Brec R, Ouvrard G, Rouxel J (1985) Relationship between structure parameters and chemical properties in some $MPS_3$ layered phases. Mater Res Bul 20: 1257–1263
73. Miki Y, Nakazato D, Ikuta H, Uchida T, Wakihara M (1995) Amorphous $MoS_2$ as the cathode of lithium secondary batteries. J Power Sources 54: 508–510
74. Jacobson AJ, Chianelli RR, Rich SM, Whittingham MS (1979) Amorphous molybdenum trisulfide: A new Lithium battery cathode. Mat Res Bull 14: 1437–1448
75. Meunier G, Dormoy R, Levasseur A (1989) New positive-electrode materials for Lithium thin film secondary batteries. Mater Sci Eng B 3: 19–23

76. Gonbeau D, Guimon C, Pfister-Guillouzo G, Levasseur A, Meunier G, Dormoy R (1991) XPS study of thin films of titanium oxysulfides. Surface Sci 254: 81–89

77. Schmidt E, Meunier G, Levasseur A (1995) Electrochemical properties of new amorphous molybdenum oxysulfide thin films. Solid State Ionics 76: 243–247

78. Yufit V, Nathan M, Golodnitsky D, Peled E (2003) Thin-film lithium and lithium-ion batteries with electrochemically deposited molybdenum oxysulfide cathodes. J Power Sources 122: 169–173

79. Shembel EM, Apostolova RD, Tysyachnyi VP, Kirsanova IV (2005) Thin-layer electrolytic molybdenum oxidisulfides for cathodes of Lithium batteries. Russ J Electrochem 41: 1305–1315

80. Martin-Litas I, Vinatier P, Levasseur A, Dupin JC, Gonbeau D (2001) Promising thin films ($WO_{1.05}S_2$ and $WO_{1.35}S_{2.2}$) as positive electrode materials in microbatteries. J Power Sources 97–98: 545–547

81. Aurbach D, Lu Z, Schechter A, Gofer Y, Gizbar H, Turgeman R, Cohen Y, Moshkovich M, Levi E (2000) Prototype systems for rechargeable magnesium batteries. Nature 407: 724–727

82. Lancry E, Levi E, Gofer Y, Levi MD, Aurbach D (2005) The effect of milling on the performance of a $Mo_6S_8$ Chevrel phase as a cathode material for rechargeable Mg batteries. J Solid State Electrochem 9: 259–266

83. Levi E, Lancry E, Gofer Y, Aurbach D (2006) The crystal structure of the inorganic surface films formed on Mg and Li intercalation compounds and the electrode performance. J Solid State Electrochem (2006) 10: 176–184

84. Petr N, Klaus M, Santhanam KSV, Otto H (1997) Electrochemically active polymers for rechargeable batteries. Chem Rev 97: 207–282

85. Kolosnitsyn VS, Karaseva EV (2008) Lithium–Sulfur batteries: Problems and solutions. Russ J Electrochem 44: 506–509

86. Vissers DR, Tomczuk Z, Steunenberg RK (1974) A preliminary investigation of high temperature Lithium/Iron Sulfide secondary cells. J Electrochem Soc 121: 665–667

87. Raleigh DO, White JT, Ogden CA (1979) Anodic corrosion rate measurements in LiCl-KCl eutectic. I. Electrochemical considerations. J Electrochem Soc 126: 1087–1093

88. Kaun TD, Nelson PA, Redey L, Vissers DR, Henriksen GL (1993) High temperature Lithium/Sulfide batteries. Electrochim Acta 38: 1269–1287

89. Marmorstein D, Yu TH, Striebel KA, McLarnon FR, Hou J, Carins EJ (2000) Electrochemical performance of lithium-sulfur cells with three different polymer electrolytes. J Power Sources 89: 219–226

90. Yuan LX, Feng JK, Ai XP, Cao YL, Chen SL, Yang HX (2006) Improved dischargeability and reversibility of sulfur cathode in a novel ionic liquid electrolyte. Electrochem Commun 8: 610–614

91. Tsipis EV, Kharton VV (2008) Electrode materials and reaction mechanisms in solid oxide fuel cells: A brief review; I. Performance-determining factors. J Solid State Electrochem 12: 1039–1060; II. Electrochemical behavior vs. materials science aspects. *ibid*: 1367–1391

92. Chen H, Cong TN, Yang W, Tan C, Li Y, Ding Y (2009) Progress in electrical energy storage system: A critical review. Prog Nat Sci 19: 291–312

93. Abraham KM, Jiang Z (1997) PEO-like polymer electrolytes with high room temperature conductivity. J Electrochem Soc 144: L136–L138

94. Park CW, Ahn JH, Ryu HS, Kim KW, Ahn HJ (2006) Room-temperature solid-state Sodium/Sulfur battery. Electrochem Solid State Lett 9: A123–A125

95. Park CW, Ryu HS, Kim KW, Ahn JH, Lee JY, Ahn HJ (2007) Discharge properties of all-solid sodium–sulfur battery using poly (ethylene oxide) electrolyte. J Power Sources 165: 450–454

96. Wang J, Yang J, Nuli Y, Holze R (2007) Room temperature Na/S batteries with sulfur composite cathode materials. Electrochem Commun 9: 31–34

97. Kim JS, Kim DY, Cho GB, Nam TH, Kim KW, Ryu HS, Ahn JH, Ahn HJ (2009) The electrochemical properties of copper sulfide as cathode material for rechargeable sodium cell at room temperature. J Power Sources 189: 864–868

98. Kim JS, Ahn HJ, Ryu HS, Kim DJ, Cho GB, Kim KW, Nam TH, Ahn JH (2008) The discharge properties of Na/Ni$_3$S$_2$ cell at ambient temperature. J Power Sources 178: 852–856

99. Cairns EJ, Shimotake H (1969) High-temperature batteries. Science 164: 1347–1355

100. Kennedy JH (1977) Thin film solid electrolyte systems. Thin Solid Films 43: 41–92

101. Linford RG (1988) Applications of solid state ionics for batteries. Solid State Ionics 28–30: 831–840

102. Takahashi T, Yamamoto O (1970) Solid ionics–solid electrolyte cells. J Electrochem Soc 4117: 1–5

103. Takahashi T, Yamamoto O (1971) Solid-state ionics—coulometric titrations and measurements of the ionic conductivity of beta Ag$_2$Se and beta Ag$_2$Te and use of these compounds in an electrochemical analog memory element. J Electrochem Soc 118: 1051–1057

104. Guo WX, Shua D, Chen HY, Li AJ, Wang H, Xiao GM, Dou CL, Peng SG, Wei WW, Zhang W, Zhou HW, Chen S (2008) Study on the structure and property of lead tellurium alloy as the positive grid of lead-acid batteries. J Alloy Compd 475: 102–109

105. Guidotti RA, Masset P (2006) Thermally activated ("thermal") battery technology: Part I: An overview. J Power Sources 161: 1443–1449

106. Masset P, Guidotti RA (2008) Thermal activated ("thermal") battery technology Part IIIa: FeS$_2$ cathode material. J Power Sources 177: 595–609

107. Masset P, Guidotti RA (2008) Thermal activated ("thermal") battery technology Part IIIb. Sulfur and oxide-based cathode materials. J Power Sources 178: 456–466

108. Janata J (1992) Chemical sensors. Anal Chem 64: 196–219

109. Bakker E, Telting-Diaz M (2002) Electrochemical sensors. Anal Chem 74: 2781–2800

110. Bakker E (2004) Electrochemical sensors. Anal Chem 76: 3285–3298

111. Bakker E, Qin Y (2006) Electrochemical sensors. Anal Chem 78: 3965–3983

112. Pejcic B, De Marco R (2006) Impedance spectroscopy: Over 35 years of electrochemical sensor optimization. Electrochim Acta 51: 6217–6229

113. Bobacka J, Ivaska A, Lewenstam A (2008) Potentiometric ion sensors. Chem Rev 108: 329–351

114. Pungor E (1998) The theory of Ion Selective Electrodes. Anal Sci 14: 249–256

115. Bakker E, Bühlmann P, Pretsch E (2004) The phase-boundary potential model. Talanta 63: 3–20

116. Lawrence NS, Davis J, Compton RG (2000) Analytical strategies for the detection of sulfide: A review. Talanta 52: 771–784

117. Zirino A, Belli SL, Van der Weele DA (1998) Copper concentration and cull activity in San Diego Bay. Electroanalysis 10: 423–427

118. De Marco R, Mackey DJ, Zirino A (1997) Response of the jalpaite membrane copper(II) ion-selective electrode in marine waters. Electroanalysis 9: 330–334

119. Kozicki MN, Mitkova M (2006) Mass transport in chalcogenide electrolyte films – materials and applications. J Non-Cryst Solids 352: 567–577

120. Baker CT, Trachtenberg I (1971) Ion Selective Electrochemical Sensors–Fe$^{3+}$, Cu$^{2+}$. J Electrochem Soc 118: 571–576

121. Jasinski R, Trachtenberg I (1973) Evaluation of the ferric ion sensitive chalcogenide glass electrode. J Electrochem Soc 120: 1169–1174

122. Jasinski R, Trachtenberg I, Rice G (1974) A chalcogenide glass electrode sensitive to cupric ions. J Electrochem Soc 121: 363–370

123. Vlasov YG, Bychkov EA, Legin AV (1994) Chalcogenide glass chemical sensors: Research and analytical applications. Talanta 41: 1059–1063

124. Vassilev V, Karadashka I, Parvanov S (2008) New chalcogenide glasses in the Ag$_2$Te–As$_2$Se$_3$–CdTe system. J Phys Chem Solids 69: 1835–1840

125. Vassilev V, Tomova K, Parvanova V, Parvanov S (2007) New chalcogenide glasses in the $GeSe_2$–$Sb_2Se_3$–PbSe system. Mater Chem Phys 103: 312–317

126. Vassilev V, Tomova K, Parvanova V (2009) The glass-forming region in the system $GeSe_2$–PbSe–PbTe. Mater Chem Phys 114: 874–878

127. Vlasov YG, Bychkov EA (1989) Sodium ion-selective chalcogenide glass electrodes. Anal Lett 22: 1125–1144

128. Vassilev VS, Boycheva SV (2005) Chemical sensors with chalcogenide glassy membranes. Talanta 67: 20–27

129. Schubert J, Schöning MJ, Schmidt C, Siegert M, Mesters St, Zander W, Kordos P, Lüth H, Legin A, Mourzina YG, Seleznev B, Vlasov YG (1999) Chalcogenide-based thin film sensors prepared by pulsed laser deposition technique. Appl Phys A Mater Sci Process 69: 803–805

130. Mourzina YG, Schubert J, Zander W, Legin A, Vlasov YG, Schöning MJ (2001) Development of multisensor systems based on chalcogenide thin film chemical sensors for the simultaneous multicomponent analysis of metal ions in complex solutions. Electrochim Acta 47: 251–258

131. Legin AV, Vlasov YG, Rudnitskaya AM, Bychkov EA (1996) Cross-sensitivity of chalcogenide glass sensors in solutions of heavy metal ions. Sens Actuators B 34: 456–461

132. De Marco R, Shackleton J (1999) Calibration of the Hg chalcogenide glass membrane ion-selective electrode in seawater media. Talanta 49: 385–391

133. De Marco R, Pejcic B, Prince K, van Riessen A (2003) A multi-technique surface study of the mercury(II) chalcogenide ion-selective electrode in saline media. Analyst 128: 742–749

134. Pejcic B, De Marco R (2004) Characterization of an $AgBr$-$Ag_2S$-$As_2S_3$-$HgI_2$ion-selective electrode membrane: a X-ray photoelectron and impedance spectroscopy approach. Appl Surf Sci 228: 378–400

135. De Marco R, Mackey DJ (2000) Calibration of a chalcogenide glass membrane ion-selective electrode for the determination of free $Fe^{3+}$ in seawater: I. Measurements in UV photooxidised seawater. Mar Chem 68: 283–294

136. Van den Berg CMG (2000) Mar Chem 71: 331–332

137. D' Orazio P (2003) Biosensors in clinical chemistry. Clin Chim Acta 334: 41–69

138. Warsinke A, Benkert A, Scheller FW (2000) Electrochemical immunoassays. Fresenius J Anal Chem 366: 622–634

139. Guilbault GG, Pravda M, Kreuzer M, O'Sullivan CK (2004) Biosensors – 42 Years and Counting. Anal Lett 37: 1481–1496

140. Guilbault GG, Montalvo J (1969) Urea specific enzyme electrode. J Am Chem Soc 91: 2164–2165

141. Di Gleria K, Hill HAO, McNeil CJ, Green MJ (1986) Homogeneous ferrocene mediated amperometric biosensors. Anal Chem 58: 1203–1205

142. Katz E, Willner I, Wang J (2004) Electroanalytical and bioelectroanalytical systems based on metal and semiconductor nanoparticles. Electroanalysis 16: 19–44

143. Pardo-Yissar V, Katz E, Wasserman J, Willner I (2003) Acetylcholine esterase-labeled CdS nanoparticles on electrodes: Photoelectrochemical sensing of the enzyme inhibitors. J Am Chem Soc 125: 622–623

144. Curri ML, Agostiano A, Leo G, Mallardi A, Cosma P, Monica MD (2002) Development of a novel enzyme/semiconductor nanoparticles system for biosensor application. Mater Sci Eng C 22: 449–452

145. Wang J (2003) Nanoparticle-based electrochemical DNA detection. Anal Chim Acta 500: 247–257

146. Willner I, Patolsky F, Wasserman J (2001) Photoelectrochemistry with controlled DNA-cross-linked CdS nanoparticle arrays. Angew Chem Int Ed 40: 1861–1864

147. Wang J, Liu G, Polsky R, Merkoçi A (2002) Electrochemical stripping detection of DNA hybridization based on cadmium sulfide nanoparticle tags. Electrochem Commun 4: 722–726

148. Wang J, Liu G, Merkoçi A (2003) Electrochemical coding technology for simultaneous detection of multiple DNA targets. J Am Chem Soc 125: 3214–3215
149. Poznyak SK, Talapin DV, Shevchenko EV, Weller H (2004) Quantum dot chemiluminescence. Nano Lett 4: 693–698
150. Zou G, Ju H (2004) Electrogenerated chemiluminescence from a CdSe nanocrystal film and its sensing application in aqueous solution. Anal Chem 76: 6871–6876
151. Ren T, Xu JZ, Tu YF, Xu S, Zhu JJ, Chen HY (2005) Electrogenerated chemiluminescence of CdS spherical assemblies. Electrochem Commun 7: 5–9
152. Jie GF, Liu B, Pan HC, Zhu JJ, Chen HY (2007) CdS nanocrystal-based electrochemiluminescence biosensor for the detection of low-density lipoprotein by increasing sensitivity with gold nanoparticle amplification. Anal Chem 79: 5574–5581
153. Fang YM, Sun JJ, Wu AH, Su XL, Chen GN (2009) Catalytic electrogenerated chemiluminescence and nitrate reduction at CdS nanotubes modified glassy carbon electrode. Langmuir 25: 555–560

# About the Editor



Fritz Scholz is a professor at the University of Greifswald in Germany. Following studies in chemistry at Humboldt University, Berlin, he obtained a Dr. rer. nat. and a Dr. sc. nat. (habilitation) from that same university. In 1987 and 1989, he worked with Alan Bond in Australia. His main interest is in electrochemistry and electroanalysis. He has published more than 250 scientific papers, and he is editor and co-author of the book "Electroanalytical Methods" (Springer 2002 and 2005; Russian Edition, BINOM 2006), co-author of the book "Electrochemistry of Immobilized Particles and Droplets" (Springer 2005), co-editor of the "Electrochemical Dictionary" (Springer 2008), and co-editor of volumes 7a and 7b of the "Encyclopedia of Electrochemistry" (Wiley-VCH 2006). In 1997, he founded the *Journal of Solid State Electrochemistry* (Springer) and has served as Editor-in-Chief since then. He served as editor of the series "Monographs in Electrochemistry" (Springer), in which modern topics of electrochemistry are presented. Scholz introduced the technique "Voltammetry of Immobilized Microparticles" for studying the electrochemistry of solid compounds and materials, and he introduced the concept of threephase electrodes to determine the Gibbs energies of ion transfer between immiscible liquids.

# About the Author



Mirtat Bouroushian received a PhD for the electrodeposition and characterization of binary and ternary selenides and tellurides, from the National Technical University of Athens (NTUA; Greece, 1998). He is currently Assistant Professor of Solid State Chemistry in the Chemical Engineering School of NTUA. His research activities apply on the electrosynthesis and photoelectrochemistry of semiconductors and the electrodeposition and characterization of metal–matrix composites. He is focused presently on the investigation of electrochemical nucleation/growth phenomena and interface charge transfer kinetics in connection with the photo-sensitization of porous titania electrodes by chalcogenide semiconductors. He has published several papers on the electrochemistry of II–VI chalcogenides and has participated in European and Greek research and educational projects. He is the author of a university textbook on *solid-state chemistry* and co-author of a *general chemistry* textbook for secondary school, as well as scientific articles for the public.

# Index